frontiers | Research Topics

Cerebrovascular imaging — from micro- to macroscopic scales

Edited by
Chengcheng Zhu, Danny J. J. Wang, Mickael Tanter, Zhaoyang Fan, Song Hu and Umar Sadat

Published in
Frontiers in Neuroscience
Frontiers in Neurology

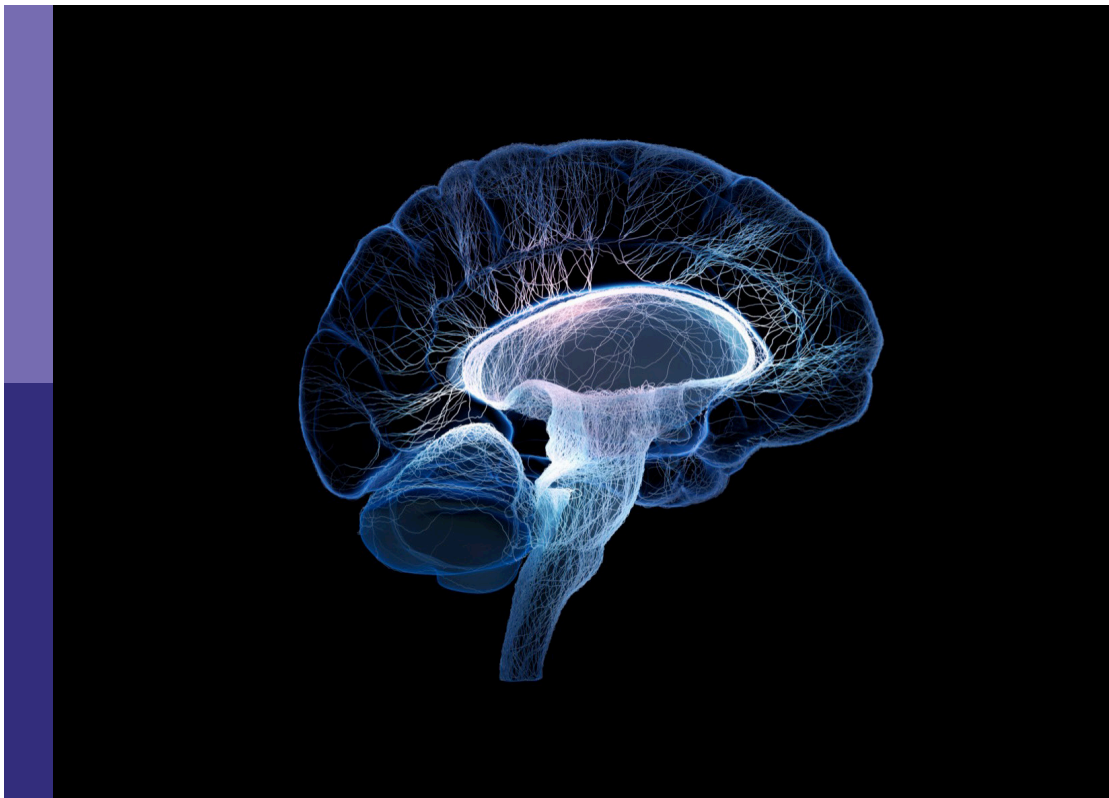

ISSN 1664-8714
ISBN 978-2-83250-949-4
DOI 10.3389/978-2-83250-949-4

About Frontiers

Frontiers is more than just an open access publisher of scholarly articles: it is a pioneering approach to the world of academia, radically improving the way scholarly research is managed. The grand vision of Frontiers is a world where all people have an equal opportunity to seek, share and generate knowledge. Frontiers provides immediate and permanent online open access to all its publications, but this alone is not enough to realize our grand goals.

Frontiers journal series

The Frontiers journal series is a multi-tier and interdisciplinary set of open-access, online journals, promising a paradigm shift from the current review, selection and dissemination processes in academic publishing. All Frontiers journals are driven by researchers for researchers; therefore, they constitute a service to the scholarly community. At the same time, the *Frontiers journal series* operates on a revolutionary invention, the tiered publishing system, initially addressing specific communities of scholars, and gradually climbing up to broader public understanding, thus serving the interests of the lay society, too.

Dedication to quality

Each Frontiers article is a landmark of the highest quality, thanks to genuinely collaborative interactions between authors and review editors, who include some of the world's best academicians. Research must be certified by peers before entering a stream of knowledge that may eventually reach the public - and shape society; therefore, Frontiers only applies the most rigorous and unbiased reviews. Frontiers revolutionizes research publishing by freely delivering the most outstanding research, evaluated with no bias from both the academic and social point of view. By applying the most advanced information technologies, Frontiers is catapulting scholarly publishing into a new generation.

What are Frontiers Research Topics?

Frontiers Research Topics are very popular trademarks of the *Frontiers journals series*: they are collections of at least ten articles, all centered on a particular subject. With their unique mix of varied contributions from Original Research to Review Articles, Frontiers Research Topics unify the most influential researchers, the latest key findings and historical advances in a hot research area.

Find out more on how to host your own Frontiers Research Topic or contribute to one as an author by contacting the Frontiers editorial office: frontiersin.org/about/contact

Cerebrovascular imaging — from micro- to macroscopic scales

Topic editors

Chengcheng Zhu — University of Washington, United States
Danny J. J. Wang — University of Southern California, United States
Mickael Tanter — Institut National de la Santé et de la Recherche Médicale - INSERM
Zhaoyang Fan — University of Southern California, United States
Song Hu — Washington University in St. Louis, United States
Umar Sadat — University of Cambridge, United Kingdom

Citation

Zhu, C., Wang, D. J. J., Tanter, M., Fan, Z., Hu, S., Sadat, U., eds. (2022). *Cerebrovascular imaging — from micro- to macroscopic scales*. Lausanne: Frontiers Media SA. doi: 10.3389/978-2-83250-949-4

Table of contents

frontiers | Frontiers in Neuroscience

TYPE Editorial
PUBLISHED 22 November 2022
DOI 10.3389/fnins.2022.1086022

OPEN ACCESS

EDITED AND REVIEWED BY
Wei Jin,
Shanghai Jiao Tong University, China

*CORRESPONDENCE
Chengcheng Zhu
zhucheng@uw.edu

SPECIALTY SECTION
This article was submitted to Brain Imaging Methods, a section of the journal Frontiers in Neuroscience

RECEIVED 31 October 2022
ACCEPTED 14 November 2022
PUBLISHED 22 November 2022

CITATION
Zhu C, Tanter M, Fan Z, Hu S, Sadat U and Wang DJJ (2022) Editorial: Cerebrovascular imaging—From micro- to macroscopic scales. *Front. Neurosci.* 16:1086022. doi: 10.3389/fnins.2022.1086022

Editorial: Cerebrovascular imaging—From micro- to macroscopic scales

Chengcheng Zhu[1]*, Mickael Tanter[2], Zhaoyang Fan[3], Song Hu[4], Umar Sadat[5] and Danny J. J. Wang[6]

[1]Department of Radiology, University of Washington, Seattle, WA, United States, [2]INSERM U1273 Physics for Medicine Paris (ESPCI), Paris, France, [3]Department of Radiology, University of Southern California, Los Angeles, CA, United States, [4]McKelvey School of Engineering, Washington University in St. Louis, St. Louis, MO, United States, [5]Department of Surgery, University of Cambridge, Cambridge, United Kingdom, [6]Department of Neurology, University of Southern California, Los Angeles, CA, United States

KEYWORDS

stroke, vessel wall imaging, MRI, perfusion, atherosclerosis, aneurysm

Editorial on the Research Topic
Cerebrovascular imaging—From micro- to macroscopic scales

Neurovascular diseases, including stroke, atherosclerosis, aneurysm, cerebral small vessel disease (cSVD), vascular cognitive impairment and dementia (VCID), and others, are major causes of death and disabilities. The prevalence of these neurovascular diseases has been steadily increasing due to the global population aging. During the past few decades, the technical advances of medical imaging methods, including MRI, CT, PET, optical and ultrasound (US) imaging, as well as photoacoustic imaging, have given the opportunities to image the neurovascular system in great details from micro to macro scales, from the capillaries (<10 um), arterioles/venules (~100 um) to large vessels (mm) including lumen, vessel wall and perivascular space.

Vessel wall imaging

While most of the vascular imaging methods focus on the flowing lumen, vessel wall MRI provides the ability to directly visualize the vessel wall, which is the source of pathology in atherosclerotic plaques, aneurysms and other vasculopathy. Most vessel MRI studies were performed at 3 Tesla due to its high signal to noise ratio (SNR) compared to 1.5 Tesla, and the use of ultra-high field 7 Tesla MRI scanners further increase the ability (Zhu et al., 2016; Rutland et al., 2020).

In this Research Topic collection, Zhang L. et al. developed a T2 prepared inversion recovery (IR) MRI sequence (T2IR-SPACE) which markedly suppressed the Cerebrospinal Fluid (CSF) signal without much SNR loss of the other tissues (i.e., vessel wall, white matter, and gray matter). Such sequence can be used in multi-contrast intracranial vessel wall imaging to achieve good CSF suppression and improve the vessel wall contrast. Kong et al. developed 3D inner-volume (IV) TSE (SPACE) sequence with optimized 2D spatially selective excitation (SSE) radio frequency (RF)

pulses, and they achieved the highest resolution (0.3 mm isotropic) *in vivo* vessel wall MRI so far by using a 7T scanner. They found clearer delineation of lenticulostriate artery (LSA) than conventional SPACE images.

Xu et al. developed automatic segmentation methods for carotid and intracranial plaques on vessel wall MRI in 124 patients using machine learning. Their method demonstrated satisfactory agreement with the manual method, with dice values of 93.8% for lumen contours and 86.0% for outer wall contours, which were higher than those obtained from the traditional U-Net, Attention U-Net, and Inception U-Net. Lindenholz et al. found an interrelationship between large vessel wall lesion burden and cerebral parenchymal manifestations often linked to small vessel disease (SVD). Li J. et al. studied 68 patients with vertebrobasilar atherosclerosis using vessel wall MRI, and found the vertebrobasilar junction (VBJ) angle over 90° might aggravate the vessel wall condition of the atherosclerotic vertebrobasilar arteries, which might serve as a potential risk factor for vertebrobasilar atherosclerosis.

Eisenmenger et al. presented 9 cases of arteriovenous malformation (AVM) and found Vessel wall "enhancement" occurs in AVMs with no prior clinical rupture. Xiao et al. presented a case of intracranial plaque with serial vessel wall MRI follow up and they found vessel wall MRI can directly visualize the morphology and signal change of plaques. The suggest early identification of patients who do not respond well to medication is critical to prevent the recurrence of cardiovascular events in these patients.

Perfusion

Perfusion imaging plays an important role in the management of patients with neurovascular diseases. Jann et al. applied 3D pseudo-continuous arterial spin labeling (pCASL) MRI in the cohort of elderly Latinx subjects and found cerebral blood flow (CBF) in the leptomeningeal and perforator middle cerebral artery (MCA) territories were the most likely candidate biomarker of Vascular Cognitive Impairment and Dementia (VCID). Shi et al. compared several software for CT perfusion measurements and found F-STROKE software had excellent agreement with the widely used analysis tool of RAPID in measuring ischemic core volume (ICV) and penumbra volume (PV). Shou et al. developed super-resolution perfusion imaging and achieved high spatial resolution (isotropic-2 mm) using 2D simultaneous multi-slice (SMS) pseudo-continuous arterial spin labeling (pCASL) and slice dithered enhanced resolution (SLIDER) technique. de Bortoli et al. used T2*-weighted imaging and ultra-small superparamagnetic iron oxide nanoparticles to obtain subtraction angiographies and steady-state cerebral blood volume (ss-CBV) maps. They found the maps agreed well with first pass dynamic susceptibility contrast MRI (DSC-MRI). They concluded that iron oxide nanoparticle-based ss-CBV could serve as a robust, non-invasive imaging surrogate marker for neocortical vessels, with the potential to reduce and refine preclinical models targeting the development and outgrowth of cerebral collateralization.

Hemodynamics

Hemodynamics plays important roles in the development and progression of vascular diseases. The hemodynamics information could be either computed using computational fluid dynamics (CFD) by using image-derived geometry or directly acquired by flow imaging. Zhai et al. performed CFD analysis in 20 unruptured and 12 ruptured pericallosal artery aneurysms (PAA) with 3D digital subtraction angiography (DSA), and found a high mean oscillatory shear index (OSI) was an independent risk factor for PAA rupture. Zhang G. et al. studied the Hemodynamics using 4D flow MRI and found increased WSS, especially during the diastolic period and in the axial direction, may be a signal of a high-risk plaque and may cause cerebrovascular events in patients with moderate carotid artery stenosis.

Deeping learning in neurovascular imaging

Zhu et al. studied a total of 632 patients with 668 MCA aneurysms (423 ruptured aneurysms) from five hospitals and quantified their radiomics and morphological features from computed tomography angiography images. They concluded integrating radiomics features into conventional models might provide additional value in ruptured MCA aneurysms classification. Shou et al. applied deep learning methods in perfusion imaging, and Xu et al. applied deep learning in vessel wall imaging.

Other research

Bretzner et al. analyzed a multi-site cohort of 4,163 acute ischemic strokes (AIS) patients with T2-FLAIR MR images with total brain and white matter hyperintensity (WMH) segmentations. They found Radiomics extracted from T2-FLAIR images of AIS patients capture microstructural damage of the cerebral parenchyma and correlate with clinical phenotypes, suggesting different radiographical textural abnormalities per cardiovascular risk profile. Li T. et al. found high-resolution flat-detector computed tomography (HR-FDCT) improves visualization of the fine structures of intracranial stents deployed for symptomatic intracranial atherosclerotic stenosis (ICAS) compared with

that visualized using conventional flat-detector computed tomography (FDCT). The concluded HR-FDCT improves assessment of stent deployment and could reduce the risk of complications. Du et al. reviewed the histological and imaging features of intimal and medial calcification within the large intracranial arteries and highlighted its clinical relevance.

Future direction

Vessel wall imaging is a hot topic with increasing research and clinical translation interests (Mossa-Basha et al., 2022) in the past decade and we include seven articles in this Research Topic. However, most of current studies were cross-sectional with limited sample sizes. Future larger scale longitudinal studies and randomized controlled trails are needed to establish vessel wall imaging markers to predict patients' outcome (Zhu and Mossa-Basha, 2021). Perfusion imaging with noninvasive ASL techniques continues to grow and translate into clinical use. Hemodynamic conditions in neurovascular disease have been studied for several decades but the clinical utility still need larger scale study to prove. Recent advances in 4D flow imaging with higher resolution and shorter scan time may facilitate its clinical translation. Deep learning is another hot topic in neurovascular imaging recently and it has great potential for image acceleration, reconstruction and automating image analysis.

Author contributions

All authors listed have made a substantial, direct, and intellectual contribution to the work and approved it for publication.

Funding

CZ was supported by US National Institute of Health (NIH) grants R01HL162743 and R00HL136883. ZF was supported by NIH grant R01HL147355.

Conflict of interest

The authors declare that the research was conducted in the absence of any commercial or financial relationships that could be construed as a potential conflict of interest.

Publisher's note

All claims expressed in this article are solely those of the authors and do not necessarily represent those of their affiliated organizations, or those of the publisher, the editors and the reviewers. Any product that may be evaluated in this article, or claim that may be made by its manufacturer, is not guaranteed or endorsed by the publisher.

References

Mossa-Basha, M., Zhu, C., Yuan, C., Saba, L., Saloner, D. A., Edjlali, M., et al. (2022). Survey of the American society of neuroradiology membership on the use and value of intracranial vessel wall MRI. *AJNR Am. J. Neuroradiol.* 43, 951–957. doi: 10.3174/ajnr.A7541

Rutland, J. W., Delman, B. N., Gill, C. M., Zhu, C., Shrivastava, R. K., Balchandani, P., et al. (2020). Emerging use of ultra-high-field 7T MRI in the study of intracranial vascularity: state of the field and future directions. *AJNR Am. J. Neuroradiol.* 41, 2–9. doi: 10.3174/ajnr.A6344

Zhu, C., Haraldsson, H., Tian, B., Meisel, K., Ko, N., Lawton, M., et al. (2016). High resolution imaging of the intracranial vessel wall at 3 and 7 T using 3D fast spin echo MRI. *Magma* 29, 559–570. doi: 10.1007/s10334-016-0531-x

Zhu, C., and Mossa-Basha, M. (2021). Wall enhancement as an emerging marker of intracranial aneurysm stability: roadmap toward a potential target for clinical trials. *Eur. J. Neurol.* 28, 3550–3551. doi: 10.1111/ene.15094

frontiers in Neuroscience

ORIGINAL RESEARCH
published: 27 January 2021
doi: 10.3389/fnins.2021.627627

Evaluation of Cerebral Blood Flow Measured by 3D PCASL as Biomarker of Vascular Cognitive Impairment and Dementia (VCID) in a Cohort of Elderly Latinx Subjects at Risk of Small Vessel Disease

*Kay Jann[1], Xingfeng Shao[1], Samantha J. Ma[1], Steven Y. Cen[2], Lina D'Orazio[2], Giuseppe Barisano[3], Lirong Yan[1], Marlena Casey[1], Jesse Lamas[1], Adam M. Staffaroni[4], Joel H. Kramer[4], John M. Ringman[2] and Danny J. J. Wang[1,2]**

[1] Laboratory of FMRI Technology, USC Mark and Mary Stevens Neuroimaging and Informatics Institute, Keck School of Medicine, University of Southern California, Los Angeles, CA, United States, [2] Department of Neurology, Keck School of Medicine, University of Southern California, Los Angeles, CA, United States, [3] Zilkha Neurogenetic Institute and Department of Physiology and Neuroscience, Keck School of Medicine, University of Southern California, Los Angeles, CA, United States, [4] Department of Neurology, Memory and Aging Center, Weill Institute for Neurosciences, University of California, San Francisco, San Francisco, CA, United States

OPEN ACCESS

Edited by:
Shantanu H. Joshi,
University of California, Los Angeles, United States

Reviewed by:
Jia Guo,
University of California, Riverside, United States
Swati Rane,
University of Washington, United States

***Correspondence:**
Danny J. J. Wang
jwang71@gmail.com

Specialty section:
This article was submitted to Brain Imaging Methods, a section of the journal Frontiers in Neuroscience

Received: 09 November 2020
Accepted: 07 January 2021
Published: 27 January 2021

Citation:
Jann K, Shao X, Ma SJ, Cen SY, D'Orazio L, Barisano G, Yan L, Casey M, Lamas J, Staffaroni AM, Kramer JH, Ringman JM and Wang DJJ (2021) Evaluation of Cerebral Blood Flow Measured by 3D PCASL as Biomarker of Vascular Cognitive Impairment and Dementia (VCID) in a Cohort of Elderly Latinx Subjects at Risk of Small Vessel Disease. Front. Neurosci. 15:627627. doi: 10.3389/fnins.2021.627627

Cerebral small vessel disease (cSVD) affects arterioles, capillaries, and venules and can lead to cognitive impairments and clinical symptomatology of vascular cognitive impairment and dementia (VCID). VCID symptoms are similar to Alzheimer's disease (AD) but the neurophysiologic alterations are less well studied, resulting in no established biomarkers. The purpose of this study was to evaluate cerebral blood flow (CBF) measured by 3D pseudo-continuous arterial spin labeling (pCASL) as a potential biomarker of VCID in a cohort of elderly Latinx subjects at risk of cSVD. Forty-five elderly Latinx subjects (12 males, 69 ± 7 years) underwent repeated MRI scans ∼6 weeks apart. CBF was measured using 3D pCASL in the whole brain, white matter and 4 main vascular territories (leptomeningeal anterior, middle, and posterior cerebral artery (leptoACA, leptoMCA, leptoPCA), as well as MCA perforator). The test-retest repeatability of CBF was assessed by intra-class correlation coefficient (ICC) and within-subject coefficient of variation (wsCV). Absolute and relative CBF was correlated with gross cognitive measures and domain specific assessment of executive and memory function, vascular risks, and Fazekas scores and volumes of white matter hyperintensity (WMH). Neurocognitive evaluations were performed using Montreal Cognitive Assessment (MoCA) and neuropsychological test battery in the Uniform Data Set v3 (UDS3). Good to excellent test-retest repeatability was achieved (ICC = 0.77–0.85, wsCV 3–9%) for CBF measurements in the whole brain, white matter, and 4 vascular territories. Relative CBF normalized by global mean CBF in the leptoMCA territory was positively correlated with the executive function composite score, while relative CBF in the leptoMCA and MCA perforator territory was positively correlated with

MoCA scores, controlling for age, gender, years of education, and testing language. Relative CBF in WM was negatively correlated with WMH volume and MoCA scores, while relative leptoMCA CBF was positively correlated with WMH volume. Reliable 3D pCASL CBF measurements were achieved in the cohort of elderly Latinx subjects. Relative CBF in the leptomeningeal and perforator MCA territories were the most likely candidate biomarker of VCID. These findings need to be replicated in larger cohorts with greater variability of stages of cSVD.

Keywords: arterial spin labeling, item response theory, white matter hyperintensity, cerebral small vessel disease, cerebral blood flow, vascular cognitive impairment and dementia

INTRODUCTION

While Alzheimer's disease (AD) is the most common cause of dementia, the contribution of vascular factors to cognitive impairment and dementia is becoming increasingly recognized (Gorelick et al., 2011). AD and cerebrovascular diseases share common risk factors such as hypertension, obesity, diabetes, and these conditions coexist in 40–50% of clinically diagnosed AD, making mixed AD-vascular dementia the most common cause of cognitive impairment in the aged (Iadecola, 2016). The clinical differentiation of AD from vascular cognitive impairment and dementia (VCID) is blurred (Schneider et al., 2007). Cerebral small vessel disease (cSVD) is the most common vascular cause of dementia, a major contributor to mixed dementia, and the cause of about one fifth of all strokes worldwide (Norrving, 2008; Pantoni, 2010). The aging population worldwide and the increase in vascular disease with age have led to projections of major growth in VCID over the next 30 years (Gorelick et al., 2011). However, the underlying mechanisms of cSVD remain poorly understood, resulting in no specific guidelines for its prevention and treatment.

The large knowledge gap in cSVD is partly because cerebral small vessels, including arterioles, capillaries, and venules, are inaccessible to existing imaging technologies. Clinical diagnosis of SVD relies on conventional MRI findings including lacunar infarcts, white matter hyperintensities (WMH), cerebral microbleeds, prominent perivascular spaces, and atrophy (Wardlaw et al., 2009). Large epidemiological studies have shown that silent cerebral infarction and WMHs are associated with both non-memory-related cognitive deficits (e.g., executive function and perceptual speed) (Mayda and Decarli, 2009; Rosenberg et al., 2015), and memory impairment (Breteler et al., 1994; DeCarli et al., 1995; Debette et al., 2010). Composite scores of MRI features of cSVD have also been proposed (Staals et al., 2015). However, these parenchymal lesions are the consequences of cSVD rather than the surrogate markers of microvascular changes and cannot guide early interventions to change the course of VCID. It is of paramount importance to identify and develop imaging markers of early microvascular changes related to cSVD for the design of future clinical trials to prevent and treat VCID.

Chronic hypoperfusion is thought to be a key mechanism of SVD and cause of WMHs on MRI. Although the etiology is not completely understood, chronic hypoperfusion may result from the narrowing of the arteriolar lumina secondary to lipohyalinosis and arteriolosclerosis (Yata et al., 2014). A recent systematic review and meta-analysis including 24 cross-sectional studies (n = 1161) showed that cerebral blood flow (CBF) is lower in subjects with more WMHs, globally and in most gray and white matter regions (Shi et al., 2016). Arterial spin labeling (ASL) perfusion MRI provides non-invasive quantitative CBF measurement with good test-retest repeatability and has been validated by PET (Kilroy et al., 2014). ASL can be standardized across major MRI platforms with 3D pseudo-continuous ASL (pCASL) (Alsop et al., 2015), which has started to be used in multi-site clinical trials. Therefore, ASL CBF may be applied as a marker of VCID caused by cSVD.

In this study we applied 3D pCASL perfusion MRI to assess the test-retest repeatability of regional CBF for an interval of ∼6 weeks as well as CBF alterations in association with cognitive impairment in a cohort of aged Latinx subjects with varying risks of vascular diseases. Latinx population is the fastest growing segment of the US population who are traditionally underrepresented in clinical research (US Census Bureau, 2016). Latinx population however are at a higher risk for AD and other dementias (Association, 2016), and cerebrovascular disease represents the fourth leading cause of death among Latinx (Heron, 2016). A prominent behavioral phenotype of cSVD is early executive dysfunction manifested by impaired capacity to use complex information, to formulate strategies, and to exercise self-control, with less pronounced episodic memory deficits compared to AD patients (Wallin et al., 2018). Therefore, ASL CBF measurements were correlated with a composite score of executive function developed using Item Response Theory (IRT) (Staffaroni et al., 2020a) and global cognitive measures as well as memory function, vascular risks, and WMHs.

MATERIALS AND METHODS

Human Subjects

Forty-five elderly Latinx subjects (12 males, 69 ± 7 years) participated in the present study as part of the MarkVCID study at the University of Southern California[1]. The inclusion criteria were: (1) Fluency in Spanish and/or English; (2) Age > 60 years; (3) Have capacity for and sign consents indicating so, or

[1]www.markvcid.org

give assent and have an appropriate surrogate (as determined by California law) to sign consent; (4) For demented subjects, have an appropriate informant who is also willing and able to accompany the subject. Non-demented subjects must also have an informant willing to participate by phone. The exclusion criteria included history of prior clinical stroke, head trauma, contraindications to MRI, abnormal renal function, pregnancy, other concurrent neurologic or psychiatric illnesses, or abnormal structural MRI (e.g., mass lesions, cystic infarction, etc.). All subjects were required to refrain from caffeine intake and nicotine use 3 h before and during study visits. The demographic and clinical information of the subjects is listed in **Table 1**.

MRI Experiments

MRI scans were performed on a Siemens 3T Prisma system (Erlangen, Germany) using a 20-channel head coil after subjects provided written informed consent according to a protocol approved by the Institutional Review Board (IRB) of the University of Southern California. Each subject underwent repeated MRI scans ∼6 weeks apart (6.7 ± 4.6 weeks). The MRI protocol included a 3D T1-weighted magnetization-prepared rapid gradient-echo (MPRAGE) scan (1 mm^3 isotropic resolution, TR/TI/TE = 2,530/1,100/1.69 ms), a 3D T2-weighted Fluid-Attenuated Inversion Recovery (FLAIR) scan (1 mm^3 isotropic resolution, TR/TI/TE = 5,000/1,800/388 ms), and a 3D gradient and spin-echo (GRASE) pCASL scan with background suppression (2.5 mm^3 isotropic resolution, 48 slices, 4 segments, TR/TE = 4,300 ms/36.8 ms, label duration = 1,500 ms, post-labeling delay = 2,000 ms, 7 label/control image pairs and one M0 image with the same imaging parameters but no background suppression were acquired in 4 min 35 s).

TABLE 1 | Demographic characteristics of 45 subjects recruited in this study.

		Count	Column N%
Sex	Male	12	26.7%
	Female	33	73.3%
Age range (years)		60–92	
Mean ± SD		69 ± 7	
Education (years)		7 ± 4	
Vascular risk factor	Diabetes	17 (of 45)	37.8%
	Hypertension	28 (of 45)	62.2%
	Hypercholesterolemia	33 (of 45)	73.3%
Global CDR scale	0 (Normal)	27	62.8%
	0.5 (Very mild dementia)	16	37.2%
Fazekas scale	0 (No WMH) Periventricular WM	6	13.3%
	1 (Mild WMH) Periventricular WM	32	71.1%
	2 (Severe WMH) Periventricular WM	7	15.6%
	0 (No WMH) Deep WM	5	11.1%
	1 (Mild WMH) Deep WM	32	71.1%
	2 (Severe WMH) Deep WM	8	17.8%

Vascular risk factors (presence of diabetes, hypertension, or hypercholesterolemia) was defined by a past diagnosis and/or current treatment for these conditions from 45 subjects. Neurocognitive performance was evaluated by global Clinical Dementia Rating (CDR) scale for 43 subjects. Severity of white matter lesions were quantified by the Fazekas scale, which is rated from 0 (absent) to 3 (large confluent areas) in periventricular white matter and deep white matter, respectively.

Clinical and Cognitive Assessments

Clinical evaluation of the participants was performed by a board-certified neurologist (JMR) using the Clinical Dementia Rating (CDR) scores. The CDR is a structured interview of the subject and informant based on which subjects were rated as: 0 (asymptomatic), 0.5 (equivocal impairment), 1 (mild), 2 (moderate), or 3 (severe dementia). All participants were rated CDR 0 or 0.5 (**Table 1**). The Clinical Dementia Rating Sum of Boxes (CDR-SOB) scores were used for correlation analyses with CBF due to the wider score range of 0–18 (O'Bryant et al., 2008). The Montreal Cognitive Assessment (MoCA) was performed on 39 participants by a licensed neuropsychologist (LD) with scores ranging from 0 to 30 (Nasreddine et al., 2005). Testing was administered in English (5, 13%) or Spanish (34, 87%), determined by the comfort level of the subjects. Neurocognitive evaluations were performed using standard neuropsychological test battery in the Uniform Data Set v3 (UDS3). Domain specific assessment of executive function was performed using scores of Trail Making B—A and a composite score of executive function developed using IRT (Staffaroni et al., 2020a). Composite scores of executive function offer advantages such as better reliability, fewer statistical comparisons, and improved power to detect longitudinal change with smaller sample sizes (Gibbons et al., 2012; Staffaroni et al., 2020b). Memory scores were derived from the Spanish English Verbal Learning Test (SEVLT) which has been shown to be appropriate and have adequate normative data for use with older Latinx persons of Mexican descent (González et al., 2002). The memory scores included Total Learned (over the learning trials), Benefit of Cues (difference between delayed free recall and delayed cued recall), and percentage retained (Delayed Free Recall / Trial 5). Overall, 43 subjects had complete behavioral and clinical assessments.

Furthermore, presence or absence of hypertension, diabetes, and hypercholesterolemia (0 or 1) was defined by a past diagnosis and/or current treatment for these conditions. Vascular risk factor (0–3) was calculated as the combination of presences of hypertension, diabetes, or hypercholesterolemia, which was used for correlation analysis with CBF.

Data Analysis

ASL data were preprocessed and quantified using SPM12 and in-house Matlab scripts. Following motion correction, pair-wise subtraction of label and control images was performed and averaged across the time series to generate mean perfusion images. Quality control metrics were generated by the program and included framewise displacement for head motion and temporal SNR. Quantitative CBF maps were generated using the standard one-compartment perfusion model (Alsop et al., 2015) using voxel-wise calibration with the M0 image. Results

were visually checked for any artifacts. Only one CBF dataset was found to have artifacts with abnormally low CBF, and this subject (66 years, F) was excluded for further analyses. CBF maps from the 1st and 2nd visit of the remaining 44 subjects were coregistered to individual T1w MRI and normalized to the Montreal Neurological Institute (MNI) template space. CBF was measured in the whole brain (WB), white matter (WM) and 4 main vascular territories [leptomeningeal anterior cerebral artery (ACA), middle cerebral artery (MCA) and posterior cerebral artery (PCA), as well as MCA perforator] using a template (Tatu et al., 1998; Wang et al., 2012). WM mask was created from tissue probability maps thresholded at 99%.

White matter hyperintensity (WMH) was segmented from T2-weighted FLAIR images using ITK-SNAP[2] (Yushkevich et al., 2006) and its semi-automatic segmentation tool for supervised classification based on random forests. Three tissue classes (WMH, non-hyperintense tissue, and CSF) were identified as training examples for the classifier, and seeds were then placed in the observed WMH. The active contour algorithm was used to iteratively expand the seeds into the WMH segmentation, which was then carefully inspected by clinical fellows and manually adjusted if necessary. The final segmentation was used to quantify the total WMH volume which was normalized by the intracranial volume (ICV) segmented and measured using SPM12 (FIL, UCL, London, United Kingdom) in each subject. Severity of white matter lesions were quantified by the Fazekas scale (Fazekas et al., 1987), which is rated from 0 (absent) to 3 (large confluent areas) in periventricular white matter and deep white matter, respectively. Since Fazekas scores of periventricular and deep WM were highly correlated, we used total Fazekas scores for correlation analysis with CBF.

The test-retest repeatability of CBF was assessed by intra-class correlation coefficient (ICC) and within-subject coefficient of variation (wsCV). Absolute and relative CBF (vs. global mean CBF) were correlated with global cognitive measures, CDR-SOB scores and domain specific assessment of executive and memory function, with age, gender, years of education and testing language as covariates. Absolute and relative CBF (normalized by global mean CBF) were also correlated with vascular risk factor, Fazekas scores, and volumes of WMH, with covariates of age and gender. Data distribution was examined using histogram and Shapiro–Wilk test which has relatively strong statistical power to be suitable for small sample size, compared to other normality tests. Logarithm transformation was applied to skewed data when necessary. For unadjusted correlation, either Pearson or Spearman correlation was used depending on normality. To examine the adjusted correlation, data were first rescaled to z scores then fit with generalized linear multivariate regression model (GLM) with covariates. The beta coefficient from the regression model using z score can approximate the correlation coefficient and be comparable between variables of interest. For Fazekas scores, since they are categorical measurements (k levels), GLM with k-1 degree of freedom ANOVA test was used as the global association test. Residual plots were used to assess the model integrity and Cook's d was used to detect outliers with extreme influence. Multivariate Adaptive Regression Spline (MARS) (Friedman, 1991) was used to explore the potential non-linear association. Scatter plots were used to illustrate the correlation with outliers highlighted. If a spline detected by MARS, the spline regression slope instead of linear regression slope was used to illustrate the potential non-linear association. Based on our hypothesis and literature evidence, we focused on CBF measurements in 3 regions for correlation with behavioral and imaging biomarkers of cSVD: leptomeningeal MCA (leptoMCA) and MCA perforator (MCAperf) territories, and WM. As an exploratory analysis, an α level of 0.05 (2-sided) was used for statistical significance without correction for multiple comparisons. SAS9.4 was used for statistical analysis.

[2]www.itksnap.org

RESULTS

Test-Retest Repeatability of CBF

Figure 1 shows CBF maps normalized to the MNI canonical space of three representative participants acquired on two visits. The three participants had above average, average and below average reproducibility of repeated CBF measurements, respectively. Mean CBF maps for visit1 and visit2 as well as the voxel-wise ICC and wsCW maps of test-retest results for all the 44 subjects are shown in **Figure 2**. Good to excellent test-retest repeatability was achieved (ICC = 0.77–0.85, wsCV 3–9%, **Figure 3**) for absolute CBF measurements in the WB [ICC(C-k) = 0.84], WM [ICC(C-k) = 0.77], and 4 vascular territories: leptomeningeal ACA (leptoACA, ICC_{abs} = 0.77, $wsCV_{abs}$ = 0.09 $\pm$ 0.07); leptomeningeal MCA (leptoMCA, ICC_{abs} = 0.85, $wsCV_{abs}$ = 0.08 $\pm$ 0.05); leptomeningeal PCA (leptoPCA, ICC_{abs} = 0.83, $wsCV_{abs}$ = 0.08 $\pm$ 0.06);, and MCA perforator territory (MCAperf, ICC_{abs} = 0.77, $wsCV_{abs}$ = 0.08 $\pm$ 0.07). For relative CBF, wsCV was calculated for test-retest repeatability since the inter-subject variation was very small due to normalization by global CBF. The wsCV of relative CBF ranged from 3 to 6% in the 4 vascular territories between repeated scans ~6 weeks apart (**Figure 3**): leptoACA ($wsCV_{rel}$ = 0.05 $\pm$ 0.04); leptoMCA ($wsCV_{rel}$ = 0.03 $\pm$ 0.03); leptoPCA ($wsCV_{rel}$ = 0.06 $\pm$ 0.05);, and MCAperf ($wsCV_{rel}$ = 0.05 $\pm$ 0.04).

Correlations Between CBF and Cognitive Scores

Global mean CBF was not significantly correlated with any cognitive scores. Relative CBF normalized by global mean CBF in the leptoMCA territory was positively correlated with the executive function composite score [**Figure 4A**, beta = 0.33, 95% CI (0.08, 0.59), P = 0.02]. Relative CBF in the MCAperf territory [**Figure 4B**, beta = 0.29, 95% CI (0.04, 0.54), P = 0.03] and leptoMCA territory [**Figure 4C**, beta = 0.36, 95% CI (0.10, 0.63), P = 0.01] was positively correlated with MoCA scores, controlling for age, gender, years of education and testing language. However, relative CBF in WM was negatively correlated with MoCA scores [**Figure 4D**, beta = −0.36, 95% CI (−0.66, −0.07),

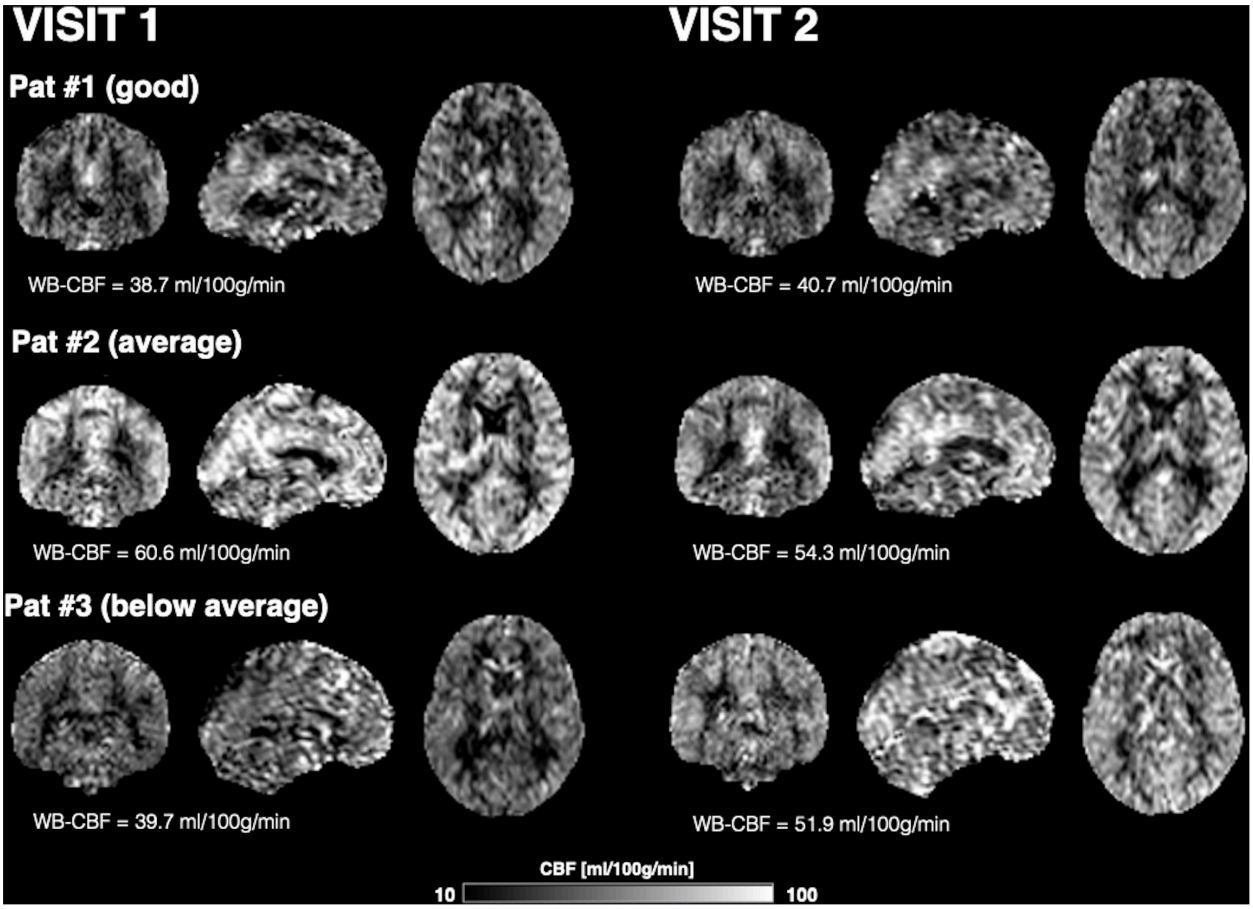

FIGURE 1 | CBF maps normalized to the MNI canonical space and displayed in coronal, sagittal, and axial views of three representative participants acquired on two visits. The three participants had above average, average and below average reproducibility of repeated CBF measurements.

P = 0.02], controlling for age, gender, years of education and testing language.

For association with memory function, no CBF measurements in leptoMCA or MCAperf territories were found to be correlated with any of the three SEVLT scores. However, relative CBF of WM was positively correlated with the Benefit of Cues score of SEVLT [beta = 0.5, 95% CI (0.09, 0.9), P = 0.022]. No CBF measurements were significantly correlated with CDR-SOB scores.

Correlations Between CBF, Vascular Risks and WMH

No CBF measurements were found to be correlated with vascular risk factor—the combination of presences of hypertension, diabetes, or hypercholesterolemia (0–3).

The WMH was found to be generally mild (WMH volume < 20 ml) in the study cohort except two subjects with WMH volume greater than 60 ml (top two dots in **Figure 5A**). We found a significant negative correlation between relative WM CBF and the log transformation of normalized WMH volume [**Figure 5A**, beta = −0.37, 95% CI (−0.64, −0.10), P = 0.01], controlling for age and gender. There was also a negative correlation between relative WM CBF and total Fazekas scores of WMH (**Figure 5B**, p = 0.03). However, relative leptoMCA CBF was positively correlated with the log transformation of normalized WMH volume [**Figure 5C**, beta = 0.37, 95% CI (0.10, 0.64), P = 0.01] and total Fazekas scores of WMH (**Figure 5D**, p = 0.02).

DISCUSSION

In this study, we evaluated CBF measurement by 3D pCASL as a potential biomarker of VCID in a cohort of elderly Latinx subjects at risk of cSVD. Good to excellent test-retest repeatability was achieved (ICC = 0.77–0.85, wsCV 3–9%) for CBF measurements in the whole brain, WM, and 4 vascular territories. Relative CBF normalized by global mean CBF in the leptoMCA territory was positively correlated with an IRT-derived composite score of executive function, while relative CBF in the MCA perforator and leptoMCA territory was positively correlated with MoCA scores of global cognitive function. Relative CBF in WM was

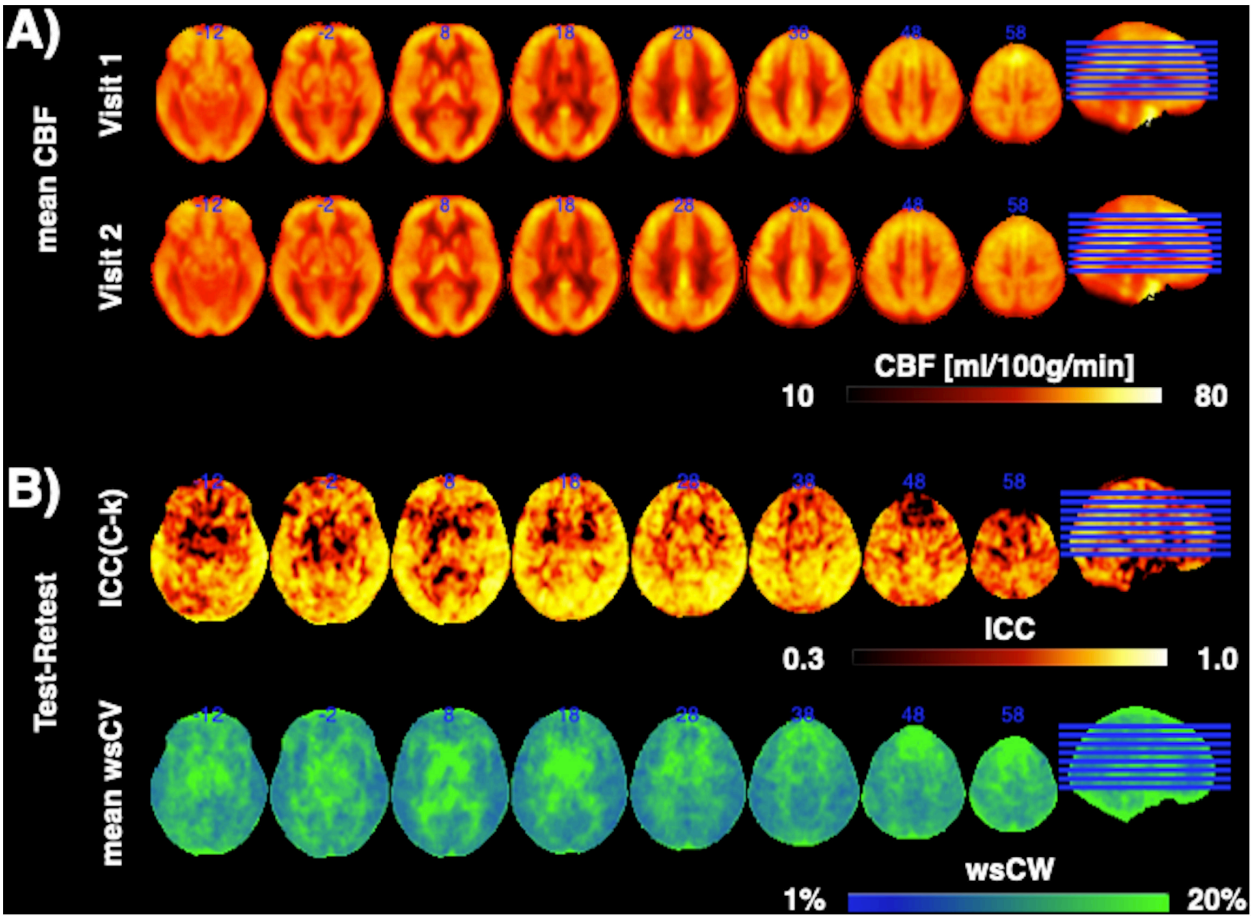

FIGURE 2 | (A) Mean CBF maps for visit1 and visit2 as well as **(B)** the voxel-wise ICC and wsCW maps of test-retest results for all the 44 subjects.

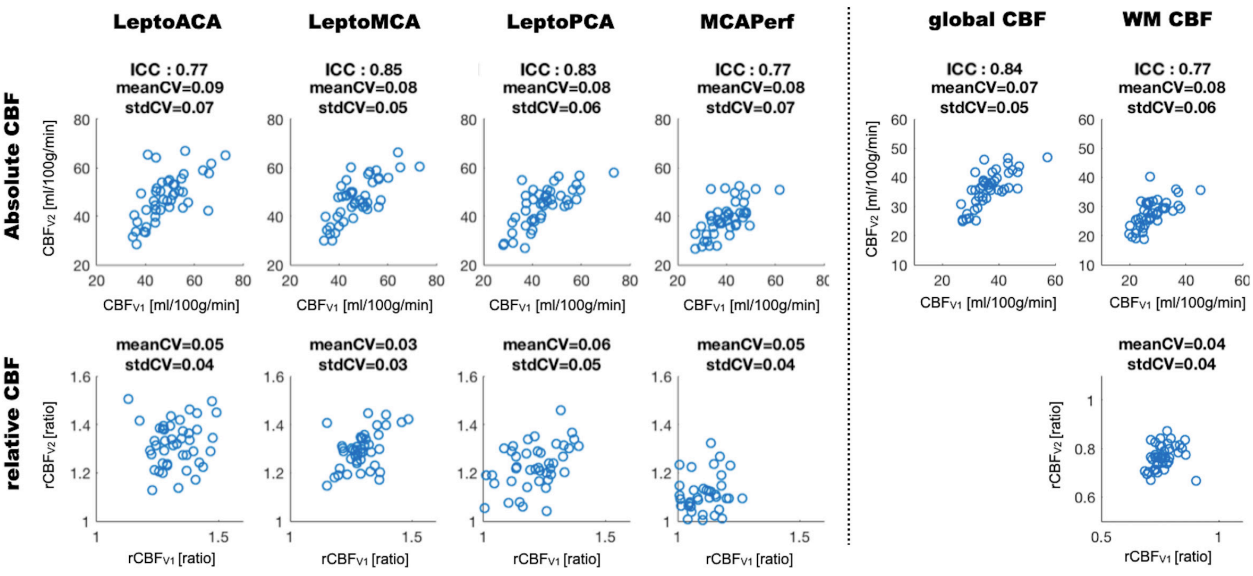

FIGURE 3 | Scatter plots of absolute and relative CBF values acquired on two visits measured in the whole brain (global CBF), white matter (WM) and 4 vascular territories. ICC and wsCV (mean and SD) of each ROI are listed for absolute CBF while wsCV values are listed for relative CBF.

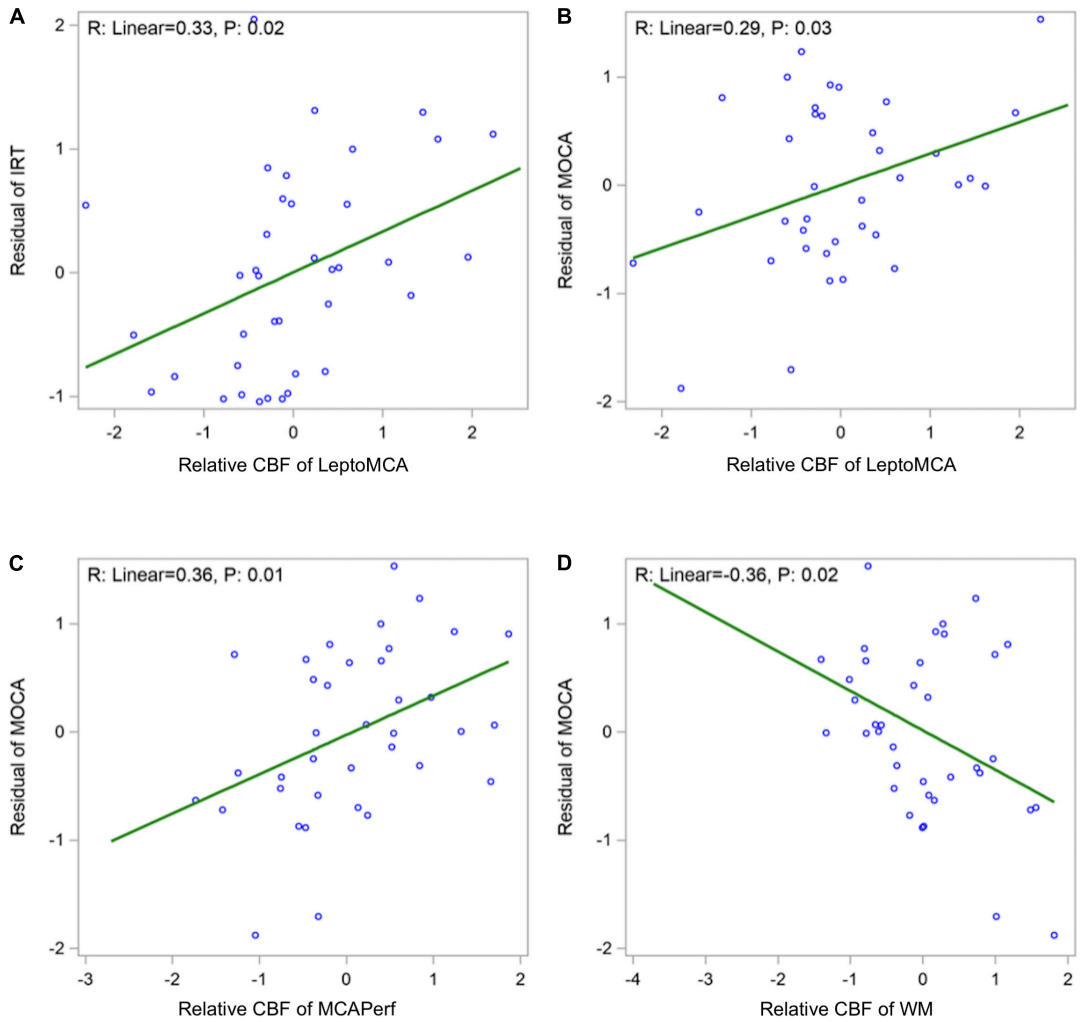

FIGURE 4 | Scatter plots showing **(A)** positive correlations between relative CBF in the leptoMCA and executive function composite score [adjusted beta = 0.33, 95% CI (0.08, 0.59), $P = 0.02$]; **(B)** positive correlation between relative CBF in the leptoMCA territory and MoCA score [β = 0.29, 95% CI (0.04, 0.54), $P = 0.03$]; **(C)** positive correlation between relative CBF in the MCAperf territory and MoCA score [β = 0.36, 95% CI (0.10, 0.63), $P = 0.01$]; **(D)** negative correlation between relative CBF in WM and MoCA scores [β = –0.36, 95% CI (–0.66, –0.07), $P = 0.02$). Final associations were controlled for age, gender, years of education and testing language, and used standardized z scores for both independent and dependent variables.

negatively correlated with WMH volume and MoCA scores, while relative leptoMCA CBF was positively correlated with WMH volume.

Test-Retest Repeatability of CBF

The test-retest repeatability of ASL CBF measurements has been evaluated using different ASL techniques in different populations. Chen et al. (2011) compared three common ASL strategies with 2D EPI readout: pCASL, pulsed (PASL) and continuous ASL (CASL) in 12 young healthy subjects at 3T, with scan intervals up to 1 week. The authors reported a wsCV on the order of 10% for GM CBF for PASL (9.2 ± 0.12%) and pCASL (8.5 ± 0.14%), with higher variability for longer scan intervals. Kilroy et al. (2014) evaluated repeatability (∼4 weeks apart) and accuracy (by comparing to 15O-PET) of pCASL with 2D EPI and 3D GRASE readout in 13 elderly subjects including six MCI and one mild AD. GRASE pCASL demonstrated a higher repeatability for regional perfusion measurements (ICC = 0.707, wsCV = 10.9%) compared to EPI pCASL (ICC = 0.362, wsCV = 15.3%). Hodkinson et al. (2013) evaluated 3D pCASL in 16 healthy male volunteers (age range: 18–50 years) in a clinical model of post-surgical pain. The inter- and intra-session reliability of the post-surgical pCASL CBF measurements were good-to-excellent (ICC > 0.6), while the repeatability of ΔCBF between pre- and post-surgical states was moderate (ICC > 0.4). Between-subjects, the pCASL CBF measurements in the post-surgical pain state and ΔCBF were both characterized as moderately reliable (ICC > 0.4) across nine ROIs. Lin et al. (2020) compared test-retest repeatability of 3D pCASL with standard (1,500 ms) and long (3,500 ms) labeling duration in 20 adult volunteers (age 56.6 ± 17.2 years) with a 1 h interval. The ICCs were generally high (> 0.85) and wsCV < 10% across

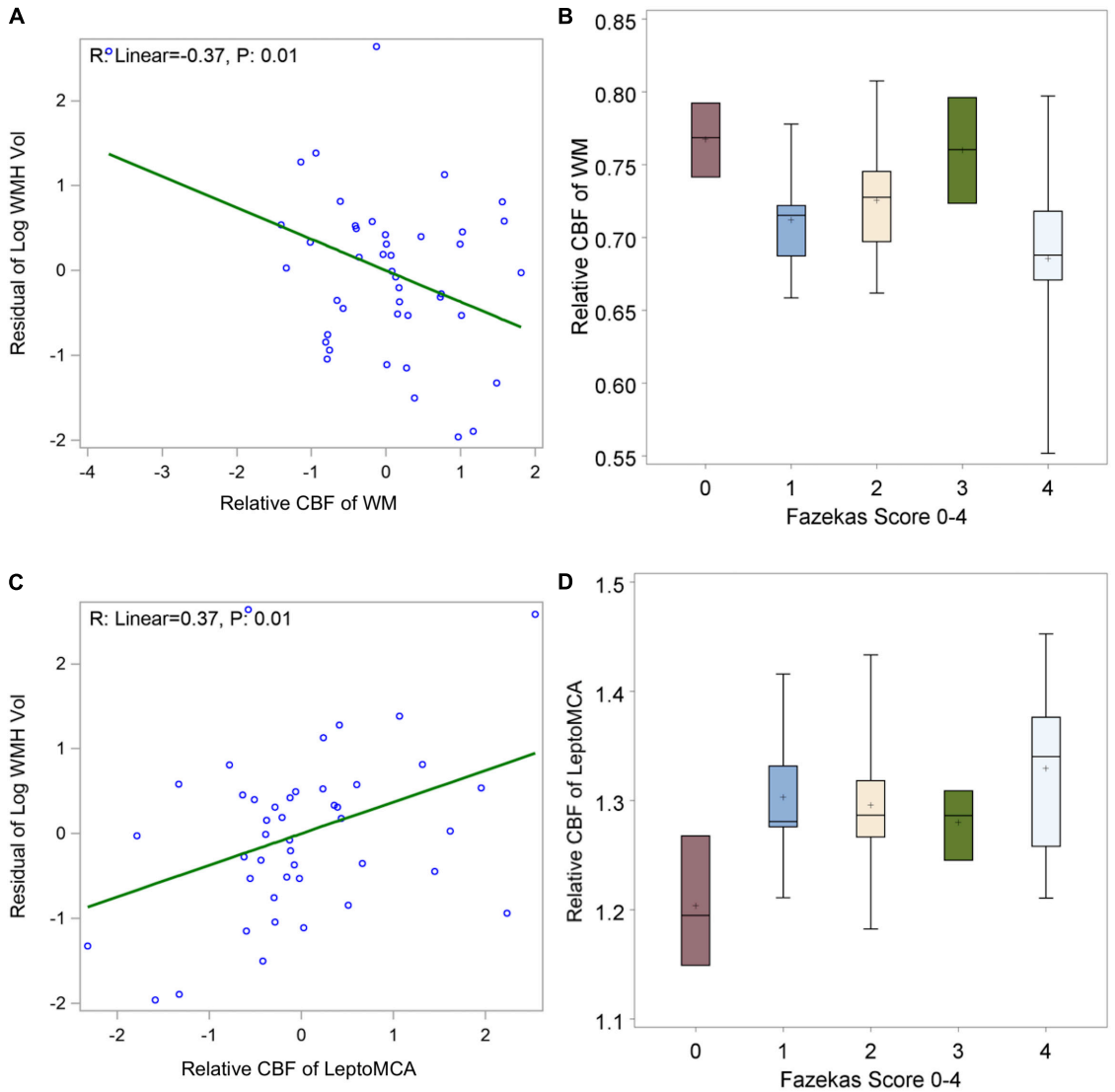

FIGURE 5 | shows **(A)** negative correlations between relative WM CBF and log transformation of normalized WMH volume [β = –0.37, 95% CI (–0.64, –0.10), *P* = 0.01 adjusted for age and gender]; **(B)** linear decreasing trend of relative WM CBF by increasing in total Fazekas scores of WMH [β = –0.02, 95% CI (–0.0004, –0.04) *P*: 0.02]; **(C)** positive correlations between relative leptoMCA CBF with the log transformation of normalized WMH volume [β = 0.37, 95% CI (0.10, 0.64), *P* = 0.01 adjusted for age and gender]; **(D)** linear increasing trend of relative leptoMCA CBF by increasing in total Fazekas scores of WMH [β = 0.03, 95% CI (0.01, 0.05) *P*: < 0.01].

lobar ROIs with the long labeling duration pCASL showing higher repeatability.

Overall our results of test-retest repeatability of 3D pCASL CBF measurements in the cohort of elderly Latinx subjects are consistent with those reported in literature. To the best of our knowledge, this is the first pCASL study in Latinx population with a moderate sample size (N = 45 recruited from communities) that is larger than those in previous studies. The scan interval of ∼6 weeks is also longer than those in previous studies, adding challenges for achieving a high repeatability. Nevertheless, the test-retest repeatability of 3D pCASL CBF measurements in our study was comparable and even higher than those reported in literature. Our data strongly support that 3D pCASL CBF measurement can be applied as an imaging biomarker in community based clinical studies/trials.

Correlation of CBF With Neurocognitive Function

In this study, relative CBF in the leptoMCA territory was correlated with executive dysfunction (Staffaroni et al., 2020b) which is considered a prominent behavioral phenotype of cSVD. In contrast, episodic memory deficits are more pronounced in patients with AD (Wallin et al., 2018). The leptoMCA territory includes a large area of cerebral cortex including the

frontal, parietal and temporal lobes. These regions comprise the default mode, dorsal attention and frontoparietal networks associated with attention and executive functions (22). A recent study also found positive associations between the executive function composite score and CBF in dorsolateral prefrontal cortex (Staffaroni et al., 2019). Therefore, it is not surprising that relative CBF in leptoMCA territory was correlated with the executive function composite score. In addition, leptoMCA relative CBF was correlated with MoCA scores of gross cognition. This finding is not surprising given the involvement of leptoMCA territory in a wide range of cognitive functions. A previous study in a cohort of Chinese patients with subcortical vascular cognitive impairment found diffuse global reductions in CBF and correlation of regional CBF with gross cognition in temporal, orbitofrontal and insular cortices (Sun et al., 2016). These areas partially overlap with the areas of the leptoMCA territory. A main difference is that the previous study did not account for the widespread global hypoperfusion, a factor that will be discussed below.

We also observed that relative CBF in the MCA perforator territory was positively correlated with MoCA scores of global cognitive function. The MCA perforator territory primarily consists of lenticulostriate arteries (LSAs) that supply important subcortical areas including the caudate nucleus, globus pallidus, putamen, and part of the posterior limb of the internal capsule (Ma et al., 2019). LSAs take origin directly from the high flow MCA with small diameters on the order of a few hundred microns (Marinković et al., 2001), therefore are particularly susceptible to damage (e.g., by hypertension) (Dichgans and Leys, 2017). Indeed, subcortical ischemic infarcts (e.g., lacunes) are a prominent hallmark of cSVD (Wardlaw et al., 2009). In addition, CBF in leptoMCA or MCA perforator territories were not associated with any of the 3 memory scores derived from the SEVLT. Relative MCAperf CBF was also correlated with retinal capillary density measured by optical coherence tomography angiography (OCTA) in the same cohort of Latinx subjects (Ashimatey et al., 2020). Our findings, in conjunction with existing evidence, prompt relative CBF in the leptomeningeal and perforator MCA territories as candidate biomarkers of VCID. However, the area of MCA perforator territory is much smaller than that of leptoMCA which may affect the reliability of CBF measurements (as indicated by lower ICC values in the former).

Previous studies have shown the advantages of using psychometrically robust composite scores over a single or multiple cognitive test scores to quantify cognitive performance (Crane et al., 2012; Gibbons et al., 2012; Staffaroni et al., 2020b). The IRT-based score used in the present study is sensitive to impairments in MCI, AD, and frontotemporal dementia (Staffaroni et al., 2020b). Furthermore, it was associated with gray matter volume of frontal, parietal, and temporal lobes, the same regions that make up the leptoMCA territory. A different IRT-based composite score of executive function derived from the NIH-EXAMINER has been shown to detect longitudinal declines in asymptomatic carriers of mutations that cause frontotemporal dementia and is sensitive to premanifest Huntington's disease (You et al., 2014), two conditions that present with executive dysfunction. This suggests these composite scores may be sensitive to the earliest changes in executive abilities. In the present study, we did not observe associations between CBF and another common metric of executive function (Trail Making B—A), providing additional evidence that an IRT-based composite score may provide a more robust measure of executive function than its component tests.

We found relative CBF in WM was negatively correlated with MoCA scores, which contradicts the positive association between MCA CBF and MoCA scores. The reason for this observation is not known. It is possible that normalization with global mean CBF may play a role in different trends of relative CBF between GM and WM regions. However, absolute CBF was not associated with behavioral measures or WMH in our study, suggesting the importance of controlling variations in global CBF with normalization for regional CBF values. This notion is in line with previous reports that inter-individual differences in global CBF are higher than within-subject CBF variations (Henriksen et al., 2012), and thus, detection of small inter-subject regional CBF variations associated with cognitive or clinical assessments requires global CBF bias correction or normalization. It also has been demonstrated that relative CBF is more sensitive in detecting regional differences across subjects compared to absolute CBF (Aslan and Lu, 2010).

Correlation of CBF With WMH

WMH is the most prominent imaging feature of cSVD (Wardlaw et al., 2009). WMHs are associated with increased risk of cognitive impairment and dementia (Alber et al., 2019), and are presumed to be caused by chronic hypoperfusion, blood-brain barrier (BBB) breakdown, dysfunction of oligodendrocyte precursor cells, and venous collagenosis (Kim et al., 2020). A recent systematic review and meta-analysis with a large pooled sample (n = 1,161) showed that CBF is lower in subjects with more WMHs (Shi et al., 2016). Several studies also investigated perfusion changes in the WMH penumbra, which is the normal appearing WM around the hyperintensities (Promjunyakul et al., 2015, 2016; Rane et al., 2018). These studies found that hypoperfusion in the WMH penumbra are associated with cognition and future WMH growth. In the present study, we found a significant negative correlation between relative WM CBF and the log transformation of normalized WMH volume, as well as total Fazekas scores of WMH. This finding is consistent with the hypothesis of chronic hypoperfusion as a main etiology of WMH in literature. However, this trend was reversed for relative CBF in leptoMCA which is positively correlated with the log transformation of normalized WMH volume and total Fazekas scores of WMH. The WMH was generally mild (WMH volume < 20 ml) in the study cohort except two subjects with WMH volume greater than 60 ml (top two dots in **Figure 5A**). Excluding these two subjects with large WMH volume, none of the reported associations between CBF and WMH were significant ($P > 0.05$). Therefore, the reported findings need to be interpreted with

caution and should be verified in larger cohorts with greater variability of WMH.

Limitations and Future Directions

There are several limitations of this study: (1) The sample size is moderate and the study cohort is all aged Latinx subjects. This is both a strength and weakness since our study is the first of its kind in a Latinx population; nevertheless, the relatively uniform cohort may not have large enough variability in the stages of cSVD (e.g., WMH); (2) Our study was performed on a single 3T MRI scanner. It would be ideal to evaluate the test-retest repeatability of ASL CBF across MRI scanners by different manufacturers, as shown by Mutsaerts et al. (2015). This has become feasible with the recommended implementation of pCASL with background suppressed 3D acquisitions across major MRI platforms (Alsop et al., 2015); (3) We did not perform correction for multiple comparisons for exploratory analyses. The sample size was only powered for reliability test, but was underpowered for testing the association with clinical outcomes. Such an exploratory analysis can provide us the insight for directing further confirmative studies with larger sample sizes.

CONCLUSION

Reliable 3D pCASL CBF measurements were achieved in the cohort of elderly Latinx subjects. Relative CBF in the leptomeningeal and perforator MCA territories were the most likely candidate biomarker of VCID. These findings need to be replicated in larger cohorts with greater variability of stages of cSVD.

DATA AVAILABILITY STATEMENT

The datasets presented in this article was collected as part of the MarkVCID consortium study at the University of Southern California (www.markvcid.org). The datasets is available by contacting the corresponding author.

ETHICS STATEMENT

The studies involving human participants were reviewed and approved by the Institutional Review Board of the University of Southern California. The patients/participants provided their written informed consent to participate in this study.

AUTHOR CONTRIBUTIONS

KJ, XS, SM, and DW developed the post processing pipeline, conducted data analysis, and wrote the manuscript. XS, KJ, SM, LY, MC, JR, LD'O, and DW carried out the experiments and collected data. SC, KJ, SM, GB, AS, JK, and JL conducted data analysis. LD'O, JL, KJ, LY, AS, JR, and DW guided experiments, discussed results, and revised manuscript. All authors edited and revised the manuscript and approved final submission.

FUNDING

This work was supported by the National Institute of Health (NIH) grant UH3-NS100614, R01-NS114382, and R01-EB028297.

REFERENCES

Alber, J., Alladi, S., Bae, H.J., Barton, D.A., Beckett, L.A., Bell, J.M. et al. (2019). White matter hyperintensities in vascular contributions to cognitive impairment and dementia (VCID): Knowledge gaps and opportunities. *Alzheimers Dement* 5, 107–117.

Alsop, D.C., Detre, J.A., Golay, X., Gunther, M., Hendrikse, J., Hernandez-Garcia, L. et al. (2015). Recommended implementation of arterial spin-labeled perfusion MRI for clinical applications: a consensus of the ISMRM perfusion study group and the european consortium for ASL in dementia. *Magn. Reson. Med.* 73, 102–116. doi: 10.1002/mrm.25197

Ashimatey, B.S., D'Orazio, L.M., Ma, S.J., Jann, K., Jiang, X., Lu, H. et al. (2020). Lower retinal capillary density in minimal cognitive impairment among older latinx adults. *Alzheimers Dement.* 12:e12071.

Aslan, S., and Lu, H. (2010). On the sensitivity of ASL MRI in detecting regional differences in cerebral blood flow. *Magn. Reson Imaging* 28, 928–935. doi: 10.1016/j.mri.2010.03.037

Association, A.S. (2016). 2016 Alzheimer's disease facts and figures. *Alzheimers Dement.* 12, 459–509. doi: 10.1016/j.jalz.2016.03.001

Breteler, M.M., van Amerongen, N.M., van Swieten, J.C., Claus, J.J., Grobbee, D.E., van Gijn, J. et al. (1994). Cognitive correlates of ventricular enlargement and cerebral white matter lesions on magnetic resonance imaging. The rotterdam study. Stroke 25, 1109–1115. doi: 10.1161/01.str.25.6.1109

Chen, Y., Wang, D.J.J., and Detre, J.A. (2011). Test-retest reliability of arterial spin labeling with common labeling strategies. *J. Magn. Reson. Imaging* 33, 940–949. doi: 10.1002/jmri.22345

Crane, P.K., Carle, A., Gibbons, L.E., Insel, P., Mackin, R.S., Gross, A. et al. (2012). Development and assessment of a composite score for memory in the Alzheimer's Disease neuroimaging Initiative (ADNI). *Brain Imaging Behav.* 6, 502–516. doi: 10.1007/s11682-012-9186-z

Debette, S., Beiser, A., DeCarli, C., Au, R., Himali, J.J., Kelly-Hayes, M. et al. (2010). Association of MRI markers of vascular brain injury with incident stroke, mild cognitive impairment, dementia, and mortality: the framingham offspring study. Stroke 41, 600–606. doi: 10.1161/strokeaha.109.570044

DeCarli, C., Murphy, D.G., Tranh, M., Grady, C.L., Haxby, J.V., Gillette, J.A. et al. (1995). The effect of white matter hyperintensity volume on brain structure, cognitive performance, and cerebral metabolism of glucose in 51 healthy adults. Neurology 45, 2077–2084. doi: 10.1212/wnl.45.11.2077

Dichgans, M., and Leys, D. (2017). Vascular cognitive impairment. *Circ. Res.* 120, 573–591.

Fazekas, F., Chawluk, J.B., Alavi, A., Hurtig, H.I., and Zimmerman, R.A. (1987). MR signal abnormalities at 1.5 T in Alzheimer's dementia and normal aging. *Am. J. Roentgenol.* 149, 351–356. doi: 10.2214/ajr.149.2.351

Friedman, J.H. (1991). Multivariate adaptive regression splines. *Annals Stat.* 19, 1–67.

Gibbons, L.E., Carle, A.C., Mackin, R.S., Harvey, D., Mukherjee, S., Insel, P. et al. (2012). A composite score for executive functioning, validated in Alzheimer's disease neuroimaging initiative (ADNI) participants with baseline mild cognitive impairment. *Brain Imaging Behav.* 6, 517–527. doi: 10.1007/s11682-012-9176-1

González, H.M., Mungas, D., and Haan, M.N. (2002). A verbal learning and memory test for english- and spanish-speaking older mexican-american adults. *Clin. Neuropsychol.* 16, 439–451. doi: 10.1076/clin.16.4.439.13908

Gorelick, P.B., Scuteri, A., Black, S.E., Decarli, C., Greenberg, S.M., Iadecola, C. et al. (2011). Vascular contributions to cognitive impairment and dementia: a statement for healthcare professionals from the american heart

association/american stroke association. *Stroke* 42, 2672–2713. doi: 10.1161/str.0b013e3182299496

Henriksen, O.M., Larsson, H.B., Hansen, A.E., Grüner, J.M., Law, I., Rostrup, E. et al. (2012). Estimation of intersubject variability of cerebral blood flow measurements using MRI and positron emission tomography. *J. Magn. Reson. Imaging* 35, 1290–1299. doi: 10.1002/jmri.23579

Heron, M., 2016. Deaths: leading causes for 2014. *Natl. Vital. Stat. Rep.* 65, 1–96.

Hodkinson, D.J., Krause, K., Khawaja, N., Renton, T.F., Huggins, J.P., Vennart, W. et al. (2013). Quantifying the test-retest reliability of cerebral blood flow measurements in a clinical model of on-going post-surgical pain: a study using pseudo-continuous arterial spin labelling. *Neuroimage Clin.* 3, 301–310. doi: 10.1016/j.nicl.2013.09.004

Iadecola, C., 2016. Vascular and metabolic factors in alzheimer's disease and related dementias: introduction. *Cell Mol. Neurobiol.* 36, 151–154 doi: 10.1007/s10571-015-0319-y

Kilroy, E., Apostolova, L., Liu, C., Yan, L., Ringman, J., Wang, D.J. et al. (2014). Reliability of two-dimensional and three-dimensional pseudo-continuous arterial spin labeling perfusion MRI in elderly populations: comparison with 15O-water positron emission tomography. *J. Magn.Reson. Imaging* 39, 931–939. doi: 10.1002/jmri.24246

Kim, H.W., Hong, J., and Jeon, J.C. (2020). Cerebral small vessel disease and alzheimer's disease: a review. *Front. Neurol.* 11:927. doi: 10.3389/fneur.2020.00927

Lin, T., Qu, J., Zuo, Z., Fan, X., You, H., Feng, F. et al. (2020). Test-retest reliability and reproducibility of long-label pseudo-continuous arterial spin labeling. *Magn Reson Imaging* 73, 111–117. doi: 10.1016/j.mri.2020.07.010

Ma, S.J., Sarabi, M.S., Yan, L., Shao, X., Chen, Y., Yang, Q. et al. (2019). Characterization of lenticulostriate arteries with high resolution black-blood T1-weighted turbo spin echo with variable flip angles at 3 and 7 tesla. *Neuroimage* 199, 184–193. doi: 10.1016/j.neuroimage.2019.05.065

Marinković, S., Gibo, H., Milisavljević, M., and Ćetković, M., (2001). Anatomic and clinical correlations of the lenticulostriate arteries. *Clin. Anatomy* 14, 190–195. doi: 10.1002/ca.1032

Mayda, A., and Decarli, C. (2009). Vascular cognitive impairment: prodrome to VaD? In:. In: Wahlund L-O, Erkinjuntti, T., Gauthier S (Eds.). *Vascular Cognitive Impairment in Clinical Practice*. Cambridge,. Cambridge University Press. 11–31. doi: 10.1017/cbo9780511575976.003

Mutsaerts, H.J.M.M., van Osch, M.J.P., Zelaya, F.O., Wang, D.J.J., Nordhoy, W., Wang, Y. et al. (2015). Multi-vendor reliability of arterial spin labeling perfusion MRI using a near-identical sequence: implications for multi-center studies. *Neuroimage* 113, 143–152. doi: 10.1016/j.neuroimage.2015.03.043

Nasreddine, Z.S., Phillips, N.A., Bédirian, V., Charbonneau, S., Whitehead, V., Collin, I. et al. (2005). The montreal cognitive assessment, MoCA: a brief screening tool for mild cognitive impairment. *J. Am. Geriat. Soc.* 53, 695–699.

Norrving, B. (2008). Lacunar infarcts: no black holes in the brain are benign. *Pract. Neurol.* 8, 222–228. doi: 10.1136/jnnp.2008.153601

O'Bryant, S.E., Waring, S.C., Cullum, C.M., Hall, J., Lacritz, L., Massman, P.J. et al. (2008). Staging dementia using clinical dementia rating scale sum of boxes scores: a texas alzheimer's research consortium study. *Arch. Neurol.* 65, 1091–1095.

Pantoni, L. (2010). Cerebral small vessel disease: from pathogenesis and clinical characteristics to therapeutic challenges. *Lancet Neurol.* 9, 689–701. doi: 10.1016/s1474-4422(10)70104-6

Promjunyakul, N., Lahna, D., Kaye, J.A., Dodge, H.H., Erten-Lyons, D. et al. (2015). Characterizing the white matter hyperintensity penumbra with cerebral blood flow measures. *Neuroimage Clin.* 8, 224–229. doi: 10.1016/j.nicl.2015.04.012

Promjunyakul, N.O., Lahna, D.L., Kaye, J.A., Dodge, H.H., Erten-Lyons, D., Rooney, W.D. et al. (2016). Comparison of cerebral blood flow and structural penumbras in relation to white matter hyperintensities: a multi-modal magnetic resonance imaging study. *J. Cereb. Blood Flow Metab.* 36, 1528–1536. doi: 10.1177/0271678x16651268

Rane, S., Koh, N., Boord, P., Madhyastha, T., Askren, M.K., Jayadev, S. et al. (2018). Quantitative cerebrovascular pathology in a community-based cohort of older adults. *Neurobiol. Aging* 65, 77–85. doi: 10.1016/j.neurobiolaging.2018.01.006

Rosenberg, G.A., Wallin, A., Wardlaw, J.M., Markus, H.S., Montaner, J., Wolfson, L. et al. (2015). Consensus statement for diagnosis of subcortical small vessel disease. *J. Cereb. Blood Flow Metab.* 36, 6–25. doi: 10.1038/jcbfm.2015.172

Schneider, J.A., Arvanitakis, Z., Bang, W., and Bennett, D.A. (2007). Mixed brain pathologies account for most dementia cases in community-dwelling older persons. *Neurology* 69, 2197–2204. doi: 10.1212/01.wnl.0000271090.28148.24

Shi, Y., Thrippleton, M.J., Makin, S.D., Marshall, I., Geerlings, M.I., de Craen, A.J. et al. (2016). Cerebral blood flow in small vessel disease: a systematic review and meta-analysis. *J. Cereb Blood Flow Metab.* 36, 1653–1667. doi: 10.1177/0271678x16662891

Staals, J., Booth, T., Morris, Z., Bastin, M.E., Gow, A.J., Corley, J. et al. (2015). Total MRI load of cerebral small vessel disease and cognitive ability in older people. *Neurobiol. Aging* 36, 2806–2811. doi: 10.1016/j.neurobiolaging.2015.06.024

Staffaroni, A.M., Asken, B.M., Casaletto, K.B., Fonseca, C., You, M., Rosen, H.J. et al. (2020a). Development and validation of the uniform data set (v3.0) executive function composite score (UDS3-EF). *Alzheimer's Dementia* 2020:12214. doi: 10.1002/alz.12214

Staffaroni, A.M., Bajorek, L., Casaletto, K.B., Cobigo, Y., Goh, S.Y.M., Wolf, A. et al. (2020b). Assessment of executive function declines in presymptomatic and mildly symptomatic familial frontotemporal dementia: NIH-EXAMINER as a potential clinical trial endpoint. *Alzheimer's Dementia* 16, 11–21.

Staffaroni, A.M., Cobigo, Y., Elahi, F.M., Casaletto, K.B., Walters, S.M., Wolf, A. et al. (2019). A longitudinal characterization of perfusion in the aging brain and associations with cognition and neural structure. *Hum Brain Mapp* 40, 3522–3533.

Sun, Y., Cao, W., Ding, W., Wang, Y., Han, X., Zhou, Y. et al. (2016). Cerebral blood flow alterations as assessed by 3D ASL in cognitive impairment in patients with subcortical vascular cognitive impairment: a marker for disease severity. *Front. Aging Neurosci.* 8:211. doi: 10.3389/fnagi.2016.00211

Tatu, L., Moulin, T., Bogousslavsky, J., and Duvernoy, H., (1998). Arterial territories of the human brain: cerebral hemispheres. *Neurology* 50, 1699–1708. doi: 10.1212/wnl.50.6.1699

US Census Bureau. (2016). *National Population Projections*. https://www.census.gov/data/tables/2017/demo/popproj/2017-summary-tables.html

Wallin, A., Román, G.C., Esiri, M., Kettunen, P., Svensson, J., Paraskevas, G.P. et al. (2018). Update on vascular cognitive impairment associated with subcortical small-vessel disease2. *J. Alzheimers Dis.* 62, 1417–1441. doi: 10.3233/jad-170803

Wang, D.J.J., Alger, J.R., Qiao, J.X., Hao, Q., Hou, S., Fiaz, R. et al. (2012). The value of arterial spin-labeled perfusion imaging in acute ischemic stroke comparison with dynamic susceptibility contrast-enhanced MRI. *Stroke* 43, 1018–U1200.

Wardlaw, J.M., Doubal, F., Armitage, P., Chappell, F., Carpenter, T., Munoz Maniega, S. et al. (2009). Lacunar stroke is associated with diffuse blood-brain barrier dysfunction. *Ann. Neurol.* 65, 194–202. doi: 10.1002/ana.21549

Yata, K., Nishimura, Y., Unekawa, M., Tomita, Y., Suzuki, N., Tanaka, T. et al. (2014). In vivo imaging of the mouse neurovascular unit under chronic cerebral hypoperfusion. *Stroke* 45, 3698–3703. doi: 10.1161/strokeaha.114.005891

You, S.C., Geschwind, M.D., Sha, S.J., Apple, A., Satris, G., Wood, K.A. et al. (2014). Executive functions in premanifest Huntington's disease. *Mov. Disord.* 29, 405–409. doi: 10.1002/mds.25762

Yushkevich, P.A., Piven, J., Hazlett, H.C., Smith, R.G., Ho, S., Gee, J.C. et al. (2006). User-guided 3D active contour segmentation of anatomical structures: significantly improved efficiency and reliability. *Neuroimage* 31, 1116–1128. doi: 10.1016/j.neuroimage.2006.01.015

Conflict of Interest: The authors declare that the research was conducted in the absence of any commercial or financial relationships that could be construed as a potential conflict of interest.

frontiers in Neuroscience

ORIGINAL RESEARCH
published: 25 February 2021
doi: 10.3389/fnins.2021.620172

Optimized Inner-Volume 3D TSE for High-Resolution Vessel Wall Imaging of Intracranial Perforating Arteries at 7T

Qingle Kong[1,2], Yue Wu[1,3,4], Dehe Weng[5], Jing An[5], Yan Zhuo[1,3,4] and Zihao Zhang[1,3,4]**

[1] State Key Laboratory of Brain and Cognitive Science, Beijing MR Center for Brain Research, Institute of Biophysics, Chinese Academy of Sciences, Beijing, China, [2] MR Collaboration, Siemens Healthcare Ltd, Beijing, China, [3] University of Chinese Academy of Sciences, Beijing, China, [4] Innovation Center for Excellence in Brain Science, Chinese Academy of Sciences, Beijing, China, [5] Siemens Shenzhen Magnetic Resonance Ltd, Shenzhen, China

The impairment of microvessels can lead to neurologic diseases such as stroke and vascular dementia. The imaging of lumen and vessel wall of perforating arteries requires an extremely high resolution due to their small caliber size. Current imaging techniques have the difficulty in observing the wall of perforating arteries. In this study, we developed a 3D inner-volume (IV) TSE (SPACE) sequence with optimized 2D spatially selective excitation (SSE) RF pulses. The optimized SSE RF pulses were designed through a series of optimization including iterative RF pulse design, trajectory optimization, and phase convention of Carr-Purcell-Meiboom-Gill (CPMG) condition to meet the perforating arteries imaging demands. High resolution of isotropic 0.30 mm within 10 min was achieved for the black- blood images of lenticulostriate artery (LSA). The LSA lumen and vessel wall were imaged by the IV-SPACE sequence simultaneously. Images obtained by the optimized RF pulse has fewer aliasing artifacts from outside of ROI than the traditional pulse. The IV-SPACE images showed clearer delineation of vessel wall and lumen of LSA than conventional SPACE images. IV-SPACE might be a promising method for detecting microvasculopathies of cerebral vascular diseases.

Keywords: vessel wall imaging, perforating arteries, 7T, high-resolution, inner-volume imaging

OPEN ACCESS

Edited by:
Song Hu,
Washington University in St. Louis, United States

Reviewed by:
Xingfeng Shao,
University of Southern California, Los Angeles, United States
Hao Li,
University of Cambridge, United Kingdom

****Correspondence:***
Yan Zhuo
yzhuo@ibp.ac.cn
Zihao Zhang
zhzhang@ibp.ac.cn

Specialty section:
This article was submitted to Brain Imaging Methods, a section of the journal Frontiers in Neuroscience

Received: *22 October 2020*
Accepted: *14 January 2021*
Published: *25 February 2021*

Citation:
Kong Q, Wu Y, Weng D, An J, Zhuo Y and Zhang Z (2021) Optimized Inner-Volume 3D TSE for High-Resolution Vessel Wall Imaging of Intracranial Perforating Arteries at 7T. Front. Neurosci. 15:620172. doi: 10.3389/fnins.2021.620172

INTRODUCTION

Lacunar infarction (LI) may be caused by lipohyalinotic small artery disease (SAD) (Fisher, 1982), atherosclerotic SAD (Caplan, 1989), and the occlusion of perforators because of parental artery atherothrombosis (Bang et al., 2002). Distinguishing the causes of LI is essential for potential guiding therapeutic intervention. Unfortunately, current imaging techniques cannot differentiate atherosclerotic from lipohyalinotic SAD (Kim and Yoon, 2013) due to the difficulty in observing the wall of small arteries. Visualization of the vessel wall of small arteries (such as perforating artery) requires extremely high spatial resolution and signal-to-noise ratio (SNR) due to their small caliber size and slow flow.

According to previous radiological studies (Mandell et al., 2017), the following features were required for vessel wall imaging (VWI) of intracranial arteries: high spatial resolution, sufficient SNR, suppression of signal in luminal blood and CSF, and multiple tissue weightings. To meet these

requirements, turbo spin echo (TSE) and its variants become the most widely used MR sequence for intracranial VWI (Van der Kolk et al., 2011; Zhu et al., 2016; Harteveld et al., 2017). And for 3D acquisition, TSE sequence with variable flip angle (named SPACE by Siemens) is usually used to obtain isotropic high-resolution images to reduce partial volume effects (Fan et al., 2017). Qiao et al. used 3D TSE to obtain 0.4 mm isotropic images to evaluate intracranial vessels at 3.0T (Qiao et al., 2011), which is the highest resolution currently reported for 3D VWI. The SPACE at 7T has higher SNR and intrinsic black blood characteristics, which is very suitable for high-resolution VWI.

Nevertheless, the isotropic 0.40 mm voxel is not sufficient to delineate the vessel wall of intracranial small arteries, of which the thickness was 0.05–0.40 mm. To visualize the thinner vasculature, the spatial resolution of VWI must be further improved. However, conventional 3D TSE employed hard pulse for excitation and required whole-brain acquisition to avoid image aliasing. As a result, high spatial resolution increased phase-encoding (PE) steps in 3D TSE, which means four times the acquisition time (TA) when the dimension of a voxel is halved.

Theoretically, TA can be shortened by increasing acceleration factors. However, too aggressive down-sampling further impaired the limited SNR of small voxels and downgraded the quality of displaying tiny structures in images. The inner volume imaging (IVI) was another way to reduce the PE steps and shorten TA. This can be achieved by limiting the excitation area to reduce the field of view (FOV) (Feinberg et al., 1985). To obtain inner volume selection, orthogonal excitation in combination with refocusing pulses (Feinberg et al., 1985), or 2D spatially selective excitation (SSE) radio frequency (RF) pulses can be used (Pauly et al., 1989). SSE was particularly suited for IVI using 3D TSE sequences because magnetization not tipped by the initial excitation pulse did not generate signal at any of the subsequent echo times so long as sufficient spoiling was included to suppress free induction decay (FID) signals produced by refocusing pulses.

Previous work has verified the feasibility of combining 2D RF pulse and 3D TSE sequence (Mitsouras et al., 2006). However, because it is a preliminary study, some limitations still exist and hinder its practical application, such as incomplete background suppression and long RF pulse durations. Background suppression is critical for inner-volume imaging, particularly when selecting a small sub-volume since the volume contributing undesired background signals is large. In addition, the RF designed method that previous work used is non-ideal in minimizing excitation error. This work designed the SSE RF pulses successfully to meet the perforating arteries (especially lenticulostriate artery, LSA) imaging demands through a series of optimization including iterative RF pulse design, trajectory optimization, and phase convention of Carr-Purcell-Meiboom-Gill (CPMG) condition (Meiboom and Gill, 1958). The optimized 2D SSE RF pulses were used to replace the excitation pulses of the conventional SPACE sequence. Inner volume (IV) imaging of SPACE (IV-SPACE) was achieved to reduce the acquisition matrix and obtain high-resolution VWI images of LSA. The LSA lumen and vessel wall were imaged by the IV-SPACE sequence with black-blood 0.30 mm isotropic resolution. The imaging results from the optimized RF pulse were compared to the traditional 2D RF pulse. The LSA vessel wall imaging from the IV-SPACE sequence was also compared with conventional SPACE.

MATERIALS AND METHODS

Subjects

With the approval of the local institutional review board, eleven healthy volunteers were recruited and scanned. Four of the subjects were male, seven females, and the average age was 26 (± 2) years. Written informed consent was obtained from all subjects.

MRI System

All scans were performed on a whole-body human 7T MR research system (Siemens Healthcare, Erlangen, Germany), with a maximum gradient amplitude of 70 mT/m and maximum gradient slew rate of 200 mT/m/ms. A 32-channel head coil was used for signal reception at 7T.

2D Spatially Selective RF Pulse Design

The traditional 2D SSE RF pulse (FA = 90°) was designed with a constant angular rate spiral-in transmit k-space trajectory, 32 turns, and a pulse length of 16.75 ms (**Figure 1**). The calculation method was described in Pauly et al. (1989). The disk diameter was 5 cm, and the excitation FOV was 17 cm to avoid excitation aliasing. These parameters were selected based on the anatomical distribution of the middle cerebra artery (MCA) and LSA. The Bloch simulation was performed to verify the performance of SSE RF pulse and phase relaxation and off-resonance were ignored.

To design the optimized RF pulse that excited the desired 2D profile, B_0 and B_1 information together with the subject's geometry were needed. Therefore, maps of the local B_0 offsets (echo time (TE) difference: 2.3 ms, scan time: 18 s) and B_1 efficiency [dual repetition time (TR) method (Insko and Bolinger, 1993), TR: 80 ms, scan time: 74 s] were acquired of a sagittal slice in the brain. A mask indicating the subject's brain was obtained from the threshold of the first echo image of the B_0 map. The position of the LSA in the sagittal plane was determined from sagittal localizer images.

Variable-density spiral trajectories were used to under-sample k-space regionally, thus reducing pulse length. The variable-density spiral-in trajectory within hardware limitations of the gradient system was designed to adequately sampled excitation k-space near the origin (XFOV = 25 cm), and under sampled in the high-frequency region (XFOV = 6 cm) (**Figure 1**). The optimized SSE RF pulses (FA = 90°) were calculated following the method described in Yip et al. (2005) and using the natural suppression mechanism of the CPMG condition. The feature of TSE sequences is that excitation and refocusing pulses must rotate the magnetization vector around orthogonal axes. If this condition is not met, echo amplitudes rapidly decrease when the refocusing angle is not precisely 180° (Meiboom and Gill, 1958). Therefore, the component of the excited magnetization that is perpendicular to the rotation axis of the refocusing pulses (i.e., the non-CPMG component) will yield echoes that quickly die away through the imaging sequence. If long echo

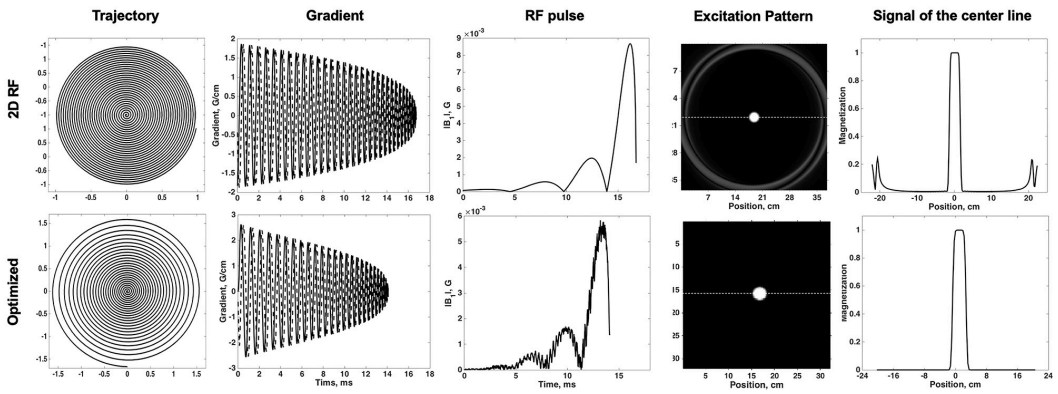

FIGURE 1 | Comparisons of the traditional 2D SSE pulse (top row) and the optimized method (bottom row): trajectory, gradient, RF pulse, excitation pattern in the excitation plane, and the signal of the center line.

trains are used with linear phase encode ordering the resulting signals are strongly suppressed. This work achieved this enhanced background suppression by performing a weighted least squares minimization like the methods proposed by Malik and Hajnal (2016). Weighting factor wr = 0.25 and regularization parameter λ = 100 was used for RF pulse designs based on pilot data performance. A typical example was shown in **Figure 1**. The pulse length was 14.10 ms. The delay time between gradient and RF pulse was corrected in the scanner. Individual pulse design processes took approximately 1 min using MATLAB (R2017b, The MathWorks, Inc., Natick, MA, United States) on a computer with a 3.1 GHz dual core processor and 8 GB RAM.

Experiment

A phantom experiment was performed to explore the performance of the traditional 2D RF pulse and the optimized RF pulse. The phantom was a sphere filled with a solution of $NiSO_4$ (T_1/T_2: 420 ms/240 ms). The IV-SPACE for phantom imaging had field of view (FOV) 190 mm × 190 mm, TR = 1500 ms, TE = 10 ms, Matrix = 144 × 144 × 128, Resolution = 1.3 ×1.3 ×1.3 mm^3, ETL = 50, TA = 2 min 5 s.

The effect of the 2D SSE pulses (two methods) was also assessed on a low resolution (1.8 ×1.8 ×1.8 mm^3) scan of the entire brain (scan time = 3 min 11 s). The local higher resolution scan of the MCA region was performed subsequently. The scan parameters were as follows: TR = 1500 ms, TE = 10 ms, Matrix = 848 ×212 ×192, Resolution = 0.3 ×0.3 ×0.3 mm^3, ETL = 30, Average = 1.6, GRAPPA = 3, TA = 9 min 57 s. High-resolution imaging was performed for both two pulses. In order to evaluate the LSA vessel wall of the IV-SPACE sequence, a 0.4 mm isotropic conventional SPACE data acquisition was also performed in this study. The detailed imaging parameters can be found in previous work (Kong et al., 2019).

Data Analysis

To quantitatively assess the degree of suppression outside of ROI which optimized method achieved, the suppression ratio was calculated for both pulses. The suppression ratio was calculated as the ratio of the average signal inside a 1 cm^2 volume within the excited inner volume to the outer volume region. In order to compare the uniformity of the signal in ROI, the ratio of standard deviation and magnitudes within the ROI was calculated for both two methods. The line profile through the excitation center was also extracted and normalized to quantitatively assess the performance of the optimized method.

Coronal MinIP (projection thickness = 18 mm) was generated with VWI images of all three methods. When generating the MinIP, the center of the slab was adjusted until the maximal number and the longest visible length of LSAs were obtained. The number of stems and branches were counted by two independent readers (Z.H.Z., Q.L.K.; 5 and 3 years of experience in VWI, respectively). Stems were defined as the LSAs that originated directly from the MCA M1, and branches were defined as daughter vessels originating from the parent LSA stems plus stems without any branches. The signal-to-noise ratio (SNR) was also calculated for all three methods. The ROI of signal was obtained from the brain tissue adjacent to LSA (circle, diameter = 5 mm). The noise was estimated as the standard deviation of the ROI (circle, diameter = 5 mm) at the margin of images without brain tissue. The ROIs were kept consistent in the images acquired by all three methods.

To demonstrate the feasibility of using IV-SPACE to visualize the LSAs vessel wall, curved multi-planar reconstruction (curved-MPR) was constructed along the MCAs and transverse minimum intensity projections (MinIP, projection thickness = 2 mm) was generated with VWI images from both IV-SPACE and conventional SPACE. The section view of LSA was built perpendicular to the center line of LSA so that the vessel wall of LSAs could be readily identified in the plane. A cut line through the vessel center was extracted and normalized to compare the wall characterization of two pulses. All the analysis was executed in OsiriX (Rosset et al., 2004).

All quantitative data were expressed as means ± standard deviations. Wilcoxon signed-rank test was used to compare the numbers of stems and branches between the pairwise comparison of the three imaging methods. A *p*-value of less than 0.05 indicated statistical significance. The intraclass correlation coefficient (ICC) was calculated and reported for the

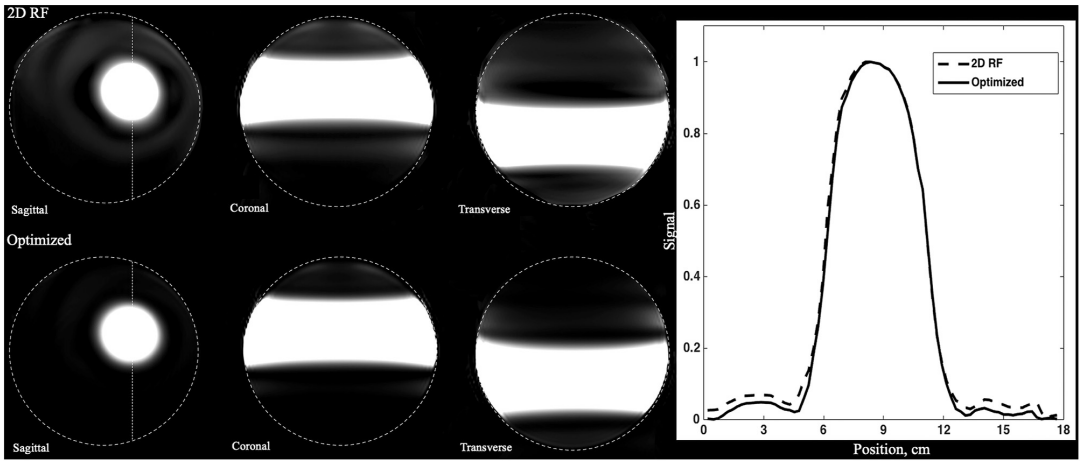

FIGURE 2 | Comparison of the phantoms excited by traditional SSE RF pulse and optimized pulse. Images were shown in the same window-level which was increased the to show the signal residuals outside the ROI. The optimized RF pulse exhibits less residual signal in the outer-volume, which is most obvious in sagittal plane. The line profile through the center of ROI was shown in right column. The solid line is for the optimized pulse and the dashed line is the traditional pulse. Optimized RF pulse has better signal suppression outside the ROI and fewer side lobes.

measurements of LSA. All statistical analyses were performed using commercial software (SPSS 22.0, IBM).

RESULTS

The Bloch simulation of the traditional 2D RF pulse and optimized RF pulse were shown in **Figure 1**. The simulation results showed that the designed SSE pulse achieved inner volume selection successfully. The phantom results of the excitation profile for two methods were shown in **Figure 2**. They were consistent with the simulation results. The images were set to have the same window level and to show the residual signal outside the ROI as much as possible. Images in **Figure 2** showed that the optimized RF pulse had less residual signal outside the ROI. The line profile through the excitation center was also extracted and normalized, as shown in the right column of **Figure 2**. The average signal outside the ROI of the image obtained by optimized RF pulse was 2%, and by traditional 2D RF pulse was 8%, which further showed that the optimized RF pulse had better signal suppression outside the ROI and fewer side lobes. The line profile before the normalization was shown in **Supplementary Figure 1**.

In order to compare the uniformity of the signal in ROI, the ratio of standard deviation and magnitudes within the ROI was calculated for both pulses. The ratio within ROI of the optimized RF pulse was 0.0016, while the 2D RF pulse was 0.0021. Obviously, the optimized RF pulse had a better uniformity in ROI, which may be due to the better correction of B_1 and B_0. The widths of the transition band of the phantom images obtained by the two pulses were similar, accounting for about 25% (1.25 / 5) of the pass bandwidth.

The B_0 and B_1 maps obtained from a volunteer for optimized RF pulse design were shown in **Figures 3C,D**. The desired target was 5 cm ×5 cm (**Figure 3A**). The mask obtained by threshold processing accurately depicted the brain contour of subjects (**Figure 3B**), which further improved the excitation accuracy. The typical excitation pattern of the 2D SSE pulses designed by the optimized method and the traditional method was shown in **Figure 4**, in a low-resolution scan across the entire brain. A large signal intensity difference between the ROI and the rest of the ROI can be observed. **Figure 4** showed that the optimized RF pulse had better suppression of signals outside the ROI, which was especially important for local high-resolution imaging. The more thorough signal suppression outside the ROI, the smaller the aliasing artifacts in the ROI of the high-resolution image.

The high-resolution 0.3 mm isotropic images obtained by the optimized RF pulse and the traditional 2D RF pulse were shown in **Figure 5**. Similar to the low-resolution results, the images obtained by the optimized RF pulse had fewer aliasing artifacts from outside of ROI, making it easier to observe the LSA vessel wall.

Finally, ten datasets were used for analysis (one was removed due to head motion). The numbers of stems and branches of the LSAs are summarized in **Table 1**. The p values of Wilcoxon signed-rank test on SNR and the numbers of stems and branches listed in **Table 2**. The numbers of stems visualized among three different methods were comparable. The number of branches visualized by 2D RF and conventional SPACE were comparable, and both them were lower than that by optimized method (Optimized vs. Conventional SPACE = 7.8 ± 1.54 vs. 7.1 ± 1.33, p = 0.002, ICC = 0.817; 2D RF vs. Optimized = 7.0 ± 1.78 vs. 7.8 ± 1.54, p = 0.001, ICC = 0.805). Optimized methods yielded a better SNR than 2D RF (p = 0.017), and both these two methods were significantly lower than conventional SPACE (Optimized vs. Conventional SPACE: p = 0.001, 2D RF vs. Conventional SPACE: $p < 0.001$).

The representative coronal MinIP images of a volunteer were shown in **Figure 6** for 2D RF (a), optimized method (b), and conventional SPACE (c). The optimization method achieves

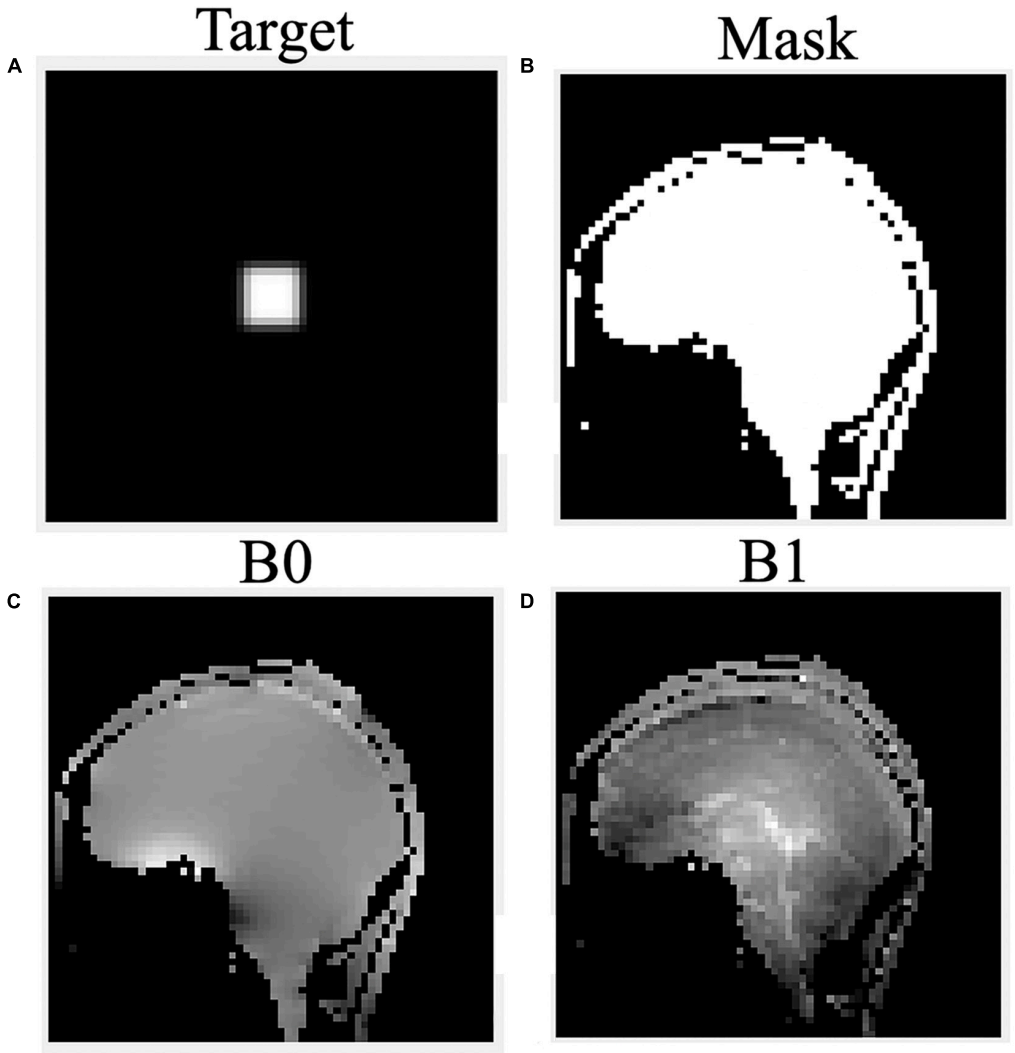

FIGURE 3 | The desired pattern **(A)**, mask **(B)**, B_0 **(C)**, and B_1 **(D)** field map for optimized RF pulse design on a volunteer.

more thorough signal suppression compare to traditional 2D RF and suffers from fewer aliasing artifacts (white arrow). Benefiting from the advantages of increased spatial resolution, the optimized method shows more branches that are invisible to conventional SPACE images (yellow arrows).

Axial images and curved multi-planar reconstruction along the MCA were shown in **Figure 7**. The lumen of an LSA in the IV-SPACE image is clearly depicted and longer than conventional SPACE.

In **Figure 8**, the section view of an LSA was shown and analyzed. The LSA vessel wall was obvious in IV-SPACE (red arrow) but almost invisible in the conventional SPACE image. The increased spatial resolution of the IV-SPACE image can be appreciated in the sharper depiction of the LSA vessel wall as compared with the conventional SPACE image. With a cut line through the vessel center, IV-SPACE images showed a significant signal drop at the lumen, which was almost absent in conventional SPACE images. **Figure 9** showed another example that the lumen and orifice of an LSA were clearly depicted in the IV-SPACE image, whereas the lumen and orifice were blurred in conventional SPACE. On the line profile extracted by IV-SPACE, the lumen and wall of the two LSAs could be clearly identified, but the signal contrast of the wall to the lumen in SPACE was weak. The wall-to-lumen signal ratio of the LSA for IV-SPACE was 2.6, and the ratio for conventional SPACE was 1.5. The contrast between the vessel wall and lumen for LSA in IV-SPACE was better than conventional SPACE.

DISCUSSION

Although optimized forms of 3D TSE imaging have become available, the adoption of 3D sequences into routine clinical imaging has been limited primarily by long image acquisition times. Long acquisition time also hinders its high-resolution

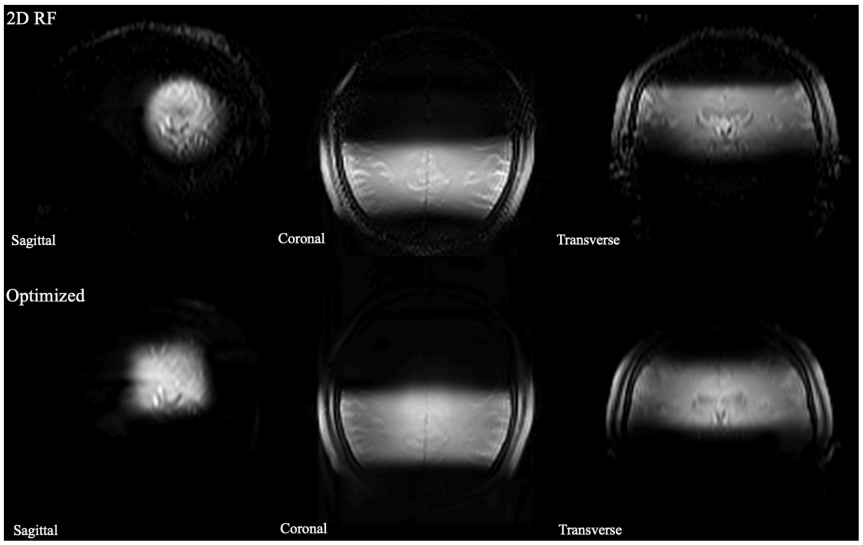

FIGURE 4 | The comparison of full-FOV IV-SPACE images using different RF pulse designs. The upper is from a traditional SSE RF pulse and the bottom is from an optimized pulse. Optimized RF pulse has better suppression of signals outside the ROI.

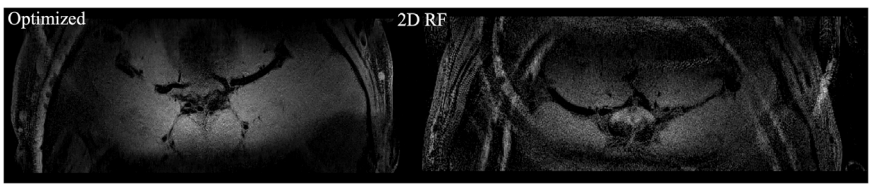

FIGURE 5 | The comparison of high resolution IV-SPACE images using a traditional 2D SSE RF pulse and an optimized RF pulse. Images obtained by the optimized RF pulse has fewer aliasing artifacts from the outer volume than the traditional pulse.

TABLE 1 | The numbers of stems and branches of LSAs and SNR among the three methods.

	Stem	Branch	SNR
Conventional SPACE	5.1 ± 0.85	7.1 ± 1.33	80.7 ± 23.36
2D RF	5.0 ± 0.86	7.0 ± 1.78	46.7 ± 5.08
Optimized	5.2 ± 0.87	7.8 ± 1.54	53.3 ± 8.57

applications. Inner volume methods offer a potential solution to this limitation by combining multidimensional RF excitations to confine coherent transverse magnetization within a given volume of interest (Alley et al., 1997; Yang et al., 1999). This enables reduced FOV imaging of an anatomic region without aliasing artifacts and with significantly reduced acquisition times or achieve high resolution. In this study, the SSE RF pulse is combined with the SPACE sequence to selectively excite the basal ganglia region where MCA and LSA are located, thereby reducing the imaging FOV and reducing the size of the sampling matrix. Multiple scans are used to improve the image SNR after increasing the scanning speed. This achieves local high-resolution LSA vessel wall imaging.

This work successfully produced a clear vessel wall image of the proximal LSA. This is the first time intracranial black-blood images with isotropic 0.30 mm resolution within 10 min have been demonstrated. The optimized SSE RF pulse is robust, and no obvious signal folding from outer excitation FOV is observed. The results demonstrate that IV-SPACE

TABLE 2 | The comparison of the numbers of stems, branches, SNR among conventional SPACE, 2D RF and optimized methods (*$p < 0.050$, **$p < 0.005$).

	Stem		Branch		SNR
	p value	ICC	*p* value	ICC	*p* value
Optimized vs. 2D RF	0.186	0.858	0.001**	0.805	0.017*
Optimized vs. conventional SPACE	0.330	0.926	0.002**	0.817	0.001**
2D RF vs. conventional SPACE	0.163	0.847	0.681	0.849	0.000**

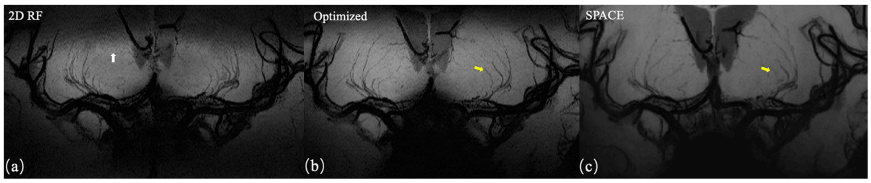

FIGURE 6 | Coronal MinIP (projection thickness = 18 mm) images of 2D SSE pulse **(a)**, optimized method **(b)**, and conventional SPACE **(c)**. The optimized method achieves better signal suppression compare to traditional 2D RF and exhibits fewer aliasing artifacts (white arrow). Due to the higher spatial resolution, the optimized method shows more branches that are invisible in conventional SPACE images (yellow arrows).

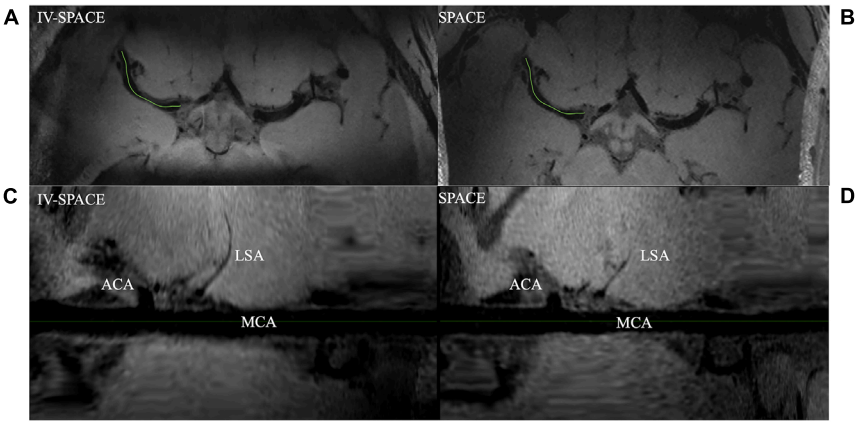

FIGURE 7 | Comparison of IV-SPACE and conventional SPACE in displaying LSA. The enlarged images at the bottom are curved-MPR results along the right MCA [the green lines in **(A,B)**] of IV-SPACE **(C)** and conventional SPACE **(D)**. The lumen of an LSA in the IV-SPACE image is clearly depicted. The visible length of the LSA is longer than that in conventional SPACE.

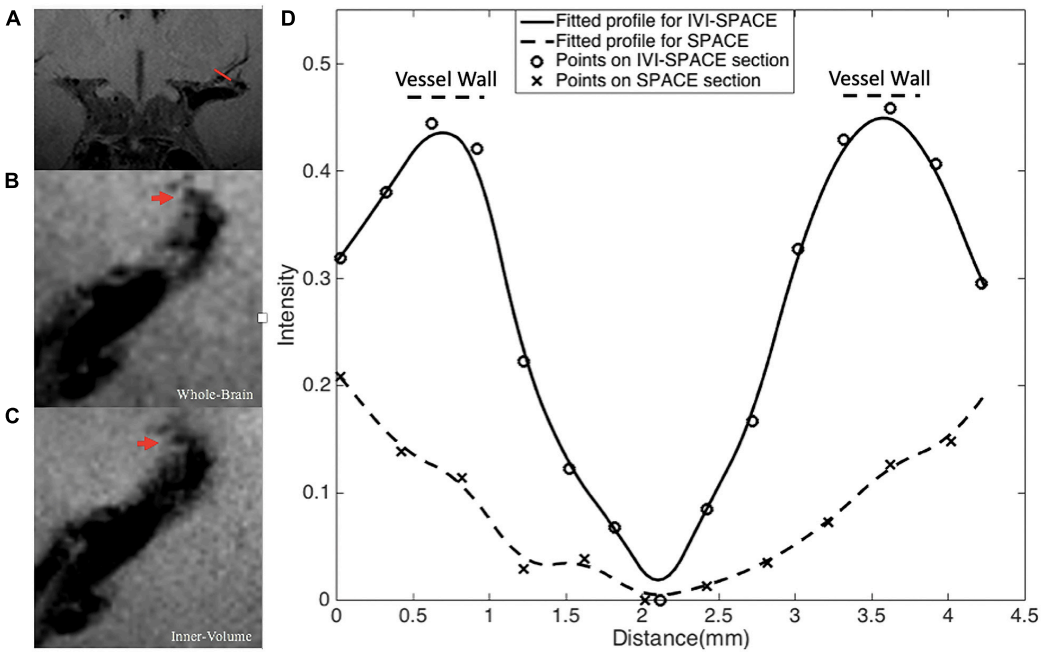

FIGURE 8 | The section view of an LSA that is only visible in the IV-SPACE image. The position of the section was at the red line in coronal view **(A)**. The sections of conventional SPACE and IV-SPACE are shown in **(B,C)**, respectively. The line profiles through the LSA lumen are also shown in **(D)**.

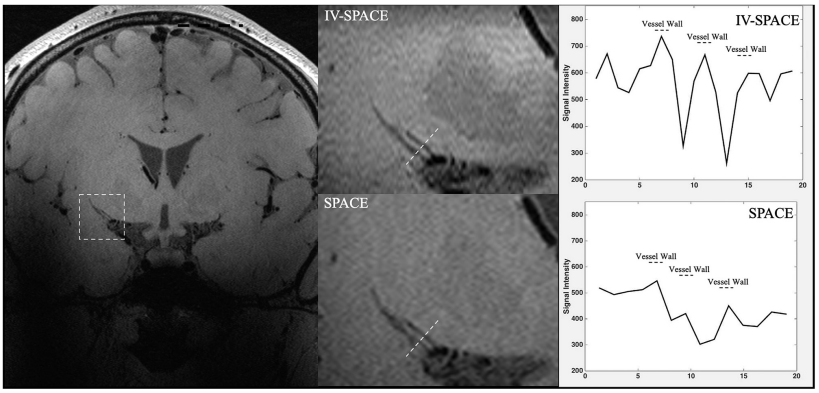

FIGURE 9 | The comparisons of IV-SPACE and conventional SPACE (using optimized RF pulse) in coronal plane. The enlarged image is displayed in the second column and line profiles through the LSA lumen is shown on the right column.

imaging of the LSA vessel wall is feasible in a population of healthy volunteers.

The numbers of stems of LSAs visualized by three methods showed no significant difference, demonstrating comparable abilities of these methods on displaying primary structures of LSAs. The higher number of branches of optimized methods may be due to the higher resolution reveals much more details. The lower number of branches in 2D RF methods may be due to interference of aliased signals caused by incomplete signal suppression outside ROI (**Figure 6**, white arrows). The optimization method achieves more thorough signal suppression and shows more details and more branches. Of course, it must be realized that the acquisition of higher resolution comes at the expense of the signal-to-noise ratio. However, the higher resolution at the expense of the SNR seems to be beneficial, because more branches are revealed, and the sacrifice of the SNR does not cause much damage to the image quality.

Conventional SPACE uses a non-selective pulse with whole-brain coverage. Slab-selective SPACE reduces the matrix size only in the head-foot direction, while the longer duration of the excitation pulse prolongs the occurrence of the first echo and reduces the SNR. In contrast, the optimized 2D SSE RF pulse reduces FOV in both the anterior-posterior and head-foot directions. Therefore, IV-SPACE needs a smaller acquisition matrix to cover MCA and LSA than conventional SPACE to achieve the same resolution. IV-SPACE can be used to reduce acquisition times or have a higher resolution. Moreover, the inherently long and symmetric slab-selective pulse requires an extra 180° pulse as the first echo to reduce the subsequent echo spacing. However, it is not needed with a spiral-in 2D SSE pulse, resulting in a stronger signal that is suitable for a perforating artery image.

A higher spatial resolution reduces the partial volume effect, so the LSA delineation is significantly improved in the IV-SPACE images in **Figure 7**. The reduction of the echo train length from 50 to 30 might also contribute to the sharpness of the vessel walls due to less signal decay (**Figure 8**). The sharper vessel wall potentially benefits the diagnosis and also the study of cerebral vascular diseases, such as the microvasculopathy in small vessel disease, quantitative evaluation of the aneurysmal wall, and microstructure of atherosclerotic plaques.

The initial results reported herein are encouraging as they demonstrate IV-SPACE to be a robust, reliable technique for imaging of LSA wall. Using the inner volume technique, it is possible to excite a small FOV without aliasing artifacts, thus yielding high-quality imaging within the selected volume of interest. As zoomed imaging reduces the acquisition matrix while maintaining acquisition time, higher spatial resolution (not previously implemented) is achieved. Thus, IV-SPACE imaging may become the preferred approach for VWI of LSA.

The work that can be done in the future is to extend the IV-SPACE sequence to 3T scanners. Due to the popularity of 3T scanners in the clinical environment, the IV-SPACE sequence may be widely used and may exhibit more advantages. The better homogeneity of the magnetic field at 3T (Ma et al., 2019) benefits the observation of the perforating arteries originating from the M2 segment, and the lower SAR value at 3T relaxed the restrictions on sequence parameters of the IV-SPACE. But the challenge of 3T is that the SNR is only half of that at 7T, which may hinder the depiction of the LSA wall clearly. Although the nominal resolution can be set to 0.30 mm, it certainly needs further improvement on the imaging sequence to compensate for the low SNR.

This study has several limitations. The first limitation is the small sample size and that only images from healthy volunteers were acquired, so it remains to be seen how these findings translate into the clinical evaluation of patients. However, vessel wall lesions generally thicken the wall, so it is believed that the IV-SPACE sequence will have a clearer depiction of the LSA wall. Another limitation is that collecting the field map and designing RF pulse for each subject is time-consuming, so some general pulse design methods should be considered for further study.

CONCLUSION

The inner-volume 3D TSE sequence was developed to achieve isotropic 0.30 mm within ten minus black-blood images within

a clinically acceptable time. A higher resolution produces sharper delineation of the vessel wall and lumen of intracranial perforating arteries. The technique is promising for the evaluation of microvasculopathies of cerebral vascular diseases.

DATA AVAILABILITY STATEMENT

The raw data supporting the conclusions of this article will be made available by the authors, without undue reservation.

ETHICS STATEMENT

The studies involving human participants were reviewed and approved by the Institutional Review Board of Beijing MRI Center for Brain Research. The patients/participants provided their written informed consent to participate in this study.

AUTHOR CONTRIBUTIONS

ZZ and QK: study concepts and design. QK, DW, and ZZ: sequence programming. QK: sequence test. QK and YW: data acquisition. QK, YW, and ZZ: data analysis and interpretation. QK: manuscript preparation. ZZ, YZ, and JA: manuscript editing. YZ and ZZ: manuscript review. All authors contributed to the article and approved the submitted version.

FUNDING

This study has received funding from the National Natural Science Foundation of China (82001804 and 8191101305), Ministry of Science and Technology of China (2017YFC1307904), Natural Science Foundation of Beijing Municipality (7191003), and Strategic Priority Research Program of Chinese Academy of Sciences (XDB32010300).

SUPPLEMENTARY MATERIAL

The Supplementary Material for this article can be found online at: https://www.frontiersin.org/articles/10.3389/fnins.2021.620172/full#supplementary-material

Supplementary Figure 1 | The line profile through the center of ROI before the normalization. The solid line is for the optimized pulse and the dashed line is the traditional pulse.

REFERENCES

Alley, M. T., Pauly, J. M., Sommer, F. G., and Pelc, N. J. (1997). Angiographic imaging with 2D RF pulses. *Magn. Reson. Med.* 37, 260–267. doi: 10.1002/mrm.1910370220

Bang, O. Y., Heo, J. H., Kim, J. Y., Park, J. H., and Huh, K. (2002). Middle cerebral artery stenosis is a major clinical determinant in striatocapsular small, deep infarction. *Arch. Neurol.* 59, 259–263. doi: 10.1001/archneur.59.2.259

Caplan, L. R. (1989). Intracranial branch atheromatous disease: a neglected, understudied, and underused concept. *Neurology* 39, 1246–1250. doi: 10.1212/WNL.39.9.1246

Fan, Z., Yang, Q., Deng, Z., Li, Y., Bi, X., Song, S., et al. (2017). Whole brain intracranial vessel wall imaging at 3 T esla using cerebrospinal fluid–attenuated T1-weighted 3 D turbo spin echo[J]. *Magn. Reson. Med.* 77, 1142–1150. doi: 10.1002/mrm.26201

Feinberg, D. A., Hoenninger, J. C., Crooks, L. E., Kaufman, L., Watts, J. C., Arakawa, M., et al. (1985). Inner volume MR imaging: technical concepts and their application. *Radiology* 156, 743–747. doi: 10.1148/radiology.156.3.4023236

Fisher, C. M. (1982). Lacunar strokes and infarcts: a review. *Neurology* 32, 871–876. doi: 10.1212/wnl.32.8.871

Harteveld, A. A., van der Kolk, A. G., van der Worp, H. B., Dieleman, N., Siero, J. C. W., Kuijf, H. J., et al. (2017). High-resolution intracranial vessel wall MRI in an elderly asymptomatic population: comparison of 3T and 7T. *Eur. Radiol.* 27, 1585–1595. doi: 10.1007/s00330-016-4483-3

Insko, E. K., and Bolinger, L. (1993). Mapping of the radiofrequency field. *J. Magn. Res.* 103, 82–85. doi: 10.1006/jmra.1993.1133

Kim, J. S., and Yoon, Y. (2013). Single subcortical infarction associated with parental arterial disease: important yet neglected sub-type of atherothrombotic stroke. *Int. J. Stroke* 8, 197–203. doi: 10.1111/j.1747-4949.2012.00816.x

Kong, Q. L., Zhang, Z. H., Yang, Q., Fan, Z. Y., Wang, B., An, J., et al. (2019). 7T TOF-MRA shows modulated orifices of lenticulostriate arteries associated with atherosclerotic plaques in patients with lacunar infarcts. *Eur. J. Radiol.* 118, 271–276. doi: 10.1016/j.ejrad.2019.07.032

Ma, S. J., Sarabi, M. S., Yan, L., Shao, X., Chen, Y., Yang, Q., et al. (2019). Characterization of lenticulostriate arteries with high resolution black-blood T1-weighted turbo spin echo with variable flip angles at 3 and 7 Tesla. *NeuroImage* 199, 184–193. doi: 10.1016/j.neuroimage.2019.05.065

Malik, S. J., and Hajnal, J. V. (2016). Phase relaxed localized excitation pulses for inner volume fast spin echo imaging. *Magn. Reson. Med.* 76, 848–861. doi: 10.1002/mrm.25996

Mandell, D. M., Mossa-Basha, M., Qiao, Y., Hess, C. P., Hui, F., Matouk, C., et al. (2017). Intracranial vessel wall MRI: principles and expert consensus recommendations of the American Society of Neuroradiology. *Am. J. Neuroradiol.* 38, 218–229. doi: 10.3174/ajnr.A4893

Meiboom, S., and Gill, D. (1958). Modified spin-echo method for measuring nuclear relaxation times. *Rev. Sci. Instrum.* 29, 688–691. doi: 10.1063/1.1716296

Mitsouras, D., Mulkern, R. V., and Rybicki, F. J. (2006). Strategies for inner volume 3D fast spin echo magnetic resonance imaging using nonselective refocusing radio frequency pulses. *Med. Phys.* 33, 173–186. doi: 10.1118/1.2148331

Pauly, J., Nishimura, D., and Macovski, A. (1989). A k-space analysis of small-tip- angle excitation. *J. Magn. Reson.* 81, 43–56. doi: 10.1016/0022-2364(89)90265-5

Qiao, Y., Steinman, D. A., Qin, Q., Etesami, M., Schär, M., Astor, B. C., et al. (2011). Intracranial arterial wall imaging using three-dimensional high isotropic resolution black blood MRI at 3.0 Tesla. *J. Magn. Reson. Imaging* 34, 22–30. doi: 10.1002/jmri.22592

Rosset, A., Spadola, L., and Ratib, O. (2004). OsiriX: an open-source software for navigating in multidimensional DICOM images. *J. Digit. Imaging* 17, 205–216. doi: 10.1007/s10278-004-1014-6

Van der Kolk, A. G., Zwanenburg, J. J. M., Brundel, M., Biessels, G. J., Visser, F., Luijten, P. R., et al. (2011). Intracranial vessel wall imaging at 7.0-T MRI. *Stroke* 42, 2478–2484. doi: 10.1161/STROKEAHA.111.620443

Yang, G. Z., Burger, P., Gatehouse, P. D., and Firmin, D. N. (1999). Locally focused 3D coronary imaging using volume-selective RF excitation. *Magn. Reson. Med.* 41, 171–178. doi: 10.1002/(SICI)1522-2594(199901)41:1<171::AID-MRM24<3.0.CO;2-5

Yip, C., Fessler, J. A., and Noll, D. C. (2005). Iterative RF pulse design for multidimensional, small-tip-angle selective excitation. *Magn. Reson. Med.* 54, 908–917. doi: 10.1002/mrm.20631

Zhu, C., Haraldsson, H., Tian, B., Meisel, K., Ko, N., Lawton, M., et al. (2016). High-resolution imaging of the intracranial vessel wall at 3 and 7 T using 3D fast spin echo MRI. *MAGMA* 29, 559–570. doi: 10.1007/s10334-016-0531-x

Conflict of Interest: QK and JA are employees of Siemens Healthcare, China. DW is an employee of Siemens Shenzhen Magnetic Resonance Ltd.

The remaining authors declare that the research was conducted in the absence of any commercial or financial relationships that could be construed as a potential conflict of interest.

frontiers in Neuroscience

ORIGINAL RESEARCH
published: 12 April 2021
doi: 10.3389/fnins.2021.608799

Baseline Cerebral Ischemic Core Quantified by Different Automatic Software and Its Predictive Value for Clinical Outcome

Zhang Shi[1†], Jing Li[1†], Ming Zhao[2,3†], Minmin Zhang[3], Tiegong Wang[1], Luguang Chen[1], Qi Liu[1], He Wang[4†], Jianping Lu[1*†] and Xihai Zhao[5]*

[1] Department of Radiology, Changhai Hospital, Naval Medical University, Shanghai, China, [2] Department of Neurology, The 983[th] Hospital of Joint Logistics Support Forces of Chinese PLA, Tianjin, China, [3] Department of Neurology, Changhai Hospital, Naval Medical University, Shanghai, China, [4] Institute of Science and Technology for Brain-Inspired Intelligence, Fudan University, Shanghai, China, [5] Department of Biomedical Engineering, Center for Biomedical Imaging Research, Tsinghua University School of Medicine, Beijing, China

OPEN ACCESS

Edited by:
Umar Sadat,
University of Cambridge,
United Kingdom

Reviewed by:
Qi Yang,
Capital Medical University, China
Beibei Sun,
Shanghai Jiao Tong University, China

****Correspondence:***
He Wang
hewang@fudan.edu.cn
Jianping Lu
cjr.lujianping@vip.163.com

[†] These authors have contributed equally to this work

Specialty section:
This article was submitted to Brain Imaging Methods, a section of the journal Frontiers in Neuroscience

Received: *21 September 2020*
Accepted: *25 February 2021*
Published: *12 April 2021*

Citation:
Shi Z, Li J, Zhao M, Zhang M, Wang T, Chen L, Liu Q, Wang H, Lu J and Zhao X (2021) Baseline Cerebral Ischemic Core Quantified by Different Automatic Software and Its Predictive Value for Clinical Outcome. Front. Neurosci. 15:608799. doi: 10.3389/fnins.2021.608799

Purpose: This study aims to investigate the agreement of three software packages in measuring baseline ischemic core volume (ICV) and penumbra volume (PV), and determine their predictive values for unfavorable clinical outcome in patients with endovascular thrombectomy (EVT).

Methods: Patients with acute ischemic stroke who underwent computed tomographic perfusion (CTP) were recruited. Baseline CTP measurements including ICV and PV were calculated by three software packages of IntelliSpace Portal (ISP), Rapid Processing of Perfusion and Diffusion (RAPID), and fast-processing of ischemic stroke (F-STROKE). All patients received EVT, and the modified Rankin scale (mRS) at 90 days after EVT was assessed to determine the clinical outcomes (favorable: mRS = 0–2; unfavorable: mRS = 3–6). The agreement of CTP measurements among three software packages was determined using intraclass correlation coefficient (ICC). The associations between CTP measurements and unfavorable clinical outcome were analyzed using logistic regression. Receiver operating characteristic curves were conducted to calculate the area under the curve (AUC) of CTP measurements in predicting unfavorable clinical outcome.

Results: Of 223 recruited patients (68.2 ± 11.3 years old; 145 males), 17.0% had unfavorable clinical outcome after EVT. Excellent agreement between F-STROKE and RAPID was found in measuring ICV (ICC 0.965; 95% CI 0.956–0.973) and PV (ICC 0.966; 95% CI 0.956–0.973). ICVs measured by three software packages were significantly associated with unfavorable clinical outcome before (odds ratios 1.012–1.018, all $P < 0.01$) and after (odds ratios 1.003–1.014, all $P < 0.05$) adjusted for confounding factors (age, gender, TOAST classification, and NIHSS on admission). In predicting unfavorable clinical outcome, ICV measured by F-STROKE showed similar performance to that measured by RAPID (AUC 0.701 vs. 0.717) but higher performance than that measured by ISP (AUC 0.629).

Conclusions: The software of F-STROKE has excellent agreement with the widely used analysis tool of RAPID in measuring ICV and PV. The ischemic core volume measured by both F-STROKE and RAPID is a stronger predictor for unfavorable clinical outcome after EVT compared to ISP.

Keywords: ischemic stroke, penumbra, computed tomography, perfusion imaging, outcome, software

INTRODUCTION

The current challenges in the management of acute ischemic stroke (AIS) owing to large-vessel occlusion (LVO) mainly include predicting the clinical outcome before endovascular thrombectomy (EVT), optimizing imaging analysis methods for patient selection, and evaluating the therapeutic strategy. Several recent studies demonstrated that the measurements of acute ischemic core volume (ICV) and penumbra volume (PV) have been considered as effective predictors for clinical outcome in patients receiving EVT (Bivard et al., 2015; Fiehler et al., 2019). It is well evidenced that endovascular therapy will be more beneficial for patients with a small infarct core and a large penumbra, whereas patients with a large ischemic core are at risk of developing unfavorable clinical outcome after EVT (Wannamaker et al., 2018). Therefore, accurately and reliably measuring ICV and PV is important for predicting clinical outcomes (Austein et al., 2016).

Computed tomographic perfusion (CTP) is widely used to evaluate cerebral ischemic status by calculating the perfusion maps of cerebral blood flow (CBF) and time to maximum (T_{max}) (Austein et al., 2016). The calculation of these quantitative CTP measurements is based on different algorithms and combined in different ways to quantitatively estimate the extent of the ischemic core and penumbral tissue (Murphy et al., 2006; Wintermark et al., 2006), which have been proved to be a predictor for clinical outcomes in patients treated with reperfusion strategies (Albers et al., 2018; Nogueira et al., 2018; Vinny et al., 2018). Recently, semi-automatic commercialized CTP software, such as brain CTP package of IntelliSpace Portal (ISP), is broadly used for measuring cerebral perfusion in the routine clinical workup. Despite the widespread utility, complex postprocessing, variability in image acquisition capabilities, and a lack of standardization of perfusion thresholds have hampered the use of ISP in clinical settings (Wintermark et al., 2006). In contrast, automatic and operator-independent CTP software packages, such as Rapid Processing of Perfusion and Diffusion (RAPID), could overcome above limitations and enable routine diagnostic workup of acute stroke, (Rose et al., 2001; Yin et al., 2015; Pinto et al., 2018) which has been utilized to quantify ischemic lesions in many randomized control trials on EVT (Straka et al., 2010). However, some disadvantages of the RAPID software package still exist. Fast-processing of ischemic stroke (F-STROKE), a fully automatic processing software, which is similar to RAPID, can segment and label large vessels, parenchyma, and cerebrospinal fluid according to their time-intensity curves. F-STROKE could avoid the incorrect labeling on those low-signal volumes, including cerebrospinal fluid and arachnoid cysts. However, whether F-STROKE could improve the accuracy in measuring ICV and PV as compared with ISP and RAPID software packages is unknown.

Furthermore, investigators reported that the final infarct core and the growth of volume of infarct region were strongly associated with clinical outcomes (Austein et al., 2016; Albers et al., 2018; Nogueira et al., 2018). However, there is no consensus on the optimal CTP measurements at baseline, which could accurately predict clinical outcomes after EVT. The predictive value of ICV and PV measured by F-STROKE for clinical outcomes in patients receiving EVT is also unclear.

In the present study, we sought to investigate the agreement of F-STROKE with ISP and RAPID software packages in measuring ICV and PV using CTP data. The second aim of this study was to determine the predictive value of ICV and PV measured by F-STROKE for unfavorable clinical outcome in patients with EVT.

MATERIALS AND METHODS

Patients

Patients with AIS who underwent CTP and referred to EVT with and without intravenous alteplase between September 2017 and December 2018 were retrospectively recruited in this study. The inclusion criteria were as follows: (1) age $\geq$ 18 years old; (2) AIS caused by LVO of the anterior circulation (the intracranial segment of internal carotid artery, M1 segment of the middle cerebral artery, or proximal M2 segment of the middle cerebral artery); and (3) National Institutes of Health Stroke Scale (NIHSS) $\geq$ 6 (acute stroke with substantial neurological deficits). Patients were excluded if they had: (1) intracranial hemorrhage; (2) the modified Rankin scale (mRS) $>$ 2 at baseline; or (3) severe motion artifacts or poor cardiac output generating erroneous CTP data. The study protocol was approved by the Institutional Review Board of Changhai Hospital of Shanghai, and all patients provided written informed consent.

Clinical Assessment

Clinical data including age; gender; medical history, including hypertension, hyperlipidemia, diabetes, smoking, drinking, and heart disease; and clinical scales including Glasgow Coma Scale, NIHSS, and mRS were collected from the medical record. The Trial of Org10172 in Acute Stroke Treatment (TOAST) classification was used to classify stroke types. The NIHSS assessment was performed at baseline (on admission), 1 and 24 h after EVT. The mRS was assessed at discharge and 90 days after EVT. The favorable clinical outcome after EVT was defined as a

90-days mRS of 0–2, and the unfavorable one was defined as a 90-days mRS of 3–6 (Albers et al., 2018; Nogueira et al., 2018).

CT Examinations

All CT scans were performed on a 256-slice CT scanner (Brilliance iCT, Philips Healthcare, Cleveland, OH, United States), which included scanning parameters (non-contrast CT) and reconstruction parameters [Computed tomographic angiography (CTA) and CTP]. The scanning parameters for helical non-contrast CT were as follows: tube voltage 120 kV, tube current 350 mAs, thickness 5 mm, slice number 30, field-of-view (FOV) 250 × 250 mm^2, and matrix 496 × 496. The imaging parameters for CTP were as follows: tube voltage 80 kV, tube current 180 mAs, whole-brain coverage in the Z-axis, FOV 220 × 220 mm^2, matrix 512 × 512, slice thickness 5 mm, and 14 consecutive phases acquired with a temporal resolution of 4 s. A total of 50 mL of iobitridol (Xenetix-350; Guerbet, France) was intravenously injected with a flow rate of 5 mL/s, followed by a 20-mL saline flush with the same flow rate. CTA was performed after 3 min once CTP was completed with the following parameters: tube voltage 120 kV, tube current 300 mAs, FOV 220 × 220 mm^2, matrix 512 × 512, slice thickness1 mm, and slice number 399. The same contrast agent was injected intravenously with the same flow rate to CTP, and the dose of contrast agent was 45 mL.

Post-processing of Computed Tomographic Perfusion Images

Computed tomographic perfusion images were processed using three common commercial software independently:

IntelliSpace Portal

Brain CTP package of ISP Version 10.1 (Philips Health System, Best, Netherlands) offers a semi-automatic way to process CTP data, including computation of delay-insensitive parameter. ISP is a software program that requires human intervention. In this analysis, one observer (ZS) who was blinded to clinical information, and the results of the analysis using other two software utilized ISP to adjust the location of the seeds in the M1 segment of middle cerebral artery and the superior sagittal sinus to obtain the arterial inflow function, venous outflow function, and cerebral mid-line. Default 2D motion correction and brain map were used. During the calculation phase, an arrival-time-insensitive method was chosen to calculate relative CBF and $T_{\max}$. To make it comparable with RAPID software, the summary map was generated with impaired perfusion as $T_{\max} > 6$s and severely impaired perfusion (considered as ischemic core) as relative CBF < 30% compared to the contralateral hemisphere.

Rapid Processing of Perfusion

Rapid processing of perfusion and diffusion (iSchemaView, Menlo Park, CA, United States) is a DICOM-In/DICOM-Out black box server, which automatically processes CT perfusion data. This software is tested and wildly used by many hospitals and research centers (Albers et al., 2018; Nogueira et al., 2018). RAPID also additionally provides a graphic user interface on the webpage to offer limited manual adjustment. It defines CBF < 30% as an ICV and relative $T_{\max} > 6$s of that in normal tissue as PV, which was the inclusion criteria of the recent clinical trials of DEFUSE 3 (Albers et al., 2018) and DAWN (Nogueira et al., 2018).

Fast-Processing of Ischemic Stroke

Fast-processing of ischemic stroke software (Version 1.0; Neuroblem Ltd. Company, Shanghai, China) is a software running on Windows 64 server. It provides a fully automatic CTP processing combined with manual rerun mechanism in a Windows graphic user interface. It segments large vessels, parenchyma, bone, cerebrospinal fluid according to their time-intensity curves and labels the region of either ischemic core or penumbra in the time-intensity curve of parenchyma, which could avoid the incorrect labeling on those low-signal volumes, such as an arachnoid cyst. Similar to RAPID (Straka et al., 2010), F-STROKE calculates (1) $T_{\max}$, (2) relative cerebral blood volume (rCBV), (3) relative CBF (rCBF), and (4) mean transit time but with only arterial inflow function input.

$$T_{\max} = \arg\max_t (r(t)) \tag{1}$$

$$\mathrm{rCBV} = H \int c_t(t)\,\mathrm{d}t \tag{2}$$

$$\mathrm{rCBF} = 60H \int c_a(t)\,\mathrm{d}t \left[\max_t (r(t))\right] \tag{3}$$

$$c_t(t) = c_a(t) \times r(t) \tag{4}$$

where $r(t)$ is tissue property, $c_t(t)$ is the perfusion image signal, $c_a(t)$ is arterial inflow function, and H is a pre-defined constant.

To make it comparable with RAPID results, thresholds of $T_{\max} > 6$s and relative CBF < 30% compared to the median relative CBF of brain tissues were configured to calculate ICV and PV, respectively. Note that using CBF with or without venous outflow function input to calculate infarct core volume is mathematically identical. Since per selection of vein output function $c_v(t)$,

$$\mathrm{CBF} \propto \frac{\mathrm{rCBF}}{\int c_v(t)\,\mathrm{d}t}$$

And when divided by median of relative CBF, $\int c_v(t)\,\mathrm{d}t$ along with other constant is eliminated as a scaling factor.

Statistical Analysis

The calculation of sample size was based on a two independent sample unpaired t-test with 0.80 power and 0.05 significance level (two sided). The ratio of favorable group vs. unfavorable group is 4:1. The mean and standard deviation (SD) of ICV in favorable group are 25.5 and 36.0, while the mean and SD are 64.5 and 62.9 in unfavorable group. Considering the image quality and follow-up censoring rate is 15–20% in our study, a sample size of 76 patients in favorable group and 19 in unfavorable group was needed based on PASS 15 software.

Mean values and SD were described for the continuous variables with normal distribution while median values and

interquartile ranges (IQRs) were calculated for continuous variables with abnormal distribution. CTP measurements were compared among three software packages using the Friedman test with Bofferoni correction or Chi-square analysis. The agreement of CTP measurements between two software packages was determined using intraclass correlation coefficient (ICC) and Bland-Altman analysis. The agreement categories include poor (ICC < 0.4), fair to good (ICC 0.4–0.75), and excellent (ICC > 0.75) agreement. Continuous variables and categorical variables were compared between patients with unfavorable and favorable clinical outcome using independent *t* test, Mann-Whitney *U* test, or Chi-square test. Univariate and multivariate logistic regression analyses were performed to calculate the odds ratios (ORs) and corresponding 95% confidence intervals (CIs) of CTP measurements in predicting unfavorable clinical outcome. Receiver operating characteristic (ROC) curves were also conducted to calculate the area under curve (AUC) of CTP measurements in discriminating unfavorable clinical outcome. ROC curves were compared using the method developed by DeLong et al. (1988). *P* values of <0.05 were considered statistically significant. All statistical analyses were performed with IBM SPSS Statistics 24.0 (SPSS Inc an IBM Company, Chicago, IL, United States).

RESULTS

Clinical Characteristics

A total of 245 patients were recruited in this study, of which 22 were excluded due to pre-stroke cases (n = 9), motion artifacts (n = 8), and poor cardiac output (n = 5). Of the remaining 223 patients, 145 are male, and the mean age was 68.2 ± 11.3 years old. **Table 1** summarized the baseline clinical characteristics of this study population. Of 223 patients, 38 (17.0%) had unfavorable clinical outcome and 185 (83.0%) patients had favorable clinical outcome after EVT, respectively. Patients with unfavorable clinical outcome had less atherosclerotic stroke (44.7 vs. 60.0%, P = 0.040) and higher NIHSS [22.4 (IQR 17.0–29.0) vs. 16.5 (IQR 12.0–22.0), P < 0.001] at baseline compared with those with favorable clinical outcome. No significant differences were found in other clinical characteristics between patients with unfavorable and favorable clinical outcome (all P > 0.05).

During EVT treatment, 63.2% of patients with unfavorable clinical outcome were beyond 6 h, whereas this percentage in those with favorable clinical outcome was 28.1%. In contrast, during EVT treatment, the prevalence of not using intravenous alteplase in patients with unfavorable clinical outcome was lower than that of those with favorable outcome (17.6 vs. 82.4%). The NIHSS [22.3 (16.8–28.0) vs. 11.7 (IQR 7.0–17.0), P < 0.001] and mRS [4.9 (4.0–5.0) vs. 1.3 (IQR 0–2.0), P < 0.001] at discharge in patients with unfavorable clinical outcomes were significantly higher than those in patients with favorable clinical outcomes. After EVT treatment, 90.1% of patients achieved successful recanalization (mTICI 2b, n = 64; mTICI 3, n = 137), while 9.9% did not (mTICI 1, n = 9; mTICI 2a, n = 13). Additionally, there were four patients suffered from fresh hemorrhage and nine with fresh infarct after EVT treatment.

Comparison and Agreement of Computed Tomographic Perfusion Measurements Among Three Software Packages

The value of ICV measured by ISP was significantly greater than that measured by RAPID [29.7 mL (IQR 11.5–56.7) vs. 13.9 mL

TABLE 1 | Baseline demographic and clinical characteristics (n = 232).

	Mean ± SD, median (IQR), or *n* (%)			
	All patients (n = 223)	**Unfavorable outcome (n = 38)**	**Favorable outcome (n = 185)**	***P* value**
Age	68.2 ± 11.3	70.9 ± 10.8	67.6 ± 11.4	0.095
Sex, male	145 (65.0)	22 (57.9)	123 (66.5)	0.312
Diabetes mellitus	45 (20.2)	9 (23.7)	36 (19.5)	0.554
Hypertension	136 (61.0)	27 (71.1)	109 (58.9)	0.163
Hyperlipidemia	25 (11.2)	5 (13.2)	20 (10.8)	0.777
Smoking	42 (18.8)	5 (13.2)	37 (20.0)	0.326
Atrial fibrillation	82 (36.8)	14 (36.8)	68 (36.8)	0.992
Valvular heart disease	32 (14.3)	5 (13.2)	27 (14.6)	0.818
Coronary atherosclerotic disease	23 (10.3)	3 (7.9)	20 (10.8)	0.773
TOAST classification				0.040
Atherosclerotic	128 (57.4)	17 (44.7)	111 (60.0)	
Cardioembolic	67 (30)	13 (34.2)	54 (29.2)	
Other	15 (6.7)	4 (10.5)	11 (5.9)	
Undetermined	13 (5.8)	4 (10.5)	9 (4.9)	
Glasgow Coma Scale	12.0 (9.0–15.0)	11.1 (9.0–14.0)	11.6 (9.0–15.0)	0.440
NIHSS on admission	17.0 (12.0–23.0)	22.4 (17.0–29.0)	16.5 (12.0–22.0)	<0.001
Thrombectomy strategy				0.583
With intravenous alteplase	36 (16.1)	5 (13.2)	31 (16.8)	
Without intravenous alteplase	187 (83.9)	33 (86.8)	154 (83.2)	

SD, standard deviation; IQR, interquartile range; TOAST, The Trial of Org10172 in Acute Stroke Treatment; NIHSS, National Institutes of Health Stroke Scale.

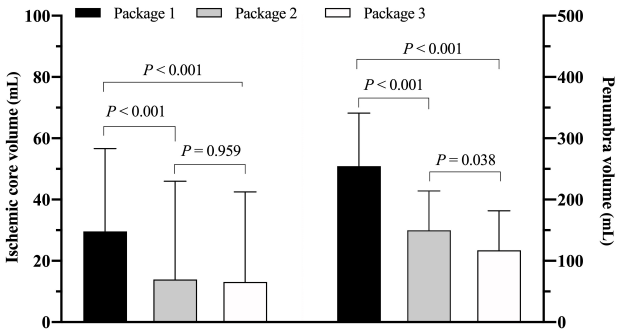

FIGURE 1 | Comparison of ischemic core volume in panel **(A)** and penumbra volume in panel **(B)** among three software packages [Package 1: IntelliSpace portal (ISP); Package 2: Rapid processing of perfusion and diffusion (RAPID); Package 3: Fast-processing of ischemic stroke (F-STROKE)].

(IQR 0–46.0), $P < 0.001$] and F-STROKE [29.7 mL (IQR 11.5–56.7) vs. 13.1 mL (IQR 0–42.5), $P < 0.001$] (**Figure 1A**). No significant difference was found in the measurement of ICV between RAPID and F-STROKE ($P = 0.959$). The PV measured by ISP was significantly greater than that measured by RAPID [254.5 mL (IQR 172.2–341.2) vs. 150.0 mL (IQR 92.0–214.0), $P < 0.001$] and F-STROKE [254.5 mL (IQR 172.2–341.2) vs. 117.1 mL (IQR 70.9–181.8), $P < 0.001$] (**Figure 1B**). The PV measured by F-STROKE was significantly smaller than that measured by RAPID ($P = 0.038$) (**Figure 1B**).

In measuring ICV, the software of ISP showed fair to good agreement with RAPID (ICC 0.693; 95% CI 0.622–0.753) and F-STROKE (ICC 0.656; 95% CI 0.578–0.722). Excellent agreement was found between RAPID and F-STROKE (ICC 0.965; 95% CI 0.956–0.973) in measuring ICV. Similarly, in measuring PV, ISP showed fair to good agreement with RAPID (ICC 0.646; 95% CI 0.567–0.714) and F-STROKE (ICC 0.604; 95% CI 0.517–0.678), but excellent agreement was found between RAPID and F-STROKE (ICC 0.966; 95% CI 0.956–0.973). The Bland-Altman analysis showed that F-STROKE (mean bias 1.6; 95% CI –19.2 to 22.4) showed smaller bias than ISP (mean bias 9.0; 95% CI –52.0 to 70.0) as compared with RAPID in measuring ICV (**Figure 2A**). Similarly, F-STROKE (mean bias 22.2; 95% CI –27.7 to 72.2) showed smaller bias than ISP (mean bias 110.2; 95% CI –76.9 to 297.2) as compared with RAPID in measuring PV (**Figure 2B**).

Association Between Computed Tomographic Perfusion Measurements and Unfavorable Clinical Outcomes

Patients with unfavorable clinical outcome had significantly larger ICV measured by all three software packages compared to those with favorable clinical outcome (all $P < 0.01$, **Figure 3**). There was no significant difference in PV measured by any software package between patients with unfavorable and favorable clinical outcome (all $P > 0.05$, **Figure 3**).

Table 2 summarized the results of the regression analysis. Univariate logistic regression showed that ICV measured by any software package was significantly associated with unfavorable clinical outcome (OR 1.012 to 1.018, all $P < 0.01$). After adjusted for confounding factors of the baseline data including age, gender, TOAST classification, and NIHSS on admission, these associations remained statistically significant (OR 1.012–1.028, all $P < 0.05$). No significant associations were found between PV measured by any software package and unfavorable clinical outcome before and after adjusted for confounding factors of the baseline data (all $P > 0.05$).

Receiver Operating Characteristic Analysis

Receiver operating characteristic analysis showed that, in predicting unfavorable clinical outcome, RAPID had the highest AUC (0.717, 95% CI 0.577–0.832), followed by F-STROKE (0.701, 95% CI 0.548–0.831) and ISP (0.629, 95% CI 0.499–0.739) (**Figure 4A**). Furthermore, in predicting unfavorable clinical outcome among the patients with complete reperfusion after EVT (mTICI = 3), the AUC values of F-STROKE (0.879, 95% CI 0.794–0.931), RAPID (0.858, 95% 0.788–0.919), and ISP (0.717, 95% CI 0.633–0.792) were significantly improved (**Figure 4B**). However, there was no significant difference in the AUC values between RAPID and F-STROKE in all patients ($z = 1.563$; $P = 0.118$) or in patients achieving the complete reperfusion ($z = 1.422$; $P = 0.155$).

DISCUSSION

This study investigated the agreement between three software packages of ISP, RAPID, and F-STROKE in measuring ICV and PV using CTP data and determine their performance in predicting unfavorable clinical outcome after EVT. We found excellent agreement and smaller bias between F-STROKE and RAPID in measuring both ICV and PV. In predicting unfavorable clinical outcome, the ICV measured by F-STROKE showed similar strength to that measured by RAPID but higher strength than that measured by ISP. Our study indicated that the software package of F-STROKE might be an alternative analysis tool for CTP data, and the measurements of F-STROKE may have the potential in predicting adverse prognosis after EVT.

In the present study, we found that the software package of F-STROKE had an excellent agreement with RAPID in measuring ICV and PV. Similar to RAPID, F-STROKE provided a fully automatic CTP processing and defined CBF < 30% as ICV and relative T_{max} > 6s of that in normal tissue as PV. In the algorithm of F-STROKE, the thresholds of T_{max} > 6s and relative CBF < 30% compared to the median relative CBF of brain tissues were calculated with only arterial inflow function input, which is similar to RAPID. The present study also showed fair to good agreement between ISP and RAPID and F-STROKE, and the bias between F-STROKE and RAPID was smaller than that between ISP and RAPID in measuring ICV and PV. This may indicate that software package with automatic segmentation and calculation would be more accurate in measuring the volume of ischemic lesions than semi-automatic software package of ISP. Although ISP could create the CTP maps and quantify ICV and PV

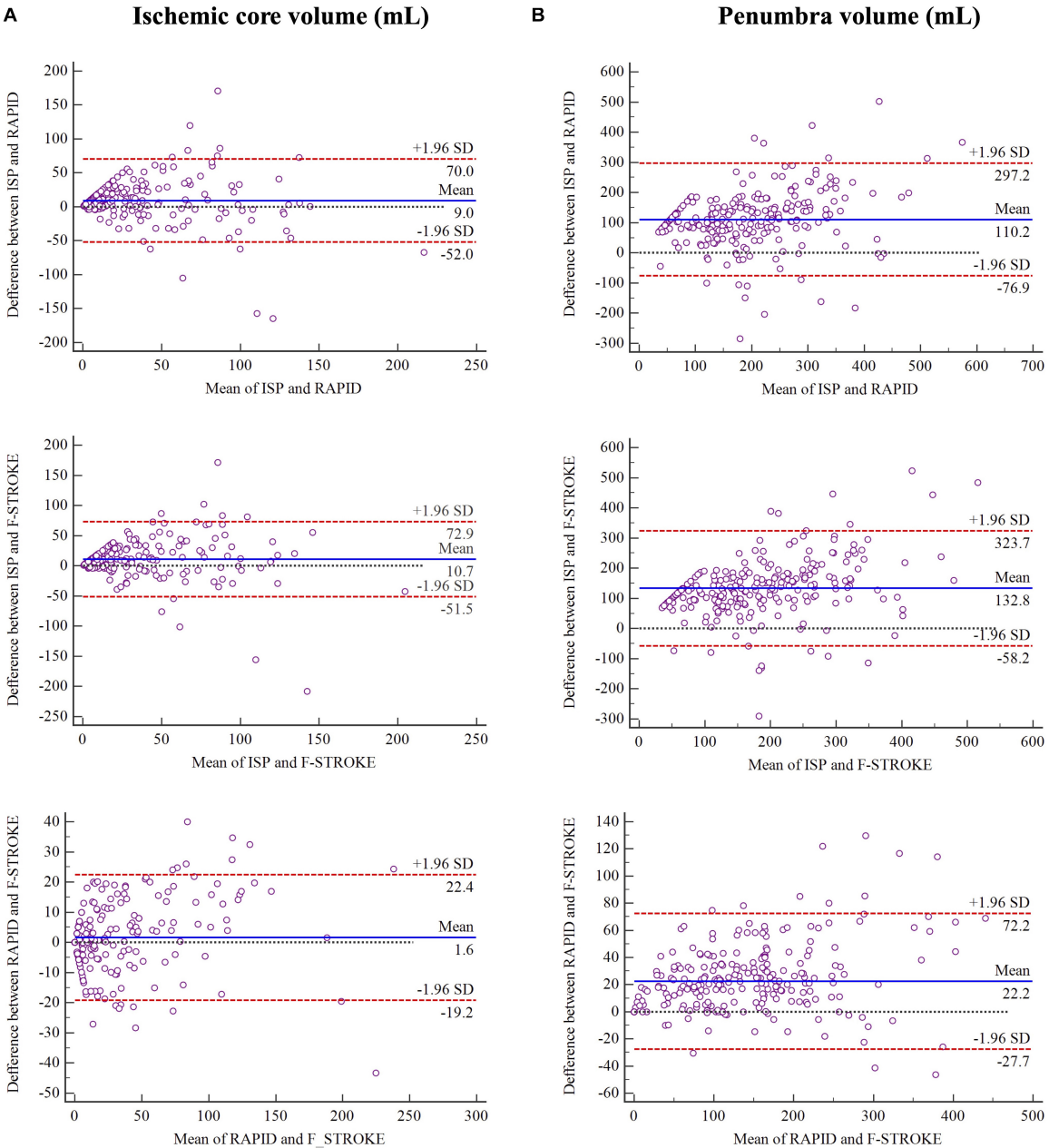

FIGURE 2 | Bland-Altman plots for the agreement and bias in measuring ischemic core volume in panel **(A)** and penumbra volume in panel **(B)** between any two software packages.

automatically, the regions of ischemic core and penumbra should be manually segmented by the radiologists, which may introduce subjective bias due to the experience and the measurements. Notably, our results illustrated that the PV measured by F-STROKE was significantly smaller than that measured by RAPID (P = 0.038). Because large vessels, parenchyma, bone, and cerebrospinal fluid were segmented by F-STROKE according to time-intensity curves and the labeled region of ischemic core in the time-intensity curve of parenchyma, this will avoid the incorrect labeling on those low-intensity volumes, such as an arachnoid cyst. Therefore, the differences identified by these two software packages could be attributed to the over the removal of cerebrospinal by RAPID (**Supplementary Figure 1**).

We found the baseline ICV measured by any software package was an independent predictor for unfavorable clinical outcome after EVT. Although some previous studies (Austein et al., 2016; Albers et al., 2018; Nogueira et al., 2018) showed that the final infarct core and the growth of volume of infarct region were strongly associated with the functional outcomes, the assessment

TABLE 2 | Association between CTP measurements and unfavorable clinical outcome.

	Univariate Logistic Regression			Multivariate Logistic Regression*		
	OR	**95% CI**	***P* value**	**OR**	**95% CI**	***P* value**
Ischemic core volume						
ISP	1.012	1.004–1.020	0.004	1.012	1.003–1.021	0.010
RAPID	1.016	1.009–1.024	<0.001	1.024	1.012–1.036	<0.001
F-STROKE	1.018	1.010–1.027	<0.001	1.028	1.014–1.042	<0.001
Penumbra volume						
ISP	1.002	1.000–1.015	0.083	1.001	0.996–1.004	0.975
RAPID	1.002	0.999–1.006	0.219	0.993	0.987–0.999	0.064
F-STROKE	1.003	0.999–1.007	0.133	0.992	0.986–0.999	0.058

**Adjustment: age, gender, TOAST classification, and NIHSS on administration. OR, odds ratio; CI, confidence interval.*

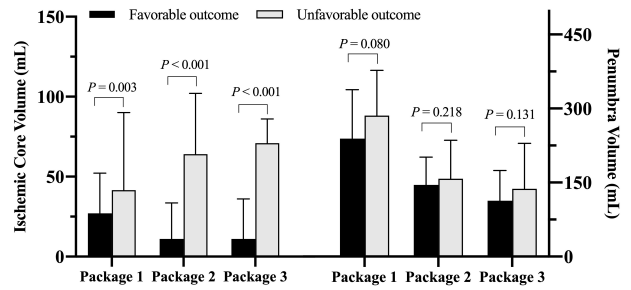

FIGURE 3 | Comparison of ischemic core volume and penumbra volume measured by three software packages between patients with favorable and unfavorable clinical outcomes after endovascular thrombectomy (EVT) (Package 1: ISP; Package 2: RAPID; Package 3: F-STROKE).

of baseline ICV was still indispensable and crucial for selecting patients before undergoing either EVT or IVT and predicting their clinical outcomes (Chen et al., 2019). Recently, Panni et al. (2019) reported that increased baseline diffusion-weighted imaging (DWI) lesion volume was the strongest predictors for 90-days mortality in stroke patients with a large ICV. However, in these studies, the attention was only paid to the large ICV, and investigators did not evaluate the relationship between ICV and the subsequent clinical outcomes. In our data, patients with smaller baseline ICV would benefit from EVT compared to those with large one regardless of the penumbral size at baseline. Our finding was similar to the previous study of International Stroke Perfusion Imaging Registry (INSPIRE) (Chen et al., 2019). This indicated that ICV might have a stronger correlation with clinical outcome compared with PV. However, Chen et al. (2019) investigated that the patients with a larger baseline ICV who underwent EVT would be achieving a greater clinical benefit compared to intravenous thrombolysis alone. But our finding considered the smaller baseline ICV as a strong predictor of favorable clinical outcome in the patients suffering from EVT, which indicated the size of injured brain tissue. Furthermore, an

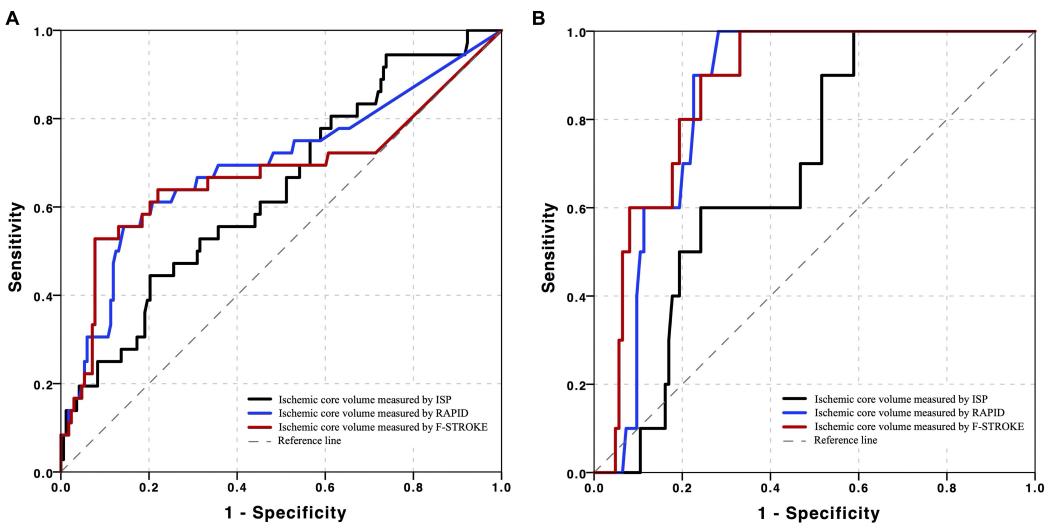

FIGURE 4 | Receiver operating characteristic (ROC) curves of ischemic core volume calculated by three computed tomographic perfusion (CTP) software packages in predicting unfavorable clinical outcomes in all the patients in panel **(A)** and patients achieved complete reperfusion in panel **(B)** after EVT.

increasing number of studies (Miles and Knuckey, 1998; Radak et al., 2017) reported that apoptosis might contribute to the death of a significant proportion of neurons during AIS, and the ischemic core of the brain experienced a sudden reduction of blood flow, overproduction of free radicals, an overload of Ca^{2+}, and excitotoxicity as well as necrosis started in the first hours after the onset of AIS in the ischemic core (Radak et al., 2017). However, apoptosis within the ischemic penumbra may occur after several hours or days. Therefore, when patients suffered from EVT within the time window of the recovery (<6 h), the ischemic region of the brain, especially in the penumbral area, would be reperfused and saved, but the ischemic core would not. This may be the molecular reason why the patients who had larger ICV achieved unfavorable outcomes.

Our data showed that, in predicting unfavorable clinical outcome, the ICV measured by F-STROKE had similar performance to that measured by RAPID. These results may be explained by our findings of excellent consistency in the measurement of ICV between F-STROKE and RAPID. F-STROKE utilized the similar algorithm and standard definition of ischemic parameters with RAPID, which is a reliable CTP software validated by many RCTs (Campbell et al., 2015; Albers et al., 2018; Nogueira et al., 2018; Vinny et al., 2018). Additionally, we found that both RAPID and F-STROKE had stronger predictive value for an unfavorable clinical outcome compared to ISP. This result may be contributed to the automatic computation based on the robust algorithm of RAPID and F-STROKE. In contrast, there was subjective bias from manual segmentation of ISP. Of note, the AUC values of ICV measured by the two automatic software packages of F-STROKE and RAPID for predicting unfavorable clinical outcome in our study were higher among patients who achieved complete recanalization after EVT. Our results are in line with the previous study by Chen et al. (2019) (AUC = 0.868).

There are several limitations to our study. First, we only explored the predictive value of baseline CTP measurements by F-STROKE for clinical outcomes of acute stroke patients after EVT. Future studies are warranted to determine the performance of ICV measured by F-STROKE in predicting clinical outcome with other treatments. Second, our study only focused on the short-term clinical outcome (mRS at 90 days) after EVT. The predictive value of CTP measurements by F-STROKE for long-term clinical outcome will be explored in future studies. And the lack of golden standard for baseline ischemic core and PV might be another important limitation. Third, we didn't do a direct comparison of the regions intensified by the three software packages since the voxels of the labeled regions could not be gotten due to the commercial reasons. And although CTP has an additional diagnostic value for detection of AIS in the anterior and posterior circulation, this study only recruited the patients with anterior circulation AIS. Further studies on both circulation ischemic status should be included together. Last, this study evaluated the consistency of two automatic software packages (F-STROKE and RAPID) in measuring CTP data. However, CTP examination has ionizing radiation and does not apply for patients with allergy to iodine or renal dysfunction. Recently, investigators demonstrated that MR perfusion, particularly dynamic susceptibility contrast (Seiler et al., 2020; Seners et al., 2020; Zhu et al., 2020) and arterial spin labeling-based perfusion techniques (Nael et al., 2013; Tan et al., 2018; Yu et al., 2018), can be reliably utilized to assess cerebral ischemic lesions. It is valuable to test the performance of F-STROKE in analyzing MR perfusion data in future studies.

DATA AVAILABILITY STATEMENT

The raw data supporting the conclusions of this article will be made available by the authors, without undue reservation.

ETHICS STATEMENT

The studies involving human participants were reviewed and approved by Institutional Review Board of Changhai Hospital of Shanghai. The patients/participants provided their written informed consent to participate in this study.

AUTHOR CONTRIBUTIONS

ZS, JLi, and MZO contributed to the study concept and design, analysis and interpretation of data, drafting/revising the manuscript for content, and statistical analysis. MZN and TW were involved in analysis and interpretation of data, drafting/revising the manuscript for content, and statistical analysis. LC performed analysis and interpretation of data. QL took part in the study concept and design, analysis, and interpretation of data. HW, JLU, and XZ contributed to the study concept and design, acquisition, analysis, and interpretation of data, and drafting/revising the manuscript for content. All authors reviewed this manuscript and approved the version to be published.

FUNDING

This research was supported by the National Key R&D Program of China (Grant No. 2018YFC1312900), National Natural Science Foundation of China (Grant Nos. 81670396, 31470910, and 81971583), and Shanghai Municipal Science and Technology Major Project (Grant Nos. 2017SHZDZX01 and 2018SHZDZX01).

ACKNOWLEDGMENTS

We would like to thank Dr. Ming Yang for providing the F-STROKE software.

SUPPLEMENTARY MATERIAL

The Supplementary Material for this article can be found online at: https://www.frontiersin.org/articles/10.3389/fnins.2021.608799/full#supplementary-material

REFERENCES

Albers, G. W., Marks, M. P., Kemp, S., Christensen, S., Tsai, J. P., Ortega-Gutierrez, S., et al. (2018). Thrombectomy for stroke at 6 to 16 hours with selection by perfusion imaging. *N. Engl. J. Med.* 378, 708–718.

Austein, F., Riedel, C., Kerby, T., Meyne, J., Binder, A., Lindner, T., et al. (2016). Comparison of perfusion CT software to predict the final infarct volume after thrombectomy. *Stroke* 47, 2311–2317. doi: 10.1161/strokeaha.116.013147

Bivard, A., Levi, C., Krishnamurthy, V., McElduff, P., Miteff, F., Spratt, N. J., et al. (2015). Perfusion computed tomography to assist decision making for stroke thrombolysis. *Brain* 138, 1919–1931. doi: 10.1093/brain/awv071

Campbell, B. C., Mitchell, P. J., Kleinig, T. J., Dewey, H. M., Churilov, L., Yassi, N., et al. (2015). Endovascular therapy for ischemic stroke with perfusion-imaging selection. *N. Engl. J. Med.* 372, 1009–1018.

Chen, C., Parsons, M. W., Levi, C. R., Spratt, N. J., Miteff, F., Lin, L., et al. (2019). Exploring the relationship between ischemic core volume and clinical outcomes after thrombectomy or thrombolysis. *Neurology* 93, e283–e292.

DeLong, E. R., DeLong, D. M., and Clarke-Pearson, D. L. (1988). Comparing the areas under two or more correlated receiver operating characteristic curves: a nonparametric approach. *Biometrics* 44, 837–845. doi: 10.2307/2531595

Fiehler, J., Thomalla, G., Bernhardt, M., Kniep, H., Berlis, A., Dorn, F., et al. (2019). Eraser. *Stroke* 50, 1275–1278.

Miles, A. N., and Knuckey, N. W. (1998). Apoptotic neuronal death following cerebral ischaemia. *J. Clin. Neurosci.* 5, 125–145. doi: 10.1016/s0967-5868(98)90027-3

Murphy, B. D., Fox, A. J., Lee, D. H., Sahlas, D. J., Black, S. E., Hogan, M. J., et al. (2006). Identification of penumbra and infarct in acute ischemic stroke using computed tomography perfusion-derived blood flow and blood volume measurements. *Stroke* 37, 1771–1777. doi: 10.1161/01.str.0000227243.96808.53

Nael, K., Meshksar, A., Liebeskind, D. S., Wang, D. J., Ellingson, B. M., Salamon, N., et al. (2013). Periprocedural arterial spin labeling and dynamic susceptibility contrast perfusion in detection of cerebral blood flow in patients with acute ischemic syndrome. *Stroke* 44, 664–670. doi: 10.1161/strokeaha.112.672956

Nogueira, R. G., Jadhav, A. P., Haussen, D. C., Bonafe, A., Budzik, R. F., Bhuva, P., et al. (2018). Thrombectomy 6 to 24 hours after stroke with a mismatch between deficit and infarct. *N. Engl. J. Med.* 378, 11–21.

Panni, P., Gory, B., Xie, Y., Consoli, A., Desilles, J. P., Mazighi, M., et al. (2019). Acute stroke with large ischemic core treated by thrombectomy. *Stroke* 50, 1164–1171.

Pinto, A., McKinley, R., Alves, V., Wiest, R., Silva, C. A., and Reyes, M. (2018). Stroke lesion outcome prediction based on mri imaging combined with clinical information. *Front. Neurol.* 9:1060. doi: 10.3389/fneur.2018.01060

Radak, D., Katsiki, N., Resanovic, I., Jovanovic, A., Sudar-Milovanovic, E., Zafirovic, S., et al. (2017). Apoptosis and acute brain ischemia in ischemic stroke. *Curr. Vasc. Pharmacol.* 15, 115–122. doi: 10.2174/1570161115666161104095522

Rose, S. E., Chalk, J. B., Griffin, M. P., Janke, A. L., Chen, F., McLachan, G. J., et al. (2001). MRI based diffusion and perfusion predictive model to estimate stroke evolution. *Magn. Reson. Imaging* 19, 1043–1053. doi: 10.1016/s0730-725x(01)00435-0

Seiler, A., Lauer, A., Deichmann, R., Nöth, U., Herrmann, E., Berkefeld, J., et al. (2020). Signal variance-based collateral index in DSC perfusion: a novel method to assess leptomeningeal collateralization in acute ischaemic stroke. *J. Cereb. Blood Flow Metab.* 40, 574–587. doi: 10.1177/0271678x19831024

Seners, P., Turc, G., Lion, S., Cottier, J. P., Cho, T. H., Arquizan, C., et al. (2020). Relationships between brain perfusion and early recanalization after intravenous thrombolysis for acute stroke with large vessel occlusion. *J. Cereb. Blood Flow Metab.* 40, 667–677. doi: 10.1177/0271678x19836288

Straka, M., Albers, G. W., and Bammer, R. (2010). Real-time diffusion-perfusion mismatch analysis in acute stroke. *J. Magn. Reson. Imaging* 32, 1024–1037. doi: 10.1002/jmri.22338

Tan, X., Guo, Y., Dun, S., and Sun, H. (2018). Crossed aphasia following cerebral infarction in a right-handed patient with atypical cerebral language dominance. *J. Neurol.* 265, 1671–1675. doi: 10.1007/s00415-018-8901-0

Vinny, P. W., Vishnu, V. Y., and Srivastava, M. V. P. (2018). Thrombectomy for stroke with selection by perfusion imaging. *N. Engl. J. Med.* 378:1849. doi: 10.1056/nejmc1803856

Wannamaker, R., Guinand, T., Menon, B. K., Demchuk, A., Goyal, M., Frei, D., et al. (2018). Computed tomographic perfusion predicts poor outcomes in a randomized trial of endovascular therapy. *Stroke* 49, 1426–1433. doi: 10.1161/strokeaha.117.019806

Wintermark, M., Flanders, A. E., Velthuis, B., Meuli, R., van Leeuwen, M., Goldsher, D., et al. (2006). Perfusion-CT assessment of infarct core and penumbra: receiver operating characteristic curve analysis in 130 patients suspected of acute hemispheric stroke. *Stroke* 37, 979–985. doi: 10.1161/01.str.0000209238.61459.39

Yin, J., Sun, H., Yang, J., and Guo, Q. (2015). Automated detection of the arterial input function using normalized cut clustering to determine cerebral perfusion by dynamic susceptibility contrast-magnetic resonance imaging. *J. Magn. Reson. Imaging* 41, 1071–1078. doi: 10.1002/jmri.24642

Yu, S., Ma, S. J., Liebeskind, D. S., Yu, D., Li, N., Qiao, X. J., et al. (2018). Aspects-based reperfusion status on arterial spin labeling is associated with clinical outcome in acute ischemic stroke patients. *J. Cereb. Blood Flow Metab.* 38, 382–392. doi: 10.1177/0271678x17697339

Zhu, G., Federau, C., Wintermark, M., Chen, H., Marcellus, D. G., Martin, B. W., et al. (2020). Comparison of MRI IVIM and MR perfusion imaging in acute ischemic stroke due to large vessel occlusion. *Int. J. Stroke.* 15, 332–342. doi: 10.1177/1747493019873515

Conflict of Interest: The authors declare that the research was conducted in the absence of any commercial or financial relationships that could be construed as a potential conflict of interest.

frontiers in Neurology

ORIGINAL RESEARCH
published: 06 May 2021
doi: 10.3389/fneur.2021.637556

Intracranial Atherosclerotic Burden and Cerebral Parenchymal Changes at 7T MRI in Patients With Transient Ischemic Attack or Ischemic Stroke

Arjen Lindenholz[1], Jeroen de Bresser[2], Anja G. van der Kolk[1,3], H. Bart van der Worp[4], Theodoor D. Witkamp[1], Jeroen Hendrikse[1] and Irene C. van der Schaaf[1]*

[1] Department of Radiology, University Medical Center Utrecht, Utrecht, Netherlands, [2] Department of Radiology, Leiden University Medical Center, Leiden, Netherlands, [3] Netherlands Cancer Institute–Antoni van Leeuwenhoek Hospital, Amsterdam, Netherlands, [4] Department of Neurology and Neurosurgery, University Medical Center Utrecht Brain Center, Utrecht University, Utrecht, Netherlands

The relevance of intracranial vessel wall lesions detected with MRI is not fully established. In this study (trial identification number: NTR2119; www.trialregister.nl), 7T MRI was used to investigate if a higher vessel wall lesion burden is associated with more cerebral parenchymal changes in patients with ischemic stroke or transient ischemic attack (TIA). MR images of 82 patients were assessed for the number of vessel wall lesions of the large intracranial arteries and for cerebral parenchymal changes, including the presence and number of cortical, small subcortical, and deep gray matter infarcts; lacunes of presumed vascular origin; cortical microinfarcts; and periventricular and deep white matter hyperintensities (WMHs). Regression analyses showed that a higher vessel wall lesion burden was associated with the presence of small subcortical infarcts, lacunes of presumed vascular origin, and deep gray matter infarcts (relative risk 1.18; 95% CI, 1.03–1.35) and presence of moderate-to-severe periventricular WMHs (1.21; 95% CI, 1.03–1.42), which are all manifestations of small vessel disease (SVD). The burden of enhancing vessel wall lesions was associated with the number of cortical microinfarcts only (1.48; 95% CI, 1.04–2.11). These results suggest an interrelationship between large vessel wall lesion burden and cerebral parenchymal manifestations often linked to SVD or, alternatively, that vascular changes occur in both large and small intracranial arteries simultaneously.

Keywords: intracranial arteries, intracranial atherosclerosis, intracranial vessel wall MR imaging, small vessel disease, large vessel disease, white matter hyperintensity

OPEN ACCESS

Edited by:
Robin Lemmens,
University Hospitals Leuven, Belgium

Reviewed by:
Mariel Kozberg,
Massachusetts General Hospital and Harvard Medical School, United States
Marieta Peycheva,
Plovdiv Medical University, Bulgaria

****Correspondence:***
Arjen Lindenholz
A.Lindenholz@umcutrecht.nl

Specialty section:
This article was submitted to Stroke, a section of the journal Frontiers in Neurology

Received: *12 January 2021*
Accepted: *22 March 2021*
Published: *06 May 2021*

Citation:
Lindenholz A, de Bresser J, van der Kolk AG, van der Worp HB, Witkamp TD, Hendrikse J and van der Schaaf IC (2021) Intracranial Atherosclerotic Burden and Cerebral Parenchymal Changes at 7T MRI in Patients With Transient Ischemic Attack or Ischemic Stroke. Front. Neurol. 12:637556. doi: 10.3389/fneur.2021.637556

INTRODUCTION

Intracranial atherosclerosis (ICAS) is an important cause of ischemic stroke (1). Historically, ICAS has been evaluated by measuring the presence of intracranial stenosis using lumenographic techniques or by detecting vessel wall calcifications that generally reflect a more advanced stage of ICAS (2–5). Over the last two decades, however, intracranial vessel wall MRI sequences have enabled *in vivo* visualization of the intracranial vessel wall itself (6–8). With these dedicated MRI sequences, both subtle (non-stenotic) and more advanced vessel wall pathology of the proximal cerebral large arteries can be assessed.

Vessel wall changes of the large intracranial arteries are frequently observed on intracranial vessel wall MR images, both in patients with cerebrovascular disease and in healthy elderly individuals, but the nature and clinical relevance of these changes have not been fully established (9–12). *Ex vivo* studies applying intracranial vessel wall MRI to postmortem samples suggest that these changes represent vessel wall disease at an early stage to halfway on the developmental timeline of ICAS (13–18). At the end of this timeline, plaque disruption, thrombus formation, and large vessel stenosis or occlusion can lead to transient ischemic attack (TIA) or ischemic stroke. The parenchymal consequences of vessel wall changes presumably reflecting less advanced ICAS, however, are less clear, hampering interpretation of these changes in clinical practice.

ICAS in the smaller arteries, arterioles, and capillaries—while difficult to visualize using vessel wall MRI due to their small caliber—or emboli disrupted from atherosclerotic plaques located in larger parent arteries may lead to (small) subcortical infarcts, deep gray matter infarcts, lacunes of presumed vascular origin, cortical microinfarcts, or white matter hyperintensities (WMHs) (19, 20). Often, these cerebrovascular changes of the small vessels and their sequelae are categorized as a separate disease entity [cerebral small vessel disease (SVD)] compared with large artery stroke, although both small and large cerebral arteries comprise one vascular bed that is physiologically connected, suggesting that pathology in one "type" of vessel bed will inevitably affect the other. Recent studies have shown evidence for this connection: for example, large (intracranial) artery disease may result in endothelial damage and blood–brain barrier damage of the smaller arteries by the release of inflammatory molecules and enzymes, while alternatively, atherosclerotic plaques located in the larger intracranial arteries may obstruct orifices of smaller branching arteries resulting in small vessel pathology (21, 22). Nevertheless, the exact role and direction of effect—cerebrovascular changes of the small arteries by large artery pathology, vice versa, or bilateral—remains to be elucidated (22).

In this study, we hypothesize that the burden of intracranial vessel wall lesions of the larger intracranial arteries might be associated with a variety of cerebral parenchymal changes, including large and small infarcts and WMHs. The purpose of this study was therefore to investigate whether a greater burden of intracranial vessel wall lesions assessed using 7-tesla (T) vessel wall MRI is associated with more cerebral parenchymal changes.

MATERIALS AND METHODS

Study Population

Between December 2009 and May 2018, patients presenting at our University hospital with TIA or ischemic stroke of the anterior circulation were eligible for inclusion in the prospective Intracranial Vessel wall Imaging (IVI) study (NTR2119, www.trialregister.nl). The main inclusion criteria were age 18 years or older and ability to undergo a 7T MRI examination within 3 months after the ischemic event. The main exclusion criteria were ischemic stroke or TIA secondary to a surgical or interventional procedure and any contraindication to 7T MR imaging or to gadolinium-containing contrast agents. A flowchart of the study inclusion is shown in **Figure 1**. The full eligibility criteria and other details of the study have been reported before (6, 23). The study was approved by the medical ethics committee of the University Medical Center Utrecht according to the guidelines of the Declaration of Helsinki of 1975, and all patients provided written informed consent. Baseline characteristics including cardiovascular risk factors and characteristics of the ischemic event [final diagnosis and subtype classified by the Trial of Org 10172 in Acute Stroke Treatment (TOAST) criteria] were recorded (24).

Imaging Protocol

Imaging was performed on a 7T whole-body system (Philips Healthcare, Best, The Netherlands) with either a 16-channel ($n = 35$) or 32-channel ($n = 47$) receive coil and a volume transmit-receive coil for transmission (Quad TR; Nova Medical, Wilmington, MA, USA). The protocol included a pre- and post-contrast T_1-weighted intracranial vessel wall sequence [magnetization-prepared inversion recovery turbo spin-echo (MPIR-TSE)], time-of-flight MR angiography (TOF-MRA), diffusion-weighted imaging (DWI), and fluid-attenuated inversion recovery (FLAIR) imaging. The post-contrast MPIR-TSE sequence was acquired 5 min after the administration of 0.1 ml/kg of a gadolinium-containing contrast agent (gadobutrol, Gadovist 1.0 mmol/ml, Bayer Schering Pharma, Newbury, UK). The TOF-MRA images were used for anatomical verification of the large intracranial vessels seen on the MPIR-TSE images. The following acquisition parameters were used for the MPIR-TSE sequence: field of view (FOV) 220 × 180 × 13 mm^3 ($n = 40$), which was extended during the study period to 250 × 250 × 190 mm^3 ($n = 42$) (23), acquired spatial resolution 0.8 × 0.8 × 0.8 mm^3, reconstructed spatial resolution 0.5 × 0.5 × 0.5 mm^3, repetition time (TR) 3,952 ms, echo time (TE) 37 ms, inversion time (TI) 1,375 ms, and acquisition time 10 min 40 s. In case of the smaller FOV sequence, the FOV was placed in such a way that all large intracranial arteries of the anterior circulation were within the imaging plane, which included the anterior cerebral arteries (ACAs; A1 and A2 segments), middle cerebral arteries (MCAs; M1 and M2 segments), and the distal parts of the internal (intracranial) carotid arteries (ICAs; clinoid, supra-clinoid, and terminal segments). Acquisition parameters for the other sequences were as follows: for the TOF-MRA, FOV 190 × 190 × 102 mm^3, acquired spatial resolution 0.4 × 0.5 × 0.6 mm^3, reconstructed spatial resolution 0.4 × 0.4 × 0.3 mm^3, TR 21 ms, TE 2.3 ms, and acquisition time 9 min 18 s; for the DWI, FOV 220 × 220 × 123 mm^3, acquired and reconstructed spatial resolution 1.5 × 1.5 × 1.5 mm^3, TR 17,659 ms, TE 57 ms, and acquisition time 6 min 10 s; and for the FLAIR sequence, FOV 250 × 250 × 190 mm^3, acquired spatial resolution 0.8 × 0.8 × 0.4 mm^3, reconstructed spatial resolution 0.5 × 0.5 × 0.5 mm^3, TR

Abbreviations: ACA, anterior cerebral artery; CI, confidence interval; FLAIR, fluid-attenuated inversion recovery; ICA, internal carotid artery; ICAS, intracranial atherosclerosis; MCA, middle cerebral artery; MPIR-TSE, magnetization-prepared inversion-recovery turbo spin echo; SVD, small vessel disease; T, tesla; TIA, transient ischemic attack; TOAST, Trial of Org 10172 in Acute Stroke Treatment; WMH, white matter hyperintensity.

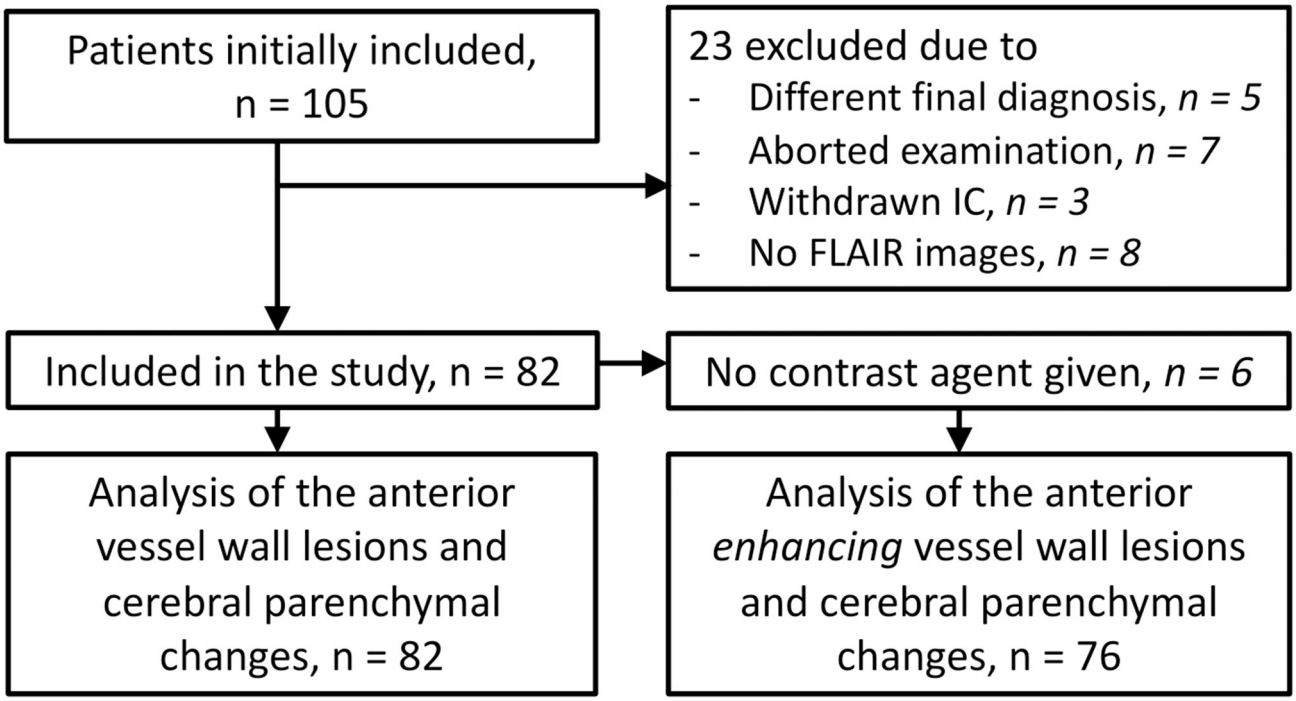

FIGURE 1 | Flowchart showing the number of participants who were included for analyses. IC, informed consent.

8,000 ms, TE 300 ms, TI 2,200 ms, and acquisition time 10 min 48 s [for more details, see Lindenholz et al. (11)].

Vessel Wall Assessment

The MR vessel wall images were scored by an expert in reading intracranial vessel wall images (AK, 9 years of experience). The reader was blinded for patient details and clinical information. Interrater reproducibility measures for the assessment of these vessel wall images have been published before [intraclass correlation coefficient, 0.93; 95% confidence interval (CI); 0.90–0.96; Dice similarity coefficient (DSC), 0.81] (25). For the current study, intracranial vessels of the anterior circulation were assessed, including the ACA (A1 and A2 segments), MCA (M1 and M2 segments), and the ICA (clinoid, supra-clinoid, and terminal segments). A vessel wall lesion was defined as a visually judged focal or diffuse vessel wall thickening of >50% compared with the neighboring vessel wall (or contralateral vessel wall in case of diffuse thickening), with or without contrast enhancement (11). Contrast enhancement was assessed by comparing pre- and post-contrast images including co-registered subtraction images using the Elastix toolbox in MeVisLab (version 2.7, MeVis Medical Solutions, Bremen, Germany) (26). Contrast enhancement of a vessel wall lesion was defined as lesion hyperintensity approximating the signal intensity of the pituitary stalk on the post-contrast MR images on at least two consecutive images using the pre-contrast MR images as a reference and the coregistered subtraction images as confirmation. Contrast-enhancing foci at the location where the ICA pierces the dura mater were classified as vasa vasorum and were not considered vessel wall enhancement. The intracranial vessel wall lesion burden was used as a continuous variable for the primary analysis and was defined as the total number of vessel wall lesions for each patient. The total number of enhancing vessel wall lesions was used as a continuous variable in the secondary analysis.

Parenchyma Assessment

The DWI and FLAIR images and T_1-weighted MPIR-TSE images were assessed for anterior circulation parenchymal changes by an expert neuroradiologist (TDW, 30 years of experience). The reader was blinded for patient details, clinical information, and vessel wall lesion assessment. The following cerebral parenchymal changes were scored: cortical infarcts and (recent) small subcortical infarcts, deep gray matter infarcts and lacunes of presumed vascular origin, cortical microinfarcts, and periventricular and deep WMHs. A recent position paper has judged all of these MR findings except for cortical infarcts (and possibly cortical microinfarcts) to be related to SVD (27).

Cortical infarcts were defined as hyperintense lesions on FLAIR imaging located in the cerebral cortex and >5 mm in diameter, with or without associated tissue loss or extension into the deep white matter. When a cortical infarct was multifocal or extending into the white matter, but with similar presumed origin, the infarct was scored as a single cortical infarct. Small subcortical infarcts and lacunes of presumed vascular origin were defined as hyperintense lesions of, respectively, 15–20 and 3–15 mm in diameter on FLAIR imaging with or without a hypointense center or cavity and local tissue loss, classified and scored according to the STRIVE criteria (27). Deep gray matter

infarcts were defined as hyperintense lesions on FLAIR imaging located in the basal ganglia or thalamus >3 mm in diameter (not specifically defined in the STRIVE criteria but derived from the position paper) (27). Cortical microinfarcts were defined as hyperintense lesions on FLAIR imaging in the cerebral cortex smaller than 5 mm in size and scored according to a recent consensus paper (20). The periventricular and deep WMHs on FLAIR imaging were also defined according to the STRIVE criteria and were scored with the Fazekas four-point scale for periventricular (0 = absent WMH lesions, 1 = "caps" or pencil-thin lining, 2 = smooth "halo," and 3 = irregular hyperintensities extending into the deep white matter) and for deep WMHs (0 = absence or a single punctate WMH lesion, 1 = multiple punctate lesions, 2 = beginning confluency of lesions, and 3 = large confluent lesions) (27, 28). The presence of any cerebral infarct in the flow territory of the anterior circulation and the WMH score (dichotomized into high, Fazekas 2 or 3; and low, Fazekas 0 or 1) were used as primary outcomes in the analyses. The number of cerebral infarcts was used as outcomes for the secondary analysis.

Statistical Analysis

Descriptive baseline statistics are presented as proportions or means. To estimate associations between intracranial vessel wall lesion burden and presence or number of cerebral parenchymal changes, appropriate regression analyses for modeling count data were performed. Age and sex were included as covariates. In the primary analyses, the association between the number of intracranial vessel wall lesions (as continuous and independent variable) and the presence of any scored cerebral parenchymal change (dichotomized outcome as dependent variable) were individually and all together investigated with a negative log-binomial regression model. A composite variable was composed of the infarcts that are often considered to be manifestations of cerebral SVD and included small subcortical and deep gray matter infarcts and lacunes of presumed vascular origin (27). In the secondary analyses, the associations between the total number of intracranial vessel wall lesions (independent variable) and the total number of infarcts (count data; classified by infarct type, dependent variable) were investigated with a negative log-binomial regression model for the number of infarcts. To assess the association between the number of enhancing intracranial vessel wall lesions (independent variable) and presence and number of the scored cerebral parenchymal changes as dependent variables, we used the same methods as in the primary and secondary analyses. Negative log-binomial regression generally provides rate ratios, which are interpretable as relative risks. Therefore, associations are presented in more commonly used relative risks. For all analyses, 95% CIs are given. A two-sided $p < 0.05$ was considered statistically significant. Statistical analyses were performed using SPSS version 21.0 (IBM SPSS Statistics, IBM Corp., Armonk, NY, USA).

RESULTS

A total of 105 patients were included in the IVI study. Twenty-three patients were excluded because of reasons listed in **Figure 1**, leaving a total of 82 patients for the current study. Baseline characteristics of the study participants are shown in **Table 1**.

TABLE 1 | Baseline characteristics.

Patient characteristics (n = 82)	
Mean age in years (range)	61 (27–85)
Men	49 (60%)
Body mass index (BMI, kg/m^2), mean (range)	26 (18–35)
Diagnosis	
Ischemic stroke	55 (67%)
Transient ischemic attack	22 (27%)
Transient monocular visual loss of vascular origin	5 (6%)
Hypertension	40 (49%)
Hyperlipidemia	39 (48%)
Diabetes mellitus	10 (12%)
Peripheral artery disease	0 (0%)
Current smoker	26 (32%)
Former smoker	27 (33%)
Atrial fibrillation	10 (12%)
Angina pectoris	4 (5%)
Myocardial infarction	5 (6%)
Average days from symptom onset to MRI in days ± SD	23 ± 34
Patients imaged without contrast agent	6 (7%)
TOAST-criteria	
Large artery atherosclerosis	44 (54%)
Cardio embolism	17 (21%)
Small-vessel occlusion	5 (6%)
Other determined etiology	5 (6%)
Undetermined	11 (13%)

Patient characteristics for the studied population.

Distribution of Intracranial Vessel Wall Lesions and Cerebral Parenchymal Changes

Sixty-two patients (75%) had a total of 193 vessel wall lesions and 35 patients (43%) a total of 81 enhancing vessel wall lesions. The total number of (enhancing) vessel wall lesions per arterial segment is shown in **Supplementary Table 1**.

Sixty-eight patients (83%) had at least one cerebral parenchymal vascular lesion. Fifty-five patients (67%) had a total of 122 cortical infarcts. One patient (1%) had a small subcortical infarct of <20 mm, 23 patients (28%) had a total of 54 lacunes of presumed vascular origin, 15 patients (18%) had a total of 21 subcortical deep gray matter infarcts, and 16 patients (20%) had a total of 43 cortical microinfarcts. For the periventricular WMHs and for the deep WMHs, 24 patients (29%) and 25 patients (30%) had a Fazekas score of 2 and 3, respectively. All details regarding the detected cerebral parenchymal changes are shown in **Supplementary Table 2**.

Intracranial Vessel Wall Lesion Burden and Cerebral Parenchymal Changes

Unadjusted and adjusted relative risks for the association between intracranial vessel wall lesion burden and the presence

of cerebral parenchymal changes are shown as primary analyses in **Table 2**. In our study population, vessel wall lesion burden was not associated with the presence of small cortical infarcts (adjusted relative risk, 1.07; 95% CI, 0.98–1.17). Neither was an association found between vessel wall lesion burden and presence of lacunes of presumed vascular origin (adjusted relative risk, 1.13; 95% CI, 0.95–1.34), deep gray matter infarcts (adjusted relative risk 1.25; 95% CI, 0.98–1.60), and cortical microinfarcts (adjusted relative risk 1.07; 95% CI, 0.85–1.36). When all subcortical infarcts were combined into one composite variable composing the infarcts often considered to be a manifestation of SVD, an association was found between vessel wall lesion burden and presence of an infarct (adjusted relative risk, 1.18; 95% CI, 1.03–1.35). In addition, the presence of moderately to severe (Fazekas 2–3) periventricular WMHs was associated with vessel wall lesion burden (adjusted relative risk, 1.21; 95% CI, 1.02–1.42). No association was found between deep WMHs and vessel wall lesion burden. An example of the presence of vessel wall lesions and a high WMH score is shown in **Figure 2**.

In the secondary analyses, we did not find an association between intracranial vessel wall lesion burden and the number of cerebral parenchymal changes of any type (**Table 3**). In the subanalyses, an association was found between the enhancing vessel wall lesion burden and the number of cortical microinfarcts (relative risk, 1.48; 95% CI, 1.04–2.11), but no other association was found between the enhancing vessel wall lesion burden and either presence (**Table 4**) or number (**Table 5**) of cerebral parenchymal changes.

DISCUSSION

In the current study, an increased vessel wall lesion burden was associated with the presence of small subcortical infarcts, lacunes of presumed vascular origin, or deep gray matter infarcts, and with the presence of moderate-to-severe periventricular WMHs. We did not find an association between intracranial vessel wall lesion burden and presence and number of large cortical infarcts and presence and number of infarcts when classified by type. In addition, the enhancing vessel wall lesion burden was only associated with the number of cortical microinfarcts.

Several of the cerebral parenchymal changes that we assessed in our study have been considered manifestations of SVD (27). SVD is generally defined by cerebral parenchymal manifestations, as SVD itself is difficult to quantify (19, 29–31). By contrast, large artery disease can be assessed directly using either lumenography techniques (stenosis) or intracranial vessel wall imaging (vessel wall lesions) (9). Many studies focus on either large vessel disease or SVD, and ongoing effort has been committed to find differences or similarities between cerebral large artery disease and SVD (32–39). Despite anatomical and pathophysiological differences between large and small intracranial vessels, the intracranial vasculature is interrelated as one vascular network. SVD has recently been described as a dynamic whole-brain disease that in some cases may share a similar etiology with large vessel disease. In this proposed "parent artery atheroma theory," atherosclerotic plaques in the large cerebral arteries (e.g., MCA) cause an occlusion at the origin of smaller branching arteries, subsequently leading to cerebral parenchymal changes reflecting SVD (21, 39). The findings in our study can support this theory, as we found an association between the presence of infarcts often related to SVD and the intracranial vessel wall lesion burden (**Table 2**). Specific microbiota, proteases, and immunoglobulins from atherosclerotic plaques can cause a cascade that harms the vessel wall endothelium and the blood–brain barrier and consequently could lead to SVD (22). This may be an alternative explanation of our findings that the co-occurrence of intracranial vessel wall lesions and parenchymal manifestations of SVD may suggest concomitant changes in both large and small intracranial vasculature.

It remains uncertain why an association was found between the enhancing vessel wall lesion burden and number of cortical microinfarcts, but not with the presence of cortical microinfarcts nor with the presence or number of any other type of infarct. This is most likely related to insufficient statistical power. Increasing evidence, including pooled data, shows that vessel wall lesion enhancement may be associated with plaque vulnerability and consequently with higher risk of ischemic events (40–42). Histopathological validation and especially follow-up studies with a larger sample size are necessary to investigate whether this applies to our study population.

Several etiologies have been described that attempt to explain different categories of WMHs, yet it remains unclear if there indeed exist distinct mechanisms for periventricular and deep WMH development and if these differences are of clinical importance (19, 43, 44). The presence of both periventricular and deep WMHs may be a result of underlying vascular changes (and subsequent loss of vascular integrity) of both large and SVD (19). Nevertheless, different associations between periventricular and deep WMHs were found in our study, and definite explanations for these discrepancies have yet to be further investigated.

In contrast to previous studies investigating ICAS as a risk factor for (large artery) ischemic stroke, in our study, no association was found between intracranial vessel wall lesion burden and presence and number of (large) cortical infarcts. This may be due to the setup of the IVI study, for which specifically ischemic stroke and TIA patients were selected, not limited to large-artery atherosclerosis according to the TOAST criteria, and without inclusion of healthy volunteers. Large numbers of patients are needed to detect small differences in this type of study population. Another explanation (especially for the number of cortical infarcts) may be the difference in definition of ICAS. Previous studies often used intracranial stenosis as a proxy for ICAS, but this represents an advanced state of ICAS (45, 46). In early-to-moderate stages of ICAS, vessel wall changes may be its only (early) sign; due to vascular remodeling, luminal narrowing often occurs in advanced stages of the disease (47).

The strength of this study is that data have been derived from a relatively large number of patients who received 7T MR vessel wall imaging; high-resolution 7T MRI has been shown superior to 3T MRI in visualizing the intracranial vessel wall because of its high contrast-to-noise ratio and has a better detection rate of especially small symptomatic and asymptomatic

TABLE 2 | Associations between the presence of parenchymal changes and the intracranial vessel wall lesion burden.

Outcome as present/absent	Unadjusted relative risk (±95% CI)	*p*-value	Adjusted relative risk (±95% CI)	*p*-value
Infarcts				
Any anterior circulation infarct	1.05 (0.99–1.12)	0.086	1.05 (0.98–1.12)	0.151
Cortical infarcts	1.06 (0.98–1.15)	0.151	1.07 (0.98–1.17)	0.129
Infarcts often caused by SVD	**1.23 (1.09–1.39)**	**0.001**	**1.18 (1.03–1.35)**	**0.017**
Small subcortical infarcts	NA		NA	NA
Lacunes of presumed vascular origin	**1.20 (1.04–1.40)**	**0.016**	1.13 (0.95–1.34)	0.174
Deep gray matter infarcts	**1.29 (1.04–1.60)**	**0.019**	1.25 (0.98–1.60)	0.069
Cortical microinfarcts	1.14 (0.93–1.38)	0.212	1.07 (0.85–1.36)	0.565
White matter hyperintensities (Fazekas grade)				
Periventricular (0/1 vs. 2/3)	**1.34 (1.16–1.55)**	**<0.001**	**1.21 (1.02–1.42)**	**0.026**
Deep (0/1 vs. 2/3)	**1.22 (1.05–1.41)**	**0.008**	1.09 (0.89–1.33)	0.417

Included for analysis, n = 82. The unadjusted and adjusted (for age and sex) relative risks including their 95% confidence interval (CI) for the presence of cerebral parenchymal changes with the total number of anterior vessel wall lesions as included variable. A $p < 0.05$ was considered to indicate a statistically significant difference shown as bold text. A log-binomial regression model was used with a robust variance estimator. White matter hyperintensity Fazekas grade is described as follows: 0 = absence or single punctate white matter hyperintensity, 1 = "caps" or pencil-thin lining or multiple punctate lesions, 2 = smooth "halo" or beginning confluency of lesions, and 3 = large confluent lesions or irregular hyperintensities extending into the deep white matter (28).

CMI, cortical microinfarct; NA, not applicable (only 1 count); SVD, small vessel disease.

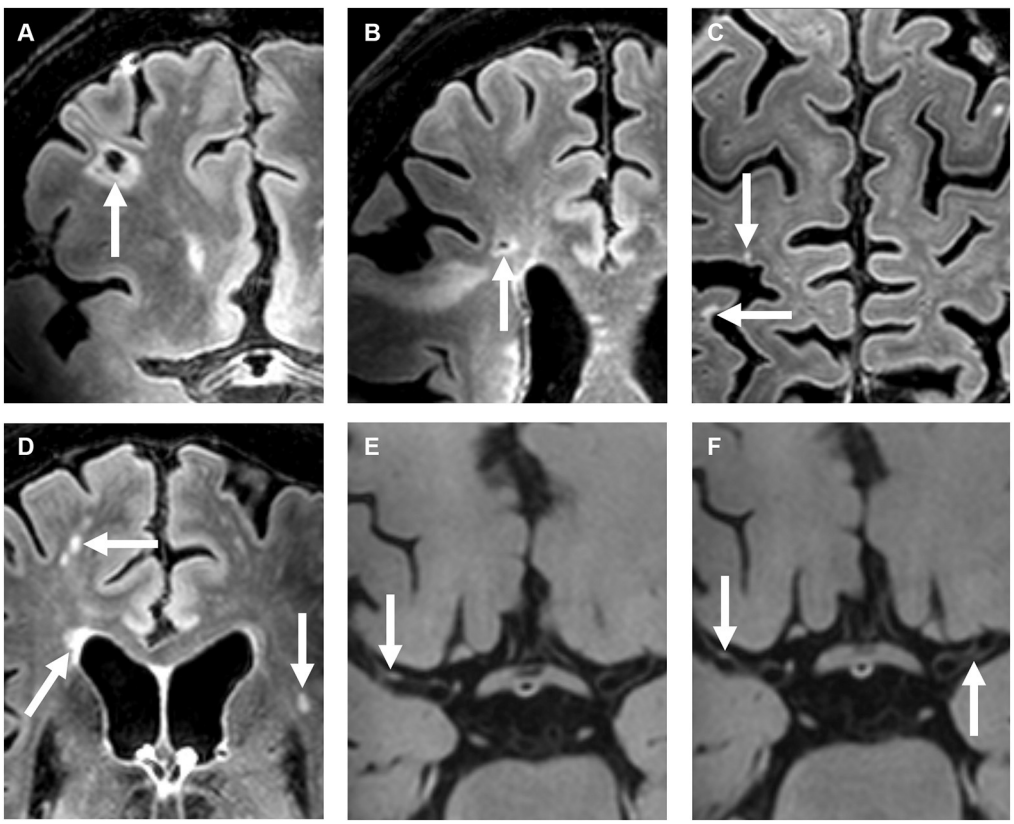

FIGURE 2 | A 72-year-old female with a right-sided ischemic stroke; imaging 25 days after symptom onset. **(A–D)** Precontrast 7T transverse FLAIR images and **(E–H)** post-contrast 7T transverse T_1-weighted MPIR-TSE vessel wall images. Lacunar infarcts are located in the right frontal [arrow in **(A)**] and right frontotemporal area [arrow in **(B)**]. Multiple cortical microinfarcts are also seen [arrows in **(C)**], as well as periventricular and deep white matter hyperintensities [arrows in **(D)**]. Note also the extensive enlarged periventricular spaces in this patient [not scored; arrows in **(E,F)**]. Vessel wall lesions are seen in the left and right middle cerebral arteries (M1 segments) [arrows in **(G,H)**].

TABLE 3 | Associations between the number of parenchymal changes and the intracranial vessel wall lesion burden.

Outcome as count	Unadjusted relative risk (±95% CI)	*p*-value	Adjusted relative risk (±95% CI)	*p*-value
Infarcts				
Any anterior circulation infarct	**1.15 (1.03–1.29)**	**0.016**	1.08 (0.96–1.21)	0.189
Cortical infarcts	1.12 (0.98–1.28)	0.102	1.08 (0.94–1.24)	0.290
Infarcts often caused by SVD	1.12 (0.97–1.31)	0.134	1.05 (0.90–1.23)	0.531
Small subcortical infarcts	NA	NA	NA	NA
Lacunes of presumed vascular origin	1.09 (0.90–1.31)	0.370	1.00 (0.79–1.26)	0.981
Deep gray matter infarcts	1.21 (0.91–1.61)	0.190	1.15 (0.84–1.58)	0.396
Cortical microinfarcts	1.23 (0.95–1.60)	0.111	1.16 (0.86–1.56)	0.333
White matter hyperintensities (Fazekas grade)				
Periventricular (0, 1, 2, or 3)	NA	NA	NA	NA
Deep (0, 1, 2, or 3)	NA	NA	NA	NA

Included for analysis, n = 82. The unadjusted and adjusted (for age and sex) relative risks including their 95% confidence interval (CI) for the number of cerebral parenchymal changes with the total number of anterior vessel wall lesions as included variable. A p < 0.05 was considered to indicate a statistically significant difference shown as bold text. For continuous count data as outcome variable, a log-binomial regression model was used with a robust variance estimator. For ordinal data as outcome variable, an ordinal regression model was used. Ordinal Fazekas grade is described as follows: 0 = absence or single punctate white matter hyperintensity, 1 = "caps" or pencil-thin lining or multiple punctate lesions, 2 = smooth "halo" or beginning confluency of lesions, and 3 = large confluent lesions or irregular hyperintensities extending into the deep white matter (28).
CMI, cortical microinfarct; NA, not applicable (groups too small for reliable statistical analyses); SVD, small vessel disease.

TABLE 4 | Associations between the presence of parenchymal changes and the enhancing intracranial vessel wall lesion burden.

Outcome as present/absent	Unadjusted relative risk (±95% CI)	*p*-value	Adjusted relative risk (±95% CI)	*p*-value
Infarcts				
Any anterior circulation infarct	1.00 (0.92–1.09)	0.957	0.99 (0.90–1.08)	0.824
Cortical infarcts	1.04 (0.95–1.14)	0.394	1.05 (0.94–1.16)	0.387
Infarcts often caused by SVD	1.06 (0.90–1.26)	0.498	1.00 (0.83–1.22)	0.975
Small subcortical infarcts	NA	NA	NA	NA
Lacunes of presumed vascular origin	1.07 (0.87–1.32)	0.537	1.00 (0.78–1.28)	0.986
Deep gray matter infarcts	0.90 (0.65–1.24)	0.508	0.83 (0.61–1.14)	0.256
Cortical microinfarcts	1.24 (0.95–1.60)	0.112	1.18 (0.93–1.49)	0.187
White matter hyperintensities (Fazekas grade)				
Periventricular (0/1 vs. 2/3)	**1.19 (0.98–1.45)**	**0.077**	1.02 (0.81–1.29)	0.858
Deep (0/1 vs. 2/3)	1.12 (0.92–1.36)	0.273	0.99 (0.80–1.24)	0.948

Included for analysis, n = 76. Six of 82 patients did not receive contrast agent. The unadjusted and adjusted (for age and sex) relative risks including their 95% confidence interval (CI) for the presence of cerebral parenchymal changes with the total number of anterior enhancing vessel wall lesions as included variable. A p < 0.05 was considered to indicate a statistically significant difference shown as bold text. A log-binomial regression model was used with a robust variance estimator. White matter hyperintensity Fazekas grade is described as follows: 0 = absence or single punctate white matter hyperintensity, 1 = "caps" or pencil-thin lining or multiple punctate lesions, 2 = smooth "halo" or beginning confluency of lesions, and 3 = large confluent lesions or irregular hyperintensities extending into the deep white matter (28).
CMI, cortical microinfarct; NA, not applicable (only 1 count); SVD, small vessel disease.

cerebral parenchymal changes (12, 48). Still, for analyzing all associations in this study, the absolute number of included patients is limited, and the inherently induced selection bias due to the design of the study may have affected the analyzed associations underestimating the true association due to reversed causality. Also, the smaller size of the subgroup analysis may have accounted for the lack of an association, which also applies for the analyses with the enhancing vessel wall lesion burden as included variable. Although we detected several trends in our analyses, most of them could not be confirmed with statistical significance. We think that this can for the most part be explained by statistical power constraints. When periventricular and deep WMHs share the same etiology, the same reason may account for the observed difference in associations between the presence of periventricular vs. deep WMHs and vessel wall lesion burden. Overall, there was an overrepresentation of patients with a Fazekas score of 1 in both periventricular and deep WMHs, implicating relatively small subgroups of patients with a different Fazekas score. Therefore, (ordinal) regression analyses could not be reliably performed among the individual Fazekas scores. Also, we based our results on multivariable models and tested seven variables of cerebral parenchymal

TABLE 5 | Associations between the number of parenchymal changes and the enhancing intracranial vessel wall lesion burden.

Outcome as count	Unadjusted relative risk (±95% CI)	*p*-value	Adjusted relative risk (±95% CI)	*p*-value
Infarcts				
Any anterior circulation infarct	1.17 (0.97–1.40)	0.096	1.10 (0.93–1.29)	0.269
Cortical infarcts	1.04 (0.93–1.15)	0.539	1.01 (0.91–1.12)	0.830
Infarcts often caused by SVD	1.01 (0.82–1.23)	0.918	0.97 (0.77–1.21)	0.773
Small subcortical infarcts	NA	NA	NA	NA
Lacunes of presumed vascular origin	1.06 (0.84–1.33)	0.636	1.00 (0.77–1.31)	0.984
Deep gray matter infarcts	0.82 (0.57–1.18)	0.278	0.75 (0.53–1.06)	0.102
Cortical microinfarcts	**1.59 (1.08–2.34)**	**0.019**	**1.48 (1.04–2.11)**	**0.032**
White matter hyperintensities (Fazekas grade)				
Periventricular (0, 1, 2, or 3)	NA	NA	NA	NA
Deep (0, 1, 2, or 3)	NA	NA	NA	NA

Included for analysis, n = 76. Six of 82 patients did not receive contrast agent. The unadjusted and adjusted (for age and sex) relative risks including their 95% confidence interval (CI) for the number of cerebral parenchymal changes with the total number of anterior enhancing vessel wall lesions as included variable. A $p < 0.05$ was considered a statistically significant difference shown as bold text. For continuous count data as outcome variable, a log-binomial regression model was used with a robust variance estimator. For ordinal data as outcome variable, an ordinal regression model was used. Ordinal score is described as follows: 0 = absence or single punctate white matter hyperintensity, 1 = "caps" or pencil-thin lining or multiple punctate lesions, 2 = smooth "halo" or beginning confluency of lesions, and 3 = large confluent lesions or irregular hyperintensities extending into the deep white matter (28). CMI, cortical microinfarct; NA, not applicable (groups too small for reliable statistical analyses); SVD, small vessel disease.

changes with the presence of (enhancing) vessel wall lesions. The Bonferroni correction for multiple testing would mean that our *p*-value of 0.05 should be divided by the nine outcome variables = 0.009, which indicates statistical significance. That approach would leave no association between (enhancing) vessel wall lesions and cerebral parenchymal changes. Furthermore, several other cerebral parenchymal changes have been recognized to reflect (chronic) vascular damage due to SVD, such as cerebral microbleeds, which were not assessed in this study (27). Ideally, the inclusion of a larger group of patients could improve the statistical reliability and enable inclusion of more potential confounders or effect modifiers, while assessment of these other cerebral parenchymal changes may contribute to a broader understanding of the potential associations between intracranial vessel wall lesion burden reflecting underlying large artery disease and the cerebral sequelae associated with SVD. Another limitation of assessing intracranial vessel wall lesion burden is the absence of a gold standard method to assess ICAS lesions found on MRI. However, this is a limitation of all studies on intracranial vessel wall MRI, and several post-mortem *ex vivo* imaging correlation studies have been performed, tentatively increasing the confidence that detected vessel wall lesions represent true ICAS (15, 18, 49). Yet the cutoff point between confirmed early-stage atherosclerotic lesions and non-pathological or natural variations of vessel wall thickness may be difficult to define.

CONCLUSIONS

Within this relatively small sample size, intracranial vessel wall lesion burden was associated with the presence of periventricular WMHs and the presence of any type of infarct often linked to SVD, while no association was found with (large) cortical infarcts. The co-occurrence of intracranial vessel wall lesions and parenchymal manifestations generally attributed to SVD tentatively suggests that either vessel wall lesions of the large intracranial parent arteries eventually result in cerebral parenchymal manifestations of SVD, e.g., by occluding the orifices of smaller branching arteries, or vascular changes occur in both large and small intracranial arteries simultaneously. In the future, studies with larger sample sizes are required to confirm these findings.

DATA AVAILABILITY STATEMENT

The original contributions generated for the study are included in the article/**Supplementary Material**, further inquiries can be directed to the corresponding author/s.

ETHICS STATEMENT

The studies involving human participants were reviewed and approved by the medical ethics committee of the University Medical Center Utrecht according to the guidelines of the Declaration of Helsinki of 1975. The patients/participants provided their written informed consent to participate in this study.

AUTHOR CONTRIBUTIONS

AL: study design, literature search, figures, data collection, data analyses, data interpretation, and writing. JdB: study design, literature search, data interpretation, and critical review of the manuscript. AvK: study design, data collection, data interpretation, and critical review of the manuscript. HvW: data interpretation and critical review of the manuscript. TW: MRI analyses. JH: study design and critical review of the manuscript. IS: study design, data interpretation, and critical review of the

manuscript. All authors contributed to the article and approved the submitted version.

FUNDING

The research of JH has received funding from the European Research Council under the European Union's Horizon 2020 Programme (H2020)/ERC grant agreement no. 637024 (HEARTOFSTROKE).

SUPPLEMENTARY MATERIAL

The Supplementary Material for this article can be found online at: https://www.frontiersin.org/articles/10.3389/fneur.2021.637556/full#supplementary-material

REFERENCES

1. Gorelick P, Wong KS, Liu L. Epidemiology. *Front Neurol Neurosci.* (2016) 40:34–46. doi: 10.1159/000448272
2. Arenillas JF. Intracranial atherosclerosis: current concepts. *Stroke*. (2011) 42 (1 Suppl):S20–3. doi: 10.1161/STROKEAHA.110.597278
3. Holmstedt CA, Turan TN, Chimowitz MI. Atherosclerotic intracranial arterial stenosis: risk factors, diagnosis, and treatment. *Lancet Neurol.* (2013) 12:1106–14. doi: 10.1016/S1474-4422(13)70195-9
4. Qureshi AI, Caplan LR. Intracranial atherosclerosis. *Lancet.* (2014) 383:984–98. doi: 10.1016/S0140-6736(13)61088-0
5. Bang OY. Intracranial atherosclerosis: current understanding and perspectives. *J Stroke.* (2014) 16:27–35. doi: 10.5853/jos.2014.16.1.27
6. van der Kolk AG, Zwanenburg JJ, Brundel M, Biessels GJ, Visser F, Luijten PR, et al. Intracranial vessel wall imaging at 7.0-T MRI. *Stroke.* (2011) 42:2478–84. doi: 10.1161/STROKEAHA.111.620443
7. Qiao Y, Steinman DA, Qin Q, Etesami M, Schar M, Astor BC, et al. Intracranial arterial wall imaging using three-dimensional high isotropic resolution black blood MRI at 3.0 Tesla. *J Magn Reson Imaging.* (2011) 34:22–30. doi: 10.1002/jmri.22592
8. Lindenholz A, Harteveld AA, Zwanenburg JJM, Siero JCW, Hendrikse J. Comparison of 3T intracranial vessel wall MRI sequences. *AJNR Am J Neuroradiol.* (2018) 39:1112–20. doi: 10.3174/ajnr.A5629
9. Mandell DM, Mossa-Basha M, Qiao Y, Hess CP, Hui F, Matouk C, et al. Intracranial vessel wall MRI: principles and expert consensus recommendations of the american society of neuroradiology. *AJNR Am J Neuroradiol.* (2016) 38:218–29. doi: 10.3174/ajnr.A4893
10. Bhogal P, Navaei E, Makalanda HL, Brouwer PA, Sjostrand C, Mandell DM, et al. Intracranial vessel wall MRI. *Clin Radiol.* (2016) 71:293–303. doi: 10.1016/j.crad.2015.11.012
11. Lindenholz A, van der Kolk AG, Zwanenburg JJM, Hendrikse J. The use and pitfalls of intracranial vessel wall imaging: how we do it. *Radiology.* (2018) 286:12–28. doi: 10.1148/radiol.2017162096
12. Harteveld AA, van der Kolk AG, van der Worp HB, Dieleman N, Siero JC, Kuijf HJ, et al. High-resolution intracranial vessel wall MRI in an elderly asymptomatic population: comparison of 3T and 7T. *Eur Radiol.* (2016) 27:1585–95. doi: 10.1007/s00330-016-4483-3
13. Harteveld AA, Denswil NP, Siero JC, Zwanenburg JJ, Vink A, Pouran B, et al. Quantitative intracranial atherosclerotic plaque characterization at 7T MRI: an *ex vivo* study with histologic validation. *AJNR Am J Neuroradiol.* (2016) 37:802–10. doi: 10.3174/ajnr.A4628
14. van der Kolk AG, Zwanenburg JJ, Denswil NP, Vink A, Spliet WG, Daemen MJ, et al. Imaging the intracranial atherosclerotic vessel wall using 7T MRI: initial comparison with histopathology. *AJNR Am J Neuroradiol.* (2015) 36:694–701. doi: 10.3174/ajnr.A4178
15. Jiang Y, Zhu C, Peng W, Degnan AJ, Chen L, Wang X, et al. *Ex-vivo* imaging and plaque type classification of intracranial atherosclerotic plaque using high resolution MRI. *Atherosclerosis.* (2016) 249:10–6. doi: 10.1016/j.atherosclerosis.2016.03.033
16. Lopez-Cancio E, Dorado L, Millan M, Reverte S, Sunol A, Massuet A, et al. The barcelona-asymptomatic intracranial atherosclerosis (AsIA) study: prevalence and risk factors. *Atherosclerosis.* (2012) 221:221–5. doi: 10.1016/j.atherosclerosis.2011.12.020
17. Qiao Y, Guallar E, Suri FK, Liu L, Zhang Y, Anwar Z, et al. MR imaging measures of intracranial atherosclerosis in a population-based study. *Radiology.* (2016) 280:860–8. doi: 10.1148/radiol.2016151124
18. Yang WJ, Wong KS, Chen XY. Intracranial atherosclerosis: from microscopy to high-resolution magnetic resonance imaging. *J Stroke.* (2017) 19:249–60. doi: 10.5853/jos.2016.01956
19. Wardlaw JM, Smith C, Dichgans M. Mechanisms of sporadic cerebral small vessel disease: insights from neuroimaging. *Lancet Neurol.* (2013) 12:483–97. doi: 10.1016/S1474-4422(13)70060-7
20. van Veluw SJ, Shih AY, Smith EE, Chen C, Schneider JA, Wardlaw JM, et al. Detection, risk factors, and functional consequences of cerebral microinfarcts. *Lancet Neurol.* (2017) 16:730–40. doi: 10.1016/S1474-4422(17)30196-5
21. Shi Y, Wardlaw JM. Update on cerebral small vessel disease: a dynamic whole-brain disease. *Stroke Vasc Neurol.* (2016) 1:83–92. doi: 10.1136/svn-2016-000035
22. Ihara M, Yamamoto Y. Emerging evidence for pathogenesis of sporadic cerebral small vessel disease. *Stroke.* (2016) 47:554–60. doi: 10.1161/STROKEAHA.115.009627
23. van der Kolk AG, Hendrikse J, Brundel M, Biessels GJ, Smit EJ, Visser F. Multi-sequence whole-brain intracranial vessel wall imaging at 7.0 tesla. *Euro Radiol.* (2013) 23:2996–3004. doi: 10.1007/s00330-013-2905-z
24. Adams HP, Jr., Bendixen BH, Kappelle LJ, Biller J, Love BB, Gordon DL, et al. Classification of subtype of acute ischemic stroke. Definitions for use in a multicenter clinical trial. TOAST. Trial of org 10172 in acute stroke treatment. *Stroke.* (1993) 24:35–41. doi: 10.1161/01.STR.24.1.35
25. Lindenholz A, van der Kolk AG, van der Schaaf IC, van der Worp HB, Harteveld AA, Dieleman N, et al. Intracranial atherosclerosis assessed with 7-T MRI: evaluation of patients with ischemic stroke or transient ischemic attack. *Radiology.* (2020) 295:162–70. doi: 10.1148/radiol.2020190643
26. Klein S, Staring M, Murphy K, Viergever MA, Pluim JP. elastix: a toolbox for intensity-based medical image registration. *IEEE Trans Med Imaging.* (2010) 29:196–205. doi: 10.1109/TMI.2009.2035616
27. Wardlaw JM, Smith EE, Biessels GJ, Cordonnier C, Fazekas F, Frayne R, et al. Neuroimaging standards for research into small vessel disease and its contribution to ageing and neurodegeneration. *Lancet Neurol.* (2013) 12:822–38. doi: 10.1016/S1474-4422(13)70124-8
28. Fazekas F, Chawluk JB, Alavi A, Hurtig HI, Zimmerman RA. MR signal abnormalities at 1.5 T in Alzheimer's dementia and normal aging. *AJR Am J Roentgenol.* (1987) 149:351–6. doi: 10.2214/ajr.149.2.351
29. Wardlaw JM, Dennis MS, Warlow CP, Sandercock PA. Imaging appearance of the symptomatic perforating artery in patients with lacunar infarction: occlusion or other vascular pathology? *Ann Neurol.* (2001) 50:208–15. doi: 10.1002/ana.1082
30. Pantoni L. Cerebral small vessel disease: from pathogenesis and clinical characteristics to therapeutic challenges. *Lancet Neurol.* (2010) 9:689–701. doi: 10.1016/S1474-4422(10)70104-6
31. Harteveld AA, De Cocker LJ, Dieleman N, van der Kolk AG, Zwanenburg JJ, Robe PA, et al. High-resolution postcontrast time-of-flight MR angiography of intracranial perforators at 7.0 Tesla. *PLoS ONE.* (2015) 10:e0121051. doi: 10.1371/journal.pone.0121051
32. Kwon HM, Lynn MJ, Turan TN, Derdeyn CP, Fiorella D, Lane BF, et al. Frequency, risk factors, and outcome of coexistent small vessel disease and intracranial arterial stenosis: results from the stenting and aggressive medical management for preventing recurrent stroke

in intracranial stenosis (SAMMPRIS) trial. *JAMA Neurol.* (2016) 73:36–42. doi: 10.1001/jamaneurol.2015.3145
33. Bang OY, Chung JW, Ryoo S, Moon GJ, Kim GM, Chung CS, et al. Brain microangiopathy and macroangiopathy share common risk factors and biomarkers. *Atherosclerosis.* (2016) 246:71–7. doi: 10.1016/j.atherosclerosis.2015.12.040
34. Mead GE, Lewis SC, Wardlaw JM, Dennis MS, Warlow CP. Severe ipsilateral carotid stenosis and middle cerebral artery disease in lacunar ischaemic stroke: innocent bystanders? *J Neurol.* (2002) 249:266–71. doi: 10.1007/s004150200003
35. Brisset M, Boutouyrie P, Pico F, Zhu Y, Zureik M, Schilling S, et al. Large-vessel correlates of cerebral small-vessel disease. *Neurology.* (2013) 80:662–9. doi: 10.1212/WNL.0b013e318281ccc2
36. Aboyans V, Lacroix P, Criqui MH. Large and small vessels atherosclerosis: similarities and differences. *Progr Cardiovas Dis.* (2007) 50:112–25. doi: 10.1016/j.pcad.2007.04.001
37. Bang OY, Joo SY, Lee PH, Joo US, Lee JH, Joo IS, et al. The course of patients with lacunar infarcts and a parent arterial lesion: similarities to large artery vs small artery disease. *Arch Neurol.* (2004) 61:514–9. doi: 10.1001/archneur.61.4.514
38. Dieleman N, van der Kolk AG, Zwanenburg JJ, Brundel M, Harteveld AA, Biessels GJ, et al. Relations between location and type of intracranial atherosclerosis and parenchymal damage. *J Cereb Blood Flow Metab.* (2016) 36:1271–80. doi: 10.1177/0271678X15616401
39. Kong Q, Zhang Z, Yang Q, Fan Z, Wang B, An J, et al. 7T TOF-MRA shows modulated orifices of lenticulostriate arteries associated with atherosclerotic plaques in patients with lacunar infarcts. *Euro J Radiol.* (2019) 118:271–6. doi: 10.1016/j.ejrad.2019.07.032
40. Qiao Y, Zeiler SR, Mirbagheri S, Leigh R, Urrutia V, Wityk R. Intracranial plaque enhancement in patients with cerebrovascular events on high-spatial-resolution MR images. *Radiology.* (2014) 271:534–42. doi: 10.1148/radiol.13122812
41. Wang Y, Liu X, Wu X, Degnan AJ, Malhotra A, Zhu C. Culprit intracranial plaque without substantial stenosis in acute ischemic stroke on vessel wall MRI: a systematic review. *Atherosclerosis.* (2019) 287:112–21. doi: 10.1016/j.atherosclerosis.2019.06.907
42. Lee HN, Ryu CW, Yun SJ. Vessel-Wall magnetic resonance imaging of intracranial atherosclerotic plaque and ischemic stroke: a systematic review and meta-analysis. *Front Neurol.* (2018) 9:1032. doi: 10.3389/fneur.2018.01032
43. Kim KW, MacFall JR, Payne ME. Classification of white matter lesions on magnetic resonance imaging in elderly persons. *Biol Psychiatry.* (2008) 64:273–80. doi: 10.1016/j.biopsych.2008.03.024
44. Rost NS, Rahman RM, Biffi A, Smith EE, Kanakis A, Fitzpatrick K, et al. White matter hyperintensity volume is increased in small vessel stroke subtypes. *Neurology.* (2010) 75:1670–7. doi: 10.1212/WNL.0b013e3181fc279a
45. Ritz K, Denswil NP, Stam OC, van Lieshout JJ, Daemen MJ. Cause and mechanisms of intracranial atherosclerosis. *Circulation.* (2014) 130:1407–14. doi: 10.1161/CIRCULATIONAHA.114.011147
46. Arenillas JF, Lopez-Cancio E, Wong KS. Biomarkers, natural course and prognosis. *Front Neurol Neurosci.* (2016) 40:93–108. doi: 10.1159/000448304
47. Qiao Y, Anwar Z, Intrapiromkul J, Liu L, Zeiler SR, Leigh R, et al. Patterns and implications of intracranial arterial remodeling in stroke patients. *Stroke.* (2016) 47:434–40. doi: 10.1161/STROKEAHA.115.009955
48. Zhu C, Haraldsson H, Tian B, Meisel K, Ko N, Lawton M, et al. High resolution imaging of the intracranial vessel wall at 3 and 7 T using 3D fast spin echo MRI. *MAGMA.* (2016) 29:559–70. doi: 10.1007/s10334-016-0531-x
49. Harteveld AA, Denswil NP, Siero JC, Zwanenburg JJ, Vink A, Pouran B, et al. Quantitative intracranial atherosclerotic plaque characterization at 7T MRI: an *ex vivo* study with histologic validation. *AJNR Am J Neuroradiol.* (2015) 37:802–10. doi: 10.3174/ajnr.A4628

Conflict of Interest: The authors declare that the research was conducted in the absence of any commercial or financial relationships that could be construed as a potential conflict of interest.

frontiers in Neuroscience

ORIGINAL RESEARCH
published: 25 June 2021
doi: 10.3389/fnins.2021.665076

T_2-Weighted Whole-Brain Intracranial Vessel Wall Imaging at 3 Tesla With Cerebrospinal Fluid Suppression

Lei Zhang[1†], Yanjie Zhu[1†], Yulong Qi[2], Liwen Wan[1], Lijie Ren[3], Yi Zhu[2], Na Zhang[1], Dong Liang[1], Ye Li[1], Hairong Zheng[1] and Xin Liu[1]*

[1] Paul C. Lauterbur Research Center for Biomedical Imaging, Shenzhen Institutes of Advanced Technology, Chinese Academy of Sciences, Shenzhen, China, [2] Department of Radiology, Peking University Shenzhen Hospital, Shenzhen, China, [3] Department of Neurology, Shenzhen No. 2 People's Hospital, Shenzhen, China

OPEN ACCESS

Edited by:
Chengcheng Zhu,
University of Washington,
United States

Reviewed by:
Bram Coolen,
University of Amsterdam, Netherlands
Haikun Qi,
ShanghaiTech University, China
Anja Van Der Kolk,
Antoni van Leeuwenhoek Hospital,
Netherlands
Nan Wang,
University of California, Los Angeles,
United States
Qin Qin,
Johns Hopkins University,
United States

***Correspondence:**
Hairong Zheng
hr.zheng@siat.ac.cn

[†] These authors have contributed equally to this work

Specialty section:
This article was submitted to Brain Imaging Methods, a section of the journal Frontiers in Neuroscience

Received: 07 February 2021
Accepted: 03 June 2021
Published: 25 June 2021

Citation:
Zhang L, Zhu Y, Qi Y, Wan L, Ren L, Zhu Y, Zhang N, Liang D, Li Y, Zheng H and Liu X (2021) T_2-Weighted Whole-Brain Intracranial Vessel Wall Imaging at 3 Tesla With Cerebrospinal Fluid Suppression. Front. Neurosci. 15:665076. doi: 10.3389/fnins.2021.665076

Background: T_2-weighted (T_2w) intracranial vessel wall imaging (IVWI) provides good contrast to differentiate intracranial vasculopathies and discriminate various important plaque components. However, the strong cerebrospinal fluid (CSF) signal in T_2w images interferes with depicting the intracranial vessel wall. In this study, we propose a T_2-prepared sequence for whole-brain IVWI at 3T with CSF suppression.

Methods: A preparation module that combines T_2 preparation and inversion recovery (T_2IR) was used to suppress the CSF signal and was incorporated into the commercial three-dimensional (3D) turbo spin echo sequence-Sampling Perfection with Application optimized Contrast using different flip angle Evolution (SPACE). This new technique (hereafter called T_2IR-SPACE) was evaluated on nine healthy volunteers and compared with two other commonly used 3D T_2-weighted sequences: T_2w-SPACE and FLAIR-SPACE (FLAIR: fluid-attenuated inversion recovery). The signal-to-noise ratios (SNRs) of the vessel wall (VW) and CSF and contrast-to-noise ratios (CNRs) between them were measured and compared among these three T_2-weighted sequences. Subjective wall visualization of the three T_2-weighted sequences was scored blindly and independently by two radiologists using a four-point scale followed by inter-rater reproducibility analysis. A pilot study of four stroke patients was performed to preliminarily evaluate the diagnostic value of this new sequence, which was compared with two conventional T_2-weighted sequences.

Results: T_2IR-SPACE had the highest CNR (11.01 $\pm$ 6.75) compared with FLAIR-SPACE (4.49 $\pm$ 3.15; $p < 0.001$) and T_2w-SPACE (−56.16 $\pm$ 18.58; $p < 0.001$). The subjective wall visualization score of T_2IR-SPACE was higher than those of FLAIR-SPACE and T_2w-SPACE (T_2IR-SPACE: 2.35 $\pm$ 0.59; FLAIR-SPACE: 0.52 $\pm$ 0.54; T_2w-SPACE: 1.67 $\pm$ 0.58); the two radiologists' scores showed excellent agreement (ICC = 0.883).

Conclusion: The T_2IR preparation module markedly suppressed the CSF signal without much SNR loss of the other tissues (i.e., vessel wall, white matter, and gray matter) compared with the IR pulse. Our results suggest that T_2IR-SPACE is a potential alternative T_2-weighted sequence for assessing intracranial vascular diseases.

Keywords: intracranial vessel wall imaging, atherosclerosis, stroke, SPACE, T_2IR

INTRODUCTION

Intracranial atherosclerotic disease is a leading cause of ischemic stroke worldwide, particularly in the Asian population (Kim and Johnston, 2011; Qureshi and Caplan, 2014). High-resolution magnetic resonance (MR) intracranial vessel wall imaging (IVWI) has been reported as a promising technique allowing direct visualization of intracranial atherosclerotic plaques (Swartz et al., 2009; Qiao et al., 2011; Zhu et al., 2016; Mandell et al., 2017; Young et al., 2019). The characterization of intracranial vessel walls using MR imaging requires suppressing the MR signal arising from luminal blood and cerebrospinal fluid (CSF) (Qiao et al., 2011; van der Kolk et al., 2013; Dieleman et al., 2014; Mandell et al., 2017; Young et al., 2019), helping to delineate both the inner and outer walls of the vessels. Early studies mainly focused on T_1-weighted IVWI because of its ability to reveal vessel wall abnormalities with (i.e., atherosclerotic plaque) or without contrast agents (i.e., intraplaque hemorrhage), and it can also help classify intracranial vasculopathy (i.e., vasculitis) (Qiao et al., 2011; van der Kolk et al., 2013; Dieleman et al., 2014; Zhang et al., 2015; Mandell et al., 2017; Young et al., 2019; Jia et al., 2020).

Recently, studies have shown that T_2-weighted IVWI has the potential to identify intracranial plaque components and classify plaque types (van der Kolk et al., 2015; Harteveld et al., 2016; Jiang et al., 2016). For example, T_2-weighted IVWI allows the identification of lipid cores and fibrous cap ruptures (Turan et al., 2013; Chung et al., 2014). Xu et al. (2010) reported that a hyperintense band adjacent to the lumen on T_2-weighted images might suggest a fibrous cap. Ryu et al. (2009) reported that the foci of T_2 hyperintensity within plaques were more frequently observed in symptomatic stenosis than in asymptomatic stenosis. Additionally, T_2-weighted IVWI can be used as a complementary tool in multi-contrast vessel wall imaging for classifying intracranial vasculopathy (Mossa-Basha et al., 2015, 2016, 2017) and detecting atherosclerotic lesions that are not visible on magnetic resonance angiography (MRA) (Li et al., 2009).

Although T_2-weighted IVWI shows great potential in clinical use, its bright CSF signal makes the outer boundary of the intracranial vessel wall indistinguishable and may lead to estimation bias in vessel wall thickness. Fluid-attenuated inversion recovery (FLAIR) imaging has been applied to three-dimensional (3D) T_2-weighted IVWI to suppress the CSF signal (Turan et al., 2013). However, using inversion recovery requires a long inversion time for adequate CSF suppression and causes a significant deficiency in the signal-to-noise ratio (SNR). Another technique that combines T_2 preparation and an inversion recovery pulse (referred to as T_2IR) was developed to suppress background tissue for flow-independent peripheral angiography (Brittain et al., 1997); its advantages of an improved SNR and reduced T_1-weighting make it suitable for various applications (i.e., cardiac MRI, vessel wall imaging, and cerebral blood mapping) (Brittain et al., 1995; Mugler et al., 2000; Wong et al., 2001; Rooney et al., 2007; Busse et al., 2008; Liu et al., 2010, 2017; Visser et al., 2010; Xie et al., 2010; Mugler, 2014; Zhao et al., 2016; Zhang D.F. et al., 2017; Qi et al., 2018; Qin et al., 2019; Zhang et al., 2019; Zi et al., 2020). The T_2IR preparation module was used to achieve a submillimeter volumetric FLAIR sequence in an ultra-high field system (Visser et al., 2010).

In the present study, we combined the T_2IR preparation module with 3D variable-flip-angle TSE- Sampling Perfection with Application optimized Contrast using different flip angle Evolution (SPACE) acquisition, called T_2IR-SPACE, and achieved high resolution IVWI at 3.0T. The performance of the new sequence was assessed in a simulation study and an *in vivo* study in healthy volunteers and patients. The preliminary work for this study was partially reported in Zhang et al. (2019).

MATERIALS AND METHODS

Pulse Sequence

The proposed T_2IR-SPACE sequence comprises two parts (**Figure 1**): a T_2IR preparation module (Brittain et al., 1997) and T_2-weighted SPACE acquisition sampling (Mugler et al., 2000; Mugler, 2014) at the null point of the CSF signal.

Figure 1B illustrates the timing diagram of the T_2IR preparation module used in the present study. This module is designed according to the Carr-Purcell Malcolm Levitt (MLEV) method (Brittain et al., 1995). First, the longitudinal magnetization is excited by a 90^o_x radiofrequency (RF) pulse. Next, four composite refocus pulses ($90^o_x - 180^o_y - 90^o_x$) are applied, with the phases alternated to minimize the adverse effects of B_1 and B_0 field inhomogeneities. Finally, a composite 90^o_x ($270^o_{-x} - 360^o_x$) pulse tips the T_2-prepared transverse magnetization down to the $-z$ axis. The pulse is designed following the composite pulse ($270^o_x - 360^o_{-x}$) of -90^o_x (Brittain et al., 1995) but with an opposite phase to tip the magnetization downward. The duration of the T_2IR module, TE_{prep}, weights the longitudinal magnetization by $-e^{-TEprep/T2}$. A spoiling gradient is applied to dephase all the remaining transverse magnetizations (not shown in **Figure 1**). The SPACE acquisition is delayed by the time of inversion (TI) from the last 90° pulse at the null point of the CSF signal. All the pulses used are hard pulses, and the durations of the 90°, 180°, 270°, and 360° RF pulses are 0.5, 1, 1.5, and 2 ms, respectively.

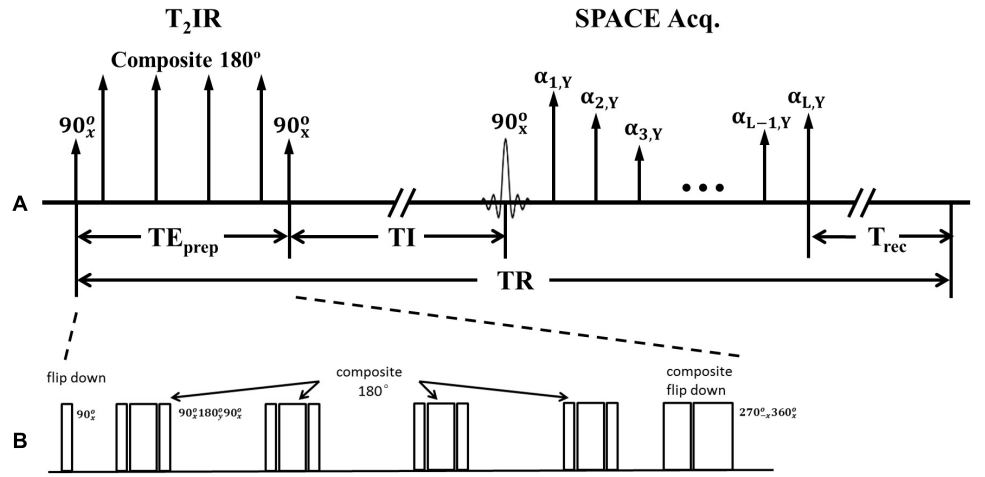

FIGURE 1 | (A) Schematic of the T_2IR preparation module followed by SPACE acquisition. **(B)** Zoom in of T_2IR preparation module.

Simulations

Bloch simulations (Busse et al., 2008; Zhang et al., 2015) were performed to investigate the signal behaviors of the intracranial vessel wall and CSF in the T_2IR-SPACE sequence. The simulation parameters were as follows: TR/TE = 2500/92 ms; echo spacing (ESP) = 4.4 ms; echo train length (ETL) = 77; TE_{prep} = 200 ms; and TI = 950 ms. The T_1 and T_2 values were 4300 and 2200 ms for CSF (Rooney et al., 2007; Liu et al., 2017), and 1200 and 50 ms for the vessel wall (Xie et al., 2010; Qi et al., 2018). The simulation was implemented and performed in MATLAB version 2010 (MathWorks, Natick, MA, United States). The optimization of the parameters of T_2IR module (TE_{prep} and TI) is provided in the Supporting Material (**Supplementary Figure 1**).

The signal evolutions of the vessel wall and CSF in conventional 3D T_2-weighted vessel wall imaging (T_2w-SPACE) and 3D T_2-weighted vessel wall imaging with a FLAIR preparation pulse to suppress CSF (FLAIR-SPACE) were also simulated and compared with the proposed T_2IR-SPACE sequence. The imaging parameters were adjusted to achieve the same spatial resolution and spatial coverage in the same scan time for all three sequences. The simulation parameters for T_2w-SPACE were the same as those for T_2IR-SPACE (**Supplementary Figure 2** shows the optimization of T_2w-SPACE). For FLAIR-SPACE, the simulation parameters were TR/TE = 6250/345 ms, ESP = 4.4 ms, ETL = 195, and TI = 2100 ms. The recently developed techniques, such as delay alternating with nutation for tailored excitation (DANTE) prepared T_2w-SPACE and AntiDrive were also compared with our proposed T_2IR-SPACE (Yang et al., 2016; Fan et al., 2017; Viessmann et al., 2017; Zhang L. et al., 2017). The Parameters for the DANTE module were: flip angle = 8°, number of pulses = 150, maximum gradient (in x, y, and z directions) = 20 mT/m, interpulse duration = 1.5 ms.

In vivo Experiments

All the experiments were performed using a 3T clinical whole-body MR system (TIM TRIO, Siemens, Erlangen) equipped with a 32-channel head coil. Nine healthy volunteers (three female; aged 24–61 years; mean age: 44.9 years) without known cerebrovascular disease were recruited for the volunteer study. Four patients (one female; aged 33–52 years) with symptoms of stroke and a diagnosis of intracranial arterial stenosis based on earlier MR angiography or computed tomography angiography were recruited for the pilot study. The patients were recruited during initial hospitalization within 30 days of symptom onset. Two more volunteers (both females, aged 62 and 29 years) were recruited to compare DANTE prepared T_2w-SPACE and AntiDrive with T_2IR-SPACE. Both studies were approved by the institutional review board, and informed consent forms were signed by all the participants before MR imaging.

For each volunteer, IVWI using whole-brain coverage was performed using T_2IR-SPACE, T_2w-SPACE, and FLAIR-SPACE. The imaging parameters were the same as those in the simulation and were summarized in **Table 1**. All the sequences were performed in the sagittal orientation. The fat suppression technique used in this study was composed of a spectral-selective pulse and spoiling gradients. GRAPPA was used to accelerate the scan time. The total scan time was 11 min 40 s for each of the three sequences.

In the patient study, three scans (T_2IR-SPACE, T_2w-SPACE, and FLAIR-SPACE, respectively) were conducted for two patients. The other two patients underwent only T_2IR-SPACE and T_2w-SPACE scans because they could not endure the long scan times. The imaging parameters were the same as those in the volunteer study.

Image Analysis

Qualitative image analysis was performed at a workstation (Syngo MultiModality Workplace, Siemens Healthcare, Germany) by two experienced radiologists (Q.Y.L. and Z.Y. with over 10 and 7 years of experience in neurovascular imaging, respectively) independently. The 3D image sets of T_2IR-SPACE, FLAIR-SPACE and T_2w-SPACE were presented to the two radiologists

TABLE 1 | Imaging parameters of the sequences evaluated in the study.

	T_2IR-SPACE	FLAIR-SPACE	T_2w-SPACE
TR/TE (ms)	2500/92	6250/345	2500/123
TE_{prep}/TI (ms)	200/950	.../2100	.../...
Echo train length	77	195	77
Common parameters			
Matrix size	288 × 288 × 224		
FOV (mm)	170 × 170 × 134.4		
Slice partial Fourier	5/8		
Bandwidth (Hz/pixel)	579		
GRAPPA/ref. lines	2/24		
Fat suppression	Yes		
Flip angle mode	T_2 var		
Voxel size (mm)	0.6 isotropic		
Scan time	11 min 40 s		

individually in a random order, with imaging information being blinded. The intracranial vascular beds were divided into three segments for assessment: Segment 1 included the M1–2 segments of the middle cerebral artery (MCA); Segment 2 included the basilar artery (BA) and V3–4 segments of VA; Segment 3 included C4–7 segments of ICA. Image quality was assessed using a four-point scale: 0 (poor), more than 50% of the vessel walls were invisible; 1 (acceptable), more than 50% of the walls were visible, but with noticeable blurring or limited SNR and CNR between the vessel wall and CSF; 2 (good), vessel walls were continuously visible but were slight blurred; 3 (excellent), vessel walls were clearly depicted with good SNR, CNR and sharpness. Scores >1 were regarded as diagnostic.

Quantitative analysis was performed at the following three vessel segments surrounded by CSF with different flow rate: the M1 segment of the MCA of both the left and right sides, BA, and internal carotid artery cavernous segment (C4, ICA) of both the left and right sides. T_2IR-SPACE, FLAIR-SPACE and T_2w-SPACE images were co-registered on the workstation using 3D image fusion functionality (Syngo Fusion, Siemens, Germany). 2D cross-sectional wall images were reconstructed by an experienced MRI scientist (Z.N.) using multiplanar reconstruction for each arterial segment; five vessel segments were reconstructed for each subject. Care was taken to ensure location matching among different scans. The SNR of the vessel wall and adjacent CSF and the contrast-to-noise ratio (CNR) between them were measured using region-of-interest (ROI) analysis. Based on the aforementioned 2D images, the ROI was manually prescribed on the images where the vessel walls were clearly visualized in all three sequences, and the mean signal intensities (S) of these sequences were obtained. The SNR is defined as SNR = S/σ, where S is the mean signal intensity of a certain tissue (VW or CSF) and σ is the noise measured as the standard deviation from an artifact-free air region of the nasal cavity. The CNR between the VW and CSF is defined as CNR = SNR_{VW}-SNR_{CSF}.

Statistical analyses were performed by using SPSS software (version 19.0; Chicago, IL, United States). The intra-reader correlation coefficient (ICC) was obtained from a two-way random model. The ICC value was interpreted as excellent, good, fair, and poor when it was between 0.75 and 1, between 0.6 and 0.74, between 0.4 and 0.59, and less than 0.4, respectively. Paired two-tailed Wilcoxon signed-rank test was performed on the data sets to determine the significance of the differences. The significance level was set at $p < 0.05/2 = 0.025$ (Bonferroni correction). The data were presented as means ± standard deviation.

RESULTS

Simulations

The simulated signal evolutions within one TR were plotted after ten repetitions of the pulse sequence until the signal evolutions reached the steady-state for subsequent repetitions. The signal evolution for T_2IR-SPACE (**Figure 2A**) comprises four parts: (I) transverse magnetization (M_{xy}) modulated by T_2 decay during the T_2IR module, in which, the M_{xy} of CSF decreases slightly because of its long T_2 value and the M_{xy} of vessel wall is close to zero at the end of the T_2IR module; (II) a second 90^o_x pulse tipping the transverse magnetization to the negative longitudinal axis, and the M_z recovering from the $-z$ axis during TI; (III) M_{xy} during the SPACE acquisition that performs around the null point of CSF; and (IV) recovery of the M_z during T_{rec}. The signal evolution for FLAIR-SPACE (**Figure 2C**) comprises three parts: (I) recovery of the M_z from the $-z$ axis after the inversion recovery pulse; (II) M_{xy} during the SPACE acquisition around the null point of CSF; and (III) recovery of M_z during the remainder of the TR. T_2w-SPACE signal evolution (**Figure 2E**) has two parts: (I) M_{xy} during the SPACE acquisition and (II) recovery of M_z during the remaining time of TR. **Figures 2B,E,F** are the magnified blocks from **Figures 2A,B,E**, showing the M_{xy} during the SPACE acquisition in T_2IR-SPACE, FLAIR-SPACE, and T_2w-SPACE, respectively. The CSF signals were well suppressed in both T_2IR-SPACE and FLAIR-SPACE (both < 0.05). The signal intensity of the vessel wall in T_2IR-SPACE (∼0.2) was almost twice that in FLAIR-SPACE (∼0.1). Although T_2w-SPACE had the highest vessel wall signal (∼0.25) among these three sequences, the unsuppressed CSF signal (∼0.5) resulted in a low contrast between the vessel wall and CSF.

In vivo Experiments

The MR scans were successfully acquired in all the participants with adequate or excellent image quality. As expected, the CSF signal was effectively suppressed in all T_2IR-SPACE images while the signal of other tissues maintained a high level. The qualitative image analysis results are summarized in **Table 2**. T_2IR SPACE showed better overall image quality when visualizing the intracranial vessel wall (reader 1, T_2IR-SPACE: 2.35 ± 0.59; FLAIR-SPACE: 0.52 ± 0.54; T_2w-SPACE: 1.671 ± 0.58). The inter-reader reliability was 0.883 (0.794–0.93; $p < 0.0001$). Representative images are shown in **Figure 3**. The vessel walls were clearly visualized at all segments of intracranial arteries on T_2IR-SPACE images, while they were almost invisible at most segments on FLAIR-SPACE images because of their low SNRs (labeled by red arrows). Additionally, the intracranial vessel wall

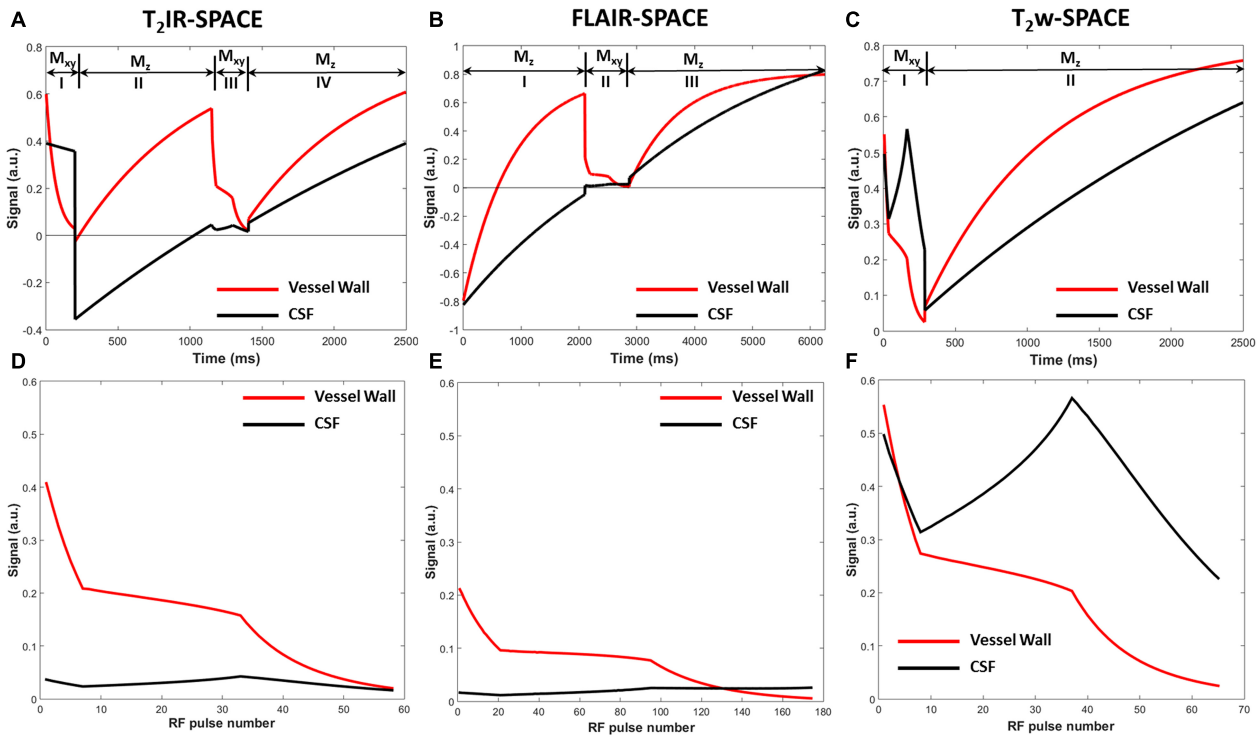

FIGURE 2 | Signal evolutions of the vessel wall and CSF for **(A)** T_2IR-SPACE, **(C)** FLAIR-SPACE, and **(E)** T_2w-SPACE sequences within one TR using Bloch simulation. Signal evolutions of transverse magnetization during the acquisition for **(B)** T_2IR-SPACE, **(D)** FLAIR-SPACE, and **(F)** T_2w-SPACE.

TABLE 2 | Comparison of the vessel wall visualization quality among T_2IR, FLAIR, and T_2w based on a four-point scale (0, poor; 1, fair; 2, good; and 3, excellent).

		T_2IR-SPACE	FLAIR-SPACE		T_2w-SPACE	
		Radiology scores (mean ± SD)	**Radiology scores (mean ± SD)**	***p*-value: vs. T_2IR**	**Radiology scores (mean ± SD)**	***p*-value: vs. T_2IR**
Reader 1	MCA	2.78 ± 0.44	0.67 ± 0.50	0.006	1.67 ± 0.50	0.008
	BA	2.22 ± 0.67	0.11 ± 0.33	0.006	1.67 ± 0.50	0.059
	ICA	2.56 ± 0.53	0.89 ± 0.33	0.006	2.11 ± 0.33	0.102
	Overall	2.52 ± 0.58	0.56 ± 0.51	<0.001	1.81 ± 0.48	<0.001
Reader 2	MCA	2.11 ± 0.33	0.22 ± 0.44	0.006	1.22 ± 0.44	0.011
	BA	2.00 ± 0.50	0.11 ± 0.33	0.006	1.44 ± 0.73	0.059
	ICA	2.44 ± 0.73	1.11 ± 0.33	0.014	1.89 ± 0.60	0.132
	Overall	2.19 ± 0.56	0.48 ± 0.58	<0.001	1.51 ± 0.64	0.001
Mean		2.35 ± 0.59	0.52 ± 0.54	<0.001	1.67 ± 0.58	0.001

could not be differentiated in T_2w-SPACE images because of the high CSF signal.

The quantitative results are summarized in **Table 3**. T_2IR-SPACE showed the best image contrast between the vessel wall (VW) and CSF (CNR: 11.01 ± 6.75) among the three sequences. As expected, the SNRs of the VW and CSF from T_2w-SPACE were the highest (VW: 50.45 ± 18.50; CSF: 106.61 ± 7.70), but the high CSF signal made delineating the outer boundary of the intracranial vessel wall challenging. The CSF signal was effectively suppressed in both T_2IR-SPACE and FLAIR-SPACE, but the T_2IR-SPACE had a much higher vessel wall signal (20.57 ± 6.07 vs. 9.40 ± 3.06; $p < 0.001$), resulting in a higher CNR between the VW and CSF (11.01 ± 6.75 vs. 4.49 ± 3.15; $p < 0.001$). The CNRs approximately agreed with the Bloch simulation predictions shown in **Figure 2**.

Imaging was successfully performed in all four patients. Among the four patients, three patients were found to have atherosclerosis plaques at the location of stenosis. One patient (female, 33 years old) was diagnosed as probable vasculitis (**Figure 4**), concentric wall thickening at MCA was more conspicuous on the T_2IR-SPACE image than on the FLAIR-SPACE and T_2w-SPACE images. **Figures 5**, **6** show the patients with atherosclerosis, in which wall thickening at the M2 segment of MCA was depicted only in T_2IR-SPACE imaging (**Figure 5**).

Figure 7 shows example images from a 62-years-old subject acquired with T_2IR-SPACE and DANTE prepared T_2w-SPACE,

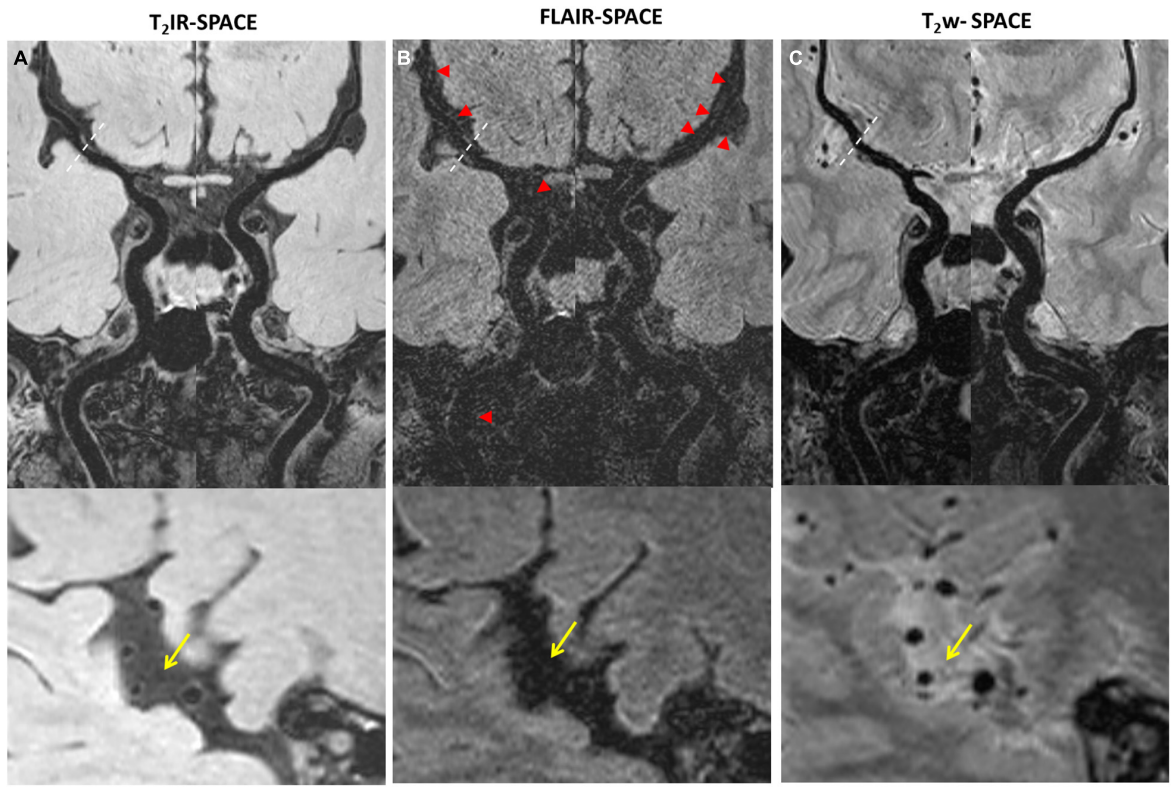

FIGURE 3 | Comparison among **(A)** T_2IR-SPACE, **(B)** FLAIR-SPACE, and **(C)** T_2w-SPACE images in a healthy 60-year-old volunteer. Curved multi-planar reconstruction images of both the left and right sides, starting from the internal carotid artery (ICA) and continuing up to the M2 segment of the middle cerebral artery (MCA), were generated for visual comparison. Bottom images show the zoomed-in image to better show the inner/outer vessel wall for each sequence, CSF area are labeled by the arrows. **(A)** The vessel walls are clearly visualized at all segments of intracranial arteries on T_2IR-SPACE. **(B)** The SNR is low on FLAIR-SPACE, and most of the intracranial vessel wall cannot be delineated (indicated by the red arrowheads). **(C)** For T_2w-SPACE, delineating the outer boundary of the intracranial artery wall is challenging.

TABLE 3 | SNR and CNR measurement results.

	T_2IR-SPACE	FLAIR-SPACE		T_2w-SPACE	
	Measurement (mean ± SD)	**Measurement (mean ± SD)**	***p*-value: vs. T_2IR**	**Measurement (mean ± SD)**	***p*-value: vs. T_2IR**
SNR: VW	20.57 ± 6.07	9.40 ± 3.06	<0.001	50.45 ± 18.50	<0.001
SNR: CSF	9.55 ± 1.87	4.91 ± 1.87	<0.001	106.61 ± 7.70	<0.001
CNR: VW-CSF	11.01 ± 6.75	4.49 ± 3.15	<0.001	−56.16 ± 18.58	<0.001

where T_1w-SPACE was also scanned as a reference standard. Wall thickening was detected at the M2 segment of the right MCA in T_2IR-SPACE (yellow arrow). This lesion was confirmed in T_1w-SPACE but could not be visualized in DANTE-SPACE. We performed T_2w-SPACE with AntiDrive in another healthy subject. The result is shown in **Figure 8**, illustrating that the CSF signal is not well suppressed and the intracranial vessel wall is not visible.

DISCUSSION

T_2IR-SPACE achieved high spatial resolution, large spatial coverage and, more importantly, remarkable CSF suppression and enhanced WM-CSF CNR. As shown in our preliminary results, T_2IR-SPACE greatly improves the ability of conventional T_2w-SPACE to differentiate vessel walls from CSF and is a potential alternative to T_2w-SPACE for assessing intracranial vascular diseases.

The subjective assessment results showed that T_2IR-SPACE had better intracranial wall visualization than the other two sequences in all vessel wall segments (**Table 2**). The subjective mean scores of T_2IR-SPACE were significantly higher than those of FLAIR-SPACE in all segments. This is because the IR pulse significantly reduced the SNR of the overall image and most parts of the intracranial vessel wall were missing in FLAIR-SPACE images, as demonstrated in both volunteer subjects and patient subjects (**Figures 3**, **4**). Moreover, the radiologist scores

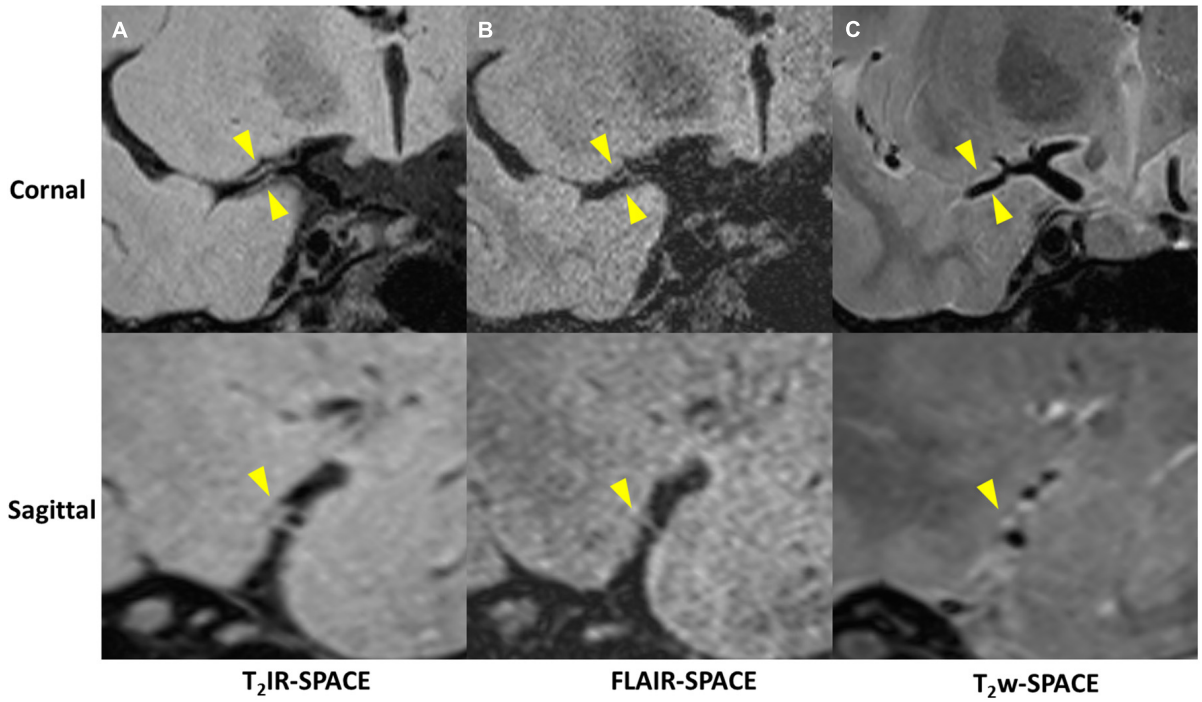

FIGURE 4 | A 33-year-old female patient diagnosed with vasculitis. **(A)** T_2IR-SPACE, **(B)** FLAIR-SPACE, and **(C)** T_2w-SPACE images. Top: coronal view of the right MCA; Bottom: sagittal view of the thickened vessel wall pointed by the arrowheads. Among the three T_2w sequences, only T_2IR-SPACE depicted concentric wall thickening on the M1 segment of the right MCA; the vessel wall was not clear on FLAIR-SPACE, and most parts of the vessel wall were missing; the vessel wall on T_2-weighted SPACE imaging appeared normal.

of T_2IR-SPACE were significantly higher than those of T_2w-SPACE in the MCA and BA segments. This is because in the two regions, and the CSF signal in T_2-weighted images was high, the outer boundary of the intracranial vessel wall was difficult to differentiate from the surrounding CSF (**Figures 3–6**), interfering with the accurate diagnosis by the radiologist. In the ICA segment, the radiologist score of T_2IR-SPACE showed little improvement without statistical significance compared with T_2w-SPACE because the intracranial vessel wall at the ICA region was not surrounded by the CSF fluid, so the high CSF signal would not influence the vessel wall visualization. Our proposed T_2IR-SPACE technique compensates for the imperfection of the above two existing approaches. It suppresses the CSF signal without much signal loss of other tissues, and the vessel wall can be clearly visualized at all segments of intracranial arteries in T_2IR-SPACE images (**Figures 3–6**).

Previous studies have demonstrated that patients with symptomatic MCA stenosis have larger wall area, plaque area and remodeling index than asymptomatic patients (Xu et al., 2010; Zhang D.F. et al., 2017; Zhao et al., 2016). A hyperintensity band adjacent to the lumen was often observed on T_2-weighted images, which was assumed to represent the fibrous cap (Xu et al., 2010; Mossa-Basha et al., 2015). In these studies, the MCA-CSF interface was used to manually trace the vessel area. The high CSF signal in T_2-weighted MRI images makes it difficult to distinguish the outer boundary of the intracranial vessel wall and results in inaccurate measurements of wall area and plaque area. T_2IR-SPACE suppresses CSF uniformly in whole-brain coverage and allows clear visualization of the interface between the MCA and CSF, which helps to characterize the features of intracranial plaques more accurately and stratify stroke risk in patients with atherosclerotic disease.

Recently, DANTE prepared SPACE and SPACE with AntiDrive have gained popularity in IVWI due to their efficient CSF suppression and superior SNR efficiency (Yang et al., 2016; Fan et al., 2017; Viessmann et al., 2017; Zhang L. et al., 2017). We compared these techniques with our proposed T_2IR-SPACE in a preliminary volunteer study. The DANTE module suppresses the CSF well around the circle of Wills but varies at distal (M2 or beyond) segments of the MCA or adjacent to the brain parenchyma (**Figure 7**, red arrowheads), because CSF fluid velocity varies in those regions and DANTE is a velocity-sensitive module, thus resulting in a heterogeneous CSF signal and interfering with accurate diagnosis by the radiologist. The T_2IR module provides robust CSF suppression regardless of the flow velocity, because this module relies on physical properties (T1 and T2) of CSF rather than the velocity of CSF. Hence, this approach is insensitive to slow flow and flow direction. In T_2w-SPACE with AntiDrive, the CSF signal is not well suppressed and the intracranial vessel wall is not visible. This is because the TR (2500 ms) is relatively long in T_2w-SPACE, although the AntiDrive pulse inverts the M_z of CSF to the negative longitudinal axis at the end of the echo train, the CSF still recovers to a relatively high value during

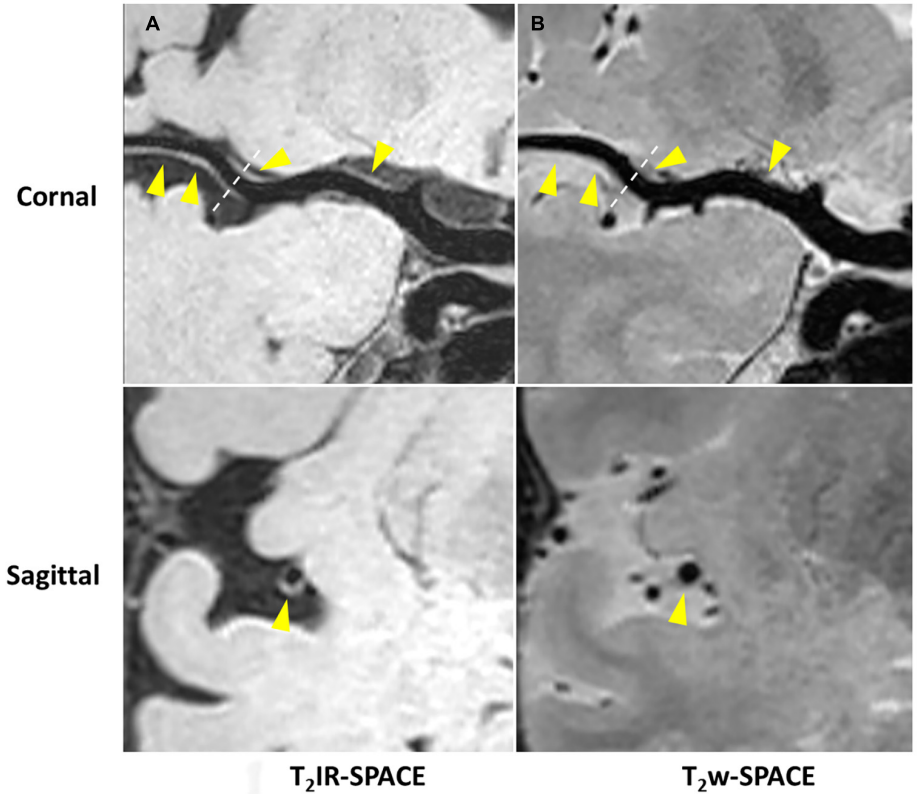

FIGURE 5 | Curved MPR of **(A)** T_2IR-SPACE and **(B)** T_2w-SPACE from a 46-year-old male patient. Top: coronal view of the right MCA; Bottom: sagittal view of artery at the location of the dashed line; Wall thickening was depicted only in T_2IR-SPACE (labeled by the arrowhead). The vessel appeared normal in T_2w-SPACE.

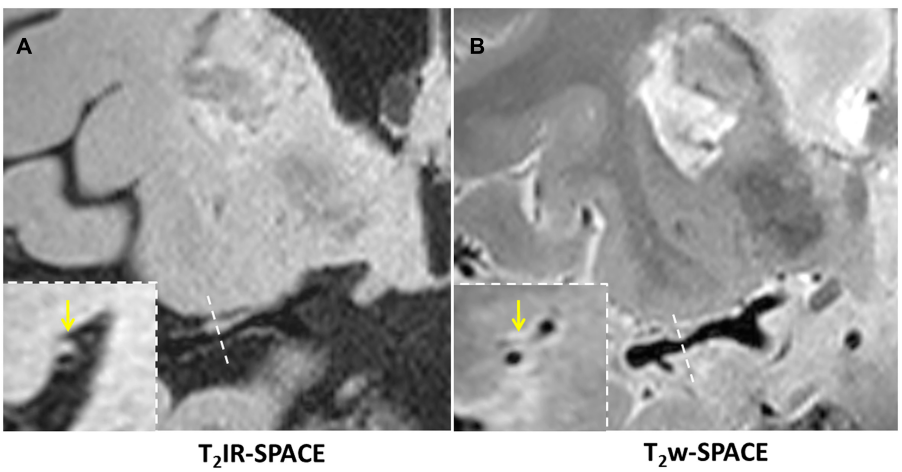

FIGURE 6 | In a 45-year-old male patient with ischemic stroke, **(A)** reconstructed T_2IR-SPACE image and **(B)** T_2w-SPACE identified a plaque at the M1 segment of the right MCA. However, the cross-sectional view (bottom dashed insert) showed eccentric wall thickening only on T_2IR-SPACE because of the signal suppression of surrounding CSF. The outer boundary of the eccentric plaque was not visible on T_2w-SPACE. The yellow arrow means the eccentric wall thickening.

the long T_{rec}. However, in T_1w-SPACE, CSF signal is already low enough and lower than the brain parenchyma due to the short TR, and the application of AntiDrive pulse would further reduce the CSF signal and improve the T1 contrast. This is the reason why AntiDrive pulse is widely used in T_1-weighted IVWI.

In this study, a composite 90° pulse was used instead of a hard pulse to tip the magnetization down with better

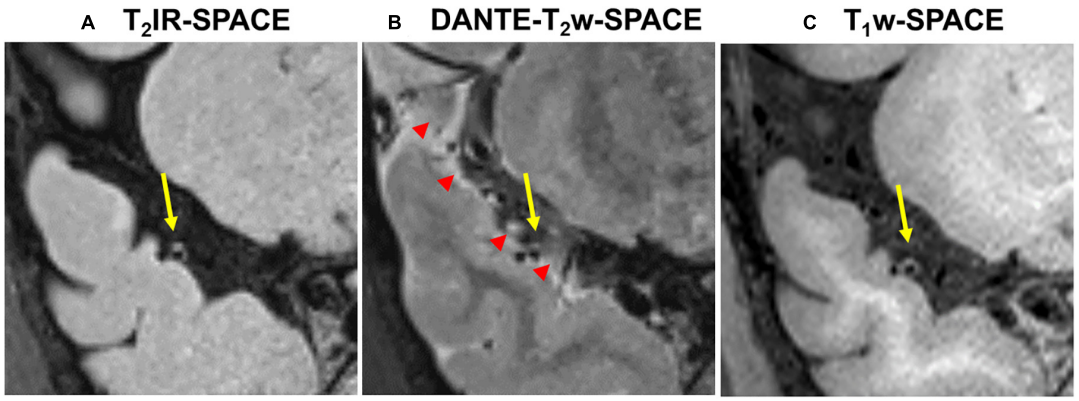

FIGURE 7 | Comparison between **(A)** T_2IR-SPACE and **(B)** DANTE prepared T_2w-SPACE in a 62-year-old subject. **(C)** T_1w-SPACE was scanned as a reference standard. The yellow arrows indicate the wall thickening which is visualized in T_2IR-SPACE and T_1w-SPACE. The red arrowheads indicate the heterogeneous CSF signal caused by the DANTE module.

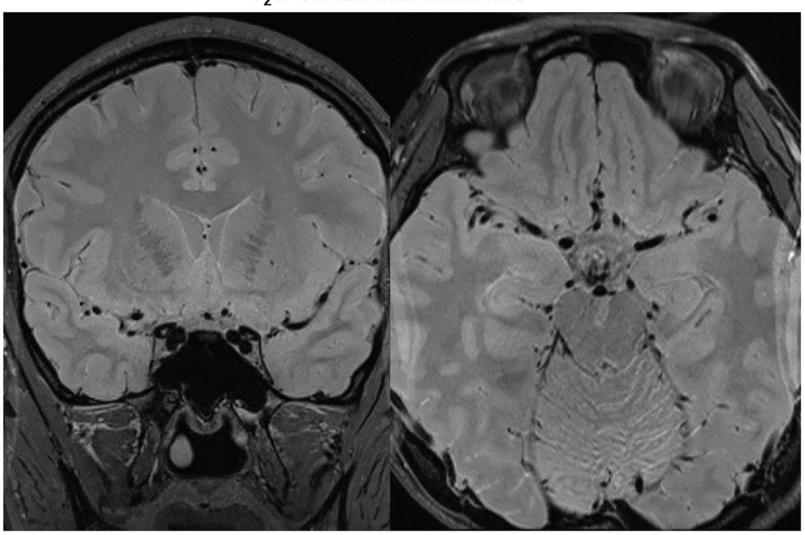

FIGURE 8 | Representative images of T_2w-SPACE with AntiDrive from a healthy subject. The CSF is not well suppressed and the intracranial vessel wall is not visible.

immunity to B_0 field inhomogeneity. However, the composite pulse has a narrower bandwidth with limited RF amplitude when implemented on a human scanner and is thus sensitive to B_1 field inhomogeneity.

This study has several limitations. One limitation of the technique is the long scan time as result of the long TR required for CSF nulling. This can not be easily compensated for by e.g., choosing a longer ETL as this would negatively impact the effective resolution of the scan. We however feel that the robustness of CSF suppression justifies the use of the sequence. Furthermore, there have efforts already using compressed sensing for IVWI for T_1-weighting imaging (Zhu et al., 2018; Jia et al., 2020) and such strategies might be used in T_2-weighting imaging to enable shortening of the scan time, thereby improving the clinical feasibility of our sequence. Second, we performed simulations and found that T_2IR-SPACE was affected by partial T_1-weighting next to the desired T_2-weighting, due to the short TI time (**Supplementary Figure 3**). We will optimize the parameters of T_2IR-SPACE to reduce the T_1-weighting in future studies. Third, the number of patients involved in this study was small. However, the present study was designed to demonstrate the feasibility and potential of T_2IR-SPACE in IVWI. Separate clinical studies involving a large patient cohort are needed to evaluate the clinical relevance for the diagnosis of intracranial vascular disease.

CONCLUSION

In the present study, we developed a new whole-brain T_2-weighted intracranial arterial wall imaging sequence with CSF

suppression. The T_2IR preparation module suppresses the CSF signal remarkably without much SNR loss of in other tissues (i.e., vessel wall, white matter, and gray matter) compared with the IR pulse. Our results suggest that T_2IR-SPACE is a potential alternative T_2-weighted sequence for assessing intracranial vascular diseases.

DATA AVAILABILITY STATEMENT

The datasets used and analyzed during this study are available from the corresponding author on reasonable request and filling out NEL-Consent redirecting to "Zenodo" with the DOI: https://doi.org/10.5281/zenodo.4145224.

ETHICS STATEMENT

The studies involving human participants were reviewed and approved by Institutional Review Board of Shenzhen Institute of Advanced Technology, Chinese Academy of Sciences; Institutional Review Board of Shenzhen Second People's Hospital. The patients/participants provided their written informed consent to participate in this study.

AUTHOR CONTRIBUTIONS

LZ and YaZ designed the sequence and experiments and drafted the manuscript. LZ performed the Bloch equation simulations. YQ and YiZ performed the subjective assessment. LW contributed to data collection. LR recruited the patients. NZ and LW measured the SNR and CNR. XL and YL contributed to the study design and helped revised the manuscript critically. XL and HZ conceived the study design and provided supervision of the whole project and critical review of the manuscript. All authors read and approved the final manuscript.

FUNDING

This study received funding from the National Natural Science Foundation of China (Grant Nos. 81801691, 61771463, 81971611, and 81830056), State Key Program of national Natural Science Foundation of China (No. 81830056), Natural Science Foundation of Guangdong Province (Grant No. 2018A 030313204), and Shenzhen Fundamental Research Program (JCYJ20180302145700745).

SUPPLEMENTARY MATERIAL

The Supplementary Material for this article can be found online at: https://www.frontiersin.org/articles/10.3389/fnins.2021.665076/full#supplementary-material

Supplementary Figure 1 | Simulated T_2IR-SPACE signal intensity of **(A)** vessel wall, **(B)** CSF, and **(C)** contrast between the vessel wall and CSF as a function of TI and TE_{prep}.

Supplementary Figure 2 | T_2w-SPACE images with different TRs in a healthy subject.

Supplementary Figure 3 | Simulation results of T_2IR-SPACE from two hypothetical tissues with the same T2 value and different T1 values **(a,b)**; the same T1 value and different T2 values **(c,d)**.

REFERENCES

Brittain, J. H., Hu, B. S., Wright, G. A., Meyer, C. H., Macovski, A., and Nishimura, D. G. (1995). Coronary angiography with magnetization-prepared T2 contrast. *Magn Reson Med.* 33, 689–696. doi: 10.1002/mrm.1910330515

Brittain, J. H., Olcott, E. W., Szuba, A., Gold, G. E., Wright, G. A., Irarrazaval, P., et al. (1997). Three-Dimen -sional flow-independent peripheral angiography. *Magn. Reson. Med.* 38:343. doi: 10.1002/mrm.1910380302

Busse, R. F., Brau, A. C., Vu, A., Michelich, C. R., Bayram, E., Kijowski, R., et al. (2008). Effects of refocusing flip angle modulation and view ordering in 3D fast spin echo. *Magn. Reson. Med.* 60, 640–649. doi: 10.1002/mrm.21680

Chung, J. W., Kim, B. J., Choi, B. S., Sohn, C. H., Bae, H. J., Yoon, B. W., et al. (2014). High-resolution magnetic resonance imaging reveals hidden etiologies of symptomatic vertebral arterial lesions. *J. Stroke Cerebrovasc. Dis.* 23, 293–302. doi: 10.1016/j.jstrokecerebrovasdis.2013.02.021

Dieleman, N., van der Kolk, A. G., Zwanenburg, J. J. M., Harteveld, A. A., Biessels, G. J., Luijten, P. R., et al. (2014). Imaging intracranial vessel wall pathology with magnetic resonance imaging: current prospects and future directions. *Circulation* 130, 192–201. doi: 10.1161/circulationaha.113.006919

Fan, Z., Yang, Q., Deng, Z., Li, Y., Bi, X., Song, S., et al. (2017). Whole-brain intracranial vessel wall imaging at 3 Tesla using cerebrospinal fluid-attenuated T1-weighted 3D turbo spin echo. *Magn. Reson. Med.* 77:1142. doi: 10.1002/mrm.26201

Harteveld, A. A., Denswil, N. P., Siero, J. C., Zwanenburg, J. J., Vink, A., Pouran, B., et al. (2016). Quantitative intracranial atherosclerotic plaque characterization at 7T MRI: An Ex vivo study with histologic validation. *AJNR Am. J. Neuroradiol.* 37, 802–810. doi: 10.3174/ajnr.a4628

Jia, S., Zhang, L., Ren, L., Qi, Y., Ly, J., Zhang, N., et al. (2020). Joint intracranial and carotid vessel wall imaging in 5 minutes using compressed sensing accelerated DANTE-SPACE. *Eur. Radiol.* 30, 119–127. doi: 10.1007/s00330-019-06366-7

Jiang, Y., Zhu, C., Peng, W., Degnan, A. J., Chen, L., Wang, X., et al. (2016). Ex-vivo imaging and plaque type classification of intracranial atherosclerotic plaque using high resolution MRI. *Atherosclerosis* 249, 10–16. doi: 10.1016/j.atherosclerosis.2016.03.033

Kim, A. S., and Johnston, S. C. (2011). Global variation in the relative burden of stroke and ischemic heart disease. *Circulation* 124, 314–323. doi: 10.1161/circulationaha.111.018820

Li, M. L., Xu, W. H., Song, L., Feng, F., You, H., Ni, J., et al. (2009). Atherosclerosis of middle cerebral artery: evaluation with high-resolution MR imaging at 3T. *Atherosclerosis* 204, 447–452. doi: 10.1016/j.atherosclerosis.2008.10.019

Liu, C. Y., Bley, T. A., Wieben, O., Brittain, J. H., and Reeder, S. B. (2010). Flow-independent T(2)-prepared inversion recovery black-blood MR imaging. *J. Magn. Reson. Imaging* 31, 248–254. doi: 10.1002/jmri.21986

Liu, D., Xu, F., Lin, D. D., van Zijl, P. C. M., and Qin, Q. (2017). Quantitative measurement of cerebral blood volume using velocity-selective pulse trains. *Magn. Reson. Med.* 77, 92–101. doi: 10.1002/mrm.26515

Mandell, D. M., Mossa-Basha, M., Qiao, Y., Hess, C. P., Hui, F., Matouk, C., et al. (2017). Vessel wall imaging study group of the American Society of N. intracranial vessel wall MRI: principles and expert consensus recommendations of the American society of neuroradiology. *AJNR Am. J. Neuroradiol.* 38, 218–229. doi: 10.3174/ajnr.a4893

Mossa-Basha, M., de Havenon, A., Becker, K. J., Hallam, D. K., Levitt, M. R., Cohen, W. A., et al. (2016). Added value of vessel wall magnetic resonance imaging in

the differentiation of moyamoya vasculopathies in a non-asian cohort. *Stroke* 47, 1782–1788. doi: 10.1161/strokeaha.116.013320

Mossa-Basha, M., Hwang, W. D., De Havenon, A., Hippe, D., Balu, N., Becker, K. J., et al. (2015). Multicontrast high-resolution vessel wall magnetic resonance imaging and its value in differentiating intracranial vasculopathic processes. *Stroke* 46, 1567–1573. doi: 10.1161/strokeaha.115.009037

Mossa-Basha, M., Shibata, D. K., Hallam, D. K., de Havenon, A., Hippe, D. S., Becker, K. J., et al. (2017). Added value of vessel wall magnetic resonance imaging for differentiation of nonocclusive intracranial vasculopathies. *Stroke* 48, 3026–3033. doi: 10.1161/strokeaha.117.018227

Mugler, J. P. III (2014). Optimized three-dimensional fast-spin-echo MRI. *J. Magn. Reson. Imaging* 39, 745–767. doi: 10.1002/jmri.24542

Mugler, J. P., Bao, S., Mulkern, R. V., Guttmann, C. R., Robertson, R. L., Jolesz, F. A., et al. (2000). Optimized single-slab three-dimensional spin-echo MR imaging of the brain. *Radiology* 216, 891–899. doi: 10.1148/radiology.216.3.r00au46891

Qi, H., Sun, J., Qiao, H., Zhao, X., Guo, R., Balu, N., et al. (2018). Simultaneous T1 and T2 mapping of the carotid plaque (SIMPLE) with T2 and inversion recovery prepared 3D radial imaging. *Magn. Reson. Med.* 80, 2598–2608. doi: 10.1002/mrm.27361

Qiao, Y., Steinman, D. A., Qin, Q., Etesami, M., Schar, M., Astor, B. C., et al. (2011). Intracranial arterial wall imaging using three-dimensional high isotropic resolution black blood MRI at 3.0 Tesla. *J. Magn. Reson. Imaging* 34, 22–30. doi: 10.1002/jmri.22592

Qin, Q., Qu, Y., Li, W., Liu, D., Shin, T., Zhao, Y., et al. (2019). Cerebral blood volume mapping using Fourier-transform-based velocity-selective saturation pulse trains. *Magn. Reson. Med.* 81, 3544–3554. doi: 10.1002/mrm.27668

Qureshi, A. I., and Caplan, L. R. (2014). Intracranial atherosclerosis. *Lancet.* 383, 984–998.

Rooney, W. D., Johnson, G., Li, X., Cohen, E. R., Kim, S. G., Ugurbil, K., et al. (2007). Magnetic field and tissue dependencies of human brain longitudinal 1H2O relaxation in vivo. *Magn. Reson. Med.* 57, 308–318. doi: 10.1002/mrm.21122

Ryu, C. W., Jahng, G. H., Kim, E. J., Choi, W. S., and Yang, D. M. (2009). High resolution wall and lumen MRI of the middle cerebral arteries at 3 tesla. *Cerebrovasc. Dis.* 27, 433–442. doi: 10.1159/000209238

Swartz, R. H., Bhuta, S. S., Farb, R. I., Agid, R., Willinsky, R. A., Terbrugge, K. G., et al. (2009). Intracranial arterial wall imaging using high-resolution 3-tesla contrast-enhanced MRI. *Neurology* 72, 627–634. doi: 10.1212/01.wnl.0000342470.69739.b3

Turan, T. N., Rumboldt, Z., and Brown, T. R. (2013). High-resolution MRI of basilar atherosclerosis: three-dimensional acquisition and FLAIR sequences. *Brain Behav.* 3, 1–3. doi: 10.1002/brb3.103

van der Kolk, A. G., Hendrikse, J., Brundel, M., Biessels, G. J., Smit, E. J., Visser, F., et al. (2013). Multi-sequence whole-brain intracranial vessel wall imaging at 7.0 tesla. *Eur. Radiol.* 23, 2996–3004. doi: 10.1007/s00330-013-2905-z

van der Kolk, A. G., Zwanenburg, J. J., Denswil, N. P., Vink, A., Spliet, W. G., Daemen, M. J., et al. (2015). Imaging the intracranial atherosclerotic vessel wall using 7T MRI: initial comparison with histopathology. *AJNR Am. J. Neuroradiol. 2015* 36, 694–701. doi: 10.3174/ajnr.a4178

Viessmann, O., Li, L., Benjamin, P., and Jezzard, P. (2017). T2-Weighted intracranial vessel wall imaging at 7 Tesla using a DANTE-prepared variable flip angle turbo spin echo readout (DANTE-SPACE). *Magn. Reson. Med.* 77:655. doi: 10.1002/mrm.26152

Visser, F., Zwanenburg, J. J. M., Hoogduin, J. M., and Luijten, P. R. (2010). High-resolution magnetization-prepared 3D-FLAIR imaging at 7.0 Tesla. *Magn. Reson. Med.* 64, 194–202. doi: 10.1002/mrm.22397

Wong, E. C., Liu, T. T., Luh, W. M., Frank, L. R., and Buxton, R. B. (2001). T(1) and T(2) selective method for improved SNR in CSF-attenuated imaging: T(2)-FLAIR. *Magn. Reson. Med.* 45, 529–532. doi: 10.1002/1522-2594(200103)45:3<529::aid-mrm1071>3.0.co;2-l

Xie, J., Bi, X., Fan, Z., Bhat, H., Shah, S., Zuehlsdorff, S., et al. (2010). 3D flow-independent peripheral vessel wall imaging using T(2)-prepared phase-sensitive inversion-recovery steady-state free precession. *J. Magn. Reson. Imaging* 32, 399–408. doi: 10.1002/jmri.22272

Xu, W. H., Li, M. L., Gao, S., Ni, J., Zhou, L. X., Yao, M., et al. (2010). *In vivo* high-resolution MR imaging of symptomatic and asymptomatic middle cerebral artery atherosclerotic stenosis. *Atherosclerosis* 212, 507–511. doi: 10.1016/j.atherosclerosis.2010.06.035

Yang, H., Zhang, X., Qin, Q., Liu, L., Wasserman, B. A., and Qiao, Y. (2016). Improved cerebrospinal fluid suppression for intracranial vessel wall MRI. *J. Magn. Reson. Imaging* 44:665. doi: 10.1002/jmri.25211

Young, C. C., Bonow, R. H., Barros, G., Mossa-Basha, M., Kim, L. J., and Levitt, M. R. (2019). Magnetic resonance vessel wall imaging in cerebrovascular diseases. *Neurosurg. Focus.* 47:E4.

Zhang, D. F., Chen, Y. C., Chen, H. Y., Zhang, W. D., Sun, J., Mao, C. N., et al. (2017). A High-Resolution MRI study of relationship between remodeling patterns and ischemic stroke in patients with atherosclerotic middle cerebral artery stenosis. *Front. Aging Neurosci.* 9:140. doi: 10.3389/fnagi.2017.00140

Zhang, L., Chung, Y. C., Ren, L. J., Zhang, N., and Liu, X. (2019). "T2 weighted whole-brain intracranial vessel wall imaging at 3 tesla with cerebrospinal fluid suppression," in *Proceedings of the 27th Annual Meeting of ISMRM, Montreal, QC*, (Canada), 1044.

Zhang, L., Zhang, N., Wu, J., Liu, X., and Chung, Y. C. (2017). High resolution simultaneous imaging of intracranial and extracranial arterial wall with improved cerebrospinal fluid suppression. *Magn. Reson. Imaging* 44:65. doi: 10.1016/j.mri.2017.08.004

Zhang, L., Zhang, N., Wu, J., Zhang, L., Huang, Y., Liu, X., et al. (2015). High resolution three dimensional intracranial arterial wall imaging at 3T using T1 weighted SPACE. *Magn. Reson. Imaging* 33, 1026–1034. doi: 10.1016/j.mri.2015.06.006

Zhao, D. L., Deng, G., Xie, B., Gao, B., Peng, C. Y., Nie, F., et al. (2016). Wall characteristics and mechanisms of ischaemic stroke in patients with atherosclerotic middle cerebral artery stenosis: a high-resolution MRI study. *Neurol. Res.* 38, 606–613. doi: 10.1179/1743132815y.0000000088

Zhu, C., Tian, B., Chen, L., Eisenmenger, L., Raithel, E., Forman, C., et al. (2018). Accelerated whole brain intracranial vessel wall imaging using black blood fast spin echo with compressed sensing (CS-SPACE). *MAGMA* . 31, 457–467. doi: 10.1007/s10334-017-0667-3

Zhu, C. C., Haraldsson, H., Tian Bing, Meisel Karl, Ko Nerissa, Lawton Michael, et al. (2016). High resolution imaging of the intracranial vessel wall at 3 and 7T using 3D fast spin echo MRI. *MAGMA* 29, 559–570. doi: 10.1007/s10334-016-0531-x

Zi, R., Zhu, D., and Qin, Q. (2020). Quantitative T2 mapping using accelerated 3D stack-of-spiral gradient echo readout. *Magn. Reson. Imaging* 73, 138–147. doi: 10.1016/j.mri.2020.08.007

Conflict of Interest: The authors declare that the research was conducted in the absence of any commercial or financial relationships that could be construed as a potential conflict of interest.

frontiers in Neuroscience

ORIGINAL RESEARCH
published: 12 July 2021
doi: 10.3389/fnins.2021.691244

OPEN ACCESS

Edited by:
Danny J. J. Wang, University of Southern California, Los Angeles, United States

Reviewed by:
Dafna Ben Bashat, The Wohl institute for Advanced Imaging, Israel
Yong Fan, University of Pennsylvania, United States

***Correspondence:**
Martin Bretzner
mbretzner@mgh.harvard.edu; martin.bretzner@gmail.com

†*The members of the MRI-GENIE GISCOME Investigators and the International and Stroke Genetics Consortium are given in Supplementary Table 1.*

Specialty section:
This article was submitted to Brain Imaging Methods, a section of the journal Frontiers in Neuroscience

Received: *05 April 2021*
Accepted: *15 June 2021*
Published: *12 July 2021*

Citation:
Bretzner M, Bonkhoff AK, Schirmer MD, Hong S, Dalca AV, Donahue KL, Giese A-K, Etherton MR, Rist PM, Nardin M, Marinescu R, Wang C, Regenhardt RW, Leclerc X, Lopes R, Benavente OR, Cole JW, Donatti A, Griessenauer CJ, Heitsch L, Holmegaard L, Jood K, Jimenez-Conde J, Kittner SJ, Lemmens R, Levi CR, McArdle PF, McDonough CW, Meschia JF, Phuah C-L, Rolfs A, Ropele S, Rosand J, Roquer J, Rundek T, Sacco RL, Schmidt R, Sharma P, Slowik A, Sousa A, Stanne TM, Strbian D, Tatlisumak T, Thijs V, Vagal A, Wasselius J, Woo D, Wu O, Zand R, Worrall BB, Maguire JM, Lindgren A, Jern C, Golland P, Kuchcinski G and Rost NS (2021) MRI Radiomic Signature of White Matter Hyperintensities Is Associated With Clinical Phenotypes. Front. Neurosci. 15:691244. doi: 10.3389/fnins.2021.691244

MRI Radiomic Signature of White Matter Hyperintensities Is Associated With Clinical Phenotypes

Martin Bretzner[1,2]*, Anna K. Bonkhoff[1], Markus D. Schirmer[1], Sungmin Hong[1], Adrian V. Dalca[1,3,4], Kathleen L. Donahue[1], Anne-Katrin Giese[1], Mark R. Etherton[1], Pamela M. Rist[1,5], Marco Nardin[1], Razvan Marinescu[1,4], Clinton Wang[1,4], Robert W. Regenhardt[1], Xavier Leclerc[2], Renaud Lopes[2,6], Oscar R. Benavente[7], John W. Cole[8], Amanda Donatti[9], Christoph J. Griessenauer[10,11], Laura Heitsch[12,13], Lukas Holmegaard[14], Katarina Jood[14], Jordi Jimenez-Conde[15], Steven J. Kittner[8], Robin Lemmens[16,17], Christopher R. Levi[18,19], Patrick F. McArdle[20], Caitrin W. McDonough[21], James F. Meschia[22], Chia-Ling Phuah[13], Arndt Rolfs[23], Stefan Ropele[24], Jonathan Rosand[25], Jaume Roquer[26], Tatjana Rundek[26], Ralph L. Sacco[26], Reinhold Schmidt[24], Pankaj Sharma[27,28], Agnieszka Slowik[29], Alessandro Sousa[8], Tara M. Stanne[14], Daniel Strbian[30], Turgut Tatlisumak[31,32], Vincent Thijs[33], Achala Vagal[34], Johan Wasselius[35,36], Daniel Woo[37], Ona Wu[3], Ramin Zand[38], Bradford B. Worrall[39], Jane M. Maguire[40], Arne Lindgren[41,42], Christina Jern[14], Polina Golland[4], Grégory Kuchcinski[2], Natalia S. Rost[1] and on behalf of the MRI-GENIE GISCOME Investigators the International and Stroke Genetics Consortium†

[1] J. Philip Kistler Stroke Research Center, Massachusetts General Hospital, Boston, MA, United States, [2] Inserm, CHU Lille, U1172 - LilNCog (JPARC) - Lille Neurosciences and Cognition, University of Lille, Lille, France, [3] A. A. Martinos Center for Biomedical Imaging, Massachusetts General Hospital, Harvard Medical School, Boston, MA, United States, [4] Computer Science and Artificial Intelligence Laboratory, Massachusetts Institute of Technology, Cambridge, MA, United States, [5] Division of Preventive Medicine, Department of Medicine, Brigham and Women's Hospital and Harvard Medical School, Boston, MA, United States, [6] CNRS, Institut Pasteur de Lille, US 41 - UMS 2014 - PLBS, Lille, France, [7] Department of Medicine, Division of Neurology, University of British Columbia, Vancouver, BC, Canada, [8] Department of Neurology, University of Maryland School of Medicine and Veterans Affairs Maryland Health Care System, Baltimore, MD, United States, [9] School of Medical Sciences, University of Campinas (UNICAMP) and the Brazilian Institute of Neuroscience and Neurotechnology (BRAINN), Campinas, Brazil, [10] Department of Neurosurgery, Geisinger, Danville, PA, United States, [11] Research Institute of Neurointervention, Paracelsus Medical University, Salzburg, Austria, [12] Division of Emergency Medicine, Washington University School of Medicine, St. Louis, MO, United States, [13] Department of Neurology, Washington University School of Medicine and Barnes-Jewish Hospital, St. Louis, MO, United States, [14] Institute of Biomedicine, Sahlgrenska Academy at University of Gothenburg, Gothenburg, Sweden, [15] Department of Neurology, Neurovascular Research Group (NEUVAS), Institut Hospital del Mar d'Investigacions Mèdiques (IMIM), Universitat Autonoma de Barcelona, Barcelona, Spain, [16] Department of Neurosciences, Experimental Neurology and Leuven Research Institute for Neuroscience and Disease (LIND), KU Leuven – University of Leuven, Leuven, Belgium, [17] VIB, Vesalius Research Center, Laboratory of Neurobiology, Department of Neurology, University Hospitals Leuven, Leuven, Belgium, [18] School of Medicine and Public Health, University of Newcastle, Newcastle, NSW, Australia, [19] Department of Neurology, John Hunter Hospital, Newcastle, NSW, Australia, [20] Division of Endocrinology, Diabetes and Nutrition, Department of Medicine, University of Maryland School of Medicine, Baltimore, MD, United States, [21] Department of Pharmacotherapy and Translational Research and Center for Pharmacogenomics, University of Florida, Gainesville, FL, United States, [22] Department of Neurology, Mayo Clinic, Jacksonville, FL, United States, [23] Centogene AG, Rostock, Germany, [24] Department of Neurology, Clinical Division of Neurogeriatrics, Medical University of Graz, Graz, Austria, [25] Henry and Allison McCance Center for Brain Health, Center for Genomic Medicine, Massachusetts General Hospital, Boston, MA, United States, [26] Department of Neurology and Evelyn F. McKnight Brain Institute, Miller School of Medicine, University of Miami, Miami, FL, United States, [27] Institute of Cardiovascular Research, Royal Holloway University of London (ICR2UL), Egham, United Kingdom, [28] Ashford and St. Peter's Hospitals, Chertsey and Ashford, United Kingdom, [29] Department of Neurology, Jagiellonian University Medical College, Krakow, Poland, [30] Division of Neurocritical Care and Emergency Neurology, Department of Neurology, Helsinki University Central Hospital, Helsinki, Finland, [31] Department of Clinica Neuroscience, Institute of Neuroscience and Physiology, Sahlgrenska Academy at University of Gothenburg, Gothenburg, Sweden, [32] Department of Neurology, Sahlgrenska University Hospital, Gothenburg, Sweden, [33] Stroke Division, Florey Institute of Neuroscience and Mental

Health, Department of Neurology Austin Health, Heidelberg, VIC, Australia, [34] Department of Radiology, University of Cincinnati College of Medicine, Cincinnati, OH, United States, [35] Department of Clinical Sciences Lund, Radiology, Lund University, Lund, Sweden, [36] Department of Radiology, Neuroradiology, Skåne University Hospital, Malmö, Sweden, [37] Department of Neurology and Rehabilitation Medicine, University of Cincinnati College of Medicine, Cincinnati, OH, United States, [38] Department of Neurology, Geisinger, Danville, PA, United States, [39] Department of Neurology and Public Health Sciences, University of Virginia, Charlottesville, VA, United States, [40] Faculty of Health, University of Technology Sydney, Ultimo, NSW, Australia, [41] Department of Neurology and Rehabilitation Medicine, Skåne University Hospital, Lund, Sweden, [42] Department of Clinical Sciences Lund, Neurology, Lund University, Lund, Sweden

Objective: Neuroimaging measurements of brain structural integrity are thought to be surrogates for brain health, but precise assessments require dedicated advanced image acquisitions. By means of quantitatively describing conventional images, radiomic analyses hold potential for evaluating brain health. We sought to: (1) evaluate radiomics to assess brain structural integrity by predicting white matter hyperintensities burdens (WMH) and (2) uncover associations between predictive radiomic features and clinical phenotypes.

Methods: We analyzed a multi-site cohort of 4,163 acute ischemic strokes (AIS) patients with T2-FLAIR MR images with total brain and WMH segmentations. Radiomic features were extracted from normal-appearing brain tissue (brain mask–WMH mask). Radiomics-based prediction of personalized WMH burden was done using ElasticNet linear regression. We built a radiomic signature of WMH with stable selected features predictive of WMH burden and then related this signature to clinical variables using canonical correlation analysis (CCA).

Results: Radiomic features were predictive of WMH burden (R^2 = 0.855 ± 0.011). Seven pairs of canonical variates (CV) significantly correlated the radiomics signature of WMH and clinical traits with respective canonical correlations of 0.81, 0.65, 0.42, 0.24, 0.20, 0.15, and 0.15 (FDR-corrected p-values$_{CV1-6} < 0.001$, p-value$_{CV7} = 0.012$). The clinical CV1 was mainly influenced by age, CV2 by sex, CV3 by history of smoking and diabetes, CV4 by hypertension, CV5 by atrial fibrillation (AF) and diabetes, CV6 by coronary artery disease (CAD), and CV7 by CAD and diabetes.

Conclusion: Radiomics extracted from T2-FLAIR images of AIS patients capture microstructural damage of the cerebral parenchyma and correlate with clinical phenotypes, suggesting different radiographical textural abnormalities per cardiovascular risk profile. Further research could evaluate radiomics to predict the progression of WMH and for the follow-up of stroke patients' brain health.

Keywords: stroke, cerebrovascular disease (CVD), MRI, radiomics, machine learning, brain health

INTRODUCTION

White matter hyperintensities (WMH) are a cardinal manifestation of small vessel disease (SVD) (Wardlaw et al., 2013). Increased WMH burden is associated with incident ischemic stroke and worse clinical outcome (Arsava et al., 2009). Beyond ischemic stroke, WMH are also associated with vascular cognitive impairment and dementia (Au et al., 2006). WMH prevalence increases with age but is also directly influenced by individual small vessel risk factors: the aggregation of cardiovascular risk factors leads to an increased WMH burden (Wardlaw et al., 2015). Hence, WMH are an imaging biomarker of brain health suggestive of neurodegeneration beyond normal brain aging (Brugulat-Serrat et al., 2019).

Structural injury of the brain has been shown to occur at the macrostructural level, in the form of WMH, but also at the microstructural level. Advanced diffusion tensor imaging (DTI) studies have shown an age-related loss of parenchymal microstructural integrity in normal-appearing white matter (NAWM) (Etherton et al., 2017a). Furthermore, perfusion-weighted imaging (PWI)-based research has also revealed age-related alterations of the blood-brain barrier with increased contrast agents' leakage (Topakian et al., 2010). However, such microstructural injuries are not visualized with conventional structural MRI sequences, and as DTI and PWI require special

acquisition times, the outlined imaging biomarkers are not currently used in clinical routine for SVD patients. Consequently, we are in need of conventional MRI-based methodologies that better quantify SVD and brain health to ensure a widespread application and translation to clinical practice.

Radiomic analyses cover a broad ensemble of high-throughput quantification methods applicable to digitalized medical images (Gillies et al., 2015). These methods automatically extract high-dimensional data, called radiomic features, by describing a given region of interest by its size, shape, histogram, and relationship between voxels. Because these techniques can capture slight differences in intensities and patterns that would remain undetected to a human reader, radiomics bear the potential to describe neuroimaging beyond what meets the naked eye, and thus might help to phenotype SVD (Lambin et al., 2012). Conceivably, they may identify early underlying brain injury at the individual level with rapid clinical translatability and thus enhance personalized care in stroke and SVD.

The aim of the current study was to assess the structural integrity of the brain using a texture analysis approach and to understand the infra-radiological footprint of WMH by exploring its relationship with cardiovascular risk profiles. To do so, we analyzed 4,163 T2 FLAIR images from a large multi-site international collaborative effort studying stroke and WMH. We sought to (a) build a robust radiomic signature of the subvisible manifestations of WMH and (b) to apply canonical correlation analysis (CCA) to investigate the relation between this latent textural expression in relation to sociodemographic information and cardiovascular risk factors, providing a potentially novel approach to improve SVD and stroke care.

MATERIALS AND METHODS

Participants

We reviewed all ischemic stroke patients included in the MRI-GENetics Interface Exploration (MRI-GENIE) study, a large international multi-site collaboration of 20 sites gathering clinical, MRI imaging, and genetic data, built on top of the NINDS Stroke Genetics Network (SiGN) study. Both study design, data collection protocols, and populations have been previously described (Giese et al., 2020).

Ethics

The MRI-GENIE project has been approved by the MGH Institutional Review Board (IRB, Protocol #: 2001P001186 and Protocol #: 2003P000836), as well as ethics boards of the collaborating institutions. All participants or health care proxy provided signed informed consent.

Data Collection and Neuroimaging Pre-processing

Clinical data were acquired within the SiGN study and comprised information on age, sex, hypertension (HTN), history of smoking, diabetes mellitus (DM), atrial fibrillation (AF). Among the 6,627 patients included across 20 sites, FLAIR images were available for 6,389 patients. Axial T2-FLAIR images were acquired between 2003 and 2011 within 48 h of the initial stroke. They had a mean in-plane resolution of 0.7 mm (range: 0.3–1.0 mm) and a through-plane resolution of 6.2 mm (range: 3.0–30.0 mm). Total brain, ventricle, and WMH segmentations were accomplished using deep learning methods described in detail previously (Schirmer et al., 2019; Dubost et al., 2020). Briefly, total brain segmentation was done using a tailored 2D-convolutional neural network for clinical T2-FLAIR data. T2-FLAIR image intensities were normalized and scaled. Successively, WMH and ventricles were automatically segmented using distinct convolutional neural network frameworks. A total of 1,353 patients were excluded after final quality control of all T2-FLAIR images and respective segmentations; this control process is described in great detail in a previous publication (Schirmer et al., 2019). To capture the underlying processes of SVD in brain parenchyma not overtly affected by WMH, we computed masks for normal-appearing brain parenchyma by subtracting ventricles and WMH masks from total brain masks, resulting in 5,031 masks. To remove any stray voxels that could impact radiomics extraction, a morphological opening operation with a 3 × 3 voxel kernel was performed on the final masks. Among those 5,031 patients, 868 were excluded for missing major clinical data (age and sex), remaining missing values (89 patients included, see **Supplementary Table 2**) were imputed using medians of distributions. As a result, a total of 4,163 patients were included across 17 different sites.

Radiomic Feature Extraction

Radiomic features were extracted using the open-source toolbox PyRadiomics V2.2.0. The full list of the radiomics extraction parameters can be found online at https://github.com/MBretzner/WMH_radiomicSign.

Briefly, to account for the discrepancy in voxel sizes and to reduce unwanted variance that could be originating from differences between centers and scanners, all features were extracted in-plane from down-sampled 1 mm × 1 mm × 6 mm T2-FLAIR images. Quantization was set to a fixed bin width of 5. Features extraction was performed outside of WMH on native and pre-filtered images. Filters included Laplacian of Gaussian (LoG) filters (with sigmas of 1, 2, and 3 mm), wavelet decompositions, and 2D Local Binary Patterns (2D-LBD). For each patient, 118 features were computed including mask statistics, shape features, first-order histogram statistics, GLCM (Gray Level Co-occurrence Matrix) features, GLRLM (Gray Level Run Length Matrix), GLDM (Gray Level Dependence Matrix), and NGTDM (Neighboring Gray Tone Difference Matrix) features. Exhaustive and didactic descriptions and formulas of every radiomic feature and filter can be found online

at https://pyradiomics.readthedocs.io/en/latest/features.html. As a result, we extracted 763 rotation invariant radiomic features per patient.

Machine Learning Approach to Build the Radiomic Signature of the WMH

To account for cerebral size differences, each WMH volume was divided by the corresponding brain volume to obtain a percentage of WMH per total brain volume. As the resultant distribution was highly skewed, it was transformed using a Box-Cox transform and is referred to as "WMH burden" in the next paragraphs.

To address the high dimensionality of the data, prediction of the WMH burden was done using an ElasticNet linear regressor. Since ElasticNet coefficient estimates are not scale-invariant, we standardized predictors, i.e., radiomics variables, to be 0 centered and have variances of the same order.

Radiomics-based predictions of WMH burden were performed in 30-times repeated nested fivefold stratified cross-validation scheme, resulting in a total of 24,990 out-of-sample predictions. Predictions were plotted against ground truth values, and R^2 values were computed with standard deviation.

To better understand the role of each class of radiomics and to rule out an association based solely on the size of the extraction mask and thus reflecting only atrophy, an ancillary prediction of the WMH burden was performed using only the radiomics features that only reflected the size and the shape of the analyzed brains. As NIHSS has been shown to be a surrogate marker of stroke volume, and to assess a hypothetical impact of stroke lesions on radiomics features, residual of the WMH burden predictions were studied per NIHSS score when available (Tong et al., 1998). To explore the potential impact of data heterogeneity across all sites, a second ancillary analysis was performed predicting WMH burden in a leave-one-site-out cross-validation scheme.

TABLE 1 | Demographic and clinical characteristics of the study population (n = 4,163).

Age	**Mean (SD)**	**62.8 (15.0)**
Female	n (%)	1,748 (42.0%)
Hypertension	n (%)	2,825 (67.9%)
Diabetes mellitus	n (%)	687 (16.5%)
Atrial fibrillation	n (%)	595 (14.3%)
Coronary artery disease	n (%)	772 (18.5%)
History of smoking	n (%)	1,331 (32.0%)
Prior stroke	n (%)	539 (12.9%)
WMH volume	Median (IQR)	4.2 mL (1.4–11.2)
NIHSS*	Median (IQR)	3 (1–6)

NIHSS, NIH Stroke Scale.
**NIHSS was available for 2,234 (53.7%) patients included.*
"Prior stroke" refers to a stroke preceding the one that led to the inclusion in the study.

The shrinkage ability of the ElasticNet regressor was leveraged to select the most predictive features of the WMH burden. The radiomic signature of the WMH was built with the features that were consistently selected across each of the 30 repetitions and therefore represented the most robust and stable predictors of WMH burden.

Understanding the Textural Footprint of Clinical Phenotypes

Association of clinical variables and the radiomic signature of WMH burden were done *via* CCA, which allows studying two multivariate variable sets concomitantly (Hotelling, 1936; Wang et al., 2020). Indeed, traditional analyses explore relationships between many to one variable, whereas CCA can study complex many-to-many correlations, truly leveraging the power of multivariate datasets. CCA can be conceived as similar to principal component analyses in the way that each side of the data (here clinical and radiomics) undergoes a factorization into a latent representation of the variables, called canonical variates (CV). The canonical correlation score of a canonical function represents the correlation between the two CV that composes it. To extract each canonical function, CCA finds combinations of factors of the two sets so that they are maximally correlated. Canonical loadings represent the correlations between variables and their latent representation (CV) and can be interpreted as the relative contribution of variables to the variates: a variable with a large loading has more impact on a variate than a variable with a smaller loading.

Radiomic features and continuous clinical variable (age) normality was assessed using the Shapiro–Wilks test and, if needed, were transformed using the R toolbox *BestNormalize* (Peterson and Cavanaugh, 2020). Significance of canonical correlations was determined *via* permutation testing (1,000 permutations) and assessed using Wilks' Lambda computed with Rao's F-approximation, p-values were corrected for multiple testing with Benjamini–Hochberg procedure (Hotelling, 1936; Wang et al., 2020). Explained variances of the canonical functions were calculated and figured in a scree plot. Loadings were calculated to discover and characterize the impact of clinical and radiomic features on each canonical function and thus to provide support for the interpretation of the relationship between the radiomics and clinical domains.

Overall, the goal of CCA is to find underlying representations that best describe the correlations between the two multi-dimensional datasets. Thus, this technique permits the estimation of the sources of maximal covariance between the clinical and the radiomics domains, highlighting the subvisible contribution of cardiovascular risk factors to T2 FLAIR imaging.

Code Availability

Radiomic features extraction, feature selection, and machine learning analyses were performed in python

3.7.6 using the toolbox *scikit-learn* (Pedregosa et al., 2011). CCA was performed in R V1.3.1056 using the toolboxes *CCA*, *vegan* (González et al., 2008; Oksanen et al., 2019). The complete codes used to perform the radiomics extraction as well as the extraction parameters and the data analysis are available here: https://github.com/MBretzner/WMH_radiomicSign.

RESULTS

Population

All patients included in MRI-GENIE have suffered an ischemic stroke. Population demographics are shown in **Table 1**. The mean age was 62.8, and there were 42% females, median WMH volume was 4.2 mL [interquartile range (IQR): 1.4–11.2]. Admission NIH stroke scale (NIHSS) was available for 2,234 (53.7%) patients; median NIHSS was 3 (IQR: 1–6). Comparison of included and excluded patients' available clinical characteristics is shown in **Supplementary Table 2**. Briefly, excluded patients were younger, had less hypertension, less coronary artery disease (CAD), less AF, but had more prior strokes. There was no difference in sex or diabetes status. Importantly NIHSS scores did not differ.

Building the Latent Radiomic Signature of the WMH Burden

The coefficient of determination of the repeated out-of-sample cross-validated predictions of the WMH burden was $R^2 = 0.855 \pm 0.011$ (**Figure 1**). The average (SD) number of selected features per repetition was 150.3 (5.6). These features represented the most relevant ones in the prediction of WMH burden. To reduce the redundancy and multicollinearity of radiomic features, we built a signature of the WMH burden by only including the features that were systematically selected in every repetition. This step resulted in the automatic selection of 68 features, which are referred to as the "radiomic signature of WMH." These features are listed in **Supplementary Table 1**.

Prediction performance of the WMH burden using radiomics that only capture the shape and size of the extraction mask but not voxel intensities was substantially lower with an R^2 of 0.41 ± 0.03. The analysis of the residual of the WMH burden predictions per available NIHSS score showed no trend suggesting an impact of stroke lesions on the predictions (**Supplementary Figure 1**).

Results of the predictions recursively holding one site out are reported in **Supplementary Table 3**. Distributions of patients Age and WMH volume per site are reported in **Supplementary Figure 2**. Briefly, when the center held-out was showing large clinical differences (mainly younger patient and/or neglectable loads of WMH), prediction performances were lower.

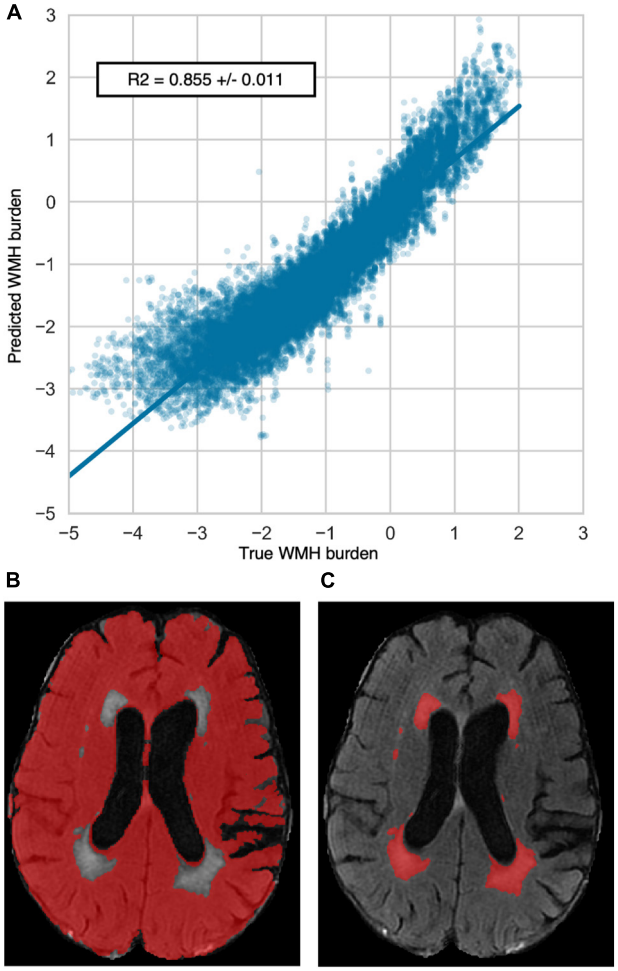

FIGURE 1 | Repeated out-of-sample cross-validated predictions of WMH burden. **(A)** Predictions of the WMH burden resulted in a coefficient of determination of $R^2 = 0.855 \pm 0.011$. Predicted and true WMH burdens show negative values due to the Box-Cox transformation of the WMH burden distribution. The bottom panels provide an illustrative example of a radiomics extraction mask **(B)** and a WMH mask **(C)**.

Clinical Phenotypes Captured by Radiomics

Aiming to discover possible links between clinical phenotypes and textural features of the radiomic signature of WMH burden, we performed a CCA.

The CCA could identify seven canonical functions (CF 1–7) correlating the radiomics with clinical variates. All seven canonical functions were significant (False discovery rate corrected p-values $CF_{1-6} < 10^{-3}$; $CF_7 = 0.012$) with respective canonical correlations of 0.81, 0.65, 0.42, 0.24, 0.20, 0.15, and 0.15. **Figure 2** contains the scree plot of the explained variance of each CF and the correlation plot of the clinical and radiomic variates of the first canonical function with patients points colored according to their age. Loadings of the clinical and the five most impactful radiomic variables (highest loadings) of the first two canonical functions are reported in **Table 2**. The bi-loading

plot in **Figure 3** provides a graphical interpretation relationship between the most impactful variables of the first two canonical functions. Loadings of the clinical variate of all canonical functions are shown in **Table 3**; loadings of the radiomics variate are presented in **Supplementary Table 1**. Variables that share the same direction along a given function have a positive covariance, whereas variables that show opposing directions have negative covariance. The magnitude of the loading reflects the strength of the association.

DISCUSSION

Radiomic features, extracted outside of the visible WMH, captured latent characteristics of WMH and could accurately predict WMH burden. Upon further analysis, seven distinct combinations of radiomics features were associated seven distinct combinations of clinical traits relevant to WMH, such as age, sex, hypertension, history of smoking, DM, and CAD. Therefore, the methods presented here provide new tools to help to understand and quantify the microstructural portion of the parenchymal deterioration due to SVD in stroke and give a radiological snapshot of brain health. Importantly, our analyses relied on basic T2-FLAIR images, as commonly acquired in clinical routine and thus do not require any advanced, more costly additional imaging sequences.

White matter hyperintensities represent a cardinal feature among radiological manifestations of brain aging and SVD. However, DTI-(Etherton et al., 2016) and PWI-based studies suggested (Promjunyakul et al., 2018) that WMH represent an end-stage macrostructural injury, embodying a surreptitious disease altering brain parenchyma. Our results support the hypothesis of WMH penumbra in cerebral SVD with a continuum between visible and invisible parenchymal damage (Maillard et al., 2011; Wardlaw et al., 2013). A major caveat of traditional advanced imaging biomarkers is their acquisition. Indeed, DTI sequences are rarely acquired routinely because of long scanning times, and PWI necessitates the injection of Gadolinium-based contrast agents. In contrast, our method can capture parenchymal microstructural integrity and hence, promises to replace additional dedicated imaging as a candidate approach to follow-up SVD progression in the clinic.

Cerebral atrophy has been shown to be associated with WMH burden (Aribisala et al., 2013). However, little is known about the relationship between the texture of the brain and WMH accumulation. By showing a twofold improvement of predictions leveraging exhaustive textural information compared to predictions restricted to radiomics describing only shape and size, our findings suggest that, beyond atrophy, textural analysis of the brain might better document WMH related damage of the brain. Therefore, one hypothesis would be that radiomics might be able to capture early-stage infra-radiological abnormalities prior to their evolution into irreversible cerebral loss, potentially bearing implications for future studies targeting WMH progression prevention.

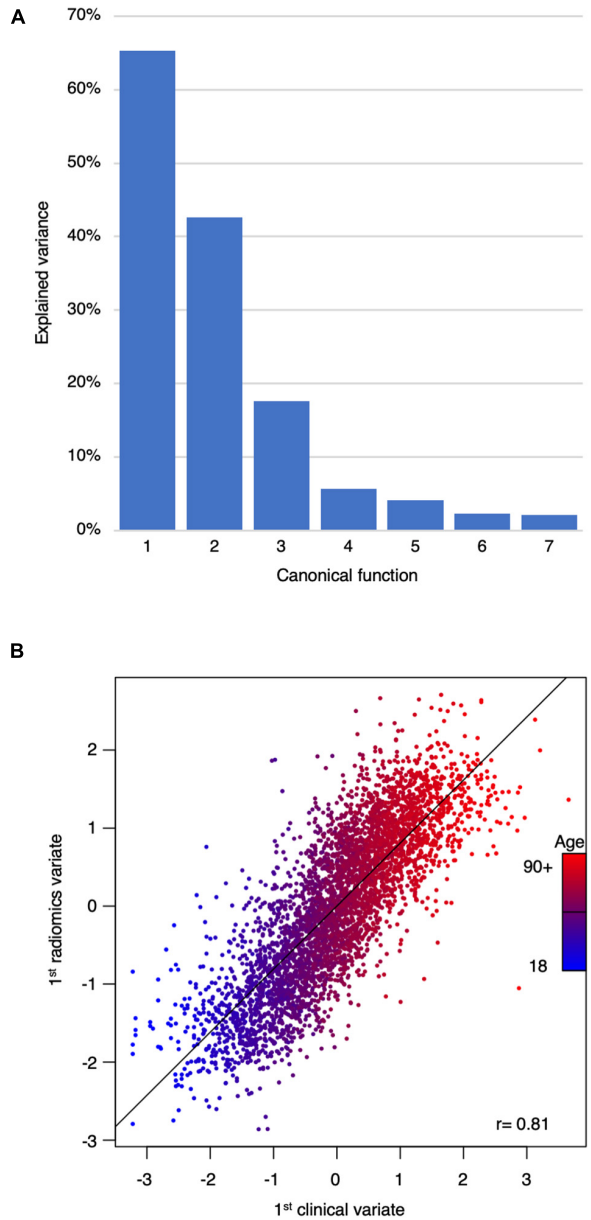

FIGURE 2 | Scree plot of the explained variance per canonical function and correlation plot between the first clinical and radiomic variates. **(A)** Scree plot of the explained variance by canonical functions. **(B)** Correlation plot of the first clinical and radiomics canonical variates. Each dot represents a patient and is colored according to age. The first canonical function mainly represented age. There was a very strong correlation between the clinical and the radiomics variates of $r = 0.81$.

By means of our CCA, we estimated the associations between the radiomic signature of WMH and SVD risk factors. The influence of cardiovascular risk factors on brain tissue was previously investigated in neuropathology and advanced imaging studies yet was rarely described by analyzing the texture of conventional imaging (Gouw et al., 2011; Wardlaw et al., 2013). Our work complement and support previous studies on MRI

TABLE 2 | Clinical and most impactful radiomic loadings of the first two canonical functions.

Clinical loadings			Radiomics loadings		
	CF 1	**CF 2**		**CF 1**	**CF 2**
AF	0.310	0.005	LoG-1mm histogram 10 percentile	−0.254	−0.128
Age	0.990	0.008	LoG-1mm GLSZM large area high gray level emphasis	−0.747	−0.008
CAD	0.260	0.097	LoG-1mm GLSZM large area low gray level emphasis	−0.743	−0.005
DM	0.127	0.009	LoG-2mm GLDM gray level non uniformity	−0.514	0.671
Hypertension	0.381	−0.057	LoG-2mm GLRLM run variance	−0.241	−0.124
Female sex	0.089	−0.993	LoG-2mm GLRLM short run low gray level emphasis	0.734	0.097
Smoking	0.069	0.180	LoG-3mm GLRLM gray level non uniformity normalized	0.300	−0.167
			LoG-3mm GLRLM short run low gray level emphasis	0.767	0.073
			Original histogram 10 percentile	−0.733	−0.071
			Original GLRLM run length non uniformity	0.662	0.221
			Original GLRLM run length non uniformity normalized	0.658	0.051
			Original GLRLM run variance	−0.801	−0.013
			Original shape major axis length	−0.263	0.696
			Original shape maximum 2D diameter column	−0.162	0.745
			Original shape mesh volume	−0.608	0.581
			Original shape minor axis length	0.046	0.709
			Original shape sphericity	−0.759	−0.172
			Original shape surface volume ratio	0.778	0.044
			Wavelet-LH GLSZM Small area high gray level emphasis	−0.413	−0.161

AF, atrial fibrillation; CAD, coronary artery disease; DM, diabetes mellitus; LoG, Laplacian of Gaussian; GLCM, Gray Level Co-occurrence matrix; GLRLM, Gray Level Run Length Matrix; GLDM, Gray Level Dependence Matrix; NGTDM, Neighboring Gray Tone Difference Matrix. Loadings assess the relative contribution of a variable to a canonical function.

textural analysis applied to SVD by Valdés et al. (2017) on gadolinium-enhanced T2-FLAIR, Bernal et al. (2020) on dynamic spectral gadolinium-enhanced T1 weighted imaging, Tozer et al. (2018) on T1 and T2-FLAIR cognitive textural biomarkers, and Shu et al. (2020) and Shao et al. (2018) who could predict the progression of WMH using radiomics extracted from, respectively, T1-FLAIR and T2-FLAIR images. Our analyses were based on a large collection of clinical T2-FLAIR images, a routine MRI sequences acquired during both acute screening and follow-up of patients with stroke and cerebrovascular disease. Therefore, it argues for the overall clinical relevance of radiomics in stroke and SVD.

Age was the clinical aspect correlating most strongly with the radiomic signature of WMH burden and is a well-established predictor of WMH (Rost et al., 2010; Giese et al., 2020). Similarly, blood-brain barrier studies using PWI highlight an age-associated increased leakage of contrast agents within WMH, but also beyond, in NAWM, showcasing a possible preclinical pathogenic step leading to cognitive decline (Wardlaw et al., 2017). Our findings also suggest the presence of age-related subvisible abnormalities that can notably be quantified on structural T2-FLAIR images. Radiomic features describing atrophy (brain size and lower sphericity) and T2-FLAIR heterogeneity, were the most strongly correlated with age. On the first canonical function, age was the main variable, however, HTN, AF, and CAD were also moderately represented, painting the picture of vascular pathological brain aging. The heterogeneity and hyperintensities of the parenchyma could have maybe captured lacunes, enlarged perivascular spaces, or microbleed, which is, along with WMH, radiological hallmarks of SVD (Wardlaw et al., 2013). Radiomics presented here could therefore portray a representation of a pathological brain aging process in stroke patients, depicting atrophic and heterogeneous parenchyma.

The second canonical function illustrated sex differences in tissue aspects in T2-FLAIR. The association of the radiomic signature with sex was mainly driven by shape radiomics capturing differences in brain size. This finding remains, however, independent from age-related atrophy since canonical functions analyze the unexplained variance from the previous function. Nevertheless, the female sex was also associated with greater linear edge density (GLRLM after LoG filtering), which might indicate some sex-specific textural differences in the loss of microstructural integrity, as suggested in DTI with previous findings reporting sex-specific fractional anisotropy values (Etherton et al., 2017b).

The third canonical function captured a profile representing mainly patients with a history of smoking, and, to a lesser extent, diabetes, which shared common textural features describing more high spatial frequency changes in intensities which could represent diffuse and fine heterogeneity throughout the brain.

The fourth canonical function characterized a specific relation between hypertension and some textural features highlighting inhomogeneity on a lower spatial frequency after wavelet decomposition, thus describing a patchy texture. Since no other cardiovascular risk factor was represented on this dimension, it describes an age-independent specific textural manifestation of hypertension on T2-FLAIR.

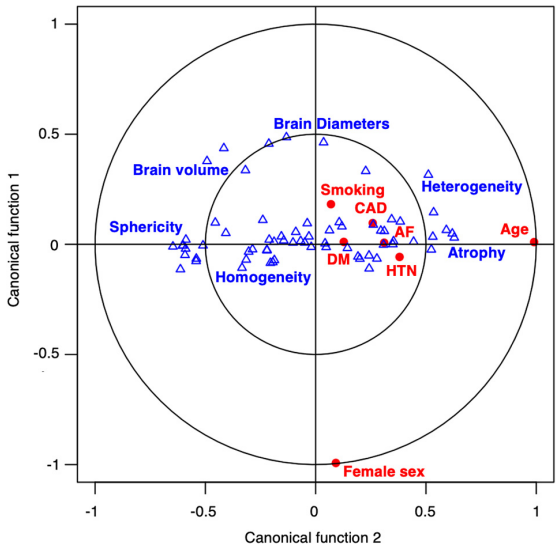

FIGURE 3 | Bi-loading plot of the variables projected over the two first canonical functions. A bi-loading plot graphically represents both the correlation of variables with canonical functions, and the correlation between variables of each set. The position of a variable relative to an axis describes the strength of the correlation of that variable with the axis, the closer to the outer circle, the stronger the correlation. Clinical variables (red dot) and radiomic features (blue triangle) are positively correlated if close or negatively correlated if diagonally opposed. Blue tags were positioned next to correlated radiomic features representing common textural concepts. On T2 FLAIR images, younger patients had larger brains and more homogeneous brain tissue (left side of the plot) whereas older patients had more atrophic and heterogeneous brains (right side of the plot).

Diabetes mellitus was mainly represented in the fifth dimension, correlating with textural features that illustrated overall less hyperintense parenchyma and especially those obtained after filtering with LoG filters. Since those filters are known to act as blob detectors, they potentially captured isolated islets of damage.

The sixth canonical function related the presence of CAD and AF to a more homogeneous texture, which was, however, combined with a high impulse response to the LoG filters of 1, 2, and 3 mm sigma that could signify the presence of spots of subvisible damage of varying size of presupposed embolic origin. On the contrary, the seventh canonical function pictured the differences separating AF from CAD and DM patients, where AF patients seemed to exhibit more patches of high spatial frequency intensity changes, which could represent zones of subtly lesioned brain.

Diabetes and AF were represented by several dimensions meaning that the diseases in question could manifest in several distinctive aspects or stages in our data. Conditional factors that could influence such diversity in presentations include the relative control of disease by treatment or lifestyle, the patient's stage of disease severity, genetic predispositions, and endophenotypes of varying severity.

As with any work on radiomics, the main pitfall remains the *curse of dimensionality*, which refers to a very high number of variables. Consequently, one of the strengths of our study was the available sample size, allowing us to truly leverage both machine learning methodologies and multivariate modeling to select and characterize relevant radiomic variables in a data-driven fashion. In fact, to date and to the best of our knowledge, this is the largest radiomics study performed on any topic. Previous work on radiomics of SVD studied smaller datasets (<250 participants) and thus did not permit powerful unsupervised feature selections (Valdés et al., 2017; Tozer et al., 2018; Bernal et al., 2020). Another added value of the present study is its multicentric design. Our study is the first to explore radiomics of SVD in a large and multicentric population including diverse ischemic stroke cohorts with patients presenting a large spectrum of age and WMH burdens. While the heterogeneity of our dataset could be perceived as a limitation for prediction performances, we think it is on the contrary strength of our study. Indeed, our algorithm was trained on very diverse patients therefore theoretically increasing its chance of success if applied to an external dataset. By implementing multiple measures, such as down-sampling and intensity normalization, to prevent differences originating from acquisition parameters discrepancies, we could reach homogeneous results across all centers while capturing relevant sources of variance, as depicted by the low error of our WMH burden predictions. Another source of unwanted variance in radiomics analyses is segmentation. Indeed, underestimation of the WMH burden, brain parenchyma, or ventricles could have impacted our radiomics based WMH burden prediction. However, we here built upon previous results obtained with state-of-the-art deep learning-based, fully automated segmentation methods that could produce consistent outlines of brains, WMH, and ventricles from T2-FLAIR (Schirmer et al., 2019; Dubost et al., 2020). Preventive measures we implemented, especially down-sampling and intensity normalization, may have come at the cost of losing pertinent information. However, that impact might have been mitigated thanks to our large sample size. We thus emphasize the capital importance of international collaborations, such as the MRI-GENIE consortium, to gather large datasets, especially in the era of quantitative imaging and personalized medicine.

Limitations and Future Directions

We acknowledge several limitations; first, stroke lesion outlines were not available and thus not accounted for. Overall, the median size of ischemic stroke lesions in this cohort is expected to be small, as the median NIHSS was 3. Moreover, the radiomic analysis conducted here provides a single value per radiomic variable per patient, averaging the textural presentation over the whole extraction zone and thus largely decreasing the impact of small lesions. Regarding large lesions, the corresponding perturbated radiomic value could have been assimilated to an outlier and then mitigated by the ElasticNet model, which includes an L1 regularization that improves its robustness to extreme values. The absence of clear trend in the analysis of the residual of WMH burden prediction per NIHSS score is in favor of a limited impact of stroke lesions on the predictions. Other SVD imaging features were also not accounted for, such as microbleeds or enlarged perivascular space, which have been previously linked to radiomic features (Valdés et al., 2017; Tozer et al., 2018).

TABLE 3 | Clinical loadings for all seven canonical functions.

	Clinical loadings						
Canonical function	**1**	**2**	**3**	**4**	**5**	**6**	**7**
AF	0.310	0.005	0.102	0.020	0.313	−0.596	0.663
Age	0.990	0.008	0.096	0.080	−0.045	0.034	0.017
CAD	0.260	0.097	0.169	−0.157	−0.214	−0.744	−0.521
DM	0.127	0.009	−0.443	−0.117	0.781	−0.050	−0.401
Hypertension	0.381	−0.057	0.067	−0.916	0.055	0.058	0.030
Female sex	0.089	−0.993	−0.015	0.056	−0.004	−0.030	0.039
Smoking	0.069	0.180	−0.903	−0.055	−0.347	−0.132	0.081

AF, atrial fibrillation; CAD, coronary artery disease; DM, diabetes mellitus.
A high loading coefficient implies a higher contribution to a canonical function. For instance, age was the most important variable when establishing the clinical variate of the first canonical function.

Secondly, we could not study the relationship between radiomics and other known WMH biomarkers such as dyslipidemia.

Thirdly, we here suggest a novel biomarker to assess the structural integrity of the brain on routine T2-FLAIR imaging. However, as with every new biomarker, the results presented here would need external validation, especially to appreciate the robustness of the features included in the radiomic signature of WMH.

Fourthly, a substantial number of patients were excluded from the analysis because of failed segmentation mainly due to image quality. While this might bias the analysis, it also highlights the challenges of processing clinical imaging in a real-world setting.

Lastly, radiomics were extracted outside of the WMH but not specifically within the white matter. Future research could evaluate the impact of co-registration and resampling on radiomics of SVD, then benchmark radiomics of NAWM against more traditional DTI metrics in the prediction of clinical outcomes and therefore provide a more straightforward method to quantify microstructural integrity.

CONCLUSION

In a large cohort of ischemic stroke patients, we demonstrated that radiomic features predicted WMH burden and were associated with clinical factors. By applying machine learning methods to radiomics analyses of T2-FLAIR images from a large multi-site ischemic stroke cohort, we could characterize the latent expression of SVD that extends beyond the visible WMH and subsequently uncover links associating cardiovascular risk factors to distinct textural patterns. Radiomics analysis may hold promise to become a cost-effective tool to quantify microstructural damage on routinely acquired images in the follow-up of SVD and stroke patients, once externally validated.

DATA AVAILABILITY STATEMENT

Data will be made available upon reasonable request and with approval from local IRBs, to replicate the results presented in this manuscript. Requests to access the data should be directed to NR: nrost@partners.org.

ETHICS STATEMENT

The studies involving human participants were reviewed and approved by the MRI-GENIE project and by the MGH Institutional Review Board (IRB, Protocol #: 2001P001186 and Protocol #: 2003P000836), as well as ethics boards of the collaborating institutions: (Albrecht-Kossel Institute for Neuroregeneration (AKOS) University of Rostock, Germany; University of Cincinnati (UC) College of Medicine, USA; Geisinger Institute, USA; Helsinki University Central Hospital, Finland; IMIM - Hospital del Mar, Spain; Imperial college of London, UK; Mayo Clinic Florida, USA; Medical University Graz, Austria; Sahlgrenska Academy at University of Gothenburg, Sweden; Skane University Hospital, Sweden; Leuven University Hospitals, Belgium; University of British Columbia, Canada; University of Maryland School of Medicine, USA; University of Miami, USA; University of Newcastle, Australia). All participants or health care proxy provided signed informed consent. The patients/participants provided their written informed consent to participate in this study.

AUTHOR CONTRIBUTIONS

MB, AB, MS, SH, ME, PR, RM, CW, RR, XL, RL, GK, and NR: conception and design of the study. MB, AB, MS, SH, ADa, KD, A-KG, ME, PR, MN, OB, JC, ADo, CG, LHo, LHe, KJ, JJ-C, SK, RL, CL, PM, CM, JMe, C-LP, AR, SR, JRs, JRq, TR, RSa, RSc, PS, ASl, ASo, TS, DS, TT, VT, AV, JC, DW, OW, RZ, BW, JM, AL, CJ, PG, and NR: acquisition and analysis of data. MB, AB, MS, ME, RM, CW, RR, XL, ReL, CG, JMe, JW, GK, and NR: drafting a significant portion of the manuscript or figures. All authors contributed to the article and approved the submitted version.

FUNDING

The MRI-GENIE study was funded by NIH NINDS (R01NS086905). MB was supported by the ISITE-ULNE

Fundation, the Société Française de Neuroradiologie, the Société Française de Radiologie, the Thérèse and René Planiol Fundation. ME was supported by the American Academy of Neurology and MGH Executive Council on Research. PR was supported by NIH K01 HL128791. TT was supported by the Helsinki University Central Hospital, Sigrid Juselius Foundation, Sahlgrenska University Hospital, and University of Gothenburg. The funders had no role in design and conduct of the study; collection, management, analysis, and interpretation of the data; preparation, review, or approval of the manuscript; and decision to submit the manuscript for publication.

ACKNOWLEDGMENTS

A copy of a public version of this manuscript has been made available on https://www.biorxiv.org (Bretzner et al., 2021).

SUPPLEMENTARY MATERIAL

The Supplementary Material for this article can be found online at: https://www.frontiersin.org/articles/10.3389/fnins.2021.691244/full#supplementary-material

REFERENCES

Aribisala, B. S., Valdés Hernández, M. C., Royle, N. A., Morris, Z., Muñoz Maniega, S., Bastin, M. E., et al. (2013). Brain atrophy associations with white matter lesions in the ageing brain: the Lothian Birth Cohort 1936. *Eur. Radiol.* 23, 1084–1092. doi: 10.1007/s00330-012-2677-x

Arsava, E. M., Rahman, R., Rosand, J., Lu, J., Smith, E. E., Rost, N. S., et al. (2009). Severity of leukoaraiosis correlates with clinical outcome after ischemic stroke. *Neurology* 72, 1403–1410. doi: 10.1212/wnl.0b013e3181a18823

Au, R., Massaro, J. M., Wolf, P. A., Young, M. E., Beiser, A., Seshadri, S., et al. (2006). Association of white matter hyperintensity volume with decreased cognitive functioning: the Framingham heart study. *Arch. Neurol.* 63, 246–250. doi: 10.1001/archneur.63.2.246

Bernal, J., Valdés-Hernández, M. D. C., Escudero, J., Viksne, L., Heye, A. K., Armitage, P. A., et al. (2020). Analysis of dynamic texture and spatial spectral descriptors of dynamic contrast-enhanced brain magnetic resonance images for studying small vessel disease. *Magn. Reson. Imaging* 66, 240–247. doi: 10.1016/j.mri.2019.11.001

Bretzner, M., Bonkhoff, A. K., Schirmer, M. D., Hong, S., Dalca, A., Donahue, K. L., et al. (2021). MRI radiomic signature of white matter hyperintensities is associated with clinical phenotypes. *bioRxiv*[Preprint] 2021.01.24.427986,

Brugulat-Serrat, A., Salvadó, G., Operto, G., Cacciaglia, R., Sudre, C. H., Grau-Rivera, O., et al. (2019). White matter hyperintensities mediate gray matter volume and processing speed relationship in cognitively unimpaired participants. *Hum. Brain Mapp.* 41, 1309–1322. doi: 10.1002/hbm.24877

Dubost, F., de Bruijne, M., Nardin, M., Dalca, A. V., Donahue, K. L., Giese, A.-K., et al. (2020). Multi-atlas image registration of clinical data with automated quality assessment using ventricle segmentation. *Med. Image Anal.* 63:101698. doi: 10.1016/j.media.2020.101698

Etherton, M. R., Wu, O., Cougo, P., Giese, A.-K., Cloonan, L., Fitzpatrick, K. M., et al. (2017a). Integrity of normal-appearing white matter and functional outcomes after acute ischemic stroke. *Neurology* 88, 1701–1708. doi: 10.1212/wnl.0000000000003890

Etherton, M. R., Wu, O., Cougo, P., Giese, A.-K., Cloonan, L., Fitzpatrick, K. M., et al. (2017b). Structural integrity of normal appearing white matter and sex-specific outcomes after acute ischemic stroke. *Stroke* 48, 3387–3389. doi: 10.1161/strokeaha.117.019258

Etherton, M. R., Wu, O., and Rost, N. S. (2016). Recent advances in leukoaraiosis: white matter structural integrity and functional outcomes after acute ischemic stroke. *Curr. Cardiol. Rep.* 18:123.

Giese, A.-K., Schirmer, M. D., Dalca, A. V., Sridharan, R., Donahue, K. L., Nardin, M., et al. (2020). White matter hyperintensity burden in acute stroke patients differs by ischemic stroke subtype. *Neurology* 95, e79–e88.

Gillies, R. J., Kinahan, P. E., and Hricak, H. (2015). . Radiomics: images are more than pictures, they are data. *Radiology* 278, 563–577. doi: 10.1148/radiol.2015151169

González, I., Déjean, S., Martin, P. G. P., and Baccini, A. C. C. A. (2008). An R package to extend canonical correlation analysis. *J. Stat. Softw.* 23, 1–14.

Gouw, A. A., Seewann, A., van der Flier, W. M., Barkhof, F., Rozemuller, A. M., Scheltens, P., et al. (2011). Heterogeneity of small vessel disease: a systematic review of MRI and histopathology correlations. *J. Neurol. Neurosurg. Psychiatry* 82, 126–135. doi: 10.1136/jnnp.2009.204685

Hotelling, H. (1936). Relations between two sets of variates. *Biometrika* 28, 321–377. doi: 10.2307/2333955

Lambin, P., Rios-Velazquez, E., Leijenaar, R., Carvalho, S., van Stiphout, R. G. P. M., Granton, P., et al. (2012). Radiomics: extracting more information from medical images using advanced feature analysis. *Eur. J. Cancer* 48, 441–446. doi: 10.1016/j.ejca.2011.11.036

Maillard, P., Fletcher, E., Harvey, D., Carmichael, O., Reed, B., Mungas, D., et al. (2011). White matter hyperintensity penumbra. *Stroke* 42, 1917–1922. doi: 10.1161/strokeaha.110.609768

Oksanen, J., Kindt, R., Legendre, P., Hara, B., Simpson, G., Solymos, P., et al. (2019). *vegan: Community Ecology Package*. Available online at: https://CRAN.R-project.org/package=vegan (accessed November 29, 2020).

Pedregosa, F., Varoquaux, G., Gramfort, A., Michel, V., Thirion, B., Grisel, O., et al. (2011). Scikit-learn: machine learning in python. *J. Mach. Learn. Res.* 12, 2825–2830.

Peterson, R. A., and Cavanaugh, J. E. (2020). Ordered quantile normalization: a semiparametric transformation built for the cross-validation era. *J. Appl. Stat.* 47, 2312–2327. doi: 10.1080/02664763.2019.1630372

Promjunyakul, N.-O., Dodge, H. H., Lahna, D., Boespflug, E. L., Kaye, J. A., Rooney, W. D., et al. (2018). Baseline NAWM structural integrity and CBF predict periventricular WMH expansion over time. *Neurology* 90, e2119–e2126.

Rost, N. S., Rahman, R., Sonni, S., Kanakis, A., Butler, C., Massasa, E., et al. (2010). Determinants of white matter hyperintensity volume in patients with acute ischemic stroke. *J. Stroke Cerebrovasc. Dis.* 19, 230–235. doi: 10.1016/j.jstrokecerebrovasdis.2009.05.007

Schirmer, M. D., Dalca, A. V., Sridharan, R., Giese, A.-K., Donahue, K. L., Nardin, M. J., et al. (2019). White matter hyperintensity quantification in large-scale clinical acute ischemic stroke cohorts – the MRI-GENIE study. *Neuroimage Clin.* 23:101884. doi: 10.1016/j.nicl.2019.101884

Shao, Y., Chen, Z., Ming, S., Ye, Q., Shu, Z., Gong, C., et al. (2018). Predicting the development of normal-appearing white matter with radiomics in the aging brain: a longitudinal clinical study. *Front. Aging Neurosci.* 10:393. doi: 10.3389/fnagi.2018.00393

Shu, Z., Shao, Y., Xu, Y., Ye, Q., Cui, S., Mao, D., et al. (2020). Radiomics nomogram based on MRI for predicting white matter hyperintensity progression in elderly adults. *J. Magn. Reson. Imaging* 51, 535–546. doi: 10.1002/jmri.26813

Tong, D. C., Yenari, M. A., Albers, G. W., O'Brien, M., Marks, M. P., and Moseley, M. E. (1998). Correlation of perfusion- and diffusion-weighted MRI with NIHSS score in acute (<6.5 hour) ischemic stroke. *Neurology* 50, 864–869. doi: 10.1212/wnl.50.4.864

Topakian, R., Barrick, T. R., Howe, F. A., and Markus, H. S. (2010). Blood–brain barrier permeability is increased in normal-appearing white matter in patients with lacunar stroke and leucoaraiosis. *J. Neurol. Neurosurg. Psychiatry* 81, 192–197. doi: 10.1136/jnnp.2009.172072

Tozer, D. J., Zeestraten, E., Lawrence, A. J., Barrick, T. R., and Markus, H. S. (2018). Texture analysis of T1-weighted and fluid-attenuated inversion recovery images detects abnormalities that correlate with cognitive decline in small vessel disease. *Stroke* 49, 1656–1661. doi: 10.1161/strokeaha.117.019970

Valdés, M. H., González-Castro, V., Chappell, F. M., Sakka, E., Makin, S., Armitage, P. A., et al. (2017). Application of Texture analysis to study small vessel disease

and blood-brain barrier integrity. *Front. Neurol.* 8:327. doi: 10.3389/fneur.2017.00327

Wang, H.-T., Smallwood, J., Mourao-Miranda, J., Xia, C. H., Satterthwaite, T. D., Bassett, D. S., et al. (2020). Finding the needle in a high-dimensional haystack: canonical correlation analysis for neuroscientists. *Neuroimage* 216:116745. doi: 10.1016/j.neuroimage.2020.116745

Wardlaw, J. M., Makin, S. J., Valdés Hernández, M. C., Armitage, P. A., Heye, A. K., Chappell, F. M., et al. (2017). Blood-brain barrier failure as a core mechanism in cerebral small vessel disease and dementia: evidence from a cohort study. *Alzheimers Dement.* 13, 634–643. doi: 10.1016/j.jalz.2016.09.006

Wardlaw, J. M., Smith, C., and Dichgans, M. (2013). Mechanisms of sporadic cerebral small vessel disease: insights from neuroimaging. *Lancet Neurol.* 12, 483–497. doi: 10.1016/s1474-4422(13)70060-7

Wardlaw, J. M., Valdés Hernández, M. C., and Muñoz-Maniega, S. (2015). What are white matter hyperintensities made of? Relevance to vascular cognitive impairment. *J. Am. Heart Assoc.* 4:001140.

Conflict of Interest: AR was employed by the company Centogene GmbH.The remaining authors declare that the research was conducted in the absence of any commercial or financial relationships that could be construed as a potential conflict of interest.

frontiers in Neuroscience

BRIEF RESEARCH REPORT
published: 21 July 2021
doi: 10.3389/fnins.2021.697432

Presence of Vessel Wall Hyperintensity in Unruptured Arteriovenous Malformations on Vessel Wall Magnetic Resonance Imaging: Pilot Study of AVM Vessel Wall "Enhancement"

Laura B. Eisenmenger[1], Jacqueline C. Junn[2], Daniel Cooke[3], Steven Hetts[3], Chengcheng Zhu[4], Kevin M. Johnson[5], Jesse M. Manunga[6], David Saloner[3], Christopher Hess[3] and Helen Kim[7]*

[1] Department of Radiology, University of Wisconsin–Madison, Madison, WI, United States, [2] Department of Radiology, Mount Sinai Hospital, New York, NY, United States, [3] Department of Radiology and Biomedical Imaging, University of California, San Francisco, San Francisco, CA, United States, [4] Department of Radiology, University of Washington, Seattle, WA, United States, [5] Department of Medical Physics, University of Wisconsin–Madison, Madison, WI, United States, [6] Division of Vascular and Endovascular Surgery, Minneapolis Heart Institute, Abbott Northwestern Hospital, Minneapolis, MN, United States, [7] Department of Anesthesia, University of California, San Francisco, San Francisco, CA, United States

OPEN ACCESS

Edited by:
Mickael Tanter, Institut National de la Santé et de la Recherche Médicale – INSERM, France

Reviewed by:
Luisa Ciobanu, CEA Saclay, France
Adil Bashir, Auburn University, United States

***Correspondence:**
Laura B. Eisenmenger
leisenmenger@uwhealth.edu

Specialty section:
This article was submitted to Brain Imaging Methods, a section of the journal Frontiers in Neuroscience

Received: *19 April 2021*
Accepted: *28 June 2021*
Published: *21 July 2021*

Citation:
Eisenmenger LB, Junn JC, Cooke D, Hetts S, Zhu C, Johnson KM, Manunga JM, Saloner D, Hess C and Kim H (2021) Presence of Vessel Wall Hyperintensity in Unruptured Arteriovenous Malformations on Vessel Wall Magnetic Resonance Imaging: Pilot Study of AVM Vessel Wall "Enhancement". Front. Neurosci. 15:697432. doi: 10.3389/fnins.2021.697432

Purpose: High-resolution vessel wall magnetic resonance imaging (VW-MRI) could provide a way to identify high risk arteriovenous malformation (AVM) features. We present the first pilot study of clinically unruptured AVMs evaluated by high-resolution VW-MRI.

Methods: A retrospective review of clinically unruptured AVMs with VW-MRI between January 1, 2016 and December 31, 2018 was performed documenting the presence or absence of vessel wall "hyperintensity," or enhancement, within the nidus as well as perivascular enhancement and evidence of old hemorrhage (EOOH). The extent of nidal vessel wall "hyperintensity" was approximated into five groups: 0, 1–25, 26–50, 51–75, and 76–100%.

Results: Of the nine cases, eight demonstrated at least some degree of vessel wall nidus "hyperintensity." Of those eight cases, four demonstrated greater than 50% of the nidus with hyperintensity at the vessel wall, and three cases had perivascular enhancement adjacent to nidal vessels. Although none of the subjects had prior clinical hemorrhage/AVM rupture, of the six patients with available susceptibility weighted imaging to assess for remote hemorrhage, only two had subtle siderosis to suggest prior sub-clinical bleeds.

Conclusion: Vessel wall "enhancement" occurs in AVMs with no prior clinical rupture. Additional studies are needed to further investigate the implication of these findings.

Keywords: arteriovenous malformation, unruptured AVM, vessel wall enhancement, MRI, vessel wall imaging

INTRODUCTION

Traditional vascular imaging has been primarily "lumenography," or imaging techniques that delineate the vascular lumen to study vascular pathology. These conventional techniques include digital subtraction angiography (DSA), computed tomography angiography (CTA), and magnetic resonance angiography (MRA) (Mandell and Shroff, 2011; Dieleman et al., 2014; Matouk et al., 2016), focusing attention to the inside of blood vessels; however, it has long been appreciated that cerebrovascular disease pathogenesis resides, in large part, within the vessel wall. High-resolution vessel wall magnetic resonance imaging (VW-MRI) represents an innovative method to evaluate the intracranial vessel wall in both healthy vessels and vascular disease.

Initially, the majority of studies were focused on steno-occlusive cerebrovascular disease such as intracranial atherosclerosis (Vergouwen et al., 2011; Skarpathiotakis et al., 2013; Mossa-Basha et al., 2015), primary central nervous system vasculitis (Mandell et al., 2012; Obusez et al., 2014; Mossa-Basha et al., 2015), reversible cerebral vasoconstriction syndrome (Mandell et al., 2012; Obusez et al., 2014; Mossa-Basha et al., 2015), drug-induced vasculopathies (Han et al., 2008), and intracranial dissections (Chung et al., 2014; Natori et al., 2014). More recently, there has been increased enthusiasm for the utilization of VW-MRI to further characterize vascular malformations, with intracranial aneurysms being the most commonly studied lesion (Matouk et al., 2013, 2016; Edjlali et al., 2014; Nagahata et al., 2016; Tian et al., 2019; Wang et al., 2019; Liu et al., 2020; Zhu et al., 2020). Current evidence suggests that vessel wall hyperintensity on post-contrast VW-MRI, often referred to as vessel wall "enhancement," is associated with ruptured (Matouk et al., 2013; Nagahata et al., 2016; Wang et al., 2019), symptomatic (Zhu et al., 2020), and unstable (Edjlali et al., 2014; Edjlali et al., 2018) aneurysms. Given the early evidence that VW-MRI may help in the identification of high risk aneurysms, VW-MRI could also be a tool to improve the identification and characterization of high risk intracranial arteriovenous malformations (AVMs); however, fewer VW-MRI studies have been performed on these more complex vascular malformations, now limited to two case series (Matouk et al., 2016; Petridis et al., 2018) and a few case reports (Omodaka et al., 2015; Komatsu et al., 2018; Bhogal et al., 2019) in only ruptured AVMs. While these reports did document vessel wall enhancement within the ruptured AVMs, it is unknown if unruptured AVMs also enhance as no studies to date have evaluated unruptured AVMs with this technique (Omodaka et al., 2015; Matouk et al., 2016; Komatsu et al., 2018; Bhogal et al., 2019). We present the first pilot study of VW-MRI in clinically unruptured brain AVMs and discuss this method's promise and limitations when applied to this type of complex vascular malformation.

MATERIALS AND METHODS

A search for AVMs at UCSF with VW-MRI between January 1, 2016 and December 31, 2018 was performed with nine cases of clinically unruptured AVMs identified. IRB approval was obtained to review the images retrospectively.

Imaging Protocol

Images for the following cases were acquired at a 3T whole-body MR scanner (GE MR750) with a standard eight-channel head coil. A T1-weighted 3D fast-spin-echo sequence (CUBE) obtained in the sagittal plane with variable refocusing flip angle was acquired both pre- and post-contrast. The parameters were: non-selective 90° excitation; TR/TE = 1000/17 ms; field of view = 18 cm × 18 cm; matrix = 300 × 300; slice thickness = 0.6 mm; number of slices 288; voxel size = 0.6 mm isotropic; echo train length of 60; ARC acceleration factor of two in phase encoding direction; scan time = 7 min 55 s, within the imaging acquisition recommendations defined by the Vessel Wall Imaging Study Group of the American Society of Neuroradiology for intracranial vessel wall imaging (Mandell et al., 2017). Post-contrast CUBE was acquired approximately 5 min after the injection of Magnevist® (gadopentetate dimeglumine) with a dose of 0.2 mL per kg of body weight.

Imaging Review

A consensus review was obtained by two board certified neuroradiologists with expertise in vascular, and specifically vessel wall, imaging (8 and 19 years of experience). The reviewers were blinded to patient history and demographics. If available, T2* gradient echo images were reviewed for the evidence of old hemorrhage (EOOH) indicated by areas of low signal adjacent to the AVM. Post-contrast VW-MRI images were reviewed for the presence or absence of vessel wall "hyperintensity" on post-contrast images within the nidus, defined as greater hyperintensity than adjacent normal arterial vessel segments. Pre-contrast VW-MRI images were reviewed for intrinsic T1 hyperintensity to confirm that hyperintensity on post-contrast imaging was due to contrast administration. Axial, coronal, and sagittal VW-MRI images were reviewed to estimate the percent of the nidal vessels with post-contrast nidal vessel wall hyperintensity. The percent volume of nidal vessel wall "hyperintensity" was approximated into five groups: 0% or absence, 1–25, 26–50, 51–75, and 76–100%. The presence or absence of perivascular enhancement was also assessed in the regions surrounding the nidus, defined as post-contrast enhancement outside of the vasculature but within 2 mm of the external aspect of the vessel wall. The original radiologic clinical reports were reviewed for content including if the reading radiologist mentioned the presence or absence of vessel wall and perivascular "enhancement." The Spetzler-Martin grade was recorded.

RESULTS

Nine subjects with clinically unruptured AVMs were identified. Subject demographics and AVM details are presented in **Table 1**. No subjects had a history of vasculitis or other systemic inflammatory process. Five subjects were female and four were

TABLE 1 | Arteriovenous malformation (AVM) case demographics and characteristics.

	Sex	Age	Presenting symptoms	Location*	S-M Grade∝	EOOH♦	% Nidus hyperintensity	Perivascular hyperintensity
Case 1	Male	51	Seizures, migraines, pain over right eye	Right posterior temporal	IV	Absent	76–100%	Present
Case 2	Female	63	Seizure	Left frontal	III	Absent	76–100%	Present
Case 3	Female	30	Headaches, blurred vision, occipital fullness	Left precuneus	I	Present	1–25%	Absent
Case 4	Female	20	Left homonymous hemianopsia	Right mesial temporal	V	Present	51–75%	Present
Case 5	Male	24	Incidentally found	Left frontoparietal	III	Absent	51–75%	Absent
Case 6	Male	49	Incidentally found	Left medial parietal	II	NA	1–25%	Absent
Case 7	Male	62	Seizure	Left central sulcus	IV	Absent	26–50%	Absent
Case 8	Female	53	Headaches, visual symptoms, imbalance	Left occipital lobe	IV	NA	1–25%	Absent
Case 9	Female	43	Headaches	Right pre- and post-central gyrus	III	NA	0%	Absent

**Location where the AVM is primarily centered.*
∝Spetzler-Martin (S-M) grade of the AVM.
♦Evidence of Old Hemorrhage (EOOH): foci of siderosis suggesting prior hemorrhage, in these cases all sub-clinical.

male ranging in age from 24 to 63 with an average age of 39. Of the nine cases, eight demonstrated at least some degree of hyperintensity on post-contrast VW-MRI at the vessel wall within the nidus (**Figure 1** and **Supplementary Figures 1**, **2**). Of those eight cases, four demonstrated greater than 50% of the nidus with hyperintensity at the vessel wall, and three cases had perivascular enhancement adjacent to nidal vessels (**Figure 2**). The original radiologic reports agreed with the consensus reviewers' assessment of the presence or absence of vessel wall and perivascular "enhancement" in all cases. Although none of our cases had prior clinically apparent hemorrhage/AVM rupture, of the six patients with available susceptibility weighted imaging to assess for subtle, remote hemorrhage, only two had a small degree of siderosis to suggest prior sub-clinical bleeds (**Figure 3**).

DISCUSSION

To our knowledge, our pilot study is the first to specifically evaluate for and demonstrate the presence and extent of vessel wall hyperintensity, often referred to as vessel wall "enhancement," on black blood, high-resolution VW-MRI in cases of clinically unruptured AVMs. We found eight of nine cases demonstrated nidal "enhancement," and three of those eight demonstrated perivascular "enhancement" adjacent to the nidus. Other than our study, there are limited publications evaluating AVMs using VW-MRI. The largest by Matouk et al. (2016) reported their findings on 13 ruptured brain AVMs concluding that VW-MRI was useful in identifying the site-of-rupture in patients with ruptured brain AVMs, although it could not do so in all patients. The authors also noted that VW-MRI was useful in demonstrating the precise spatial relationship of blood products adjacent to angioarchitectural vascular structures, thereby helping to further target attention to areas of potential interest. Thick vessel wall enhancement was demonstrated in all ruptured vascular structures in their series; however, the authors did caution that multiple components of the AVMs demonstrated mesh-like and complex, flow-related enhancement (Matouk et al., 2016). One case series did evaluate black blood MRI in ruptured and unruptured AVMs finding "enhancement" in the nidus of five out of six unruptured AVMs (Petridis et al., 2018). The authors suggest that this may be due to inflammation; however, this study did not evaluate the extent of nidal involvement, and the black blood sequence used had a resolution of 0.9 mm (Petridis et al., 2018), lower than what is recommended for VW-MRI (Mandell et al., 2017). Even though several review articles on VW-MRI have also anecdotally commented on the potential use of VW-MRI in intracranial AVMs (Young et al., 2019), we found only three additional case reports with the use of VW-MRI, all of which had rupture sites involving intranidal aneurysms that demonstrated associated vessel wall "enhancement" (Omodaka et al., 2015; Komatsu et al., 2018; Bhogal et al., 2019). Prior to our pilot study, no study has evaluated the presence

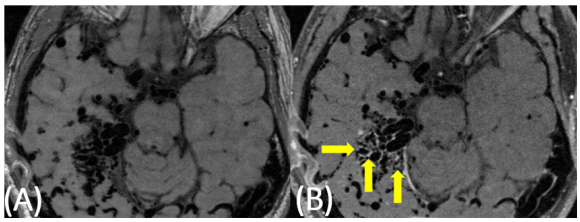

FIGURE 1 | 51-year-old man with a large AVM centered in the right temporoparietal lobe. On pre-contrast VW-MRI **(A)**, no intrinsic T1 hyperintensity is present. On post-contrast VW-MRI **(B)**, there were multiple areas of hyperintensity at the vessel wall within the nidus (yellow arrows).

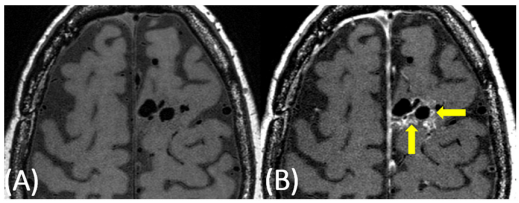

FIGURE 2 | 63-year-old female with a predominantly left frontal AVM. On pre-contrast VW-MRI **(A)**, no intrinsic T1 hyperintensity is present. On post-contrast VW-MRI **(B)**, there were multiple areas of hyperintensity at the vessel wall as well as perivascular hyperintensity within the nidus (yellow arrows).

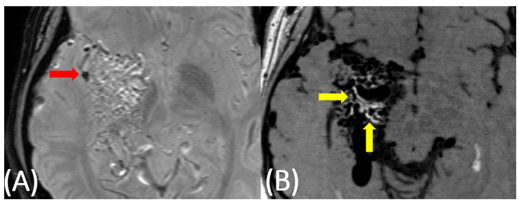

FIGURE 3 | 20-year-old female with a right temporoparietal AVM with a small area of sub-clinical evidence of prior hemorrhage on susceptibility-weighted imaging (**A**, red arrow). On post-contrast VW-MRI **(B)**, there were multiple areas of hyperintensity at the vessel wall (yellow arrows).

and extent of vessel wall hyperintensity, or "enhancement," in this high a number of clinically unruptured AVMs. In addition, our study is the first in unruptured AVMs to follow the American Society of Neuroradiology's vessel wall imaging recommendations regarding the VW-MRI sequence parameters used for evaluating the intracranial vessels (Mandell et al., 2017).

Vessel wall magnetic resonance imaging has been more extensively used to study intracranial aneurysms, identifying the site of aneurysm rupture (Matouk et al., 2013; Kondo et al., 2014; Hu et al., 2016; Nagahata et al., 2016) as well as unstable, symptomatic aneurysms (Edjlali et al., 2014; Edjlali et al., 2018; Zhu et al., 2020) and sites of aneurysm inflammation (Hu et al., 2016; Larsen et al., 2018). Although intracranial AVMs are much more complex shunting vascular malformations, one may speculate that areas of enhancement within AVMs may also be indicative of high risk features. This is relevant to patient care and risk stratification as the decision to treat unruptured brain AVMs remains controversial, especially after the publication of the ARUBA trial (A Randomized Trial of Unruptured Brain AVMs) and SIVMS (Scottish Intracranial Vascular Malformation Study) prospective, population-based cohort study (Al-Shahi Salman et al., 2014; Mohr et al., 2014). Both studies concluded that a conservative, non-interventional approach was associated with the best clinical outcomes; however, the methods and results of both studies remain highly controversial with many experts feeling these studies unfairly portrayed treatment outcomes as compared to watchful waiting (Elhammady and Heros, 2017; Magro et al., 2017). Philosophically, the guiding principle for any treatment strategy is the achievement of the desired result—in this case AVM obliteration—while posing minimal harm to the patient in order to provide improved outcomes. Methods of AVM treatment include surgical resection, Gamma Knife radiosurgery, embolization, and combinations of these methods, often in a staged manner overtime; however, these treatments are not without significant morbidity and, in some cases, mortality (Matouk et al., 2013). It stands to reason that identification of higher risk AVMs, as well as specific high risk AVM features, would prove to be instrumental in the improved risk stratification of these lesions for treatment and better patient outcomes. VW-MRI could be another tool in the characterization of AVMs.

Although many studies support the relationship between vessel wall "enhancement" and vessel rupture and/or instability, several complicating factors exist in the imaging of vascular lesions. For one, some studies are now finding that a proportion of vascular malformations that enhance demonstrate persistent and stable "enhancement" over time with no symptomatology or subsequent rupture (Tian et al., 2019). This persistent hyperintensity on imaging could indicate remodeled vessel wall without active inflammation as well as true persistent inflammatory changes; however, more studies and larger, longitudinal studies are needed to investigate if symptomology, rupture, and/or mortality are associated with vessel wall hyperintensity as well as histopathologic correlation with sites of enhancement versus non-enhancement. Future longitudinal VW-MRI studies evaluating unruptured AVMs should follow untreated patients over several years to truly understand the implications of AVM "enhancement" presence and extent on AVM risk and patient outcomes. Apparent vessel wall "enhancement" can also be misinterpreted from vasa vasorum, adjacent veins, and endovascular interventions such as mechanical thrombectomy or embolization causing altered flow (Mandell et al., 2017); however, maybe one of the hardest things to discern is the contributions of the VW-MRI sequences themselves to the appearance of vessel wall hyperintensity.

The third main complicating factor that can occur during the imaging of vascular lesions relates to complex blood flow within the area of abnormality. Vessel wall imaging requires high contrast-to-noise ratio (CNR) and spatial resolution in addition to blood flow and cerebral spinal fluid (CSF) suppression, yielding the appearance of

black blood which allows for the clear visualization of the vessel wall. Some of the most commonly employed VW-MRI sequences are variable refocusing flip angle (VRFA) sequences with T1 or proton density-weighted pre- and post-contrast imaging (VISTA; Philips Healthcare), sampling perfection with application-optimized contrasts by using different flip angle evolutions (SPACE; Siemens), and CUBE software (GE Healthcare) (Young et al., 2019). While VRFA sequences are adequate in most cases, because gadolinium shortens T1 relaxation time, "black blood" suppression in areas of abnormal or even normal in-plane flow can be diminished, potentially causing unsuppressed contrast in flowing blood, artifactually appearing as vessel wall contrast "enhancement." Examples of this are seen with turbulence and recirculation within aneurysms, slow flow within dilated lumens, and retrograde filling of distal collateral branches with proximal occlusion (Mandell et al., 2017; Tian et al., 2019); however, this altered blood flow leading to potential incomplete suppression on VFRA sequences may in and off itself be a high risk feature, such as areas of low wall sheer stress in aneurysms (Boussel et al., 2008), although this hypothesis has yet to be well investigated. Preparation pulses can be helpful in cases where this flow-related artifact is occurring, such as motion-sensitized driven equilibrium (MSDE) which uses flow-sensitive dephasing gradients (Young et al., 2019). Another approach to optimize blood and CSF suppression is delayed alternating nutation for tailored excitation (DANTE), a preparation pulse that uses a series of low flip angle non-selective pulses interleaved with gradient pulses of short repetition times (Mossa-Basha et al., 2016; Fan et al., 2017; Mandell et al., 2017; Tan et al., 2018). In the current pilot study, the imaging was obtained in the clinical setting and evaluated retrospectively; therefore, while the VW-MRI sequence parameters follow the American Society of Neuroradiology's intracranial vessel wall imaging recommendations, no additional blood suppression sequences were compared to the CUBE imaging. Ideally, future studies would confirm our findings as well as compare "enhancement" presence and extent utilizing different VW-MRI sequences in AVMs.

These complicating factors are likely to be even more confounding in cases of intracranial AVMs given the higher rates of blood flow in the feeding arteries, the more complex network of abnormal vessels in the AVM nidus, the potential presence of intranidal aneurysms and/or pseudoaneurysms, as well as altered morphology and blood flow in the draining veins. While the previous case series and case reports focus on sites of AVM rupture (Omodaka et al., 2015; Matouk et al., 2016; Komatsu et al., 2018; Petridis et al., 2018; Bhogal et al., 2019), our brief report highlights the complexity of vessel wall hyperintensity patterns in AVMs, and not in ruptured AVMs, but in clinically unruptured lesions. If AVM data are found to be similar to aneurysm VW-MRI data, that may mean AVMs with vessel wall "enhancement" are more unstable and require a new paradigm in AVM risk classification. In addition, although all cases in our study were clinically unruptured, two of six with susceptibility-weighted imaging demonstrated evidence of subclinical old hemorrhages. Our findings illustrate the need for more extensive research in these cases as well as the need for longitudinal monitoring of VW-MRI signal within brain AVMs, evaluation for both clinically evident and subclinical hemorrhage through susceptibility-weighted imaging, and the correlation of imaging findings with histopathologic analysis.

Our study does have multiple limitations. First, due to the retrospective nature of this case series, the VW-MRI sequence utilized was the variable refocusing flip angle CUBE (GE Healthcare) sequence, which does not have any additional suppression pulses to assist in the elimination of flow-related artifacts or other causes of incomplete blood signal suppression. Second, these are cases of intracranial AVMs with no prior clinical rupture. While a number of our cases had susceptibility-weighted MRI sequences acquired to confirm the absence of only prior hemorrhage (lack of hemosiderin staining), a couple of the cases do not. Future prospective studies should include susceptibility-weighted imaging in all cases. Third, given the small number of subjects and lack of long-term follow-up, it is hard to derive any meaningful conclusions regarding the implications of the AVM "enhancement." Larger, longitudinal studies are needed to discern if there is any increased risk of symptomology, rupture, and/or mortality associated with the presence, amount, degree, or pattern of vessel wall hyperintensity. In addition, histopathologic correlation with sites of enhancement versus non-enhancement is needed to fully understand the findings of both our pilot study of clinically unruptured AVMs and the prior reports of ruptured cases; however, our case series is essential in that it highlights the complexity of these lesions and the need for this type of AVM research.

CONCLUSION

To our knowledge, this is the largest pilot study of clinically unruptured AVMs evaluated by high-resolution VW-MRI, demonstrating varying degrees of vessel wall hyperintensity, or "enhancement," in the majority of the cases. While a portion of the hyperintensity could be due to incomplete blood suppression, given the high percentage of involvement within the nidus in several of the cases, this brief report illustrates that vessel wall enhancement occurs even in AVMs with no prior rupture. Larger, longitudinal studies are needed to more fully understand the implications of this intranidal "enhancement" including whether or not the presence, degree, morphology, and/or location of the hyperintensity has any increased risk of morbidity or mortality. Our findings illustrate the need for more extensive research in these cases including future studies with histopathologic analysis.

DATA AVAILABILITY STATEMENT

The original contributions presented in the study are included in the article/**Supplementary Material**. Further inquiries can be directed to the corresponding author/s.

ETHICS STATEMENT

The studies involving human participants were reviewed and approved by the UCSF IRB. Written informed consent for participation was not required for this study in accordance with the national legislation and the institutional requirements.

AUTHOR CONTRIBUTIONS

LE, JJ, DC, SH, CZ, KJ, JM, DS, CH, and HK contributed to the study design. LE and JJ collected the data. LE wrote the first draft. All authors contributed to editing and drafting of the final draft and agreed with the submitted version.

FUNDING

LE's effort on this work was supported by the Clinical and Translational Science Award (CTSA) program, through the NIH National Center for Advancing Translational Sciences (NCATS), grant UL1TR002373 and KL2TR002374, as well as the Wisconsin Alzheimer's Disease Research Center grant P30-AG062715. CZ is supported by the US National Institutes of Health (NIH) grant R00HL136883.

SUPPLEMENTARY MATERIAL

The Supplementary Material for this article can be found online at: https://www.frontiersin.org/articles/10.3389/fnins.2021.697432/full#supplementary-material

Supplementary Figure 1 | 30-year-old female with a predominantly left occipital AVM. On pre-contrast VW-MRI **(A)**, no intrinsic T1 hyperintensity is present. On post-contrast VW-MRI **(B)**, there was only one area of hyperintensity near the vessel wall (yellow arrow). No perivascular hyperintensity was present.

Supplementary Figure 2 | 24-year-old male with a left frontoparietal AVM. On pre-contrast VW-MRI **(A)**, no intrinsic T1 hyperintensity is present; however, there were multiple areas of hyperintensity at the vessel wall (yellow arrows) on post-contrast VW-MRI **(B)**. No perivascular hyperintensity was present.

REFERENCES

Al-Shahi Salman, R., White, P. M., Counsell, C. E., du Plessis, J., van Beijnum, J., Josephson, C. B., et al. (2014). Outcome after conservative management or intervention for unruptured brain arteriovenous malformations. *JAMA* 311, 1661–1669. doi: 10.1001/jama.2014.3200

Bhogal, P., Lansley, J., Wong, K., Udani, S. D., Uff, C., Wadley, J., et al. (2019). Vessel wall enhancement of a ruptured intra-nidal aneurysm in a brain arteriovenous malformation. *Int. Neuroradiol.* 25, 310–314. doi: 10.1177/1591019918824796

Boussel, L., Rayz, V., McCulloch, C., Martin, A., Acevedo-Bolton, G., Lawton, M., et al. (2008). Aneurysm growth occurs at region of low wall shear stress: patient-specific correlation of hemodynamics and growth in a longitudinal study. *Stroke* 39, 2997–3002. doi: 10.1161/strokeaha.108.521617

Chung, J. W., Kim, B. J., Choi, B. S., Sohn, C. H., Bae, H. J., Yoon, B. W., et al. (2014). High-resolution magnetic resonance imaging reveals hidden etiologies of symptomatic vertebral arterial lesions. *J. Stroke Cerebrovasc. Dis.* 23, 293–302. doi: 10.1016/j.jstrokecerebrovasdis.2013.02.021

Dieleman, N., van der Kolk, A. G., Zwanenburg, J. J., Harteveld, A. A., Biessels, G. J., Luijten, P. R., et al. (2014). Imaging intracranial vessel wall pathology with magnetic resonance imaging: current prospects and future directions. *Circulation* 130, 192–201. doi: 10.1161/circulationaha.113.006919

Edjlali, M., Gentric, J. C., Regent-Rodriguez, C., Trystram, D., Hassen, W. B., Lion, S., et al. (2014). Does aneurysmal wall enhancement on vessel wall MRI help to distinguish stable from unstable intracranial aneurysms? *Stroke* 45, 3704–3706. doi: 10.1161/strokeaha.114.006626

Edjlali, M., Guedon, A., Ben Hassen, W., Boulouis, G., Benzakoun, J., Rodriguez-Regent, C., et al. (2018). Circumferential thick enhancement at vessel wall MRI has high specificity for intracranial aneurysm instability. *Radiology* 289, 181–187. doi: 10.1148/radiol.2018172879

Elhammady, M. S., and Heros, R. C. (2017). Editorial: the ARUBA study: where do we go from here? *J. Neurosurg.* 126, 481–485. doi: 10.3171/2015.7.jns151408

Fan, Z., Yang, Q., Deng, Z., Li, Y., Bi, X., Song, S., et al. (2017). Whole-brain intracranial vessel wall imaging at 3 Tesla using cerebrospinal fluid-attenuated T1-weighted 3D turbo spin echo. *Magn. Reson. Med.* 77, 1142–1150. doi: 10.1002/mrm.26201

Han, J. S., Mandell, D. M., Poublanc, J., Mardimae, A., Slessarev, M., Jaigobin, C., et al. (2008). BOLD-MRI cerebrovascular reactivity findings in cocaine-induced cerebral vasculitis. *Nat. Clin. Pract. Neurol.* 4, 628–632. doi: 10.1038/ncpneuro0918

Hu, P., Yang, Q., Wang, D. D., Guan, S. C., and Zhang, H. Q. (2016). Wall enhancement on high-resolution magnetic resonance imaging may predict an unsteady state of an intracranial saccular aneurysm. *Neuroradiology* 58, 979–985. doi: 10.1007/s00234-016-1729-3

Komatsu, K., Takagi, Y., Ishii, A., Kikuchi, T., Yamao, Y., Fushimi, Y., et al. (2018). Ruptured intranidal aneurysm of an arteriovenous malformation diagnosed by delay alternating with nutation for tailored excitation (DANTE)-prepared contrast-enhanced magnetic resonance imaging. *Acta Neurochir.* 160, 2435–2438. doi: 10.1007/s00701-018-3713-7

Kondo, R., Yamaki, T., Mouri, W., Sato, S., Saito, S., Nagahata, M., et al. (2014). [Magnetic resonance vessel wall imaging reveals rupture site in subarachnoid hemorrhage with multiple cerebral aneurysms]. *No Shinkei Geka* 42, 1147–1150.

Larsen, N., von der Brelie, C., Trick, D., Riedel, C. H., Lindner, T., Madjidyar, J., et al. (2018). Vessel wall enhancement in unruptured intracranial aneurysms: an indicator for higher risk of rupture? High-resolution MR imaging and correlated histologic findings. *AJNR Am. J. Neuroradiol.* 39, 1617–1621. doi: 10.3174/ajnr.a5731

Liu, X., Zhang, Z., Zhu, C., Feng, J., Liu, P., Kong, Q., et al. (2020). Wall enhancement of intracranial saccular and fusiform aneurysms may differ in intensity and extension: a pilot study using 7-T high-resolution black-blood MRI. *Eur. Radiol.* 30, 301–307. doi: 10.1007/s00330-019-06275-9

Magro, E., Gentric, J. C., Darsaut, T. E., Ziegler, D., Msi, Bojanowski, M. W., et al. (2017). Responses to ARUBA: a systematic review and critical analysis for the design of future arteriovenous malformation trials. *J. Neurosurg.* 126, 486–494. doi: 10.3171/2015.6.jns15619

Mandell, D. M., Matouk, C. C., Farb, R. I., Krings, T., Agid, R., terBrugge, K., et al. (2012). Vessel wall MRI to differentiate between reversible cerebral vasoconstriction syndrome and central nervous system vasculitis: preliminary results. *Stroke* 43, 860–862. doi: 10.1161/strokeaha.111.626184

Mandell, D. M., Mossa-Basha, M., Qiao, Y., Hess, C. P., Hui, F., Matouk, C., et al. (2017). Intracranial vessel wall MRI: principles and expert consensus recommendations of the American Society of Neuroradiology. *AJNR Am. J. Neuroradiol.* 38, 218–229. doi: 10.3174/ajnr.a4893

Mandell, D. M., and Shroff, M. (2011). On MR imaging of the intracranial vessel wall. *Can. J. Neurol. Sci.* 38, 4–5. doi: 10.1017/s0317167100011021

Matouk, C. C., Cord, B. J., Yeung, J., Malhotra, A., Johnson, M. H., and Minja, F. J. (2016). High-resolution vessel wall magnetic resonance imaging in intracranial aneurysms and brain arteriovenous malformations. *Top. Magn. Reson. Imaging* 25, 49–55. doi: 10.1097/rmr.0000000000000084

Matouk, C. C., Mandell, D. M., Gunel, M., Bulsara, K. R., Malhotra, A., Hebert, R., et al. (2013). Vessel wall magnetic resonance imaging identifies the site of rupture in patients with multiple intracranial aneurysms: proof of principle. *Neurosurgery* 72, 492–496;discussion6.

Mohr, J. P., Parides, M. K., Stapf, C., Moquete, E., Moy, C. S., Overbey, J. R., et al. (2014). Medical management with or without interventional therapy for unruptured brain arteriovenous malformations (ARUBA): a multicentre, non-blinded, randomised trial. *Lancet* 383, 614–621. doi: 10.1016/s0140-6736(13)62302-8

Mossa-Basha, M., Alexander, M., Gaddikeri, S., Yuan, C., and Gandhi, D. (2016). Vessel wall imaging for intracranial vascular disease evaluation. *J. Neurointerv. Surg.* 8, 1154–1159. doi: 10.1136/neurintsurg-2015-012127

Mossa-Basha, M., Hwang, W. D., De Havenon, A., Hippe, D., Balu, N., Becker, K. J., et al. (2015). Multicontrast high-resolution vessel wall magnetic resonance imaging and its value in differentiating intracranial vasculopathic processes. *Stroke* 46, 1567–1573. doi: 10.1161/strokeaha.115.009037

Nagahata, S., Nagahata, M., Obara, M., Kondo, R., Minagawa, N., Sato, S., et al. (2016). Wall enhancement of the intracranial aneurysms revealed by magnetic resonance vessel wall imaging using three-dimensional turbo spin-echo sequence with motion-sensitized driven-equilibrium: a sign of ruptured aneurysm? *Clin. Neuroradiol.* 26, 277–283. doi: 10.1007/s00062-014-0353-z

Natori, T., Sasaki, M., Miyoshi, M., Ohba, H., Oura, M. Y., Narumi, S., et al. (2014). Detection of vessel wall lesions in spontaneous symptomatic vertebrobasilar artery dissection using T1-weighted 3-dimensional imaging. *J. Stroke Cerebrovasc. Dis.* 23, 2419–2424. doi: 10.1016/j.jstrokecerebrovasdis.2014.05.019

Obusez, E. C., Hui, F., Hajj-Ali, R. A., Cerejo, R., Calabrese, L. H., Hammad, T., et al. (2014). High-resolution MRI vessel wall imaging: spatial and temporal patterns of reversible cerebral vasoconstriction syndrome and central nervous system vasculitis. *AJNR Am. J. Neuroradiol.* 35, 1527–1532. doi: 10.3174/ajnr.a3909

Omodaka, S., Endo, H., Fujimura, M., Niizuma, K., Sato, K., Matsumoto, Y., et al. (2015). High-grade cerebral arteriovenous malformation treated with targeted embolization of a ruptured site: wall enhancement of an intranidal aneurysm as a sign of ruptured site. *Neurol. Med. Chir.* 55, 813–817. doi: 10.2176/nmc.cr.2015-0052

Petridis, A. K., Dibue-Adjei, M., Cornelius, J. F., Suresh, M. P., Li, L., Kamp, M. A., et al. (2018). Contrast enhancement of vascular walls of intracranial high flow malformations in black blood MRI indicates high inflammatory activity. *Chin. Neurosurg. J.* 4:13.

Skarpathiotakis, M., Mandell, D. M., Swartz, R. H., Tomlinson, G., and Mikulis, D. J. (2013). Intracranial atherosclerotic plaque enhancement in patients with ischemic stroke. *AJNR Am. J. Neuroradiol.* 34, 299–304. doi: 10.3174/ajnr.a3209

Tan, H. W., Chen, X., Maingard, J., Barras, C. D., Logan, C., Thijs, V., et al. (2018). Intracranial vessel wall imaging with magnetic resonance imaging: current techniques and applications. *World Neurosurg.* 112, 186–198. doi: 10.1016/j.wneu.2018.01.083

Tian, B., Toossi, S., Eisenmenger, L., Faraji, F., Ballweber, M. K., Josephson, S. A., et al. (2019). Visualizing wall enhancement over time in unruptured intracranial aneurysms using 3D vessel wall imaging. *J. Magn. Reson. Imaging* 50, 193–200. doi: 10.1002/jmri.26553

Vergouwen, M. D., Silver, F. L., Mandell, D. M., Mikulis, D. J., Krings, T., and Swartz, R. H. (2011). Fibrous cap enhancement in symptomatic atherosclerotic basilar artery stenosis. *Arch. Neurol.* 68:676.

Wang, X., Zhu, C., Leng, Y., Degnan, A. J., and Lu, J. (2019). Intracranial aneurysm wall enhancement associated with aneurysm rupture: a systematic review and meta-analysis. *Acad. Radiol.* 26, 664–673. doi: 10.1016/j.acra.2018.05.005

Young, C. C., Bonow, R. H., Barros, G., Mossa-Basha, M., Kim, L. J., and Levitt, M. R. (2019). Magnetic resonance vessel wall imaging in cerebrovascular diseases. *Neurosurg. Focus* 47:E4.

Zhu, C., Wang, X., Eisenmenger, L., Shi, Z., Degnan, A., Tian, B., et al. (2020). Wall enhancement on black-blood MRI is independently associated with symptomatic status of unruptured intracranial saccular aneurysm. *Eur. Radiol.* 30, 6413–6420. doi: 10.1007/s00330-020-07063-6

Disclaimer: The content is solely the responsibility of the authors and does not necessarily represent the official views of the NIH.

Conflict of Interest: The authors declare that the research was conducted in the absence of any commercial or financial relationships that could be construed as a potential conflict of interest.

frontiers in Neuroscience

ORIGINAL RESEARCH
published: 11 August 2021
doi: 10.3389/fnins.2021.721268

Classifying Ruptured Middle Cerebral Artery Aneurysms With a Machine Learning Based, Radiomics-Morphological Model: A Multicentral Study

*Dongqin Zhu[1], Yongchun Chen[1], Kuikui Zheng[1], Chao Chen[1], Qiong Li[1,2], Jiafeng Zhou[1], Xiufen Jia[1], Nengzhi Xia[1], Hao Wang[1], Boli Lin[1], Yifei Ni[3], Peipei Pang[4] and Yunjun Yang[5]**

[1] Department of Radiology, The First Affiliated Hospital of Wenzhou Medical University, Wenzhou, China, [2] Department of Radiology, Wenzhou Central Hospital, Wenzhou, China, [3] The First School of Medicine, Wenzhou Medical University, Wenzhou, China, [4] GE Healthcare China Co., Ltd., Shanghai, China, [5] Department of Nuclear Medicine, The First Affiliated Hospital of Wenzhou Medical University, Wenzhou, China

OPEN ACCESS

Edited by:
Danny J. J. Wang,
University of Southern California,
United States

Reviewed by:
Chengcheng Zhu,
University of Washington,
United States
Shanshan Wang,
Shenzhen Institutes of Advanced Technology, Chinese Academy of Sciences (CAS), China

***Correspondence:**
Yunjun Yang
yyjunjim@163.com

Specialty section:
This article was submitted to Brain Imaging Methods, a section of the journal Frontiers in Neuroscience

Received: 06 June 2021
Accepted: 26 July 2021
Published: 11 August 2021

Citation:
Zhu D, Chen Y, Zheng K, Chen C, Li Q, Zhou J, Jia X, Xia N, Wang H, Lin B, Ni Y, Pang P and Yang Y (2021) Classifying Ruptured Middle Cerebral Artery Aneurysms With a Machine Learning Based, Radiomics-Morphological Model: A Multicentral Study. Front. Neurosci. 15:721268. doi: 10.3389/fnins.2021.721268

Objective: Radiomics and morphological features were associated with aneurysms rupture. However, the multicentral study of their predictive power for specific-located aneurysms rupture is rare. We aimed to determine robust radiomics features related to middle cerebral artery (MCA) aneurysms rupture and evaluate the additional value of combining morphological and radiomics features in the classification of ruptured MCA aneurysms.

Methods: A total of 632 patients with 668 MCA aneurysms (423 ruptured aneurysms) from five hospitals were included. Radiomics and morphological features of aneurysms were extracted on computed tomography angiography images. The model was developed using a training dataset (407 patients) and validated with the internal (152 patients) and external validation (73 patients) datasets. The support vector machine method was applied for model construction. Optimal radiomics, morphological, and clinical features were used to develop the radiomics model (R-model), morphological model (M-model), radiomics-morphological model (RM-model), clinical-morphological model (CM-model), and clinical-radiomics-morphological model (CRM-model), respectively. A comprehensive nomogram integrating clinical, morphological, and radiomics predictors was generated.

Results: We found seven radiomics features and four morphological predictors of MCA aneurysms rupture. The R-model obtained an area under the receiver operating curve (AUC) of 0.822 (95% CI, 0.776, 0.867), 0.817 (95% CI, 0.744, 0.890), and 0.691 (95% CI, 0.567, 0.816) in the training, temporal validation, and external validation datasets, respectively. The RM-model showed an AUC of 0.848 (95% CI, 0.810, 0.885), 0.865 (95% CI, 0.807, 0.924), and 0.721 (95% CI, 0.601, 0.841) in the three datasets. The CRM-model obtained an AUC of 0.856 (95% CI, 0.820, 0.892), 0.882 (95% CI, 0.828,

0.936), and 0.738 (95% CI, 0.618, 0.857) in the three datasets. The CRM-model and RM-model outperformed the CM-model and M-model in the internal datasets ($p < 0.05$), respectively. But these differences were not statistically significant in the external dataset. Decision curve analysis indicated that the CRM-model obtained the highest net benefit for most of the threshold probabilities.

Conclusion: Robust radiomics features were determined related to MCA aneurysm rupture. The RM-model exhibited good ability in classifying ruptured MCA aneurysms. Integrating radiomics features into conventional models might provide additional value in ruptured MCA aneurysms classification.

Keywords: computed tomography angiography, decision support techniques, intracranial aneurysm, machine learning, middle cerebral artery, nomograms

INTRODUCTION

Middle cerebral artery (MCA) aneurysm is the most common subtype of unruptured aneurysms (Huttunen et al., 2010; Can et al., 2015). With the improvement of imaging techniques, unruptured aneurysms have become more frequently detected (Greving et al., 2014). But therapeutic decision-making for them is controversial. On the one hand, many unruptured aneurysms stay asymptomatic and never rupture (Korja et al., 2014). The prophylactic treatment such as current endovascular and microsurgical interventions carries the risk of procedure-related complications (Naggara et al., 2010; Zhu et al., 2020). On the other hand, once the aneurysm ruptures, the outcome is catastrophic (Vlak et al., 2011). Therefore, it is vital to screen out rupture-prone aneurysms.

Previous studies have identified that morphological features were associated with aneurysms rupture (Lindgren et al., 2016; Zhu et al., 2020). Researchers have constructed various computational methods using morphological features to evaluate the aneurysms-rupture risk (Zhang et al., 2019; Tanioka et al., 2020; Zhu et al., 2020). However, those morphological features are measured on two-dimensional images and might be affected by different readers or projections. It could impair the comparability of results.

Radiomics is an emerging technology that extracts high-throughput data from medical images (Zhou et al., 2018; Hua et al., 2020; Tomaszewski and Gillies, 2021). Recently, radiomics is frequently used in cerebrovascular disease researches (Chen et al., 2021; Zhu D. et al., 2021; Zhu D. Q. et al., 2021). Several researchers have scoped to the whole-brain aneurysms and proved that radiomics features were related to aneurysms rupture status (Liu et al., 2019; Ou et al., 2021). Regretfully, they did not analyze the features' robustness, which can be easily affected by a slight change in image-scanning protocols or regions of interest (ROIs) segmentation (Mackin et al., 2015; Choe et al., 2019). Moreover, the predictive ability of radiomics in those studies was not validated by any external validation dataset, which leads to the uncertainness of their results' generalizability (Collins et al., 2015; Lambin et al., 2017).

To the best of our knowledge, few studies have predicted the rupture of the location-specific aneurysm with robust radiomics features. In this study, we included a large sample of 668 MCA aneurysms. We aimed to (1) determine whether there are robust radiomics features that can classify ruptured MCA aneurysms; and (2) evaluate the additional value of combining morphological and radiomics features in classifying ruptured MCA aneurysm.

MATERIALS AND METHODS

Our study was approved by the Medical Ethics Committee of our hospital.

Study Population and Clinical Data

We performed a retrospective and multicentral study using the data from five hospitals (hospitals A, B, C, D, and E). MCA aneurysms with available computed tomography angiography (CTA) data were included. Exclusion criteria were as follows: fusiform MCA aneurysms, aneurysms combined with vascular diseases (such as Moyamoya disease and arteriovenous malformations), aneurysms with a size <3 mm, aneurysms with poor-quality images and patients underwent surgery or interventional therapy before CTA examination (see **Supplementary Methods**, **Supplementary Digital Content 1**, which illustrates details about CTA image scanning).

Patients with MCA aneurysms seen in hospital A from January 2009 to December 2019 were allocated to the training and the internal validation datasets. The training dataset encompassed the patients from the earlier period (2009–2017). The patients from the more recent period (2018–2019) were attributed to the temporal validation dataset (internal validation dataset) (Collins et al., 2015; Al-Shahi Salman et al., 2018). For external validation, MCA aneurysms cases in four hospitals, including hospital B (from January 2018 to December 2020), hospital C (from January 2018 to December 2020), hospital D (from January 2017 to October 2019), and hospital E (from September 2019 to March 2020), were merged to one external validation dataset (Lambin et al., 2017).

Clinical data such as age, sex, history of hypertension (a diagnosis of hypertension previously made by another physician or use of antihypertensive drugs), cigarette smoking (previous smoker or current smoker), and aneurysm side were collected. Rupture status of aneurysms was evaluated using

the following criterion: (1) for patients with subarachnoid hemorrhage (SAH), aneurysms adjacent to the cisternal clots were judged ruptured, and those aneurysms not adjacent to the cisternal clots were judged on digital subtraction angiography (DSA). (2) Asymptomatic patients without SAH were identified to be unruptured (Shi et al., 2021).

Morphological Predictors Discovery

Morphological features such as aneurysm location (divided into M1, the proximal segment of the middle cerebral artery; Mbif, main middle cerebral artery bifurcation; Mdist, distal middle cerebral artery), aneurysm size, vessel size, aneurysm height, perpendicular height, aspect ratio (AR), size ratio (SR), aneurysm angle, flow angle, vessel angle, daughter dome, and irregular shape were measured as described in previous studies (Can et al., 2015; Chen et al., 2020; Zhu et al., 2020; **Figure 1C**; see **Supplementary Methods**, **Supplementary Digital Content 2**, which illustrates detailed definitions of morphological features).

We implemented univariate analysis to find morphological factors that were associated with MCA aneurysm rupture. After that, the multivariable logistic regression was performed to identify independent morphological predictors of MCA aneurysm rupture.

Optimal Radiomics Signature Detection

The workflow process of radiomics analysis is shown in **Figures 1A,B**. ROIs of aneurysms were manually segmented by a neuroradiologist on each slice of CTA images (**Figure 1A**). Then, 50 aneurysms were randomly selected to be re-segmented by another neuroradiologist. We calculated the inter-class correlation coefficient (ICC) to evaluate the inter-observer reproducibility.

As the images were acquired from different CT scanners with different parameters, we performed data preprocessing before radiomics feature extraction (Lambin et al., 2017; Morin et al., 2018; Chen et al., 2021). Image resampling and gray-level discretization were used to reduce the variability of radiomics features (Shafiq-Ul-Hassan et al., 2018). A total of 1316 radiomics features were extracted from each ROI (see **Supplementary Digital Content 3**, which illustrates the possible pathophysiologic meaning of the features). All radiomics features were standardized by z-score to eliminate unit limits of each feature (Yang et al., 2019; see **Supplementary Methods**, **Supplementary Digital Content 4**, for further details about radiomics analysis).

Figure 1B indicates the feature selection procedure. Firstly, features with poor reproducibility (an ICC of <0.7) were excluded. After that, we used two different kinds of schemes to select informative radiomics features: (1) the minimum redundancy maximum relevance (mRMR) method was performed to rank the top 50 rupture-associated features while minimizing intra-feature correlation (Ding and Peng, 2005; Castiglioni et al., 2019), and then we used the least absolute shrinkage and selection operator (LASSO) method to select optimal features from those 50 features (Sauerbrei et al., 2007) ("mRMR-LASSO method"); (2) only LASSO method was used to selected optimal features ("LASSO method") (see **Supplementary Methods**, **Supplementary Digital Content 5**, for further detailed information of mRMR and LASSO). We applied the logistics regression model to build radiomics signatures. Discrimination ability of the "mRMR-LASSO model" and "LASSO model" were compared. The features with better performance were used for subsequent analysis. Moreover, we calculated the Rad score through a linear combination of selected features by multiplying with their LASSO coefficients (Huang et al., 2016).

Machine Learning Models Development and Validation

Support vector machine (SVM) is a supervised machine learning method that classifies data points by maximizing the distance between classes in a high-dimensional space (Orru et al., 2012). We applied SVM with a 10-fold cross-validation to construct models. As shown in **Figure 1D**, optimal radiomics features were introduced into the radiomics model (R-model). The morphological predictors of aneurysm rupture were introduced into the morphological model (M-model). Optimal radiomics features and morphological features were put together to generate the radiomics-morphological model (RM-model). Models were trained using the training dataset and validated in the temporal and external validation datasets. Variance inflation factor (VIF) was used to detect multicollinearity of the enrolled features, and a VIF of ≥ 5 was considered as multicollinearity (Akinwande et al., 2015).

The model performance was evaluated using the receiver operating characteristic (ROC) curve. The DeLong test was used for comparisons of an area under the receiver operating curves (AUCs) of different models (DeLong et al., 1988). The decision curve analysis (DCA) was applied to assess the clinical utility of the models. Besides, net reclassification improvement (NRI) (Pencina et al., 2011) was calculated to evaluate the improvement in the discrimination ability of different models.

Nomogram Construction and Evaluation

To provide an easy and visualized rupture risk-scoring system, we constructed a comprehensive nomogram. The top five rupture-associated factors among the Rad score, clinical and morphological features were selected using the mRMR method. These five factors were used to generate the nomogram. The discrimination of the nomogram was assessed with ROC curves. The agreement between predicted rupture and observed rupture was evaluated using the calibration curve and the Hosmer–Lemeshow test (Kramer and Zimmerman, 2007). The discrimination and calibration of the nomogram were appraised in the training and validation datasets.

Statistical Analysis

Categorical variables are presented as counts (with percentages), while continuous variables are presented as medians [interquartile range, (IQR)]. We used Student t-tests or Mann–Whitney U tests to evaluate the differences in continuous variables. Differences in categorical variables were assessed using the χ^2 test or Fisher exact test (two-tailed). A p-value of <0.05

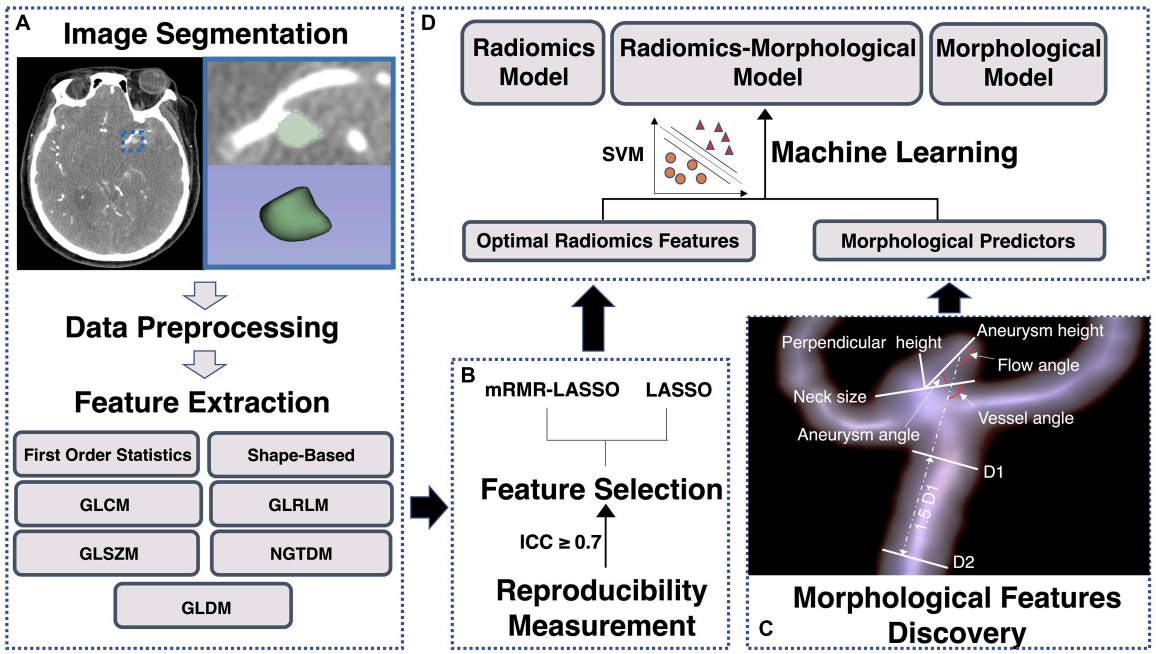

FIGURE 1 | A flowchart of radiomics analysis and radiomics-clinical model construction. **(A)** The process of regions of interest (ROIs) segmentation; **(B)** the process of optimal radiomics features detection; **(C)** the process of morphological predictors discovery; and **(D)** the process of machine learning models development and validation. GLCM, gray level co-occurrence matrix; GLDM, gray level dependence matrix; GLRLM, grey level run-length matrix; GLSZM, gray level size zone matrix; NGTDM, neighboring gray tone difference matrix; SVM, support vector machine.

indicates a statistical difference. Statistical analysis and model construction were conducted using SPSS (version 24.0) and R (version 3.6.1).

RESULTS

Clinical and Morphological Characteristics

A total of 632 patients with 668 MCA aneurysms (423 ruptured aneurysms) from five hospitals were included in our study. Multiple aneurysms were presented in 132 (20.9%) patients. Thirty-two of the 132 (24.2%) patients have bilateral MCA aneurysms. There were 407, 152, and 73 patients with 438, 155, and 75 aneurysms in the training, temporal validation, and external validation datasets. **Table 1** shows the clinical and morphological characteristics of the training dataset (see **Supplementary Digital Content 6**, which shows characteristics of validation datasets). In univariate analysis, patients with ruptured aneurysms were younger and were less common to have a history of hypertension ($p < 0.05$).

For morphological features, the mean ICC value of the nine morphological features was 0.924. The kappa value of the irregular shape and daughter dome is 0.603 and 0.838, respectively (p-value for all <0.001). Vessel size, aneurysm size, neck size, AR, SR, aneurysm height, perpendicular height, aneurysm angle, irregular shape, and daughter dome were associated with aneurysm rupture ($p < 0.05$). The result of multivariate analysis (**Table 2**) indicates that SR [odds ratio (OR), 1.607 (95% CI, 1.309, 1.973); $p < 0.001$], neck size [OR, 0.690 (95% CI, 0.596, 0.799), $p < 0.001$], multiplicity [OR, 0.389 (95% CI, 0.244, 0.621), $p < 0.001$], and daughter dome [OR, 2.987 (95% CI, 1.650, 5.406), $p < 0.001$] were independent predictors of MCA aneurysms rupture.

Optimal Radiomics Features Detection

The mean ICC value of the overall 1316 radiomics features was 0.751. Eight hundred and eighty-one radiomics features showed a high interobserver agreement (an ICC value of ≥0.7). As shown in **Table 3**, the "mRMR-LASSO model" presented an AUC of 0.767 and 0.828 in the training and temporal validation dataset, respectively. The "mRMR-LASSO model" presented a higher discrimination ability than the "LASSO model." Therefore, those features selected using the "mRMR-LASSO method" were used for R-model construction. The Rad score was calculated (see **Supplementary Results**, **Supplementary Digital Content 7**, which indicates the Rad score calculation formula).

Machine Learning Models Construction and Evaluation

The performance of the models was shown in **Table 4** and **Figure 2**. The R-model obtained an AUC of 0.822 (95% CI, 0.776, 0.867) in the training dataset. In the temporal and external validation dataset, the R-model presented an AUC of 0.817 (95% CI, 0.744, 0.890) and 0.691 (95% CI, 0.567, 0.816), respectively. Four morphological predictors, including SR, neck

TABLE 1 | Baseline characteristics of patients in the training dataset.

Variables	Unruptured (*N* = 141)	Ruptured (*N* = 297)	*p*-Value
Age[a]	59.0 (53.0, 69.0)	55.0 (48.0, 64.3)	0.004
Female[a]	77.0 (54.6%)	173.0 (58.2%)	0.472
Hypertension[b]	75.0 (68.8%)	149.0 (55.4%)	0.016
Smoking[c]	30.0 (28.0%)	77.0 (28.6%)	0.909
Location			0.016
M1	51.0 (36.2%)	72.0 (24.2%)	
Mbif	85.0 (60.3%)	219.0 (73.7%)	
Mdist	5.0 (3.5%)	6.0 (2.0%)	
Side			0.862
Right	81.0 (57.4%)	168.0 (56.6%)	
Left	60.0 (42.6%)	129.0 (43.4%)	
Multiplicity	63.0 (44.7%)	66.6 (22.2%)	<0.001
Vessel size (mm)	2.5 (2.1, 2.8)	2.4 (2.0, 2.6)	0.002
Aneurysm size (mm)	5.6 (4.0, 7.8)	6.7 (5.0, 9.1)	0.001
Neck size (mm)	4.2 (3.3, 5.5)	3.9 (3.1, 4.8)	0.018
Aspect ratio	0.8 (0.5, 1.1)	1.0 (0.8, 1.4)	<0.001
Size ratio	1.6 (1.0, 2.3)	2.3 (1.6, 3.4)	<0.001
Aneurysm height (mm)	4.1 (2.6, 5.4)	5.1 (3.9, 6.9)	<0.001
Perpendicular height (mm)	3.3 (2.3, 4.6)	4.1 (3.0, 5.5)	<0.001
Aneurysm angle (°)	65.4 (53.5, 81.4)	61.4 (48.1, 76.5)	0.014
Vessel angle (°)	57.1 (37.4, 77.7)	64.3 (41.4, 78.4)	0.134
Flow angle (°)	135.8 (111.4, 158.5)	137.8 (116.2, 159.2)	0.319
Daughter dome	18.0 (12.8%)	102.0 (34.3%)	<0.001
Irregular shape	48.0 (34.0%)	179.0 (60.3%)	<0.001

[a] *3/438 (0.68%) missing values.*
[b] *60/438 (13.70%) missing values.*
[c] *62/438 (14.16%) missing values.*
M1, the proximal segment of the middle cerebral artery; Mbif, main middle cerebral artery bifurcation; Mdist, distal middle cerebral artery.

TABLE 2 | Univariate and multivariable analysis of morphological and clinical features associated with aneurysm rupture.

Variables	Univariate analysis			Multivariate analysis		
	Odds ratio	95% CI	*p*-Value	Odds ratio	95% CI	*p*-Value
Neck size (mm)	0.864	0.770, 0.970	0.018	0.690	0.596, 0.799	< 0.001
Daughter dome	3.574	2.063, 6.192	< 0.001	2.987	1.650, 5.406	< 0.001
Size ratio	1.478	1.240, 1.761	< 0.001	1.607	1.309, 1.973	< 0.001
Multiplicity	0.354	0.230, 0.544	< 0.001	0.389	0.244, 0.621	< 0.001
Aneurysm height (mm)	1.169	1.074, 1.272	< 0.001	–	–	0.407
Location	1.825	1.178, 2.827	0.016	–	–	0.385
Aneurysm size (mm)	1.080	1.009, 1.156	0.001	–	–	0.735
Aspect ratio	2.813	1.754, 4.511	< 0.001	–	–	0.814
Vessel size (mm)	0.526	0.357, 0.776	0.002	–	–	0.747
Perpendicular height (mm)	1.110	1.015, 1.212	< 0.001	–	–	0.731
Aneurysm angle (°)	0.987	0.976, 0.998	0.014	–	–	0.215
Irregular shape	2.939	1.934, 4.468	< 0.001	–	–	0.100
Hypertension	0.625	0.387, 1.011	0.016	–	–	0.055
Age	0.974	0.954, 0.994	0.004	–	–	0.012

CI, confidence interval.

size, multiplicity, and daughter dome, were used to construct the M-model. The M-model obtained an AUC of 0.798 (95% CI, 0.749, 0.846), 0.751 (95% CI, 0.674, 0.828), and 0.624 (95% CI, 0.490, 0.759) in the training, temporal, and external validation datasets, respectively. The *p*-values from the DeLong test of the statistical comparison of the ROC curves are given in **Table 5**.

The optimal radiomics features and morphological predictors were enrolled in the RM-model. The RM-model exhibited good

TABLE 3 | Performance of the "LASSO model" and "mRMR-LASSO model."

Datasets	Method	Feature count	AUC (95% CI)	ACC	SEN	SPE	*p*-Value
Training dataset	LASSO	7	0.693 (0.638, 0.747)	0.717	0.811	0.518	0.003
	mRMR-LASSO	7	0.767 (0.718, 0.816)	0.774	0.869	0.574	
Temporal validation dataset	LASSO	7	0.767 (0.689, 0.845)	0.735	0.735	0.736	0.092
	mRMR-LASSO	7	0.828 (0.759, 0.897)	0.806	0.928	0.667	

p-Values were derived from the DeLong test comparing AUCs between radiomics signatures built by two feature selection methods.
AUC, area under the receiver operating curve; ACC, accuracy; CI, confidence interval; SEN, sensitivity; SPE, specificity.

TABLE 4 | Performance of the radiomics, morphological, radiomics-morphological, clinical-morphological, and clinical-radiomics-morphological models.

Datasets	Models	AUC (95% CI)	ACC	SEN	SPE	PPV	NPV
Training dataset	R-model	0.822 (0.776, 0.867)	0.826	0.912	0.645	0.844	0.778
	M-model	0.798 (0.749, 0.846)	0.733	0.680	0.844	0.902	0.556
	RM-model	0.848 (0.810, 0.885)	0.795	0.788	0.809	0.897	0.644
	CM-model	0.811 (0.770, 0.853)	0.758	0.761	0.752	0.866	0.599
	CRM-model	0.856 (0.820, 0.892)	0.756	0.707	0.858	0.913	0.582
Temporal validation dataset	R-model	0.817 (0.744, 0.890)	0.800	0.928	0.653	0.755	0.887
	M-model	0.751 (0.674, 0.828)	0.690	0.590	0.806	0.778	0.630
	RM-model	0.865 (0.807, 0.924)	0.813	0.855	0.764	0.807	0.821
	CM-model	0.795 (0.723, 0.867)	0.755	0.819	0.681	0.747	0.766
	CRM-model	0.882 (0.828, 0.936)	0.832	0.928	0.722	0.794	0.897
External validation dataset	R-model	0.691 (0.567, 0.816)	0.693	0.721	0.656	0.738	0.636
	M-model	0.624 (0.490, 0.759)	0.680	0.953	0.313	0.651	0.833
	RM-model	0.721 (0.601, 0.841)	0.733	0.744	0.719	0.780	0.676
	CM-model	0.738 (0.621, 0.855)	0.747	0.860	0.594	0.740	0.760
	CRM-model	0.738 (0.618, 0.857)	0.760	0.767	0.750	0.805	0.706

R-model, radiomics model; M-model, morphological model; RM-model, radiomics-morphological model; CM-model, clinical-morphological model; CRM-model, clinical-radiomics-morphological model; AUC, area under the receiver operating curve; ACC, accuracy; CI, confidence interval; PPV, positive predictive value; NPV, negative predictive value. SEN, sensitivity; SPE, specificity.

TABLE 5 | The *p*-values of the DeLong test of the statistical comparison of the ROC curves in all datasets.

	Training dataset	Temporal validation dataset	External validation dataset
R-model vs. M-model	0.458	0.211	0.457
M-model vs. RM-model	0.041	0.005	0.224
R-model vs. RM-model	0.176	0.115	0.559
R-model vs. CM-model	0.743	0.685	0.603
M-model vs. CM-model	0.515	0.212	0.106
R-model vs. CRM-model	0.078	0.041	0.407
M-model vs. CRM-model	0.018	0.002	0.152
RM-model vs. CRM-model	0.176	0.096	0.378
CM-model vs. CRM-model	0.038	0.018	0.993

R-model, radiomics model; M-model, morphological model; RM-model, radiomics-morphological model; CM-model, clinical-morphological model; CRM-model, clinical-radiomics-morphological model.

ability in classifying ruptured MCA aneurysms, with an AUC of 0.848 (95% CI, 0.810, 0.885), accuracy of 0.795, sensitivity of 0.788, and specificity of 0.809 in the training dataset. We further validated the RM-model in two validation datasets. The AUC of RM-model for ruptured MCA aneurysms classification was 0.865 (95% CI, 0.807, 0.924) and 0.721 (95% CI, 0.601, 0.841) in the temporal and external validation datasets, respectively (**Figure 2** and **Table 4**). Multicollinearity was not observed between those selected radiomics features and morphological predictors (VIF for all <2).

Compared with the single R-model and M-model, the RM-model achieved a higher AUC. In the training dataset, the RM-model outperformed the M-model [AUC (95% CI), 0.848 (0.810, 0.885) vs. 0.798 (0.749, 0.846), $p = 0.041$]. In the validation datasets, the RM-model tended to have a better presented higher AUC than the single M-model. The difference was statistically

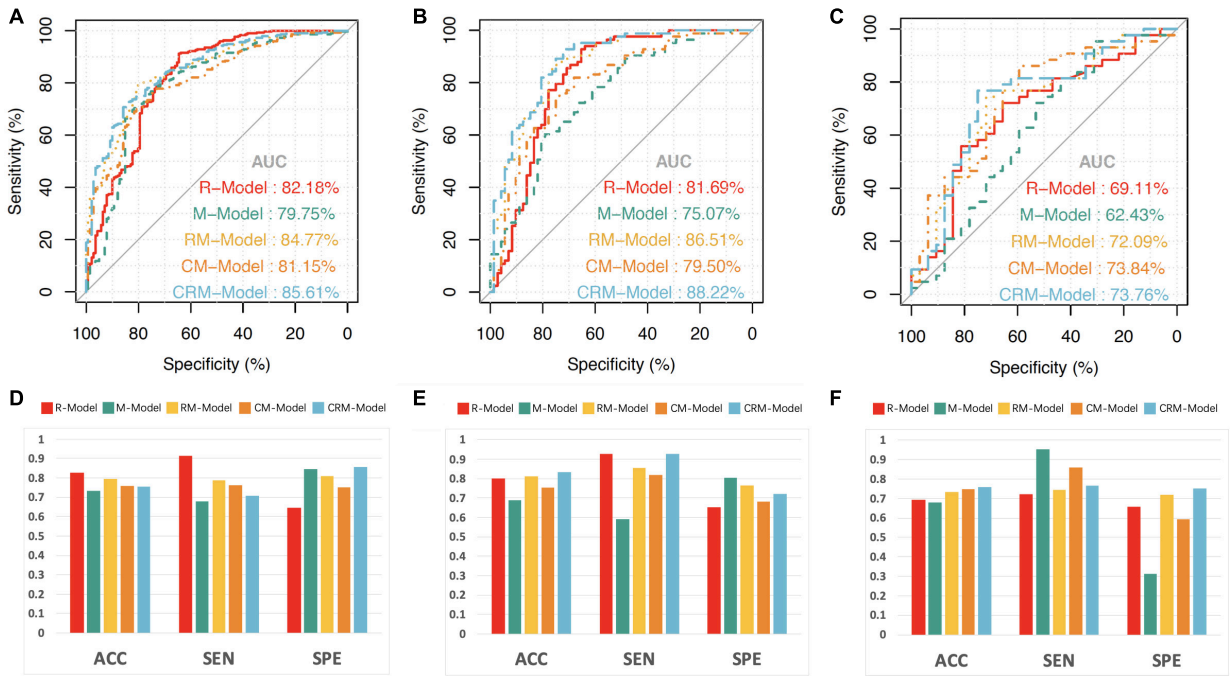

FIGURE 2 | The receiver operating characteristic (ROC) curves, accuracy, sensitivity, and specificity of the radiomics model (R-model), morphological model (M-model), radiomics-morphological model (RM-model), clinical-morphological model (CM-model); and clinical-radiomics-morphological model (CRM-model). The ROC curves of the three models in training **(A)**, temporal validation **(B)**, and external validation datasets **(C)**. The accuracy, sensitivity, and specificity of the three models in the training **(D)**, temporal validation **(E)**, and external validation datasets **(F)**. ACC, accuracy; SEN, sensitivity; SPE, specificity.

significant in the temporal validation dataset ($p < 0.005$) while it was not statistically significant in the external validation dataset ($p = 0.224$).

We further added clinical features (hypertension, smoking, age, and sex) into the M-model and RM-model to construct the clinical-morphological model (CM-model) and clinical-radiomics-morphological model (CRM-model). As it was shown in **Table 4** and **Figure 2**, the CRM-model obtained an AUC (95% CI) of 0.856 (0.820, 0.892), 0.882 (0.828, 0.936), and 0.738 (0.618, 0.857) in the three datasets, respectively. The CRM-model outperformed the CM-model in the training and temporal validation datasets ($p < 0.05$). However, the difference was not observed in the external validation dataset. We further calculated NRI to evaluate the improvement of discrimination by adding radiomics features to CM-model. We found that adding radiomics features to CM-mode improved the net reclassification indices in the three datasets (additive NRI, 52.40%, 89.66%, and 24.62%, respectively). This indicated that compared to the CM-model, the CRM-model correctly reclassified 52.40%, 89.66%, and 24.62% cases in the three datasets, respectively.

With respect to clinical utility, the DCA (**Figure 3B**) indicated that the RM-model had a higher overall net benefit in distinguishing ruptured aneurysms than the single R-model and M-model for most of the threshold probabilities. The CRM-model obtained the highest net benefit for most of the threshold probabilities. Combining radiomics features to conventional models resulted in an extra net-benefit compared with the M-model and CM-model.

Nomogram Construction and Evaluation

The shape, vessel size, AR, multiplicity, and Rad score were incorporated into the comprehensive nomogram (**Figure 3A**). The nomogram presented satisfying discrimination ability with an AUC of 0.771 (95% CI, 0.723, 0.818), 0.823, (95% CI, 0.757, 0.889), and 0.709 (95% CI, 0.592, 0.827) in the training, temporal validation, and external validation datasets, respectively. The calibration curve (**Figures 3C–E**) and the Hosmer–Lemeshow test (p = 0.731, 0.325, and 0.067, in the three datasets, respectively) indicate good calibration.

DISCUSSION

This study developed and validated ruptured MCA aneurysms classification models based on radiomics and morphological features in a large and multicentral dataset (a total of 668 MCA aneurysms were enrolled). It was proved that robust radiomics features extracted from CTA images could classify ruptured MCA aneurysms. The RM-model could identify more than 74% ruptured MCA aneurysms with a specificity of 72–81%. Additionally, we provided an easy and visualized rupture risk-scoring system for MCA aneurysm patients through the nomogram.

In this study, a total of 1316 radiomics features were extracted for each aneurysm. Among those numerous radiomics features, the features indicating image heterogeneity

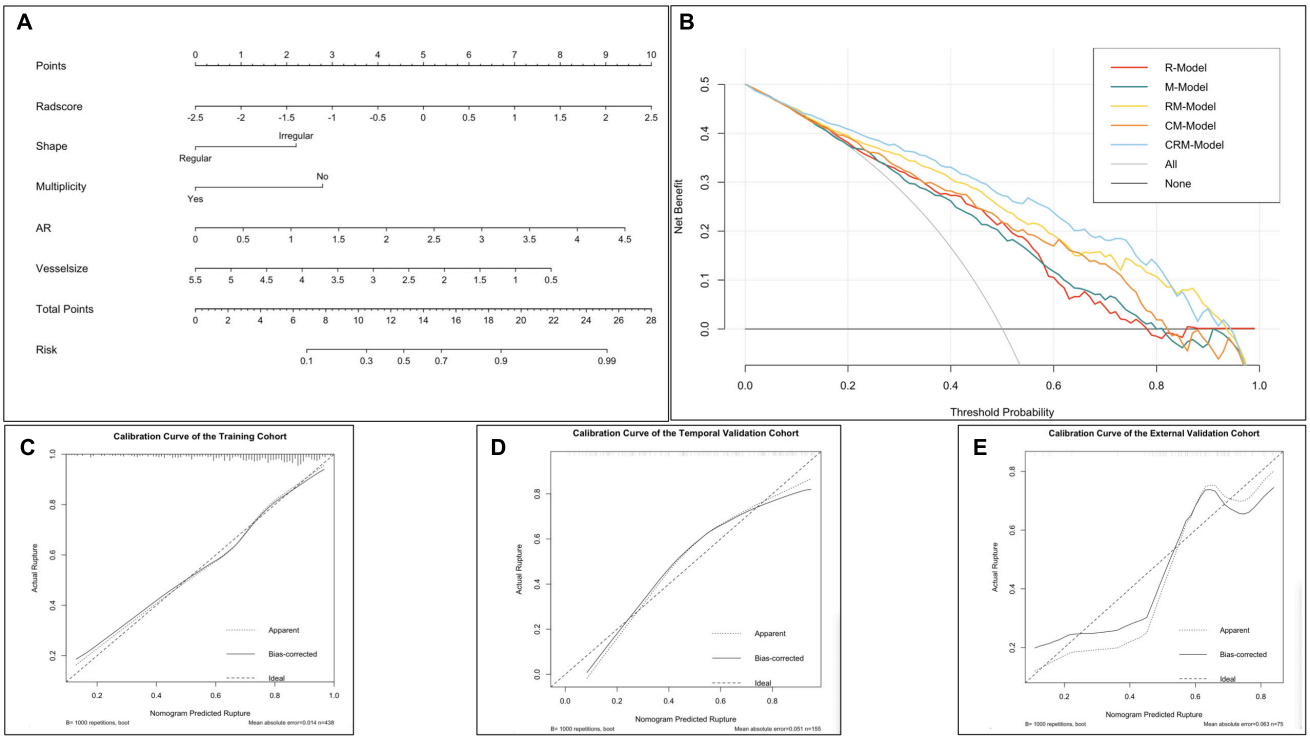

FIGURE 3 | The comprehensive nomogram for classifying ruptured MCA aneurysm and decision curve analysis in the overall patients. **(A)** The comprehensive nomogram for predicting aneurysm rupture. **(B)** Decision curve analysis in overall patients. The *y*-axis indicates the net benefit; the *x*-axis indicates threshold probability. The gray line represents the assumption that all aneurysms rupture. The black line represents the assumption that no aneurysm ruptures. The red line, green line, gold line, orange line, and blue line represent the net benefit of the radiomics model (R-model), morphological model (M-model), radiomics-morphological model (RM-model), clinical-morphological model (CM-model), and clinical-radiomics-morphological model (CRM-model), respectively. Calibration of the nomogram in the training **(C)**, temporal validation **(D)**, and external validation datasets **(E)**.

(e.g., Dependence Non-Uniformity Normalized, Cluster Shade, and Variance) were screened out as the optimal signature for ruptured aneurysms classification. This is in agreement with the study of Ou et al. (2021). The possible explanation for this is that CTA image heterogeneity is caused by the contrast maldistribution in the vessel lumen. The uneven distribution of contrast indicates turbulent flow (George et al., 2016; Aghayev et al., 2018; Ou et al., 2021), which was one of the risk factors for aneurysms rupture (Lv et al., 2020). Therefore, we speculate that CTA-derived radiomics features might imply the hemodynamics condition of aneurysms.

Unlike former research (Liu et al., 2019; Ou et al., 2021), shape radiomics features were not selected for model construction. We exclude some shape features before the feature selection due to their poor interobserver agreement (e.g., the shape radiomics features Sphericity and Flatness obtained an ICC value of 0.536 and 0.590, respectively). Only highly stable features were used in the model construction procedure. The temporal and external validation datasets further verified the robustness and generalizability of the results.

It is generally acknowledged that vessel wall degradation and abnormal morphological condition are related to aneurysms' rupture. We found that daughter dome, multiplicity, neck size, and SR were independent predictors for MCA aneurysm rupture, which have been reported by other researchers (Can et al., 2015; Zhang et al., 2019; Ou et al., 2020; Tanioka et al., 2020; Zhu et al., 2020).

Both radiomics and morphological features originate from CTA images, but their biological meanings and analysis procedures are different. Radiomics features describe the shape and texture characteristics of aneurysms from the micro point of view (Lambin et al., 2017; Xu et al., 2019), while the morphological features measure the macroscopic observation of the aneurysms. Radiomics features are three-dimensional derived, high-through biomarkers but lacking clinical interpretability. Meanwhile, those morphological features are two-dimensional measured features with relatively less information, but they are still fundamental tools for aneurysm evaluation. Though the statistically significant improvement in AUC of adding radiomics was not observed in the external dataset, considering its objectivity and its extra net-benefit in DCA, radiomics could be a possible choice in clinical practice, enabling better patient management.

Aneurysms rupture leads to catastrophic consequences. Preventive treatment for high rupture risk patients

is necessary. However, preventive treatments for low rupture risk patients may cause more harm than good due to operation-related complications (Naggara et al., 2010). Therefore, except for stratifying rupture-prone aneurysms, accurate identification of aneurysms at a relatively low rupture risk is also essential. Compared to the CM-model (which is routinely used in clinical practice), the CRM-model obtained a higher specificity, positive predictive value (PPV), and the CRM-model correctly reclassified 52.40%, 89.66%, and 24.62% patients in the three datasets, respectively. This indicated that adding radiomics features to conventional models might not only classify ruptured aneurysms but also help in recognizing unruptured aneurysms, which may reduce unnecessary treatment for unruptured aneurysms patients.

There are some limitations in this study. First, this is a retrospective, cross-sectional study without the longitudinal follow-up of aneurysms, which might inherently cause biases. Second, the aneurysms' morphological changes after rupture were not considered because it is hard to collect the morphological change before and after the aneurysm rupture due to ethical issues. Third, most patients with SAH history were excluded because of their surgery experience. This could cause potential selection bias. Forth, images from external validation datasets contain different scanning protocols, which might affect the validation results. We performed image resampling and gray-level discretization to reduce the variability of images. Moreover, samples from the other four hospitals were merged into one external validation dataset. The good results further indicated the robustness of the models.

CONCLUSION

In conclusion, we analyzed the MCA aneurysms rupture by clinical, radiomics, and morphological features using multicentral data. We answered two critical questions: (1) Robust radiomics features could classify ruptured MCA aneurysms. (2) The integration of radiomics into conventional clinical and morphological models might provide additional benefit in ruptured MCA aneurysms classification. An easy and visualized rupture risk-scoring nomogram was generated. This may aid in the rupture-risk assessment of MCA aneurysms.

DATA AVAILABILITY STATEMENT

The original contributions presented in the study are included in the article/**Supplementary Material**, further inquiries can be directed to the corresponding author/s.

ETHICS STATEMENT

The studies involving human participants were reviewed and approved by the Medical Ethics Committee of the First Affiliated Hospital of Wenzhou Medical University. Written informed consent for participation was not required for this study in accordance with the national legislation and the institutional requirements.

AUTHOR CONTRIBUTIONS

DZ wrote the manuscript. DZ, PP, and YC interpreted the data and prepared the tables and figures. JZ, YC, and KZ revised the manuscript for intellectual content. CC, QL, JZ, NX, HW, BL, YN, and XJ acquired the data. YY contributed to the conception and the design of the study. All co-authors read and revised the manuscript.

FUNDING

This study was supported by the Wenzhou Major Program of Science and Technology Innovation (Grant No. ZY2020012), the Health Foundation for Creative Talents in Zhejiang Province, China (Grant No. 2016), the Project Foundation for the College Young and Middle-aged Academic Leader of Zhejiang Province, China (Grant No. 2017), and Basic Research Project of Wenzhou (Grant No. Y2020164).

SUPPLEMENTARY MATERIAL

The Supplementary Material for this article can be found online at: https://www.frontiersin.org/articles/10.3389/fnins.2021.721268/full#supplementary-material

REFERENCES

Aghayev, A., Giannopoulos, A. A., Gronsbell, J., George, E., Cai, T., Steigner, M. L., et al. (2018). Common First-Pass CT Angiography Findings Associated With Rapid Growth Rate in Abdominal Aorta Aneurysms Between 3 and 5 cm in Largest Diameter. *AJR Am. J. Roentgenol.* 210, 431–437. doi: 10.2214/AJR.17.18094

Akinwande, M. O., Dikko, H. G., and Samson, A. (2015). Variance Inflation Factor: As a Condition for the Inclusion of Suppressor Variable(s) in Regression Analysis. *Open J. Stat.* 05, 754–767. doi: 10.4236/ojs.2015.57075

Al-Shahi Salman, R., Frantzias, J., Lee, R. J., Lyden, P. D., Battey, T. W. K., Ayres, A. M., et al. (2018). Absolute risk and predictors of the growth of acute spontaneous intracerebral haemorrhage: a systematic review and meta-analysis of individual patient data. *Lancet Neurol.* 17, 885–894. doi: 10.1016/S1474-4422(18)30253-9

Can, A., Ho, A. L., Dammers, R., Dirven, C. M., and Du, R. (2015). Morphological parameters associated with middle cerebral artery aneurysms. *Neurosurgery* 76, 721–726. doi: 10.1227/neu.0000000000000713

Castiglioni, I., Gallivanone, F., Soda, P., Avanzo, M., Stancanello, J., Aiello, M., et al. (2019). AI-based applications in hybrid imaging: how to build smart and truly multi-parametric decision models for radiomics. *Eur. J. Nucl. Med. Mol. Imaging* 46, 2673–2699. doi: 10.1007/s00259-019-04414-4

Chen, Q., Xia, T., Zhang, M., Xia, N., Liu, J., and Yang, Y. (2021). Radiomics in Stroke Neuroimaging: Techniques, Applications, and Challenges. *Aging Dis* 12, 143–154. doi: 10.14336/AD.2020.0421

Chen, Y., Lin, B., Zhou, J., Chen, L., Yang, Y., and Zhao, B. (2020). Morphological predictors of middle cerebral artery bifurcation aneurysm rupture. *Clin. Neurol. Neurosurg.* 192:105708. doi: 10.1016/j.clineuro.2020.105708

Choe, J., Lee, S. M., Do, K. H., Lee, G., Lee, J. G., Lee, S. M., et al. (2019). Deep Learning-based Image Conversion of CT Reconstruction Kernels Improves Radiomics Reproducibility for Pulmonary Nodules or Masses. *Radiology* 292, 365–373. doi: 10.1148/radiol.2019181960 PubMed

Collins, G. S., Reitsma, J. B., Altman, D. G., and Moons, K. G. M. (2015). members of the Tg. Transparent Reporting of a Multivariable Prediction Model for Individual Prognosis or Diagnosis (TRIPOD): The TRIPOD Statement. *Eur. Urol.* 67, 1142–1151. doi: 10.1016/j.eururo.2014.11.025

DeLong, E. R., DeLong, D. M., and Clarke-Pearson, D. L. (1988). Comparing the areas under two or more correlated receiver operating characteristic curves: a nonparametric approach. *Biometrics* 44, 837–845. doi: 10.2307/2531595

Ding, C., and Peng, H. (2005). Minimum redundancy feature selection from microarray gene expression data. *J. Bioinform. Comput. Biol.* 3, 185–205. doi: 10.1142/s0219720005001004

George, E., Giannopoulos, A. A., Aghayev, A., Rohatgi, S., Imanzadeh, A., Antoniadis, A. P., et al. (2016). Contrast inhomogeneity in CT angiography of the abdominal aortic aneurysm. *J. Cardiovasc. Comput. Tomogr.* 10, 179–183. doi: 10.1016/j.jcct.2015.11.006

Greving, J. P., Wermer, M. J., Brown, R. D. Jr., Morita, A., Juvela, S., Yonekura, M., et al. (2014). Development of the PHASES score for prediction of risk of rupture of intracranial aneurysms: a pooled analysis of six prospective cohort studies. *Lancet Neurol.* 13, 59–66. doi: 10.1016/S1474-4422(13)70263-1

Hua, W., Xiao, T., Jiang, X., Liu, Z., Wang, M., Zheng, H., et al. (2020). Lymph-vascular space invasion prediction in cervical cancer: Exploring radiomics and deep learning multilevel features of tumor and peritumor tissue on multiparametric MRI. *Biomedical. Signal Proc. Control* 58:101869. doi: 10.1016/j.bspc.2020.101869

Huang, Y. Q., Liang, C. H., He, L., Tian, J., Liang, C. S., Chen, X., et al. (2016). Development and Validation of a Radiomics Nomogram for Preoperative Prediction of Lymph Node Metastasis in Colorectal Cancer. *J. Clin. Oncol.* 34, 2157–2164. doi: 10.1200/JCO.2015.65.9128

Huttunen, T., von und zu Fraunberg, M., Frosen, J., Lehecka, M., Tromp, G., Helin, K., et al. (2010). Saccular intracranial aneurysm disease: distribution of site, size, and age suggests different etiologies for aneurysm formation and rupture in 316 familial and 1454 sporadic eastern Finnish patients. *Neurosurgery* 66, 631–638.

Korja, M., Lehto, H., and Juvela, S. (2014). Lifelong rupture risk of intracranial aneurysms depends on risk factors: a prospective Finnish cohort study. *Stroke* 45, 1958–1963. doi: 10.1161/STROKEAHA.114.005318

Kramer, A. A., and Zimmerman, J. E. (2007). Assessing the calibration of mortality benchmarks in critical care: The Hosmer-Lemeshow test revisited. *Crit. Care Med.* 35, 2052–2056. doi: 10.1097/01.CCM.0000275267.64078.B0

Lambin, P., Leijenaar, R. T. H., Deist, T. M., Peerlings, J., de Jong, E. E. C., van Timmeren, J., et al. (2017). Radiomics: the bridge between medical imaging and personalized medicine. *Nat. Rev. Clin. Oncol.* 14, 749–762. doi: 10.1038/nrclinonc.2017.141

Lindgren, A. E., Koivisto, T., Bjorkman, J., von Und Zu Fraunberg, M., Helin, K., and Jaaskelainen, J. E. (2016). Irregular Shape of Intracranial Aneurysm Indicates Rupture Risk Irrespective of Size in a Population-Based Cohort. *Stroke* 47, 1219–1226. doi: 10.1161/strokeaha.115.012404

Liu, Q., Jiang, P., Jiang, Y., Ge, H., Li, S., Jin, H., et al. (2019). Prediction of Aneurysm Stability Using a Machine Learning Model Based on PyRadiomics-Derived Morphological Features. *Stroke* 50, 2314–2321. doi: 10.1161/STROKEAHA.119.025777

Lv, N., Karmonik, C., Chen, S., Wang, X., Fang, Y., Huang, Q., et al. (2020). Wall Enhancement, Hemodynamics, and Morphology in Unruptured Intracranial Aneurysms with High Rupture Risk. *Transl. Stroke Res.* 11, 882–889. doi: 10.1007/s12975-020-00782-4

Mackin, D., Fave, X., Zhang, L., Fried, D., Yang, J., Taylor, B., et al. (2015). Measuring Computed Tomography Scanner Variability of Radiomics Features. *Invest. Radiol.* 50, 757–765. doi: 10.1097/RLI.0000000000000180

Morin, O., Vallieres, M., Jochems, A., Woodruff, H. C., Valdes, G., Braunstein, S. E., et al. (2018). A Deep Look Into the Future of Quantitative Imaging in Oncology: A Statement of Working Principles and Proposal for Change. *Int. J. Radiat. Oncol. Biol. Phys.* 102, 1074–1082. doi: 10.1016/j.ijrobp.2018.08.032

Naggara, O. N., White, P. M., Guilbert, F., Roy, D., Weill, A., and Raymond, J. (2010). Endovascular treatment of intracranial unruptured aneurysms: systematic review and meta-analysis of the literature on safety and efficacy. *Radiology* 256, 887–897. doi: 10.1148/radiol.10091982 PubMed

Orru, G., Pettersson-Yeo, W., Marquand, A. F., Sartori, G., and Mechelli, A. (2012). Using Support Vector Machine to identify imaging biomarkers of neurological and psychiatric disease: a critical review. *Neurosci Biobehav Rev* 36, 1140–1152. doi: 10.1016/j.neubiorev.2012.01.004

Ou, C., Chong, W., Duan, C. Z., Zhang, X., Morgan, M., and Qian, Y. A. (2021). preliminary investigation of radiomics differences between ruptured and unruptured intracranial aneurysms. *Eur. Radiol.* 31, 2716–2725. doi: 10.1007/s00330-020-07325-3

Ou, C., Liu, J., Qian, Y., Chong, W., Zhang, X., Liu, W., et al. (2020). Rupture Risk Assessment for Cerebral Aneurysm Using Interpretable Machine Learning on Multidimensional Data. *Front Neurol* 11:570181. doi: 10.3389/fneur.2020.570181

Pencina, M. J., D'Agostino, R. B. Sr., and Steyerberg, E. W. (2011). Extensions of net reclassification improvement calculations to measure usefulness of new biomarkers. *Stat. Med.* 30, 11–21. doi: 10.1002/sim.4085

Sauerbrei, W., Royston, P., and Binder, H. (2007). Selection of important variables and determination of functional form for continuous predictors in multivariable model building. *Stat. Med.* 26, 5512–5528. doi: 10.1002/sim.3148

Shafiq-Ul-Hassan, M., Latifi, K., Zhang, G., Ullah, G., Gillies, R., and Moros, E. (2018). Voxel size and gray level normalization of CT radiomic features in lung cancer. *Sci. Rep.* 8:10545. doi: 10.1038/s41598-018-28895-9

Shi, Z., Chen, G. Z., Mao, L., Li, X. L., Zhou, C. S., Xia, S., et al. (2021). Machine Learning-Based Prediction of Small Intracranial Aneurysm Rupture Status Using CTA-Derived Hemodynamics: A Multicenter Study. *AJNR Am. J. Neuroradiol.* 2021:7034. doi: 10.3174/ajnr.A7034

Tanioka, S., Ishida, F., Yamamoto, A., Shimizu, S., Sakaida, H., Toyoda, M., et al. (2020). Machine Learning Classification of Cerebral Aneurysm Rupture Status with Morphologic Variables and Hemodynamic Parameters. *Radiol. Artif Intell* 2:e190077. doi: 10.1148/ryai.2019190077

Tomaszewski, M. R., and Gillies, R. J. (2021). The Biological Meaning of Radiomic Features. *Radiology* 298, 505–516. doi: 10.1148/radiol.2021202553

Vlak, M. H., Algra, A., Brandenburg, R., and Rinkel, G. J. (2011). Prevalence of unruptured intracranial aneurysms, with emphasis on sex, age, comorbidity, country, and time period: a systematic review and meta-analysis. *Lancet Neurol.* 10, 626–636. doi: 10.1016/S1474-4422(11)70109-0

Xu, X., Zhang, H. L., Liu, Q. P., Sun, S. W., Zhang, J., Zhu, F. P., et al. (2019). Radiomic analysis of contrast-enhanced CT predicts microvascular invasion and outcome in hepatocellular carcinoma. *J. Hepatol.* 70, 1133–1144. doi: 10.1016/j.jhep.2019.02.023

Yang, L., Gu, D., Wei, J., Yang, C., Rao, S., Wang, W., et al. (2019). A Radiomics Nomogram for Preoperative Prediction of Microvascular Invasion in Hepatocellular Carcinoma. *Liver Cancer* 8, 373–386. doi: 10.1159/000494099

Zhang, J., Can, A., Mukundan, S., Steigner, M., Castro, V. M., Dligach, D., et al. (2019). Morphological Variables Associated With Ruptured Middle Cerebral Artery Aneurysms. *Neurosurgery* 85, 75–83. doi: 10.1093/neuros/nyy213 PubMed

Zhou, Y., Xu, J., Liu, Q., Li, C., Liu, Z., Wang, M., et al. (2018). A Radiomics Approach With CNN for Shear-Wave Elastography Breast Tumor Classification. *IEEE Trans. Biomed. Eng.* 65, 1935–1942. doi: 10.1109/TBME.2018.2844188

Zhu, D., Zhang, M., Li, Q., Liu, J., Zhuang, Y., Chen, Q., et al. (2021). Can perihaematomal radiomics features predict haematoma expansion? *Clin. Radiol.* 2021:003. doi: 10.1016/j.crad.2021.03.003

Zhu, D. Q., Chen, Q., Xiang, Y. L., Zhan, C. Y., Zhang, M. Y., Chen, C., et al. (2021). Predicting intraventricular hemorrhage growth with a machine learning-based, radiomics-clinical model. *Aging* 13, 12833–12848. doi: 10.18632/aging.202954

Zhu, W., Li, W., Tian, Z., Zhang, Y., Wang, K., Zhang, Y., et al. (2020). Stability Assessment of Intracranial Aneurysms Using Machine Learning Based on Clinical and Morphological Features. *Transl. Stroke Res.* 11, 1287–1295. doi: 10.1007/s12975-020-00811-2

Conflict of Interest: PP was employed by the company GE Healthcare China Co., Ltd., Shanghai.

The remaining authors declare that the research was conducted in the absence of any commercial or financial relationships that could be construed as a potential conflict of interest.

Publisher's Note: All claims expressed in this article are solely those of the authors and do not necessarily represent those of their affiliated organizations, or those of the publisher, the editors and the reviewers. Any product that may be evaluated in this article, or claim that may be made by its manufacturer, is not guaranteed or endorsed by the publisher.

frontiers in Neuroscience

ORIGINAL RESEARCH
published: 11 August 2021
doi: 10.3389/fnins.2021.678358

Differences in Wall Shear Stress Between High-Risk and Low-Risk Plaques in Patients With Moderate Carotid Artery Stenosis: A 4D Flow MRI Study

*Guiling Zhang[1], Shun Zhang[1], Yuanyuan Qin[1], Jicheng Fang[1], Xiangyu Tang[1], Li Li[1], Yiran Zhou[1], Di Wu[1], Su Yan[1], Weiyin Vivian Liu[2] and Wenzhen Zhu[1]**

[1] Department of Radiology, Tongji Hospital, Tongji Medical College, Huazhong University of Science and Technology, Wuhan, China, [2] Magnetic Resonance Research, General Electric Healthcare, Beijing, China

OPEN ACCESS

Edited by:
Chengcheng Zhu,
University of Washington,
United States

Reviewed by:
Tae Kim,
University of Pittsburgh, United States
Dalin Tang,
Worcester Polytechnic Institute,
United States
Gador Canton,
University of Washington,
United States

***Correspondence:**
Wenzhen Zhu
zhuwenzhen8612@163.com

Specialty section:
This article was submitted to Brain Imaging Methods, a section of the journal Frontiers in Neuroscience

Received: 09 March 2021
Accepted: 15 July 2021
Published: 11 August 2021

Citation:
Zhang G, Zhang S, Qin Y, Fang J, Tang X, Li L, Zhou Y, Wu D, Yan S, Liu WV and Zhu W (2021) Differences in Wall Shear Stress Between High-Risk and Low-Risk Plaques in Patients With Moderate Carotid Artery Stenosis: A 4D Flow MRI Study. Front. Neurosci. 15:678358. doi: 10.3389/fnins.2021.678358

This study aimed to evaluate the difference in wall shear stress (WSS) (axial, circumferential, and 3D) between high-risk and low-risk plaques in patients with moderate carotid artery stenosis and to identify which time points and directions play the dominant roles in determining the risk associated with plaques. Forty carotid arteries in 30 patients were examined in this study. All patients underwent high-resolution vessel wall (HRVW) imaging, diffusion-weighted imaging (DWI), and 4D flow MRI; HRVW imaging and DWI were used to separate low- and high-risk plaque. Twenty-four high-risk plaques and 16 low-risk plaques were enrolled. An independent-sample *t*-test was used to compare WSS between low- and high-risk plaques in the whole cardiac cycle and at 20 different time points in the cardiac cycle. The study found that patients with high-risk plaques had higher WSS than those with low-risk plaques throughout the entire cardiac cycle ($p < 0.05$), but the changes varied at the 20 different time points. The number of non-significant differences ($p > 0.05$) was less in diastole than in systole across different time points. The axial WSS values were higher than the circumferential WSS values; the difference in axial WSS values between high- and low-risk plaques was more significant than the difference in circumferential WSS, whereas 3D WSS values best reflected the difference between high-risk and low-risk plaques because they showed significant differences at every time point. In conclusion, increased WSS, especially during the diastolic period and in the axial direction, may be a signal of a high-risk plaque and may cause cerebrovascular events in patients with moderate carotid artery stenosis. Additionally, WSS can provide hemodynamic information and help clinicians make more appropriate decisions for patients with plaques.

Keywords: plaque risk, 4D flow MRI, wall shear stress, high resolution vessel wall imaging, stroke

INTRODUCTION

High-risk plaques that easily rupture and cause thrombosis or embolism are the predominant cause of cerebrovascular events (Falk et al., 2013). Conservative treatments such as pharmacological interventions can be used in patients with low-risk plaques, while proactive treatment such as stent placement or endovascular thrombectomy is usually utilized in those with high-risk plaques (Adamson et al., 2015). Plaques with a stenosis rate greater than 70% are independently associated with acute ischemic stroke and are defined as high-risk plaques, whereas patients with less than 30% stenosis are treated with medicine or prescribed for imaging follow-up (Bodle et al., 2013). However, for patients with moderate stenosis (a stenosis rate of 30–70%), treatments cannot be selected based on the stenosis alone; further examinations are needed to identify the high-risk plaques and take proactive treatments (Kernan et al., 2014; Bonati et al., 2015; Brott et al., 2016). Therefore, detecting high-risk plaques with moderate stenosis is of great importance.

High-risk plaques tend to be characterized by a large plaque volume, a necrotic lipid core, positive remodeling, peripheral neovascularization, a thin fibrous cap, microcalcification, intraplaque hemorrhage (IPH) and chronic inflammation (Adamson et al., 2015). Carotid endarterectomy provides the pathological tissue sections needed to identify between high- and low-risk plaques. However, this procedure is invasive; therefore, there is a pressing need for an accurate imaging method to identify high-risk and low-risk plaques in patients with moderate stenosis. Advanced imaging methods available to identify plaque risk are generally classified according to their basis: morphology or hemodynamics. A breakthrough has been made in morphological assessment with the development of high-resolution vessel wall (HRVW) imaging (Cai et al., 2005; Makowski et al., 2011; Qiao et al., 2014). HRVW can help identify stroke mechanisms, determine the degree and pathology of stenoses, and identify non-stenotic plaques and potentially high-risk plaque components (Bodle et al., 2013), but it still cannot completely distinguish high-risk from low-risk plaques by morphology alone, especially in the case of atypical plaques, due to limitations in resolution, an uncertain relationship with pathology, and morphological complexity and diversity. Therefore, the application of hemodynamics in combination with HRVW is useful and even essential in the determination of plaque risk.

Wall shear stress (WSS) is the most commonly reported risk indicator in hemodynamic research and is considered the most useful hemodynamic parameter for assessing plaques. It is generally accepted that low WSS may promote plaque formation by activating inflammatory processes (Matlung et al., 2012; Peiffer et al., 2013; Hung et al., 2015; Zhang et al., 2017). However, it remains controversial whether high WSS causes plaque rupture (Groen et al., 2008) or protects plaques from rupturing (Malek et al., 1999; Cheng et al., 2006). Further studies are needed to identify the relationship between WSS and plaque risk. 4D flow MRI is a novel method to non-invasively measure hemodynamic parameters *in vivo*. Compared to the traditional method, computational fluid dynamics (CFD), which relies on a fluid mechanics model based on idealized assumptions in a simulation to acquire hemodynamic information, 4D flow MRI directly measures blood velocity to compute hemodynamic values. The results of 4D flow MRI results are considered more realistic and reliable than those of CFD (Dyverfeldt et al., 2015). In addition, 4D flow MRI can dynamically and visually display hemodynamic changes across different cardiac cycles and can be used to explore the relationship between high- and low-risk plaques for different flow directions and plaque locations (Sotelo et al., 2018; Rizk et al., 2019).

HRVW imaging combined with the 4D flow MRI technique was used in our study to explore the differences in WSS between high- and low-risk plaques in patients with moderate stenosis. We aim to identify whether WSS is a predictor of high-risk plaques and which directions of blood flow and phases of the cardiac cycle play the most important roles in atherosclerosis. This study provides information on the hemodynamic aspects of plaque imaging and can help with further clinical treatments in atherosclerotic patients.

MATERIALS AND METHODS

Subjects

We recruited 34 patients with carotid plaques from January 2019 to June 2020. The stenosis rate of all plaques was initially assessed to be 30–70%, three patients with low-quality imaging and one patient whose actual stenosis rate was greater than 70% were excluded from the study. Ultimately, 40 carotid arteries of 30 patients were included: 10 patients had bilateral carotid plaques, and the 20 remaining patients had one healthy carotid artery each. Twenty-four had high-risk plaques, and 16 had low-risk plaques. High-risk plaques were defined as follows: (1) HRVW imaging: showed potentially high-risk plaque characteristics, including heterogeneous signal, a thin fibrous cap, IPH, a lipid core, or obvious partially enhanced signal. The enhancement was quantified as follows: [signal intensity of plaque (post-contrast)/signal intensity of gray matter (post-contrast)]/[signal intensity of plaque (pre-contrast)/signal intensity of gray matter (pre-contrast)]; when this value was greater than 1, the plaque was enhanced. (2) Cerebrovascular events had occurred, with definite hyperintense lesions identified in the ipsilateral brain parenchyma on DWI (**Figure 1**). Low-risk plaques were defined as follows: (1) HRVW imaging: did not show potentially high-risk plaque components and did not show enhancement. (2) No obvious lesion was identified in the ipsilateral brain parenchyma on DWI (**Figure 2**; Adamson et al., 2015; Zhang R. Y. et al., 2020).

Examination Protocol

All patients underwent 4D flow MRI, HRVW 3D T1-weighted imaging (T1WI), and DWI. The 4D flow MRI scans were conducted using a 3.0-T MRI scanner (GE Medical Systems, Discovery MR750, Waukesha, WI, United States) with an eight-channel head–neck coil. The 4D flow MRI data were

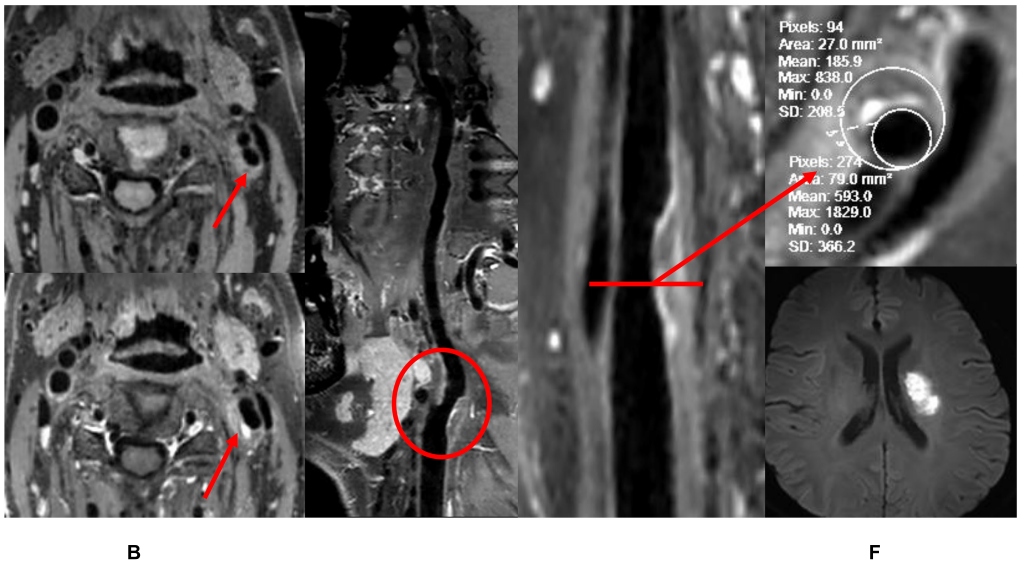

FIGURE 1 | The definition of high-risk plaque. **(A)** Pre-enhanced HRVW 3D T1 image, inhomogeneous intensity was seen in the plaque. **(B)** Post-enhanced HRVW 3D T1 image. Hyperintensity was seen in the plaque. **(C,D)** Reconstruction map of post-enhanced HRVW 3D T1 image. The whole vessel and a plaque shown in red circle were better displayed. **(E)** Section image perpendicular to the lumen in the plaque lesion. Stenosis rate was determined in this section. **(F)** DWI. Hyperintensity was seen in left basal ganglia, indicating cerebrovascular events occurred.

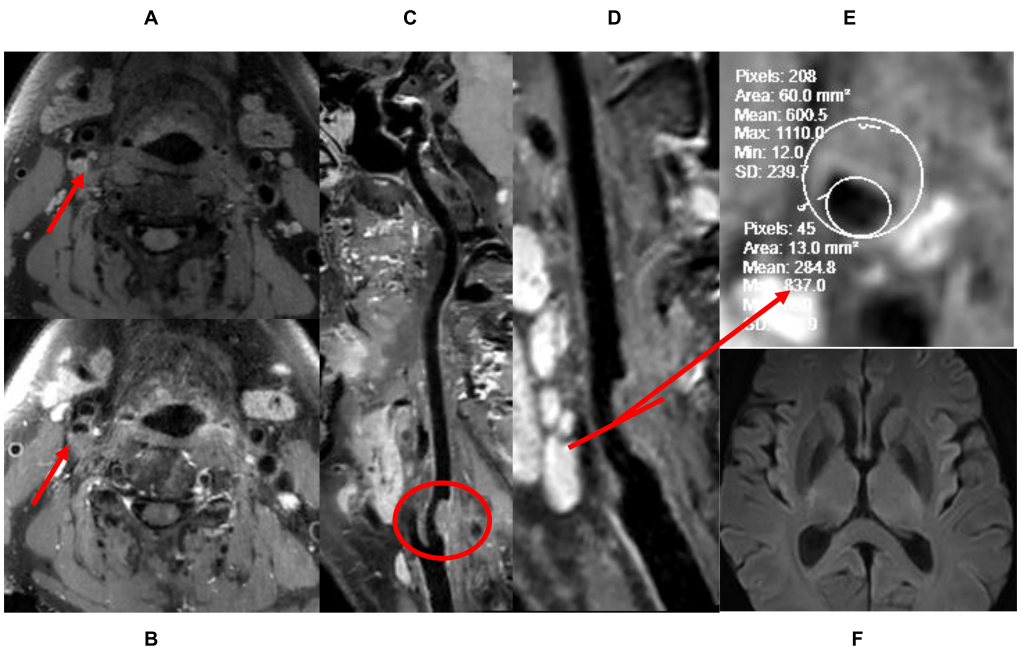

FIGURE 2 | The definition of low-risk plaque. **(A)** Pre-enhanced HRVW 3D T1 image. Intensity is homogeneous was seen in the plaque. **(B)** Post-enhanced HRVW 3D T1 image. No abnormal intensity was seen in the plaque. **(C,D)** Reconstruction map of post-enhanced HRVW 3D T1 image. Better display of the whole vessel and the plaque shown in red circle. **(E)** Section image, perpendicular to the lumen located in the plaque lesion. The stenosis rate can be determined in this section. **(F)** DWI. No abnormal hyperintensity was found in the whole brain, indicating no cerebrovascular events occurred.

acquired using a volumetric, time-resolved phase-contrast method. The scanning parameters were as follows: TR = 4.1 ms, TE = 2.1 ms, flip angle = 8°, FOV = 240 × 240 mm^2, matrix size = 128 × 128, NEX = 1 and receiver bandwidth = ± 62.5 kHz. Velocity encoding (VENC) was set at 100 cm/s to prevent aliasing artifacts. Twenty frames were reconstructed through

view sharing. The total scan time of the 4D flow was approximately 4–6 min depending on the heart rate of each subject (Zhang G. et al., 2020). DWI and HRVW imaging were conducted immediately after the 4D flow MRI. A 32-channel head coil combined with a soft coil attached to the neck with only a slight space between neck and neck coil was used at a 3T MR scanner (UMR780, United Imaging Healthcare, Shanghai, China). The DWI parameters were as follows: TR = 4,049 ms, TE = 48 ms, thickness = 5 mm, flip angle = 90°, FOV = 230 × 220 mm^2, B values = 0 and 1,000 s/mm^2, voxel size = 1.60*1.44*5.00 mm, and scan time 1min54s. HRVW imaging was performed with 3D-TIWI matrix before and after an injectable gadolinium-based contrast agent, gadobenate dimeglumine injection (Bracco Sine Pharmaceutical Corp., Ltd.; Shanghai, China), was administered intravenously (0.1 mmol/kg of body weight); 5 min after the contrast agent was administered, we conducted post-enhancement HRVW. The parameters were as follows: TR = 750 ms, TE = 23.7 ms, FOV = 220 mm × 180 mm, slice thickness = 0.66 mm, voxel size = 0.65 × 0.65 × 0.66 mm, and scan time = 7 min 13 s.

Data Analysis

As displayed in **Figure 3**, 4D flow MRI data were imported into the CVI42 software (Version 5.6.6, Circle Cardiovascular Imaging, Calgary, Canada) for preprocessing and parameter calculation; the analysis steps included the following: (1) preprocessing: the preprocessing step consisted of automatic offset correction, signal aliasing correction, correction of flow direction, and dynamic previewing of images in all directions to identify and exclude images with poor quality. (2) Segmentation: the target vessel was segmented parallel to the centerline, which was traced along the vessel. (3) Calculation: the analysis plane was placed perpendicular to the centerline at the narrowest part of the carotid artery, and velocity (maximum and mean), axial WSS (maximum and mean), and circumferential WSS (maximum and mean) were measured at 20 time points. WSS was calculated

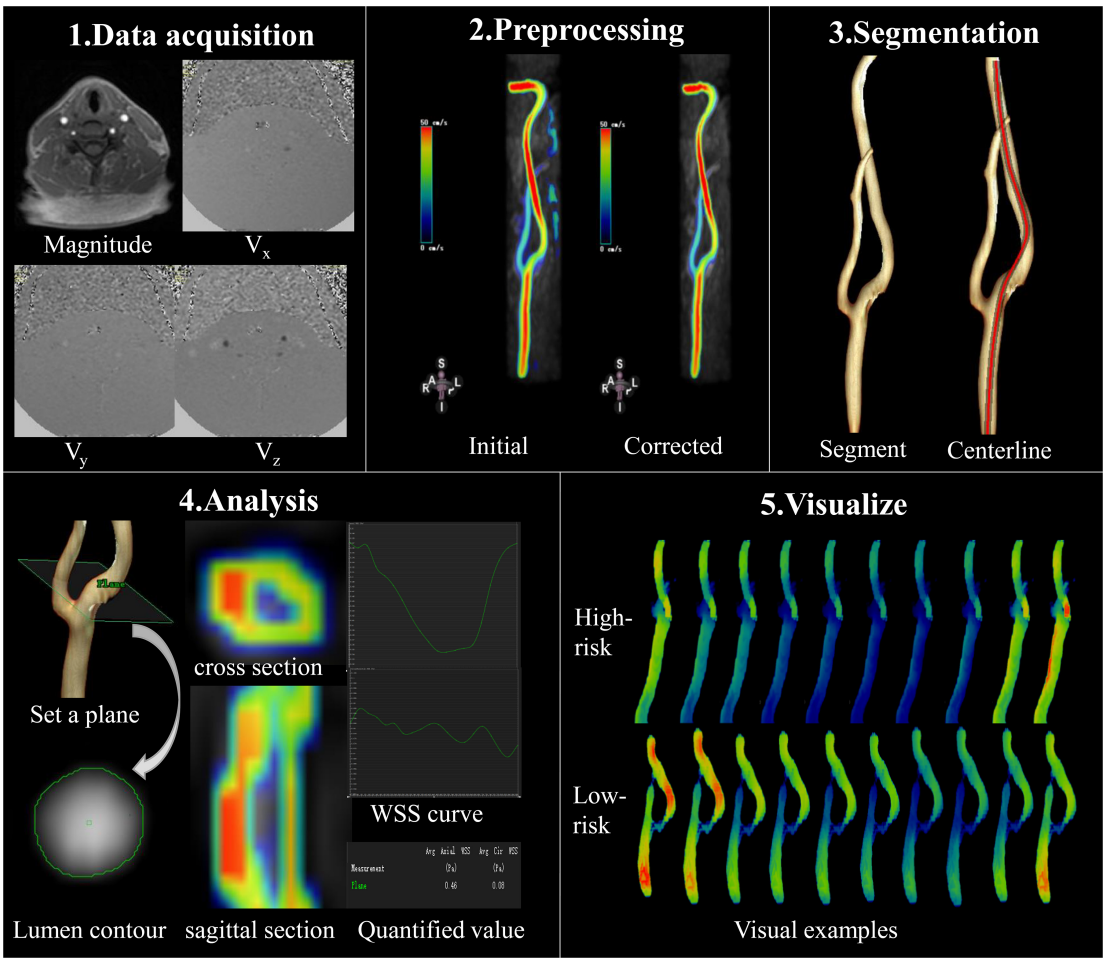

FIGURE 3 | Data acquisition and analysis workflow for 4D flow MRI. **(1)** Data acquisition: PC-MRI with three-directional velocity information is collected. **(2)** Preprocessing: data preprocessing corrects for errors due to noise, aliasing, and eddy current. **(3)** Segmentation: the centerline was segmented parallel traced along the target vessel. **(4)** Analysis: the plane is set at the narrowed segment of the lumen and segment of the lumen contour in magnitude-coded image manually, then we can get the cross section and sagittal section visually, as well as the axial and circumferential WSS curve and the quantified values. **(5)** Visualize: examples of WSS evaluated by 4D flow MRI at different time points; 4D flow MRI can display hemodynamic changes dynamically and visually in different cardiac cycles.

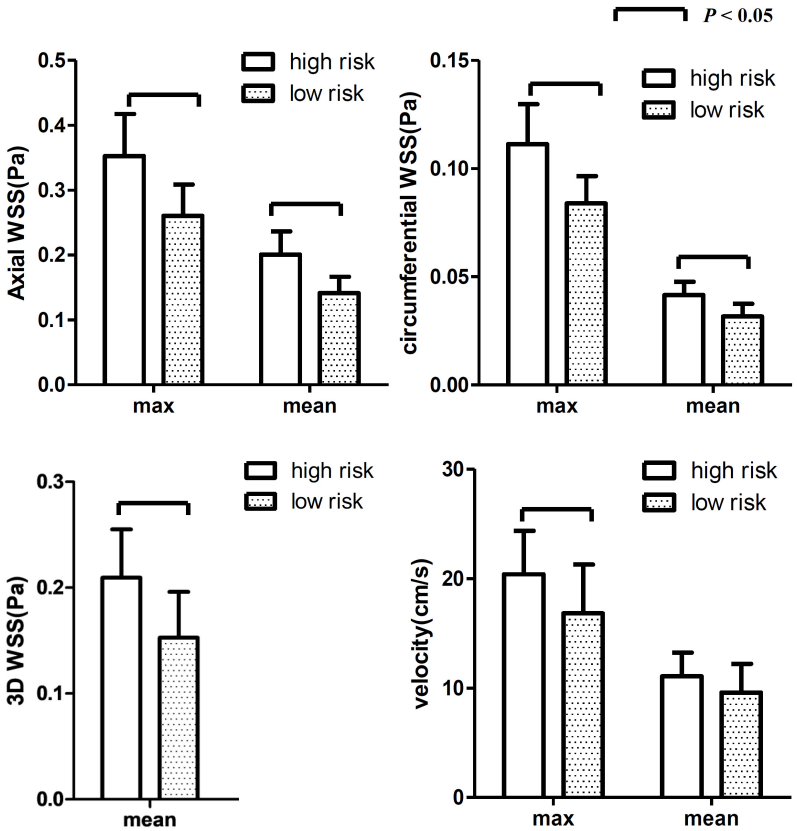

FIGURE 4 | The differences in WSS (axial, circumferential, and 3D) and velocity at all 20 time points. The WSS values were higher in the high-risk group than those in the low-risk group. Both max and mean WSS values between the two groups were found significant, while no significant difference was found for mean velocity.

based on the method described by Markl (Stalder et al., 2008). The 3D WSS reflected the total WSS along the plane tangent to the local vessel surface, and was decomposed into axial and circumferential components. Axial and circumferential WSS represent the WSS along the blood flow direction and the vessel circumference. The stenosis rate was calculated using HRVW imaging data and the equation for stenosis rate = D_s/D_d or D_s/D_p), in which D_s is the diameter of the narrowed segment of the lumen, D_d is the diameter of the distal lumen next to the narrowed segment, and D_p is the diameter of the proximal lumen next to the narrow segment. All statistical analyses were performed with SPSS (Version 19.0.0 IBM, Armonk, NY, United States). The stenosis rate and volume were compared using independent-sample *t*-tests. The WSS and velocity values displayed normal distributions according to a normality test. An independent-sample *t*-test was used to compare WSS (axial, circumferential and 3D) and velocity between low- and high-risk plaques over the entire cardiac cycle and at 20 different time points; $p < 0.05$ was considered statistically significant.

RESULTS

The demographics of the patients with high-risk plaques and low-risk plaques are shown in **Table 1**. There were no significant differences in stenosis or volume between the high-risk and low-risk groups. Among the 30 patients (20 male, 56.3 ± 9.5 years), 19 patients had hypertension, 6 patients had hyperlipidemia, 16 patients were active smokers, and 6 patients had diabetes. The mean heart rate was 75.0 ± 10.8 times/min.

The maximum and mean values of axial, circumferential, and 3D WSS and velocity at all time points were all higher in the high-risk plaque group than those in the low-risk plaque group. **Figure 4** shows that the differences were significant except for mean velocity ($p = 0.061$).

The differences at each time point were also analyzed separately. **Figures 4**, **5** show that the value of axial WSS was significantly higher than that of circumferential WSS, the WSS was 0.18 ± 0.08 Pa (mean ± SD) in the axial direction and 0.04 ± 0.02 Pa (mean ± SD) in the circumferential direction ($P < 0.001$), and the WSS value in the axial direction was more than four times that in the circumferential direction. The differences in circumferential WSS at half of the time points were non-significant, whereas non-significant maximum and mean axial WSS values were observed at only one time point and three time points, respectively. The difference in 3D WSS was significantly different between the two groups at all time points. The trend of 3D WSS more closely resembled that of axial WSS than that of circumferential WSS, but 3D WSS was more stable than axial WSS at all different time points.

TABLE 1 | Patient demographic data.

Characteristics	N (%)	P
Patient characteristic*		
Age (years)[a]	56.3 ± 9.5	
Male	20 (66.7%)	
Smoke	16 (53.3%)	
Hypertension	19 (63.3%)	
Diabetes	6 (20.0%)	
Hyperlipidemia	6 (20.0%)	
Heart rate (times/min)[a]	75.0 ± 10.8	
Plaque identification†		
High-risk	24 (60.0%)	
Low-risk	16 (40.0%)	
Stenosis rate[a]†		0.359
High-risk	53.2 ± 7.9	
Low-risk	50.9 ± 7.4	
Volume in the stenosis lumen (ml)[a]†		0.965
High-risk	3.6 ± 2.0	
Low-risk	3.5 ± 1.3	

[a]*Mean (± SD).*
**For the entire cohort of 30 patients.*
†*For the 40 carotid arteries with 40 plaques.*

The WSS and velocity differed between systole and diastole within a cardiac cycle. As displayed in **Figure 5**, WSS was higher in the high-risk plaque group than in the low-risk plaque group at each time point, but the difference was non-significant ($p > 0.05$) at a few time points, especially during systole. The number of non-significant differences in each WSS variable was as follows: 1 (systole) in maximum axial WSS, 2 (systole) and 1 (diastole) in mean axial WSS, 6 (systole) and 4 (diastole) in maximum circumferential WSS, and 10 (systole) and 1 (diastole) in mean circumferential WSS. Velocity was higher in the high-risk plaque group than in the low-risk plaque group, except for the first time point (systole) for mean velocity, and the differences in the maximum diastolic velocity were all significant (all $p < 0.05$).

Figure 3 (5.Visualize) displayed the cases of dynamic changes in 3D WSS at different time points. The WSS in the high-risk plaque group increased at stenosis, and the degree of changes varied at different time points. The WSS of low-risk plaques declined in the stenotic location.

DISCUSSION

WSS plays an important role in the development of atherosclerosis. We studied the difference in WSS in vessels with similar degrees of stenosis using 4D flow MRI. Our study demonstrated that high-risk plaques had higher WSS than low-risk plaques. The WSS changes varied at different points of the cardiac cycle, and diastolic WSS may have a greater impact on plaque stability than systolic WSS. The axial WSS values were significantly higher than the circumferential WSS values. Additionally, 3D WSS best reflected the difference between high-risk and low-risk plaques in that it had a smaller standard deviation than the other WSS parameters, and it showed a significant difference at every time point. 4D flow is a notable emerging technology to display changes in any hemodynamic parameters at different time points in the cardiac cycle visually and dynamically; it is an *in vivo* technology and provides multidirectional and multi-time-phase information. Its hemodynamic measures can be combined with anatomical information to help clinicians make more accurate judgments based on a patient's clinical condition.

Vessel stenosis greater than 70% is independently associated with cerebrovascular events and is considered a high-risk feature. Studies have found that moderate stenosis is also associated with a high incidence of cerebrovascular events (Bodle et al., 2013), and stenosis is not an independent predictor in defining plaque risk (Shi et al., 2018; Shi et al., 2020). Therefore, it is of great importance to identify high-risk plaques in patients with moderate stenosis (Shi et al., 2021). Previous studies have mostly addressed HRVW imaging, whereas *in vivo* hemodynamic studies have been less extensively discussed. WSS is the force generated by blood flow and is directly perpendicular to the vessel wall and the plaque. The "axial" here intended as the direction aligned with the tangent to the vessel's centerline and the main flow direction, and the "circumferential" intended as the direction was along the lumen circumference, orthogonal to the axial direction and centerline (Stalder et al., 2008; Morbiducci et al., 2015). Measurements at time points represent different times in the cardiac cycle; the magnitude of the force varies with the contraction of the heart. High WSS was related to induce specific changes in endothelial cell behavior, exacerbating inflammation and stimulating progression of the atherosclerotic lipid core in the vessel wall; it was a possible causative factor to promote the development of high-risk plaques (Eshtehardi et al., 2017). Understanding the detailed changes in plaque WSS can help clinicians apply more active treatments when a plaque shows high WSS, especially in diastolic and axial WSS.

Previous studies (Groen et al., 2007; Tuenter et al., 2016) found that ulcers formed exclusively at locations of high WSS, and a higher maximum WSS was significantly associated with the presence of IPH. Gijsen et al. (2011) found that plaque regions exposed to high WSS were subject to increasing strain over time, indicating that high WSS was likely to increase lipid deposition. These studies roughly corresponded to ours, although our study was more detailed in that we investigated axial, circumferential, and 3D WSS *in vivo* using 4D flow MRI. WSS can affect the function of vascular endothelial and smooth muscle cells, and high WSS induces specific changes in endothelial cell behavior, for example, by modifying gene expression, which may contribute to the onset and progression of atherosclerosis (Castier et al., 2005; White et al., 2011; Eshtehardi et al., 2017).

The ability to detect hemodynamic changes at different time points in the cardiac cycle is a feature of 4D flow MRI, and studies about these changes in the carotid artery are rare. A 4D flow MRI study of WSS changes in regurgitant semilunar valvular lesions by Rizk et al. (2019) found that in the presence of pulmonary and aortic regurgitation, WSS was elevated in comparison with controls and showed a diastolic peak. In contrast, Geiger et al. (2018) found that systolic WSS was not significantly altered in bicuspid aortic valve (BAV) patients. Our research also found that

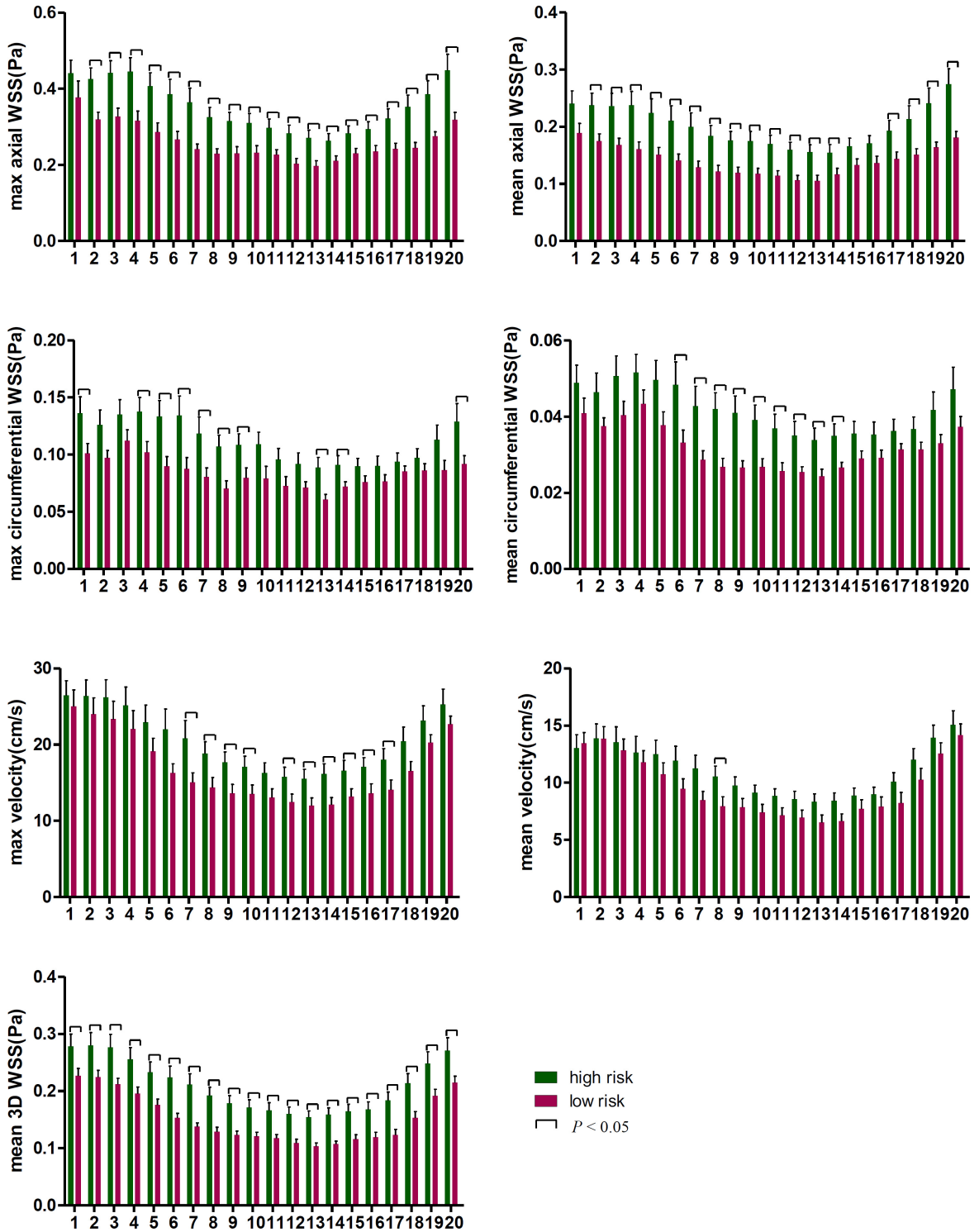

FIGURE 5 | The WSS differences at every time point in the cardiac cycle. The first time point was the start of the rapid ejection period, with 1–5 time points and 16–20 time points representing systole and 6–15 time points representing diastole.

WSS values were increased throughout the entire cardiac cycle, but the difference in diastolic WSS was more significant than that in systolic WSS. Although previous work explored different diseases than our study did, these prior studies explained the role of diastole in the presence of disease; this role cannot be ignored and may be a considerable contributing factor to some

cardiovascular diseases. The diastolic period lasts longer than the systolic period, consequently affecting the vessel wall longer; therefore, diastole may play a more important role in WSS.

Choi et al. (2015) explored the relationship between axial WSS and plaque, finding that upstream axial plaque stress increased with lesion severity and that axial plaque stress showed a negative correlation with lesion length. These results were complementary to ours. Furthermore, we further compared the contributions of axial WSS and circumferential WSS to plaque risk, and we found that axial WSS may be more meaningful in the assessment of plaque risk and in the selection of treatment strategies for patients with atherosclerotic plaque. Studies on other diseases, such as Marfan syndrome and BAV (Bissell et al., 2013; Wang et al., 2016; Guala et al., 2019), found that these patients exhibited reduced axial and circumferential WSS, but in different locations, circumferential WSS was reduced in the distal ascending aorta and in the proximal descending aorta in patients with Marfan syndrome, whereas axial WSS displayed more dilatation at the aortic root, and greater circumferential WSS was positively associated with dilatation in the ascending aorta in BAV patients. 3D WSS is the summation of the axial and circumferential WSS, Patients with high-risk plaques had greater WSS than those with low-risk plaques, but some differences in the axial and circumferential WSS were not statistically significant. When the differences in axial and circumferential WSS were combined for analysis, the difference in 3D WSS was significant at every time point. Further investigations will be needed in the future to address the specific reason, but it can be speculated that shear stress acting on the vessel wall axially rather than circumferentially plays a key role in high-risk plaques.

Some limitations in our study should be mentioned. First, our criteria for high-risk plaques required not only imaging results but also cerebrovascular events. A few patients had cerebrovascular events but no high-risk imaging signs, or vice versa, and were not included in the high-risk group. This may limit the applicability of our results in the clinic. However, the purpose of our study is to identify the hemodynamic differences between high- and low-risk plaques; thus, the criteria for including high-risk plaques are stricter than those that are used in clinic. We believe that the inclusion of unmatched data in future studies will enrich this area of research. Second, the geometries and multi-slice (measuring several planes along the vessel), multi-segment (showing the external or internal wall of the internal carotid artery, where the stenosis presented) models of the carotid arteries, which have been discussed in previous studies, were not investigated in this study, although they may provide more detailed and comprehensive information. Third, the amount of sample data is relatively small, and a larger dataset is need for further verification in the future.

CONCLUSION

In conclusion, 4D flow MRI can display hemodynamic changes dynamically and visually across cardiac cycles. Patients with high-risk plaques were found to have higher WSS than those with low-risk plaques. The increases in axial WSS were greater than those in circumferential WSS. Diastolic WSS was more influential than systolic WSS in determining plaque outcomes. High WSS, especially diastolic and axial WSS, may be related to atherosclerotic plaque rupture and cause cerebrovascular events in patients with moderate carotid artery stenosis.

DATA AVAILABILITY STATEMENT

The original contributions presented in the study are included in the article/supplementary material, further inquiries can be directed to the corresponding author/s.

ETHICS STATEMENT

The studies involving human participants were reviewed and approved by the Institutional Review Board of Tongji Hospital, Tongji Medical College, Huazhong University of Science and Technology, Wuhan, China. Written informed consent for participation was not required for this study in accordance with the national legislation and the institutional requirements.

AUTHOR CONTRIBUTIONS

GZ and WZ were responsible for the study concepts and design. GZ, SZ, YQ, XT, LL, WL, and WZ were responsible for literature research. GZ, JF, YZ, DW, and WZ were responsible for the clinical studies. GZ and SY were responsible for the statistical analysis. All the authors were guarantors of integrity of the entire study and responsible for the experimental studies and data analysis, manuscript preparation and editing, and final approval.

FUNDING

This work was supported by the National Natural Science Foundation of China (Nos. 81730049, 81570462, 81801666, and 81873890).

REFERENCES

Adamson, P. D., Dweck, M. R., and Newby, D. E. (2015). The vulnerable atherosclerotic plaque: in vivo identification and potential therapeutic avenues. *Heart* 101, 1755–1766. doi: 10.1136/heartjnl-2014-307099

Bissell, M. M., Hess, A. T., Biasiolli, L., Glaze, S. J., Loudon, M., Pitcher, A., et al. (2013). Aortic dilation in bicuspid aortic valve disease: flow pattern is a major contributor and differs with valve fusion type. *Circ. Cardiovasc. Imaging* 6, 499–507. doi: 10.1161/CIRCIMAGING.113.000528

Bodle, J. D., Feldmann, E., Swartz, R. H., Rumboldt, Z., Brown, T., and Turan, T. N. (2013). High-resolution magnetic resonance imaging: an emerging tool for evaluating intracranial arterial disease. *Stroke* 44, 287–292. doi: 10.1161/STROKEAHA.112.664680

Bonati, L. H., Dobson, J., Featherstone, R. L., Ederle, J., van der Worp, H. B., de Borst, G. J., et al. (2015). Long-term outcomes after stenting versus endarterectomy for treatment of symptomatic carotid stenosis: the International Carotid Stenting Study (ICSS) randomised trial. *Lancet* 385, 529–538. doi: 10.1016/S0140-6736(14)61184-3

Brott, T. G., Howard, G., Roubin, G. S., Meschia, J. F., Mackey, A., Brooks, W., et al. (2016). Long-term results of stenting versus endarterectomy for carotid-artery stenosis. *N. Engl. J. Med.* 374, 1021–1031. doi: 10.1056/NEJMoa1505215

Cai, J., Hatsukami, T. S., Ferguson, M. S., Kerwin, W. S., Saam, T., Chu, B., et al. (2005). In vivo quantitative measurement of intact fibrous cap and lipid-rich necrotic core size in atherosclerotic carotid plaque: comparison of high-resolution, contrast-enhanced magnetic resonance imaging and histology. *Circulation* 112, 3437–3444. doi: 10.1161/CIRCULATIONAHA.104.528174

Castier, Y., Brandes, R. P., Leseche, G., Tedgui, A., and Lehoux, S. (2005). p47phox-dependent NADPH oxidase regulates flow-induced vascular remodeling. *Circ. Res.* 97, 533–540. doi: 10.1161/01.RES.0000181759.63239.21

Cheng, C., Tempel, D., van Haperen, R., van der Baan, A., Grosveld, F., Daemen, M. J., et al. (2006). Atherosclerotic lesion size and vulnerability are determined by patterns of fluid shear stress. *Circulation* 113, 2744–2753. doi: 10.1161/CIRCULATIONAHA.105.590018

Choi, G., Lee, J. M., Kim, H. J., Park, J. B., Sankaran, S., Otake, H., et al. (2015). Coronary artery axial plaque stress and its relationship with lesion geometry: application of computational fluid dynamics to coronary CT angiography. *JACC Cardiovasc. Imaging* 8, 1156–1166. doi: 10.1016/j.jcmg.2015.04.024

Dyverfeldt, P., Bissell, M., Barker, A. J., Bolger, A. F., Carlhall, C. J., Ebbers, T., et al. (2015). 4D flow cardiovascular magnetic resonance consensus statement. *J. Cardiovasc. Magn. Reson* 17:72. doi: 10.1186/s12968-015-0174-5

Eshtehardi, P., Brown, A. J., Bhargava, A., Costopoulos, C., Hung, O. Y., Corban, M. T., et al. (2017). High wall shear stress and high-risk plaque: an emerging concept. *Int. J. Cardiovasc. Imaging* 33, 1089–1099. doi: 10.1007/s10554-016-1055-1

Falk, E., Nakano, M., Bentzon, J. F., Finn, A. V., and Virmani, R. (2013). Update on acute coronary syndromes: the pathologists view. *Eur. Heart J.* 34, 719–728. doi: 10.1093/eurheartj/ehs411

Geiger, J., Rahsepar, A. A., Suwa, K., Powell, A., Ghasemiesfe, A., Barker, A. J., et al. (2018). 4D flow MRI, cardiac function, and T1 -mapping: association of valve-mediated changes in aortic hemodynamics with left ventricular remodeling. *J. Magn. Reson Imaging* 48, 121–131. doi: 10.1002/jmri.25916

Gijsen, F. J. H., Mastik, F., Schaar, J. A., Schuurbiers, J. C. H., van der Giessen, W. J., de Feyter, P. J., et al. (2011). High shear stress induces a strain increase in human coronary plaques over a 6-month period. *Eurointervention* 7, 121–127. doi: 10.4244/Eijv7i1a20

Groen, H. C., Gijsen, F. J., van der Lugt, A., Ferguson, M. S., Hatsukami, T. S., van der Steen, A. F., et al. (2007). Plaque rupture in the carotid artery is localized at the high shear stress region: a case report. *Stroke* 38, 2379–2381. doi: 10.1161/STROKEAHA.107.484766

Groen, H. C., Gijsen, F. J., van der Lugt, A., Ferguson, M. S., Hatsukami, T. S., Yuan, C., et al. (2008). High shear stress influences plaque vulnerability Part of the data presented in this paper were published in Stroke 2007;38:2379-81. *Neth. Heart J.* 16, 280–283. doi: 10.1007/BF03086163

Guala, A., Teixido-Tura, G., Dux-Santoy, L., Granato, C., Ruiz-Munoz, A., Valente, F., et al. (2019). Decreased rotational flow and circumferential wall shear stress as early markers of descending aorta dilation in Marfan syndrome: a 4D flow CMR study. *J. Cardiovasc. Magn. Reson.* 21:63. doi: 10.1186/s12968-019-0572-1

Hung, O. Y., Brown, A. J., Ahn, S. G., Veneziani, A., Giddens, D. P., and Samady, H. (2015). Association of wall shear stress with coronary plaque progression and transformation. *Interv. Cardiol. Clin.* 4, 491–502. doi: 10.1016/j.iccl.2015.06.009

Kernan, W. N., Ovbiagele, B., Black, H. R., Bravata, D. M., Chimowitz, M. I., Ezekowitz, M. D., et al. (2014). Guidelines for the prevention of stroke in patients with stroke and transient ischemic attack: a guideline for healthcare professionals from the American Heart Association/American Stroke Association. *Stroke* 45, 2160–2236. doi: 10.1161/STR.0000000000000024

Makowski, M. R., Wiethoff, A. J., Blume, U., Cuello, F., Warley, A., Jansen, C. H., et al. (2011). Assessment of atherosclerotic plaque burden with an elastin-specific magnetic resonance contrast agent. *Nat. Med.* 17, 383–388. doi: 10.1038/nm.2310

Malek, A. M., Alper, S. L., and Izumo, S. (1999). Hemodynamic shear stress and its role in atherosclerosis. *JAMA* 282, 2035–2042. doi: 10.1001/jama.282.21.2035

Matlung, H. L., Neele, A. E., Groen, H. C., van Gaalen, K., Tuna, B. G., van Weert, A., et al. (2012). Transglutaminase activity regulates atherosclerotic plaque composition at locations exposed to oscillatory shear stress. *Atherosclerosis* 224, 355–362. doi: 10.1016/j.atherosclerosis.2012.07.044

Morbiducci, U., Gallo, D., Cristofanelli, S., Ponzini, R., Deriu, M. A., Rizzo, G., et al. (2015). A rational approach to defining principal axes of multidirectional wall shear stress in realistic vascular geometries, with application to the study of the influence of helical flow on wall shear stress directionality in aorta. *J. Biomech.* 48, 899–906. doi: 10.1016/j.jbiomech.2015.02.027

Peiffer, V., Sherwin, S. J., and Weinberg, P. D. (2013). Does low and oscillatory wall shear stress correlate spatially with early atherosclerosis? A systematic review. *Cardiovasc. Res.* 99, 242–250. doi: 10.1093/cvr/cvt044

Qiao, Y., Zeiler, S. R., Mirbagheri, S., Leigh, R., Urrutia, V., Wityk, R., et al. (2014). Intracranial plaque enhancement in patients with cerebrovascular events on high-spatial-resolution MR images. *Radiology* 271, 534–542. doi: 10.1148/radiol.13122812

Rizk, J., Latus, H., Shehu, N., Mkrtchyan, N., Zimmermann, J., Martinoff, S., et al. (2019). Elevated diastolic wall shear stress in regurgitant semilunar valvular lesions. *J. Magn. Reson. Imaging* 50, 763–770. doi: 10.1002/jmri.26680

Shi, Z., Li, J., Zhao, M., Peng, W. J., Meddings, Z., Jiang, T., et al. (2020). Quantitative histogram analysis on intracranial atherosclerotic plaques a high-resolution magnetic resonance imaging study. *Stroke* 51, 2161–2169. doi: 10.1161/Strokeaha.120.029062

Shi, Z., Zhao, M., Li, J., Meddings, Z., Shi, Y. B., Jiang, T., et al. (2021). Association of hypertension with both occurrence and outcome of symptomatic patients with mild intracranial atherosclerotic stenosis: a prospective higher resolution magnetic resonance imaging study. *J. Magn. Reson. Imaging* 54, 76–88. doi: 10.1002/jmri.27516

Shi, Z., Zhu, C. C., Degnan, A. J., Tian, X., Li, J., Chen, L. G., et al. (2018). Identification of high-risk plaque features in intracranial atherosclerosis: initial experience using a radiomic approach. *Eur. Radiol.* 28, 3912–3921. doi: 10.1007/s00330-018-5395-1

Sotelo, J., Dux-Santoy, L., Guala, A., Rodriguez-Palomares, J., Evangelista, A., Sing-Long, C., et al. (2018). 3D axial and circumferential wall shear stress from 4D flow MRI data using a finite element method and a laplacian approach. *Magn. Reson. Med.* 79, 2816–2823. doi: 10.1002/mrm.26927

Stalder, A. F., Russe, M. F., Frydrychowicz, A., Bock, J., Hennig, J., and Markl, M. (2008). Quantitative 2D and 3D phase contrast MRI: optimized analysis of blood flow and vessel wall parameters. *Magn. Reson. Med.* 60, 1218–1231. doi: 10.1002/mrm.21778

Tuenter, A., Selwaness, M., Lorza, A. A., Schuurbiers, J. C. H., Speelman, L., Cibis, M., et al. (2016). High shear stress relates to intraplaque haemorrhage in asymptomatic carotid plaques. *Atherosclerosis* 251, 348–354. doi: 10.1016/j.atherosclerosis.2016.05.018

Wang, H. H., Chiu, H. H., Tseng, W. Y., and Peng, H. H. (2016). Does altered aortic flow in marfan syndrome relate to aortic root dilatation? *J. Magn. Reson. Imaging* 44, 500–508. doi: 10.1002/jmri.25174

White, S. J., Hayes, E. M., Lehoux, S., Jeremy, J. Y., Horrevoets, A. J., and Newby, A. C. (2011). Characterization of the differential response of endothelial cells exposed to normal and elevated laminar shear stress. *J. Cell Physiol.* 226, 2841–2848. doi: 10.1002/jcp.22629

Zhang, B., Gu, J., Qian, M., Niu, L., Zhou, H., and Ghista, D. (2017). Correlation between quantitative analysis of wall shear stress and intima-media thickness in atherosclerosis development in carotid arteries. *Biomed. Eng. Online* 16:137. doi: 10.1186/s12938-017-0425-9

Zhang, G., Wang, Z., Zhang, S., Qin, Y., Yao, Y., Tang, X., et al. (2020). Age and anatomical location related hemodynamic changes assessed by 4D flow MRI in the carotid arteries of healthy adults. *Eur. J. Radiol.* 128:109035. doi: 10.1016/j.ejrad.2020.109035

Zhang, R. Y., Zhang, Q. W., Ji, A. H., Lv, P., Zhang, J. J., Fu, C. X., et al. (2020). Identification of high-risk carotid plaque with MRI-based radiomics

and machine learning. *Eur. Radiol.* 31, 3116–3126. doi: 10.1007/s00330-020-07361-z

Conflict of Interest: The authors declare that the research was conducted in the absence of any commercial or financial relationships that could be construed as a potential conflict of interest.

Publisher's Note: All claims expressed in this article are solely those of the authors and do not necessarily represent those of their affiliated organizations, or those of the publisher, the editors and the reviewers. Any product that may be evaluated in this article, or claim that may be made by its manufacturer, is not guaranteed or endorsed by the publisher.

frontiers in Neuroscience

ORIGINAL RESEARCH
published: 27 August 2021
doi: 10.3389/fnins.2021.655594

Application of High-Resolution Flat Detector Computed Tomography in Stent Implantation for Intracranial Atherosclerotic Stenosis

Tengfei Li[1,2†], Yuting Wang[3†], Ji Ma[1,2], Michael Levitt[4], Mahmud Mossa-Basha[5], Chengcheng Shi[1,2], Yuncai Ran[6], Jianzhuang Ren[1,2], Xinwei Han[1,2] and Chengcheng Zhu[5*]*

[1] Department of Interventional Radiology, First Affiliated Hospital of Zhengzhou University, Zhengzhou, China, [2] Interventional Institute of Zhengzhou University, Zhengzhou, China, [3] Department of Radiology, Sichuan Provincial People's Hospital, University of Electronic Science and Technology of China, Chengdu, China, [4] Department of Neurological Surgery, University of Washington, Seattle, WA, United States, [5] Department of Radiology, University of Washington, Seattle, WA, United States, [6] Department of Magnetic Resonance, First Affiliated Hospital of Zhengzhou University, Zhengzhou, China

OPEN ACCESS

Edited by:
Ayman Sabry El-Baz, University of Louisville, United States

Reviewed by:
Qi Yang, Capital Medical University, China
Youngkyoo Jung, University of California, Davis, United States

***Correspondence:**
Xinwei Han
xinwei_han@163.com
Chengcheng Zhu
zhucheng@uw.edu

[†] These authors have contributed equally to this work

Specialty section:
This article was submitted to Brain Imaging Methods, a section of the journal Frontiers in Neuroscience

Received: *19 January 2021*
Accepted: *09 August 2021*
Published: *27 August 2021*

Citation:
Li T, Wang Y, Ma J, Levitt M, Mossa-Basha M, Shi C, Ran Y, Ren J, Han X and Zhu C (2021) Application of High-Resolution Flat Detector Computed Tomography in Stent Implantation for Intracranial Atherosclerotic Stenosis. Front. Neurosci. 15:655594. doi: 10.3389/fnins.2021.655594

Objective: To evaluate the utility of high-resolution flat-detector computed tomography (HR-FDCT) compared with conventional flat-detector computed tomography (FDCT) for stent placement in symptomatic intracranial atherosclerotic stenosis (ICAS).

Methods: We retrospectively reviewed the clinical data of 116 patients with symptomatic ICAS who underwent stent implantation. Images were acquired using conventional FDCT [voxel size = 0.43 mm (isotropic)] and HR-FDCT [voxel size = 0.15 mm (isotropic)]. Immediately after stent deployment, dual-volume three-dimensional (3D) fusion images were obtained from 3D digital subtraction angiography (DSA) and HR-FDCT. The image quality for stent visualization was graded from 0 to 2 (0: not able to assess; 1: limited, but able to assess; 2: clear visualization), and the stent-expansion status ("full," "under-expanded" or "poor apposition") was recorded.

Results: A total of 116 patients with symptomatic ICAS were treated successfully using 116 stents (58 Neuroform^{TM} EZ, 42 Enterprise^{TM}, and 16 Apollo^{TM}). The mean pre-stent stenosis was 80.5 ± 6.4%, which improved to 20.8 ± 6.9% after stenting. Compared with FDCT, HR-FDCT improved visualization of the fine structures of the stent to improve the image quality that significantly (mean score: 1.63 ± 0.60 *vs*. 0.41 ± 0.59, $P < 0.001$). In 19 patients, stent under-expansion ($n = 11$) or poor apposition ($n = 8$) was identified by HR-FDCT but not by conventional FDCT. After balloon dilatation, stent malapposition was shown to have improved on HR-FDCT. None of the 19 patients with stent malapposition experienced short-term complications during hospitalization or had in-stent stenosis at 6-month follow-up.

Conclusion: High-resolution flat-detector computed tomography (HR-FDCT) improves visualization of the fine structures of intracranial stents deployed for symptomatic ICAS compared with that visualized using conventional FDCT. High-resolution flat-detector computed tomography improves assessment of stent deployment and could reduce the risk of complications.

Keywords: flat detector CT, intracranial atherosclerosis, stenosis, stent, complications

INTRODUCTION

Intracranial atherosclerotic stenosis (ICAS) is a major cause of ischemic stroke. In the USA, ICAS accounts for 5–10% of ischemic strokes, and it is a more common stroke etiology in Asian, African, and Hispanic populations (Gorelick et al., 2008). Intracranial atherosclerotic stenosis is the source of stroke in as many as 30–50% of cases among Chinese populations (Leung et al., 1993).

Initially, ICAS is treated with non-invasive medical therapy that seeks to reduce the risk of cerebral infarction (Qureshi and Caplan, 2014; Heit and Wintermark, 2018). However, patients who develop recurrent cerebral infarction or recurrent transient ischemic attacks (TIAs) despite optimal medical therapy may be considered for more aggressive treatment, including cerebral arterial angioplasty and/or stent placement (Qureshi and Caplan, 2014; Heit and Wintermark, 2018). Optimal visibility of the intracranial stent is limited using digital subtraction angiography (DSA) applications (Kato et al., 2020). Although some radiopaque elements of intracranial stents may be observed *via* fluoroscopy during treatment, local distortion or incomplete expansion of the stent may be difficult to identify due to limited angiographic angles or the presence of bony or metal obstructions (Li et al., 2019). Incomplete expansion of the stent is an important potential risk factor for stent thrombosis and prolonged duration of stent endothelialization (Foin et al., 2014). Improving intraprocedural imaging of stent placement during ICAS treatment could minimize risks and improve outcomes (Zaidat et al., 2015; Wang and Wang, 2017; Alexander et al., 2019).

High-resolution flat-detector computed tomography (HR-FDCT) technology (syngo DynaCT Micro, Siemens Healthineers, Forchheim, Germany) was developed recently. This technology allows for improved visualization of fine anatomical features or the features of implanted devices during angiographic procedures. Compared with conventional FDCT, HR-FDCT provides higher spatial resolution and reduced artifacts from the cone beam (Yuki et al., 2016; Li et al., 2019). Instead of 2 × 2-pixel binning during read-out from flat-detector imaging, this technology employs a non-binning technique. The exposure conditions and image-processing algorithms have been optimized, and the spatial resolution improved from 0.43 to 0.15 mm.

High-resolution flat-detector computed tomography (HR-FDCT) has been reported to improve the visibility of various intracranial stents for stent-assisted aneurysm embolization when compared with that obtained with conventional FDCT (Yuki et al., 2016; Shintai et al., 2018; Li et al., 2019; Zhang et al., 2019). However, *in vivo* research on the use of this technique to evaluate stent placement for symptomatic ICAS is scarce.

We assessed the *in vivo* image quality of HR-FDCT, its utility for guiding intravascular procedures, and the possible influence on the postoperative outcome. In this way, we aimed to evaluate comprehensively the utility of HR-FDCT for stent placement in symptomatic ICAS.

MATERIALS AND METHODS

Ethical Approval of the Study Protocol

The protocol for this retrospective study was approved by the Ethics Committee of the Biomedical Research Department within First Affiliated Hospital of Zhengzhou University (Zhengzhou, China). The procedures followed were in accordance with the Helsinki Declaration of 1975 and its later amendments.

Inclusion and Exclusion Criteria

Patients were eligible for inclusion in this study if: (i) a TIA or minor stroke (Fischer et al., 2010) had occurred <90 days before stent placement and was attributed to an angiographically verified >50% stenosis of a major intracranial artery supplying the stroke territory; (ii) the stenosis was located in the intracranial internal carotid artery, M1 segment of the middle cerebral artery, intracranial vertebral artery, or basilar artery, and the diameter of the artery adjacent to the stenosis was 2.0–4.0 mm; (iii) the National Institutes of Health Stroke Scale (NIHSS) score was <9 upon presentation; (iv) patient age was 30–80 years; (v) the patient had at least one risk factor for atherosclerosis (hypertension, diabetes mellitus, hyperlipidemia, hyperhomocysteinemia, or smoking); (vi) ischemic stroke or TIA occurred despite the patient receiving standard medical therapy (antiplatelet or anticoagulant medication); (vii) symptomatic ICAS was treated with a single intracranial stent: Neuroform EZ™ (Stryker Neurovascular, Fremont, CA, United States), Enterprise™ (Codman Neuro, Raynham, MA, United States), or Apollo™ (MicroPort Medical, Shanghai, China).

Patients were excluded if they: (i) were treated with a single or combined drug-eluting balloon or drug-eluting stents; (ii) underwent stenting combined with bypass surgery; (iii) had clinically defined non-atherosclerotic ICAS (e.g., vasculitis, arterial dissection).

Patient Selection

Consecutive patients who underwent stent implantation in First Affiliated Hospital of Zhengzhou University between June 2017 and December 2018 for treatment of symptomatic ICAS were identified retrospectively by reviewing medical records.

Demographic (age, sex) and clinical information, (risk factors for atherosclerosis) were recorded. Lesion characteristics, including the location and Mori classification, were documented. With regard to the Mori classification, type-A lesions were concentric and <5 mm in length, type-B lesions were eccentric lesions 5–10 mm in length, and type-C lesions were longer than 10 mm and excessively tortuous (Mori et al., 1998).

Image Acquisition

Preprocedural preparation and the stenting procedure were undertaken as described previously (Jiang et al., 2007; Vajda et al., 2012; Xu et al., 2019), and included clopidogrel (p.o.) for 3-6 months and long-term aspirin (p.o.). Preprocedural vascular stenosis and postoperative residual stenosis were measured manually using calipers on images from catheter angiography.

Immediately after stent deployment, FDCT and HR-FDCT were carried out using the same imaging unit as a routine procedure in our institution for optimal care of patients. Whole-brain FDCT was acquired to exclude parenchymal or subarachnoid hemorrhage, and to determine whether to add heparin and/or tirofiban into postprocedural treatment. We used the following parameters for whole-brain FDCT: acquisition time = 20 s; X-ray tube voltage = 109 kV; tube current = 460 mA; total angle = 200°; 496 frames; zoom size = 48 cm; voxel size = 0.49 mm (isotropic).

Subsequently, HR-FDCT was acquired with the region of interest limited to the stent-placement area (to verify that the stent was fully expanded) using the following parameters: acquisition time = 20 s; X-ray tube voltage = 109 kV; tube current = 460 mA; total angle = 200°; 496 frames; zoom size = 22 cm; voxel size = 0.15 mm (isotropic). The radiation dose for FDCT was 85.3 mGy, and that for HR-FDCT was 294 mGy.

Three-dimensional FDCT and HR-FDCT images were reconstructed automatically on a three-dimensional (3D) workstation (Siemens Healthineers).

After the two acquisitions stated above had been completed, patients underwent 3D-DSA for 5 s for confirmation of vessel patency. 3D-DSA was done using the following parameters: acquisition time for each rotation = 5 s; X-ray tube voltage = 70 kVp; tube current = 460 mA, total angle = 200°; 397 frames; zoom size = 48 cm; voxel size = 0.43 mm (isotropic). For contrast-enhanced DSA, undiluted contrast media (370 mg/mL; Ultravist^{TM}; Bayer, Bayer Leverkusen, Germany) was injected at 2.5 mL/s for 5 s, and the scan was started with a 1-s delay. 3D-DSA images and HR-FDCT were fused and displayed as dual-volume (syngo 3D–3D fusion, Siemens Healthineers) to evaluate the vessel-wall apposition of the implanted stent. During 3D–3D fusion, the 3D-DSA images were first reconstructed into two volumes (i.e., we subtracted the volume of 3D vessels and the mask volume of the skull and brain tissues) with identical 3D coordinates. Then, the mask volume was fused with HR-FDCT based on rigid registration of bony structures. Hence, a fusion matrix between 3D-DSA and HR-FDCT was generated. Through application of the same fusion matrix between the subtracted volume and HR-FDCT, the 3D-vessel could be fused with a clearly reconstructed stent from HR-FDCT. If malapposition of the stent was observed, the interventionalist carried out balloon angioplasty to expand the stent further. Follow-up HR-FDCT could be undertaken to confirm stent deployment after angioplasty depending on the interventionalist's clinical judgment. Stent malapposition was described as "stent under-expansion" (partially opened stent) or "poor apposition" (presence of a gap between the stent trunk and the parent-artery wall, or a gap between the distal or proximal flare of the stent and the parent artery).

Stenosis Evaluation

The preoperative and postoperative/residual stenosis was calculated according to the warfarin–aspirin symptomatic intracranial disease (WASID) method (Samuels et al., 2000) on DSA images, The success of stenting was defined as complete coverage of the lesion by the stent, resulting in a residual stenosis of $\leq$30% with good anterograde blood flow.

Retrospective Evaluation of the Image Quality of FDCT and HR-FDCT

Patients were divided into three groups based on the type of stent deployed (Neuroform, Enterprise, or Apollo). For each stent group, two sets of 3D images (FDCT and HR-FDCT) were anonymized and randomized for evaluation after all procedures had been completed for the included patients. Two experienced neuro-interventionalists (with 12 years and 36 years of experience, respectively) blinded to the procedural results evaluated the image quality independently.

The evaluation criteria were: 0 (the image quality was poor and defined as inadequate delineation between the stent lumen and stent strut, or no visualization of the stent lumen); 1 (the image quality was good and defined as visualization of a mildly inhomogeneous stent lumen, but with the patency of the stent lumen interpretable); 2 (images of excellent quality, the lesion area appeared as a homogeneous stent lumen with clear delineation of the stent strut) (**Figure 1**) (Jang et al., 2012).

Postoperative Management and Follow-Up

Vital signs were monitored after stenting. Systolic pressure was maintained at 90–110 mmHg for >48 h. If the NIHSS score or modified Rankin Scale (mRS) score changed, CT and/or magnetic resonance imaging of the head was done. At 1-month clinical follow-up, the scores for the mRS and NIHSS were used to assess functional outcome.

Statistical Analyses

SPSS 22.0 (IBM, Armonk, NY, United States) was used for statistical analyses. Data with a normal distribution and continuous data are presented as the mean ± SD. Ratings for image quality were evaluated using chi-square or Fisher's exact tests. Inter-observer agreement between the two raters was analyzed using Kappa ($\geq$ 0.75 was considered "good agreement") values. $P < 0.05$ was considered significant.

RESULTS

Patients and Stenting

Consecutive ICAS patients (n = 146) were screened for inclusion. Thirty patients were excluded from the study [12 patients with deployment of single or combined drug-eluting balloons or drug-eluting stents; 18 patients without follow-up DSA/computed tomography angiography (CTA)]. Hence, 116 patients (71 males and 45 females; mean age, 54 ± 11 years) formed the study cohort. The median time from the initial TIA or stroke event to stent placement was 21.7 (range, 14–56) days. The characteristics of patients at baseline are shown in **Table 1**.

Overall, 116 patients were treated with 116 intracranial stents (58 Neuroform EZ, 42 Enterprise, and 16 Apollo). Mean preprocedural stenosis was 80.5 ± 6.4%, and mean postprocedural residual stenosis was 20.8 ± 6.9% (internal carotid artery 19.1 ± 6.8%, middle cerebral artery 22.3 ± 7.6%, vertebral artery 20.4 ± 6.7%, basilar artery 18.9 ± 5.2%). The success rate for the technical procedure was 100%.

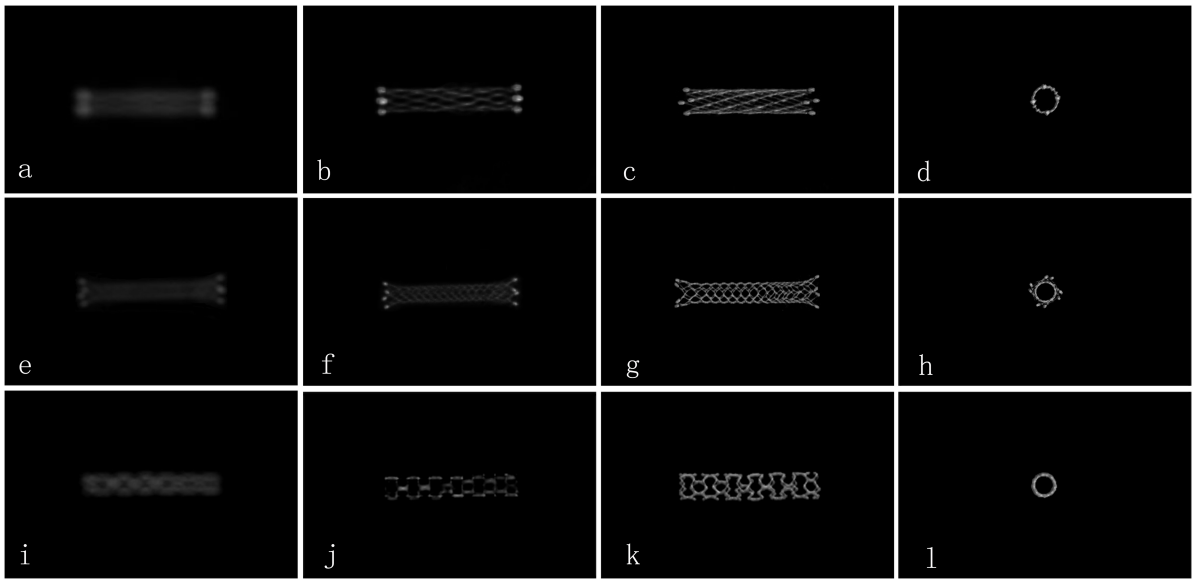

FIGURE 1 | Comparison of the image quality for different types of stents by FDCT and HR-FDCT *in vitro* (representative cases). **(a–d)** Neuroform^{TM} EZ stent with image-quality scores of 0, 1, 2, and 2 points; **(e–h)** Enterprise^{TM} stent with image-quality scores of 0, 1, 2, and 2 points; **(i–l)** Apollo^{TM} stent with image-quality scores of 0, 1, 2, and 2 points. Panels **(a,e,i)** were images by FDCT, and the rest were images by HR-FDCT.

Comparison Between FDCT and HR-FDCT

Both readers showed excellent agreement for assessment of image quality (κ = 0.92). The inter-rater agreement was excellent for each type of stent used (κ = 0.89 for Neuroform EZ, 0.94 for Enterprise, and 0.95 for Apollo). Compared with reconstructed images from FDCT, reconstructed images from HR-FDCT showed significant improvement in visualization of stent structure and assessment of stent deployment (mean score: 1.63 ± 0.60 *vs.* 0.41 ± 0.59, $P < 0.001$) (**Table 2** and **Figures 2–5**). The improvement of image quality was significant ($P < 0.05$) for each stent type.

TABLE 1 | Baseline patient characteristics (n = 116).

Baseline characteristics	No. (%)
Age	54 ± 11
Male	71 (61.2)
Female	45 (38.8)
Risk factor	
Hyperlipidemia	87(75.0)
Hypertension	77(66.4)
Smoking	52 (44.8)
Diabetes mellitus	31 (26.7)
Hyper-homocysteinemia	29 (25.0)
Other factors	
Qualifying stroke event	47 (40.5)
Relevant regional infarct	89 (76.7)
Lesion location	
Internal carotid artery	22 (19.0)
Middle cerebral artery	36 (30.0)
Vertebral artery	26 (22.4)
Basilar artery	32 (25.6)
Lesion morphology	
Mori Type A	49 (42.2)
Mori Type B	56 (48.3)
Mori Type C	11 (9.5)

Balloon Angioplasty

By reviewing the HR-FDCT images during the interventional procedure, patients who had stent malapposition were identified and underwent additional balloon angioplasty. According to the reconstruction images obtained from HR-FDCT, 11 stents (seven Neuroform EZ and four Enterprise) were found to be under-expanded. The involved arterial segments were four in intracranial carotid arteries, three in middle cerebral arteries, one in the basilar artery, and three in vertebral arteries. After balloon angioplasty, all stents expanded fully (**Figure 5**). According to the reconstruction of 3D fusion images obtained from 3D-DSA combined with HR-FDCT, eight stents (four Neuroform EZ and four Enterprise) were found to have poor apposition. The involved arterial segments were four in intracranial carotid arteries, two in middle cerebral arteries, and two in vertebral arteries. After balloon angioplasty, stent malapposition improved, as confirmed by an additional HR-FDCT scan.

Complications During Hospitalization

One patient had postprocedural intraparenchymal hemorrhage and was discharged 50 days later with a moderate permanent neurological deficit (NIHSS score = 6, mRS score = 3). Six patients

TABLE 2 | Evaluation of images obtained with FDCT and HR-FDCT (Neuroform EZ stent, *n* = 58; Enterprise stent, *n* = 42; Apollo stent, *n* = 16).

Stent	Visibility score[a]	Method		*P*	Average Score of Image quality	
		Dyna CT	Dyna micro-CT		Dyna CT	Dyna micro-CT
Total	0	75	7	< 0.001*	0.41 ± 0.59	1.63 ± 0.60
	1	35	29			
	2	6	80			
Neuroform EZ	0	35	2	< 0.001*	0.43 ± 0.57	1.69 ± 0.54
	1	21	14			
	2	2	42			
Enterprise	0	30	3	< 0.001*	0.33 ± 0.57	1.60 ± 0.63
	1	10	11			
	2	2	28			
Apollo	0	10	2	0.005*	0.50 ± 0.73	1.5 ± 0.73
	1	4	4			
	2	2	10			

**p < 0.05, Significant difference in quality between FDCT and HR-FDCT images (Neuroform EZ stent, p < 0.001; Enterprise stent, p < 0.001; Apollo stent, p = 0.005).*
[a]0 = the image quality was poor and defined as inadequate delineation between the stent lumen and stent strut due to severe beaming artifacts, as well as no visualization of the stent lumen due to image noise; 1 = the image quality was good and defined as visualization of a mildly inhomogeneous stent lumen, but with the patency of the stent lumen interpretable; 2 = images of excellent quality, the lesion area appeared as a homogeneous stent lumen with clear delineation of the stent strut.

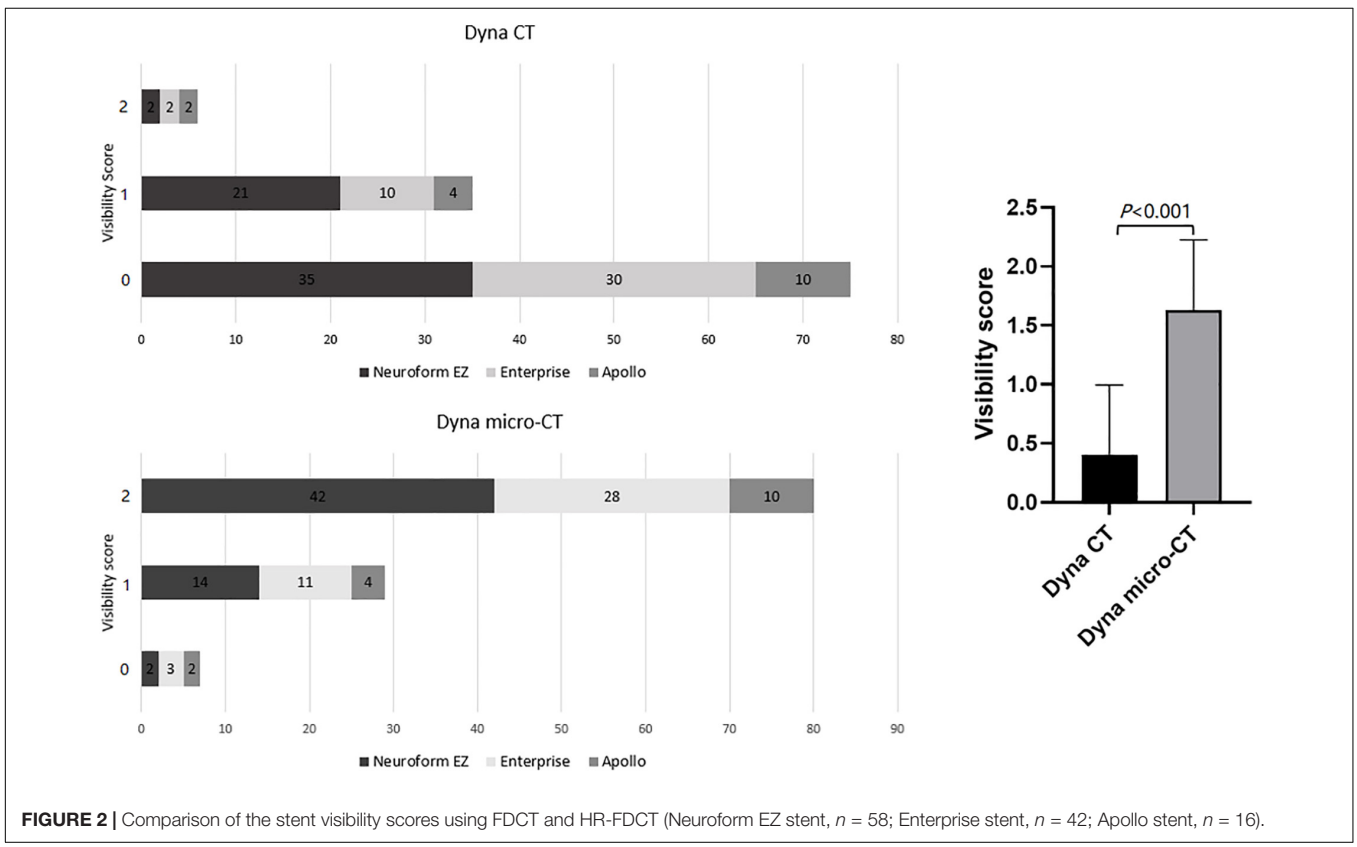

FIGURE 2 | Comparison of the stent visibility scores using FDCT and HR-FDCT (Neuroform EZ stent, *n* = 58; Enterprise stent, *n* = 42; Apollo stent, *n* = 16).

had postprocedural ischemic stroke, though DSA confirmed patency in blood flow through the stents in all cases and stroke was assumed to be a result of perforator occlusion based on the infarct pattern. Of these six patients, three had a permanent minor neurological deficit with a mRS score of 1, 1, and 2 and NHISS score of 1, 1, and 2, respectively, at 1 month. There were no cases of acute thrombosis or hemorrhagic complications in the remaining 109 patients. There were no complications among the 19 patients that necessitated balloon angioplasty.

Follow-Up

A total of 114 patients had adequate follow-up data after surgery. The duration of follow-up was 6–25.3 (median, 12.9) months. The mRS score at 6 months was 0 (*n* = 88),

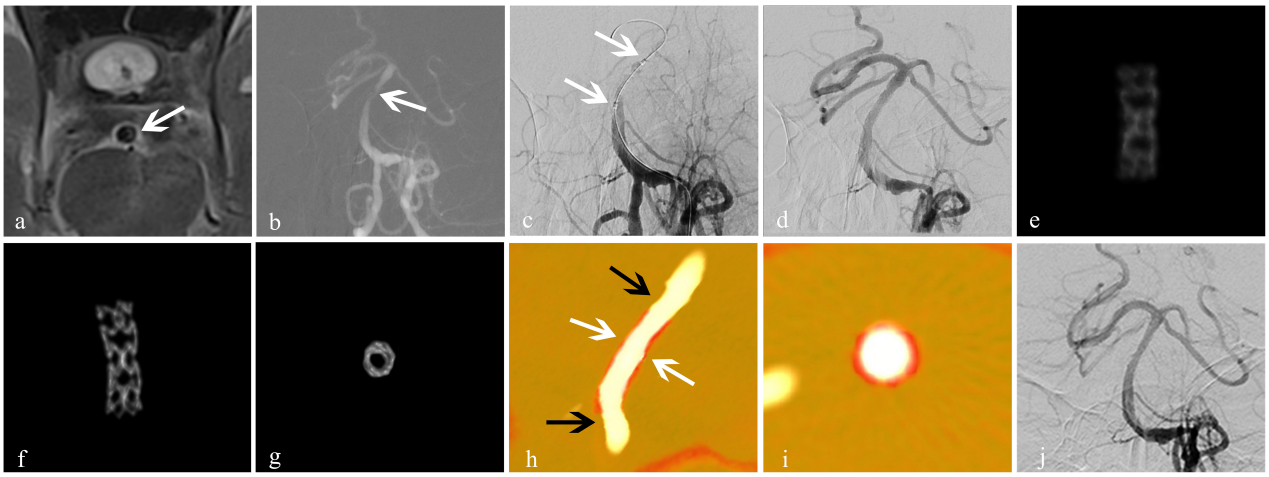

FIGURE 3 | Treatment for an atherosclerotic stenosis in the basilar artery with the Apollo^{TM} stent. A 56-year-old man presented with dizziness of 2-week duration. **(a)** High-resolution MRI showed stenosis of the basal-artery trunk (white arrow); **(b)** 2D-DSA showed severe stenosis (80%) of the basilar-artery trunk (white arrow); **(c)** an Apollo balloon-expandable stent measuring 2.5 mm × 8 mm was placed (white arrow); **(d)** DSA showed improved blood flow with good expansion of the stent, and residual stenosis was 5%; **(e)** conventional FDCT showed the blurred metal struts of the stent with an image-quality score of 0; **(f,g)** HR-FDCT showed that the stent struts were clear and expanded completely, and image quality was improved significantly with a score of 2; **(h,i)** Dual volume three-dimensional fusion images showed good apposition of the stent to the vessel wall (stent, white arrow; vessel wall, black arrow); **(j)** follow-up DSA at 6 months showed durable stent patency. Panels **(e–g)** were obtained *in vivo*.

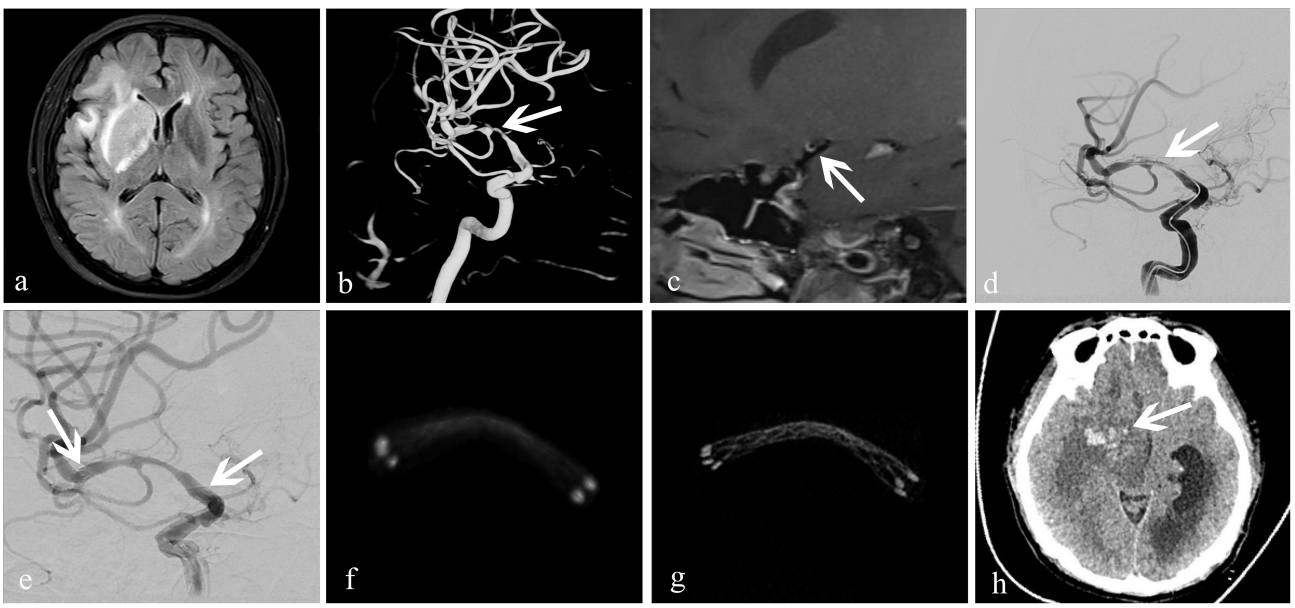

FIGURE 4 | Treatment of an atherosclerotic stenosis in the right middle cerebral artery with the Enterprise^{TM} stent. A 52-year-old woman who presented with left-limb weakness of 12-day duration. **(a)** MRI showed subacute cerebral infarction in the right temporal lobe and basal ganglia; **(b)** 3D-DSA revealed severe stenosis (83%) at the bifurcation of the right middle cerebral artery (white arrow); **(c)** high-resolution MRI showed that the stenosis was atherosclerotic (white arrow); **(d,e)** dilation using a Gateway^{TM} balloon was done followed by insertion of an Enterprise stent measuring 4.5 mm × 22 mm (white arrow). Residual stenosis was 28%; the two arrows in **(e)** showed both ends of the stent. **(f)** conventional FDCT showed a good position of the distal and proximal stent markers, but the stent itself was poorly visualized with an image-quality score of 0; **(g)** HR-FDCT showed good deployment of the stent, and the image quality was improved significantly with a score of 2; **(h)** 6-h later, CT of the head showed cerebral parenchymal hemorrhage (white arrow) in the former infarction area at right basal ganglia.

1 (n = 24), 2 (n = 1), and 3 (n = 1). In the follow-up window, 3.5% (4/114) of patients had ischemic strokes, of which one resulted in permanent disability and three were minor strokes. Also, 3.5% (4/114) of patients had a TIA. Mortality was 2.6% (3/114), none of which were from neurological causes.

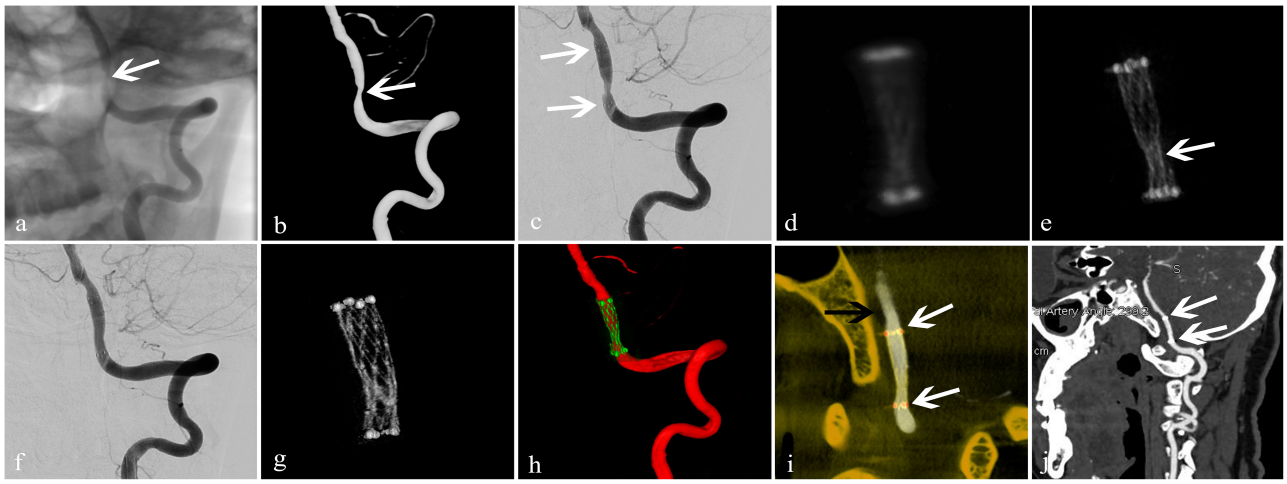

FIGURE 5 | Treatment of an arteriosclerotic stenosis of the V4 segment of the left vertebral artery using the Neuroform^{TM} EZ stent. A 67-year-old man presented with dizziness and instability while standing of 6-day duration. **(a,b)** 2D and 3D-DSA showed 78% stenosis of the V4 segment of the left vertebral artery (white arrow); **(c)** dilation using a Gateway^{TM} balloon was done followed by insertion of a Neuroform EZ stent measuring 3.0 mm × 15 mm (white arrow) with 50% residual stenosis; **(d)** conventional FDCT showed full expansion of the proximal and distal stent markers but poor visualization of the stent itself with an image-quality score of 0; **(e)** HD-FDCT showed the stent was partially expanded with an image-quality score of 1 (white arrow); **(f)** angioplasty with a Gateway balloon was undertaken again with a 3.0 mm × 9 mm balloon to treat stent under-expansion. Review by 2D-DSA showed that stenosis was improved significantly (residual stenosis = 11%); **(g)** after balloon angioplasty, HD-FDCT was done again and confirmed that the stent was fully expanded; **(h,i)** Dual-volume 3D fusion images showed good apposition of the stent to the vessel wall (stent, white arrow; vessel wall, black arrow); **(j)** 6-month follow-up CTA showed durable stent patency (white arrow).

A total of 97 patients had follow-up imaging data at 6 months (36 cases by CTA, 61 by DSA); 14 (14.4%) (seven Neuroform EZ, five Enterprise, and two Apollo) showed in-stent stenosis, of which six were symptomatic; three of those were treated with balloon angioplasty. The remaining eight asymptomatic cases were treated conservatively. Regarding the causes of in-stent stenosis, three patients had poor control of hyperglycemia or hypertension, and one patient had poor medication compliance. In the remaining 10 patients, the possible causes were a relatively higher degree of post-stent residual stenosis, vascular endothelial injury due to balloon angioplasty, poor response to antiplatelet medication, and/or prolonged time of vascular endothelialization.

In the 19 patients with stent malapposition who underwent balloon angioplasty, a deterioration of neurological function was not observed in the clinical follow-up (mean, 9.1 months). In addition, in-stent stenosis was not observed at 6-month follow-up DSA.

DISCUSSION

HR-FDCT has helped improve stent visualization during neurointerventional procedures (Clarençon et al., 2017; Kuriyama et al., 2018; Srinivasan et al., 2018). Studies have explored its utility in patients with intracranial aneurysms [(Caroff et al., 2014; Shintai et al., 2018; Kato et al., 2020). However, few reports have focused on the clinical application of HR-FDCT in stent placement for symptomatic ICAS.

In our relatively large patient cohort (n = 116), HR-FDCT improved the visualization of fine structures of the stent, which helped detection of stent malapposition. Nineteen cases of stent under-expansion or poor apposition were identified by HR-FDCT but were not seen by FDCT because of artifacts caused by the metal in the wire mesh and lower spatial resolution. After balloon angioplasty, stent malapposition improved on HR-FDCT. None of the 19 patients with stent malapposition experienced short-term complications during hospitalization or had in-stent stenosis at 6-month follow-up.

Stent under-expansion and poor apposition can lead to an increased risk of acute thrombosis or delayed ischemia after deployment. Balloon angioplasty is often necessary if malapposition is detected (Sheng et al., 2014). Flat-detector computed tomography and HR-FDCT could be utilized for different purposes according to their strengths and limitations. Flat-detector computed tomography could be employed to visualize the whole brain for exclusion of intracranial bleeding due to its large field of view (can be up to 30 × 40 cm) but has limited spatial resolution when compared with HR-FDCT. The latter could be used only for visualizing a small field of view (16 × 16 cm) to compromise for signal read-out burden if pixel binning was not adopted. Caroff and colleagues used HR-FDCT (Vaso CT; Philips, Amsterdam, the Netherlands) to observe stent-assisted embolization of intracranial aneurysms. They found that HR-FDCT could be used to assess stent deployment and reduce the risk of thromboembolic events (Caroff et al., 2014). We garnered similar findings in that HR-FDCT aided stent apposition, and serious complications (e.g., acute thrombosis) did not occur during or after intervention.

Among the six patients in our study with ischemic stroke during the perioperative period, three had basilar-artery stenosis

and the post-stenting infarctions were located in the pons. The remaining three cases had a stenosis in the middle cerebral artery and the post-stenting infarctions were located in the basal ganglia. Considering that (i) postprocedural DSA did not show an apparent filling defect in the stent or large-artery occlusion, and (ii) the infarct pattern, perforator territory infarcts involving pontine and medial lenticulostriate perforators were favored.

The Stenting vs. Aggressive Medical Management for Preventing Recurrent Stroke in Intracranial Stenosis (SAMMPRIS) trial reported a high prevalence of periprocedural complications in the stenting arm (14.7% higher than that in the medical-therapy arm) (Derdeyn et al., 2014). However, the Post Market Surveillance Study of the Wingspan Stent System (WEAVE) trial reported a much lower prevalence of periprocedural complication (2.6%) for on-label intracranial stenting. That result suggested that the previously reported high prevalence of complications might have been due to inexperienced interventionalists, poor selection of patients, and immature standards of practice for intracranial stenting (Alexander et al., 2019). Those results indicated that careful selection of patients and experienced operators, if aided by additional tools such as HR-FDCT, can achieve excellent safety and efficacy for ICAS stenting.

Post-stent restenosis is an important factor affecting the extension and application of stenting in ICAS. We found that the overall prevalence of stent restenosis and prevalence of restenosis of a single stent type were lower than those reported by a multicenter, large-sample study which used FDCT (Jiang et al., 2012). In that study, the overall prevalence of stent restenosis was 23.3%, whereas that for the Apollo stent was 20.3% and that for the self-expandable stent was 27.9%. Many variables were involved in the two studies, but the lower prevalence of restenosis in our study (14.4% overall) could be attributed (at least in part) to the use of HR-FDCT as well as the strict criteria on which stent placement was decided.

Our study had three main limitations. First, this was a single-center, retrospective study, and some selection biases may have been present. Second, the prevalence of restenosis may have been over- or underestimated because only 53.5% (61/114) of patients underwent follow-up studies using angiography. Third, the Wingspan stent-delivery system was not used in the present study. Although it is approved for intracranial stenosis in the USA, it has been criticized for its rigidity and open-cell design with radial force (Feng et al., 2015; Du et al., 2018). Off-label use of several other types of intracranial stents has been used to treat intracranial stenosis [e.g., Neuroform (Du et al., 2018; Xu et al., 2019) and Enterprise (Feng et al., 2015; Huang et al., 2019; Salik et al., 2019)].

CONCLUSION

High-resolution flat-detector computed tomography (HR-FDCT) improves visualization of the fine structures of intracranial stents deployed for symptomatic ICAS compared with that using conventional FDCT. High-resolution flat-detector computed tomography improves assessment of stent deployment and could reduce the risk of complications.

DATA AVAILABILITY STATEMENT

The original contributions presented in the study are included in the article/supplementary material, further inquiries can be directed to the corresponding authors.

ETHICS STATEMENT

The studies involving human participants were reviewed and approved by Ethics committee of Biomedical Research of the First Affiliated Hospital of Zhengzhou University. The patients/participants provided their written informed consent to participate in this study.

AUTHOR CONTRIBUTIONS

TL, JM, CS, YR, and JR were responsible for patient recruitment, data acquisition, and/or analysis. TL, YW, XH, and CZ contributed to the study design. TL contributed to the imaging optimization. TL, YW, and CZ contributed to the statistical analysis and drafting of the manuscript. ML, MM-B, and XH critically revised the manuscript. All authors read and approved the final manuscript.

FUNDING

This work was supported by a grant from the National Natural Science Foundation of China (81801806) and the Medical Science and Technology Research Project of Henan Province (KYDZ2020120441).

ACKNOWLEDGMENTS

We thank Jia-Jia Ge and Bing Yan from Siemens for their invaluable assistance in this work.

REFERENCES

Alexander, M. J., Zauner, A., Chaloupka, J. C., Baxter, B., Callison, R. C., Gupta, R., et al. (2019). WEAVE trial: final results in 152 on-label patients. *Stroke* 50, 889–894. doi: 10.1161/strokeaha.118.023996

Caroff, J., Mihalea, C., Neki, H., Ruijters, D., Ikka, L., Benachour, N., et al. (2014). Role of C-arm VasoCT in the use of endovascular WEB flow disruption in intracranial aneurysm treatment. *AJNR Am. J. Neuroradiol.* 35, 1353–1357. doi: 10.3174/ajnr.a3860

Clarençon, F., Di Maria, F., Gabrieli, J., Shotar, E., Degos, V., Nouet, A., et al. (2017). Clinical impact of flat panel volume CT angiography in evaluating the accurate intraoperative deployment of flow-diverter stents. *AJNR Am. J. Neuroradiol.* 38, 1966–1972. doi: 10.3174/ajnr.a343

Derdeyn, C. P., Chimowitz, M. I., Lynn, M. J., Fiorella, D., Turan, T. N., Janis, L. S., et al. (2014). Aggressive medical treatment with or without stenting in high-risk patients with intracranial artery stenosis (SAMMPRIS): the final results of a randomised trial. *Lancet* 383, 333–341. doi: 10.1016/s0140-6736(13)62038-3

Du, Z., Mang, J., Yu, S., Tian, C., Cao, X., Liu, X., et al. (2018). Weighing in on the off-label use: initial experience of neuroform EZ stenting for intracranial arterial stenosis in 45 patients. *Front. Neurol.* 9:852. doi: 10.3389/fneur.2018.00852

Feng, Z., Duan, G., Zhang, P., Chen, L., Xu, Y., Hong, B., et al. (2015). Enterprise stent for the treatment of symptomatic intracranial atherosclerotic stenosis: an initial experience of 44 patients. *BMC Neurol.* 15:187. doi: 10.1186/s12883-015-0443-9

Fischer, U., Baumgartner, A., Arnold, M., Nedeltchev, K., Gralla, J., De Marchis, G. M., et al. (2010). What is a minor stroke? *Stroke* 41, 661–666.

Foin, N., Gutiérrez-Chico, J. L., Nakatani, S., Torii, R., Bourantas, C. V., Sen, S., et al. (2014). Incomplete stent apposition causes high shear flow disturbances and delay in neointimal coverage as a function of strut to wall detachment distance: implications for the management of incomplete stent apposition. *Circ. Cardiovasc. Interv.* 7, 180–189. doi: 10.1161/circinterventions.113.000931

Gorelick, P. B., Wong, K. S., Bae, H. J., and Pandey, D. K. (2008). Large artery intracranial occlusive disease: a large worldwide burden but a relatively neglected frontier. *Stroke* 39, 2396–2399. doi: 10.1161/strokeaha.107.505776

Heit, J. J., and Wintermark, M. (2018). New developments in clinical ischemic stroke prevention and treatment and their imaging implications. *J. Cereb. Blood Flow Metab.* 38, 1533–1550. doi: 10.1177/0271678x17694046

Huang, C. M., Hong, Y. F., Xing, S. H., Xu, K., Xu, C. K., Zhang, W. J., et al. (2019). Thirty-Day outcomes of the enterprise stent in treating hypoperfusion of symptomatic intracranial stenosis. *World Neurosurg.* 129, e429–e435.

Jang, J. H., Lim, Y. S., Lee, Y. J., Yoo, W. J., Sung, M. S., and Kim, B. S. (2012). Evaluation of middle cerebral artery stents using multidetector row CT angiography *in vivo* study: comparison of the three different kernels. *Acta Radiol.* 53, 456–460. doi: 10.1258/ar.2012.110659

Jiang, W. J., Cheng-Ching, E., Abou-Chebl, A., Zaidat, O. O., Jovin, T. G., Kalia, J., et al. (2012). Multicenter analysis of stenting in symptomatic intracranial atherosclerosis. *Neurosurgery* 70, 25–30. doi: 10.1227/neu.0b013e31822d274d

Jiang, W. J., Xu, X. T., Jin, M., Du, B., Dong, K. H., and Dai, J. P. (2007). Apollo stent for symptomatic atherosclerotic intracranial stenosis: study results. *AJNR Am. J. Neuroradiol.* 28, 830–834.

Kato, N., Yuki, I., Ishibashi, T., Ikemura, A., Kan, I., Nishimura, K., et al. (2020). Visualization of stent apposition after stent-assisted coiling of intracranial aneurysms using high resolution 3D fusion images acquired by C-arm CT. *J. Neurointerv. Surg.* 12, 192–196. doi: 10.1136/neurintsurg-2019-014966

Kuriyama, T., Sakai, N., Beppu, M., Sakai, C., Imamura, H., Masago, K., et al. (2018). Quantitative analysis of conebeam CT for delineating stents in stent-assisted coil embolization. *AJNR Am. J. Neuroradiol.* 39, 488–493. doi: 10.3174/ajnr.a5533

Leung, S. Y., Ng, T. H., Yuen, S. T., Lauder, I. J., and Ho, F. C. (1993). Pattern of cerebral atherosclerosis in Hong Kong Chinese. severity in intracranial and extracranial vessels. *Stroke* 24, 779–786. doi: 10.1161/01.str.24.6.779

Li, T. F., Ma, J., Han, X. W., Fu, P. J., Niu, R. N., Luo, W. Z., et al. (2019). Application of high-resolution C-Arm CT combined with streak metal artifact removal technology for the stent-assisted embolization of intracranial aneurysms. *AJNR Am. J. Neuroradiol.* 40, 1752–1758.

Mori, T., Fukuoka, M., Kazita, K., and Mori, K. (1998). Follow-up study after intracranial percutaneous transluminal cerebral balloon angioplasty. *AJNR Am. J. Neuroradiol.* 19, 1525–1533.

Qureshi, A. I., and Caplan, L. R. (2014). Intracranial atherosclerosis. *Lancet* 383, 984–998.

Salik, A. E., Selcuk, H. H., Zalov, H., Kilinc, F., Cirak, M., and Kara, B. (2019). Medium-term results of undersized angioplasty and stenting for symptomatic high-grade intracranial atherosclerotic stenosis with enterprise. *Interv. Neuroradiol.* 25, 484–490. doi: 10.1177/1591019919832244

Samuels, O. B., Joseph, G. J., Lynn, M. J., Smith, H. A., and Chimowitz, M. I. (2000). A standardized method for measuring intracranial arterial stenosis. *AJNR Am. J. Neuroradiol.* 21, 643–646.

Sheng, L., Li, J., Li, H., Li, G., Chen, G., Xiang, W., et al. (2014). Evaluation of cerebral arteriovenous malformation using 'dual vessel fusion' technology. *J. Neurointerv. Surg.* 6, 667–671. doi: 10.1136/neurintsurg-2013-010980

Shintai, K., Matsubara, N., and Izumi, T. (2018). High-resolution cone beam CT for evaluation of vascular channel in intracranial partial thrombosed aneurysm. *Nagoya. J. Med. Sci.* 80, 279–284.

Srinivasan, V. M., Chintalapani, G., Camstra, K. M., Effendi, S. T., Cherian, J., Johnson, J. N., et al. (2018). Fast acquisition cone-beam computed tomography: initial experience with a 10 s protocol. *J. Neurointerv. Surg.* 10, 916–920. doi: 10.1136/neurintsurg-2017-013475

Vajda, Z., Schmid, E., Güthe, T., Klötzsch, C., Lindner, A., Niehaus, L., et al. (2012). The modified Bose method for the endovascular treatment of intracranial atherosclerotic arterial stenoses using the enterprise stent. *Neurosurgery* 70, 91–101. doi: 10.1227/neu.0b013e31822dff0f

Wang, D., and Wang, Y. (2017). Opening already occluded middle cerebral artery, internal carotid artery or other cerebral arteries: when, where, how and why? *Stroke Vasc. Neurol.* 2, 106–107. doi: 10.1136/svn-2017-000107

Xu, H., Quan, T., Zaidat, O. O., Chen, D., Wang, Z., Yuan, Y., et al. (2019). Neuroform EZ stenting for symptomatic intracranial artery stenosis: 30 days outcomes in a high-volume stroke center. *Front. Neurol.* 10:428. doi: 10.3389/fneur.2019.00428

Yuki, I., Kambayashi, Y., Ikemura, A., Abe, Y., Kan, I., Mohamed, A., et al. (2016). High-Resolution C-Arm CT and metal artifact reduction software: a novel imaging modality for analyzing aneurysms treated with stent-assisted coil embolization. *AJNR Am. J. Neuroradiol.* 37, 317–323. doi: 10.3174/ajnr.a4509

Zaidat, O. O., Fitzsimmons, B. F., Woodward, B. K., Wang, Z., Killer-Oberpfalzer, M., Wakhloo, A., et al. (2015). Effect of a balloon-expandable intracranial stent vs medical therapy on risk of stroke in patients with symptomatic intracranial stenosis: the VISSIT randomized clinical trial. *JAMA* 313, 1240–1248. doi: 10.1001/jama.2015.1693

Zhang, Q., Zhao, H., Sun, Q., Han, J., Zhang, H., Shan, T., et al. (2019). Clinical evaluation of volume of interest imaging combined with metal artifact reduction reconstruction techniques in coiling and stent assisted coiling during neurointerventional procedures. *J. Neurointerv. Surg.* 11, 205–210. doi: 10.1136/neurintsurg-2018-013886

Conflict of Interest: The authors declare that the research was conducted in the absence of any commercial or financial relationships that could be construed as a potential conflict of interest.

frontiers in Neuroscience

CASE REPORT
published: 20 October 2021
doi: 10.3389/fnins.2021.739178

Case Report: Serial MR Vessel Wall Imaging Visualizes the Response of Intracranial Plaques and Assists in Decision-Making

Jiayu Xiao [1,2†], Matthew M. Padrick [3†], Shlee S. Song [3], Zhaoyang Fan [1,2,4] and Konrad H. Schlick [3*]*

[1] Departments of Radiology, Keck School of Medicine of USC, Los Angeles, CA, United States, [2] Biomedical Imaging Research Institute, Department of Biomedical Sciences, Cedars-Sinai Medical Center, Los Angeles, CA, United States, [3] Department of Neurology, Cedars-Sinai Medical Center, Los Angeles, CA, United States, [4] Departments of Radiation Oncology, Keck School of Medicine of USC, Los Angeles, CA, United States

OPEN ACCESS

Edited by:
Lun-De Liao,
National Health Research Institutes (Taiwan), Taiwan

Reviewed by:
Yuting Wang,
Sichuan Academy of Medical Sciences and Sichuan Provincial People's Hospital, China
Bing Zhang,
Nanjing Drum Tower Hospital, China

***Correspondence:**
Konrad H. Schlick
konrad.schlick@cshs.org
Zhaoyang Fan
zhaoyang.fan@med.usc.edu

[†] These authors have contributed equally to this work and share first authorship

Specialty section:
This article was submitted to Brain Imaging Methods, a section of the journal Frontiers in Neuroscience

Received: 10 July 2021
Accepted: 22 September 2021
Published: 20 October 2021

Citation:
Xiao J, Padrick MM, Song SS, Fan Z and Schlick KH (2021) Case Report: Serial MR Vessel Wall Imaging Visualizes the Response of Intracranial Plaques and Assists in Decision-Making. Front. Neurosci. 15:739178. doi: 10.3389/fnins.2021.739178

Intracranial atherosclerotic disease (ICAD) is a dynamic process that leads to ischemic stroke. Symptomatic ICAD patients still suffer a high recurrent rate even under standard treatment. In this case report, to better understand the response of intracranial atherosclerotic plaques to medication, serial MR imaging was added to standard clinical workup in a 47-year-old male patient with acute occipital lobe infarction at baseline, 3-month, 6-month, and 12-month post index stroke to directly visualize the morphology and signal change of plaques. We noticed that one of the plaques showed dramatic worsening at 3-month imaging follow-up despite a decrease in low-density lipoprotein level. Early identification of patients who do not respond well to medication is critical to prevent the recurrence of cardiovascular events in ICAD patients.

Keywords: intracranial atherosclerosis, stroke, plaque, vessel wall imaging, follow-up study

INTRODUCTION

Intracranial atherosclerotic disease (ICAD) represents a significant risk factor for ischemic stroke worldwide, and patients with symptomatic ICAD experience a high rate of recurrent stroke (Holmstedt et al., 2013). Therefore, active monitoring of intracranial atherosclerotic lesions has been crucial for the secondary prevention of stroke. Current clinical practice relies on physical examinations, laboratory tests, and conventional imaging modalities like CT angiography or MR angiography (MRA), which mainly focus on the assessment of luminal stenosis. In recent years, the value of magnetic resonance vessel wall imaging (MR-VWI) in directly characterizing the morphological features of intracranial atherosclerotic plaques has been explored (Song et al., 2021). In this case report, we used MR-VWI to directly probe atherosclerotic lesions in an effort to reveal lesion-level response to medical treatment.

CASE DESCRIPTION

A 47-year-old man presented with headache and vertigo. Before the index stroke event, the patient had been diagnosed with hyperlipidemia for more than 10 years without being regularly monitored or taking lipid-lowering medications. He had no history of hypertension, diabetes, or smoking. CT angiography reported a thrombosed right vertebral artery (VA) V4 segment with luminal

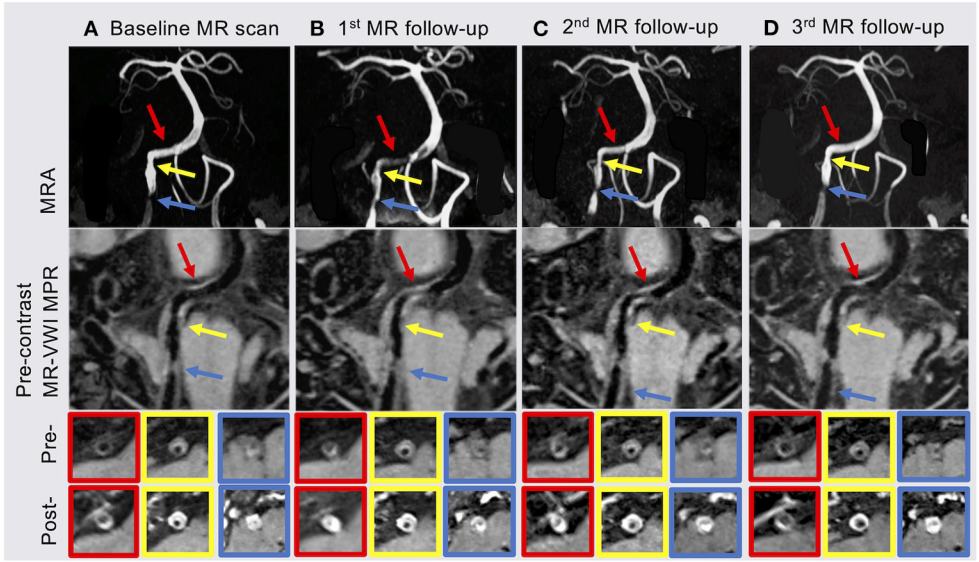

FIGURE 1 | (A) Baseline MR scan showed two plaques in the proximal (blue arrow) and middle (yellow arrow) of the right vertebral artery (VA) V4 segment. **(B)** The patient underwent the 1st MR follow-up scan 3 months after index stroke. MRA and MR-VWI showed a new plaque (red arrow) in the distal right VA V4 segment with severe stenosis and high enhancement ratio (ER). **(C)** Most of plaque features showed slightly regression at the 2nd follow-up MR scan 6 months after index stroke. **(D)** The 3rd follow-up MR scan 12 months after index stroke showed that the degree of stenosis, plaque-wall contrast ratio (CR) and ER of the plaque in the distal right VA V4 segment were back to baseline and slightly improved in the other two plaques. MRA, MR angiography; MR-VWI, MR vessel wall imaging; MPR, multiplanar reconstruction; Pre-, pre-contrast MR-VWI; Post-, post-contrast MR-VWI.

irregularities, with concerns for focal dissection, atherosclerosis, or both. This prompted initiation of intravenous heparin. Routine brain MR revealed an acute occipital lobe infarction and a slight increase in pre-contrast T1-weighted signal within the right VA V4 segment. Other laboratory findings included low-density lipoprotein (LDL) of 123 mg/dL and hemoglobin A1c of 5.7%.

Due to the uncertainty involved with the lesion on the right V4 segment, further neurovascular imaging including 3D time-of-flight MRA and pre- and post-contrast MR-VWI (Fan et al., 2017; Yang et al., 2017) was pursued. MRA revealed two stenotic lesions in the right VA (**Figure 1** yellow and blue arrows). Eccentric wall thickening, presence of hyper-intensity on pre-contrast MR-VWI and strong contrast enhancement on post-contrast MR-VWI highly suggested atherosclerotic disease rather than dissection. We quantified the degree of stenosis, pre-contrast plaque-wall contrast ratio (CR), and post-contrast plaque enhancement ratio (ER) at individual lesions using previously published methods (Wu et al., 2018). Specifically, 3D MR-VWI images were reformatted to cross-sectional views, and mean signal intensity was quantified with manually drawn regions of interest. Plaque-wall CR was calculated as the signal intensity ratio between the brightest region within the plaque and the adjacent normal-looking vessel wall. Plaque ER was calculated as the normalized signal intensity ratio between the post-contrast plaque and pre-contrast plaque. Reliability of these quantitative measurements was excellent in patients with ICAD as shown in a recent paper (Zhang et al., 2021). In the meantime, an asymptomatic plaque was also observed in the proximal V4 segment of the left vertebral artery. While in this patient, the left vertebral artery did not converge with the right vertebral artery to form the basilar artery. Quantitative analyses were not performed on this plaque because no significant changes were visualized.

High dose statin (atorvastatin 80 mg daily) and dual antiplatelet therapy (aspirin 325 mg daily and clopidogrel 75 mg daily) was initiated. The patient was hospitalized for 5 days. He was discharged with a minor headache and a National Institutes of Health Stroke Scale score of 0. Two months later, direct LDL level showed a decrease to 95 mg/dL at clinical follow-up. There were no adverse effects from the statin therapy noted. At this point, ezetimibe 10 mg daily was initiated by his cardiologist for further lowering the LDL level. However, statin therapy was stopped thereafter due to miscommunication between the patient and cardiologist.

At 3 months after the index stroke, a follow-up MR scan was performed. Despite the moderate regression of LDL and an appreciable drop in plaque-wall CR and/or plaque ER in the two originally identified lesions, a new lesion in the distal right VA with a diffusive and severe lumen narrowing and strong vessel wall enhancement was observed (**Figure 1** red arrow). The degree of stenosis of the distal lesion increased from 24.42 to 80.11% and ER increased from 2.20 to 2.59. Therefore, high dose statin was resumed.

At 6 months after the index stroke, the patient was unable to tolerate ezetimibe due to a persistent skin rash, thus was placed

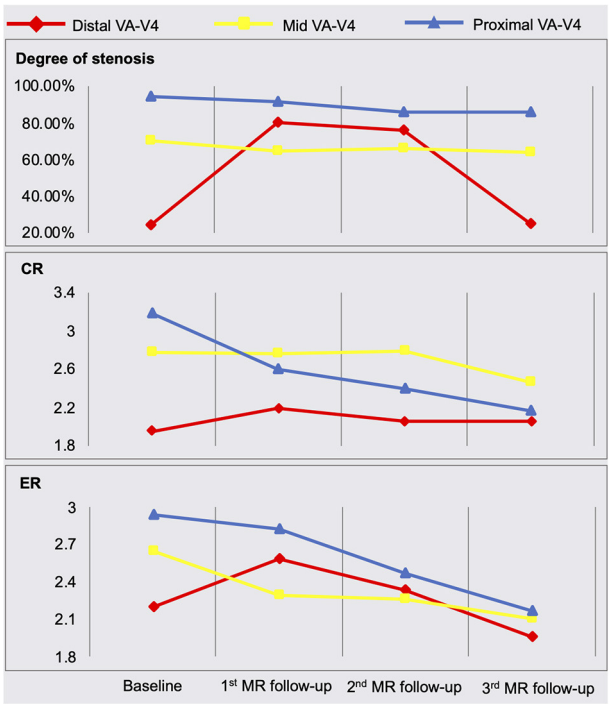

FIGURE 2 | Quantitative measurement results of plaque features. MRA, MR angiography; MR-VWI, MR vessel wall imaging; VA, vertebral artery; CR, plaque-wall contrast ratio; ER, plaque enhancement ratio.

on the PCSK-9 inhibitor evolocumab (140 mg subcutaneously every 2 weeks), which led to a drastic reduction in LDL from 67 mg/dL at 6 months to 18 mg/dL at 11 months.

MRA and MR-VWI scans were performed at 6- and 12-month post index stroke. Compared with the 3-month scan, patient's 6-month MRA showed a slight regression of lumen at the plaque in the distal right VA, but plaque ER measured on MR-VWI substantially reduced. Twelve months after the index stroke, both degree of stenosis measured on MRA and plaque ER measured on MR-VWI regressed to the baseline level at the plaque in the distal right VA. CR and ER of the other two plaques slightly improved while the degree of stenosis remained unchanged. During this period, the patient's condition has been stable without any new symptoms.

The quantitative measurement results of plaque features are shown in **Figure 2**. A schematic diagram showing the time course of clinical management and MR examinations is presented in **Figure 3**.

DISCUSSION

Serum lipid biomarkers are widely accepted to monitor ICAD patients' responses to treatment; however, these are systemic rather than lesion-specific markers. MR-VWI can more specifically interrogate each atherosclerotic lesion and provide information beyond the severity of stenosis. Previous studies (Chen et al., 2018; Chung et al., 2020) focused on investigating the treatment effect of specific medical therapies using MR-VWI before and after 6-month treatment. In contrast, we performed serial MR-VWI at multiple time points (from 1 week after symptom onset through 1 year), with a focus on demonstrating that serial MR-VWI may reveal lesion-level response or resistance during medical treatment, which may not be adequately captured by routine assessments such as laboratory test. Another noteworthy novelty in our study is that we used a 3D whole-brain rather than 2D MR-VWI approach, which allowed for the detection of new plaques at other locations and the quantification of the signal contrast between plaque and normal vessel wall. As seen in the baseline and 3 months follow-up MR scans, the subsequently identified lesion in the distal VA, although not recognized in MRA, showed considerably high plaque-wall CR and plaque ER in MR-VWI and rapidly developed severe stenosis, indicating its active atherosclerotic activities (Wu et al., 2018).

In our case, we monitored the patient's LDL level and reinforced lifestyle modifications as standard of care. Additionally, we monitored imaging features including the degree of stenosis, plaque-wall CR (which might be related to intraplaque hemorrhage), and plaque ER (a marker of inflammation) (Mandell et al., 2017). Despite a decrease in serum LDL, this patient's plaque showed dramatic worsening based on these imaging features at 3 months. The underlying reasons for this mismatch of controlled LDL and plaque-worsening remain unclear. A probable reason could be due to the fact that they probe the response or resistance from different aspects, i.e., one at a systematic level and the other at a lesion level. However, there might be other confounding factors that we are not aware of given the drastic deterioration in such a short time period. A large-scale prospective study is warranted to explore the incidence of mismatches between systemic blood biomarkers and plaque features, and the added value of MR-VWI in the management of symptomatic ICAD patients.

The LDL reduction and plaque rapid progression observed in this case illustrate how serial imaging examinations can complement systemic biomarkers and assist in the management of secondary stroke prevention. Due to miscommunication, atorvastatin was discontinued for 1 month, during which time, only ezetimibe was used for lipid-lowering. The discontinuation of atorvastatin could be found out and corrected by the treating physician at the 3-month clinical visit. However, the 3-month MR-VWI results did propel the physician to prescribe a more intensive therapy and target an LDL level <20 mg/dL as a recent study has shown that further lowering of LDL beyond the current target (100 mg/dL) would further reduce cardiovascular risk (Sabatine et al., 2018). This case involved a non-standard therapy. However, it is not uncommon to see in clinical practice that an originally prescribed standard treatment plan can be compromised due to miscommunication or poor compliance. In this representative case, our findings highly suggest that serial MR-VWI may early detect lesion-level response or resistance during medical treatment, and this information can be supplemental to routine assessments such as laboratory test in guiding treatment plans. A treatment plan may be modified in a timely manner to better achieve secondary stroke

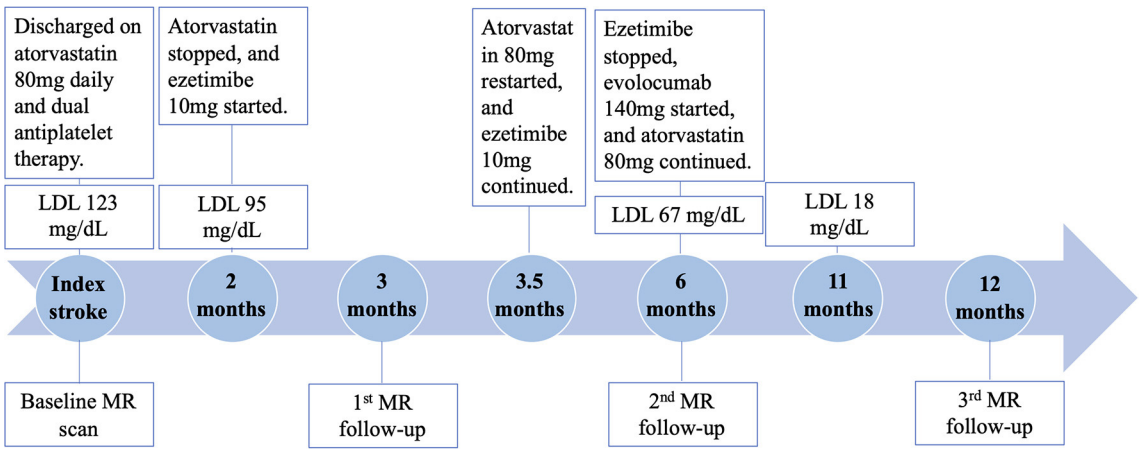

FIGURE 3 | Timeline of clinical management and MR examinations.

prevention (Xiao et al., 2021). Of course, large-scale clinical trials are warranted to validate this hypothesis.

Since treatment responses may differ in individuals due to different pharmacodynamics and treatment compliance, longitudinal assessment is necessary for ICAD. However, there is not enough evidence about the best follow-up interval. The patient underwent his follow-up imaging at 3, 6, and 12 months following our ongoing research protocol. Physicians typically follow up with stroke patients and make decisions on medical management at 3 months. Therefore, we chose to repeat imaging at 3 months to provide more information to clinical practice. In this case report, given the notable plaque progression seen on the first follow-up scan, we postulate that repeat MR-VWI as soon as 3 months post ischemic stroke may be reasonable.

Additionally, PSCK-9 inhibitor effect on ICAD plaques should be explored further, as there may be an underlying mechanism beyond plummeting serum LDL level. Further, the expected temporal concordance between LDL levels and MR-VWI features will need to be elucidated, if any are present.

In this work, plaque composition and its change process were not investigated. This is because we used an MR-VWI protocol that involves a T1-weighted sequence only. This protocol features relatively short scan time and capability of quantifying temporal changes associated with intraplaque hemorrhage and inflammation. However, certain important plaque components, such as fibrous cap and lipid core, cannot be detected because several reasons: (1) the small size of intracranial vessels, (2) the limited spatial resolution, (3) the lack of additional contrast weighting such as T2-weighting. A high-resolution multi-contrast protocol would make MR-VWI challenging for both patients and clinical workflow.

In summary, this case report sheds light on the importance of the promising combination of serum biomarkers and lesion-specific imaging tools in the decision-making of stroke patients.

DATA AVAILABILITY STATEMENT

The original contributions presented in the study are included in the article/supplementary material, further inquiries can be directed to the corresponding authors.

ETHICS STATEMENT

The studies involving human participants were reviewed and approved by Ethics Committee of Cedars-Sinai Medical Center. The patients/participants provided their written informed consent to participate in this study.

AUTHOR CONTRIBUTIONS

JX and MP interpreted the data and drafted the manuscript. SS, ZF, and KS contributed substantially to the design of the work and revised it critically for important intellectual content. All authors contributed to the article and approved the submitted version.

FUNDING

SS and ZF received salary support from the NIH/NHLBI grant # R01HL147355.

REFERENCES

Chen, X., Wang, S., Lin, L., Li, Y., and Zhang, H. (2018). Drug effect of atorvastatin on middle cerebral atherosclerotic stenosis and high resolution NMR diagnosis. *Pak. J. Pharm. Sci.* 31, 1169–1173.

Chung, J. W., Cha, J., Lee, M. J., Yu, I. W., Park, M. S., Seo, W. K., et al. (2020). Intensive statin treatment in acute ischaemic stroke patients with intracranial atherosclerosis: a high-resolution magnetic resonanceimaging study (STAMINA-MRI Study). *J. Neurol. Neurosurg. Psychiatry* 91, 204–211. doi: 10.1136/jnnp-2019-320893

Fan, Z., Yang, Q., Deng, Z., Li, Y., Bi, X., Song, S., et al. (2017). Whole-brain intracranial vessel wall imaging at 3 Tesla using cerebrospinal fluid-attenuated T1-weighted 3D turbo spin echo. *Magn. Reson. Med.* 77, 1142–1150. doi: 10.1002/mrm.26201

Holmstedt, C. A., Turan, T. N., and Chimowitz, M. I. (2013). Atherosclerotic intracranial arterial stenosis: risk factors, diagnosis, and treatment. *Lancet Neurol.* 12, 1106–1114. doi: 10.1016/S1474-4422(13)70195-9

Mandell, D. M., Mossa-Basha, M., Qiao, Y., Hess, C. P., Hui, F., Matouk, C., et al. (2017). Intracranial vessel wall MRI: principles and expert consensus recommendations of the American Society of Neuroradiology. *AJNR Am. J. Neuroradiol.* 38, 218–229. doi: 10.3174/ajnr.A4893

Sabatine, M. S., Wiviott, S. D., Im, K., Murphy, S. A., and Giugliano, R. P. (2018). Efficacy and safety of further lowering of low-density lipoprotein cholesterol in patients starting with very low levels: a meta-analysis. *JAMA Cardiol.* 3, 823–828. doi: 10.1001/jamacardio.2018.2258

Song, J. W., Pavlou, A., Xiao, J., Kasner, S. E., Fan, Z., and Messe, S. R. (2021). Vessel wall magnetic resonance imaging biomarkers of symptomatic intracranial atherosclerosis: a meta-analysis. *Stroke* 52, 193–202. doi: 10.1161/STROKEAHA.120.031480

Wu, F., Ma, Q., Song, H., Guo, X., Diniz, M. A., Song, S. S., et al. (2018). Differential features of culprit intracranial atherosclerotic lesions: a whole-brain vessel wall imaging study in patients with acute ischemic stroke. *J. Am. Heart Assoc.* 7:e009705. doi: 10.1161/JAHA.118.009705

Xiao, J., Song, S. S., Schlick, K. H., Xia, S., Jiang, T., Han, T., et al. (2021). Disparate trends of atherosclerotic plaque evolution in stroke patients under 18-month follow-up: a 3D whole-brain magnetic resonance vessel wall imaging study. *Neuroradiol. J.* 23:19714009211026920. doi: 10.1177/19714009211026920

Yang, Q., Deng, Z., Bi, X., Song, S. S., Schlick, K. H., Gonzalez, N. R., et al. (2017). Whole-brain vessel wall MRI: a parameter tune-up solution to improve the scan efficiency of three-dimensional variable flip-angle turbo spin-echo. *J. Magn. Reson. Imaging* 46, 751–757. doi: 10.1002/jmri.25611

Zhang, N., Liu, X., Xiao, J., Song, S. S., and Fan, Z. (2021). Plaque morphologic quantification reliability of 3D whole-brain vessel wall imaging in patients with intracranial atherosclerotic disease: a comparison with conventional 3D targeted vessel wall imaging. *J. Magn. Reson. Imaging* 54, 166–174. doi: 10.1002/jmri.27550

Conflict of Interest: The authors declare that the research was conducted in the absence of any commercial or financial relationships that could be construed as a potential conflict of interest.

frontiers in Neuroscience

ORIGINAL RESEARCH
published: 29 October 2021
doi: 10.3389/fnins.2021.737525

Super-Resolution Arterial Spin Labeling Using Slice-Dithered Enhanced Resolution and Simultaneous Multi-Slice Acquisition

*Qinyang Shou, Xingfeng Shao and Danny J. J. Wang**

Laboratory of FMRI Technology, USC Mark and Mary Stevens Neuroimaging and Informatics Institute, Keck School of Medicine, University of Southern California, Los Angeles, CA, United States

Purpose: To achieve high spatial resolution (isotropic-2 mm) perfusion imaging using 2D simultaneous multi-slice (SMS) pseudo-continuous arterial spin labeling (pCASL) and slice dithered enhanced resolution (SLIDER) technique for super-resolution reconstruction.

Methods: The SLIDER-SMS pCASL with a multiband factor of 4 was implemented at 3T with three numbers of slice shift (2/3/4) for the slice thickness of 4/6/8 mm, respectively. Super-resolution reconstruction was performed with singular value decomposition and different levels of Tikhonov regularizations. Temporal and spatial signal-to-noise ratio (SNR) as well as spatial blurring effects of super-resolution ASL images were measured in five healthy subjects and compared with those of reference high-resolution ASL images.

Results: Compared to conventional 2D SMS ASL, super-resolution ASL images with isotropic-2-mm resolution yielded 42, 61, and 88% higher spatial SNR, and 18, 55, and 105% higher temporal SNR with slice shift number of 2/3/4, respectively. Spatial blurring effect increased for SLIDER reconstruction from two to four slice shifts.

Conclusion: The proposed SLIDER-SMS pCASL technique can achieve whole-brain high-resolution perfusion images with ∼15-min scan time and improved SNR compared to standard 2D SMS pCASL. Caution needs to be exercised on quantifying and controlling blurring effects of SLIDER reconstruction.

Keywords: super-resolution (SR), arterial spin label (ASL) MRI, perfusion, simultaneous multi slice, slice dithered enhanced resolution (SLIDER)

OPEN ACCESS

Edited by:
Ze Wang,
University of Maryland, Baltimore, United States

Reviewed by:
Tae Kim,
University of Pittsburgh, United States
Andrew S. Nencka,
Medical College of Wisconsin, United States
Xiufeng Li,
University of Minnesota Twin Cities, United States

***Correspondence:**
Danny J. J. Wang
jwang71@gmail.com

Specialty section:
This article was submitted to Brain Imaging Methods, a section of the journal Frontiers in Neuroscience

Received: *07 July 2021*
Accepted: *05 October 2021*
Published: *29 October 2021*

Citation:
Shou Q, Shao X and Wang DJJ (2021) Super-Resolution Arterial Spin Labeling Using Slice-Dithered Enhanced Resolution and Simultaneous Multi-Slice Acquisition. Front. Neurosci. 15:737525. doi: 10.3389/fnins.2021.737525

INTRODUCTION

Arterial spin labeling (ASL) is a perfusion imaging technique that can quantitatively measure cerebral blood flow (CBF) without using an exogenous contrast agent. Due to the relatively low signal-to-noise ratio (SNR), existing ASL methods generally have a coarse resolution of 3–4 mm resulting in partial volume effects when analyzing perfusion of small brain structures and cerebral cortex with a thickness of a few mm. Segmented 3D acquisitions and pseudo-continuous ASL

(pCASL) are recommended for ASL imaging to achieve a sufficient SNR(Alsop et al., 2015). However, there remain challenges for achieving a high spatial resolution with 3D ASL including spatial blurring along the slice direction due to the modulation of k-space signals by the transverse (T2) relaxation and susceptibility to (intersegment) head motion.

Simultaneous multi-slice (SMS) is a fast imaging technology that simultaneously excites multiple slices and resolves each slice with parallel imaging techniques (Feinberg et al., 2010; Setsompop et al., 2012). When applied to ASL imaging, SMS can reduce the effect of signal decay due to longitudinal (T1) relaxation and improve spatial coverage and/or resolution compared to standard 2D ASL (Feinberg et al., 2013; Kim et al., 2013; Li et al., 2015; Wang et al., 2015). Compared to 3D imaging, 2D SMS has the potential benefits of reduced spatial blurring and improved robustness to head motion. Furthermore, a constrained slice-dependent background suppression (CSD-BS) scheme has been proposed to suppress the background signal in brain tissue to improve the SNR for 2D SMS pCASL (Shao et al., 2018).

Super-resolution techniques achieve high spatial resolution from one or multiple low-resolution images with reconstruction algorithms, which have been proven effective in MRI (Ben-Eliezer et al., 2010; Setsompop et al., 2018; Vu et al., 2018; Greenspan et al., 2002). The SLIce Dithered Enhanced Resolution (SLIDER) (Setsompop et al., 2015) technique is a super-resolution technique that utilizes sub-voxel spatial shifts in the slice direction to achieve a $\sqrt{n}$ fold gain (n is the number of spatially shifted thick slices) in SNR efficiency, given the same number of measurements and without considering physiological noise or parallel imaging factors. SLIDER has been successfully applied for SMS diffusion MRI and BOLD fMRI to achieve submillimeter spatial resolutions (Setsompop et al., 2015; Vu et al., 2018). This method may provide a potential technique for high-resolution ASL by increasing both resolution and SNR efficiency while still achieving a wide imaging coverage.

The purpose of this study was to present a super-resolution (iso-2-mm) perfusion imaging technique by integrating SLIDER with 2D SMS pCASL and CSD-BS, herein termed as SLIDER-SMS pCASL. We first presented the theoretical framework and then demonstrated *in vivo* experimental results by comparison with a reference high-resolution 2D SMS pCASL.

MATERIALS AND METHODS

Theoretical Framework

Figure 1 shows the diagram for SLIDER-SMS pCASL which combined SMS imaging, SLIDER super-resolution with the optimized CSD-BS scheme (Shao et al., 2018). In this study, six SMS slice groups with a multiband (MB) factor of 4 were employed to achieve whole-brain coverage. The detailed SMS scheme is shown in **Figure 2**. In SLIDER, N sets of 2D slices are acquired with sub-voxel spatial shifts in the slice direction, and high-resolution thin-slice images are reconstructed by applying a "deblurring" algorithm. Three options for SLIDER acquisition are shown in **Figure 1B**, namely, SLIDER2, SLIDER3, and SLIDER4 for two, three, and four sets of shifted slices with the thickness of 4, 6, and 8 mm, respectively. In our study, the reference high-resolution SMS pCASL images with 2-mm slice thickness (termed as reference ASL images hereafter) were acquired in two scans, each with a 100% inter-slice gap, to match the image acquisition time of super-resolution scans and to minimize cross talk between thin slices. The CSD-BS method employs slice-dependent pre-modulation MB RF pulses for each group of SMS slices before the pCASL pulse train as well as two inversion pulses during the post-labeling delay (PLD), so that the longitudinal magnetization (M_z) of each group of SMS slices reaches the nulling point just before the readout of each respective slice group.

The theoretical SNR for the super-resolution images ($SNR_{SLIDER-SMS}$) reconstructed with this method compared to the SNR of reference ASL images (SNR_{ref}) with the same number of measurements and without considering physiological noise or parallel imaging factors can be expressed by the following equation:

$$SNR_{SLIDER-SMS} = \sqrt{N_{set}} \times SNR_{ref} \quad (1)$$

where N_{set} is the number of shifted image sets, since the potential thin slices have been sampled for N_{set} times.

However, this equation only applies to non-SMS-accelerated acquisitions. For SLIDER-SMS pCASL, image noise caused by g-factor should be considered and can be expressed as the following equation:

$$var_{SLIDER-SMS} = g^2_{SLIDER-SMS} \times var_{thermal} + var_{physio} \quad (2)$$

where $g_{SLIDER-SMS}$ is the g-factor for SLIDER-SMS reconstruction (Breuer et al., 2009), *var* represents noise variance, and the subscript represents the respective physiological and thermal noise. When N measurements (N_{meas}) are averaged for ASL, the image noise variance can be expressed by

$$var_{SLIDER-SMS,N_{meas}} = g^2_{SLIDER} \times \frac{var_{thermal}}{N_{meas}} + \frac{var_{physio}}{N'_{meas}} \quad (3)$$

where N'_{meas} is between 1 and N_{meas} depending on the temporal correlation of physiological noise. The labeling duration and PLD of an ASL scan are much longer than the image acquisition time. In order to keep the total scan time constant for SLIDER2/3/4 and reference ASL scans (for fair comparison of SNR efficiency), we used fewer repetitions for SLIDER acquisitions with more shifted slices (N_{set}). For example, in SLIDER2, two scans were acquired with 40 repetitions in each scan, whereas in SLIDER4, four scans were acquired with only 20 repetitions in each scan. Therefore, the SNR efficiency for the proposed SLIDER-SMS pCASL can be expressed by

$$SNR_{SLIDER-SMS} = \sqrt{N_{set}} \times SNR_{ref,SMS} \times \sqrt{\frac{\frac{var_{physio}}{N'_{full}} + g^2_{ref,SMS} \times \frac{var_{thermal}}{N_{full}}}{\frac{var_{physio}}{N'_{meas}} + g^2_{SLIDER-SMS} \times \frac{var_{thermal}}{N_{meas}}}} \quad (4)$$

where N_{full} is the number of measurements of the reference ASL scan, N'_{full} is between 1 and N_{full} depending on the temporal

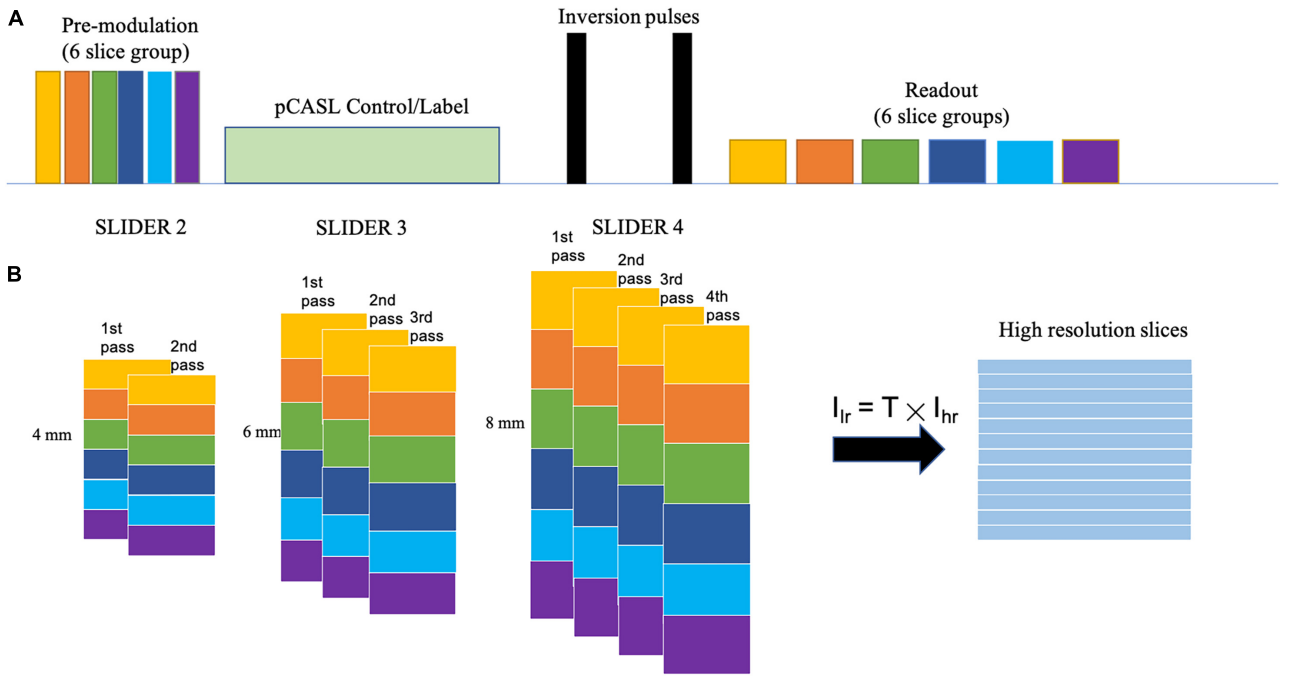

FIGURE 1 | SLIDER acquisition scheme. **(A)** SMS-EPI pCASL acquisition sequence for each set of low-resolution images, with constrained slice dependent background suppression. **(B)** Acquisition scheme for SLIDER2, SLIDER3, and SLIDER4; different numbers of scans with slice shift are needed, 2 for SLIDER2, 3 for SLIDER3, and 4 for SLIDER4. Then, high-resolution images can be reconstructed.

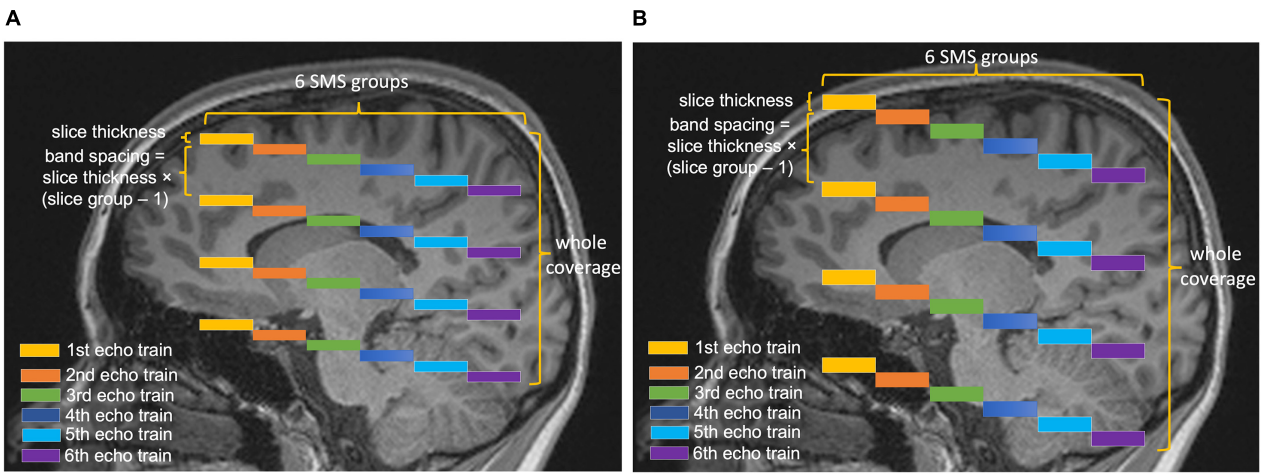

FIGURE 2 | Diagram of the SMS scheme. Six slice groups with a total slice number of 24 are acquired in each TR. The band spacing is adjusted according to the slice thickness to avoid slice cross talk. The center is aligned in different conditions, so that the slice thickness of **(A)** 4 mm and **(B)** 8 mm will have different coverages in the slice direction.

correlation of physiological noise, and $g_{ref,SMS}$ is the g-factor for the SMS acquisition of the reference ASL images. Because the coil g-factor generally decreases with larger spacing between slice groups for SMS reconstruction and physiological noise cannot be suppressed as effective as thermal noise by averaging, Eq. (4) predicts that the SNR efficiency of SLIDER ASL will increase with thicker acquired slices and a higher number of shifted slices (N_{set}). This hypothesis will be tested by *in vivo* experiment below.

The reconstruction of SLIDER acquisition can be viewed as solving an inverse problem of the following equation:

$$A \times I_{hr} = I_{lr} \quad (5)$$

where I_{lr} is the combined low-resolution images acquired, A is the forward model constructed according to the acquisition, and I_{hr} is the high-resolution images to be reconstructed. In this

study, a Toeplitz matrix was used as the forward model, which assumes a perfect slice profile, and singular value decomposition with Tikhonov regularization was used to calculate the pseudo-inversion of the A matrix (Setsompop et al., 2018).

$$I_{hr} = (A^T A + \lambda I)^{-1} A^T I_{lr} = A_{inv\_tik} I_{lr} \quad (6)$$

The regularization parameter λ was chosen between 0.1, 0.3, and 0.5 to serve as different regularization levels. A larger regularization parameter will cause less noise amplification but more spatial blurring in the reconstructed images, which will be evaluated below.

MRI Experiments

Five healthy subjects (age = 24.6 ± 1.7 years, four males) were scanned on a Siemens 3T Prisma scanner using a 32-channel head coil, after they provided written consent according to the protocol approved by the institutional review board of the University of Southern California. The imaging parameters for SLIDER-SMS pCASL included the following: in-plane resolution of 2 mm × 2 mm, field of view (FOV) of 192 mm, matrix size of 96 × 96, TR = 5,000 ms, TE = 20 ms. The MB factor was 4, and the number of slice groups was 6 with 24 total slices acquired for each TR. The acquisition of each SMS slice group took 45 ms, i.e., total 270 ms for six slice groups. Blipped CAIPI was applied to avoid voxel tilting (Setsompop et al., 2012). The labeling duration for pCASL was 1,500 ms, and the PLD was 1,800 ms. The labeling plane was placed 90 mm below the center of the most superior slice group and was adjusted in acquisitions of the shifted slices so that the labeling plane was at the same location across all the conditions. The optimized parameters for CSD-BS including the timing of the two inversion pulses were calculated according to (Shao et al., 2018). Two/three/four sets of low-resolution images with slice thickness of 4, 6, and 8 mm were acquired for SLIDER2/3/4 scans, respectively. The spacing between bands was adjusted according to the slice thickness (20, 30, and 40 mm for slice thickness of 4, 6, and 8 mm, respectively) to avoid inter-slice cross talk. A detailed SMS scheme is shown in **Figure 2**. A single-band reference scan was acquired before each of the SMS pCASL scans for SMS image reconstruction. For SLIDER2, each of the two SMS pCASL scans had 40 measurements with a duration of 6 min 45 s. For SLIDER3, each of the scan had 26 measurements and the total scan time was 4 min 35 s × 3 = 13 min 45 s. For SLIDER4, each of the scan had 20 measurements and the total scan time was 3 min 20 s × 4 = 13 min 20 s. In this way, the total scan time for each of the SLIDER methods was about 14 min. Reference ASL images were acquired by two interleaved high-resolution SMS pCASL scans (2 mm × 2 mm × 2 mm) with a 100% slice gap in each scan and, with the same background suppression parameters, were acquired as the benchmark. M0 images were acquired before each ASL scan with the same resolution. A high-resolution (iso-0.8 mm) structural MRI was acquired using a T1-weighted MPRAGE scan in each subject.

The raw k-space data of the SMS scans were processed offline using custom Matlab programs. First, raw data were corrected for N/2 phase shift caused by EPI acquisition. Second, the unaliased MB images were reconstructed using slice-GRAPPA (Setsompop et al., 2012) with a kernel size of 5 × 5 derived from the single-band references. Then, each scan was corrected for rigid head motion using SPM12[1] and combined into a full data matrix. SLIDER reconstruction was applied to achieve 2-mm isotropic M0 and perfusion images according to Eq. 6 with three different λs (0.1, 0.3, and 0.5). The numbers of 2-mm slices reconstructed were 48, 48, 72, and 96 for reference ASL and SLIDER2/3/4 scans, respectively. A principal component analysis (PCA)-based denoising algorithm (Shao et al., 2017) was further applied for both super-resolution and reference ASL scans. In our experiment, PCA reduced the overall noise level in all conditions but did not impact the comparison of super-resolution reconstructions. The spatial SNR (sSNR) and temporal SNR (tSNR) values with and without PCA denoising are listed in **Supplementary Table 1**. In addition, the g-factor maps for each SMS reconstruction of the SLIDER condition were calculated using the definition in Breuer et al. (2009) with the slice-GRAPPA kernel and the measured noise-covariance matrix.

Data Analysis

Both the reference ASL images and the reconstructed super-resolution images were evaluated by SNR in the gray matter (GM) region of interest (ROI). The GM probability map was obtained by segmentation of the MPRAGE structural images using SPM12, which was co-registered to the reference ASL M0 images. A threshold of 0.9 was applied on the probability map to obtain the GM mask. We used the definition in Feinberg et al. (2013) to calculate SNR. Even- and odd-numbered perfusion images were averaged, and then added and subtracted to generate the sum and difference images. The sSNR was calculated as the mean of the sum image divided by $1/\sqrt{2}$ of the standard deviation (SD) of the difference image within the GM ROI. This definition of SNR calculation can reduce the effect of inhomogeneous noise distribution. tSNR was calculated by the mean signal divided by the SD across time frames within the GM ROI. To evaluate the spatial blurring effect of SLIDER reconstructions, Pearson correlation coefficients of the reconstructed image volumes and the volumes shifted one slice (2 mm) down were calculated by collapsing all voxels into a vector. Furthermore, sSNR and tSNR measurements were repeated with intentionally applied spatial smoothing along slice direction on SLIDER2, 3 and reference ASL images to match the spatial blurring of SLIDER4. A nonparametric Kruskal–Wallis test with *post hoc* Wilcoxon signed-rank test was performed to compare SNR measurements between SLIDER and reference ASL scans, while two-way ANOVA and *post hoc* Wilcoxon signed-rank test were performed to compare slice blurring effects.

Pixel-wise correlations were performed between the reconstructed SLIDER images and reference ASL image within the brain mask. Difference images between the SLIDER and reference ASL images were obtained along with histograms of pixel values within the brain mask for each SLIDER condition. One sample *t*-test and Kolmogorov–Smirnov test were performed to test whether the difference images had zero mean and normal distribution, respectively.

[1] fil.ion.ucl.ac.uk/spm/software/spm12

Cerebral blood flow maps were calculated for each SLIDER and reference ASL images, respectively. Slice-dependent PLD correction was performed before quantification. Seven small brain regions (caudate, putamen, etc.) were segmented from the T1-weighted image by Freesurfer v7.1.1 and then co-registered to the M0 image of each condition. The mean CBF values were extracted from these ROIs and were compared across experimental conditions using two-way repeated measures ANOVA and *post hoc* Wilcoxon signed-rank test.

RESULTS

Slice Dithered Enhanced Resolution-Simultaneous Multi-Slice Pseudo-Continuous Arterial Spin Labeling Perfusion Images

Figure 3 shows the center 40 axial slices of the reconstructed super-resolution perfusion images with SLIDER2/3/4 and reference ASL images of a representative subject, respectively. All SLIDER reconstructions shown in **Figure 3** used a regularization parameter of $\lambda = 0.1$. The reconstructed perfusion images for SLIDER2/3/4 scans show good quality without visible artifacts and with clear contrast between gray and white matter as the reference ASL perfusion images. Scatter plots of pixel-wise correlations between the reconstructed SLIDER and reference ASL images are shown in **Supplementary Figure 1**. There were good correlations with reference ASL images in all three SLIDER conditions (0.73 for SLIDER2, 0.76 for SLIDER3, and 0.73 for SLIDER4, $p < 0.0001$). **Supplementary Figure 2** shows the difference images and associated histograms between the SLIDER and reference ASL images. The difference images had zero mean and followed normal distribution ($p > 0.05$ for all three conditions).

The zoomed slices show that the SNR of SLIDER reconstructions is higher than the reference ASL images. **Figure 4** shows the reconstructed super-resolution perfusion images in sagittal and coronal views with different regularization parameters, respectively. Using our experimental paradigm, the three SLIDER methods had different coverages in the slice direction with the largest coverage in SLIDER4 (96 slices), and narrower coverages in SLIDER3 (72 slices) and SLIDER2 (48 slices). SLIDER4 can even cover the labeling plane, as shown by the red arrow. **Figure 4** also shows that as the regularization parameter λ increases, the SNR of the perfusion image increases, but there is more spatial blurring. The full slices of SLIDER2/3/4 ASL images are shown in **Supplementary Figure 3**.

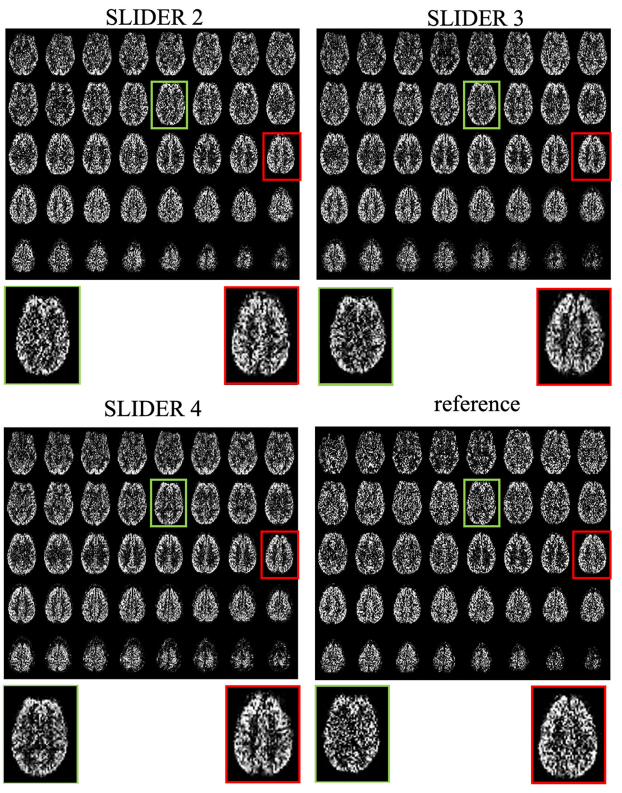

FIGURE 3 | SLIDER super-resolution reconstructed ASL images and acquired reference ASL images in the axial direction. The reconstructed images follow the reference images well, with an improved SNR. The red and green boxes and zoomed images show two slices with SNR improvement.

Signal-to-Noise Ratio Comparison Between Super-Resolution and Reference Arterial Spin Labeling

Figure 5 shows the spatial and temporal SNR values of the reconstructed images for all five subjects ($\lambda = 0.1$) (the details of each subject are included in **Table 1**). **Figure 6** shows the sSNR and tSNR map of a typical subject. The Kruskal–Wallis test showed significant differences in spatial and temporal SNR across the reconstructed super-resolution images and the reference ASL images ($p < 0.01$ for sSNR and $p < 0.005$ for tSNR). SLIDER4, 3, and 2 improved sSNR by 88, 61, and 42%, respectively, compared to the reference ASL images. TSNR was increased by 105, 55, and 18% using SLIDER4, 3, and 2, respectively, compared to reference ASL images. The trend of such SNR improvement is stable across the five subjects. *Post hoc* Wilcoxon signed-rank test showed that SLIDER can significantly improve sSNR ($p < 0.05$) and tSNR ($p < 0.01$).

The g-factor maps in the sagittal plane for the three SMS acquisitions are shown in **Supplementary Figure 4**. The mean g-factor value in the brain across five subjects for SLIDER2 is 1.28 ± 0.06, that for SLIDER3 is 1.38 ± 0.07, and that for SLIDER4 is 1.34 ± 0.06.

The calculated regional CBF values in seven small regions (including four subcortical structures and three cortical areas) of the brain are shown in **Figure 7**. The mean CBF values of SLIDER2/3/4 and reference across seven ROIs were 57.46 ± 6.89, 53.12 ± 7.57, 51.41 ± 6.74, and 56.51 ± 6.61 ml/100 g/min, respectively. Two-way ANOVA showed significant differences between these four conditions ($p < 0.0001$). The *post hoc* Wilcoxon signed-rank test showed no significant difference between SLIDER2 and reference ($p = 0.59$). There were significant

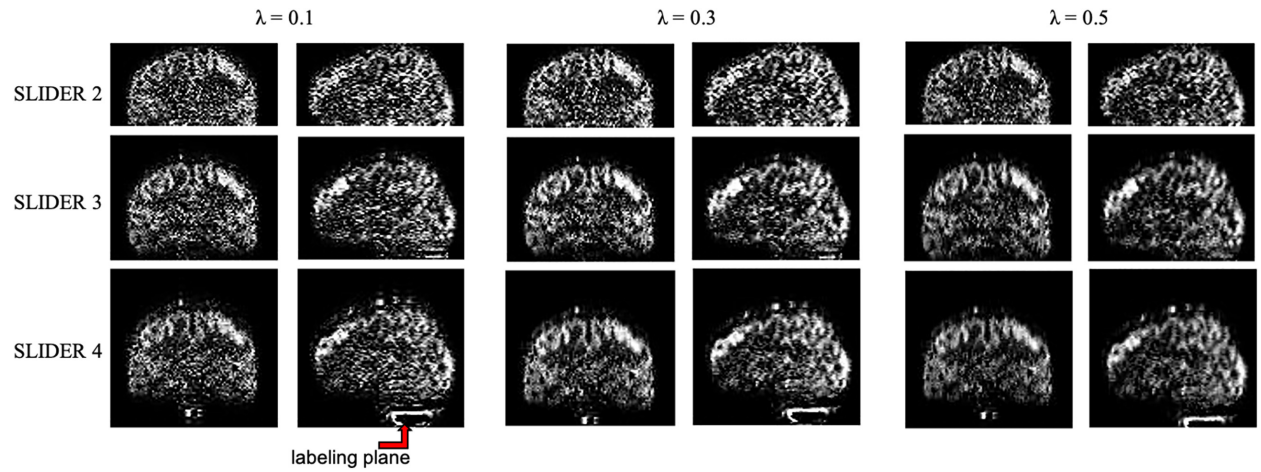

FIGURE 4 | SLIDER super-resolution reconstructed image in the sagittal and coronal direction. SLIDER2 has a brain coverage of 96 mm, SLIDER3 has a brain coverage of 144 mm, and SLIDER4 has a brain coverage of 192 mm. SLIDER4 can reach the labeling plane, as marked by the red arrow. Larger regularization parameters will lead to more spatial blurring.

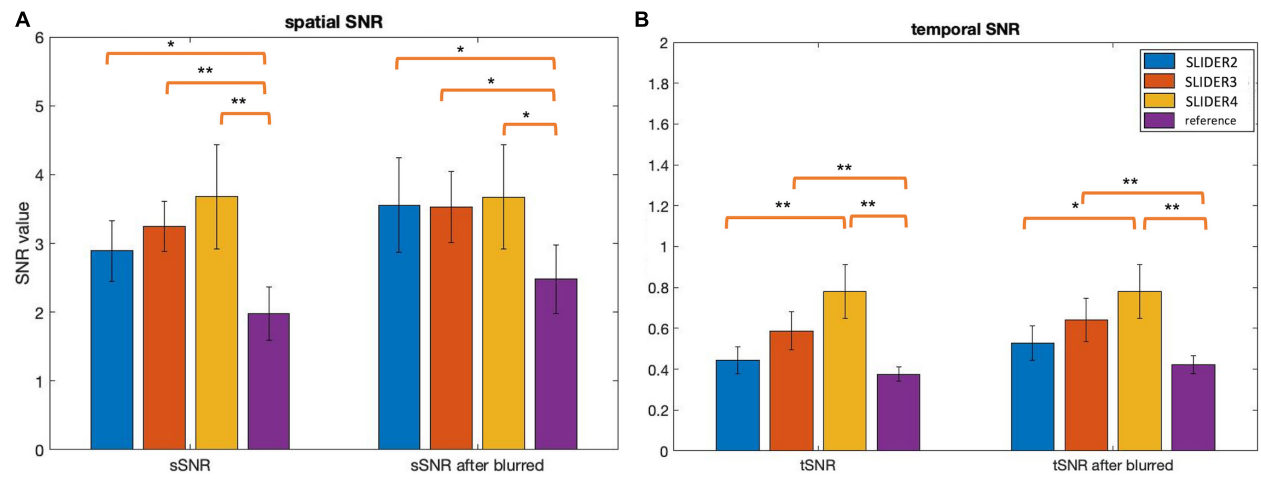

FIGURE 5 | Spatial and temporal SNR before and after controlling slice blurring. **(A)** Spatial SNR (sSNR) and **(B)** temporal SNR (tSNR) of SLIDER2/3/4 and reference scans before (left) and after applying a Gaussian kernel to control slice blurring (right). *$p < 0.05$; **$p < 0.01$. Error bars stand for standard deviation.

differences between SLIDER3/4 and reference ($p < 0.05$ for SLIDER3 and $p < 0.005$ for SLIDER4.

Spatial Blurring Evaluation

Table 2 shows the spatial blurring effect of SLIDER reconstructions, indicated by the correlation coefficient of the reconstructed image volume and the volume shifted one slice down in each subject. Two-way ANOVA showed that both SLIDER reconstructions and increased λ caused blurring in the slice direction, compared to the reference ASL images ($p < 0.0001$ for both factors). The *post hoc* Wilcoxon signed-rank test showed that SLIDER2 with the regularization parameter of λ = 0.1 had a minimum blurring effect with no statistical difference compared to the reference image ($p = 0.88$). SLIDER3 with λ = 0.1 slightly increased the slice correlation ($p < 0.05$), and SLIDER4 increased more ($p < 0.01$). The *post hoc* Wilcoxon signed-rank test also showed that the regularization parameter λ had influences on the slice blurring effects, with greater blurring effects induced by a larger regularization parameter ($p < 0.01$ was found between two λs in all SLIDER conditions).

To further investigate the relationship between spatial blurring and SNR, additional slice blurring was applied using a Gaussian kernel with the full width at half maximum (FWHM) of 1.16 voxels for SLIDER2, 1.06 voxels for SLIDER3, and 1.18 voxels for the reference ASL image along the slice direction on SLIDER2/3 and reference ASL images to match that of SLIDER4 (see **Supplementary Table 2** for burring evaluation before and after applying Gaussian kernel). **Figure 5** shows the spatial and temporal SNR before and after applying the Gaussian kernel (the details of subjects are included in **Table 1**). As shown in

TABLE 1 | Spatial and temporal SNR of the super-resolution reconstructed images and reference images for all five subjects.

	sSNR	sSNR (after blurred)	tSNR	tSNR (after blurred)
Sub1 (SLIDER2)	3.06	3.89	0.49	0.59
Sub1 (SLIDER3)	3.19	3.58	0.62	0.68
Sub1 (SLIDER4)	3.68	3.68	0.81	0.81
Sub1 (reference)	2.13	2.72	0.39	0.44
Sub2 (SLIDER2)	3.17	4.01	0.51	0.60
Sub2 (SLIDER3)	3.36	3.77	0.69	0.75
Sub2 (SLIDER4)	3.45	3.45	0.82	0.82
Sub2 (reference)	2.06	2.62	0.40	0.45
Sub3 (SLIDER2)	2.18	2.82	0.37	0.43
Sub3 (SLIDER3)	2.76	3.11	0.48	0.52
Sub3 (SLIDER4)	2.74	2.74	0.59	0.59
Sub3 (reference)	1.35	1.71	0.32	0.35
Sub4 (SLIDER2)	3.28	4.25	0.48	0.58
Sub4 (SLIDER3)	3.77	4.24	0.65	0.72
Sub4 (SLIDER4)	4.84	4.84	0.95	0.95
Sub4 (reference)	2.4	3.04	0.40	0.46
Sub5 (SLIDER2)	2.17	2.81	0.38	0.44
Sub5 (SLIDER3)	2.63	2.96	0.50	0.54
Sub5 (SLIDER4)	3.66	3.66	0.73	0.73
Sub5 (reference)	1.83	2.30	0.37	0.42
Mean ± SD (SLIDER2)	2.77 ± 0.55	3.56 ± 0.69	0.45 ± 0.07	0.53 ± 0.09
Mean ± SD (SLIDER3)	3.14 ± 0.46	3.53 ± 0.51	0.59 ± 0.10	0.64 ± 0.11
Mean ± SD (SLIDER4)	3.67 ± 0.76	3.67 ± 0.76	0.78 ± 0.13	0.78 ± 0.13
Mean ± SD (reference)	1.95 ± 0.40	2.48 ± 0.50	0.38 ± 0.03	0.42 ± 0.05

"After blurred" means additional Gaussian smoothing in the slice direction has been applied to the image to match the blurring level of SLIDER4.

Figure 5, SLIDER2/3/4 have similar sSNR after matching the level of spatial blurring, which still outperforms that of the reference ASL scan ($p < 0.001$). For tSNR, SLIDER4 still has the highest tSNR, while SLIDER3, SLIDER2, and reference scans have lower tSNR ($p < 0.01$).

DISCUSSION

Advantages of Slice Dithered Enhanced Resolution-Simultaneous Multi-Slice Arterial Spin Labeling

In this work we presented super-resolution perfusion imaging using SLIDER and SMS pCASL with an optimized CSD-BS scheme. The SLIDER-reconstructed super-resolution images had significantly higher spatial and temporal SNR compared to the reference ASL images. The results are consistent with the theoretical estimation of SNR efficiency improvements due to super-resolution acquisitions of thicker slices. Since the number of slices that can be acquired for ASL is limited by TR and T1 relaxation, using a thicker slice will result in not only higher SNR but also a larger spatial coverage in the slice direction. This is shown in **Figure 4**, where SLIDER2/3/4 had a coverage of 96, 144, and 192 mm, respectively.

In this study, SLIDER reconstruction is found to improve the spatial and temporal SNR of reference ASL images, and the SNR improvement is greater with increased number of shifted slice groups. We also controlled the total scan time (∼14 min) to be identical across the three SLIDER methods and reference ASL for a fair comparison of SNR efficiency. The calculated g-factors were similar for SLIDER2, 3, and 4 with 20, 30, and 40 band spacing, respectively, suggesting a minor role the g-factor plays in determining the SNR of SLIDER ASL techniques in our study (see Eq. 4). While thermal random noise can be effectively suppressed by averaging following the rule of square root of N measurements, physiological noise is more complex with temporal correlations at specific frequencies. Therefore, noise reduction through averaging is less effective for physiological noise than thermal noise. These factors may have contributed to a higher SNR efficiency for SLIDER reconstructions with a high number of shifted slice groups. However, we did not systematically characterize thermal and physiological noise during ASL scans which should be performed in future studies (Moeller et al., 2006).

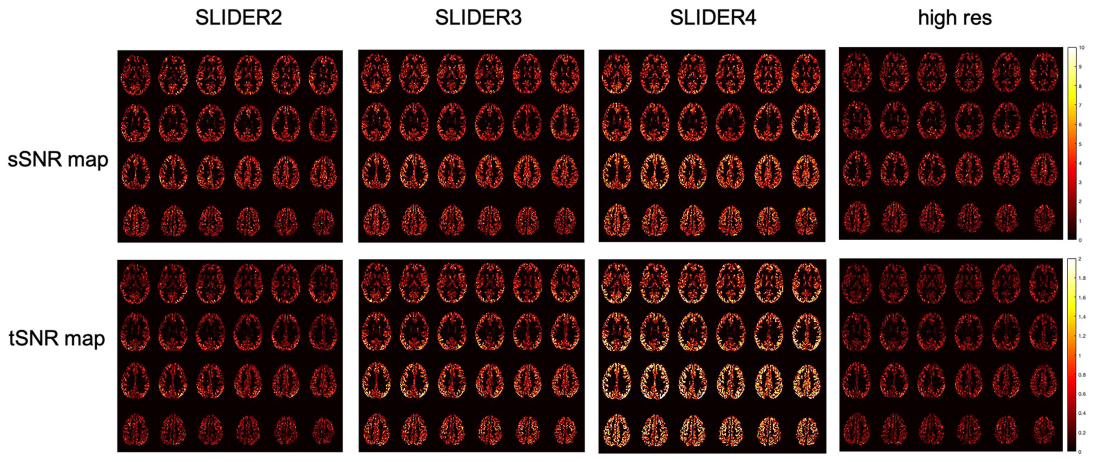

FIGURE 6 | Spatial SNR (sSNR) map and temporal SNR (tSNR) map of a representative subject in different SLIDER conditions and reference ASL scan.

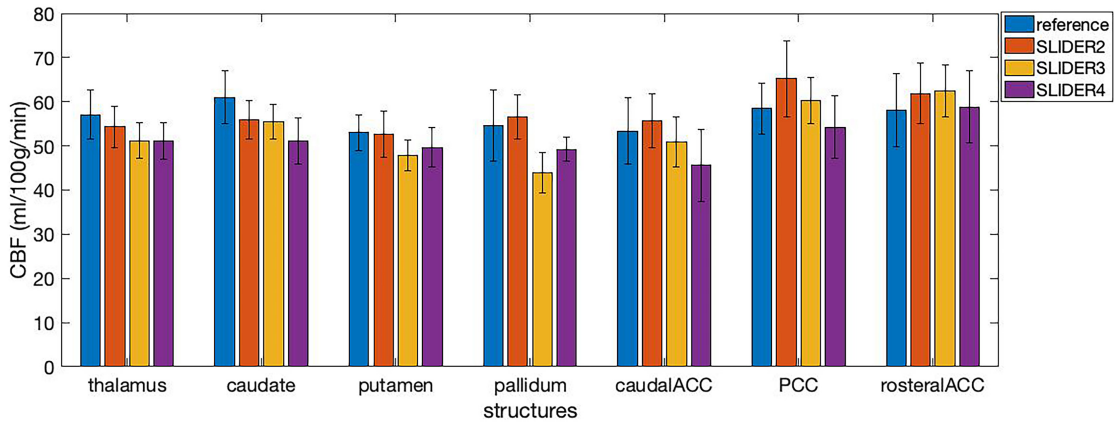

FIGURE 7 | Cerebral blood flow values in seven small brain structures acquired under different SLIDER and reference conditions. ACC, anterior cingulate cortex; PCC, posterior cingulate cortex. Error bars stand for stand deviation.

TABLE 2 | Slice blurring evaluation using autocorrelation of the reconstructed volume.

Correlation	SLIDER2 λ = 0.1	SLIDER2 λ = 0.3	SLIDER2 λ = 0.5	SLIDER3 λ = 0.1	SLIDER3 λ = 0.3	SLIDER3 λ = 0.5	SLIDER4 λ = 0.1	SLIDER4 λ = 0.3	SLIDER4 λ = 0.5	Reference ASL
Sub1	0.40	0.60	0.67	0.48	0.71	0.78	0.59	0.81	0.86	0.42
Sub2	0.41	0.55	0.62	0.51	0.72	0.78	0.63	0.82	0.87	0.41
Sub3	0.33	0.57	0.65	0.45	0.73	0.8	0.47	0.77	0.84	0.24
Sub4	0.43	0.64	0.7	0.55	0.78	0.84	0.64	0.85	0.9	0.40
Sub5	0.25	0.51	0.59	0.37	0.67	0.76	0.52	0.79	0.86	0.32
Mean ± SD	0.36 ± 0.07	0.57 ± 0.05	0.65 ± 0.04	0.47 ± 0.07	0.72 ± 0.04	0.80 ± 0.03	0.57 ± 0.07	0.81 ± 0.03	0.87 ± 0.02	0.36 ± 0.08

λ is the regularization parameter used in SLIDER reconstruction.

One advantage of the proposed SLIDER4 ASL technique is its wide coverage of 192 mm in the slice direction. There are some potential applications that may take advantage of such large coverage. For example, the labeling plane can be visualized with this method in coronal and sagittal images, which is not available for most of the ASL scans. In addition, B0 field inhomogeneity may distort the labeling plane; therefore, there is value to directly visualize the labeling plane. On the other hand, such large coverage would potentially allow measurement of perfusion in deep brain structures such as the brain stem, cerebellum, and even the spinal cord. These deep brain structures are key hubs of the structural and functional networks of the human brain, but so far very few perfusion measurements have been performed in these key deep brain structures.

Spatial Blurring of Slice Dithered Enhanced Resolution-Simultaneous Multi-Slice Arterial Spin Labeling

The spatial blurring effect should be taken into consideration when evaluating the results. **Table 2** shows that SLIDER reconstructions resulted in a small degree of slice blurring which increased with a greater number of shifted slice groups. A larger regularization parameter λ also caused a greater degree of slice blurring and reduced slice resolution as well as data fidelity. When additional slice blurring was applied, the improvement of sSNR of all the three SLIDER methods reached a similar level. For tSNR, however, SLIDER4 remained superior to SLIDER2/3 with matched slice blurring. This is because tSNR is prone to be affected by temporal fluctuation such as physiological noise while spatial blurring has more impact on sSNR. In a previous study on SLIDER, the authors suggested using λ∼0.1 which will not cause much blurring effect (Setsompop et al., 2015). Based on our experience, we also recommend the use of λ∼0.1 for SLIDER ASL as a tradeoff between imaging resolution and SNR.

Supplementary Figure 5 shows American College of Radiology (ACR) phantom images reconstructed with SLIDER2/3/4 (λ = 0.1) in comparison with reference phantom images. A small degree of spatial blurring can be observed in SLIDER3/4 reconstructed phantom images, which is consistent with our *in vivo* results on SLIDER ASL. From the quantitative CBF results in seven small brain structures, we found that the mean CBF values were reduced using SLIDER3/4 compared to the reference scan, likely due to blurring effects of SLIDER3/4 reconstructions. Although there was no significant difference between SLIDER2 and reference, the small sample size of our study may be a factor. Therefore, we recommend caution on quantifying and controlling blurring effects of SLIDER reconstruction for CBF quantification using the proposed SLIDER ASL method.

Limitations of Slice Dithered Enhanced Resolution-Simultaneous Multi-Slice Arterial Spin Labeling

There are several limitations of our study. First, as a pilot study our sample size is small. There are some restrictions with the imaging protocol, e.g., there was no slice gap applied as the SLIDER reconstruction requires overlapping thick slices to resolve the thin slices. This may potentially induce slice cross talk and saturation effects. An alternative approach to solve this problem would be to improve the slice profile with longer RF duration or using Shinnar–Le-Roux (SLR) pulse design (Setsompop et al., 2018). We only acquired six MB slice groups within a TR in all of ASL scans, resulting in two passes for the reference high-resolution ASL scan. The main reason is that the efficiency of the CSD-BS scheme for suppressing background signals will decrease with more MB slice groups. Also, the total scan time of our method is around 14 min, making it susceptible to motion artifacts. This problem could be addressed with advanced imaging acceleration methods and image denoising methods such as deep learning (Xie et al., 2020). We also acknowledge that absolute CBF quantification using the proposed SLIDER ASL method awaits further validation since we observed variations in CBF across scan conditions in small brain structures. We also notice that MB factors higher than 4 can be used for larger number of slices and alternative methods for SNR calculation such bootstrapping (Riffe et al., 2007).

Future Directions

In this work, we utilized SLIDER for the super-resolution reconstruction of ASL images to achieve isotropic-2-mm resolution perfusion images. Other more advanced super-resolution techniques such as gSLIDER (Setsompop et al., 2018) have been proposed for diffusion MRI. gSLIDER uses Hadamard encoding to achieve orthogonal basis; therefore, no regularization is needed for image reconstruction. For ASL, SLIDER SMS offers the technical simplicity and advantage for rapidly acquiring whole-brain images. The comparison of SLIDER and gSLIDER ASL may be included in future works. Further studies may also compare SLIDER reconstruction with high-resolution 3D ASL acquisitions, since 3D data tend to have higher SNR with larger FOV but with more slice blurring (FWHM on the order of 1.5 voxel size) (Vidorreta et al., 2014).

CONCLUSION

We presented super-resolution perfusion imaging using SLIDER with 2D SMS pCASL. In conjunction with optimized CSD-BS, this technique can push the resolution of whole-brain ASL imaging to isotropic-2 mm and higher for fine-grained studies on brain perfusion. Caution needs to be exercised on quantifying and controlling blurring effects of SLIDER reconstruction.

DATA AVAILABILITY STATEMENT

The raw data supporting the conclusions of this article will be made available by the authors, without undue reservation.

ETHICS STATEMENT

The studies involving human participants were reviewed and approved by the Institutional Review Board of the University of Southern California. The patients/participants provided their written informed consent to participate in this study.

AUTHOR CONTRIBUTIONS

QS designed the experiments and conducted data processing and analysis. XS helped with data processing and provided support for improvements on experiments. DW designed and supervised the experiments. All authors drafted the manuscript.

FUNDING

This work was supported by the National Institute of Health (NIH) grant UH3-NS100614, R01-NS114382, and R01-EB028297.

SUPPLEMENTARY MATERIAL

The Supplementary Material for this article can be found online at: https://www.frontiersin.org/articles/10.3389/fnins.2021.737525/full#supplementary-material

REFERENCES

Alsop, D. C., Detre, J. A., Golay, X., Guenther, M., Hendrikse, J., Hernandez-Garcia, L., et al. (2015). Recommended implementation of arterial spin-labeled perfusion MRI for clinical applications: a consensus of the ISMRM perfusion study group and the European consortium for ASL in dementia. *Magn. Reson. Med.* 73, 102–116. doi: 10.1002/mrm.25197

Ben-Eliezer, N., Irani, M., and Frydman, L. (2010). Super-resolved spatially encoded single-scan 2D MRI. *Magn. Reson. Med. Off. J. Int. Soc. Magn. Reson. Med.* 63, 1594–1600. doi: 10.1002/mrm.22377

Breuer, F. A., Kannengiesser, S. A., Blaimer, M., Seiberlich, N., Jakob, P. M., and Griswold, M. A. (2009). General formulation for quantitative G-factor calculation in GRAPPA reconstructions. *Magn. Reson. Med.* 62, 739–746. doi: 10.1002/mrm.22066

Feinberg, D. A., Beckett, A., and Chen, L. (2013). Arterial spin labeling with simultaneous multi-slice echo planar imaging. *Magn. Reson. Med.* 70, 1500–1506. doi: 10.1002/mrm.24994

Feinberg, D. A., Moeller, S., Smith, S. M., Auerbach, E., Ramanna, S., Gunther, M., et al. (2010). Multiplexed echo planar imaging for sub-second whole brain FMRI and fast diffusion imaging. *PLoS One* 5:e15710. doi: 10.1371/journal.pone.0015710

Greenspan, H., Oz, G., Kiryati, N., and Peled, S. (2002). MRI inter-slice reconstruction using super-resolution. *Magn. Reson. Imaging* 20, 437–446. doi: 10.1016/S0730-725X(02)00511-8

Kim, T., Shin, W., Zhao, T., Beall, E. B., Lowe, M. J., and Bae, K. T. (2013). Whole brain perfusion measurements using arterial spin labeling with multiband acquisition. *Magn. Reson. Med.* 70, 1653–1661. doi: 10.1002/mrm.24880

Li, X., Wang, D., Auerbach, E. J., Moeller, S., Ugurbil, K., and Metzger, G. J. (2015). Theoretical and experimental evaluation of multi-band EPI for high-resolution whole brain pCASL imaging. *Neuroimage* 106, 170–181. doi: 10.1016/j.neuroimage.2014.10.029

Moeller, S., Van de Moortele, P. F., Goerke, U., Adriany, G., and Ugurbil, K. (2006). Application of parallel imaging to fMRI at 7 Tesla utilizing a high 1D reduction factor. *Magn. Reson. Med. Off. J. Int. Soc. Magn. Reson. Med.* 56, 118–129. doi: 10.1002/mrm.20934

Riffe, M. J., Blaimer, M., Barkauskas, K. J., Duerk, J. L., and Griswold, M. A. (2007). SNR estimation in fast dynamic imaging using bootstrapped statistics. *Proc. Intl. Soc. Mag. Reson. Med.* 16:1879. doi: <doi>

Setsompop, K., Bilgic, B., Nummenmaa, A., Fan, Q., Cauley, S., Huang, S., et al. (2015). SLIce dithered enhanced resolution simultaneous multislice (SLIDER-SMS) for high resolution (700 um) diffusion imaging of the human brain. *Proc. ISMRM* 24:339. doi: <doi>

Setsompop, K., Fan, Q., Stockmann, J., Bilgic, B., Huang, S., Cauley, S. F., et al. (2018). High-resolution in vivo diffusion imaging of the human brain with generalized slice dithered enhanced resolution: simultaneous multislice (gSlider-SMS). *Magn. Reson. Med.* 79, 141–151. doi: 10.1002/mrm.26653

Setsompop, K., Gagoski, B. A., Polimeni, J. R., Witzel, T., Wedeen, V. J., and Wald, L. L. (2012). Blipped-controlled aliasing in parallel imaging for simultaneous multislice echo planar imaging with reduced g-factor penalty. *Magn. Reson. Med.* 67, 1210–1224. doi: 10.1002/mrm.23097

Shao, X., Tisdall, M. D., Wang, D. J., and van der Kouwe, A. J. W. (2017). Prospective motion correction for 3D GRASE pCASL with volumetric navigators. *Proc. ISMRM* 25:680. doi: <doi>

Shao, X., Wang, Y., Moeller, S., and Wang, D. J. J. (2018). A constrained slice-dependent background suppression scheme for simultaneous multislice pseudo-continuous arterial spin labeling. *Magn. Reson. Med.* 79, 394–400. doi: 10.1002/mrm.26643

Vidorreta, M., Balteau, E., Wang, Z., De Vita, E., Pastor, M. A., Thomas, D. L., et al. (2014). Evaluation of segmented 3D acquisition schemes for whole-brain high-resolution arterial spin labeling at 3 T. *NMR Biomed.* 27, 1387–1396. doi: 10.1002/nbm.3201

Vu, A. T., Beckett, A., Setsompop, K., and Feinberg, D. A. (2018). Evaluation of SLIce dithered enhanced resolution simultaneous multislice (SLIDER-SMS) for human fMRI. *Neuroimage* 164, 164–171. doi: 10.1016/j.neuroimage.2017.02.001

Wang, Y., Moeller, S., Li, X., Vu, A. T., Krasileva, K., Ugurbil, K., et al. (2015). Simultaneous multi-slice turbo-FLASH imaging with CAIPIRINHA for whole brain distortion-free pseudo-continuous arterial spin labeling at 3 and 7 T. *Neuroimage* 113, 279–288. doi: 10.1016/j.neuroimage.2015.03.060

Xie, D., Li, H., Yang, H., Bai, L., Wang, T., Zhou, F., et al. (2020). Denoising arterial spin labeling perfusion MRI with deep machine learning. *Magn. Reson. Imaging* 68, 95–105. doi: 10.1016/j.mri.2020.01.005

Conflict of Interest: The authors declare that the research was conducted in the absence of any commercial or financial relationships that could be construed as a potential conflict of interest.

Publisher's Note: All claims expressed in this article are solely those of the authors and do not necessarily represent those of their affiliated organizations, or those of the publisher, the editors and the reviewers. Any product that may be evaluated in this article, or claim that may be made by its manufacturer, is not guaranteed or endorsed by the publisher.

frontiers in Neuroscience

BRIEF RESEARCH REPORT
published: 18 November 2021
doi: 10.3389/fnins.2021.759806

Risk Factors for Pericallosal Artery Aneurysm Rupture Based on Morphological Computer-Assisted Semiautomated Measurement and Hemodynamic Analysis

Xiaodong Zhai[1,2], Jiewen Geng[1,2], Chengcheng Zhu[3], Jiaxing Yu[1,2], Chuanjie Li[1,2,4], Nan Jiang[1,2], Sishi Xiang[1,2], Gang Fang[5], Peng Hu[1,2] and Hongqi Zhang[1,2]**

[1] Department of Neurosurgery, Xuanwu Hospital, Capital Medical University, Beijing, China, [2] China International Neuroscience Institute, Beijing, China, [3] Department of Radiology, University of Washington School of Medicine, Seattle, WA, United States, [4] Department of Neurosurgery, Shunyi District Hospital, Beijing, China, [5] Department of R&D, UnionStrong (Beijing) Technology Co., Ltd., Beijing, China

OPEN ACCESS

Edited by:
Mojtaba Kordestani,
University of Windsor, Canada

Reviewed by:
Milad Moradi Heydarloo,
University of Windsor, Canada
Milad Rezamand,
University of Windsor, Canada
Alireza Mirzaee,
Islamic Azad University, Dariun Branch, Iran

***Correspondence:**
Peng Hu
doctor_hupeng@163.com
Hongqi Zhang
xwzhanghq@163.com

Specialty section:
This article was submitted to Brain Imaging Methods, a section of the journal Frontiers in Neuroscience

Received: 17 August 2021
Accepted: 29 October 2021
Published: 18 November 2021

Citation:
Zhai X, Geng J, Zhu C, Yu J, Li C, Jiang N, Xiang S, Fang G, Hu P and Zhang H (2021) Risk Factors for Pericallosal Artery Aneurysm Rupture Based on Morphological Computer-Assisted Semiautomated Measurement and Hemodynamic Analysis. Front. Neurosci. 15:759806. doi: 10.3389/fnins.2021.759806

Background: Although pericallosal artery aneurysms (PAAs) are relatively uncommon, accounting for only 1–9% of all intracranial aneurysms (IAs), they exhibit a considerably high propensity to rupture. Nevertheless, our current knowledge of the risk factors for PAA rupture is still very limited. To fill this gap, we investigated rupture risk factors for PAAs based on morphological computer-assisted semiautomated measurement (CASAM) and hemodynamic analysis.

Methods: Patients with PAAs were selected from the IA database in our institute and their baseline data were collected. Morphological parameters were measured in all enrolled patients by applying CASAM. Computational fluid dynamics simulation (CFD) was performed to evaluate the hemodynamic difference between ruptured and unruptured PAAs.

Results: From June 2017 to June 2020, among 2141 patients with IAs in our institute, 47 had PAAs (2.2%). Thirty-one patients (mean age 57.65 ± 9.97 years) with 32 PAAs (20 unruptured and 12 ruptured) were included in the final analysis. Comparing with unruptured PAAs, ruptured PAAs had significantly higher aspect ratio (AR), mean normalized wall shear stress (NWSS), and mean oscillatory shear index (OSI) values than the unruptured PAAs (all $P < 0.05$) in univariate analyses. Multivariable analysis showed that a high mean OSI was an independent risk factor for PAA rupture (OR = 6.45, 95% CI 1.37–30.32, $P = 0.018$).

Conclusion: This preliminary study indicates that there are morphological and hemodynamic differences between ruptured and unruptured PAAs. In particular, a high mean OSI is an independent risk factor for PAA rupture. Further research with a larger sample size is warranted in the future.

Keywords: intracranial aneurysm, pericallosal artery aneurysm, risk of rupture, morphology parameters, hemodynamic analysis

INTRODUCTION

Pericallosal artery aneurysms (PAAs), also known as distal anterior cerebral artery (DACA) aneurysms, are defined as intracranial aneurysms (IAs) located on the anterior cerebral artery (ACA) distal to the anterior communicating artery (Dinc et al., 2017; Petr et al., 2017). Aneurysm rupture lead to subarachnoid hemorrhage (SAH), a devastating condition with a high mortality rate of 30–40% (Morita et al., 2012; Li et al., 2013; Molyneux et al., 2015). Despite accounting for only a small percentage (1–9%) of all IAs, PAAs merit special attention due to their considerably high propensity to rupture (Lehecka et al., 2008b; Gross et al., 2014; Thompson et al., 2015; Korja et al., 2017). Multiple previous studies have reported that the odds ratio for a proportion of ruptured PAAs compared with IAs at all other locations is in the range of 2.5–4.7, indicating the higher rupture risk of PAAs (Weir et al., 2002; Bijlenga et al., 2013; Gross et al., 2014). Therefore, identifying high-rupture-risk PAAs and subsequently providing selective therapy are of critical importance to these patients.

Unfortunately, knowledge of the risk factors of PAAs for rupture remains limited due to the rarity of these lesions. Previous studies demonstrated that certain morphological parameters, e.g., aneurysm diameter, aspect ratio (AR), size ratio (SR), and irregular shape, are highly correlated with IA rupture (Ryu et al., 2011; Kashiwazaki et al., 2013; Greving et al., 2014; Wang et al., 2021). Degenerative remodeling of the artery wall caused by abnormal hemodynamics is believed to play an important role in the progression and rupture of IAs (Meng et al., 2007, 2014; Kulcsar et al., 2011; Tanaka et al., 2018). Thus, rupture risk evaluation based on morphological and hemodynamic parameters is critical for the identification of patients with PAAs at high risk for rupture.

We previously reported our initial experiences of morphological risk factor analysis for PAAs based on manual morphological measurements, which provided a solid basis for further exploration (Zhai et al., 2020). The present study goes a step further by providing a more detailed analysis of rupture risk factors for PAAs based on more advanced morphological computer-assisted semiautomated measurement (CASAM) and hemodynamic analysis.

MATERIALS AND METHODS

Patient Selection

We retrospectively reviewed our prospectively collected database of 2141 consecutive patients with IAs who underwent microsurgery or interventional therapy between June 2017 and June 2020. Traumatic, dissecting, and fusiform aneurysms were excluded prior to the initial screening. Of those patients, 47 had PAAs, accounting for 2.20% of the 2141 patients with IAs. Of the 47 patients with PAAs, 16 had two-dimensional (2D) digital subtraction angiography (DSA) data only, which did not fulfill the requirements of CASAM and hemodynamic analysis. Therefore, the present analysis included the remaining 31 patients with 32 PAAs (20 unruptured and 12 ruptured) who underwent three-dimensional (3D) DSA in the final analysis. Baseline and clinical patient data were collected from the medical records and the aneurysm database.

Computer-Assisted Semiautomated Measurement

The morphological parameters were measured in all enrolled patients with 3D DSA data using CASAM, the methodology for which was presented in detail in our previous report (Geng et al., 2020). As shown in **Figure 1**, the main steps followed in the CASAM procedure are as follows: (1) importing of original DSA tomographic data (**Figure 1A**); (2) 3D blood vessel reconstruction (**Figure 1B**); (3) manual selection of the region of interest (ROI) of the vessel where the aneurysm is located (**Figure 1C**); (4) automated extraction of the centerline and segmentation of the aneurysm (**Figure 1D**); and (5) computer-assisted automated measurement of 3D morphological parameters and exportation of all parameters (**Figures 1E–H**). CASAM enabled us to acquire the following morphological and derived parameters: (1) diameter (D): the maximum distance from the center of aneurysm neck to a point on the sac; (2) neck width (N): the maximum diameter in the neck plane; (3) width (W): the maximum distance between two points in the aneurysm sac perpendicular to the diameter of the aneurysm; (4) height (H): the maximum distance from the plane of the neck to the surface of the aneurysm; (5) flow angle (FA): the angle between the direction of blood flow and the diameter of the aneurysm; (6) parent artery diameter (PA): the mean diameter of parent artery between 3.0 cm upstream of the neck and 3.0 cm downstream; (7) AR: the ratio of the diameter of the aneurysm to the width of the aneurysm neck, AR = D/N; (8) SR: the ratio of the diameter of the aneurysm to the diameter of the parent artery, SR = D/PA; and (9) D/W: the ratio of the diameter to the width of the aneurysm. All CASAM procedures were completed by one experienced neurointerventionist due to the perfect interclass consistency of CASAM. Aneurysms with irregular shape, defined as having lobular or daughter sacs, was identified by two experienced neuroradiologists according to a previous study (Lindgren et al., 2016). If there was any disagreement, it was resolved by a third reader with 25 years of experience in neurovascular imaging.

Image Reconstruction and Computational Fluid Dynamics Modeling

For this study, pre-treatment patient-specific 3D-DSA data of all PAAs were obtained. The methods for image reconstruction and computational fluid dynamics simulation (CFD) simulation of hemodynamic studies were detailed in our previous publications (Hu et al., 2015a,b; Qin et al., 2017). Firstly, 3D models were generated with Raw DICOM format images and processed using Mimics medical software (Version 19.0, Materialise, Leuven, Belgium) and Geomagic Studio version 12.0 (Geomagic Inc., Cary, NC, United States), saved as standard tessellation language format as the input for the next step (Qin et al., 2017; Liu et al., 2021).

Each patient-specific 3D model was subdivided into the aneurysm sac and parent artery regions before meshing.

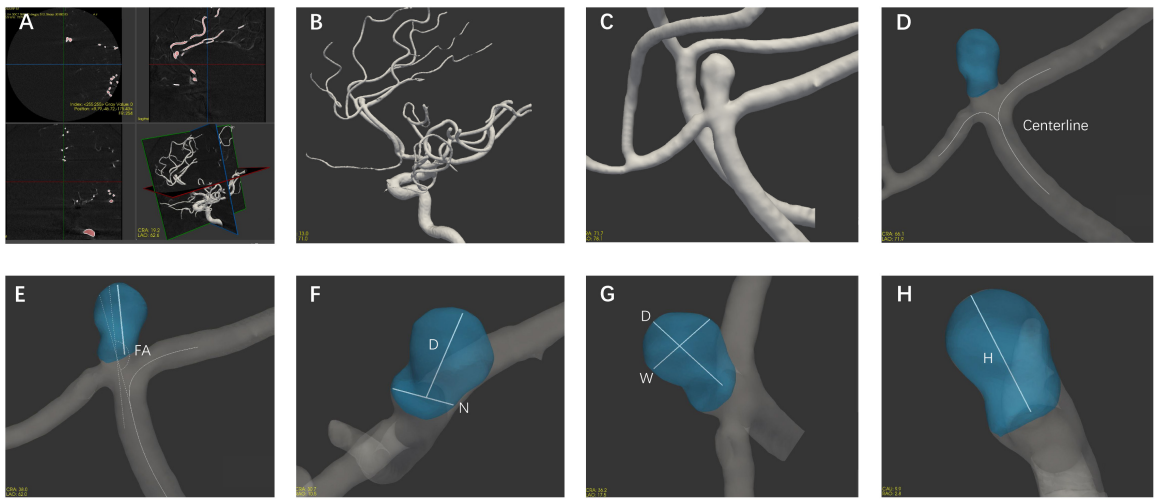

FIGURE 1 | Flow chart of the CASAM method for measuring the morphological parameters of aneurysms. **(A)** Import of original data; **(B)** 3D vessel reconstruction; **(C)** selection of region of interest; **(D)** segmentation of aneurysm using centerline method; and **(E–H)** measurement of morphological parameters of aneurysm and export of all parameters. D, diameter; N, neck width; W, width; H, height; FA, flow angle; PA, parent artery diameter.

TABLE 1 | Baseline and morphological characteristics of the included patients and aneurysms.

Variable		Unruptured (*n* = 19 Patients; *n* = 20 aneurysms)	Ruptured (*n* = 12 Patients; *n* = 12 aneurysms)	*P*-value
Age		57.37 ± 5.6	58.08 ± 14.81	0.875
Gender	Male	5 (26.3%)	5 (41.7%)	0.620
	Female	14 (73.7%)	7 (58.3%)	
Hypertension		13 (68.4%)	10 (83.3%)	0.433
Heart disease		1 (5.3%)	2 (16.7%)	0.543
Irregular shape		6 (30.0%)	7 (58.3%)	0.227
Location	Side wall	4 (20.0%)	2 (16.7%)	0.99
	Bifurcation	16 (80.0%)	10 (83.3%)	
Side	Left	9 (45.0%)	7 (58.3%)	0.716
	Right	11 (55.0%)	5 (41.7%)	
Multiple aneurysms		11 (55.0%)	6 (50.0%)	0.990
Located in anterior A3		12 (60.0%)	7 (58.3%)	0.99
Diameter (mm)		3.38 ± 2.18	3.77 ± 1.98	0.619
Width (mm)		3.77 ± 1.68	3.6 ± 1.33	0.771
Height (mm)		2.84 ± 1.51	2.96 ± 1.78	0.843
Neck (mm)		4.14 ± 2.38	3.26 ± 0.78	0.223
Flow angle (°)		126.07 ± 24.26	121.34 ± 40.55	0.681
PA		1.93 ± 0.44	1.65 ± 0.48	0.105
SR		1.87 ± 1.28	2.43 ± 1.51	0.272
AR		0.82 ± 0.33	1.15 ± 0.57	0.045
D/W		0.87 ± 0.33	1.04 ± 0.32	0.181

As defined in previous studies, the anterior A3 site is located at the bifurcation of the callosomarginal artery in the A3 segment (Lehecka et al., 2008a,b). PA, parent artery diameter; AR, aspect ratio; SR, size ratio; D/W, diameter/width.

TABLE 2 | Hemodynamic parameters of the ruptured and unruptured PAA groups.

Variable	Unruptured (*n* = 20 aneurysms)	Ruptured (*n* = 12 aneurysms)	*P*-value
Maximum CHP	0.7105 ± 0.1457	0.7574 ± 0.1274	0.364
Minimum CHP	0.0025 ± 0.0025	0.0021 ± 0.0017	0.677
Mean CHP	0.1376 ± 0.0863	0.1702 ± 0.0805	0.298
LSA ratio	0.1522 ± 0.2503	0.3009 ± 0.3508	0.172
Maximum NP	1.768 ± 0.595	1.7205 ± 0.4972	0.818
Minimum NP	0.7974 ± 0.182	0.8974 ± 0.3714	0.314
Mean NP	1.2419 ± 0.2256	1.2968 ± 0.1703	0.474
Maximum NWSS	4.2334 ± 2.6437	3.3775 ± 1.9244	0.338
Minimum NWSS	0.0874 ± 0.1233	0.0354 ± 0.0469	0.102
Mean NWSS	0.8427 ± 0.5945	0.4221 ± 0.2955	0.012
Maximum OSI	0.2518 ± 0.122	0.309 ± 0.0927	0.173
Minimum OSI	0.0002 ± 0.0001	0.0002 ± 0.0001	0.981
Mean OSI	0.0082 ± 0.0046	0.0186 ± 0.0148	0.035
Maximum RRT	6.8361 ± 12.3628	23.5218 ± 51.7724	0.294
Minimum RRT	0.0068 ± 0.0052	0.0092 ± 0.0143	0.587
Mean RRT	0.2572 ± 0.6068	0.4791 ± 1.0488	0.452
Maximum WSSG	5772.4965 ± 5047.1299	7295.3502 ± 4775.8222	0.406
Minimum WSSG	10.6517 ± 14.4013	5.0299 ± 6.1093	0.211
Mean WSSG	525.0274 ± 353.7077	559.3032 ± 620.3051	0.843

NWSS, normalized wall shear stress; NP, normalized pressure; OSI, oscillatory shear index; WSSG, wall shear stress gradient; LSA, low-shear area; CHP, combined hemodynamic parameter; RRT, relative residence time.

Parent artery was defined as a 20-mm long segment of vessel surrounding the aneurysm sac. Then, the geometry of each 3D model was imported into ICEM CFD software (ANSYS Inc., Canonsburg, PA, United States). Different mesh sizes were set for different parts. For the inlet, outlet, and sac, we chose a mesh size of 0.1 mm, which is appropriate for aneurysms in the typical size range; for the parent artery, we used a mesh size of 0.3 mm.

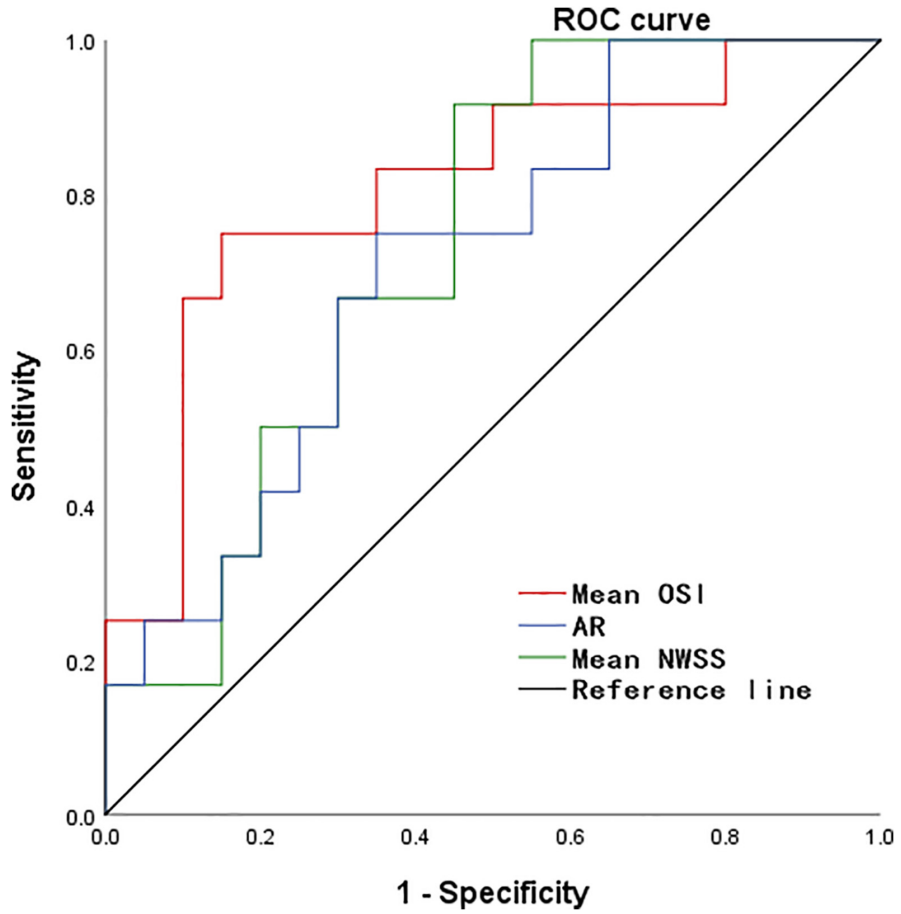

FIGURE 2 | The ROC curve for predicting PAA rupture. ROC, receiver operating characteristic, NWSS, normalized wall shear stress; OSI, oscillatory shear index; AR, aspect ratio.

The total number of finite-volume tetrahedral grid elements was approximately 1 million, and four layers of prism elements were used for the CFD simulations. The elements number was set based on grid-independence analysis to obtain high quality simulation results. The Navier–Stokes equations were the governing equations employed in the current study.

After meshing, ANSYS CFX 18.0 (ANSYS Inc.) was used for hemodynamic simulation. For the model, blood was assumed to be a Newtonian fluid with a density of 1060 kg/m^3 and a dynamic viscosity of 0.0035 N s/m^2. The vessel wall was assumed to be rigid with a no-slip boundary. Because the patient-specific boundary conditions were not available, the inflow boundary condition was a representative pulsatile velocity profile obtained from the average normal human (Ford et al., 2005). A traction-free boundary condition was applied to all outlets (Cebral et al., 2005). Initial pressure and velocity were set to zero. Three cardiac cycles were simulated to minimize transient numerical errors. The results from the third simulated cardiac cycle were collected as output for the final analyses. Validation of these methods (consistency, reliability) has been demonstrated in our previous publication (Hu et al., 2015a,b). A flowchart demonstrating an outline of the image reconstruction and CFD procedures is included in **Supplementary Figure 1**.

Hemodynamic Analysis

Several common and important hemodynamic parameters were quantified and used to characterize the hemodynamics of IAs. Normalized wall shear stress (NWSS) and normalized pressure (NP), defined as the WSS and pressure of the aneurysm wall divided by that of the parent artery wall, respectively, were calculated to allow comparisons among different patients (Jou et al., 2008; Yuan et al., 2020). The wall shear stress gradient (WSSG) was calculated based on the simulated pulsatile flow simulations (Hu et al., 2015a,b). The oscillatory shear index (OSI) is a non-dimensional parameter that is defined as the directional change in WSS during the cardiac cycle (Soldozy et al., 2019). The combined hemodynamic parameter (CHP) can be defined as a weighted average of the WSS and OSI so that each hemodynamic parameter contributes proportionately to the final CHP (Cho et al., 2018). The relative residence time (RRT) is a marker of disturbed blood flow, that incorporates particle variability during the cardiac cycle (Riccardello et al., 2018). Ultimately, hemodynamic parameters, including NWSS, NP, WSSG, CHP,

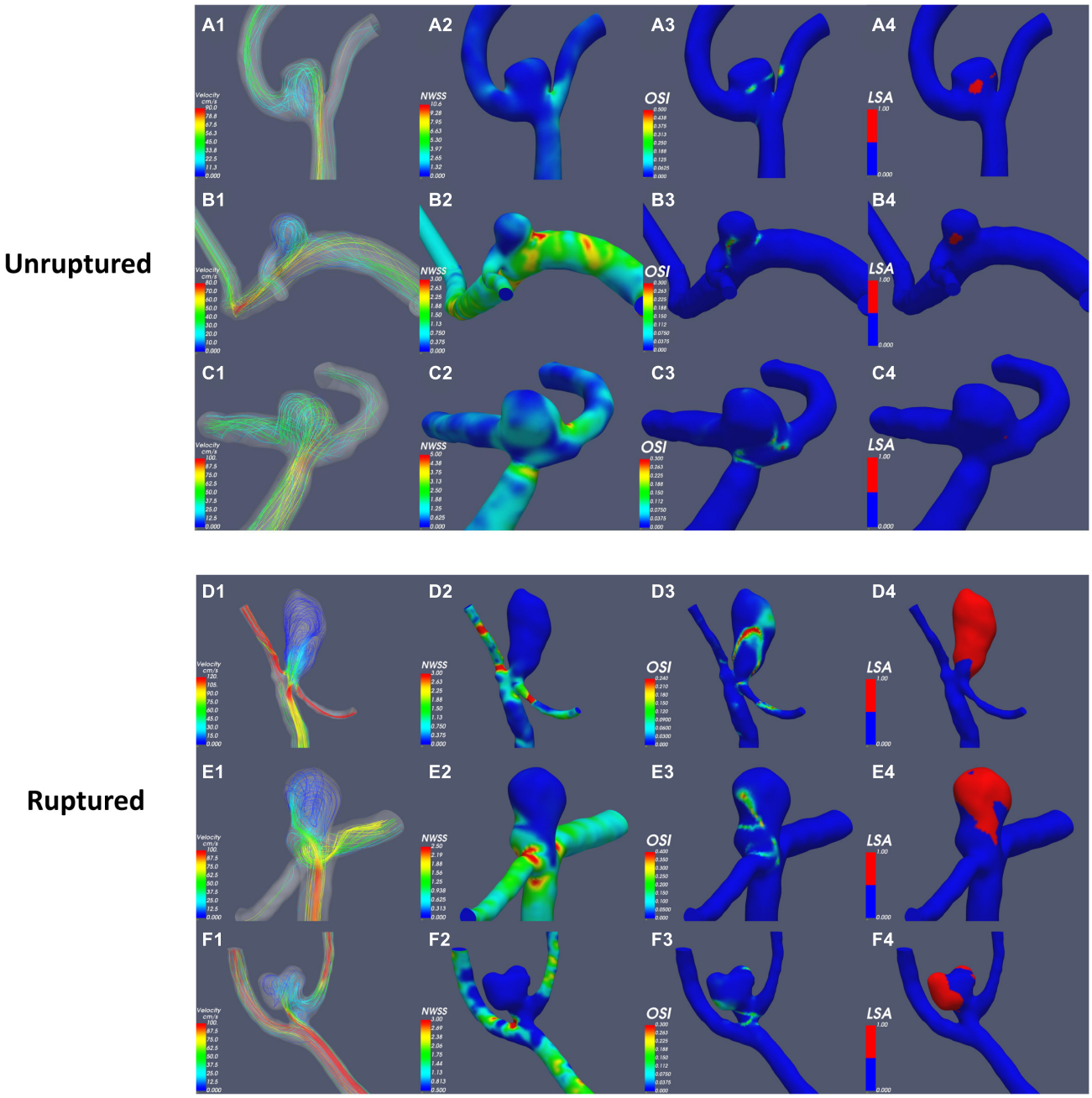

FIGURE 3 | Comparison of hemodynamic parameters between typical ruptured and unruptured PAAs. NWSS, normalized wall shear stress; OSI, oscillatory shear index; LSA, low-shear area.

RRT, and OSI, were calculated to evaluate the hemodynamic difference between the ruptured and unruptured PAAs. To ensure repeatability, all measurements were conducted at least twice.

Statistical Methods

Continuous variables were presented as the mean ± SD, and categorial variables were presented as absolute numbers with percentages. Data were tested for normality by constructing P–P and Q–Q plots. Categorical variables were compared between groups using the Pearson χ^2 test, continuity correction, and a two-tailed Fisher's exact test. Continuous variables were compared between groups using Student's *t*-test. We also evaluated the predictive value of factors that were statistically significant in the univariate analysis by receiver operating characteristic (ROC) analysis. A multivariable binary logistic regression analysis was performed including significant factors in univariate analysis. Statistical significance was defined as $P < 0.05$. Statistical analysis was performed using

SPSS Statistics version 24.0 software (IBM Corp., Armonk, NY, United States).

RESULTS

The mean age of the patients in the PAA cohort was 57.65 ± 9.97 years (range: 33–84 years). A total of 59.4% (19/32) of the PAAs were located at the bifurcation of the callosomarginal artery in the A3 segment, and no significant difference in baseline and morphological characteristics was detected between the ruptured and unruptured groups. Overall, there was little significant difference in the baseline and morphologic characteristics between ruptured and unruptured PAAs, and only AR was significantly higher in the ruptured group than in the unruptured group ($P = 0.045$) (**Table 1**).

According to the results of the quantitative hemodynamic analysis shown in **Table 2**, the mean OSI was significantly higher in the ruptured group than in the unruptured group ($P = 0.035$), and the mean NWSS was significantly lower in the ruptured group than in the unruptured group ($P = 0.012$). ROC curve analysis was performed to evaluate the predictive value of the variables for the rupture of PAAs (**Figure 2**). The largest AUC was that of the mean OSI (AUC = 0.808), and the AUC of mean NWSS (AUC = 0.733) ranked second, followed by the AUC of the AR (AUC = 0.712). The optimal threshold for mean OSI was 0.009875 with 75.0% sensitivity and 85.0% specificity. The optimal threshold for the mean NWSS was 0.78, which provided 91.7% sensitivity and 55.0% specificity. The optimal threshold for AR was 0.82, with a sensitivity of 75% and specificity of 65%. Factors in univariate analysis with $P < 0.05$ were subsequently used in a multivariable binary logistic regression analysis, including AR, mean NWSS, and mean OSI. The results of the multivariate analysis indicated that a high mean OSI was significantly associated with PAA rupture (OR = 6.45, 95% CI 1.37–30.32, $P = 0.018$). Multiple vital hemodynamic parameters are compared between several typical ruptured and unruptured typical PAAs in **Figure 3**.

DISCUSSION

To the best of our knowledge, this is the first study that assess hemodynamics and morphology simultaneously to evaluate the rupture risk of PAAs. In the present study, the results of the univariate analysis revealed that ruptured PAAs had significantly higher AR, mean NWSS, and mean OSI values than unruptured PAAs. AR represents the diameter-to-neck ratio, high AR of ruptured PAAs means that they have a relatively small neck area that limits the blood flow in the aneurysm sac and induces relatively slow and inconsistent flow in the aneurysm sac (Nader-Sepahi et al., 2004; Tateshima et al., 2010). As AR increases, vortices gradually appear in the aneurysm sac, and the flow velocity decreases (Ujiie et al., 1999; Tykocki et al., 2014). Most previous studies have indicated that AR is positively correlated with the risk of aneurysm rupture, consistent with our results (Ryu et al., 2011; Soldozy et al., 2019).

WSS is the frictional force induced by blood flow acting on the endothelium of the vessel wall, whose direction is parallel to local blood flow (Soldozy et al., 2019). For comparisons among different patients, NWSS was calculated for the hemodynamic analysis; this variable is defined as the WSS of the aneurysm wall divided by that of the parent artery wall. Low WSS was usually considered to be associated with aneurysm rupture (Miura et al., 2013; Soldozy et al., 2019), consistent with our finding that ruptured PAAs had significantly lower NWSS. OSI is a non-dimensional parameter that is defined as the directional change in WSS during the cardiac cycle; this frequency-based parameter has been used to quantify IA rupture (Soldozy et al., 2019). Our results indicated that a high mean OSI was an independent risk factor for PAA rupture (OR = 6.45, 95% CI 1.37–30.32, $P = 0.018$). OSI reflects the temporal variation in the blood flow direction, and the temporal variations in blood flow can be illustrated by the continuously emerging and disappearing vortices of blood flow throughout the cardiac cycle (Can and Du, 2016; Soldozy et al., 2019). OSI reflects the shape of the aneurysm and its parent artery because aneurysmal geometry and hemodynamics are intertwined, consistent with our finding (see above) that ruptured PAAs tend to have a relatively elongated shape as well as inconsistent flow.

Despite comprehensive screen, in an aneurysm cohort of 2141 patients, only 2.20% of them had PAAs. The primary limitation of this study was the small sample size, which might limit its generalizability. Second, the 3D DSA examination used for the hemodynamic study was not administered to all patients with PAAs, which caused a certain degree of selective bias. To overcome these limitations, further analysis with more adequate data is warranted in the future.

CONCLUSION

This study suggested that there were morphological and hemodynamic differences between ruptured and unruptured PAAs. In particular, a high mean OSI is an independent risk factor for PAA rupture. These findings should be considered preliminary until confirmed in larger studies.

DATA AVAILABILITY STATEMENT

The original contributions presented in the study are included in the article/**Supplementary Material**, further inquiries can be directed to the corresponding authors.

ETHICS STATEMENT

The studies involving human participants were reviewed and approved by the Ethics Committee of Xuanwu Hospital. The patients/participants provided their written informed consent to participate in this study. Written informed consent was obtained from the individual(s) for the publication of any potentially identifiable images or data included in this article.

AUTHOR CONTRIBUTIONS

XZ, JG, CZ, CL, JY, NJ, SX, GF, PH, and HZ contributed to the conception, design, analysis, and interpretation of the data as well as to drafting the manuscript and revising it critically. All authors have read and approved the final version of the manuscript.

FUNDING

This work was supported by the National Key R&D Program of China with grant 2016YFC1300800, Beijing Municipal Administration of Hospitals' Ascent Plan with grant DFL20180801, and the Beijing Scientific and Technologic Project (Z201100005520021).

SUPPLEMENTARY MATERIAL

The Supplementary Material for this article can be found online at: https://www.frontiersin.org/articles/10.3389/fnins.2021.759806/full#supplementary-material

Supplementary Figure 1 | Flowchart of image reconstruction and CFD procedures based on patient-specific angiogram.

REFERENCES

Bijlenga, P., Ebeling, C., Jaegersberg, M., Summers, P., Rogers, A., Waterworth, A., et al. (2013). Risk of rupture of small anterior communicating artery aneurysms is similar to posterior circulation aneurysms. *Stroke* 44, 3018–3026.

Can, A., and Du, R. (2016). Association of hemodynamic factors with intracranial aneurysm formation and rupture: systematic review and meta-analysis. *Neurosurgery* 78, 510–520. doi: 10.1227/NEU.0000000000001083

Cebral, J. R., Castro, M. A., Burgess, J. E., Pergolizzi, R. S., Sheridan, M. J., and Putman, C. M. (2005). Characterization of cerebral aneurysms for assessing risk of rupture by using patient-specific computational hemodynamics models. *AJNR Am. J. Neuroradiol.* 26, 2550–2559.

Cho, K. C., Choi, J. H., Oh, J. H., and Kim, Y. B. (2018). Prediction of thin-walled areas of unruptured cerebral aneurysms through comparison of normalized hemodynamic parameters and intraoperative images. *Biomed. Res. Int.* 2018:3047181. doi: 10.1155/2018/3047181

Dinc, N., Lescher, S., Quick-Weller, J., Berkefeld, J., Platz, J., Senft, C., et al. (2017). Outcome, prognostic factors, and follow-up results after subarachnoid hemorrhage from pericallosal artery aneurysms. *World Neurosurg.* 99, 566–571.

Ford, M. D., Alperin, N., Lee, S. H., Holdsworth, D. W., and Steinman, D. A. (2005). Characterization of volumetric flow rate waveforms in the normal internal carotid and vertebral arteries. *Physiol. Meas* 26, 477–488. doi: 10.1088/0967-3334/26/4/013

Geng, J., Hu, P., Ji, Z., Li, C., Li, L., Shen, J., et al. (2020). Accuracy and reliability of computer-assisted semi-automated morphological analysis of intracranial aneurysms: an experimental study with digital phantoms and clinical aneurysm cases. *Int. J. Comput. Assist. Radiol. Surg.* 15, 1749–1759. doi: 10.1007/s11548-020-02218-8

Greving, J. P., Wermer, M. J., Brown, R. D. Jr., Morita, A., Juvela, S., Yonekura, M., et al. (2014). Development of the PHASES score for prediction of risk of rupture of intracranial aneurysms: a pooled analysis of six prospective cohort studies. *Lancet Neurol.* 13, 59–66. doi: 10.1016/S1474-4422(13)70263-1

Gross, B. A., Lai, P. M., and Du, R. (2014). Impact of aneurysm location on hemorrhage risk. *Clin. Neurol. Neurosurg.* 123, 78–82. doi: 10.1016/j.clineuro.2014.05.014

Hu, P., Qian, Y., Lee, C. J., Zhang, H. Q., and Ling, F. (2015a). The energy loss may predict rupture risks of anterior communicating aneurysms: a preliminary result. *Int. J. Clin. Exp. Med.* 8, 4128–4133.

Hu, P., Qian, Y., Zhang, Y., Zhang, H. Q., Li, Y., Chong, W., et al. (2015b). Blood flow reduction of covered small side branches after flow diverter treatment: a computational fluid hemodynamic quantitative analysis. *J. Biomech.* 48, 895–898. doi: 10.1016/j.jbiomech.2015.02.015

Jou, L. D., Lee, D. H., Morsi, H., and Mawad, M. E. (2008). Wall shear stress on ruptured and unruptured intracranial aneurysms at the internal carotid artery. *AJNR Am. J. Neuroradiol.* 29, 1761–1767. doi: 10.3174/ajnr.A1180

Kashiwazaki, D., Kuroda, S., and Sapporo SAH Study Group (2013). Size ratio can highly predict rupture risk in intracranial small (<5 mm) aneurysms. *Stroke* 44, 2169–2173. doi: 10.1161/strokeaha.113.001138

Korja, M., Kivisaari, R., Rezai Jahromi, B., and Lehto, H. (2017). Size and location of ruptured intracranial aneurysms: consecutive series of 1993 hospital-admitted patients. *J. Neurosurg.* 127, 748–753. doi: 10.3171/2016.9.JNS161085

Kulcsar, Z., Ugron, A., Marosfoi, M., Berentei, Z., Paal, G., and Szikora, I. (2011). Hemodynamics of cerebral aneurysm initiation: the role of wall shear stress and spatial wall shear stress gradient. *AJNR Am. J. Neuroradiol.* 32, 587–594. doi: 10.3174/ajnr.a2339

Lehecka, M., Porras, M., Dashti, R., Niemela, M., and Hernesniemi, J. A. (2008b). Anatomic features of distal anterior cerebral artery aneurysms: a detailed angiographic analysis of 101 patients. *Neurosurgery* 63, 219–228, discussion 228-219. doi: 10.1227/01.NEU.0000310695.44670.32

Lehecka, M., Lehto, H., Niemela, M., Juvela, S., Dashti, R., Koivisto, T., et al. (2008a). Distal anterior cerebral artery aneurysms: treatment and outcome analysis of 501 patients. *Neurosurgery* 62, 590–601, discussion 590-601. doi: 10.1227/01.neu.0000317307.16332.03

Li, M. H., Chen, S. W., Li, Y. D., Chen, Y. C., Cheng, Y. S., Hu, D. J., et al. (2013). Prevalence of unruptured cerebral aneurysms in Chinese adults aged 35 to 75 years: a cross-sectional study. *Ann. Intern Med.* 159, 514–521. doi: 10.7326/0003-4819-159-8-201310150-00004

Lindgren, A. E., Koivisto, T., Björkman, J., von Und Zu Fraunberg, M., Helin, K., Jääskeläinen, J. E., et al. (2016). Irregular shape of intracranial aneurysm indicates rupture risk irrespective of size in a population-based cohort. *Stroke* 47, 1219–1226. doi: 10.1161/STROKEAHA.115.012404

Liu, X., Haraldsson, H., Wang, Y., Kao, E., Ballweber, M., Martin, A. J., et al. (2021). A volumetric metric for monitoring intracranial aneurysms: repeatability and growth criteria in a longitudinal MR imaging study. *AJNR Am. J. Neuroradiol.* 42, 1591–1597. doi: 10.3174/ajnr.A7190

Meng, H., Tutino, V. M., Xiang, J., and Siddiqui, A. (2014). High WSS or low WSS? Complex interactions of hemodynamics with intracranial aneurysm initiation, growth, and rupture: toward a unifying hypothesis. *AJNR Am. J. Neuroradiol.* 35, 1254–1262. doi: 10.3174/ajnr.a3558

Meng, H., Wang, Z., Hoi, Y., Gao, L., Metaxa, E., Swartz, D. D., et al. (2007). Complex hemodynamics at the apex of an arterial bifurcation induces vascular remodeling resembling cerebral aneurysm initiation. *Stroke* 38, 1924–1931. doi: 10.1161/STROKEAHA.106.481234

Miura, Y., Ishida, F., Umeda, Y., Tanemura, H., Suzuki, H., Matsushima, S., et al. (2013). Low wall shear stress is independently associated with the rupture status of middle cerebral artery aneurysms. *Stroke* 44, 519–521.

Molyneux, A. J., Birks, J., Clarke, A., Sneade, M., and Kerr, R. S. C. (2015). The durability of endovascular coiling versus neurosurgical clipping of ruptured cerebral aneurysms: 18 year follow-up of the UK cohort of the International Subarachnoid Aneurysm Trial (ISAT). *Lancet* 385, 691–697. doi: 10.1016/S0140-6736(14)60975-2

Morita, A., Kirino, T., Hashi, K., Aoki, N., Fukuhara, S., Hashimoto, N., et al. (2012). The natural course of unruptured cerebral aneurysms in a Japanese cohort. *N. Engl. J. Med.* 366, 2474–2482. doi: 10.1056/NEJMoa1113260

Nader-Sepahi, A., Casimiro, M., Sen, J., and Kitchen, N. D. (2004). Is aspect ratio a reliable predictor of intracranial aneurysm rupture? *Neurosurgery* 54, 1343–1347, discussion 1347-1348. doi: 10.1227/01.neu.0000124482.03676.8b

Petr, O., Coufalova, L., Bradac, O., Rehwald, R., Glodny, B., and Benes, V. (2017). Safety and efficacy of surgical and endovascular treatment for distal anterior cerebral artery aneurysms: a systematic review and meta-analysis. *World Neurosurg.* 100, 557–566. doi: 10.1016/j.wneu.2016.11.134

Qin, H., Yang, Q., Zhuang, Q., Long, J., Yang, F., and Zhang, H. (2017). Morphological and hemodynamic parameters for middle cerebral artery bifurcation aneurysm rupture risk assessment. *J. Korean Neurosurg. Soc.* 60, 504–510. doi: 10.3340/jkns.2017.0101.009

Riccardello, G. J. Jr., Shastri, D. N., Changa, A. R., Thomas, K. G., Roman, M., Prestigiacomo, C. J., et al. (2018). Influence of relative residence time on side-wall aneurysm inception. *Neurosurgery* 83, 574–581. doi: 10.1093/neuros/nyx433

Ryu, C. W., Kwon, O. K., Koh, J. S., and Kim, E. J. (2011). Analysis of aneurysm rupture in relation to the geometric indices: aspect ratio, volume, and volume-to-neck ratio. *Neuroradiology* 53, 883–889. doi: 10.1007/s00234-010-0804-4

Soldozy, S., Norat, P., Elsarrag, M., Chatrath, A., Costello, J. S., Sokolowski, J. D., et al. (2019). The biophysical role of hemodynamics in the pathogenesis of cerebral aneurysm formation and rupture. *Neurosurg. Focus* 47:E11. doi: 10.3171/2019.4.FOCUS19232

Tanaka, K., Takao, H., Suzuki, T., Fujimura, S., Uchiyama, Y., Otani, K., et al. (2018). Relationship between hemodynamic parameters and cerebral aneurysm initiation. *Annu. Int. Conf. IEEE Eng. Med. Biol. Soc.* 2018, 1347–1350.

Tateshima, S., Chien, A., Sayre, J., Cebral, J., and Vinuela, F. (2010). The effect of aneurysm geometry on the intra-aneurysmal flow condition. *Neuroradiology* 52, 1135–1141.

Thompson, B. G., Brown, R. D. Jr., Amin-Hanjani, S., Broderick, J. P., Cockroft, K. M., Connolly, E. S. Jr., et al. (2015). Guidelines for the management of patients with unruptured intracranial aneurysms: a guideline for healthcare professionals from the American Heart Association/American Stroke Association. *Stroke* 46, 2368–2400.

Tykocki, T., Nauman, P., and Dow Enko, A. (2014). Morphometric predictors of posterior circulation aneurysms risk rupture. *Neurol. Res.* 36, 733–738. doi: 10.1179/1743132813y.0000000306

Ujiie, H., Tachibana, H., Hiramatsu, O., Hazel, A. L., Matsumoto, T., Ogasawara, Y., et al. (1999). Effects of size and shape (aspect ratio) on the hemodynamics of saccular aneurysms: a possible index for surgical treatment of intracranial aneurysms. *Neurosurgery* 45, 119–129, discussion 129-130. doi: 10.1097/00006123-199907000-00028

Wang, Y., Cheng, M., Liu, S., Xie, G., Liu, L., Wu, X., et al. (2021). Shape related features of intracranial aneurysm are associated with rupture status in a large Chinese cohort. *J. Neurointerv. Surg. [Online ahead of print]* neurintsurg–2021–017452. doi: 10.1136/neurintsurg-2021-017452

Weir, B., Disney, L., and Karrison, T. (2002). Sizes of ruptured and unruptured aneurysms in relation to their sites and the ages of patients. *J. Neurosurg.* 96, 64–70. doi: 10.3171/jns.2002.96.1.0064

Yuan, J., Li, Z., Jiang, X., Lai, N., Wang, X., Zhao, X., et al. (2020). Hemodynamic and morphological differences between unruptured carotid-posterior communicating artery bifurcation aneurysms and infundibular dilations of the posterior communicating artery. *Front. Neurol.* 11:741. doi: 10.3389/fneur.2020.00741

Zhai, X. D., Yu, J. X., Li, C. J., Ren, J., Ji, Z., He, C., et al. (2020). Morphological characteristics of pericallosal artery aneurysms and their high propensity for rupture. *World Neurosurg.* 133, e320–e326.

Conflict of Interest: GF was employed by the company UnionStrong (Beijing) Technology Co., Ltd.

The remaining authors declare that the research was conducted in the absence of any commercial or financial relationships that could be construed as a potential conflict of interest.

Publisher's Note: All claims expressed in this article are solely those of the authors and do not necessarily represent those of their affiliated organizations, or those of the publisher, the editors and the reviewers. Any product that may be evaluated in this article, or claim that may be made by its manufacturer, is not guaranteed or endorsed by the publisher.

frontiers in Neuroscience

ORIGINAL RESEARCH
published: 26 November 2021
doi: 10.3389/fnins.2021.756577

Three-Dimensional Iron Oxide Nanoparticle-Based Contrast-Enhanced Magnetic Resonance Imaging for Characterization of Cerebral Arteriogenesis in the Mouse Neocortex

Till de Bortoli[1,2†], Philipp Boehm-Sturm[2,3,4†], Stefan P. Koch[2,3,4], Melina Nieminen-Kelhä[1,2], Lars Wessels[1,2], Susanne Mueller[2,3,4], Giovanna D. Ielacqua[5], Jan Klohs[5], Peter Vajkoczy[1,2] and Nils Hecht[1,2]*

[1] Department of Neurosurgery, Charité-Universitätsmedizin Berlin, Corporate Member of Freie Universität Berlin, Humboldt-Universität zu Berlin, Berlin, Germany, [2] Center for Stroke Research Berlin (CSB), Berlin, Germany, [3] Department of Experimental Neurology, Charité-Universitätsmedizin Berlin, Corporate Member of Freie Universität Berlin, Humboldt-Universität zu Berlin, Berlin, Germany, [4] NeuroCure Cluster of Excellence and Charité Core Facility 7T Experimental MRIs, Charité-Universitätsmedizin Berlin, Corporate Member of Freie Universität Berlin, Humboldt-Universität zu Berlin, Berlin, Germany, [5] Institute for Biomedical Engineering, University of Zurich and ETH Zürich, Zurich, Switzerland

Purpose: Subsurface blood vessels in the cerebral cortex have been identified as a bottleneck in cerebral perfusion with the potential for collateral remodeling. However, valid techniques for non-invasive, longitudinal characterization of neocortical microvessels are still lacking. In this study, we validated contrast-enhanced magnetic resonance imaging (CE-MRI) for *in vivo* characterization of vascular changes in a model of spontaneous collateral outgrowth following chronic cerebral hypoperfusion.

Methods: C57BL/6J mice were randomly assigned to unilateral internal carotid artery occlusion or sham surgery and after 21 days, CE-MRI based on T2*-weighted imaging was performed using ultra-small superparamagnetic iron oxide nanoparticles to obtain subtraction angiographies and steady-state cerebral blood volume (ss-CBV) maps. First pass dynamic susceptibility contrast MRI (DSC-MRI) was performed for internal validation of ss-CBV. Further validation at the histological level was provided by *ex vivo* serial two-photon tomography (STP).

Results: Qualitatively, an increase in vessel density was observed on CE-MRI subtraction angiographies following occlusion; however, a quantitative vessel tracing

OPEN ACCESS

Edited by:
Chengcheng Zhu, University of Washington, United States

Reviewed by:
Qi Yang, Capital Medical University, China
Zhang Shi, Fudan University, China

***Correspondence:**
Nils Hecht
nils.hecht@charite.de

†These authors share first authorship

Specialty section:
This article was submitted to Brain Imaging Methods, a section of the journal Frontiers in Neuroscience

Received: *10 August 2021*
Accepted: *02 November 2021*
Published: *26 November 2021*

Citation:
de Bortoli T, Boehm-Sturm P, Koch SP, Nieminen-Kelhä M, Wessels L, Mueller S, Ielacqua GD, Klohs J, Vajkoczy P and Hecht N (2021) Three-Dimensional Iron Oxide Nanoparticle-Based Contrast-Enhanced Magnetic Resonance Imaging for Characterization of Cerebral Arteriogenesis in the Mouse Neocortex. Front. Neurosci. 15:756577. doi: 10.3389/fnins.2021.756577

analysis was prone to errors in our model. Measurements of ss-CBV reliably identified an increase in cortical vasculature, validated by DSC-MRI and STP.

Conclusion: Iron oxide nanoparticle-based ss-CBV serves as a robust, non-invasive imaging surrogate marker for neocortical vessels, with the potential to reduce and refine preclinical models targeting the development and outgrowth of cerebral collateralization.

Keywords: contrast-enhanced MRI, cerebral blood volume, iron oxide nanoparticles, stroke, cerebrovascular disease, vessel imaging

INTRODUCTION

Cerebral collateral remodeling (cerebral arteriogenesis) represents an endogenous rescue mechanism to cope with chronic cerebral hypoperfusion and determines the severity and outcome of hemodynamic stroke (Brozici et al., 2003; Todo et al., 2008; Menon et al., 2013; Lima et al., 2014). Despite this critical importance of collateral arteries, their clinical and neuroradiological assessment remains challenging because standard neuroimaging methods to study collateral circulation are hampered by a low spatial resolution (Shuaib et al., 2011; Campbell et al., 2013). High spatial detail is important because next to the basal and leptomeningeal vasculature (Buschmann et al., 2003; Kitagawa et al., 2005; Schneider et al., 2007), arteriolar remodeling also occurs at the level of the subsurface resistance vessels (Hecht et al., 2012, 2015; Marushima et al., 2019) that represent a bottleneck to cortical perfusion (Nishimura et al., 2007).

For high-resolution imaging of the cerebral vasculature, contrast enhanced magnetic resonance imaging (CE-MRI) with ultrasmall, carbohydrate-coated superparamagnetic iron oxide nanoparticles and gradient echo or susceptibility weighted imaging has previously been reported (Iv et al., 2018; Buch et al., 2021). The resulting contrast to noise ratios are generally higher for these particles due to an exceptionally high transverse relaxivity compared to conventional gadolinium chelates based contrast agents (Rohrer et al., 2005; Plock et al., 2015; Knobloch et al., 2018). Although high-resolution angiographies are technically feasible in humans (Liu et al., 2018), animal models are needed for validation of such techniques to allow reliable, dynamic assessment of cerebrovascular development and remodeling in health and disease. Thus far, different approaches have been described to quantify iron oxide nanoparticle-based CE-MRI: On the one hand, blood volume fraction estimated by steady state cerebral blood volume (ss-CBV) measurements using a biophysical model in the static dephasing regime may serve as an *indirect* marker of gross total blood vessel volume (Boxerman et al., 1995). Technically, ss-CBV benefits from the long circulating half-time of iron oxide nanoparticles, which permits high-resolution assessment of perfused vasculature in the context of MRI (Plock et al., 2015). On the other hand, contrast enhanced magnetic resonance *angiography* (CE-MRA) was shown to allow *direct* detection of small-caliber parenchymal blood vessels in the mouse cerebral cortex using a semi-automated vessel tracing algorithm that permits diameter quantification among blood vessels enhanced at steady-state (Klohs et al., 2012). These findings are highly relevant, because non-invasive, longitudinal characterization of the cerebral vasculature has immediate implications for reduction and refinement of animal experiments next to understanding the etiology and course of neurovascular and neurodegenerative diseases. The current dilemma is that the reliability of both indirect but also direct CE-MRI techniques remains unclear, because a systematic validation against the actual cerebral angioarchitecture has not yet been performed. Therefore, the aim of the present study was to validate iron oxide nanoparticle-based CE-MRI for blood vessel quantification in a preclinical mouse model of chronic cerebral hypoperfusion and spontaneous collateral remodeling by testing a previously reported vessel tracing algorithm and analyzing steady state blood volume maps (ss-CBV) against serial two-photon (STP) tomography.

MATERIALS AND METHODS

Ethics Statement

Experiments were permitted by the local ethics committee on animal research (Landesamt für Gesundheit und Soziales, Berlin, Germany; LAGeSo G0186/16) and in conformity with the German Law for Animal Protection and the National Institute of Health Guidelines for Care and Use of Laboratory Animals. Experiments were reported following the ARRIVE guidelines.

Animals and Surgery

Sixteen male C57BL/6J mice aged 12 weeks and an initial body weight ranging from 27 to 32 g (Charles River WIGA GmbH, Sulzfeld, Germany) were randomly assigned to permanent unilateral internal carotid artery occlusion (ICAO) for stimulation of spontaneous cerebral arteriogenesis (n = 8) or sham surgery (Sham) (n = 8), as previously described (Hecht et al., 2012). Briefly, mice were anesthetized with 70 mg/kg ketamine and 16 mg/kg xylazine and body temperature was maintained at 37°C. Animals were positioned supine and the right-sided ICA was exposed by a midline neck incision. For ICAO, the right ICA was permanently ligated with 8/0 silk. For Sham, the ICA was exposed but no ligation was performed. The skin was sutured with 6/0 nylon. Mice were kept in an enriched environment with free access to food and water.

Magnetic Resonance Imaging

On Day 21 after surgery, a venous catheter was placed into the femoral vein and CE-MRI was acquired at 7 Tesla with a

small animal MR scanner (Bruker BioSpin GmbH, Ettlingen, Germany) using a transmit/receive mouse head cryoprobe (Bruker BioSpin GmbH, Ettlingen, Germany). Mice weight at Day 21 was 34.1 ± 9.7 g for ICAO and 30.2 ± 7.2 g for Sham. Researchers performing the CE-MRI were blinded to the group assignment. The MRI protocol included the following sequences:

- T2-weighted MRI [2D Rapid Acquisition with Relaxation Enhancement (RARE), 39 contiguous 0.4 mm-thick slices, field of view (FOV) = $(18.72\ mm)^2$, $(80\ \mu m)^2$ in plane resolution, repetition time/effective echo time (TR/TE) = 4.2s/33 ms, echo spacing 11 ms, RARE factor 8, bandwidth (BW) = 32.9 kHz, 2 averages, acquisition time (TA) = 4:03 min].
- CE-MRA of the cortex by acquiring T2*-weighted images [3D fast-low-angle-shot, FOV = 13.52 mm^3 × 16.64 mm^3 × 5.2 mm^3, $(65\ \mu m)^3$ resolution, TR/TE = 54 ms/3.9 ms, FA = 20°, BW = 50 kHz, partial Fourier imaging (PFT) in frequency encoding direction with factor 1.33, TA = 29:57 min per image] first pre-injection and then post-injection of ultrasmall, superparamagnetic iron oxide nanoparticles (Ferumoxytol, AMAG Pharmaceuticals, Waltham, MA) through the femoral vein. Iron oxide nanoparticles (0.300 mmol/l) were diluted 1:3 (volume/volume) in 0.9% sodium chloride and 1.6753 μl per gram bodyweight of the diluted contrast agent was injected as a single bolus over 2–3 s, which yielded a final contrast agent concentration of 300 μmol Fe/kg bodyweight.
- Dynamic susceptibility contrast (DSC)-MRI during iron oxide nanoparticle injection [single shot gradient-echo echo-planar imaging, 15 contiguous 0.4 mm slices, FOV = 18.72 × 18.72 mm^2, $(293\ \mu m)^2$ resolution, TR/TE = 400 ms/7.2 ms, FA = 50°, BW = 200 kHz, PFT = 1.5 in phase encoding direction, 200 repetitions, TA = 1:20 min].

T2-weighted sequences and DSC-MRI FOV covered the whole brain, whereas the CE-MRA FOV only covered the dorsal neocortex. A set of 5 saturation slices with identical geometry was used to suppress aliasing artifacts originating from the signal of the ventral part of the brain.

Blood Vessel Staining

To visualize cerebral blood vessels for histological analysis, mice received an *in vivo* injection of 100 μl fluorescein-labeled Lectin [DyLight 488 Labeled Lycopersicon Esculentum (Tomato) Lectin, DL-1174, Vector Laboratories, Burlingame, CA] though the femoral vein to stain endothelial cells of perfused blood vessels. Next, the animals were transcardially perfused with 4% paraformaldehyde in phosphate buffered saline and the isolated brains were stored in the same solution at 4°C for 72 h and then kept in 0.1% sodium azide in phosphate buffered saline.

Histology

For the purpose of 3R and resource conservation during histological analysis, animals were randomly assigned to two groups: In the first group, n = 4 ICAO and n = 4 Sham animals were used to validate our animal model and confirm neocortical vascular remodeling on Day 21 after unilateral ICAO by confocal laser scanning microscopy (Leica TCS SP8, Leica Camera AG, Wetzlar, Germany) of whole-mount brain sections of 80 μm thickness with 1.5 × 1.5 × 8.9 μm^3 [X × Y (plane) × Z (depth)] voxel resolution and laser excitation at 488 nm. The resulting confocal cerebral blood vessel volume (CBV) was defined as confocal-CBV by the fraction of Lectin-positive voxels from all tissue voxels in the right-sided neocortex (**Supplementary Figures 1**, **2**).

After neocortical vessel outgrowth following ICAO was confirmed, n = 2 ICAO and n = 1 Sham animals were used in the second group to validate our iron oxide nanoparticle-based ss-CBV method at whole brain level by using serial two-photon tomography (STP) of perfused brains that was generated with a commercially available platform (TissueVision, Newton, MA, United States) (Ragan et al., 2012). Briefly, block-face 2-photon imaging of brains was performed by slicing 50 μm sections with measurements of two 25 μm optical planes per slice and three channels (RGB) leading to a final resolution of 1.2 μm × 1.2 μm in plane and 25 μm slice thickness. The resulting serial two-photon cerebral blood volume was defined as STP-CBV.

Image Processing

Image co-registration was used to compare MRI and histological data and to annotate brain regions from the Allen brain atlas. MR image pre-processing was performed in ImageJ (v1.52e)[1] according to the following steps: First, all images were transformed to the resolution of the CE-MRI scan using nearest-neighbor interpolation. Second, fixed relations in image geometry planning during acquisition were used to transform images to a final FOV = 18.72 mm^3 × 18.72 mm^3 × 15.2 mm^3, $(65\ \mu m)^3$ isotropic resolution and matching geometry without image registration techniques. Manual correction of shifts due to scanner imperfections were corrected in steps of one voxel using a custom ImageJ plugin and 3 degrees of freedom and nearest neighbor interpolation. T2-weighted images were warped to the Allen brain atlas using the MATLAB (v. R2014a, MathWorks, Natick, MA, United States) toolbox ANTx (Koch et al., 2019). The calculated registration was then applied to all other MRI measurements. Histology images were registered to the Allen brain atlas using custom MATLAB tools (R2016a, The MathWorks, Inc., Natick, MA, United States) (Koch et al., 2019). The following steps were performed to transform STP data to the Allen brain atlas:

- Background removal by filtering the sum of RGB images (2D Gaussian filter, standard deviation of 11) on the first of the optical planes (resulting mask was applied to the second).

[1] https://imagej.nih.gov/ij/

- Generation of (A) an anatomical image for later image registration from autofluorescence images in the red channel and (B) a vessel image by feeding the RGB-channel images into a principal component analysis and extracting the 2nd principal component.
- Automated identification of vasculature on the vessel image by closing gaps with 3 × 3 pixel kernel, removing salt and pepper noise with 2D median filter with a 9 × 9 kernel, clustering into spatially connected objects removing objects with <5 connected pixels and binarization (values > 0 set to 1).
- Down-sampling of the binarized vessel image to the resolution of the Allen template (voxel size: 0.025 μm^3 × 0.025 μm^3 × 0.025 μm^3) using bilinear interpolation. This led to an image containing values between 0 and 1 representing the fraction of 1s of the high-resolution vessel image in the low-resolution voxel, i.e., a map of STP-CBV. This map and the down-sampled template-like image were saved as nifti-files.
- Registration of STP-CBV map via template-like image (moving image) onto the Allen mouse template (fixed image) in Elastix using a rigid body transformation, followed by affine transformation and a subsequent B-spline transformation (Klein et al., 2010; Shamonin et al., 2013).

Vessel Tracing Analysis Based on Contrast Enhanced Magnetic Resonance Angiography

Angiograms from CE-MRI (=CE-MRA) were generated by subtraction of image intensities $S_{pre} - S_{post}$. From these, vessel densities were calculated by a vessel tracing algorithm as described previously (Klohs et al., 2012). Based on previous findings in our model and as suggested by the results from our confocal-CBV analysis (**Supplementary Figures 1**, **2**), we hypothesized an increase in vessel densities in the right-sided neocortex of ICAO animals compared to Sham (Hecht et al., 2012, 2015; Marushima et al., 2019).

Steady State Cerebral Blood Volume Analysis From Iron Oxide Nanoparticle-Based Contrast-Enhanced Magnetic Resonance Imaging

The change in transverse relaxation rate $\Delta R_2^* = 1/TE \times \ln(S_{pre}/S_{post})$ was calculated using ImageJ and ss-CBV was defined using the biophysical model of Yablonsky and Haacke via ss-CBV = $3/(4\pi\gamma\Delta\chi B_0)\Delta R_2^*$ with the gyromagnetic ratio $\gamma = 2.67502 \times 10^8$ rad/s/T and susceptibility difference $\Delta\chi = 0.282 \times 10^{-8}$ (CGS units) between blood and tissue at

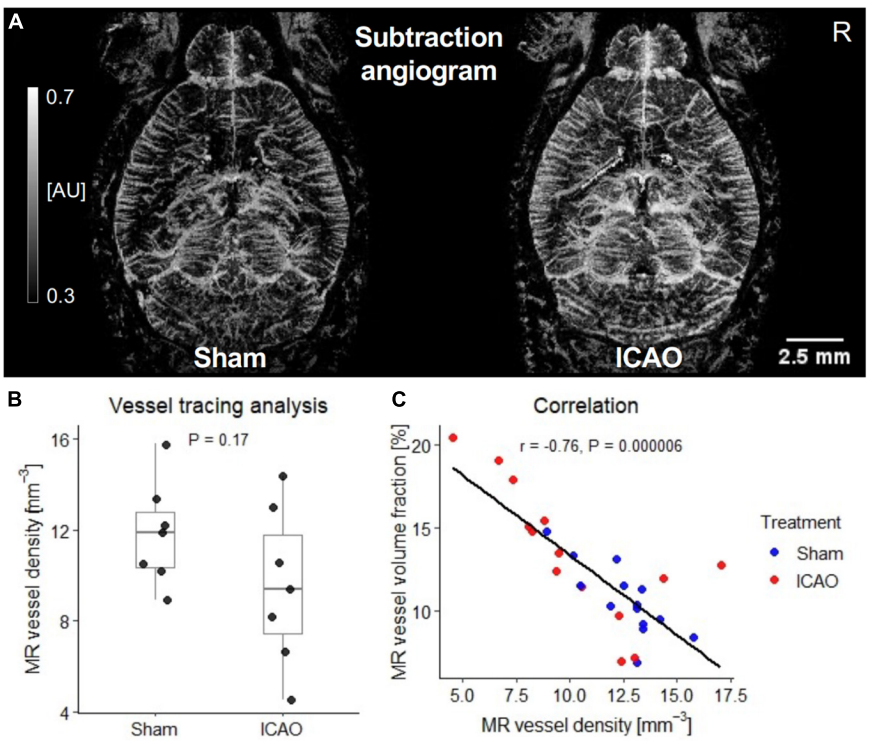

FIGURE 1 | Quantitative contrast enhanced magnetic resonance angiography (CE-MRA) subtraction angiogram analysis 21 days after ICAO or Sham. **(A)** Iron oxide nanoparticle-based MR subtraction angiograms in gray-scaled arbitrary units (AU) clearly visualized a stronger enhancement across both hemispheres on Day 21 after ICAO compared to Sham. **(B)** In contrast to this clearly visualized effect, semi-automated MR vessel density analysis yielded a lower instead of higher vessel density in the right neocortex after ICAO (n = 7 per group). **(C)** Relationship between MR vessel density and the corresponding vessel volume fraction in neocortex measurements from both hemispheres described by Spearman's rank correlation coefficient (n = 28).

B_0 = 7 T (Lemasson et al., 2016) assuming linear increase with contrast agent dose and saturation of iron magnetization above 4.7 T (Yablonskiy and Haacke, 1994; Lemasson et al., 2015).

Dynamic Susceptibility Contrast Relative Cerebral Blood Volume Analysis From Iron Oxide Nanoparticle-Based Dynamic Susceptibility Contrast Magnetic Resonance Imaging

Dynamic susceptibility contrast relative cerebral blood volume was calculated using DSCoMAN Version 1.0 (Duke University Medical Center, Durham, NC, United States) (Boxerman et al., 2006). Using ImageJ, raw DSC-MRI images were manually converted into a stack with xyztc order, one channel, 15 slices, and 200 frames. Pixel width and height were set to 0.2925 mm, voxel depth to 0.4 mm. The frame interval was set to 0.4 s, the origin to 0.0 pixels. A timetable was imported. Next, the DSCoMAN GUI was started within ImageJ to calculate raw perfusion images. The first 20 timepoints were excluded for the analysis of rCBV. Last baseline time, last time, slice locations, time points, echo time (msec), whole brain threshold, noise SDs, as well as parameter for last baseline time computation were not modified from the values automatically given by DSCoMAN. The resulting rCBV map was scaled as the raw DSC-MRI images above and saved as a nifti file.

Statistical Analyses and Methods to Prevent Bias

Since no data on CE-MRI was available for our mouse model, we chose an exploratory study design with similar sample size to the original study describing the mouse model with histological methods (Hecht et al., 2012). A total of 16 mice underwent MRI measurements. The researchers performing the MRI measurements were blinded to the group assignment. One animal was excluded because of clots in the brain after iron oxide nanoparticle injection, one animal died during the MRI protocol leading to the final group size of 7 per group. All analysis was performed blinded to group assignment. A volume-of-interest of the right neocortex for vessel tracing was defined manually by a blinded researcher and no iterations were made in the analysis. The right-sided neocortex defined by the Allen Mouse Brain Atlas was chosen as volume-of-interest for ss-CBV and DSC-rCBV analysis prior to the analysis (**Supplementary Figure 3**; Lein et al., 2007). Analysis of volume-of-interests in processed images was performed using custom code. Plots and statistics were performed using R version 4.0. Individual data points were visualized together with a summarized mean value ± standard deviation. Data were statistically described by the *p*-value derived from 2-sided Student's t-tests after passing a Shapiro-Wilk normality test. Spearman's rank correlation coefficient (*r*) was used to describe the correlation between ss-CBV and h-CBV.

RESULTS

Assessment of Vessel Density With Semi-Automated Blood Vessel Tracing Algorithm

Blood vessels in the right neocortex 21 days after ICAO or sham surgery were precisely visualized in a three-dimensional space after subtraction of post-contrast from pre-contrast images. As expected from previous findings[11] and our confocal modal validation (**Supplementary Figures 1**, **2**), more neocortical vessels were visible on CE-MRA subtraction angiograms 3 weeks after ICAO throughout both hemispheres (**Figure 1A**). Unexpectedly, however, vessel densities calculated by a previously described, semi-automated vessel tracing algorithm tended to be lower in ICAO than in Sham-treated animals (Sham: 11.8 ± 2.3 mm^{-3}; ICAO: 9.5 ± 3.5 mm^{-3}; p = 0.17; n = 7 per group; **Figure 1B**). Thus, although measurements within the ICAO group displayed large MR vessel volumes that visually corresponded well to the subtraction angiograms, the tracing analysis did not translate these effects into an increased

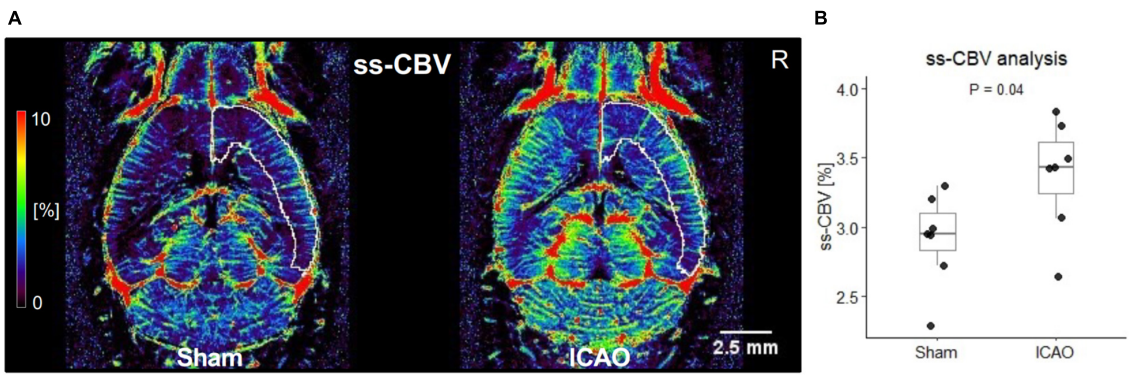

FIGURE 2 | Steady state-cerebral blood volume (ss-CBV) analysis 21 days after ICAO or Sham. **(A)** Iron oxide nanoparticle-based ss-CBV maps color-coding the fraction of blood volume per voxel brain tissue in percent (%). The white frames illustrate the right-sided neocortex as defined by the Allen Mouse Brain Atlas. **(B)** Group comparison in the right-sided neocortex ipsilateral to the permanent ICA-occlusion shows an increase in ss-CBV after ICAO (n = 7 per group).

MR vessel density. Additionally, we compared MR vessel densities for both groups and hemispheres with corresponding MR vessel volumes in a *post hoc* analysis and, interestingly, MR vessel densities were in strong negative correlation to MR vessel volumes (r = -0.76; p = 0.000006; n = 28; **Figure 1C**).

Assessment of Vessel Density With Iron Oxide Nanoparticle-Based Steady State Cerebral Blood Volume and Dynamic Susceptibility Contrast-Relative Cerebral Blood Volume

Next, we explored whether ss-CBV maps could serve as a surrogate marker for parenchymal blood vessel imaging (**Figure 2A**) and found a significant increase of ss-CBV in the right neocortex following ICAO (Sham: 2.9 ± 0.3%; ICAO: 3.4 ± 0.4%; p = 0.04; n = 7 per group; **Figure 2B**). Cerebral hemodynamics were also assessed by DSC-MRI, which serves as a commonly applied technique for blood volume mapping by MRI. For between-subject comparisons of relative DSC-CBV (DSC-rCBV) in the parenchyma, the right hemisphere was normalized to the mean value of all measured voxels (**Figure 3A**). In agreement with our parenchymal ss-CBV analysis but at clearly lower spatial resolution (**Figure 3B**), a significant increase in DSC-rCBV following ICAO was noted for the right neocortex (Sham: 1.13 ± 0.02 AU; ICAO: 1.24 ± 0.02 AU; p = 0.000002; n = 7 per group; **Figure 3C**). To confirm the internal validity of our ss-CBV blood volume analysis, neocortical ss-CBV and DSC-rCBV measurements from both hemispheres were normalized and compared with each other using a Bland-Altman plot that yielded a mean difference of 0.000007 AU with limits of agreement of –0.07 to 0.07 AU; n = 14; **Figure 3D**).

Histological Validation of Iron Oxide Nanoparticle-Based Steady State-Cerebral Blood Volume Against Serial Two-Photon Tomography

Next, ss-CBV findings were histologically validated at the whole brain level by correlating ss-CBV to corresponding STP-CBV from STP angiographies. For this purpose, 406 regions of the Allen brain atlas were covered with MRI and STP modalities to permit a direct comparison of ss-CBV against STP-CBV across those regions. Importantly, blood vessels according to ss-CBV were accurately traceable by STP (**Figure 4**) and a correlation analysis across 406 brain regions from the Allen brain atlas demonstrated good correlation between ss-CBV and STP-CBV in the mouse neocortex (Mean r = 0.57; $p < 0.000001$; Sham: n = 1; ICAO: n = 2; **Figure 4**).

DISCUSSION

In this study, we show that iron oxide nanoparticle-based ss-CBV maps serve as a valid surrogate marker for semi-quantitative assessment of cerebral blood vessels and spontaneous collateral outgrowth in the mouse neocortex with higher resolution and improved contrast compared to rCBV determined by DSC: 21 days after permanent ICAO, spontaneous outgrowth of neocortical blood vessels was mirrored by an increase of ss-CBV, which corresponded to confocal model validation and correlated well with vessel density assessed by STP. The significance of this work is that iron oxide nanoparticle-based ss-CBV can help to refine and reduce experimental protocols by serving as a novel surrogate for longitudinal characterization of cerebrovascular remodeling.

The endogenous outgrowth of collaterals represents the most powerful mechanism to cope with chronic cerebral hypoperfusion (Schaper and Scholz, 2003) and a growing body of evidence has shown preclinical effectiveness of therapeutic stimulation of collateral vessel growth in the murine brain (Buschmann et al., 2003; Schneeloch et al., 2004; Schneider et al., 2007; Duelsner et al., 2012; Hecht et al., 2012, 2015; Marushima et al., 2019). Consequently, longitudinal imaging of development, outgrowth, and remodeling of cerebral collaterals in models of health and disease remains of high interest but is also affected by the ongoing effort to replace, reduce, and refine (3Rs) animal experiments (Blakemore et al., 2012). Although the natural dynamics of cerebral collateral outgrowth and remodeling cannot be completely replaced by *ex vivo* modeling, we believe that reliable establishment of non-invasive, high-resolution CE-MRI has meaningful potential for reduction and refinement because CE-MRI facilitates an improved, longitudinal study design and intra-individual analysis with higher statistical power at the benefit of using a non-invasive technology (Nesselroade and Ram, 2004). For assessment of large caliber vessels, this hypothesis is supported by recent findings showing standardized and reliable time-of-flight (TOF) MR angiography for quantitative, longitudinal characterization of collateralization at the level of the Circle of Willis in mice (Foddis et al., 2020; Knauss et al., 2020). For assessment of collateral remodeling at the level of penetrating arterioles, however, the resolution of TOF MR angiography is too low and CE-MRA using a blood pooling agent could be better suited (Klohs et al., 2012). In order to test the feasibility and validity of iron oxide nanoparticle-based CE-MRA for quantification of parenchymal vascular remodeling, we therefore deliberately chose a previously characterized model of unilateral attenuation of cerebral perfusion in mice, in which collateral remodeling not only occurs within the basal and leptomeningeal vasculature, but also within the parenchymal resistance vessels in the neocortex of both hemispheres (Hecht et al., 2012). We clearly observed a higher (micro)vascular density in iron oxide nanoparticle-based CE-MRA subtraction angiograms on Day 21 after chronic hypoperfusion in the right hemisphere as the predefined region of interest that has predominantly been found hemodynamically impaired after right-sided ICAO (Hecht et al., 2012). The vessel density in the left hemisphere contralateral to ICAO also seemed to increase in line with previous findings (Hecht et al., 2012), however, including the left hemisphere as the second region of interest would have underpowered our analysis. However, the observation of increased vessel density in the right hemisphere did *not* translate into a higher vessel density

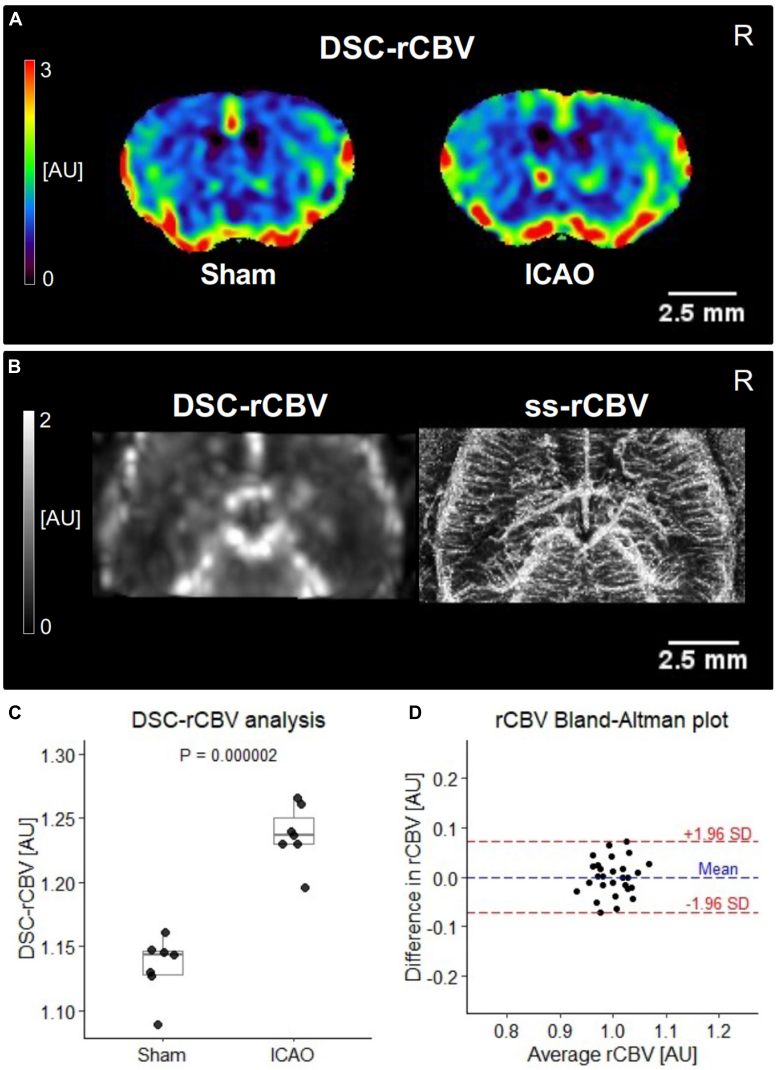

FIGURE 3 | Internal cerebral blood volume (CBV) validation. **(A)** Color-coded normalized dynamic susceptibility contrast-relative cerebral blood volume (DSC-rCBV) maps in arbitrary units (AU). **(B)** Comparison of normalized DSC-rCBV and ss-CBV map resolution for the same animal. **(C)** Comparison of iron oxide nanoparticle-based DSC-rCBV at Day 21 (n = 7 per group). **(D)** Bland-Altman comparison of DSC-rCBV and ss-CBV in the right- and the left-sided neocortex (n = 28). The average of ss-CBV and DSC-rCBV is plotted against their difference. A mean difference of 0.000007 AU in rCBV with limits of agreement between -0.07 and 0.07 AU was noted.

using a previously established semi-automated vessel tracing algorithm. Considering the generally intact blood-brain barrier within the parenchymal vasculature following unilateral ICAO (Hecht et al., 2015), this unexpected finding could be explained by blooming artifacts that confounded the algorithm especially in animals with ICAO and collateral remodeling, because increasing vessel volumes possibly results in an inability of the algorithm to correct for overlapping blood vessels on subtraction angiograms. Thus, semi-automated vessel tracing algorithms for CE-MRA subtraction angiograms may require individual validation depending on the underlying model of disease.

Under the hypothesis that cerebral blood volume maps could serve as a more robust surrogate marker for vessel density assessment, we then calculated ss-CBV with the cylinder model of blood vessels in the static dephasing regime of the MR signal to mitigate the limitation of interfering blooming artifacts (Boxerman et al., 1995). The effect of iron oxide nanoparticle dosage for ss-CBV is largely independent of concentration and the method has proven valid within a large range of concentrations both theoretically (Yablonskiy and Haacke, 1994) and experimentally (Tropres et al., 2004). In the present study, a significant increase in ss-CBV on Day 21 after ICAO was noted. Assuming equal contrast agent concentration and pulse sequence among all measurements, this higher ss-CBV after ICAO most likely represents an intraparenchymal vessel volume increase due to remodeling of the neocortical vasculature in line with our previous observations in the murine neocortex (Hecht et al., 2012, 2015; Marushima et al., 2019). For internal validation,

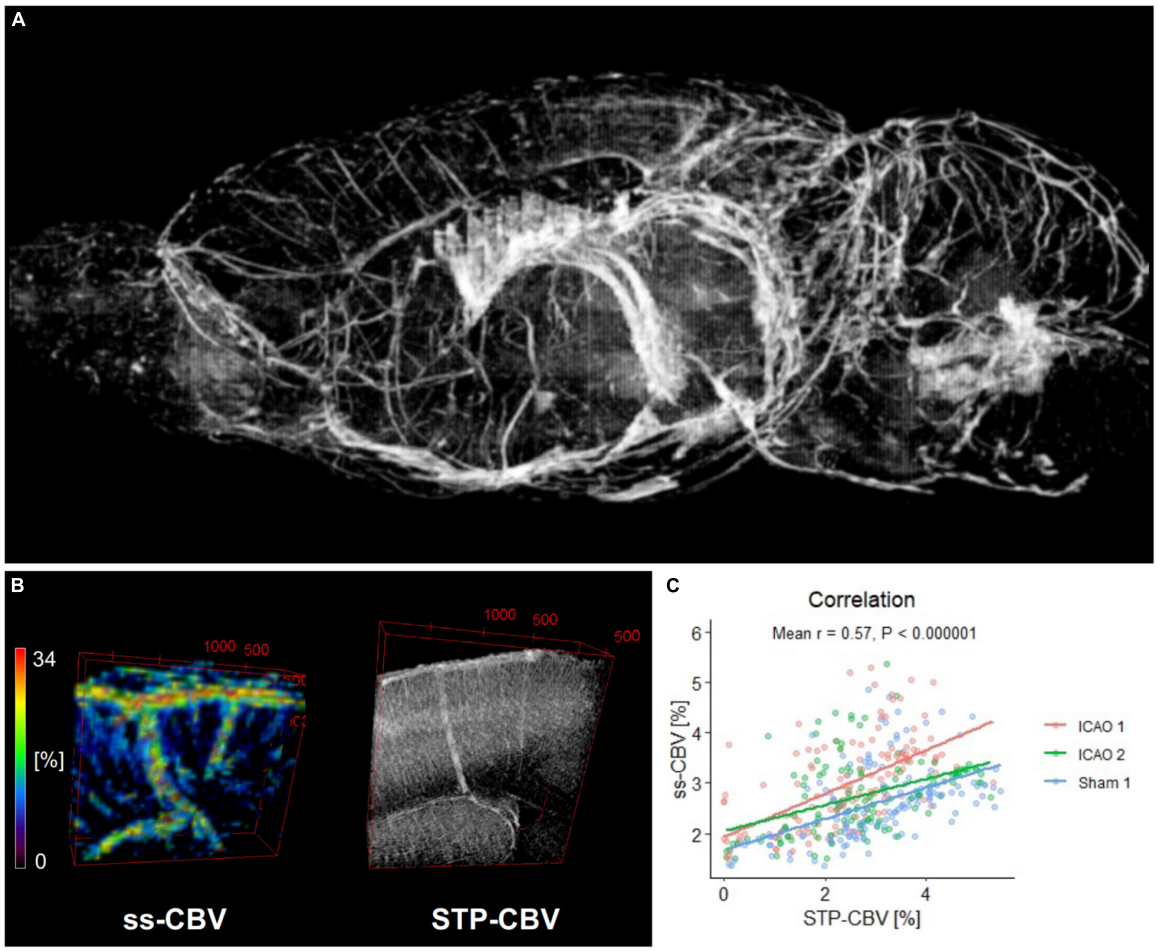

FIGURE 4 | Validation of ss-CBV against 3D serial two-photon tomography (STP). **(A)** Whole-brain histologic angiography: Perfused blood vessels were stained *in vivo* with lectin from Lycopersicon esculentum and measured by STP. The image shows a 3D reconstruction of large- and medium-size blood vessels of the cerebral vascular tree using the ImageJ plugin Volume Viewer (arbitrary units). **(B)** Panel shows corresponding maps of iron oxide nanoparticle-based ss-CBV and STP-CBV (including the capillary bed) reconstructed from STP (unit: volume percent). **(C)** Positive and significant correlation between STP-CBV and ss-CBV among 406 brain regions defined by the Allen murine brain atlas in 3 mice described by the mean Spearman's rank correlation coefficient.

ss-CBV was additionally compared to DSC-rCBV because DSC represents one of the most widely applied techniques for MRI-based CBV estimation. In our present setup, we found that both techniques can easily be combined in one protocol by low resolution fast imaging during bolus injection of the iron oxide nanoparticle (DSC-rCBV) followed by high resolution imaging after the blood pool agent has reached equilibrium concentration in plasma (ss-CBV). Importantly, ss-CBV was paralleled by DSC-rCBV values within limits of agreement but at clearly higher image resolution and contrast, which is explained by the strong effect of iron oxide nanoparticles on T2* shortening, the absence of contrast agent leakage, and the possibility of longer image acquisition time during steady-state blood volume mapping using iron oxide nanoparticles compared to bolus techniques with rapid first-pass effect, such as conventional blood volume mapping based on DSC (Guckel et al., 1994; Bremer et al., 2003; Wu et al., 2003; Varallyay et al., 2013). For definite morphological validation, ss-CBV was then compared to co-registered histology based on 3D whole brain STP. The significant correlation between ss-CBV and histological STP-CBV supported the hypothesis that ss-CBV can serve as a robust surrogate for blood vessel assessment. Importantly, for the first time we provide a systematic morphological validation of iron oxide nanoparticle-based ss-CBV maps by co-registering a comprehensive and corresponding complete histological data set, which is highly relevant considering that our atlas registration approach eliminates selection bias introduced by region-of-interest-based analyses and remains unaffected by inter-rater heterogeneity. Therefore, ss-CBV maps could serve as a method of choice for robust, semi-quantitative, and longitudinal blood vessel assessment at the level of the neocortical vasculature.

Alternative emerging approaches to quantify ferumoxytol enhanced vasculature are susceptibility weighted imaging (SWI) and quantitative susceptibility mapping (QSM), which even enabled us to distinguish between vessel diameters (Liu et al., 2018; Buch et al., 2020; Shen et al., 2020). However, none

of the studies performed histological validation and to our best knowledge, no SWI/QSM protocol for the mouse has been published in the context of cerebral microangiography. Furthermore, QSM studies require sophisticated postprocessing, which needs to be fed by complex simulations. Due to robustness, we decided for ss-CBV in this study, since the disadvantage of insensitivity of vessel diameter is an advantage at the same time: the results have no bias toward any vessel diameter. Thus, ss-CBV currently represents a more established parameter also applicable to very small vessels and independent of resolution.

Limitations

Clinically, iron oxide nanoparticle-based CE-MRA and ss-CBV maps could serve as a non-invasive alternative to digital subtraction angiography for longitudinal assessment of vascular malformations, brain tumor vascularity, anti-angiogenic treatment effects but also for improved planning of neurosurgical or radiosurgical procedures (Varallyay et al., 2013; Iv et al., 2018; Huang et al., 2019). However, clinical application has been limited to proof-of-concept studies and off-label use due to missing regulatory approval, which is mainly attributed to the concern that the carbohydrate coating of the nanoparticles could be associated with an increased risk of severe allergic response. On the other hand, the safety profile of iron oxide nanoparticles has been reported similar to iodinated contrast agents used for contrast-enhanced CT imaging (Vasanawala et al., 2016). Additionally, there is increasing awareness of permanent gadolinium deposition in the brain and its unknown risk (Gulani et al., 2017) and iron-based contrast agents may be considered as a suitable alternative (Boehm-Sturm et al., 2018).

A main limitation in the present study is the sample size. However, we deliberately decided to only use animals from one sex and a single model of disease because we believe that this optimizes the reliability of our findings by reducing the complexity of the model. Second, the lack of coherence to the previously published vessel tracing algorithm for CE-MRA underlines that such approaches may require individual validation depending on the used model or the diversity of the cohort, including the use of subjects of both sexes and different mouse strains. Third, validation of ss-CBV measurements were naturally limited by the fact that our STP vessel stain only reflected blood vessel walls rather than appreciate the entire volume of the vessel lumen as it is done by ss-CBV. On the other hand, the fact that ss-CBV recognizes the entire vessel lumen also explains why this method seems particularly useful for microvascular vessel volume quantification, because histological CBV may underestimate vessel density in areas of large surface vessels (Di Giovanna et al., 2018). Forth, although ss-CBV offers the possibility to determine vessel density based on perfused blood volume with the benefit of being extremely robust, ss-CBV is unable to distinguish between vessel diameters. For this purpose, vessel size imaging and quantitative blood oxygen level dependent imaging make use of more advanced biophysical models of spin echo MR signal in tissue (Kiselev and Novikov, 2018) but are currently limited by high noise level and low spatial resolution (Boehm-Sturm et al., 2013). MR vascular fingerprinting is a promising first attempt to reduce noise by simulating the MR signal in realistic tissue and finding a best match to the measured signal (Lemasson et al., 2016), which may soon enable vessel size sensitive imaging at similarly high resolution presented here while reducing impact of noise. In the future, automated machine-learning analyses of comprehensive histological and MR angiograms may help overcome the limitations of previous and the present work and yield further insights into neurovascular imaging correlates with the possibility of reliable clinical translation (Di Giovanna et al., 2018; Todorov et al., 2019).

DATA AVAILABILITY STATEMENT

The datasets presented in this study can be found in online repositories. The names of the repository/repositories and accession number(s) can be found below: https://gin.g-node.org/tdebortoli/CE_MRI.git.

ETHICS STATEMENT

The animal study was reviewed and approved by the local ethics committee on animal research (Landesamt für Gesundheit und Soziales, Berlin, Germany; LAGeSo approval number G0186/16).

AUTHOR CONTRIBUTIONS

NH and PB-S conceived and designed the study. NH drafted the Ethics committee proposal and supervised the project. TB performed the animal surgeries, tissue preparation for histology, confocal model validation analysis, and drafted the figures. PB-S, SK, and SM designed the MRI protocols. TB, PB-S, and SK performed the MRI validation analysis. TB and NH performed the statistical analysis. TB, PB-S, and NH created the first draft of the manuscript. All authors were involved in analysis and interpretation of the data and contributed to critical revision of the final manuscript.

FUNDING

NH was BIH Clinical Fellow funded by Stiftung Charité. SM, SK, and PB-S were funded by the German Federal Ministry of Education and Research (BMBF, Center for Stroke Research Berlin 01EO1301), the BMBF under the ERA-NET NEURON scheme (01EW1811), and the German Research Foundation (DFG, Project BO 4484/2-1 and EXC NeuroCure). MRI measurements were supported by Charité 3R| Replace – Reduce – Refine.

SUPPLEMENTARY MATERIAL

The Supplementary Material for this article can be found online at: https://www.frontiersin.org/articles/10.3389/fnins.2021.756577/full#supplementary-material

REFERENCES

Blakemore, C., MaCarthur Clark, J., Nevalainen, T., Oberdorfer, M., and Sussman, A. (2012). Implementing the 3Rs in neuroscience research: a reasoned approach. *Neuron* 75, 948–950. doi: 10.1016/j.neuron.2012.09.001

Boehm-Sturm, P., Farr, T. D., Adamczak, J., Jikeli, J. F., Mengler, L., Wiedermann, D., et al. (2013). Vascular changes after stroke in the rat: a longitudinal study using optimized magnetic resonance imaging. *Contrast Media Mol. Imaging* 8, 383–392. doi: 10.1002/cmmi.1534

Boehm-Sturm, P., Haeckel, A., Hauptmann, R., Mueller, S., Kuhl, C. K., and Schellenberger, E. A. (2018). Low-Molecular-weight iron chelates may be an alternative to gadolinium-based contrast agents for T1-weighted Contrast-enhanced MR Imaging. *Radiology* 286, 537–546. doi: 10.1148/radiol.2017170116

Boxerman, J. L., Hamberg, L. M., Rosen, B. R., and Weisskoff, R. M. (1995). MR contrast due to intravascular magnetic susceptibility perturbations. *Magn. Reson. Med.* 34, 555–566.

Boxerman, J. L., Schmainda, K. M., and Weisskoff, R. M. (2006). Relative cerebral blood volume maps corrected for contrast agent extravasation significantly correlate with glioma tumor grade, whereas uncorrected maps do not. *AJNR Am. J. Neuroradiol.* 27, 859–867.

Bremer, C., Mustafa, M., Bogdanov, A. Jr., Ntziachristos, V., Petrovsky, A., and Weissleder, R. (2003). Steady-state blood volume measurements in experimental tumors with different angiogenic burdens a study in mice. *Radiology* 226, 214–220. doi: 10.1148/radiol.2261012140

Brozici, M., van der Zwan, A., and Hillen, B. (2003). Anatomy and functionality of leptomeningeal anastomoses: a review. *Stroke* 34, 2750–2762. doi: 10.1161/01.STR.0000095791.85737.65

Buch, S., Subramanian, K., Jella, P. K., Chen, Y., Wu, Z., Shah, K., et al. (2021). Revealing vascular abnormalities and measuring small vessel density in multiple sclerosis lesions using USPIO. *Neuroimage Clin.* 29:102525. doi: 10.1016/j.nicl.2020.102525

Buch, S., Wang, Y., Park, M. G., Jella, P. K., Hu, J., Chen, Y., et al. (2020). Subvoxel vascular imaging of the midbrain using USPIO-Enhanced MRI. *Neuroimage* 220:117106. doi: 10.1016/j.neuroimage.2020.117106

Buschmann, I. R., Busch, H. J., Mies, G., and Hossmann, K. A. (2003). Therapeutic induction of arteriogenesis in hypoperfused rat brain via granulocyte-macrophage colony-stimulating factor. *Circulation* 108, 610–615. doi: 10.1161/01.CIR.0000074209.17561.99

Campbell, B. C., Christensen, S., Tress, B. M., Churilov, L., Desmond, P. M., Parsons, M. W., et al. (2013). Failure of collateral blood flow is associated with infarct growth in ischemic stroke. *J. Cereb. Blood Flow Metab.* 33, 1168–1172. doi: 10.1038/jcbfm.2013.77

Di Giovanna, A. P., Tibo, A., Silvestri, L., Mullenbroich, M. C., Costantini, I., Allegra Mascaro, A. L., et al. (2018). Whole-Brain vasculature reconstruction at the single capillary level. *Sci. Rep.* 8:12573. doi: 10.1038/s41598-018-30533-3

Duelsner, A., Gatzke, N., Glaser, J., Hillmeister, P., Li, M., Lee, E. J., et al. (2012). Granulocyte colony-stimulating factor improves cerebrovascular reserve capacity by enhancing collateral growth in the circle of Willis. *Cerebrovasc. Dis.* 33, 419–429. doi: 10.1159/000335869

Foddis, M., Winek, K., Bentele, K., Mueller, S., Blumenau, S., Reichhart, N. N., et al. (2020). An exploratory investigation of brain collateral circulation plasticity after cerebral ischemia in two experimental C57BL/6 mouse models. *J. Cereb. Blood Flow Metab.* 40, 276–287. doi: 10.1177/0271678X19827251

Guckel, F., Brix, G., Rempp, K., Deimling, M., Rother, J., and Georgi, M. (1994). Assessment of cerebral blood volume with dynamic susceptibility contrast enhanced gradient-echo imaging. *J. Comput. Assist. Tomogr.* 18, 344–351. doi: 10.1097/00004728-199405000-00002

Gulani, V., Calamante, F., Shellock, F. G., Kanal, E., Reeder, S. B., and International Society for Magnetic Resonance in, M. (2017). Gadolinium deposition in the brain: summary of evidence and recommendations. *Lancet Neurol.* 16, 564–570. doi: 10.1016/S1474-4422(17)30158-8

Hecht, N., He, J., Kremenetskaia, I., Nieminen, M., Vajkoczy, P., and Woitzik, J. (2012). Cerebral hemodynamic reserve and vascular remodeling in C57/BL6 mice are influenced by age. *Stroke* 43, 3052–3062. doi: 10.1161/STROKEAHA.112.653204

Hecht, N., Marushima, A., Nieminen, M., Kremenetskaia, I., von Degenfeld, G., Woitzik, J., et al. (2015). Myoblast-mediated gene therapy improves functional collateralization in chronic cerebral hypoperfusion. *Stroke* 46, 203–211. doi: 10.1161/STROKEAHA.114.006712

Huang, Y., Yecies, D., Bruckert, L., Parker, J. J., Ho, A. L., Kim, L. H., et al. (2019). Stereotactic laser ablation for completion corpus callosotomy. *J .Neurosurg. Pediatr.* 1–9. doi: 10.3171/2019.5.PEDS19117 [Epub ahead of print].

Iv, M., Choudhri, O., Dodd, R. L., Vasanawala, S. S., Alley, M. T., Moseley, M., et al. (2018). High-resolution 3D volumetric contrast-enhanced MR angiography with a blood pool agent (ferumoxytol) for diagnostic evaluation of pediatric brain arteriovenous malformations. *J. Neurosurg. Pediatr.* 22, 251–260. doi: 10.3171/2018.3.PEDS17723

Kiselev, V. G., and Novikov, D. S. (2018). Transverse NMR relaxation in biological tissues. *Neuroimage* 182, 149–168. doi: 10.1016/j.neuroimage.2018.06.002

Kitagawa, K., Yagita, Y., Sasaki, T., Sugiura, S., Omura-Matsuoka, E., Mabuchi, T., et al. (2005). Chronic mild reduction of cerebral perfusion pressure induces ischemic tolerance in focal cerebral ischemia. *Stroke* 36, 2270–2274. doi: 10.1161/01.STR.0000181075.77897.0e

Klein, S., Staring, M., Murphy, K., Viergever, M. A., and Pluim, J. P. (2010). Elastix: a toolbox for intensity-based medical image registration. *IEEE Trans. Med. Imaging* 29, 196–205. doi: 10.1109/TMI.2009.2035616

Klohs, J., Baltes, C., Princz-Kranz, F., Ratering, D., Nitsch, R. M., Knuesel, I., et al. (2012). Contrast-enhanced magnetic resonance microangiography reveals remodeling of the cerebral microvasculature in transgenic ArcAbeta mice. *J .Neurosci.* 32, 1705–1713. doi: 10.1523/JNEUROSCI.5626-11.2012

Knauss, S., Albrecht, C., Dirnagl, U., Mueller, S., Harms, C., Hoffmann, C. J., et al. (2020). A Semiquantitative non-invasive measurement of PcomA patency in C57BL/6 mice explains variance in ischemic brain damage in filament MCAo. *Front. Neurosci.* 14:576741. doi: 10.3389/fnins.2020.576741

Knobloch, G., Colgan, T., Wiens, C. N., Wang, X., Schubert, T., Hernando, D., et al. (2018). Relaxivity of ferumoxytol at 1.5 T and 3.0 T. *Invest. Radiol.* 53, 257–263. doi: 10.1097/RLI.0000000000000434

Koch, S., Mueller, S., Foddis, M., Bienert, T., von Elverfeldt, D., Knab, F., et al. (2019). Atlas registration for edema-corrected MRI lesion volume in mouse stroke models. *J. Cereb. Blood Flow Metab.* 39, 313–323. doi: 10.1177/0271678X17726635

Lein, E. S., Hawrylycz, M. J., Ao, N., Ayres, M., Bensinger, A., Bernard, A., et al. (2007). Genome-wide atlas of gene expression in the adult mouse brain. *Nature* 445, 168–176. doi: 10.1038/nature05453

Lemasson, B., Bouchet, A., Maisin, C., Christen, T., Le Duc, G., Remy, C., et al. (2015). Multiparametric MRI as an early biomarker of individual therapy effects during concomitant treatment of brain tumours. *NMR Biomed.* 28, 1163–1173. doi: 10.1002/nbm.3357

Lemasson, B., Pannetier, N., Coquery, N., Boisserand, L. S., Collomb, N., Schuff, N., et al. (2016). MR vascular fingerprinting in stroke and brain tumors models. *Sci. Rep.* 6:37071. doi: 10.1038/srep37071

Lima, F. O., Furie, K. L., Silva, G. S., Lev, M. H., Camargo, E. C., Singhal, A. B., et al. (2014). Prognosis of untreated strokes due to anterior circulation proximal intracranial arterial occlusions detected by use of computed tomography angiography. *JAMA Neurol.* 71, 151–157. doi: 10.1001/jamaneurol.2013.5007

Liu, S., Brisset, J. C., Hu, J., Haacke, E. M., and Ge, Y. (2018). Susceptibility weighted imaging and quantitative susceptibility mapping of the cerebral vasculature using ferumoxytol. *J. Magn. Reson. Imaging* 47, 621–633. doi: 10.1002/jmri.25809

Marushima, A., Nieminen, M., Kremenetskaia, I., Gianni-Barrera, R., Woitzik, J., Degenfeld, G. V., et al. (2019). Balanced single-vector co-delivery of VEGF/PDGF-BB improves functional collateralization in chronic cerebral ischemia. *J. Cereb. Blood Flow Metab.* 40, 404–419. doi: 10.1177/0271678X18818298

Menon, B. K., Smith, E. E., Coutts, S. B., Welsh, D. G., Faber, J. E., Goyal, M., et al. (2013). Leptomeningeal collaterals are associated with modifiable metabolic risk factors. *Ann. Neurol.* 74, 241–248. doi: 10.1002/ana.23906

Nesselroade, J. R., and Ram, N. (2004). Studying intraindividual variability: what we have learned that will help us understand lives in context. *Res. Hum. Dev.* 1, 9–29. doi: 10.1080/15427609.2004.9683328

Nishimura, N., Schaffer, C. B., Friedman, B., Lyden, P. D., and Kleinfeld, D. (2007). Penetrating arterioles are a bottleneck in the perfusion of neocortex. *Proc. Natl. Acad. Sci. U.S.A.* 104, 365–370. doi: 10.1073/pnas.0609551104

Plock, N., Facius, A., Lahu, G., Wood, N., Frigo, T., Deveney, A., et al. (2015). Population pharmacokinetic meta-analysis to bridge ferumoxytol plasma

pharmacokinetics across populations. *Clin. Pharmacokinet* 54, 385–395. doi: 10.1007/s40262-014-0203-9

Ragan, T., Kadiri, L. R., Venkataraju, K. U., Bahlmann, K., Sutin, J., Taranda, J., et al. (2012). Serial two-photon tomography for automated ex vivo mouse brain imaging. *Nat. Methods* 9, 255–258. doi: 10.1038/nmeth.1854

Rohrer, M., Bauer, H., Mintorovitch, J., Requardt, M., and Weinmann, H. J. (2005). Comparison of magnetic properties of MRI contrast media solutions at different magnetic field strengths. *Invest. Radiol.* 40, 715–724. doi: 10.1097/01.rli.0000184756.66360.d3

Schaper, W., and Scholz, D. (2003). Factors regulating arteriogenesis. *Arterioscler Thromb. Vasc. Biol.* 23, 1143–1151. doi: 10.1161/01.ATV.0000069625.11230.96

Schneeloch, E., Mies, G., Busch, H. J., Buschmann, I. R., and Hossmann, K. A. (2004). Granulocyte-macrophage colony-stimulating factor-induced arteriogenesis reduces energy failure in hemodynamic stroke. *Proc .Natl. Acad. Sci .U.S.A.* 101, 12730–12735. doi: 10.1073/pnas.0404880101

Schneider, U. C., Schilling, L., Schroeck, H., Nebe, C. T., Vajkoczy, P., and Woitzik, J. (2007). Granulocyte-macrophage colony-stimulating factor-induced vessel growth restores cerebral blood supply after bilateral carotid artery occlusion. *Stroke* 38, 1320–1328. doi: 10.1161/01.STR.0000259707.43496.71

Shamonin, D. P., Bron, E. E., Lelieveldt, B. P., Smits, M., Klein, S., Staring, M., et al. (2013). Fast parallel image registration on CPU and GPU for diagnostic classification of Alzheimer's disease. *Front. Neuroinform.* 7:50. doi: 10.3389/fninf.2013.00050

Shen, Y., Hu, J., Eteer, K., Chen, Y., Buch, S., Alhourani, H., et al. (2020). Detecting sub-voxel microvasculature with USPIO-enhanced susceptibility-weighted MRI at 7 T. *Magn. Reson. Imaging* 67, 90–100. doi: 10.1016/j.mri.2019.12.010

Shuaib, A., Butcher, K., Mohammad, A. A., Saqqur, M., and Liebeskind, D. S. (2011). Collateral blood vessels in acute ischaemic stroke: a potential therapeutic target. *Lancet Neurol.* 10, 909–921. doi: 10.1016/S1474-4422(11)70195-8

Todo, K., Kitagawa, K., Sasaki, T., Omura-Matsuoka, E., Terasaki, Y., Oyama, N., et al. (2008). Granulocyte-macrophage colony-stimulating factor enhances leptomeningeal collateral growth induced by common carotid artery occlusion. *Stroke* 39, 1875–1882. doi: 10.1161/STROKEAHA.107.503433

Todorov, M. I., Paetzold, J. C., Schoppe, O., Tetteh, G., Efremov, V., Völgyi, K., et al. (2019). Automated analysis of whole brain vasculature using machine learning. *BioRxiv* [Preprint]. doi: 10.1101/613257

Tropres, I., Lamalle, L., Farion, R., Segebarth, C., and Remy, C. (2004). Vessel size imaging using low intravascular contrast agent concentrations. *MAGMA* 17, 313–316. doi: 10.1007/s10334-004-0067-3

Varallyay, C. G., Nesbit, E., Fu, R., Gahramanov, S., Moloney, B., Earl, E., et al. (2013). High-resolution steady-state cerebral blood volume maps in patients with central nervous system neoplasms using ferumoxytol, a superparamagnetic iron oxide nanoparticle. *J. Cereb. Blood Flow Metab.* 33, 780–786. doi: 10.1038/jcbfm.2013.36

Vasanawala, S. S., Nguyen, K. L., Hope, M. D., Bridges, M. D., Hope, T. A., Reeder, S. B., et al. (2016). Safety and technique of ferumoxytol administration for MRI. *Magn. Reson. Med.* 75, 2107–2111. doi: 10.1002/mrm.26151

Wu, E. X., Wong, K. K., Andrassy, M., and Tang, H. (2003). High-resolution in vivo CBV mapping with MRI in wild-type mice. *Magn. Reson. Med.* 49, 765–770. doi: 10.1002/mrm.10425

Yablonskiy, D. A., and Haacke, E. M. (1994). Theory of NMR signal behavior in magnetically inhomogeneous tissues: the static dephasing regime. *Magn. Reson. Med.* 32, 749–763. doi: 10.1002/mrm.1910320610

Conflict of Interest: The authors declare that the research was conducted in the absence of any commercial or financial relationships that could be construed as a potential conflict of interest.

Publisher's Note: All claims expressed in this article are solely those of the authors and do not necessarily represent those of their affiliated organizations, or those of the publisher, the editors and the reviewers. Any product that may be evaluated in this article, or claim that may be made by its manufacturer, is not guaranteed or endorsed by the publisher.

frontiers in Neuroscience

ORIGINAL RESEARCH
published: 05 January 2022
doi: 10.3389/fnins.2021.789852

Vertebrobasilar Junction Angle Over 90°: A Potential Imaging Marker Associated With Vertebrobasilar Atherosclerosis

*Jia Li[1,2], Wen-Jie Yang[3], Lu Zheng[4], Heng Du[2], Winnie Chiu-Wing Chu[5], Thomas Wai-Hong Leung[6] and Xiang-Yan Chen[2]**

[1] Department of Critical Care Medicine, Ruijin Hospital, Shanghai Jiao Tong University School of Medicine, Shanghai, China, [2] Department of Health Technology and Informatics, The Hong Kong Polytechnic University, Kowloon, Hong Kong SAR, China, [3] Department of Diagnostic Radiology and Nuclear Medicine, University of Maryland, Baltimore, Baltimore, MD, United States, [4] Department of Neurology, The Third Affiliated Hospital of Sun Yat-sen University, Guangzhou, China, [5] Department of Imaging and Interventional Radiology, Prince of Wales Hospital, The Chinese University of Hong Kong, Shatin, Hong Kong SAR, China, [6] Division of Neurology, Department of Medicine and Therapeutics, Prince of Wales Hospital, The Chinese University of Hong Kong, Shatin, Hong Kong SAR, China

OPEN ACCESS

Edited by:
Umar Sadat,
University of Cambridge,
United Kingdom

Reviewed by:
Zhen-Ni Guo,
First Affiliated Hospital of Jilin University, China
David Wack,
University at Buffalo, United States

***Correspondence:**
Xiang-Yan Chen
fiona.chen@polyu.edu.hk

Specialty section:
This article was submitted to Brain Imaging Methods, a section of the journal Frontiers in Neuroscience

Received: 05 October 2021
Accepted: 23 November 2021
Published: 05 January 2022

Citation:
Li J, Yang W-J, Zheng L, Du H, Chu WC-W, Leung TW-H and Chen X-Y (2022) Vertebrobasilar Junction Angle Over 90°: A Potential Imaging Marker Associated With Vertebrobasilar Atherosclerosis. Front. Neurosci. 15:789852. doi: 10.3389/fnins.2021.789852

Objective: Whether the cerebral vascular variations play an important role in the progression of intracranial atherosclerosis is yet largely unclear. We aimed to investigate the relationship between the magnitude of the vertebrobasilar junction (VBJ) angle and the imaging features of vertebrobasilar artery atherosclerosis.

Methods: Adult patients with acute ischemic stroke or transient ischemic attack undergoing a 3.0-tesla vessel wall magnetic resonance imaging (VW-MRI) scanning were consecutively included. Imaging features of vertebrobasilar artery atherosclerosis were assessed on the reconstructed short axis of VW-MRI at the most stenotic site. The VBJ angle degree was measured on magnetic resonance angiography and classified into the angle ≥90° or <90°.

Results: Among 68 patients (mean age = 63.5 ± 9.4 years old; 63.2% were male) with vertebrobasilar atherosclerosis, 33 had a VBJ angle ≥90° and 35 had a VBJ angle <90°. Compared to the vertebrobasilar plaques with VBJ angle <90°, those with VBJ angle ≥90° had a heavier plaque burden (84.35 vs. 70.58%, $p < 0.001$) and higher prevalence of intraplaque hemorrhage (17.1 vs. 3.3%, $p = 0.01$). In the regression analyses, the VBJ angle ≥90° was also robustly associated with plaque burden (odds ratio, 1.11; 95% confidential interval, 1.043–1.18; $p = 0.001$) and intraplaque hemorrhage (odds ratio, 5.776; 95% confidential interval, 1.095–30.46; $p = 0.039$) of vertebrobasilar atherosclerosis.

Conclusion: The VBJ angle over 90° might aggravate the vessel wall condition of the atherosclerotic vertebrobasilar arteries, which might serve as a potential risk factor for vertebrobasilar atherosclerosis.

Keywords: intracranial atherosclerosis, vertebrobasilar circulation, vertebrobasilar junction angle, cerebral vascular variation, plaque imaging feature

INTRODUCTION

Ischemic stroke (IS) due to intracranial large artery atherosclerosis poses a major threat to the global public health and economy (Kaul et al., 2018; Kim et al., 2020; Wang et al., 2020). Up to 25% of acute ischemic events entail the brain tissues supported by the vertebrobasilar artery system and still carries increasing risks of stroke-related disability and stroke recurrence (Savitz and Caplan, 2005; Sparaco et al., 2019).

Geometric variants commonly exist in the vertebrobasilar artery system and may exert a strong influence on the formation of vertebrobasilar atherosclerosis mainly *via* the direct impact on the vertebrobasilar circulation hemodynamics (Yu et al., 2018; Xu et al., 2019; Zhou et al., 2020). Notably, the confluence angles of the vertebrobasilar junction (VBJ) vary from 10° to 160° (Ravensbergen et al., 1996, 1998). Previous research showed that patients with deep pontine lacunar infarction had significantly larger VBJ angles than healthy individuals (Jeong et al., 2015). Furthermore, the larger VBJ angles were also revealed in robust relevance to the hemodynamic alteration, thereby leading to the proneness to vertebrobasilar atherosclerosis in the numerical and experimental models (Ravensbergen et al., 1996, 1998; Zhang et al., 2016). Nevertheless, little clinical evidence from stroke patients could be provided to ascertain the relationship between the varying VBJ angle degrees and the progression of vertebrobasilar atherosclerosis.

With the utilization of high-resolution vessel wall magnetic resonance imaging (VW-MRI), the imaging features of vertebrobasilar artery atherosclerosis can be evaluated quantitatively and qualitatively in patients with acute ischemic stroke (AIS) attributed to intracranial large-artery atherosclerotic stenosis. In this hospital-based study, we aimed to determine the association of the VBJ angle magnitude with the imaging characterization of vertebrobasilar atherosclerosis assessed on VW-MRI.

MATERIALS AND METHODS

Study Population

Consecutive adult patients with IS or transient ischemic attack (TIA) who underwent VW-MRI at the Prince of Wales Hospital from 2015 to 2020 for intracranial large artery stenosis were retrospectively included in this study. The inclusion criteria for this study were as follows: (1) First-ever AIS or TIA within 7 days; (2) Presence of the bilateral vertebral arteries (VAs) and the basilar artery (BA) shown on magnetic resonance angiography (MRA); (3) The intracranial segments of the VAs completely covered by VW-MRI; (4) Atherosclerotic plaques on the intracranial VA and the BA detected by VW-MRI; (5) Good image quality for the imaging analyses. Subjects were excluded when meeting the following conditions: (1) Non-atherosclerotic stenosis, such as moyamoya disease, vasculitis, and dissection; (2) Clinical evidence of cardioembolism, including valvular heart disease and atrial fibrillation; (3) Coexistent moderate to severe carotid artery stenosis; (4) History of vascular malformation, brain tumor, or cerebral interventional or vascular surgical procedure. The patient baseline clinical data were recorded (age, sex, hypertension, hyperlipidemia, diabetes, and current smoking status). The study was approved by the Joint Chinese University of Hong Kong-New Territories East Cluster Clinical Research Ethics Committee (the Joint CUHK-NTEC CREC, No. 2015.011) and followed the 1975 Declaration of Helsinki. The written informed consents were signed by all the patients or their family members.

Imaging Protocol

All VW-MRI exams were performed using a 3.0-tesla Achieva MR system (Philips Healthcare, Cleveland, OH, United States) with an 8-channel head coil in this study. As described in our previous VW-MRI study (Li et al., 2020), the imaging protocol included a 3-dimensional T1-weighted (T1w) Volumetric ISotropically Turbo spin echo Acquisition (VISTA) sequence before and after the administration of a gadolinium-containing contrast agent (Dotarem, Gadoteric acid 0.5 mmol/ml; Guerbet, Roissy CdG Cedex, France) (0.1 ml/kg to each subject) and a 3-dimensional Time-Of-Flight (TOF) MRA sequence. The T1w VISTA sequence parameters were as follows: field of view (FOV) 200 mm × 167 mm × 45 mm, acquired resolution 0.6 mm × 0.6 mm × 1.0 mm, and repetition time (TR)/echo time (TE) 1,500/36 ms. The TOF MRA sequence was acquired using FOV 200 mm × 200 mm × 56 mm, acquired resolution 0.4 mm × 0.6 mm × 0.7 mm, and TR/TE 23/3.5 ms.

Measuring the Vertebrobasilar Junction Angle Magnitude

Two raters (JL and HD) blind to the patient clinical information independently measured the degrees of the VBJ angles on TOF MRA imaging using OsiriX DICOM Viewer (Geneva, Switzerland) (**Figure 1**). The VBJ angle referred to the relevant angle between the two inner vessel walls of the bilateral VAs (Ravensbergen et al., 1998). The measurement of the VBJ angle magnitude was carried out independently of the subsequent assessment of the vertebrobasilar artery plaques.

Quantitatively and Qualitatively Evaluating the Vertebrobasilar Plaques

Another two raters (W-JY and LZ) also blind to the patient clinical data independently determined the imaging features of vertebrobasilar atherosclerosis on VW-MRI (**Figure 2**). Atherosclerotic plaques along the bilateral intracranial VA segments and the BA were identified as vessel wall thickening on the matched pre- and post-contrast T1w images, according to a previously published definition (Yang et al., 2021).

The quantitative measurements of vertebrobasilar artery plaques were performed on the reconstructed cross-sectional images at the narrowest luminal site by using VesselMass software (Leiden University Medical Center, Netherlands) based on the prior methods (Guo et al., 2018; Wang et al., 2018; Yang et al., 2020). The adjacent plaque-free, non-tortuous, normal vessel segment proximal or distal to the lesion was used as the reference site. The vessel–cerebrospinal fluid interface was manually traced to measure vessel area ($VA_{measure}$). The blood–intima interface

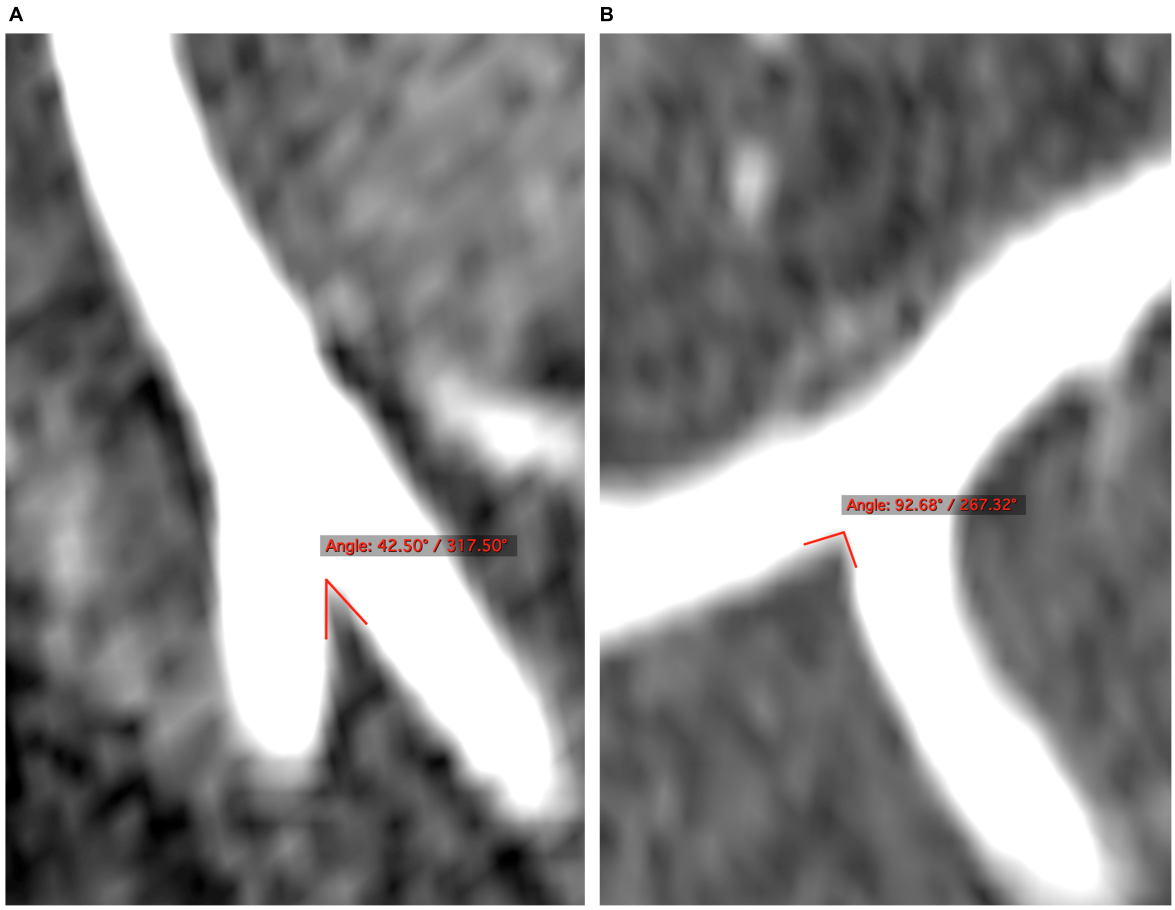

FIGURE 1 | The degrees of the VBJ confluence angles are examined on the 3-dimensional reconstructed cross sections of MRA. **(A,B)** The VBJ angles less than and more than 90°, respectively. MRA, magnetic resonance angiography; VBJ, vertebrobasilar junction.

was used for determining lumen area (LA). Wall area (WA) was defined as $VA_{measure}$ – LA. Luminal stenosis percentage was calculated as (1 – lesion LA/reference LA) × 100%. Plaque burden was defined as (lesion WA/lesion $VA_{measure}$) × 100%. Wall area index was determined by lesion WA/reference WA. Remodeling index (RI) was defined as lesion $VA_{measure}$/reference $VA_{measure}$. The remodeling pattern was designated as positive (RI ≥ 1.05) or non-positive (RI < 1.05). Plaque eccentricity index was defined as (maximum wall thickness – minimum wall thickness)/maximum wall thickness. Each plaque was classified as eccentric (eccentricity index ≥0.5) or concentric (eccentricity index <0.5).

A round area of 10–12 mm^2 at the normal gray matter near the plaque lesion was manually drawn on both pre- and post-contrast T1w images to measure the signal intensity of gray matter ($SI_{gray-matter}$). The signal intensity of plaque (SI_{plaque}) normalized to $SI_{gray-matter}$ was measured on the matched pre- and post-contrast T1w images to determine the plaque contrast enhancement: Plaque enhancement index = [(SI_{plaque}/$SI_{gray-matter}$ on post-contrast T1w images) – (SI_{plaque}/$SI_{gray-matter}$ on pre-contrast T1w images)]/(SI_{plaque}/$SI_{gray-matter}$ on pre-contrast T1w images) × 100%.

Hypointensity or hyperintensity in the plaque by comparison with the signal intensity of the adjacent normal gray matter tissue on the pre-contrast T1w image was recorded (Yang et al., 2016). The presence of intraplaque hemorrhage (IPH) was recognized as a region of high signal within the plaque (over 150% of the signal intensity of adjacent vessel-wall area) on the pre-contrast T1w images (Yang et al., 2020).

A plaque was classified as symptomatic if it was the only or the most enhanced plaque in the territory of brain infarct or neurological symptom (Yang et al., 2020). It was defined as asymptomatic plaque if the plaque was out of the territory of brain infarct or neurological symptom or the plaque was not the most enhanced in the corresponding ischemic territory (Yang et al., 2020).

Statistical Analysis

All statistical data were analyzed using the SPSS version 26.0 (IBM, NY, United States). The distribution of the VBJ angles was displayed using GraphPad Prism 8.0 (GraphPad Software Inc., San Diego, CA, United States). Variables were shown as mean ± standard deviation (SD), median [interquartile range (IQR)], or number (percentage), when appropriate. The

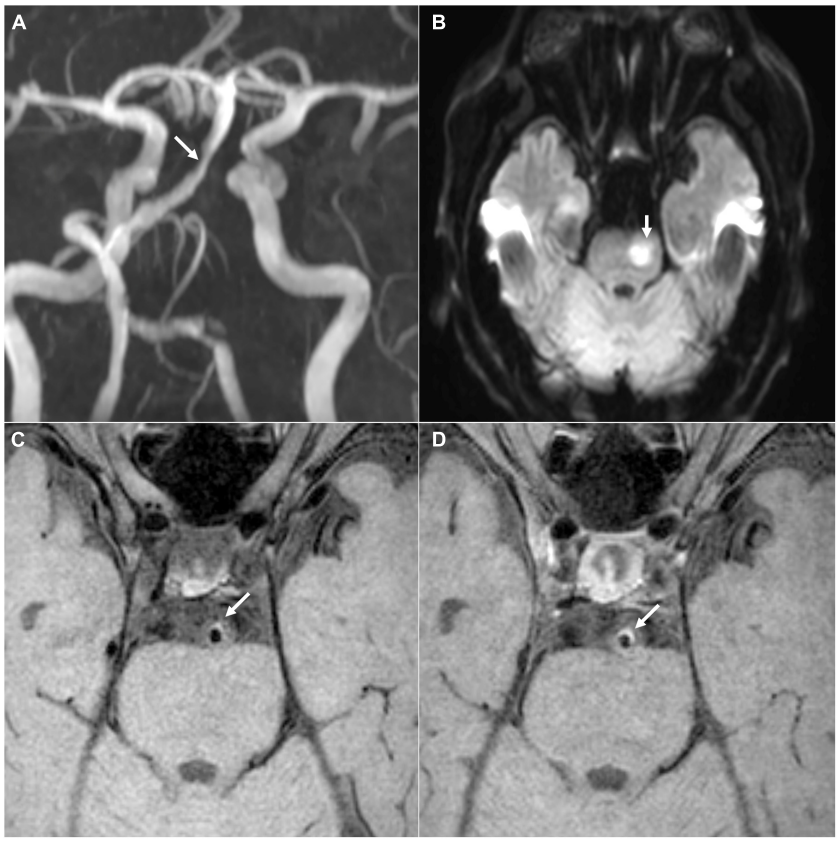

FIGURE 2 | A representative case of acute ischemia in vertebrobasilar circulation. **(A)** The MRA image shows stenosis in the BA (white arrow). **(B)** The diffusion-weighted image shows acute infarction in the BA territory (white arrow). **(C,D)** The pre- and post-contrast T1-weighted images show the BA plaque as a symptomatic lesion, respectively (white arrows). BA, basilar artery; MRA, magnetic resonance angiography.

baseline clinical features of subjects with vertebrobasilar artery atherosclerosis were compared between the VBJ angles ≥90° and the angles <90° by using *t*-test, chi-square test, or Fisher's exact test. The imaging characterizations of vertebrobasilar atherosclerotic plaques were compared between the cases with VBJ angle ≥90° and those with VBJ angle <90° by using Mann–Whitney *U* test, chi-square test, or Fisher's exact test. Univariate and multivariate logistic regression analyses were carried out to further estimate the relationship between the VBJ angle magnitude and the imaging features of vertebrobasilar artery atherosclerosis. A p-value < 0.05 was regarded as statistically significant. Inter-rater reliability was determined by intraclass correlation or Cohen κ coefficient with 95% confidence interval (CI). A coefficient >0.81 was considered as excellent.

RESULTS

Patient Demographic and Clinical Characteristics

A total of 68 patients (mean age, 63.53 ± 9.42 years; 43 male) with vertebrobasilar artery atherosclerosis were included in this study. The patient clinical characteristics on admission were summarized in **Table 1**.

The degrees of the VBJ angles varied from 29.45° to 124.20° (median, 85.18°; IQR, 68.34°–108.02°) in patients with vertebrobasilar atherosclerosis (**Figure 3**). According to the VBJ angle magnitude exceeding 90° or not, all the patients were subsequently categorized into two groups: 33 with VBJ angle ≥90° and 35 with VBJ angle <90°. Yet, no statistical significance was observed in the difference of the baseline clinical features between the two groups (all p-values > 0.05), as shown in **Table 1**.

Vertebrobasilar Artery Atherosclerosis and the Vertebrobasilar Junction Angle Magnitude

In total, 131 vertebrobasilar atherosclerotic plaques were detected in all the subjects, including 70 within the VBJ angles ≥90° and 61 within the VBJ angles <90°. The comparisons of the vertebrobasilar plaque imaging features between the groups with VBJ angle ≥90° and <90° were illustrated in **Table 2**.

As shown in **Table 2**, the VBJ angles ≥90° possessed more vertebrobasilar artery plaques with symptomatic status (20.0 vs. 4.9%, p-value = 0.01), hypointensity signal (51.4 vs. 31.1%, p-value = 0.019), and IPH (17.1 vs. 3.3%, p-value = 0.01) than

TABLE 1 | Baseline clinical characteristics of patients with vertebrobasilar artery atherosclerosis between the VBJ angles ≥90° and <90°.

Parameters	All subjects (*n* = 68)	Subjects with VBJ angle ≥90° (*n* = 33)	Subjects with VBJ angle <90° (*n* = 35)	*p*-value
Age, years, mean ± SD	63.53 ± 9.42	62.97 ± 9.69	64.06 ± 9.25	0.638
Male/female, n	43/25	22/11	21/14	0.569
Hypertension, n (%)	54 (79.4%)	26 (78.8%)	28 (80.0%)	0.902
Hyperlipidemia, n (%)	39 (57.4%)	21 (63.6%)	18 (51.4%)	0.309
Diabetes, n (%)	27 (39.7%)	11 (33.3%)	16 (45.7%)	0.297
Smoking, n (%)	18 (26.5%)	9 (27.3%)	9 (25.7%)	0.884
Index event				0.107
Stroke, n (%)	61 (89.7%)	32 (97.0%)	29 (82.9%)	
TIA, n (%)	7 (10.3%)	1 (3.0%)	6 (17.1%)	

SD, standard deviation; TIA, transient ischemic attack; VBJ angle, vertebrobasilar junction angle.

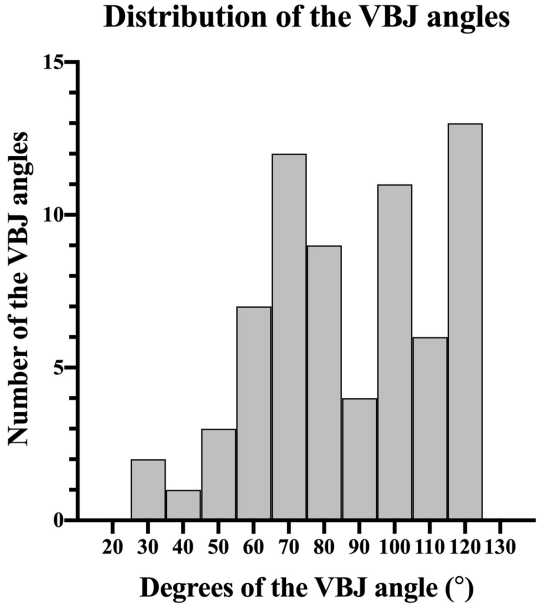

FIGURE 3 | Histograms showing the distribution of the VBJ angles in patients with vertebrobasilar artery atherosclerosis. VBJ, vertebrobasilar junction.

the VBJ angles <90°. However, no statistical significance was found in the difference of plaque hyperintensity signal, plaque wall morphology, or arterial remodeling pattern between the VBJ angles ≥90° and the angles <90° (all *p*-values > 0.05; **Table 2**).

Moreover, compared to the vertebrobasilar plaques with VBJ angle <90°, those with VBJ angle ≥90° had significantly higher percentages of luminal stenosis (73.89 vs. 45.68%, *p*-value < 0.001; **Table 2**) and plaque burden (84.35 vs. 70.58%, *p*-value < 0.001; **Table 2**). There were no significant differences observed in other plaque imaging characteristics between the two groups, such as wall area index, RI, plaque eccentricity index, and plaque enhancement index (all *p*-values > 0.05; **Table 2**).

TABLE 2 | Imaging characteristics of vertebrobasilar artery atherosclerosis between the VBJ angles ≥90° and <90°.

Features	Plaques with VBJ angle ≥90° (*n* = 70)	Plaques with VBJ angle <90° (*n* = 61)	*p*-value
Symptomatic status, n (%)	14 (20.0%)	3 (4.9%)	0.010
Hypointensity signal, n (%)	36 (51.4%)	19 (31.1%)	**0.019**
Hyperintensity signal, n (%)	19 (27.1%)	14 (23.0%)	0.581
IPH, n (%)	12 (17.1%)	2 (3.3%)	**0.010**
Plaque wall morphology			0.272
Eccentric, n (%)	40 (57.1%)	29 (47.5%)	
Concentric, n (%)	30 (42.9%)	32 (52.5%)	
Arterial remodeling			0.740
Positive, n (%)	51 (72.9%)	46 (75.4%)	
Non-positive, n (%)	19 (27.1%)	15 (24.6%)	
Luminal stenosis, %, median (IQR)	73.89 (53.81-85.12)	45.68 (35.24-66.32)	**<0.001**
Plaque burden, %, median (IQR)	84.35 (75.24-89.88)	70.58 (64.89-77.73)	**<0.001**
Wall area index, median (IQR)	35.89 (12.43-63.88)	31.80 (12.67-47.45)	0.190
Remodeling index, median (IQR)	1.31 (1.03-1.98)	1.45 (1.03-1.73)	0.761
Eccentricity index, median (IQR)	0.57 (0.36-0.69)	0.48 (0.33-0.66)	0.299
Enhancement index, %, median (IQR)	38.83 (18.42-57.91)	32.43 (12.37-45.34)	0.131

IPH, intraplaque hemorrhage; IQR, interquartile range; VBJ angle, vertebrobasilar junction angle.
The bold values are highlighted that they are less than 0.05.

TABLE 3 | Univariate and multivariate regression for independent correlation between the imaging characteristics of vertebrobasilar atherosclerosis and the VBJ angles ≥90°.

	Univariate model		Multivariate model[a]	
	OR 95% CI	*p*-value	OR 95% CI	*p*-value
Hypointensity signal	2.341 (1.143–4.792)	**0.02**	1.395 (0.569–3.418)	0.466
IPH	6.103 (1.308–28.476)	**0.021**	5.776 (1.095–30.46)	**0.039**
Luminal stenosis	1.048 (1.028–1.07)	**<0.001**	1.015 (0.986–1.044)	0.319
Plaque burden	1.137 (1.085–1.191)	**<0.001**	1.11 (1.043–1.18)	**0.001**

CI, confidential interval; IPH, intraplaque hemorrhage; OR, odds ratio; VBJ angle, vertebrobasilar junction angle.
[a]*Adjusted for age, sex, hypointensity signal, intraplaque hemorrhage, luminal stenosis, and plaque burden.*
The bold values are highlighted that they are less than 0.05.

Univariate and Multivariate Analyses

In the univariate analysis, the VBJ angles ≥90° were related to plaque hypointensity signal (odds ratio, 2.341; 95% CI, 1.143–4.792; *p*-value = 0.02), IPH (odds ratio, 6.103; 95% CI, 1.308–28.476; *p*-value = 0.021), luminal stenosis (odds ratio, 1.048; 95%

CI, 1.028–1.07; p-value < 0.001), and plaque burden (odds ratio, 1.137; 95% CI, 1.085–1.191; p-value < 0.001) in vertebrobasilar artery atherosclerosis, as displayed in **Table 3**.

In the multivariate analysis adjusted for potential confounders, the VBJ angles ≥90° were still shown in strong association with IPH (odds ratio, 5.776; 95% CI, 1.095–30.46; p-value = 0.039; **Table 3**) and plaque burden (odds ratio, 1.11; 95% CI, 1.043–1.18; p-value = 0.001; **Table 3**) caused by vertebrobasilar atherosclerosis. Yet, the VBJ angles ≥90° were not strongly associated with plaque hypointensity signal and luminal stenosis in vertebrobasilar atherosclerosis.

Inter-Rater Reliability

Inter-rater reliability on the measurement of the VBJ angle magnitude was excellent (the intra-observer reliability: coefficient = 0.907, 95% CI 0.814–0.955; the inter-observer reliability: coefficient = 0.860, 95% CI 0.728–0.931). Inter-rater reliability on the quantitative and qualitative evaluation of the plaque imaging features was substantial to excellent, which was reported in our previous VW-MRI studies (Dieleman et al., 2016; Yang et al., 2016).

DISCUSSION

In this hospital-based study, firstly, we found that the plaques in the VBJ angles over 90° were more likely to cause acute infarcts and/or acute stroke symptoms in vertebrobasilar circulation. Secondly, the VBJ angles above 90° were observed in significant correlation with higher prevalence of plaque hypointensity signal and IPH and higher degrees of luminal stenosis and plaque burden in vertebrobasilar artery atherosclerosis. Thirdly, logistic regression analyses further revealed that the relevance of the VBJ angles more than 90° to IPH and plaque burden in vertebrobasilar atherosclerosis remained robust.

Using 3-dimensional TOF MRA imaging, our study showed the striking variations in the magnitude of the VBJ angles among patients with vertebrobasilar artery atherosclerosis, ranging from 29.45° to 124.20°. This observation was consistent with the previous research reporting that the geometric variability of the VBJ angle magnitude was generally found in autopsy human brains (Ravensbergen et al., 1996, 1998). Interestingly, a larger VBJ angle magnitude was subsequently highlighted to have an effect on the development of atherosclerotic plaques in the experimental and numerical analyzing models (Ravensbergen et al., 1996, 1998; Zhang et al., 2016).

Two causes could be given. First, the degrees of the VBJ angle might strongly affect the patterns of cerebral hemodynamics that acted on the intracranial vessel walls (Ravensbergen et al., 1996, 1998; Ritter and Ringelstein, 2002). Notably, the complex patterns of blood flow and the reduced levels of wall shear stress were revealed in the models of the larger VBJ angles, which led to the formation of atherosclerosis (Ravensbergen et al., 1996, 1998). Second, the VBJ angle magnitude might also make a direct impact on the activity of vascular smooth muscle cells (VSMCs) of the vertebrobasilar arteries to develop atherosclerosis (Zhang et al., 2016). In particular, the VBJ angle structure of 90°could significantly attenuate the reaction of VSMCs to the local change in the hemodynamic force and result in the higher expressions of the pro-atherosclerotic mediators in the VSMCs (Zhang et al., 2016). Accordingly, we speculated that the geometry of the VBJ angles over 90° might deteriorate the vessel wall conditions of the vertebrobasilar arteries to grow atherosclerotic plaques mainly through the influence on the hemodynamic pattern and the vascular activity.

This hypothesis could be largely supported by our findings. Firstly, the VBJ angles exceeding 90° were robustly related to heavier plaque burden of the atherosclerotic vertebrobasilar arteries. It is notable that the degree of plaque burden in intracranial large artery atherosclerosis was suggested as a better indicator of the luminal narrowing severity than other conventional imaging values (Wang et al., 2019; Ran et al., 2020; Wu et al., 2020). Secondly, a significant increase in the prevalence of the vertebrobasilar plaques with IPH was found in the VBJ angles over 90°. As a representative imaging marker for high-risk plaque, IPH in vertebrobasilar circulation atherosclerosis was revealed in significant correlation with the plaque vulnerability and rupture, regardless of whether the stenotic grade was high or low (Shi et al., 2018, 2020; Zhu et al., 2018). More importantly, the logistic regression models in our study indicated that the VBJ angles above 90° were independently related to plaque burden and IPH in vertebrobasilar atherosclerosis. Therefore, the VBJ angle structure over 90° was robustly associated with a high-risk vessel wall condition of vertebrobasilar artery atherosclerosis.

Our observations are of potential clinical importance. Although further verification is required, we initially find that the symptomatic atherosclerotic plaques causing acute infarctions and/or acute ischemic signs in vertebrobasilar circulation were more likely to be located in the VBJ angles above 90°, rather than those below 90°. Given the stroke mechanisms varying among symptomatic patients with vertebrobasilar artery atherosclerotic stenosis (Samaniego et al., 2019; Schaafsma et al., 2019), subsequent research is urgently needed to determine if the VBJ angle geometry exceeding 90° is an independent risk factor for stroke occurrence and stroke patterns.

The present study had limitations. Firstly, any causal relationship between the VBJ angle magnitude and vertebrobasilar artery atherosclerosis could not be concluded from this observational study. Secondly, despite the consistency with the prior findings of a low prevalence of symptomatic vertebrobasilar artery atherosclerotic disease (Marquardt et al., 2009; Kim et al., 2013), further exploration of the association between the VBJ angle degrees and the infarct patterns was not allowed in this study due to a relatively small study population. Thirdly, we did not perform any flow dynamic analysis but may inspire future study directions.

CONCLUSION

Utilizing high-resolution VW-MRI, significant differences in the imaging characteristics of vertebrobasilar artery atherosclerosis were observed between the VBJ angles more than 90° and the angles less than 90°. The structure of the larger degrees of the VBJ angle might be a risk factor for vertebrobasilar

atherosclerosis. Further research is still required to investigate the underlying hemodynamic mechanisms depending on the increasing magnitude of the VBJ angles.

DATA AVAILABILITY STATEMENT

The raw data supporting the conclusions of this article will be made available by the authors, without undue reservation.

ETHICS STATEMENT

The studies involving human participants were reviewed and approved by the Joint Chinese University of Hong Kong-New Territories East Cluster Clinical Research Ethics Committee. The patients/participants provided their written informed consent to participate in this study.

AUTHOR CONTRIBUTIONS

JL analyzed imaging data and drafted the manuscript. W-JY and LZ recruited patients and analyzed imaging data. HD participated in analyzing imaging data. WC and TL participated in study coordination and patient recruitment. X-YC conceived the study, participated in its design and coordination, and revised the manuscript. All authors contributed to the article and approved the submitted version.

FUNDING

This work was supported by the General Research Fund from Research Grants Council (GRF, Reference No. 14112916) and Health and Medical Research Fund (HMRF, Project No. 04152586) in Hong Kong.

REFERENCES

Dieleman, N., Yang, W., Abrigo, J. M., Chu, W. C., van der Kolk, A. G., Siero, J. C., et al. (2016). Magnetic resonance imaging of plaque morphology, burden, and distribution in patients with symptomatic middle cerebral artery stenosis. *Stroke* 47, 1797–1802.

Guo, R., Zhang, X., Zhu, X., Liu, Z., and Xie, S. (2018). Morphologic characteristics of severe basilar artery atherosclerotic stenosis on 3d high-resolution mri. *BMC Neurol.* 18:206. doi: 10.1186/s12883-018-1214-1

Jeong, S. K., Lee, J. H., Nam, D. H., Kim, J. T., Ha, Y. S., Oh, S. Y., et al. (2015). Basilar artery angulation in association with aging and pontine lacunar infarction: a multicenter observational study. *J. Atheroscler. Thromb.* 22, 509–517. doi: 10.5551/jat.26245

Kaul, S., Alladi, S., Jabeen, S. A., Bandaru, V., Ankem, U., Mekala, S., et al. (2018). Intracranial atherosclerosis is the most common stroke subtype: Ten-year data from hyderabad stroke registry (india). *Ann. Indian Acad. Neurol.* 21, 209–213. doi: 10.4103/aian.AIAN_86_18

Kim, J., Thayabaranathan, T., Donnan, G. A., Howard, G., Howard, V. J., Rothwell, P. M., et al. (2020). Global stroke statistics 2019. *Int. J. Stroke* 15, 819–838. doi: 10.1177/1747493020909545

Kim, Y. J., Lee, J. H., Choi, J. W., Roh, H. G., Chun, Y. I., Lee, J. S., et al. (2013). Long-term outcome of vertebral artery origin stenosis in patients with acute ischemic stroke. *BMC Neurol.* 13:171. doi: 10.1186/1471-2377-13-171

Li, J., Zheng, L., Yang, W. J., Sze-To, C. Y., Leung, T. W., and Chen, X. Y. (2020). Plaque wall distribution pattern of the atherosclerotic middle cerebral artery associates with the circle of willis completeness. *Front. Neurol.* 11:599459. doi: 10.3389/fneur.2020.599459

Marquardt, L., Kuker, W., Chandratheva, A., Geraghty, O., and Rothwell, P. M. (2009). Incidence and prognosis of > or = 50% symptomatic vertebral or basilar artery stenosis: prospective population-based study. *Brain* 132, 982–988. doi: 10.1093/brain/awp026

Ran, Y., Wang, Y., Zhu, M., Wu, X., Malhotra, A., Lei, X., et al. (2020). Higher plaque burden of middle cerebral artery is associated with recurrent ischemic stroke: a quantitative magnetic resonance imaging study. *Stroke* 51, 659–662. doi: 10.1161/STROKEAHA.119.028405

Ravensbergen, J., Krijger, J. K., Hillen, B., and Hoogstraten, H. W. (1996). The influence of the angle of confluence on the flow in a vertebro-basilar junction model. *J. Biomech.* 29, 281–299. doi: 10.1016/0021-9290(95)00064-x

Ravensbergen, J., Ravensbergen, J. W., Krijger, J. K., Hillen, B., and Hoogstraten, H. W. (1998). Localizing role of hemodynamics in atherosclerosis in several human vertebrobasilar junction geometries. *Arterioscler. Thromb. Vasc. Biol.* 18, 708–716. doi: 10.1161/01.atv.18.5.708

Ritter, M. A., and Ringelstein, E. B. (2002). The venturi effect and cerebrovascular ultrasound. *Cerebrovasc. Dis.* 14, 98–104. doi: 10.1159/000064736

Samaniego, E. A., Shaban, A., Ortega-Gutierrez, S., Roa, J. A., Hasan, D. M., Derdeyn, C., et al. (2019). Stroke mechanisms and outcomes of isolated symptomatic basilar artery stenosis. *Stroke Vasc. Neurol.* 4, 189–197. doi: 10.1136/svn-2019-000246

Savitz, S. I., and Caplan, L. R. (2005). Vertebrobasilar disease. *N. Engl. J. Med.* 352, 2618–2626.

Schaafsma, J. D., Silver, F. L., Kasner, S. E., Caplan, L. R., Rose-Finnell, L., Charbel, F. T., et al. (2019). Infarct patterns in patients with atherosclerotic vertebrobasilar disease in relation to hemodynamics. *Cerebrovasc. Dis. Extra* 9, 123–128. doi: 10.1159/000503091

Shi, Z., Li, J., Zhao, M., Peng, W., Meddings, Z., Jiang, T., et al. (2020). Quantitative histogram analysis on intracranial atherosclerotic plaques: a high-resolution magnetic resonance imaging study. *Stroke* 51, 2161–2169. doi: 10.1161/STROKEAHA.120.029062

Shi, Z., Zhu, C., Degnan, A. J., Tian, X., Li, J., Chen, L., et al. (2018). Identification of high-risk plaque features in intracranial atherosclerosis: initial experience using a radiomic approach. *Eur. Radiol.* 28, 3912–3921. doi: 10.1007/s00330-018-5395-1

Sparaco, M., Ciolli, L., and Zini, A. (2019). Posterior circulation ischaemic stroke-a review part I: anatomy, aetiology and clinical presentations. *Neurol. Sci.* 40, 1995–2006. doi: 10.1007/s10072-019-03977-2

Wang, M., Wu, F., Yang, Y., Miao, H., Fan, Z., Ji, X., et al. (2018). Quantitative assessment of symptomatic intracranial atherosclerosis and lenticulostriate arteries in recent stroke patients using whole-brain high-resolution cardiovascular magnetic resonance imaging. *J. Cardiovasc. Magn. Reson.* 20:35. doi: 10.1186/s12968-018-0465-8

Wang, Y., Liu, X., Wu, X., Degnan, A. J., Malhotra, A., and Zhu, C. (2019). Culprit intracranial plaque without substantial stenosis in acute ischemic stroke on vessel wall mri: a systematic review. *Atherosclerosis* 287, 112–121. doi: 10.1016/j.atherosclerosis.2019.06.907

Wang, Y. J., Li, Z. X., Gu, H. Q., Zhai, Y., Jiang, Y., Zhao, X. Q., et al. (2020). China stroke statistics 2019: a report from the national center for healthcare quality management in neurological diseases, china national clinical research center for neurological diseases, the chinese stroke association, national center for chronic and non-communicable disease control and prevention, chinese center for disease control and prevention and institute for global neuroscience and stroke collaborations. *Stroke Vasc. Neurol.* 5, 211–239. doi: 10.1136/svn-2020-000457

Wu, F., Yu, H., and Yang, Q. (2020). Imaging of intracranial atherosclerotic plaques using 3.0 t and 7.0 t magnetic resonance imaging-current trends and future perspectives. *Cardiovasc. Diagn. Ther.* 10, 994–1004. doi: 10.21037/cdt.2020.02.03

Xu, Z., Li, M., Hou, Z., Lyu, J., Zhang, N., Lou, X., et al. (2019). Association between basilar artery configuration and vessel wall features: a prospective

high-resolution magnetic resonance imaging study. *BMC Med. Imaging* 19:99. doi: 10.1186/s12880-019-0388-3

Yang, W. J., Abrigo, J., Soo, Y. O., Wong, S., Wong, K. S., Leung, T. W., et al. (2020). Regression of plaque enhancement within symptomatic middle cerebral artery atherosclerosis: a high-resolution MRI study. *Front. Neurol.* 11:755. doi: 10.3389/fneur.2020.00755

Yang, W. J., Chen, X. Y., Zhao, H. L., Niu, C. B., Zhang, B., Xu, Y., et al. (2016). Postmortem study of validation of low signal on fat-suppressed t1-weighted magnetic resonance imaging as marker of lipid core in middle cerebral artery atherosclerosis. *Stroke* 47, 2299–2304. doi: 10.1161/STROKEAHA.116.013398

Yang, W. J., Wasserman, B. A., Zheng, L., Huang, Z. Q., Li, J., Abrigo, J., et al. (2021). Understanding the clinical implications of intracranial arterial calcification using brain ct and vessel wall imaging. *Front. Neurol.* 12:619233. doi: 10.3389/fneur.2021.619233

Yu, J., Zhang, S., Li, M. L., Ma, Y., Dong, Y. R., Lou, M., et al. (2018). Relationship between the geometry patterns of vertebrobasilar artery and atherosclerosis. *BMC Neurol.* 18:83. doi: 10.1186/s12883-018-1084-6

Zhang, Y., Menon, N. V., Li, C., Chan, V., and Kang, Y. (2016). The role of bifurcation angles on collective smooth muscle cell biomechanics and the implication in atherosclerosis development. *Biomater. Sci.* 4, 430–438. doi: 10.1039/c5bm00329f

Zhou, L., Yan, Y., Du, H., Ni, X., Wang, G., and Wang, Q. (2020). Plaque features and vascular geometry in basilar artery atherosclerosis. *Medicine (Baltimore)*. 99:e19742. doi: 10.1097/MD.0000000000019742

Zhu, C., Tian, X., Degnan, A. J., Shi, Z., Zhang, X., Chen, L., et al. (2018). Clinical significance of intraplaque hemorrhage in low- and high-grade basilar artery stenosis on high-resolution MRI. *AJNR Am. J. Neuroradiol.* 39, 1286–1292. doi: 10.3174/ajnr.A5676

Conflict of Interest: The authors declare that the research was conducted in the absence of any commercial or financial relationships that could be construed as a potential conflict of interest.

Publisher's Note: All claims expressed in this article are solely those of the authors and do not necessarily represent those of their affiliated organizations, or those of the publisher, the editors and the reviewers. Any product that may be evaluated in this article, or claim that may be made by its manufacturer, is not guaranteed or endorsed by the publisher.

frontiers in Neurology

REVIEW
published: 24 January 2022
doi: 10.3389/fneur.2021.789035

Histology-Verified Intracranial Artery Calcification and Its Clinical Relevance With Cerebrovascular Disease

Heng Du[1], *Wenjie Yang*[2] *and Xiangyan Chen*[1]*

[1] Department of Health Technology and Informatics, The Hong Kong Polytechnic University, Kowloon, Hong Kong SAR, China, [2] Department of Diagnostic Radiology and Nuclear Medicine, School of Medicine, University of Maryland, Baltimore, MD, United States

Intracranial artery calcification (IAC) was regarded as a proxy for intracranial atherosclerosis (ICAS). IAC could be easily detected on routine computer tomography (CT), which was neglected by clinicians in the previous years. The evolution of advanced imaging technologies, especially vessel wall scanning using high resolution-magnetic resonance imaging (HR-MRI), has aroused the interest of researchers to further explore the characteristics and clinical impacts of IAC. Recent histological evidence acquired from the human cerebral artery specimens demonstrated that IAC could mainly involve two layers: the intima and the media. Accumulating evidence from histological and clinical imaging studies verified that intimal calcification is more associated with ICAS, while medial calcification, especially the internal elastic lamina, contributes to arterial stiffness rather than ICAS. Considering the highly improved abilities of novel imaging technologies in differentiating intimal and medial calcification within the large intracranial arteries, this review aimed to describe the histological and imaging features of two types of IAC, as well as the risk factors, the hemodynamic influences, and other clinical impacts of IAC occurring in intimal or media layers.

Keywords: intracranial artery calcification, histology, imaging, clinical relevance, cerebrovascular disease

OPEN ACCESS

Edited by:
Chengcheng Zhu,
University of Washington,
United States

Reviewed by:
Hyungjong Park,
Keimyung University, South Korea
Wang Lingling,
Shanghai JiaoTong University, China

***Correspondence:**
Xiangyan Chen
fiona.chen@polyu.edu.hk

Specialty section:
This article was submitted to Endovascular and Interventional Neurology, a section of the journal Frontiers in Neurology

Received: *05 October 2021*
Accepted: *21 December 2021*
Published: *24 January 2022*

Citation:
Du H, Yang W and Chen X (2022) Histology-Verified Intracranial Artery Calcification and Its Clinical Relevance With Cerebrovascular Disease. Front. Neurol. 12:789035. doi: 10.3389/fneur.2021.789035

INTRODUCTION

Calcification is widely located in all vascular beds (1, 2), especially in the advanced stages of atherosclerosis along with intraplaque hemorrhage, hemosiderin deposition, and lumen surface disruption (3). Over the last decades, significant progress has been made in clinical research on intracranial artery calcification (IAC). IAC in the intracranial internal carotid artery (ICA) was demonstrated as an independent risk factor for ischemic stroke which accounted for up to 75% of all strokes (4). Currently, most studies on IAC are based on computer tomography (CT) which is capable of providing overall views of single or multiple calcifications. Calcification score and volume (5), which were initially used for assessing coronary arteries, are now widely applied to qualitative and quantitative measurements in exploring the clinical relevance of IAC (6). Despite substantial research on IAC, the correlation of IAC with stroke is controversial. In the Rotterdam study, many of the ischemic strokes were either in the vascular territories that were separate from IAC or caused by other conditions, for instance, cardiac source embolism or by the coexisting penetrating artery diseases (4). Furthermore,

despite the association of IAC and intraplaque hemorrhage (7), calcified atherosclerotic plaques in the middle cerebral arteries (MCAs) seemed to be more stable than the non-calcified plaques (8). The pathophysiology of IAC and stroke remains unclear.

There are two major patterns of IAC, one involving the intima and the other involving the media. Recent histopathologic evidence showed that medial calcification was predominantly present in both the intracranial internal carotid arteries (ICAs) (9) and vertebral arteries (VAs) (10), bringing about new considerations on the importance of IAC patterns in further clinical studies. In this review, we intended to discuss the histopathological features of IAC, its manifestation in CT and MRI as well as its clinical relevance, which may benefit in developing a better understanding of calcification and related diseases.

METHODS

Literature searching was performed in PubMed, with a search filter using words, such as "intracranial artery calcification," "intimal calcification," "medial calcification," and "stroke." All articles were extracted according to title and abstract. Most of the articles were original clinical studies. The full texts of the relevant articles were assessed independently. The references of the relevant articles were selected additionally for further evidence. Three hundred and sixty-eight articles about either the intracranial artery or the extracranial artery were screened. Articles based on autopsies, CT, and magnetic resonance imaging (MRI) were included. Articles focused on biochemical or genetic studies were excluded.

For studies based on autopsies, the identification of intimal or medial calcification in the intracranial artery was based on pathological evidence. Calcifications were identified as sharply demarcated, acellular spots, and areas. Calcification type was determined by adding the calcification areas in all slides to a summed intimal and medial calcification burden. If the summed area of medial calcification was larger than the summed area of intimal calcification, the patient was categorized by histology as a medial dominant and vice versa.

For studies based on brain CT, the definition of intimal or medial calcification in the intracranial artery was based on circularity (1 for dot, 2 for $<90°$, 3 for 90–270°, and 4 for 270–360°), thickness (1 for thick IAC $\geq$1.5 mm and 3 for thin IAC $<$1.5 mm), and morphology (0 for indistinguishable, 1 for irregular/patchy and 4 for continuous) on brain CT. A summed score from 1 to 6 indicated predominant intimal calcification and 7 to 11 indicated predominant medial calcification. For studies based on MRI, the identification of IAC pattern is yet to be studied.

IMAGING MEASUREMENT ON IAC AND THE EXISTING DEFECTS

Intracranial artery calcification is widely detected by brain CT scan due to its accessibility and reliability (11). In order to achieve quantitative analysis, semiautomatic custom-made methods are used *via* software, such as ImageJ (12) or MATLAB (13). The "volume" of IAC is calculated by multiplying the number, size, and the increment of pixels. Agatston score (14), which represents the area of calcified plaque multiplied by the weighted value assigned to its highest Hounsfield unit, has also been applied in the studies. Deficiently, Agatston score and calcium volume are both in demand for the slice thickness of 3 mm and for images without gantry tilts (6), and both are time-consuming and sometimes inaccessible for neurologists during clinical practice. In contrast, visual grading systems are comparatively more convenient for assessments. According to the previous grading criteria, the score increases as calcification extends either in the thickness or in the circumference (15–17).

However, since IAC embodied in the intima and media of intracranial arteries can vary in morphology and prevalence, the misleading effect of the Agatston score or the overall volume should not be neglected. In 2017, a new grading system was put forward by Kockelkoren et al. (18) which distinguished the intimal and medial calcification after comparing the histology and CT features of IAC. Circularity, thickness, and morphology were counted separately (**Table 1**) based on the distinct features of intimal and medial calcification. Of note, the grading order of thickness was conversed ("thick" represents one point and "thin" represents three points), and morphology was added into counting compared to prior grading systems (19).

One of the shortages of the visual systems is the subjectivity between distinct grading scales, which is the notable obstacle in maintaining consistencies. Another considerable defect is the interference by adjacent bony structures, for instance, the skull base around the carotid siphon and the VA (6). Recently, high-resolution MRI (HR-MRI) has been applied to evaluate lesions of intracranial vessel walls (20). By presenting hypointensity, IAC can be detected by HR-MRI. Revealing the ultrastructure of the vessel wall, the HR-MRI enables the neurologists to identify the calcium deposits at different locations (e.g., superficial and deep) and their positional relationship with other plaque components (21). By comparing the autopsy and multi-contrast HR-MRI, Jiang et al. (22) accomplished a remarkable

TABLE 1 | Scoring system [by Kockelkoren et al. (18)] for distinguishing intimal calcification from medial calcification.

Characteristic: circularity, thickness, and morphology		Points
Circularity	Absent	0
	Dot(s)	1
	<90 degrees	2
	96–270 degrees	3
	270–360 degrees	4
Thickness	Absent	0
	Thick $\geq$ 1.5 mm	1
	Thin < 1.5 mm	3
Morphology	Indistinguishable	0
	Irregular/Patchy	1
	Continuous	4

< 7: Dominant intimal; ≥ 7: Dominant non-intimal.

differentiation between lipid core (isointense/hyperintense), fibrous cap (isointense), and calcification (hypointense) on T1 sequence. The combination of HR-MRI and CT will presumably benefit both diagnosis and differentiation of IAC and, in addition, will indicate a necessity for the classification of IAC located at different layers of the vessel wall (intima and media).

HISTOLOGICAL FEATURES OF CALCIFICATIONS

The structure of the wall of the intracranial arteries consists of three layers: the intima (the inner layer), the media (the middle layer), and the adventitia (the outer layer). Different from extracranial arteries which are rich in elastin filaments, intracranial arteries own characteristic features with a denser internal elastic lamina, a thinner media with few elastic fibers, a less abundant adventitia, and an absence of external elastic lamina (23). Vascular calcification, resembling osteogenesis, reflects an osteochondrogenic transformation of smooth muscle cells. Traditionally, calcification is deemed to imply atherosclerosis. Studies in the early 20th century conducted by Mönckeberg confirmed that the origination of medial calcification was independent of atherosclerosis (24). Due to different histological features, calcifications in the intima and the media ought to be discussed separately.

INTIMAL CALCIFICATION

Intimal calcification is characterized by subintimal lipid deposition and macrophage accumulation (25). The intimal layer comprises endothelial cells and the subendothelial connective tissue. During atherosclerosis, inflammation intrudes and the intima becomes thickened gradually with the formation

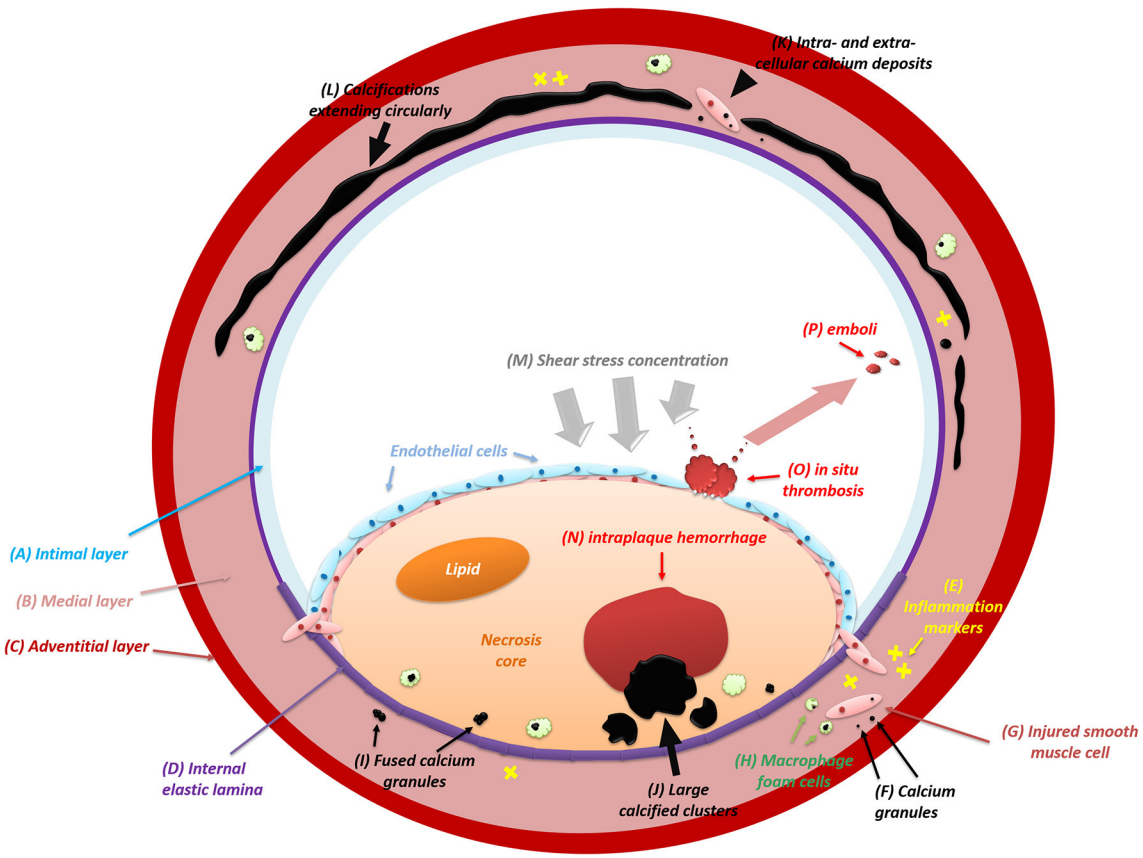

FIGURE 1 | The formation and distribution of intracranial artery calcifications (intimal and medial). IAC mainly involves the intimal layer (A) and the medial layer (B) instead of the adventitial layer (C). During the initial process of atherosclerosis, inflammation (E) infiltrates constantly and intimal calcifications begin to emerge. Usually, calcifications appear as calcium granules (F) within or outside the injured smooth muscle cells (G) and scatter diffusely among extracellular materials. Some of the calcium deposits will be internalized by macrophage foam cells (H). After growing in size with continuous fusion (I) of adjacent granules, calcified deposits will turn into large structures (J). Eventually, with the intima (A) ulcerated by large calcifications, *in situ* thrombosis (O) will adhere to the bare surface of the lesion and release emboli (P) subsequently. In some cases, the shear stress upon the arterial wall will be concentrated (M) on the lesion where large intimal calcifications are present. The elevated shear stress will result in the deformation and rupture of neovessels inside the lesion, leading to intraplaque hemorrhage (N). At first, medial calcifications are irregular calcium deposits (K) distributed intra-cellularly in the vascular muscle cells (G) and extra-cellularly near damaged elastic fibers (D) in the medial layer (B). After confluent extending (L) up to incomplete circumference, medial calcification will distort the architecture of the medial layer and then involve the entire circumference of the vessel wall.

of calcification (26). While absent in primary types, calcium deposits begin to occur as atherosclerosis advances. **Figure 1** shows the formation and distribution of intimal calcification. Initially appearing as granules within or outside the injured smooth muscle cells, calcifications diffusely scatter among extracellular materials and some of which are internalized by macrophage foam cells. With a continuous fusion of adjacent granules, calcified granules will turn into larger clusters containing lumps and plates of calcium (24). In some cases, large calcifications may ulcerate the intima, leading to subsequent occlusions (27).

Intimal calcifications frequently occur as thick and patchy clusters (18, 28). Similar to extracranial arteries, histological evidence indicates that intimal calcification frequently [85 (9) and 100% (10)] coexists with intracranial atherosclerosis (ICAS), but its prevalence among all-stage ICAS lesions is not comparatively high [62% (9) and 69% (10)]. This discrepancy could be attributed to the presence of intimal calcification, which is mainly in the progressive ICAS lesions instead of pre-ICAS lesions (10).

Vasa vasorum is a microvasculature network in vessel walls that delivers oxygen and nutrition (29) and transports inflammatory mediators (30–32) that could contribute to atherosclerosis. In 2018, Zheng et al. (33) first reported the association between the density of intraplaque calcification and the presence of adventitial vasa vasorum in *ex vivo* VA specimens, indicating a mutual basis of calcification and ICAS. However, whether intimal or medial calcification is associated with vasa vasorum is yet unknown.

MEDIAL CALCIFICATION

The medial layer of the intracranial vessel wall consists of smooth muscle cells and an elastin-rich extracellular matrix. The normal thickness of the media in the middle cerebral artery (MCA), basilar artery (BA), and VA ranges from 0.15 to 0.19 mm, and it tends to decrease during pathological changes such as atherosclerosis (3). Medial calcifications are deposits of hydroxyapatite with a high degree of crystallization (34). In **Figure 1**, the formation and extension of medial calcification is briefly drawn. A four-stage criterion is applied to distinguish the calcified lesion in the media layer (35): (1) irregular distribution of intracellular deposits in the vascular muscle cells and in the extra-cellular deposits near damaged elastic fibers in the media (colored in blue or violet) on H&E staining; (2) confluent calcification extending up to incomplete circumference with subendothelial hyperplasia in the intima; (3) calcifications distorting the architecture of media and involving the entire circumference; (4) calcification foci of bone formation.

Focal inflammation also plays a role in medial calcification. A high level of inflammatory markers like C-reactive protein, CD40, and CD154 can be identified in the vicinity of the calcified media (36). The anomalous expression of mineral-regulating proteins may contribute to the process. In patients with chronic kidney disease (CKD), rapid development of medial calcification in the extracranial arteries is observed, partly due to mineral dysregulation stemming from the primary renal disorder (35). Endoplasmic reticulum stress (37) and inflammasome activation (38) may have an impact on the medial calcification, but the key pathogenesis remains hidden.

Medial calcifications appear as thin, continuous, and circular lesions (18, 28). The formation of medial calcification is thought to be independent of atherosclerosis. In intracranial ICAs, the earliest calcifications are located in the medial layer and are unrelated to ICAS (39). More than 60% of non-atherosclerotic medial calcifications in the intracranial ICAs which extend over half of the circumference are irrelevant to the occurrence of the intimal calcification or ICAS while the prevalence of concurrent calcifications is merely 9% (9).

THE PREVALENCE AND DISTRIBUTION OF IAC

The highest prevalence of IAC is found in intracranial ICA (60–80%), followed by that in intracranial VA (17–35%), compared to BA (2.5–7%) and MCA (5%) (40–42). On histology, a low prevalence (3%) of IAC in the major intracranial arteries of Caucasians was reported (43). However, the prevalence of IAC in that of Chinses adults was higher [27.9% in MCA (44) and 39% in the major intracranial arteries (10)].

Different intracranial arteries may have a diverse frequency of IAC. Homburg et al. (45) reported a low prevalence of calcified ICAS lesions (23%) in the distal branches of the circle of Willis. Comparatively, the cavernous and carotid siphon are the most common sites of calcification in ICAs due to their tortuous anatomical configuration (15, 46). Among all segments of VA, the intracranial part is most frequently affected by calcification (40). Left intracranial VA is found more frequently calcified than the right, and most of the IACs in the vertebrobasilar arteries are focal lesions (47), but the mechanism of the left-and-right difference is unclear.

While intimal calcifications tend to occur in all major intracranial arteries (ICA, MCA, VA, and BA) and are always concurrent with ICAS (9, 10), medial calcification is more predominantly present in ICA (9) and VA (10). Histological findings demonstrated that medial calcification contributed more to the total calcified cross-sectional surface area of the carotid artery than the intimal calcification (79 vs. 14%) (9), which indicates their difference in the imaging feature (cluster vs. circular). However, it was also identified that 36% of the medial calcification also had a maximally affected circumference of $<$50%, meaning a potential cluster-like pattern (9). As a result, the overall calcification on CT scan might not serve as an accurate proxy of atherosclerosis.

CLINICAL RELEVANCE OF IAC

Risk Factors

Age (48–50) is an independent risk factor for IAC. In 2005, a CT-based study consisting of 490 consecutive cases demonstrated a high prevalence of calcification (69.4%), among which patients with IAC were significantly older (40). Diabetes (51–53) and CKD (54, 55) are two other major risk factors. As for gender

TABLE 2 | Comparison of risk factors between intimal and medial calcification (intracranial and periphery arteries).

Study authors and year	Subjects	Sample size	Risk factors	
			Intimal calcification	Medial calcification
Vos et al. (60)	Intracranial ICAs of patients with acute ischemic stroke who received CT scans	1,132	Male, smoking, hypertension,	Age, diabetes mellitus, previous vascular disease
Compagne et al. (62)	Intracranial ICAs of patients who received CT scans and underwent thrombectomy	344	Male, smoking, pre-stroke with mRS $\leq$2	Age, atrial fibrillation, diabetes mellitus, myocardial infarction, hypertension
Golüke et al. (61)	Intracranial ICAs of patients with mixed dementia who received CT scans	1,992	Male, hypertension, smoking, myocardial infarction	Diabetes mellitus
Zwakenberg et al. (63)	Femoral arteries of patients who received CT scans	718	Smoking, history of peripheral arterial disease, higher osteonectin level	Age, diabetes, HbA1c, higher ankle brachial index (ABI), higher dp-ucMGP level

TABLE 3 | Summary of the difference between intimal calcification and medial calcification.

IAC pattern	Pathological feature		Risk factor (difference)	Clinical impact	
	Formation	Morphology		Stroke mechanism	Clinical prognosis
Intimal calcification	(1) Related to atherosclerosis, often in advanced stages; (2) Inflammation associated; (3) Granules initially, fuse into large lumps and plates of calcium (4) May ulcerate the intima	Thick / patchy clusters	Male gender; Smoking	(1) Elevated shear stress causing IPH; (2) Hypoperfusion (luminal stenosis)	With lower incidence of hemorrhage after intravenous-thrombolysis
Medial calcification	(1) Irrelevant to atherosclerosis; (2) Inflammation associated; (3) Four-stage formation: from deposits to confluent calcification involving the entire circumference	Thin, often in a circular pattern	Aging; Diabetes mellitus; Chronic kidney disease;	(1) Arterial stiffness; (2) Possibly worse perfusion in microvascular beds	With a trend toward worse outcome which may improve more after endovascular treatment

difference, women are found with milder calcification than men (12, 56), but there is a contradictory finding, too (57). Opposite findings were also reported about hypertension (58, 59). One hypothesis suggests that IAC- induced arterial stiffening may act as a cause for the elevated pulse pressure.

Although intimal calcification and medial calcification share mutual risk factors, such as age and higher pulse pressure (39, 60, 61), there are some differences in other traditional risk factors (**Table 2**). After differentiating into different IAC patterns (intimal and medial), male gender and smoking were found to be independently associated with intimal calcification, while aging and diabetes mellitus were more related to medial calcification (60, 64).

Plaque Vulnerability

The association of IAC with plaque vulnerability remains controversial, which is partially due to the unclassified calcification patterns. A CT study showed that asymptomatic MCA plaques had a higher frequency of IAC compared to symptomatic MCA plaques (8), implying that IAC has a protective effect on the intracranial arteries. On the other hand, micro embolic signals in the intracranial ICA ipsilateral to acute MCA infarct were more frequently detected by transcranial Doppler (TCD) in patients with a higher extent of calcification (widest arc of IAC $\geq$ 90°) than those with the lower extent of calcification (13). However, in the TCD-based study (13), patients were diagnosed with concomitant MCA stenosis; hence the embolic signals in the temporal window originated exactly from the calcified lesion of ICA was indistinguishable. Moreover, latent carotid calcification is also related to the risk of cardio-aortic embolism (65), which can be a major interference in emboli detection.

So far, knowledge of the plaque vulnerability in different IAC patterns is still limited. In contrast, the link between calcification and plaque vulnerability in the coronary artery and the carotid artery is more thoroughly studied, which may serve as a reference. In coronary atherosclerosis, the superficial calcified nodule is an independent risk factor for plaque rupture (66). One of the most vulnerable sites is the junction between calcification and soft plaque within the fibrous cap, where the shear stress tends to increase and eventually causes rupture (67). In the carotid artery, superficial calcification in the plaque was related to intraplaque hemorrhage (IPH) (7, 68), a strong predictor for ipsilateral cerebrovascular events (69–71). One possible explanation about the pathophysiology of calcification related to IPH is the change of focal pressure. Due to the presence of calcification, the shear stress of the blood flow is increased and concentrated on the plaque surface (**Figure 2**) (72, 73), which may cause the deformation and rupture of neovessels inside the plaque (74). Compared to superficial calcifications, deep calcium tends to show irrelevance to IPH in the carotid artery (7). Since "deep" calcified deposits are more possibly located in the medial

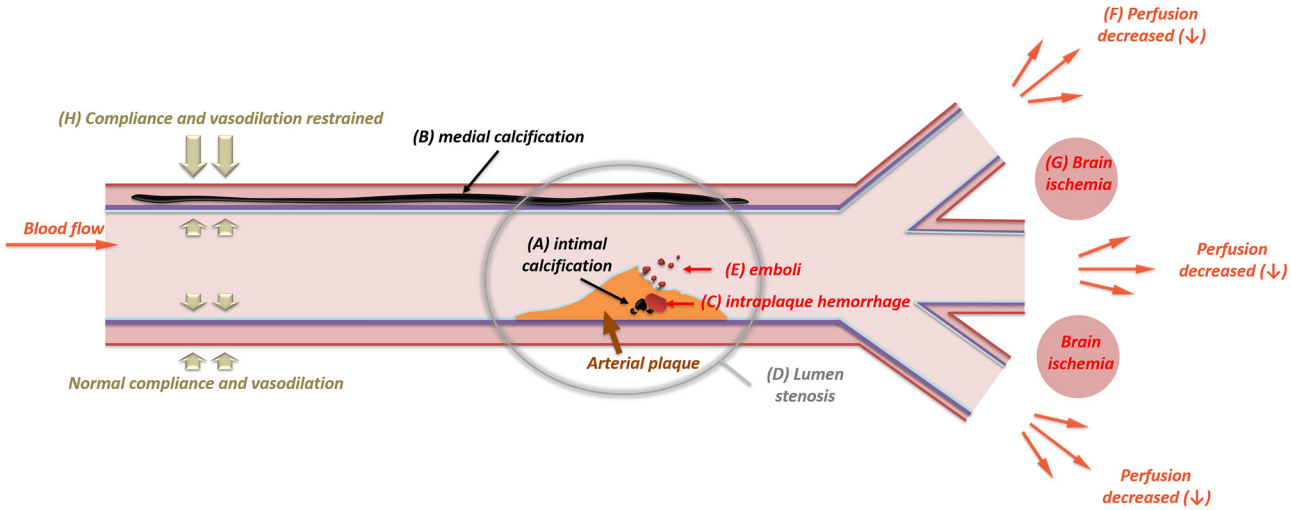

FIGURE 2 | The impact of intracranial artery calcifications (intimal and medial) on ischemic stroke. The presence of intimal calcification (A) may induce intraplaque hemorrhage (C). Intraplaque hemorrhage is one of the major causes for the rapid expanding of arterial plaque, which will then result in luminal stenosis (D). In some cases, the intima will be ulcerated by large calcification, leading to distal embolism (E). With an increase in the stenotic degree, the perfusion of the downward vascular territory will decrease (F), leading to brain ischemia (G) in the border zone of adjacent vascular branches. Unlike intimal calcifications, medial calcification (B) mainly causes arterial stiffness. The stiffened arterial wall will have limited compliance and vasodilation (H), which can be measured through carotid-femoral pulse wave velocity, systolic flow velocity, and pulsatile index.

(or adventitia) layer, medial calcification appears to be unrelated to plaque vulnerability.

Hemodynamic Impact

Intimal calcification is related to atherosclerotic luminal stenosis (10), a pivotal cause of territorial hypoperfusion and artery-to-artery embolism (**Figure 2**) (75). Previous studies have revealed the correlation between luminal stenosis and the severity (thickness and circularity) of calcification in the intracranial ICA (76, 77). In contrast, medial calcification seems to be more associated with vascular remodeling than luminal narrowing (78) in the vertebral artery and coronary artery (79). No significant correlation between medial calcification and luminal stenosis has been established yet (10). Medial calcification is thought to affect arterial stiffening, resulting in compliance deterioration and vasodilation limitation (**Figure 2**) (80). However, in previous studies about intracranial arteries, the IAC pattern was seldom categorized. Notwithstanding, the correlation of medial calcification is still partially deducible. Patients with IAC have higher carotid-femoral pulse wave velocity (81). Additionally, in the MCA and VA, heavier IAC may lead to elevated systolic flow velocity and pulsatile index, which indicate high resistance within the cerebral vasculature (82). IAC may also protect the artery from vasospasm under the circumstance of aneurysmal subarachnoid hemorrhage (83).

Arterial wall stiffening caused by calcification is an independent risk factor for all-cause mortality (84). Compagne et al. reported a trend toward worse outcomes in patients with medial calcification who would benefit more after endovascular thrombectomy compared to intimal calcification (62). Severe calcification is associated with incomplete arterial revascularization after mechanical thrombectomy (85) and prolonged procedural times during endovascular therapy (86). Besides the luminal stenosis caused by IAC, arterial stiffness is also a detrimental factor in the process of endovascular thrombectomy that blocks the extraction of thrombus and therefore increases the passes of the retriever. Furthermore, patients with heavier IAC burden in either the anterior (87) or posterior (88) circulation tend to have poor clinical outcomes after endovascular thrombectomy. It is conceivable that the loss of elasticity may decrease the microvascular cerebral perfusion, resulting in arterial flow stasis and diffuse thrombogenesis. In some diseases, IAC is found protective. Patients with IAC tend to suffer less often from arterial dissection than those without arterial dissection (60). Whether stiffening acts as a reason is unknown.

IAC in Cerebrovascular Events

Intracranial artery calcification has drawn attention as an independent risk factor for stroke (4). Chen et al. (41) first described a high prevalence of IAC in Chinese adults with ischemic stroke. An upgoing incidence of early vascular events lies toward the severity of IAC in ischemic stroke or transient ischemic attack (89). Patients with heavier calcification are at a higher risk of suffering from large cerebral artery occlusion (90) and recurrent ischemic stroke (91, 92). However, despite the fact that ischemic stroke is a condition with divergent causes including large artery atherosclerosis, cardiovascular embolism,

small vessel disease, and other determined or undetermined etiology, prior studies mostly focused on the association of IAC with all causes of stroke. The Rotterdam study revealed the association of IAC with stroke (4), but many of the stroke events were in the vascular territories that were separated from IAC and were led by other vascular disorders (93). In a prospective study on patients with ischemic stroke, the presence and score of IAC were found to be associated with recurrent stroke events (94). However, patients with vascular events had more intracranial atherosclerotic plaques, which may also account for infarction. The coexistence of IAC, atherosclerotic plaque, and luminal narrowing makes it difficult to be determined. In contrast to these findings, a protective effect of calcification was reported (8), but further studies with larger sample size and more specific IAC classifications are needed.

Intracranial artery calcification also has an impact on lacunar infarcts and white matter hyperintensity (42, 95), presumably resulting from an injured vascular tone and vasodilatory after endothelial impairment (96, 97). Erbay et al. (98) reported a weak link of IAC to white matter hyperintensities after adjusting for age. In terms of cerebral hemorrhage, significant expansion of hematoma was observed in the presence of IAC (99). Evidence showed that IAC was a predictor for microbleeds (52, 100) and hemorrhagic transformation after intravenous thrombolysis (101, 102). Medial calcification seemed more correlated to hemorrhagic complications after intravenous thrombolytic therapy (103). The increased frequency of microbleeds in patients with IAC may be due to microvascular impairment (104). Recently, a possible link was reported between Fahr's disease (familial idiopathic basal ganglia calcification) and calcified small vessels that supply the basal ganglia (105). It is conceivable that small vessel impairment may be attributed to IAC since it systemically affects multiple vessel beds.

The pathophysiology of calcification leading to cerebrovascular disease has not been fully elucidated. Intimal calcification often coexists with atherosclerosis, during which endothelial function will be impaired (106) and the permeability of the brain-blood barrier may increase subsequently. Medial calcification can lead to arterial stiffness by damaging the elastic fiber around the internal elastic lamina of the medial layer. With deterioration in compliance, distal cerebral microvascular with increased blood pressure will be vulnerable to rupture.

Intracranial Artery Calcification With Cognitive Disorder

The association between cognitive disorder and IAC has been studied in recent years. A cross-sectional study with 1992 recruited patients who were diagnosed with different types of cognitive dysfunction (107) revealed a high incidence (about 95%) of intracranial internal carotid artery calcification (61). Cognitive impairment had been observed among patients diagnosed with IAC and concurrent conditions, such as chronic hypoparathyroidism (108) and hemodialysis (109) that could directly result in irregular serum calcium. Among patients without such conditions, the risk of dementia could also rise with larger IAC volume (110), despite the influence of stroke. Additionally, patients with larger IAC volume (111) or area (112) were found to perform worse during neuropsychological assessments. However, the link between IAC and type of dementia or cognitive disorder turned uncertain after adjustment for age and gender. Similar findings were reported in the severity of mixed dementia, which was identified as "not associated" with IAC after additional adjustment for cardiovascular risk (61). The correlation of IAC to cognitive dysfunction remained unclear. One possible cause could be the focus only on IAC in the intracranial ICA, since the prevalence of IAC in other vessel beds is comparatively much lower.

Due to its long preclinical stage in which subtle cognitive deficits could only be revealed by dedicated neuropsychological tests (113), dementia or cognitive decline is always barely noticed by patients until the emergence of evident symptoms. Whether IAC can serve as a bio-marker for early screening of dementia or cognitive decline might depend on further studies including a large number of recruited patients with more intracranial arteries.

DISCUSSION

Intracranial artery calcification includes two major types: intimal calcification and medial calcification, in which the histopathological features are different from each other. **Table 3** shows the main difference between intimal calcification and medial calcification. Intimal calcification is more related to focal atherosclerotic lesion while medial calcification tends to spread over the medial layer. Non-atherosclerotic medial calcification is predominantly present in both the intracranial ICA and VA while intimal calcification can occur in all major cerebral arteries. Due to different histological features of intimal and medial calcification, the traditional quantitative measurement could be insufficient to reflect on accurate clinical information, indicating a demand for new measurements by CT or MRI.

Intimal calcification differs from medial calcification in risk factors, the association with plaque vulnerability, and the hemodynamic impact. It plays a critical role in IPH and luminal stenosis while medial calcification is more connected to arterial stiffness and vasodilation. The causal correlation of calcification with infarction and the influence of separate IAC patterns are unknown,. IAC is considered a risk factor for cerebral small vessel disease, most likely due to endothelial dysfunction. The pathophysiology underlying the IAC-inducing stroke is still unclear. Further histological, imaging, and clinical evidence that are based on different IAC subtypes are required in future studies.

AUTHOR CONTRIBUTIONS

HD and XC contributed to the conception and design of the study. WY and XC organized the database. HD wrote the first draft of the manuscript. All authors contributed to manuscript revision, read, and approved the submitted version.

REFERENCES

1. Iribarren C, Sidney S, Sternfeld B, Browner WS. Calcification of the aortic arch: risk factors and association with coronary heart disease, stroke, and peripheral vascular disease. *JAMA*. (2000) 283:2810–5. doi: 10.1001/jama.283.21.2810
2. Alexopoulos D, Toulgaridis T, Davlouros P, Christodoulou J, Sitafidis G, Hahalis G, et al. Prognostic significance of coronary artery calcium in asymptomatic subjects with usual cardiovascular risk. *Am Heart J.* (2003) 145:542–8. doi: 10.1067/mhj.2003.169
3. Yang WJ, Wong KS, Chen XY. Intracranial atherosclerosis: from microscopy to high-resolution magnetic resonance imaging. *J Stroke.* (2017) 19:249–60. doi: 10.5853/jos.2016.01956
4. Bos D, Portegies ML, van der Lugt A, Bos MJ, Koudstaal PJ, Hofman A, et al. Intracranial carotid artery atherosclerosis and the risk of stroke in whites: the rotterdam study. *JAMA Neurol.* (2014) 71:405–11. doi: 10.1001/jamaneurol.2013.6223
5. Ahn SS, Nam HS, Heo JH, Kim YD, Lee SK, Han KH, et al. Ischemic stroke: measurement of intracranial artery calcifications can improve prediction of asymptomatic coronary artery disease. *Radiology.* (2013) 268:842–9. doi: 10.1148/radiol.13122417
6. Subedi D, Zishan US, Chappell F, Gregoriades ML, Sudlow C, Sellar R, et al. Intracranial carotid calcification on cranial computed tomography: visual scoring methods, semiautomated scores, and volume measurements in patients with stroke. *Stroke.* (2015) 46:2504–9. doi: 10.1161/STROKEAHA.115.009716
7. Lin R, Chen S, Liu G, Xue Y, Zhao X. Association between carotid atherosclerotic plaque calcification and intraplaque hemorrhage: a magnetic resonance imaging study. *Arterioscler Thromb Vasc Biol.* (2017) 37:1228–33. doi: 10.1161/ATVBAHA.116.308360
8. Baek JH, Yoo J, Song D, Kim YD, Nam HS, Heo JH. The protective effect of middle cerebral artery calcification on symptomatic middle cerebral artery infarction. *Stroke.* (2017) 48:3138–41. doi: 10.1161/STROKEAHA.117.017821
9. Vos A, Van Hecke W, Spliet WG, Goldschmeding R, Isgum I, Kockelkoren R, et al. Predominance of nonatherosclerotic internal elastic lamina calcification in the intracranial internal carotid artery. *Stroke.* (2016) 47:221–3. doi: 10.1161/STROKEAHA.115.011196
10. Yang WJ, Zheng L, Wu XH, Huang ZQ, Niu CB, Zhao HL, et al. Postmortem study exploring distribution and patterns of intracranial artery calcification. *Stroke.* (2018) 49:2767–9. doi: 10.1161/STROKEAHA.118.022591
11. Ahn SS, Nam HS, Heo JH, Kim YD, Lee SK, Han K, et al. Quantification of intracranial internal carotid artery calcification on brain unenhanced CT: evaluation of its feasibility and assessment of the reliability of visual grading scales. *Eur Radiol.* (2013) 23:20–7. doi: 10.1007/s00330-012-2586-z
12. de Weert TT, Cakir H, Rozie S, Cretier S, Meijering E, Dippel DW, et al. Intracranial internal carotid artery calcifications: association with vascular risk factors and ischemic cerebrovascular disease. *AJNR Am J Neuroradiol.* (2009) 30:177–84. doi: 10.3174/ajnr.A1301
13. Wu XH, Chen XY, Fan YH, Leung TW, Wong KS. High extent of intracranial carotid artery calcification is associated with downstream microemboli in stroke patients. *J Stroke Cerebrovasc Dis.* (2017) 26:442–7. doi: 10.1016/j.jstrokecerebrovasdis.2016.10.007
14. Agatston AS, Janowitz WR, Hildner FJ, Zusmer NR, Viamonte M Jr, et al. Quantification of coronary artery calcium using ultrafast computed tomography. *J Am Coll Cardiol.* (1990) 15:827–32. doi: 10.1016/0735-1097(90)90282-T
15. Babiarz LS, Yousem DM, Wasserman BA, Wu C, Bilker W, Beauchamp NJ Jr. Cavernous carotid artery calcification and white matter ischemia. *AJNR Am J Neuroradiol.* (2003) 24:872–7.
16. Tao XX, Li GF, Wu YL, Liu YS, Zhao Y, Shi YH, et al. Relationship between intracranial internal carotid artery calcification and enlarged cerebral perivascular space. *Neuroradiology.* (2017) 59:577–86. doi: 10.1007/s00234-017-1838-7
17. Woodcock RJ Jr, Goldstein JH, Kallmes DF, Cloft HJ, Phillips CD. Angiographic correlation of CT calcification in the carotid siphon. *AJNR Am J Neuroradiol.* (1999) 20:495–9.
18. Kockelkoren R, Vos A, Van Hecke W, Vink A, Bleys RL, Verdoorn D, et al.B. De vis, computed tomographic distinction of intimal and medial calcification in the intracranial internal carotid artery. *PLoS ONE.* (2017) 12:e0168360. doi: 10.1371/journal.pone.0168360
19. Wu XH, Chen XY, Wang LJ, Wong KS. Intracranial artery calcification and its clinical significance. *J Clin Neurol.* (2016) 12:253–61. doi: 10.3988/jcn.2016.12.3.253
20. Touzé E, Toussaint JF, Coste J, Schmitt E, Bonneville F, Vandermarcq P, et al. Reproducibility of high-resolution MRI for the identification and the quantification of carotid atherosclerotic plaque components: consequences for prognosis studies and therapeutic trials. *Stroke.* (2007) 38:1812–9. doi: 10.1161/STROKEAHA.106.479139
21. Jiang Y, Zhu C, Peng W, Degnan AJ, Chen L, Wang X, et al. Ex-vivo imaging and plaque type classification of intracranial atherosclerotic plaque using high resolution MR. *Atherosclerosis*. (2016) 249:10–6. doi: 10.1016/j.atherosclerosis.2016.03.033
22. Jiang Y, Peng W, Tian B, Zhu C, Chen L, Wang X, et al. Identification and quantitative assessment of different components of intracranial atherosclerotic plaque by *ex vivo* 3T high-resolution multicontrast MRI. *AJNR Am J Neuroradiol.* (2017) 38:1716–22. doi: 10.3174/ajnr.A5266
23. Ritz K, Denswil NP, Stam OC, van Lieshout JJ, Daemen MJ. Cause and mechanisms of intracranial atherosclerosis. *Circulation.* (2014) 130:1407–14. doi: 10.1161/CIRCULATIONAHA.114.011147
24. Stary HC, Natural history of calcium deposits in atherosclerosis progression and regression. *Z Kardiol*. (2000). 89(Suppl. 2):28–35. doi: 10.1007/s003920070097
25. Abedin M, Tintut Y, Demer LL. Vascular calcification: mechanisms and clinical ramifications. *Arterioscler Thromb Vasc Biol.* (2004) 24:1161–70. doi: 10.1161/01.ATV.0000133194.94939.42
26. Wu M, Rementer C, Giachelli CM. Vascular calcification: an update on mechanisms and challenges in treatment. *Calcif Tissue Int.* (2013) 93:365–73. doi: 10.1007/s00223-013-9712-z
27. Janzen J, Vuong PN. Arterial calcifications: morphological aspects and their pathological implications. *Z Kardiol.* (2001) 90(Suppl. 3):6–11. doi: 10.1007/s003920170044
28. Boström K, Demer LL. Regulatory mechanisms in vascular calcification. *Crit Rev Eukaryot Gene Expr.* (2000) 10:151–8. doi: 10.1615/CritRevEukarGeneExpr.v10.i2.40
29. Ritman EL, Lerman A. The dynamic vasa vasorum. *Cardiovasc Res.* (2007) 75:649–58. doi: 10.1016/j.cardiores.2007.06.020
30. Herrmann J, Lerman LO, Rodriguez-Porcel M, Holmes DR Jr, Richardson DM, et al. Coronary vasa vasorum neovascularization precedes epicardial endothelial dysfunction in experimental hypercholesterolemia. *Cardiovasc Res.* (2001) 51:762–6. doi: 10.1016/S0008-6363(01)00347-9
31. Moulton KS, Vakili K, Zurakowski D, Soliman M, Butterfield C, Sylvin E, et al. Inhibition of plaque neovascularization reduces macrophage accumulation and progression of advanced atherosclerosis. *Proc Natl Acad Sci U S A.* (2003) 100:4736–41. doi: 10.1073/pnas.0730843100
32. Gössl M, Versari D, Mannheim D, Ritman EL, Lerman LO, Lerman A. Increased spatial vasa vasorum density in the proximal LAD in hypercholesterolemia–implications for vulnerable plaque-development. *Atherosclerosis.* (2007) 192:246–52. doi: 10.1016/j.atherosclerosis.2006.07.004
33. Zheng L, Yang WJ, Niu CB, Zhao HL, Wong KS, Leung TWH, et al. Correlation of adventitial vasa vasorum with intracranial atherosclerosis: a postmortem study. *J Stroke.* (2018) 20:342–9. doi: 10.5853/jos.2018.01263
34. Schlieper G, Aretz A, Verberckmoes SC, Krüger T, Behets GJ, Ghadimi R, et al. Ultrastructural analysis of vascular calcifications in uremia. *J Am Soc Nephrol.* (2010) 21:689–96. doi: 10.1681/ASN.2009080829
35. Lanzer P, Boehm M, Sorribas V, Thiriet M, Janzen J, Zeller T, et al. Medial vascular calcification revisited: review and perspectives. *Eur Heart J.* (2014) 35:1515–25. doi: 10.1093/eurheartj/ehu163
36. Amann K. Media calcification and intima calcification are distinct entities in chronic kidney disease. *Clin J Am Soc Nephrol.* (2008) 3:1599–605. doi: 10.2215/CJN.02120508

37. Duan X, Zhou Y, Teng X, Tang C, Qi Y. Endoplasmic reticulum stress-mediated apoptosis is activated in vascular calcification. *Biochem Biophys Res Commun.* (2009) 387:694–9. doi: 10.1016/j.bbrc.2009.07.085
38. Wen C, Yang X, Yan Z, Zhao M, Yue X, Cheng X, et al. Nalp3 inflammasome is activated and required for vascular smooth muscle cell calcification. *Int J Cardiol.* (2013) 168:2242–7. doi: 10.1016/j.ijcard.2013.01.211
39. Bartstra JW, van den Beukel TC, Van Hecke W, Mali W, Spiering W, Koek HL, J, et al. Intracranial arterial calcification: prevalence, risk factors, and consequences: jacc review topic of the week. *J Am Coll Cardiol.* (2020) 76:1595–604. doi: 10.1016/j.jacc.2020.07.056
40. Chen XY, Lam WW, Ng HK, Fan YH, Wong KS. The frequency and determinants of calcification in intracranial arteries in Chinese patients who underwent computed tomography examinations. *Cerebrovasc Dis.* (2006) 21:91–7. doi: 10.1159/000090206
41. Chen XY, Lam WW, Ng HK, Fan YH, Wong KS. Intracranial artery calcification: a newly identified risk factor of ischemic stroke. *J Neuroimaging.* (2007) 17:300–3. doi: 10.1111/j.1552-6569.2007.00158.x
42. Chung PW, Park KY, Moon HS, Kim YB, Youn YC, Byun JS, et al. Intracranial internal carotid artery calcification: a representative for cerebral artery calcification and association with white matter hyperintensities. *Cerebrovasc Dis.* (2010) 30:65–71. doi: 10.1159/000314622
43. Denswil NP, van der Wal AC, Ritz K, de Boer OJ, Aronica E, Troost D, et al. Atherosclerosis in the circle of Willis: spatial differences in composition and in distribution of plaques. *Atherosclerosis.* (2016) 251:78–84. doi: 10.1016/j.atherosclerosis.2016.05.047
44. Chen XY, Wong KS, Lam WW, Zhao HL, Ng HK. Middle cerebral artery atherosclerosis: histological comparison between plaques associated with and not associated with infarct in a postmortem study. *Cerebrovasc Dis.* (2008) 25:74–80. doi: 10.1159/000111525
45. Homburg PJ, Plas GJ, Rozie S, van der Lugt A, Dippel DW. Prevalence and calcification of intracranial arterial stenotic lesions as assessed with multidetector computed tomography angiography. *Stroke.* (2011) 42:1244–50. doi: 10.1161/STROKEAHA.110.596254
46. Bleeker L, Marquering HA, van den Berg R, Nederkoorn PJ, Majoie CB. Semi-automatic quantitative measurements of intracranial internal carotid artery stenosis and calcification using CT angiography. *Neuroradiology.* (2012) 54:919–27. doi: 10.1007/s00234-011-0998-0
47. Pikija S, Magdič J, Hojs-Fabjan T. Calcifications of vertebrobasilar arteries on CT: detailed distribution and relation to risk factors in 245 ischemic stroke patients. *Biomed Res Int.* (2013) 2013:918970. doi: 10.1155/2013/918970
48. Sohn YH, Cheon HY, Jeon P, Kang SY. Clinical implication of cerebral artery calcification on brain CT. *Cerebrovasc Dis.* (2004) 18:332–7. doi: 10.1159/000080772
49. Mak HK, Wong CW, Yau KK, Wong WM, Gu J, Khong PL, et al. Computed tomography evaluation of intracranial atherosclerosis in Chinese patients with transient ischemic attack or minor ischemic stroke–its distribution and association with vascular risk factors. *J Stroke Cerebrovasc Dis.* (2009) 18:158–63. doi: 10.1016/j.jstrokecerebrovasdis.2008.09.011
50. Wong KS, Huang YN, Yang HB, Gao S, Li H, Liu JY, et al. A door-to-door survey of intracranial atherosclerosis in Liangbei County, China. *Neurology.* (2007) 68:2031–4. doi: 10.1212/01.wnl.0000264426.63544.ee
51. van der Toorn JE, Engelkes SR, Ikram MK, Ikram MA, Vernooij MW, Kavousi M, et al. Vertebrobasilar artery calcification: prevalence and risk factors in the general population. *Atherosclerosis.* (2019) 286:46–52. doi: 10.1016/j.atherosclerosis.2019.05.001
52. Chen YC, Wei XE, Lu J, Qiao RH, Shen XF, Li YH. Correlation between intracranial arterial calcification and imaging of cerebral small vessel disease. *Front Neurol.* (2019) 10:426. doi: 10.3389/fneur.2019.00426
53. Gao X, Song J, Watase H, Hippe DS, Zhao X, Canton G, et al. Differences in carotid plaques between symptomatic patients with and without diabetes mellitus. *Arterioscler Thromb Vasc Biol.* (2019) 39:1234–1239. doi: 10.1161/ATVBAHA.118.312092
54. Gusbeth-Tatomir P, Covic A. Causes and consequences of increased arterial stiffness in chronic kidney disease patients. *Kidney Blood Press Res.* (2007) 30:97–107. doi: 10.1159/000100905
55. Bugnicourt JM, Chillon JM, Massy ZA, Canaple S, Lamy C, Deramond H, et al. High prevalence of intracranial artery calcification in stroke patients with CKD: a retrospective study. *Clin J Am Soc Nephrol.* (2009) 4:284–90. doi: 10.2215/CJN.02140508
56. Bos D, van der Rijk MJ, Geeraedts TE, Hofman A, Krestin GP, Witteman JC, et al. Intracranial carotid artery atherosclerosis: prevalence and risk factors in the general population. *Stroke.* (2012) 43:1878–84. doi: 10.1161/STROKEAHA.111.648667
57. van Gils MJ, Bodde MC, Cremers LG, Dippel DW, **van der Lugt A**. Determinants of calcification growth in atherosclerotic carotid arteries; a serial multi-detector CT angiography study. *Atherosclerosis.* (2013) 227:95–9. doi: 10.1016/j.atherosclerosis.2012.12.017
58. Koton S, Tashlykov V, Schwammenthal Y, Molshatzki N, Merzeliak O, Tsabari R, et al. Cerebral artery calcification in patients with acute cerebrovascular diseases: determinants and long-term clinical outcome. *Eur J Neurol.* (2012) 19:739–45. doi: 10.1111/j.1468-1331.2011.03620.x
59. Ovesen C, Abild A, Christensen AF, Rosenbaum S, Hansen CK, Havsteen I, et al. Prevalence and long-term clinical significance of intracranial atherosclerosis after ischaemic stroke or transient ischaemic attack: a cohort study. *BMJ Open.* (2013) 3:e003724. doi: 10.1136/bmjopen-2013-003724
60. Vos A, Kockelkoren R, de Vis JB, van der Schouw YT, van der Schaaf IC, Velthuis BK, et al. Risk factors for atherosclerotic and medial arterial calcification of the intracranial internal carotid artery. *Atherosclerosis.* (2018) 276:44–49. doi: 10.1016/j.atherosclerosis.2018.07.008
61. Golüke NMS, de Brouwer EJM, de Jonghe A, Claus JJ, Staekenborg SS, Emmelot-Vonk MH, et al. Intracranial artery calcifications: risk factors and association with cardiovascular disease and cognitive function. *J Neuroradiol.* (2020) doi: 10.1016/j.neurad.2020.08.001. [Epub ahead of print].
62. Compagne KCJ, Clephas PRD, Majoie C, Roos Y, Berkhemer OA, van Oostenbrugge RJ, et al. Intracranial carotid artery calcification and effect of endovascular stroke treatment. *Stroke.* (2018) 49:2961–8. doi: 10.1161/STROKEAHA.118.022400
63. Zwakenberg SR, de Jong PA, Hendriks EJ, Westerink J, Spiering W, de Borst GJ, et al. Intimal and medial calcification in relation to cardiovascular risk factors. *PLoS ONE.* (2020) 15:e0235228. doi: 10.1371/journal.pone.0235228
64. Kauw F, de Jong PA, Takx RAP, de Jong H, Kappelle LJ, Velthuis BK, et al. Effect of intravenous thrombolysis in stroke depends on pattern of intracranial internal carotid artery calcification. *Atherosclerosis.* (2021) 316:8–14. doi: 10.1016/j.atherosclerosis.2020.11.019
65. Yilmaz A, Akpinar E, Topcuoglu MA, Arsava EM. Clinical and imaging features associated with intracranial internal carotid artery calcifications in patients with ischemic stroke. *Neuroradiology.* (2015) 57:501–6. doi: 10.1007/s00234-015-1494-8
66. Naghavi M, Libby P, Falk E, Casscells SW, Litovsky S, Rumberger J, et al. From vulnerable plaque to vulnerable patient: a call for new definitions and risk assessment strategies: Part I. *Circulation.* (2003) 108:1664–72. doi: 10.1161/01.CIR.0000087480.94275.97
67. Nicoll R, Henein MY. Arterial calcification: friend or foe? *Int J Cardiol.* (2013) 167:322–7. doi: 10.1016/j.ijcard.2012.06.110
68. Xu X, Ju H, Cai J, Cai Y, Wang X, Wang Q. High-resolution MR study of the relationship between superficial calcification and the stability of carotid atherosclerotic plaque. *Int J Cardiovasc Imaging.* (2010) 26(Suppl. 1):143–50. doi: 10.1007/s10554-009-9578-3
69. Altaf N, MacSweeney ST, Gladman J, Auer DP. Carotid intraplaque hemorrhage predicts recurrent symptoms in patients with high-grade carotid stenosis. *Stroke.* (2007) 38:1633–5. doi: 10.1161/STROKEAHA.106.473066
70. Turc G, Oppenheim C, Naggara O, Eker OF, Calvet D, Lacour JC, et al. Relationships between recent intraplaque hemorrhage and stroke risk factors in patients with carotid stenosis: the HIRISC study. *Arterioscler Thromb Vasc Biol.* (2012) 32:492–9. doi: 10.1161/ATVBAHA.111.239335
71. McNally JS, McLaughlin MS, Hinckley PJ, Treiman SM, Stoddard GJ, Parker DL, et al. Intraluminal thrombus, intraplaque hemorrhage, plaque thickness, and current smoking optimally predict carotid stroke. *Stroke.* (2015) 46:84–90. doi: 10.1161/STROKEAHA.114.006286
72. Li ZY, Howarth S, Tang T, Graves M, U-King-Im JM, Gillard JH. Does calcium deposition play a role in the stability of atheroma? Location may be the key. *Cerebrovasc Dis.* (2007) 24:452–9. doi: 10.1159/000108436
73. Zhongzhao T, Jing H, Sadat U, Mercer JR, Xiaoyan W, Bahaei NS, et al. How does juxtaluminal calcium affect critical mechanical conditions in

carotid atherosclerotic plaque? An exploratory study. *IEEE Trans Biomed Eng.* (2014) 61:35–40. doi: 10.1109/TBME.2013.2275078
74. Teng Z, He J, Degnan AJ, Chen S, Sadat U, Bahaei NS, et al. Critical mechanical conditions around neovessels in carotid atherosclerotic plaque may promote intraplaque hemorrhage. *Atherosclerosis.* (2012) 223:321–6. doi: 10.1016/j.atherosclerosis.2012.06.015
75. Feng X, Chan KL, Lan L, Abrigo J, Liu J, Fang H, et al. Stroke mechanisms in symptomatic intracranial atherosclerotic disease: classification and clinical implications. *Stroke.* (2019) 50:2692–9. doi: 10.1161/STROKEAHA.119.025732
76. Suzuki M, Ozaki Y, Komura S, Nakanishi A. Intracranial carotid calcification on CT images as an indicator of atheromatous plaque: analysis of high-resolution CTA images using a 64-multidetector scanner. *Radiat Med.* (2007) 25:378–85. doi: 10.1007/s11604-007-0153-3
77. Kassab MY, Gupta R, Majid A, Farooq MU, Giles BP, Johnson MD, et al. Extent of intra-arterial calcification on head CT is predictive of the degree of intracranial atherosclerosis on digital subtraction angiography. *Cerebrovasc Dis.* (2009) 28:45–8. doi: 10.1159/000219296
78. Pikija S, Magdic J, Knific A. Are arterial calcifications a marker of remodeling in vertebrobasilar territory? *Stroke.* (2014) 45:874–6. doi: 10.1161/STROKEAHA.113.003518
79. Sangiorgi G, Rumberger JA, Severson A, Edwards WD, Gregoire J, Fitzpatrick LA, et al. Arterial calcification and not lumen stenosis is highly correlated with atherosclerotic plaque burden in humans: a histologic study of 723 coronary artery segments using nondecalcifying methodology. *J Am Coll Cardiol.* (1998) 31:126–33. doi: 10.1016/S0735-1097(97)00443-9
80. Park KY, Kim YB, Moon HS, Suh BC, Chung PW. Association between cerebral arterial calcification and brachial-ankle pulse wave velocity in patients with acute ischemic stroke. *Eur Neurol.* (2009) 61:364–70. doi: 10.1159/000210549
81. Zhang J, Li Y, Wang Y, Niu W, Zhang Y, Gao P, et al. Arterial stiffness and asymptomatic intracranial large arterial stenosis and calcification in hypertensive chinese. *Am J Hypertens.* (2011) 24:304–9. doi: 10.1038/ajh.2010.246
82. Wu X, Wang L, Zhong J, Ko J, Shi L, Soo Y, et al. Impact of intracranial artery calcification on cerebral hemodynamic changes. *Neuroradiology.* (2018) 60:357–63. doi: 10.1007/s00234-018-1988-2
83. Hussein HM, Zacharatos H, Cordina S, Lakshminarayan K, Ezzeddine MA. Intracranial vascular calcification is protective from vasospasm after aneurysmal subarachnoid hemorrhage. *J Stroke Cerebrovasc Dis.* (2014) 23:2687–93. doi: 10.1016/j.jstrokecerebrovasdis.2014.06.013
84. Vlachopoulos C, Aznaouridis K, Stefanadis C. Prediction of cardiovascular events and all-cause mortality with arterial stiffness: a systematic review and meta-analysis. *J Am Coll Cardiol.* (2010) 55:1318–27. doi: 10.1016/j.jacc.2009.10.061
85. Hernández-Pérez M, Bos D, Dorado L, Pellikaan K, Vernooij MW, López-Cancio E, et al. Intracranial carotid artery calcification relates to recanalization and clinical outcome after mechanical thrombectomy. *Stroke.* (2017) 48:342–7. doi: 10.1161/STROKEAHA.116.015166
86. Haussen DC, Gaynor BG, Johnson JN, Peterson EC, Elhammady MS, Aziz-Sultan MA, et al. Carotid siphon calcification impact on revascularization and outcome in stroke intervention. *Clin Neurol Neurosurg.* (2014) 120:73–7. doi: 10.1016/j.clineuro.2014.02.021
87. Lee SJ, Hong JM, Lee M, Huh K, Choi JW, Lee JS. Cerebral arterial calcification is an imaging prognostic marker for revascularization treatment of acute middle cerebral arterial occlusion. *J Stroke.* (2015) 17:67–75. doi: 10.5853/jos.2015.17.1.67
88. Diprose WK, Diprose JP, Tarr GP, Sutcliffe J, McFetridge A, Brew S, et al. Vertebrobasilar artery calcification and outcomes in posterior circulation large vessel occlusion thrombectomy. *Stroke.* (2020) 51:1301–4. doi: 10.1161/STROKEAHA.119.027958
89. Lee JG, Lee KB, Roh H, Ahn MY, Bae HJ, Lee JS, et al. Intracranial arterial calcification can predict early vascular events after acute ischemic stroke. *J Stroke Cerebrovasc Dis.* (2014) 23:e331–7. doi: 10.1016/j.jstrokecerebrovasdis.2013.12.022
90. Tsang ACO, Lau KK, Tsang FCP, Tse MMY, Lee R, Lui WM. Severity of intracranial carotid artery calcification in intracranial atherosclerosis-related occlusion treated with endovascular thrombectomy. *Clin Neurol Neurosurg.* (2018) 174:214–6. doi: 10.1016/j.clineuro.2018.09.030
91. Kong WY, Tan BY, Ellis ES, Ngiam NJ, Goh WG, Sharma VK, et al. Intracranial artery calcium burden predicts recurrent cerebrovascular events in transient ischaemic attack patients. *J Stroke Cerebrovasc Dis.* (2019) 28:2332–6. doi: 10.1016/j.jstrokecerebrovasdis.2019.05.027
92. Wu X, Bos D, Ren L, Leung TW, Chu WC, Wong LKS, et al. Intracranial arterial calcification relates to long-term risk of recurrent stroke and post-stroke mortality. *Front Neurol.* (2020) 11:559158. doi: 10.3389/fneur.2020.559158
93. Chimowitz MI, Caplan LR. Is calcification of intracranial arteries important and how? *JAMA Neurol.* (2014) 71:401–2. doi: 10.1001/jamaneurol.2013.6224
94. Bugnicourt JM, Leclercq C, Chillon JM, Diouf M, Deramond H, Canaple S, et al. Presence of intracranial artery calcification is associated with mortality and vascular events in patients with ischemic stroke after hospital discharge: a cohort study. *Stroke.* (2011) 42:3447–53. doi: 10.1161/STROKEAHA.111.618652
95. Bos D, Ikram MA, Elias-Smale SE, Krestin GP, Hofman A, Witteman JC, et al. Calcification in major vessel beds relates to vascular brain disease. *Arterioscler Thromb Vasc Biol.* (2011) 31:2331–7. doi: 10.1161/ATVBAHA.111.232728
96. Knottnerus IL, Ten Cate H, Lodder J, Kessels F, van Oostenbrugge RJ. Endothelial dysfunction in lacunar stroke: a systematic review. *Cerebrovasc Dis.* (2009) 27:519–26. doi: 10.1159/000212672
97. Ramadan MM, Mahfouz EM, Gomaa GF, El-Diasty TA, Alldawi L, Ikrar T, et al. Evaluation of coronary calcium score by multidetector computed tomography in relation to endothelial function and inflammatory markers in asymptomatic individuals. *Circ J.* (2008) 72:778–85. doi: 10.1253/circj.72.778
98. Erbay S, Han R, Baccei S, Krakov W, Zou KH, Bhadelia R, et al. Intracranial carotid artery calcification on head CT and its association with ischemic changes on brain MRI in patients presenting with stroke-like symptoms: retrospective analysis. *Neuroradiology.* (2007) 49:27–33. doi: 10.1007/s00234-006-0159-z
99. Pektezel MY, Arsava EM, Gocmen R, Topcuoglu MA. Intracerebral hematoma expansion and intracranial internal carotid artery calcifications. *Clin Neurol Neurosurg.* (2021) 200:106361. doi: 10.1016/j.clineuro.2020.106361
100. Chung PW, Park KY, Kim JM, Shin DW, Ha SY. Carotid artery calcification is associated with deep cerebral microbleeds. *Eur Neurol.* (2014) 72:60–3. doi: 10.1159/000358513
101. Lin TC, Chao TH, Shieh Y, Lee TH, Chang YJ, Lee JD, et al. The impact of intracranial carotid artery calcification on the development of thrombolysis-induced intracerebral hemorrhage. *J Stroke Cerebrovasc Dis.* (2013) 22:e455–62. doi: 10.1016/j.jstrokecerebrovasdis.2013.05.008
102. Yu Y, Zhang FL, Qu YM, Zhang P, Zhou HW, Luo Y, et al. Intracranial calcification is predictive for hemorrhagic transformation and prognosis after intravenous thrombolysis in non-cardioembolic stroke patients. *J Atheroscler Thromb.* (2021) 28:356–64. doi: 10.5551/jat.55889
103. Gocmen R, Arsava EM, Oguz KK, Topcuoglu MA. Atherosclerotic intracranial internal carotid artery calcification and intravenous thrombolytic therapy for acute ischemic stroke. *Atherosclerosis.* (2018) 270:89–94. doi: 10.1016/j.atherosclerosis.2018.01.035
104. Fisher M, French S, Ji P, Kim RC. Cerebral microbleeds in the elderly: a pathological analysis. *Stroke.* (2010) 41:2782–5. doi: 10.1161/STROKEAHA.110.593657
105. Wang C, Li Y, Shi L, Ren J, Patti M, Wang T, et al. Mutations in SLC20A2 link familial idiopathic basal ganglia calcification with phosphate homeostasis. *Nat Genet.* (2012) 44:254–6. doi: 10.1038/ng.1077
106. Deanfield JE, Halcox JP, Rabelink TJ. Endothelial function and dysfunction: testing and clinical relevance. *Circulation.* (2007) 115:1285–95. doi: 10.1161/CIRCULATIONAHA.106.652859
107. Claus JJ, Staekenborg SS, Roorda JJ, Stevens M, Herderschee D, van Maarschalkerweerd W, et al. Low prevalence of mixed dementia in a cohort of 2,000 elderly patients in a memory clinic setting. *J Alzheimers Dis.* (2016) 50:797–806. doi: 10.3233/JAD-150796

108. Kowdley KV, Coull BM, Orwoll ES. Cognitive impairment and intracranial calcification in chronic hypoparathyroidism. *Am J Med Sci.* (1999) 317:273–7. doi: 10.1016/S0002-9629(15)40527-0
109. Cho NJ, Park S, Lee EY, Oh SW, Oh HG, Gil HW. Association of intracranial artery calcification with cognitive impairment in hemodialysis patients. *Med Sci Monit.* (2019) 25:5036–43. doi: 10.12659/MSM.914658
110. Bos D, Vernooij MW, de Bruijn RF, Koudstaal PJ, Hofman A, Franco OH, et al. Atherosclerotic calcification is related to a higher risk of dementia and cognitive decline. *Alzheimers Dement.* (2015) 11:639–47.e1. doi: 10.1016/j.jalz.2014.05.1758
111. Bos D, Vernooij MW, Elias-Smale SE, Verhaaren BF, Vrooman HA, Hofman A, et al. Atherosclerotic calcification relates to cognitive function and to brain changes on magnetic resonance imaging. *Alzheimers Dement.* (2012) 8(5 Suppl):S104–11. doi: 10.1016/j.jalz.2012.01.008
112. Kao HW, Liou M, Chung HW, Liu HS, Tsai PH, Chiang SW, et al. High agatston calcium score of intracranial carotid artery: a significant risk factor for cognitive impairment. *Medicine.* (2015) 94:e1546. doi: 10.1097/MD.0000000000001546
113. Amieva H, Jacqmin-Gadda H, Orgogozo JM, Le Carret N, Helmer C, Letenneur L, et al. The 9 year cognitive decline before dementia of the Alzheimer type: a prospective population-based study. *Brain.* (2005) 128:1093–101. doi: 10.1093/brain/awh451

Conflict of Interest: The authors declare that the research was conducted in the absence of any commercial or financial relationships that could be construed as a potential conflict of interest.

frontiers | Frontiers in Neuroscience

ORIGINAL RESEARCH
published: 01 June 2022
doi: 10.3389/fnins.2022.888814

Deep Learning-Based Automated Detection of Arterial Vessel Wall and Plaque on Magnetic Resonance Vessel Wall Images

*Wenjing Xu[1,2†], Xiong Yang[3†], Yikang Li[4], Guihua Jiang[5], Sen Jia[1], Zhenhuan Gong[3], Yufei Mao[3], Shuheng Zhang[3], Yanqun Teng[3], Jiayu Zhu[3], Qiang He[3], Liwen Wan[1], Dong Liang[1], Ye Li[1], Zhanli Hu[1], Hairong Zheng[1], Xin Liu[1] and Na Zhang[1]**

[1] Paul C. Lauterbur Research Center for Biomedical Imaging, Shenzhen Institute of Advanced Technology, Chinese Academy of Sciences, Shenzhen, China, [2] Faculty of Information Technology, Beijing University of Technology, Beijing, China, [3] United Imaging Healthcare Co., Ltd., Shanghai, China, [4] Department of Computing, Imperial College London, London, United Kingdom, [5] Department of Radiology, Guangdong Second Provincial General Hospital, Guangzhou, China

OPEN ACCESS

Edited by:
Chengcheng Zhu,
University of Washington,
United States

Reviewed by:
Maysam Orouskhani,
Shenzhen University, China
Zhang Shi,
Fudan University, China

***Correspondence:**
Na Zhang
na.zhang@siat.ac.cn

† These authors have contributed equally to this work

Specialty section:
This article was submitted to Brain Imaging Methods, a section of the journal Frontiers in Neuroscience

Received: 03 March 2022
Accepted: 21 April 2022
Published: 01 June 2022

Citation:
Xu W, Yang X, Li Y, Jiang G, Jia S, Gong Z, Mao Y, Zhang S, Teng Y, Zhu J, He Q, Wan L, Liang D, Li Y, Hu Z, Zheng H, Liu X and Zhang N (2022) Deep Learning-Based Automated Detection of Arterial Vessel Wall and Plaque on Magnetic Resonance Vessel Wall Images. Front. Neurosci. 16:888814. doi: 10.3389/fnins.2022.888814

Purpose: To develop and evaluate an automatic segmentation method of arterial vessel walls and plaques, which is beneficial for facilitating the arterial morphological quantification in magnetic resonance vessel wall imaging (MRVWI).

Methods: MRVWI images acquired from 124 patients with atherosclerotic plaques were included. A convolutional neural network-based deep learning model, namely VWISegNet, was used to extract the features from MRVWI images and calculate the category of each pixel to facilitate the segmentation of vessel wall. Two-dimensional (2D) cross-sectional slices reconstructed from all plaques and 7 main arterial segments of 115 patients were used to build and optimize the deep learning model. The model performance was evaluated on the remaining nine-patient test set using the Dice similarity coefficient (DSC) and average surface distance (ASD).

Results: The proposed automatic segmentation method demonstrated satisfactory agreement with the manual method, with DSCs of 93.8% for lumen contours and 86.0% for outer wall contours, which were higher than those obtained from the traditional U-Net, Attention U-Net, and Inception U-Net on the same nine-subject test set. And all the ASD values were less than 0.198 mm. The Bland–Altman plots and scatter plots also showed that there was a good agreement between the methods. All intraclass correlation coefficient values between the automatic method and manual method were greater than 0.780, and greater than that between two manual reads.

Conclusion: The proposed deep learning-based automatic segmentation method achieved good consistency with the manual methods in the segmentation of arterial vessel wall and plaque and is even more accurate than manual results, hence improved the convenience of arterial morphological quantification.

Keywords: deep learning, MR vessel wall imaging, automatic segmentation, plaques, automated detection

INTRODUCTION

Confirming and risk stratifying vulnerable plaques is especially important for the clinical prevention and treatment of ischemic stroke. Magnetic resonance vessel wall imaging (MRVWI) can directly visualize arterial vessel walls and characterize vulnerable plaques. It has been widely used as an emerging non-invasive imaging modality for evaluating and identifying patients at risk for ischemic stroke (Loewe et al., 1998; Frank, 2001; Burtea et al., 2012; Dieleman et al., 2014).

Quantitative morphologic measurements of the arterial vessel wall and plaques based on MRVWI have been proven to have good reproducibility (Mandell et al., 2017; Saba et al., 2018; Zhang et al., 2018) and suggested to be imaging markers to monitor the progression and regression of ischemic stroke during medical management or drug development (Adams et al., 2004; Minarro-Gimenez et al., 2018). However, quantitative measurements are currently of limited use in clinical practice because manual segmentation of the vessel wall and plaque is labor intensive and requires continuous training of personnel (Qiao et al., 2011). It usually takes a trained expert more than 30 min to analyze MRVWI images of one patient from the manual reconstruction of two-dimensional (2D) slices to the manual segmentation of the vessel wall and plaque. In addition, the main challenge of MRVWI-based segmentation is the low contrast between the vessel wall and the surrounding tissues, which causes the accuracy of segmentation to depend heavily on the knowledge and experience of experts.

Over the past years, several studies have used computer-aided diagnosis to improve the efficiency and accuracy of segmentation and reduce the burden on doctors for the interpretation of medical images (Ladak et al., 1999; Sakellarios et al., 2012; Jodas et al., 2018). However, these methods sometimes require user intervention. With the widespread application of artificial intelligence in the field of medical image analysis, convolutional neural networks (CNNs) have achieved important breakthroughs in image segmentation tasks (Anwar et al., 2018; Yamashita et al., 2018; Maier et al., 2019; Dutta et al., 2020; Ohsaka, 2020; Taghanaki et al., 2021). Compared with traditional automatic segmentation methods, CNNs can automatically learn abundant image features to achieve fast and more accurate segmentation. Some studies have used CNN to achieve carotid arterial vessel segmentation (Tsakanikas et al., 2020; Zhu et al., 2021). In addition, some other studies used CNN to segment carotid arterial vessel wall. Among them, Chen et al., 2019 developed tractlet refinement and polar transformation for carotid artery localization and vessel wall segmentation and achieved high accuracy (Chen et al., 2019). Samber et al. (2020) used CNN to the task of delineating carotid vessel walls based on 2D T2-weighted MRVWI images. However, all these studies are aimed at the segmentation of carotid arterial vessels or vessel walls. There is a paucity of study on the automatic segmentation of intracranial arterial vessel wall. Recently, Shi et al. (2019) made a preliminary attempt to automatically segment the intracranial arterial vessel wall using a U-Net-like fully convolutional network based on whole-brain MRVWI images of 56 patients. As we know, atherosclerosis is a diffuse disease that can occur in any artery. It is more important and clinically significant to estimate the effect of a segmentation model based on MRVWI images including more arteries (intracranial and carotid arteries) in a larger patient population.

In this study, a fully automated method for the segmentation of the arterial lumen and vessel wall based on intra- and extracranial MRVWI images was developed and evaluated in a large cohort of patients with ischemic stroke.

MATERIALS AND METHODS

Study Population

The prospective study was approved by the local institutional review board, and all patients gave the informed consent. From January 2019 to April 2020, 129 consecutive patients (age range 46–78 years, mean age 58.6 ± 18.9 years) requiring high-resolution MRVWI scans in 3 centers were recruited for the study.

Image Acquisition

All MRVWI images were acquired using a T1-weighted 3D-variable flip-angle fast spin-echo (FSE) sequence, namely MATRIX (Modulated flip Angle Technique in Refocused Imaging with extended echo train) on a 3T whole-body MR system (uMR780, United Imaging Healthcare Co., Ltd., Shanghai, China). The imaging parameters were as follows: sagittal imaging orientation, repetition time (TR)/echo time (TE) = 800/13.92 ms, field of view = 230 mm × 192 mm × 154 mm, matrix size = 384 × 320 × 256, spatial resolution = 0.6 mm × 0.6 mm × 0.6 mm without interpolation, echo train length = 46, receiver bandwidth = 600 Hz/pixel, compress sensing-based acceleration rate (uCS) = 5.2, scan time = 4 min and 49 s. The study was approved by the local institutional review board, and informed consent was waived for the retrospective study.

Image Preprocessing

A dedicated plaque analysis software (uWS PlaqueTool, United Imaging Healthcare Co., Ltd., Shanghai, China) was used for image preprocessing. First, curved-planar reconstruction for all intracranial and carotid arterial segments were automatically performed using centerline extraction algorithm. Then, 2D cross-sectional slices were reconstructed for all plaques and seven main arterial segments: the common carotid artery (CCA), the internal carotid artery (ICA) and bifurcation, the anterior cerebral artery (ACA), the middle cerebral artery (MCA), the basilar artery (BA), the vertebral artery (VA), and the posterior cerebral artery (PCA), and manually delineated the lumen and outer wall contours by five experienced radiologists with more than 6 years of experience. Representative images processed with the automatic workflow are shown in **Figure 1**.

Five patients were excluded from training database due to the poor image quality with motion artifacts. A total of 13,962 2D MRVWI slices were reconstructed from 7 arterial segments of 124 patients, of which, 9,073 slices and 3,889 slices reconstructed from 115 patients were used as the training and validation sets to

build and optimize the model. In total, 1,000 slices reconstructed from the remaining 9 patients were used as the test set to evaluate the obtained model. These slices of the nine patients were manually delineated twice to compare the results of the deep learning CNN-based approach with the variability of the data between two manual reads to see if the variance between the CNN and ground truth was within the variability of assessment of expert readers.

For most slices derived from normal arterial segments or segments with slightly thickened vessel walls, an ellipse tracing tool composed of four coordinate points is used for quick delineation. For some slices with irregular shapes of the lumen and vessel wall caused by large and complex plaques, a free-shape tracing tool composed of multiple coordinate points is used for more accurate delineation. Due to the large amount of data to be labeled, five readers independently performed the above delineation on different data and cross-checked the delineation results to ensure that each slice was delineated by at least two readers by consensus. When there is discrepancy between the labeling and checking readers, a third senior reader was invited for the final decision by consensus. To avoid model overfitting, the training dataset was expanded by nearly six times from 9,073 to 54,438 slices through rotation, translation, and padding. Then, each slice was interpolated to 0.075 mm × 0.075 mm

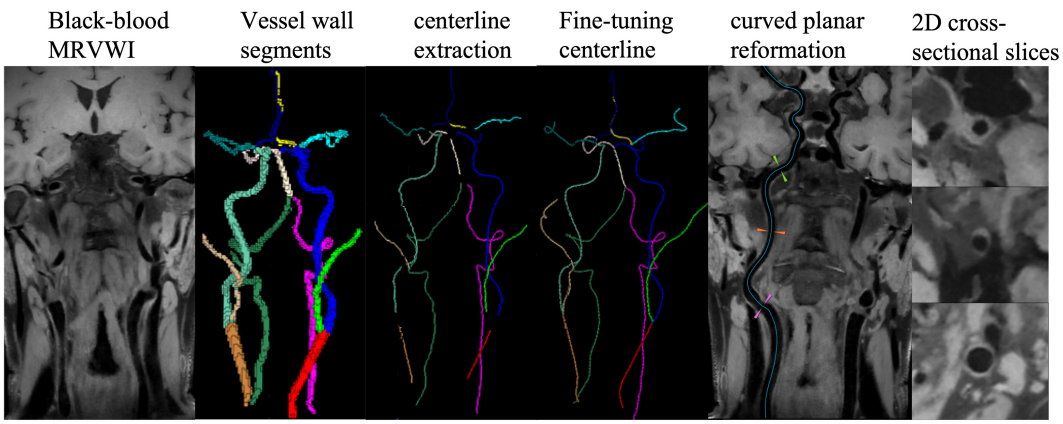

FIGURE 1 | The workflow for proposed centerline extraction of intracranial and carotid artery.

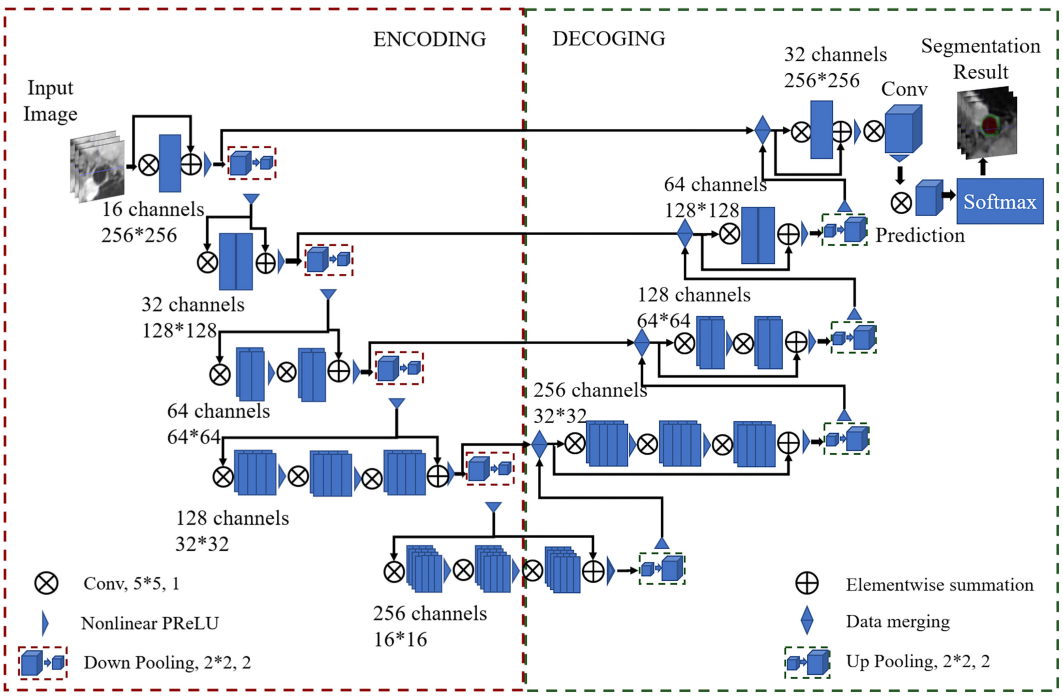

FIGURE 2 | The architecture of the proposed CNN-based VWISegNet.

TABLE 1 | The segmentation results for lumen contours and vessel wall contours of different methods.

		U-Net (mean ± SD)	VWISegNet (mean ± SD)	Attention U-Net (mean ± SD)	Inception U-Net (mean ± SD)
DSC (%)	Lumen	86.7 ± 16.9	93.8 ± 6.3	92.0 ± 8.5	86.8 ± 17.4
	Vessel wall	73.1 ± 14.6	86.0 ± 9.0	79.7 ± 9.8	74.3 ± 16.4

DSC, Dice similarity coefficient.

for reducing the morphologic measurement error and resized to 256 × 256 pixels and grayscale normalized as follows to reduce the inconsistent characteristics of the images.

$$\text{norm} = \left(\frac{x_i - x_{\min}}{x_{\max} - x_{\min}} \times (x_{\text{maxv}} - x_{\text{minv}}) + x_{\text{minv}} \right) \quad (1)$$

where x_i denotes the pixel value, and x_{minv} and x_{maxv} represent upper and lower bounds of normalized. Here, $x_{\text{minv}} = 0$, $x_{\text{maxv}} = 1$.

In summary, the proposed model was trained on 54,438 2D MRVWI slices, validated on 3,889 slices, and tested on 1,000 slices.

Vessel Wall Segmentation

A U-Net-like (Ronneberger et al., 2015) multiclass deep learning architecture was proposed to segment the vessel wall and lumen, named VWISegNet. The main architecture of the network is shown in **Figure 2**. It consists of an encoder path and an asymmetric decoder path followed by a pixelwise classifier that enables precise pixel classification. The two branches were connected by a skip connection. A filter with a size of 5 × 5 and stride of 1 was applied to all the convolutional layers to extract fine features from the resized images. Compared with the traditional U-Net network, the VWISegNet has more residual units, and these residual units can better propagate information between the low and high levels, alleviating vanishing gradient problem and allowing the network to obtain better results.

A convolutional layer with a $K = 2$ kernel and stride of 2 is used for downsampling as a substitute for the pooling layer in the encoder path. Instead of directly downsampling, each layer adds a residual unit that achieves fast convergence and better network performance. Utilizing a 1 × 1 kernel size with a stride of 1 subsequently performed beyond the last stage to generate outputs of the same size as the input images. In the process of training, convolution kernel size was decided by considering the influence of the perception field and computational efficiency. The 5 × 5 convolution kernel can obtain a larger perception field and can extract image features better. The 20 epochs are run at a learning rate of 3e−5 with a batch size of 32.

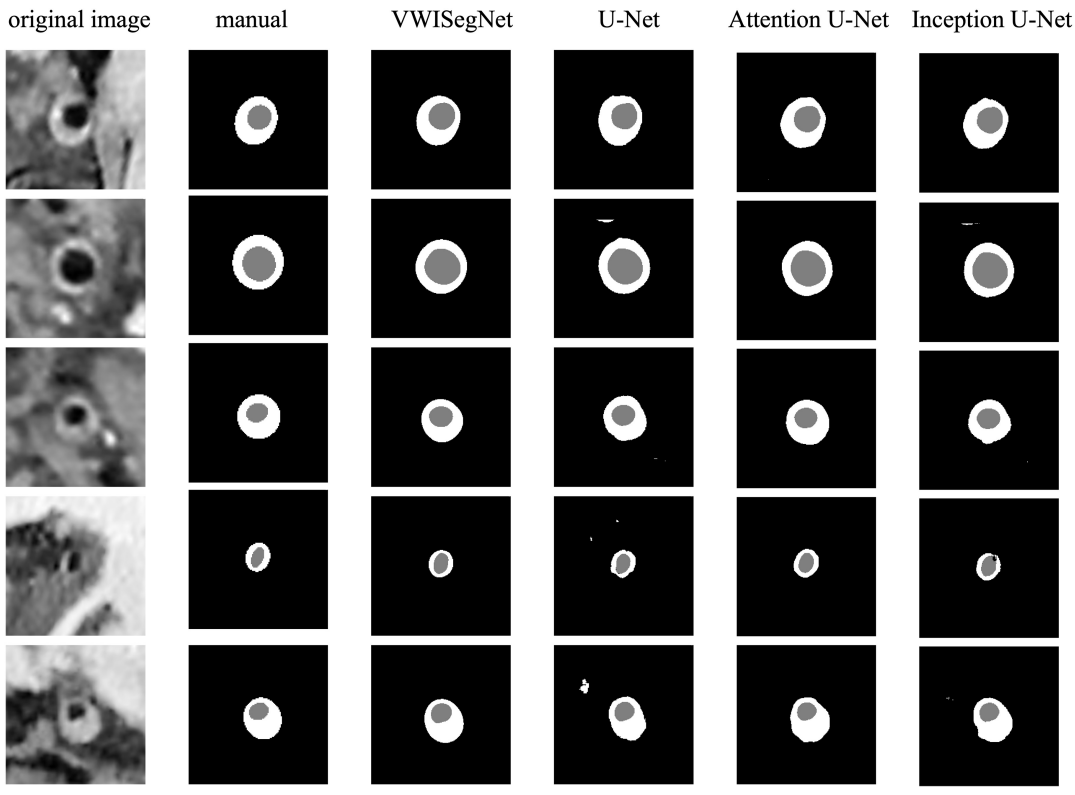

FIGURE 3 | A representative comparison between the proposed VWISegNet and the traditional U-Net, Attention U-Net, and Inception U-Net on the segmentation of vessel wall.

With 20 epochs of training, our network model was sufficiently converged and very stable. The Dice loss function is selected for calculating the loss of the lumen and the outer wall. Adaptive moment estimation (Adam) is used to optimize the model with a momentum of 0.9. The parametric rectified linear units (PReLU) function is used as the activation function. PReLU avoids the "dead features" problem caused by zero gradient. In this article, the filter size of 2 × 2 is the common size in the upsampling and downsampling.

Since traditional U-Net is some sort of standard for medical image segmentation, the proposed VWISegNet was compared with respect to the performance to this benchmark and recently published Attention U-Net, and Inception U-Net on the same test data. In addition, the VWISegNet was compared with champion group results of the Carotid Artery Vessel Wall Segmentation Challenge[1] held MICCAI 2021 and SMRA 2021 on their dataset.

Evaluation Indicators and Statistical Analysis

The Dice similarity coefficient (DSC) and the average surface distance (ASD) were used to quantitatively evaluate the similarity between automatic and manual segmentation results (Bertels et al., 2019; Eelbode et al., 2020). ASD is obtained by calculating the average of all the distances from each point on the automatic segmentation boundary to the corresponding point on the ground-truth boundary. To evaluate the accuracy of the proposed

[1]https://vessel-wall-segmentation.grand-challenge.org/

TABLE 2 | The DSC and ASD for the lumen and the vessel wall when comparing automatic and manual method on the nine-subject test set.

		Mean ± SD	ACA	CCA	ICA	MCA	BA	PCA	VA
DSC (%)	Lumen	93.8 ± 0.764	93.6	94.7	94.3	93.8	94.1	92.3	94.2
	Vessel wall	86.0 ± 1.866	84.6	88.3	87.7	85.7	87.6	83.9	84.0
ASD (mm)	Lumen	0.068 ± 0.016	0.063	0.064	0.098	0.056	0.060	0.057	0.080
	Vessel wall	0.095 ± 0.048	0.093	0.124	0.198	0.099	0.074	0.053	0.138

DSC, Dice similarity coefficient; ASD, average surface distance; SD, standard deviation.

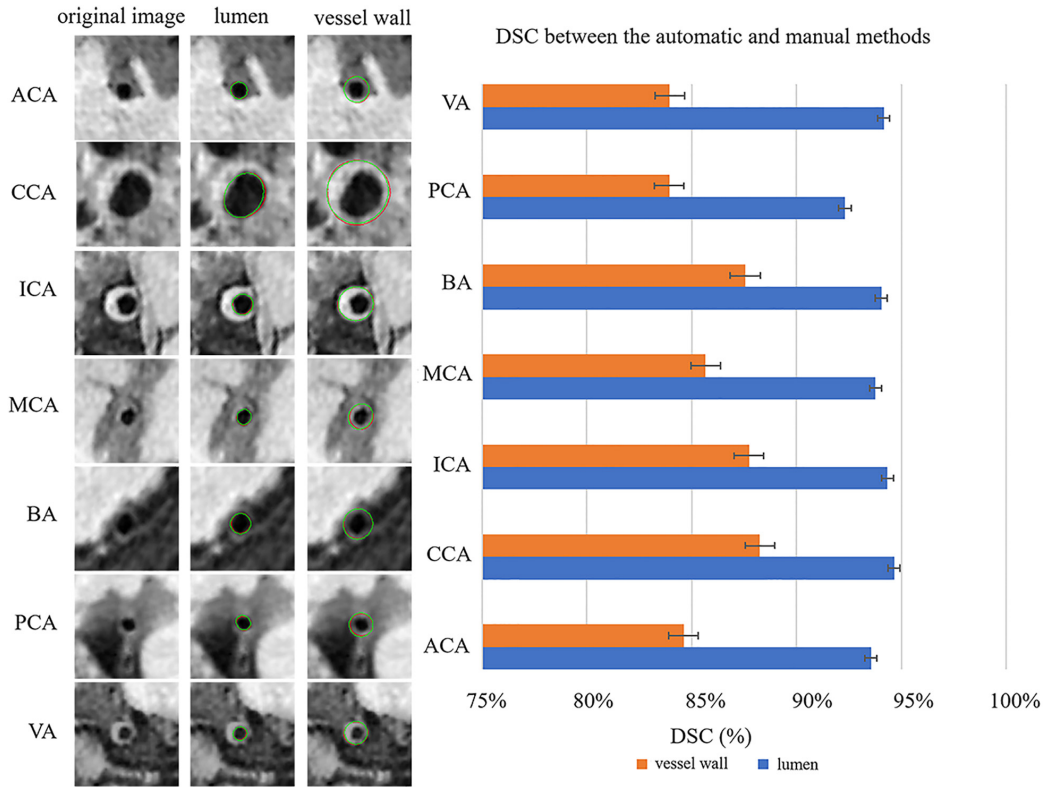

FIGURE 4 | Representative images and DSCs between the automatic and manual methods for the seven arterial segments. On the left, the first column represents the original cross-sectional slices reconstructed from MR vessel wall images; in the second column, the red contours represent the automatic segmentation results of the lumen, and the green contours represent the manual segmentation results of the lumen. In the third column, the red contour represents the automatically segmented results of the outer vessel wall, and the green contour represents the manual segmentation results of the outer vessel wall. The DSCs of the seven arterial segments are shown on the right using a bar plot.

automatic segmentation method for the estimation of arterial vessel wall morphological parameters, the lumen area, vessel wall area, mean wall thickness, and normalized wall index calculated using the automatic segmentation method were also compared with those calculated using the manual segmentation method.

Statistical analyses were performed using SPSS (version 19.0, NY, United States). The Bland–Altman, scatter plot, and intraclass correlation coefficient (ICC) were used to evaluate the agreement between the automatic and manual methods and between two manual reads for the lumen and vessel wall measurement. An ICC value of less than 0.4 was considered poor agreement, a value of 0.4–0.75 was considered good agreement, and a value of 0.75 or greater was considered excellent agreement.

RESULTS

The VWISegNet model converged after 5,000 iterations within 3 epochs. The plots of convergence for both training and validation data are shown in **Supplementary Figures 1**, **2**, respectively. The mean of DSC reached 93.8 ± 6.3% for lumen contours and 86.0 ± 9.0% for outer wall contours on the nine-subject test set. These DSC values were higher than those obtained from the traditional U-Net, Attention U-Net, and Inception U-Net. The segmentation results for lumen contours and vessel wall contours of different methods are summarized in **Table 1**. Representative results of the proposed VWISegNet, the traditional U-Net, Attention U-Net, and Inception U-Net on the segmentation of vessel wall are shown in **Figure 3**. The training convergence plot of U-Net, Attention U-Net, and Inception U-Net are shown in **Supplementary Figures 3–5**, respectively. The ASD of the proposed VWISegNet was 0.068 ± 0.016 and 0.095 ± 0.048 mm for the lumen and the outer wall contours, respectively. The DSC and ASD for the lumen and the vessel wall when comparing the automatic and manual methods on the nine-subject test set are summarized in **Table 2**. Compared with the Carotid Artery Vessel Wall Segmentation Challenge, VWISegNet achieved the better segmentation performance. The DSC and the difference in lumen area, outer wall area, and normalized wall index measured by VWISegNet and manual method were 78.1 ± 15.2%, 0.063 ± 0.134, 0.065 ± 0.106, and 0.067 ± 0.066, respectively. However, the champion group of the challenge achieved a lower

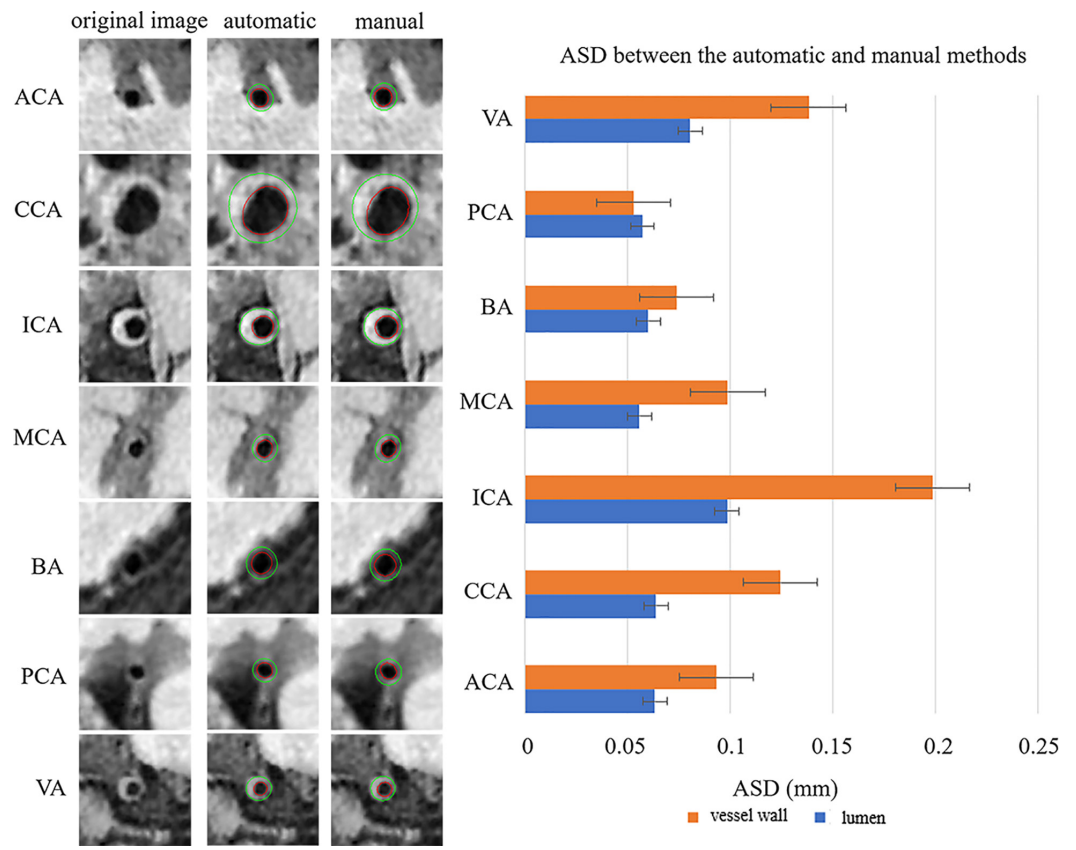

FIGURE 5 | Representative images and the ASDs between the automatic and manual methods for the seven arterial segments. On the left, the first column represents the original cross-sectional slices reconstructed from MR vessel wall images, the second column represents the automatically segmented lumen contour and outer vessel wall contour, and the third column represents the manual segmentation results of lumen and outer vessel wall contours of the seven arterial segments. The red contour represents the lumen, and the green contour represents the outer vessel wall. The ASDs of the seven arterial segments are shown on the right using a bar plot. The standard deviation (SD) represents the amount of dispersion of the variable and is calculated as the root square of the variance. ASD, average surface distance.

DSC of 77.5 ± 14.5%, and a larger difference in lumen area, outer wall area, and normalized wall index, which were 0.086 ± 0.256, 0.072 ± 0.159, and 0.080 ± 0.071, respectively. The VWISegNet achieved a Hausdorff distance of 0.321 ± 0.852, which was not good as that of 0.246 ± 0.443 achieved by champion group of the challenge.

Figure 4 shows the automatic segmentation DSC results of the lumen and outer vessel wall contours on seven arterial segments

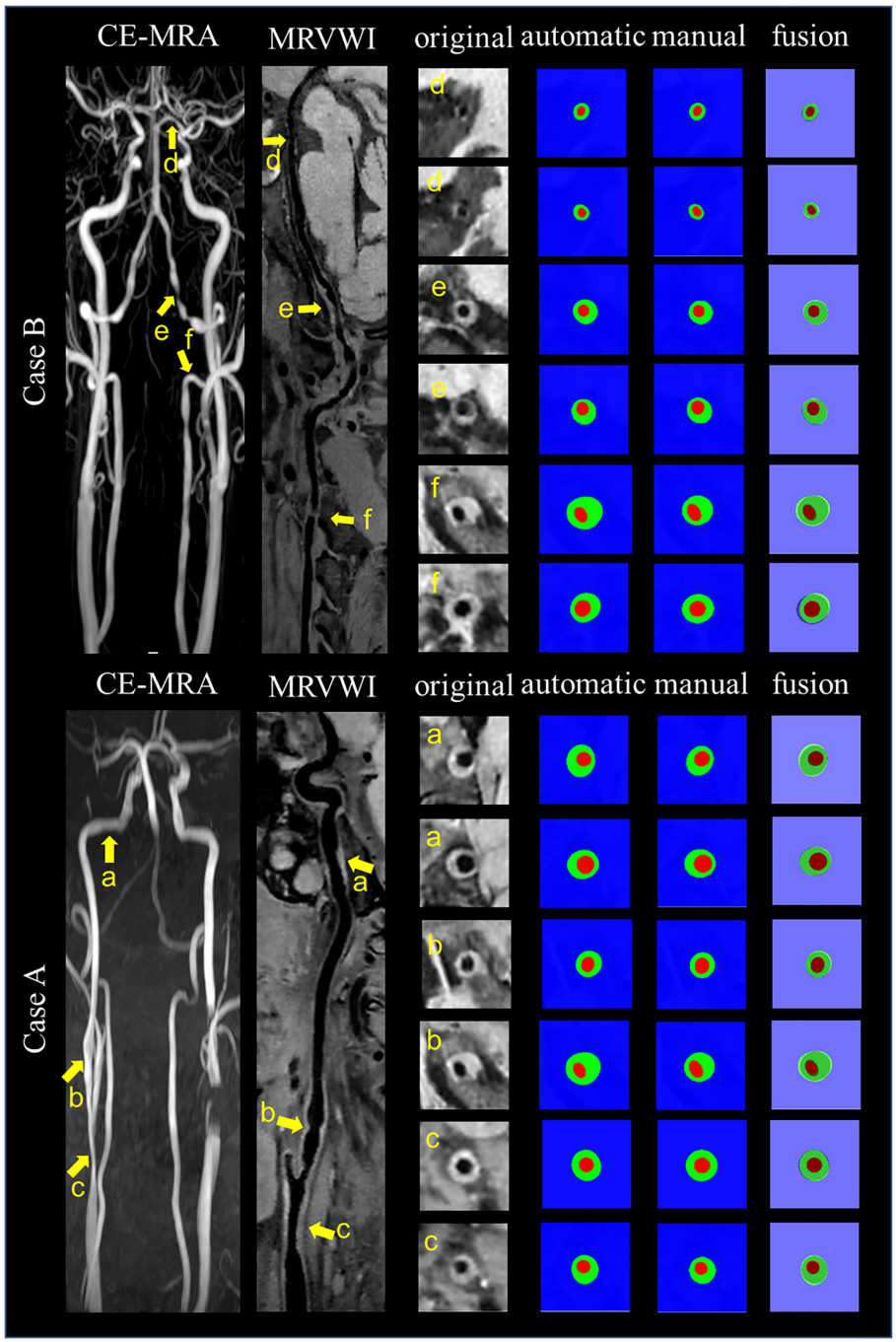

FIGURE 6 | Representative images and segmentation results from two clinical cases. Case A and Case B represent the images with anterior circulation and posterior circulation, respectively. Case A shows three stenoses at the right CCA to ICA (arrows a, b, and c on the CE-MRA image), corresponding plaques (arrows a, b, and c on the MR vessel wall image), original cross-sectional slices reconstructed from the plaques (a–c), the automatic and manual segmentation results for the plaques, and the segmentation results of fusion from left to right. Case B shows three stenoses at the left VA to PCA (arrows d, e, and f on CE-MRA image), corresponding plaques (arrows d, e, and f on MR vessel wall image), original cross-sectional slices reconstructed from the plaques (d–f), the automatic and manual segmentation results for the plaques, and the segmentation results of fusion from left to right.

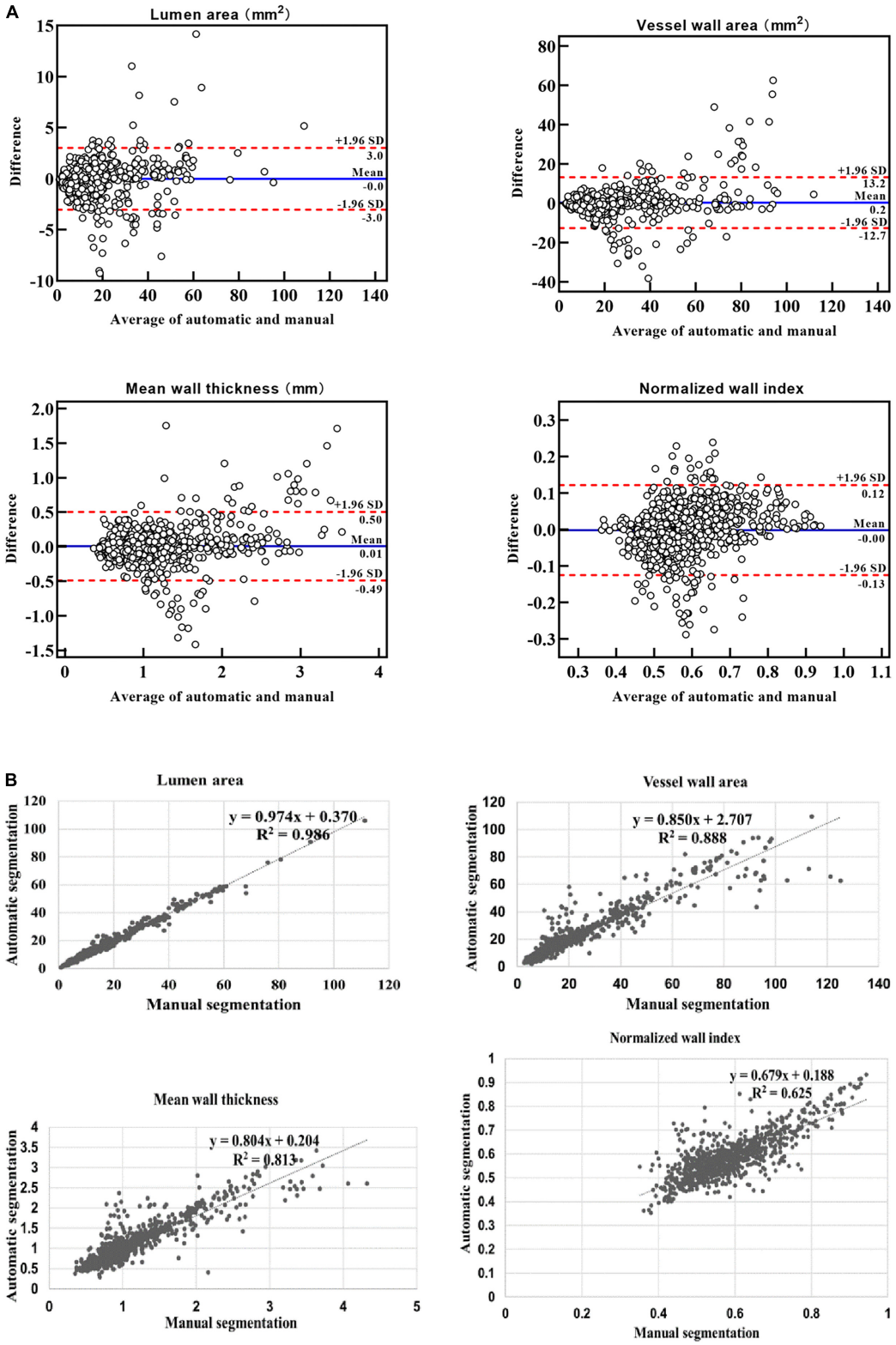

FIGURE 7 | Bland–Altman plots and scatter plots between the automatic method and manual method for the lumen area, wall area, mean wall thickness, and normalized wall index. In panel **(A)**, the blue lines indicate the mean difference, and the red line represents the 95% CI (computed through average difference ±1.96 SD of the difference). CI, confidence intervals; SD, standard deviation. In panel **(B)**, the *x*-axis shows the manual segmentation value. The *y*-axis represents the automatic segmentation value.

TABLE 3 | The agreement of lumen and vessel wall measurements (ICC values with 95% CI) between automatic and manual segmentation methods and between two manual reads.

	Lumen area (mm^2)	Vessel wall area (mm^2)	Mean wall thickness (mm)	Normalized wall index
ICC (GT1-X) (95% CI)	0.987 (0.985–0.989)	0.936 (0.928–0.943)	0.896 (0.883–0.907)	0.782 (0.756–0.805)
ICC (GT2-X) (95% CI)	0.988 (0.986–0.989)	0.951 (0.944–0.956)	0.907 (0.896–0.918)	0.797 (0.773–0.819)
ICC (GT1-GT2) (95% CI)	0.987 (0.985–0.988)	0.926 (0.916–0.934)	0.877 (0.862–0.891)	0.704 (0.671–0.734)

ICC, intraclass correlation coefficient; CI, confidence intervals; ICC (GT1-X), ICC analysis between first manual read and automatic read; ICC (GT2-X), ICC analysis between second manual read and automatic read; ICC (GT1–GT2), ICC analysis between two manual reads.

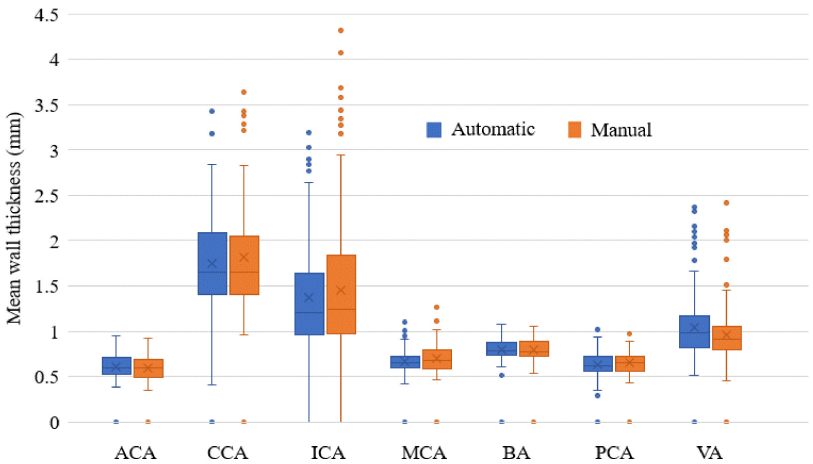

FIGURE 8 | The mean wall thickness of seven arterial segments. Boxplot shows the median with 25th and 75th percentiles. The "×" symbol points the mean and "o" shows the outliers.

and their manual segmentations for reference. All the DSC values were greater than 80%, especially for lumen contour detection, and the DSC values were all greater than 83.9%. The lowest DSC value for the lumen contour was 92.3% of the PCA, and the highest DSC value was 94.7% of the CCA. For the outer wall contour, the lowest and highest DSC values were 83.9% of the PCA and 88.3% of the CCA. In general, a DSC higher than 70.0% is a good segmentation result. **Figure 5** shows the automatic segmentation ASD results of the lumen and outer wall contours on seven arterial segments and their manual segmentations for reference. The lowest ASD value for the lumen contour was 0.056 of the MCA. For the outer wall contour, the lowest ASD was 0.053 for PCA. ICA had the highest values for both the lumen and outer wall among the seven segments. The DSC and ASD results indicated that the proposed automatic segmentation method was able to provide a reasonable segmentation result of lumen and outer wall contours. As shown in **Figure 6**, two representative segmentation results of plaques in the anterior circulation and posterior circulation show visually consistent delineation of the lumen and outer wall contours.

The Bland–Altman plots (Giavarina, 2015) for the lumen area, vessel wall area, mean wall thickness, and normalized wall index when comparing the proposed automatic segmentation method with the manual segmentation method are shown in **Figure 7A**. Random bias scattering patterns between the mean differences were observed. The mean differences between the two methods were −0.002 for the lumen area, 0.246 for the vessel wall area, 0.006 mm for the mean wall thickness, and −0.002 for the normalized wall area, which implied that there was a good agreement with a small bias between the two methods. **Figure 7B** shows the scatter plots for the four measurements between the automatic segmentation method and the manual segmentation method. The R^2 values of the lumen area, vessel wall area, mean wall thickness, and normalized wall index were 0.986, 0.888, 0.625, and 0.813, respectively.

In addition, the ICC values between the automatic and manual segmentation methods and between two manual reads for the four measurements are summarized in **Table 3**. The automatic segmentation method provided an excellent agreement with both manual methods in the measurement of lumen area, vessel wall area, mean wall thickness, and normalized wall index, with all ICC values greater than 0.780. For all the measurements, the ICC values between the automatic segmentation method and the manual method were greater than that between two manual reads. More specifically, the mean wall thickness of seven arterial segments was compared using a boxplot when comparing automatic and manual results. As shown in **Figure 8**, for each of the seven arterial segments, the mean value difference was not more than 0.100 mm between the automatic and manual segmentation methods.

DISCUSSION

A fast and accurate detection method of vessel wall and lumen contours is useful for clinically efficient and accurate quantitative

assessment of plaques, which is essential for evaluating plaque progression and treatment effects. In this study, an automatic segmentation approach using a CNN-based deep learning technique was proposed to segment the contour of the vessel wall and lumen on MRVWI images and achieved good-to-excellent agreement with the manual method. With this proposed method, automatic segmentation of the main arterial segments of intracranial and carotid arteries of one subject can be completed in a few minutes. With this potential advancement, it is likely to be used for rapid and accurate quantitative assessment of plaques during MRI scans, thereby assisting in identifying plaques and patients at risk of stroke.

The proposed fully automatic segmentation method achieved DSC larger than 80.0 and 90.0% for the segmentation of outer wall contour and lumen contour, respectively. In particular, the DSC result of the CCA was the best, reaching more than 94.7 and 88.3% for the lumen and the outer wall contours, respectively. The reason may be that CCA is larger than other carotid or intracranial arterial segments—the average diameter of the CCA lumen is 6–7 mm. Therefore, the higher signal-to-noise ratio and contrast-to-noise ratio of the CCA vessel wall facilitate segmentation of the lumen and vessel wall. Compared to previous study with DSC achieved of 88.9 and 76.7% for lumen and vessel wall, respectively (Shi et al., 2019), our automatic segmentation method showed comparatively a better agreement with the manual method. This could be explained by the fact that more training and validation samples and a network structure with more residual units were used in this study. Compared with previous studies for carotid artery segmentation (Chen et al., 2019; Samber et al., 2020), our results are close to but lower than these segmentation results. In addition, the Hausdorff distance of the VWISegNet was not good as the champion group of the Carotid Artery Vessel Wall Segmentation Challenge. The reason maybe that these studies were all only based on carotid artery segmentation, whereas our study is based on the segmentation of both intracranial and carotid arteries. The larger size of carotid artery than intracranial artery was more conducive to segmentation.

All the ASD values are less than 0.198 mm, which also exhibited the good segmentation consistency of the proposed automatic segmentation method with the manual method. And our results are also significantly lower than the previous study by Zhu et al. (2021), which achieved ASD values of 0.682 and 0.960 mm for lumen and vessel wall segmentation, respectively. Generally, a larger DSC value corresponds to a smaller ASD value. Although CCA has the largest DSC values for both the lumen and vessel wall, in our study, the smallest ASD value was found in MCA for the lumen and PCA for the vessel wall. It is supposed that the large contour size of CCA may have caused a larger error, with the MCA and PCA being relatively smaller segments. ICA has the highest ASD value for both the lumen and outer wall among the seven segments, possibly because ICA has the highest probability of plaques, and the highest number of plaques results in poor image quality. Therefore, a larger error result in the highest ASD value of ICA. If the point on the automatic segmentation boundary is overlapped with the corresponding point on the ground-truth boundary, the distance is 0. If the corresponding points on the two boundaries are not overlapped, the distance is a multiple of the interpolation resolution 0.075 mm. Therefore, the average of all the distances may be less than 0.075 mm. The lower value of ASD, the more similar between the automatic segmentation result and the manual result.

In addition, the Bland–Altman plots and scatter plots of lumen area, vessel wall area, mean wall thickness, and normalized wall index also showed a good agreement between the automatic and manual methods. However, the outliers in the Bland–Altman plots indicated that for some small arterial segments (such as the MCA) and some arterial segments with a low contrast-to-noise ratio between the vessel wall and surrounding tissues, the error between automatic segmentation and manual segmentation was relatively larger. For the ICC analysis, ICC values between the automatic segmentation method and each manual method were greater than that between two manual reads. This suggested that the proposed automatic method could not only replace manual method to reduce the workload of the radiologist and increase the convenience but also improved the accuracy of the segmentation results.

Comparing with U-Net, the proposed VWISegNet demonstrated higher DSC for both lumen and vessel wall segmentation and hence the better segmentation performance. This maybe benefit from the more residual units of VWISegNet, which can better extract image features and achieve faster convergence.

There are several potential limitations of this study. First, the sample size of data with plaques is relatively small for deep learning-based segmentation. However, the segmentation of normal arterial vessel walls is the basis for plaque segmentation and recognition. Second, although the dataset was collected from three different centers, they were all acquired with the same protocol. The dataset acquired from different MRI systems is warranted to train a segmentation model in the next work to ensure that the model can be performed on a more diverse multicenter dataset. Third, this study is based on 2D segmentation of what is inherently a 3D problem. The 2D slices are needed to be reconstructed from the acquired 3D MRVW images, and then the segmentation is performed on the 2D slices. In addition, the proposed segmentation method is aimed at the situation where there is only one artery in the 2D slice. However, there may be many different arteries on the 2D slice. It is believed that incorporating 3D context information into the model will make it possible to distinguish different blood vessels and improve the segmentation results. Finally, in the future work, the computer-aided detection (CADe) system for MRVW images is expected to do the detection and segmentation at the same time.

CONCLUSION

In conclusion, the proposed deep learning-based high-performing, automatic segmentation method has achieved good consistency with manual methods in terms of arterial morphologic measurements and is even more accurate than

manual results, which could potentially be useful for monitoring plaque progression and clinical treatment effects.

DATA AVAILABILITY STATEMENT

All data generated or analyzed during this study are included in this published article and its **Supplementary Material**.

ETHICS STATEMENT

The studies involving human participants were reviewed and approved by the Shenzhen Institutes of Advanced Technology, Chinese Academy of Sciences, Shenzhen, China. The patients/participants provided their written informed consent to participate in this study.

AUTHOR CONTRIBUTIONS

WX: data acquisition, analysis, training model, interpretation, and drafted the manuscript. XY: data acquisition, analysis, training model, and interpretation. YIL, GJ, SJ, and ZG: data acquisition and analysis. YM, SZ, YT, and JZ: statistical analysis and interpretation of data. QH, LW, and DL: study design, data interpretation, and revise the manuscript. YEL, ZH, HZ, and XL: conception and design of the study. NZ: study design, provided supervision, and critical review of the manuscript. All authors read and approved the final manuscript.

FUNDING

This study was partially supported by the National Natural Science Foundation of China (81830056), the Key Laboratory for Magnetic Resonance and Multimodality Imaging of Guangdong Province (2020B1212060051), the Shenzhen Basic Research Program (JCYJ20180302145700745 and KCXFZ202002011010360), and the Guangdong Innovation Platform of Translational Research for Cerebrovascular Diseases.

ACKNOWLEDGMENTS

We thank Laura G. Smith and Gill Edward for their help in conducting the imaging experiments.

SUPPLEMENTARY MATERIAL

The Supplementary Material for this article can be found online at: https://www.frontiersin.org/articles/10.3389/fnins.2022.888814/full#supplementary-material

Supplementary Figure 1 | The plot of convergence for training data.

Supplementary Figure 2 | The plot of convergence for validation data.

Supplementary Figure 3 | The training convergence plot of U-Net.

Supplementary Figure 4 | The training convergence plot of Attention U-Net.

Supplementary Figure 5 | The training convergence plot of Inception U-Net.

REFERENCES

Adams, G. J., Greene, J., Vick, G. W., Harrist, D., Kimball, K. T., Karmonik, C., et al. (2004). Tracking regression and progression of atherosclerosis in human carotid arteries using high-resolution magnetic resonance imaging. *Magnet. Resonan. Imaging* 22, 1249–1258. doi: 10.1016/j.mri.2004.08.020

Anwar, S. M., Majid, M., Qayyum, A., Awais, M., Alnowami, M., and Khan, M. K. (2018). Medical image analysis using convolutional neural networks: a review. *J. Med. Syst.* 42:226. doi: 10.1007/s10916-018-1088-1

Bertels, J., Eelbode, T., Berman, M., Vandermeulen, D., Maes, F., Bisschops, R., et al. (2019). Optimizing the dice score and jaccard index for medical image segmentation: theory and practice. *Med. Image Comput. Comp. Assisted Intervent. Miccai 2019 Pt II* 11765, 92–100.

Burtea, C., Ballet, S., Laurent, S., Rousseaux, O., Dencausse, A., Gonzalez, W., et al. (2012). Development of a magnetic resonance imaging protocol for the characterization of atherosclerotic plaque by using vascular cell adhesion molecule-1 and apoptosis-targeted ultrasmall superparamagnetic iron oxide derivatives. *Arterioscleros. Thromb. Vascul. Biol.* 32, E103–E103. doi: 10.1161/ATVBAHA.112.245415

Chen, L., Sun, J., Canton, G., Balu, N., Zhao, X., Li, R., et al. (2019). Automated artery localization and vessel wall segmentation of magnetic resonance vessel wall images using tracklet refinement and polar conversion. *IEEE Access.* 8, 217603–217614. doi: 10.1109/access.2020.3040616

Dieleman, N., Van Der Kolk, A. G., Zwanenburg, J. J. M., Harteveld, A. A., Biessels, G. J., Luijten, P. R., et al. (2014). Imaging intracranial vessel wall pathology with magnetic resonance imaging current prospects and future directions. *Circulation* 130, 192–201. doi: 10.1161/CIRCULATIONAHA.113.006919

Dutta, P., Upadhyay, P., De, M., Khalkar, R. G., Medical Image, Analysis Using, et al. (2020). *International Conference on Inventive Computation Technologies (ICICT), 2020*. San Jose, CA: ICICT.

Eelbode, T., Bertels, J., Berman, M., Vandermeulen, D., Maes, F., Bisschops, R., et al. (2020). Optimization for medical image segmentation: theory and practice when evaluating with dice score or jaccard index. *IEEE Transact. Med. Imaging* 39, 3679–3690. doi: 10.1109/TMI.2020.3002417

Frank, H. (2001). Characterization of atherosclerotic plaque by magnetic resonance imaging. *Am. Heart J.* 141, S45–S48.

Giavarina, D. (2015). Understanding bland altman analysis. *Biochem. Med.* 25, 141–151. doi: 10.11613/BM.2015.015

Jodas, D. S., Pereira, A. S., and Tavares, J. M. R. S. (2018). Automatic segmentation of the lumen in magnetic resonance images of the carotid artery. *Vipimage* 2017, 92–101. doi: 10.1007/978-3-319-68195-5_10

Ladak, H. M., Milner, J. S., and Steinman, D. A. (1999). *Rapid 3d Segmentation of the Carotid Bifurcation from Serial Mr Images*. London: The John P. Robarts Research Institute.

Loewe, C., Oberhuber, G., Loewe, R., and Frank, H. (1998). Delineation and characterization of atherosclerotic plaque lesions by magnetic resonance imaging. *Zeitschrift Fur Kardiol.* 87, 622–629.

Maier, A., Syben, C., Lasser, T., and Riess, C. (2019). A gentle introduction to deep learning in medical image processing. *Zeitschrift für Medizinische Physik* 29, 86–101. doi: 10.1016/j.zemedi.2018.12.003

Mandell, D. M., Mossa-Basha, M., Qiao, Y., Hess, C. P., Hui, F., Matouk, C., et al. (2017). Intracranial vessel wall mri: principles and expert consensus recommendations of the american society of neuroradiology. *Am. J. Neuroradiol.* 38, 218–229. doi: 10.3174/ajnr.A4893

Minarro-Gimenez, J. A., Martinez-Costa, C., Karlsson, D., Schulz, S., and Goeg, K. R. (2018). Qualitative analysis of manual annotations of clinical text with snomed Ct. *PLoS One* 13:209547. doi: 10.1371/journal.pone.0209547

Ohsaka, A. (2020). Artificial intelligence (Ai) and hematological diseases: establishment of a peripheral blood convolutional neural network (Cnn)-based

digital morphology analysis system. *[Rinshô ketsueki]. Jap. J. Clin. Hematol.* 61, 564–569.

Qiao, Y., Steinman, D. A., Qin, Q., Etesami, M., Schar, M., Astor, B. C., et al. (2011). Intracranial arterial wall imaging using three-dimensional high isotropic resolution black blood Mri at 3.0 tesla. *J. Magnet. Resonan. Imaging* 34, 22–30. doi: 10.1002/jmri.22592

Ronneberger, O., Fischer, P., and Brox, T. (2015). U-Net: convolutional networks for biomedical image segmentation. *Med. Image Comput. Comput. Assisted Intervent. Pt III* 9351, 234–241. doi: 10.1007/978-3-319-24574-4_28

Saba, L., Yuan, C., Hatsukami, T. S., Balu, N., Qiao, Y., Demarco, J. K., et al. (2018). Carotid artery wall imaging: perspective and guidelines from the asnr vessel wall imaging study group and expert consensus recommendations of the american society of neuroradiology. *Am. J. Neuroradiol.* 39, E9–E31. doi: 10.3174/ajnr.A5488

Sakellarios, A. I., Stefanou, K., Siogkas, P., Tsakanikas, V. D., Bourantas, C. V., Athanasiou, L., et al. (2012). Novel methodology for 3d reconstruction of carotid arteries and plaque characterization based upon magnetic resonance imaging carotid angiography data. *Magnet. Resonan. Imaging* 30, 1068–1082. doi: 10.1016/j.mri.2012.03.004

Samber, D. D., Ramachandran, S., Sahota, A., Naidu, S., Pruzan, A., Fayad, Z. A., et al. (2020). Segmentation of carotid arterial walls using neural networks. *World J. Radiol.* 12, 1–9. doi: 10.4329/wjr.v12.i1.1

Shi, F., Yang, Q., Guo, X., Qureshi, T. A., Tian, Z., Miao, H., et al. (2019). Intracranial vessel wall segmentation using convolutional neural networks. *IEEE Transact. Biomed. Enginee.* 66, 2840–2847. doi: 10.1109/TBME.2019.2896972

Taghanaki, S. A., Abhishek, K., Cohen, J. P., Cohen-Adad, J., and Hamarneh, G. (2021). Deep semantic segmentation of natural and medical images: a review. *Artific. Intellig. Rev.* 54, 137–178. doi: 10.1007/s10462-020-09854-1

Tsakanikas, V. D., Siogkas, P. K., Mantzaris, M. D., Potsika, V. T., Kigka, V. I., Exarchos, T. P., et al. (2020). A deep learning oriented method for automated 3d reconstruction of carotid arterial trees from Mr imaging. *Annu. Int. Conf. IEEE Eng. Med. Biol. Soc.* 2020, 2408–2411. doi: 10.1109/EMBC44109.2020.9176532

Yamashita, R., Nishio, M., Do, R. K. G., and Togashi, K. (2018). Convolutional neural networks: an overview and application in radiology. *Insights Imaging* 9, 611–629. doi: 10.1007/s13244-018-0639-9

Zhang, N., Zhang, F., Deng, Z., Yang, Q., Diniz, M. A., Song, S. S., et al. (2018). 3d whole-brain vessel wall cardiovascular magnetic resonance imaging: a study on the reliability in the quantification of intracranial vessel dimensions. *J. Cardiovasc. Magn. Reson.* 20:39. doi: 10.1186/s12968-018-0453-z

Zhu, C., Wang, X., Teng, Z., Chen, S., Huang, X., Xia, M., et al. (2021). Cascaded residual U-net for fully automatic segmentation of 3d carotid artery in high-resolution multi-contrast Mr images. *Phys. Med. Biol.* 66:045033. doi: 10.1088/1361-6560/abd4bb

Conflict of Interest: XY, ZG, YM, SZ, YT, JZ, and QH were employed by United Imaging Healthcare Co., Ltd.

The remaining authors declare that the research was conducted in the absence of any commercial or financial relationships that could be construed as a potential conflict of interest.

Frontiers in Neuroscience

Provides a holistic understanding of brain function from genes to behavior

Part of the most cited neuroscience journal series which explores the brain - from the new eras of causation and anatomical neurosciences to neuroeconomics and neuroenergetics.

Discover the latest Research Topics

See more →

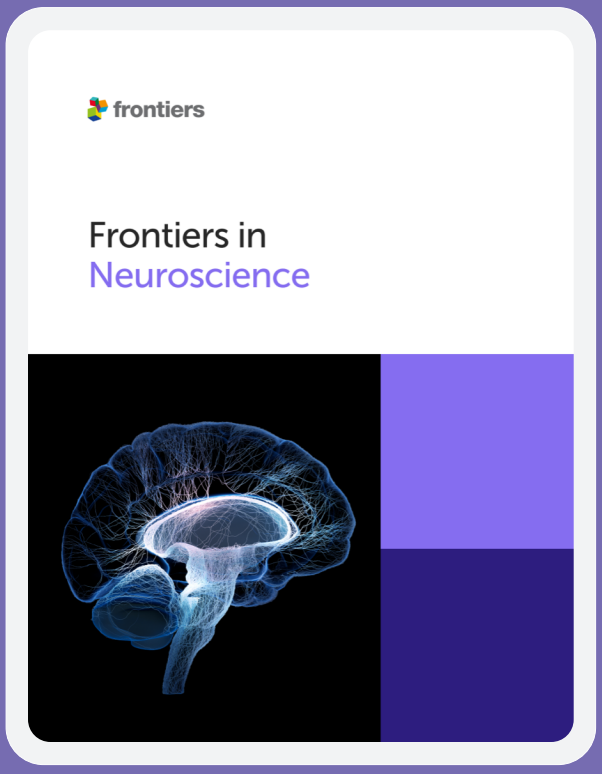

Frontiers

Avenue du Tribunal-Fédéral 34
1005 Lausanne, Switzerland
frontiersin.org

Contact us

+41 (0)21 510 17 00
frontiersin.org/about/contact